



Second United States Microgravity Laboratory: One Year Report, Volume 1

M. Vlasse, Editor

Marshall Space Flight Center, Marshall Space Flight Center, Alabama

D. McCauley, Editor

University of Alabama in Huntsville, Huntsville, Alabama

C. Walker, Editor

Universities Space Research Association, Huntsville, Alabama

The NASA STI Program Office...in Profile

Since its founding, NASA has been dedicated to the advancement of aeronautics and space science. The NASA Scientific and Technical Information (STI) Program Office plays a key part in helping NASA maintain this important role.

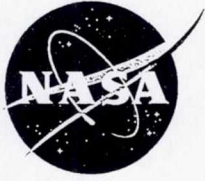
The NASA STI Program Office is operated by Langley Research Center, the lead center for NASA's scientific and technical information. The NASA STI Program Office provides access to the NASA STI Database, the largest collection of aeronautical and space science STI in the world. The Program Office is also NASA's institutional mechanism for disseminating the results of its research and development activities. These results are published by NASA in the NASA STI Report Series, which includes the following report types:

- **TECHNICAL PUBLICATION.** Reports of completed research or a major significant phase of research that present the results of NASA programs and include extensive data or theoretical analysis. Includes compilations of significant scientific and technical data and information deemed to be of continuing reference value. NASA's counterpart of peer-reviewed formal professional papers but has less stringent limitations on manuscript length and extent of graphic presentations.
- **TECHNICAL MEMORANDUM.** Scientific and technical findings that are preliminary or of specialized interest, e.g., quick release reports, working papers, and bibliographies that contain minimal annotation. Does not contain extensive analysis.
- **CONTRACTOR REPORT.** Scientific and technical findings by NASA-sponsored contractors and grantees.
- **CONFERENCE PUBLICATION.** Collected papers from scientific and technical conferences, symposia, seminars, or other meetings sponsored or cosponsored by NASA.
- **SPECIAL PUBLICATION.** Scientific, technical, or historical information from NASA programs, projects, and mission, often concerned with subjects having substantial public interest.
- **TECHNICAL TRANSLATION.** English-language translations of foreign scientific and technical material pertinent to NASA's mission.

Specialized services that complement the STI Program Office's diverse offerings include creating custom thesauri, building customized databases, organizing and publishing research results...even providing videos.

For more information about the NASA STI Program Office, see the following:

- Access the NASA STI Program Home Page at <http://www.sti.nasa.gov>
- E-mail your question via the Internet to help@sti.nasa.gov
- Fax your question to the NASA Access Help Desk at (301) 621-0134
- Telephone the NASA Access Help Desk at (301) 621-0390
- Write to:
NASA Access Help Desk
NASA Center for AeroSpace Information
800 Elkridge Landing Road
Linthicum Heights, MD 21090-2934



Second United States Microgravity Laboratory: One Year Report, Volume 1

M. Vlasse, Editor

Marshall Space Flight Center, Marshall Space Flight Center, Alabama

D. McCauley, Editor

University of Alabama in Huntsville, Huntsville, Alabama

C. Walker, Editor

Universities Space Research Association, Huntsville, Alabama

National Aeronautics and
Space Administration

Marshall Space Flight Center

Acknowledgments

The untiring efforts and dedication of the STS-73 payload and orbiter crews, mission and program managers, and mission operations personnel were critical to the completion of the mission's objectives and are sincerely appreciated. The editors wish to thank the Office of Life and Microgravity Science and Applications (OLMSA) and the Microgravity Research Division (MRD) at NASA Headquarters for their support and encouragement. The editors also wish to thank the NASA Marshall Space Flight Center's Public Affairs Office for their help in publicizing the results of the USML-2 mission, as well as all of the investigators for contributing to this document.

Marcus Vlasse
NASA Marshall Space Flight Center
USML-2 Mission Scientist

Mark Lee
NASA Headquarters
USML-2 Program Scientist

Compilers and editors—

Dannah McCauley, University of Alabama in Huntsville/NASA MSFC
Charles Walker, Universities Space Research Association/NASA MSFC

Available from:

NASA Center for AeroSpace Information
800 Elkridge Landing Road
Linthicum Heights, MD 21090-2934
(301) 621-0390

National Technical Information Service
5285 Port Royal Road
Springfield, VA 22161
(703) 487-4650

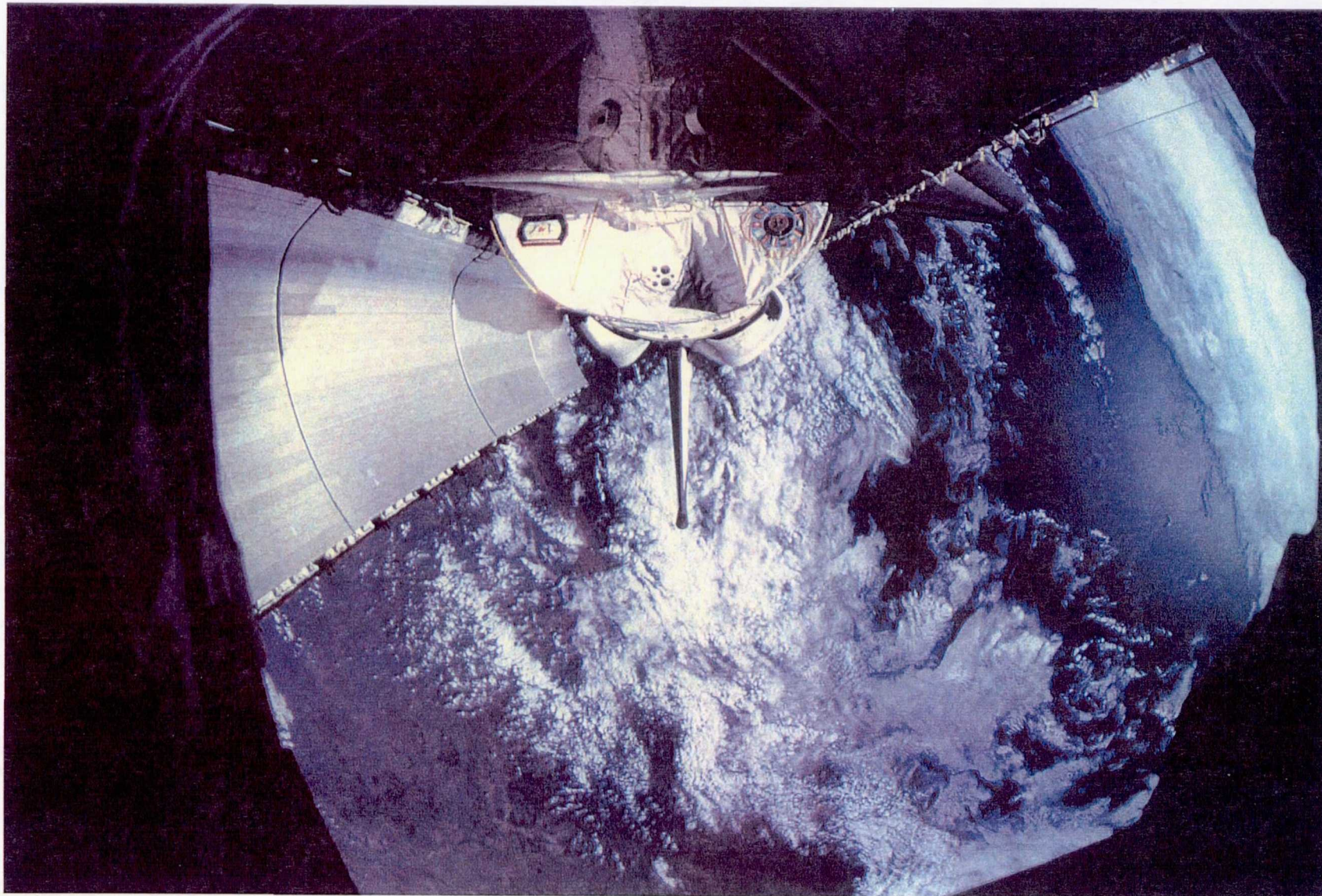


Figure 1. USML-2 payload bay view from Shuttle window.



Figure 2. USML-2 payload crewmembers; red team: Albert Sacco and Kathryn Thornton, blue team: Catherine Coleman and Fred Leslie.

TABLE OF CONTENTS

TABLE OF CONTENTS	v
LIST OF FIGURES	vii
LIST OF TABLES	xxiii
AUTHORS INDEX	xxv
ACRONYMS	xxviii
KEY WORD INDEX	xxxii
MISSION INFORMATION	xliv
INTRODUCTION	xlvi
USML-2 EXPERIMENTS	
EXPERIMENT I: Orbital Processing of High-Quality Zn-Alloyed CdTe Compound Semiconductors David J. Larson	1-1
EXPERIMENT II: Vapor Transport Crystal Growth of Mercury Cadmium Telluride in Microgravity—USML-2 Heribert Wiedemeier	2-17
EXPERIMENT III: Zeolite Crystal Growth in Microgravity—The USML-2 Mission Albert Sacco, Jr.	3-35
EXPERIMENT IV: USML-2 Drop Dynamics Experiment Taylor G. Wang	4-61
EXPERIMENT V: Science and Technology of Surface Controlled Oscillations: Report on USML-2 Results Robert E. Apfel	5-137
EXPERIMENT VI: Surface Tension Driven Convection Experiment-2 (STDCE-2) Simon X. Ostrach	6-147
EXPERIMENT VII: The Geophysical Fluid Flow Cell Experiment on USML-2 John E. Hart	7-185
EXPERIMENT VIII: Environmental Conditions in the Astroculture™ Plant Chamber During the USML-2 Mission Raymond J. Bula	8-209

EXPERIMENT IX: Astroculture: Growth and Starch Accumulation of Potato Tuber	9-219
Theodore W. Tibbitts	
EXPERIMENT X: USML-2/STS-73 One-Year Post-Flight Summary of the Commercial Generic Bioprocessing Apparatus (CGBA) Payload	10-229
Louis Stodieck	
EXPERIMENT XI: Protein Crystal Growth in Microgravity: PCAM and DCAM	11-261
Daniel C. Carter	
EXPERIMENT XII: Commercial Protein Crystal Growth Glovebox and Middeck Experiments	12-279
Lawrence J. DeLucas	
EXPERIMENT XIII: The Study of Dopant Segregation Behavior During the Growth of GaAs in Microgravity on USML-2	13-293
David H. Matthiesen	
EXPERIMENT XIV: Directional Solidification of Gallium-Doped Germanium in Crystal Growth Furnace (CGF) on USML-2	14-337
Manfred Lichtensteiger	

LIST OF FIGURES

Figure	Title	Page
Figure 1.	USML-2 payload bay view from Shuttle window.	iii
Figure 2.	USML-2 payload crewmembers; red team: Albert Sacco and Kathryn Thornton, blue team: Catherine Coleman and Fred Leslie.	iv
 EXPERIMENT I:		
Figure 1.	USML-2 Ampoule configurations: (a) cylindrical with liquid constraint; and (b) tapered to maximize growth without wall contact.	1-10
Figure 2.	Typical temperature/time/position of the optimized USML-2 primary flight ex- periment.	1-11
Figure 3.	USML-2 tapered sample configuration after crystal growth: (a) unit gravity; and (b) microgravity.	1-12
Figure 4.	USML-2 SWBT of the tapered microgravity sample surface showing the absence of twins in the region solidified without wall contact and the reappearance of twinning as wall contact is reestablished.	1-13
Figure 5	Typical {111} facet at bubble surface on surface of USML-2 cylindrical microgravity sample.	1-14
Figure 6.	Transmission SMT showing dislocation structure within USML-1 microgravity sample.	1-15
Figure 7.	Defect structures typical of USML-1 unit gravity: (a) and microgravity; and (b) samples (original magnification $\times 200$).	1-16
Figure 8.	X-ray triple crystal spectrograph of USML-1 flight sample showing low lattice strain and low mechanical strain in the microgravity sample.	1-16
 EXPERIMENT II:		
Figure 1.	Optical photomicrographs of $\text{Hg}_{1-x}\text{Cd}_x\text{Te}$ epitaxial layers as-grown at 545°C on (100) oriented CdTe substrates under reduced (a) and normal (b) gravity condi- tions after 2.5-hour growth time (at a magnification of $\times 200$).	2-30
Figure 2.	Optical photomicrographs of chemically etched $\text{Hg}_{1-x}\text{Cd}_x\text{Te}$ epitaxial layers as- grown at 545°C on (100) oriented CdTe substrates under reduced (a) and normal (b) gravity conditions after 2.5-hour growth time (at a magnification of $\times 500$).	2-30

Figure 3.	Optical photomicrographs of $\text{Hg}_{1-x}\text{Cd}_x\text{Te}$ epitaxial islands as-grown at 545 °C on (100) oriented CdTe substrates under reduced (a) and normal (b) gravity conditions after 1.5-hour growth time (at a magnification of $\times 200$).	2-31
Figure 4.	Optical photomicrographs of chemically etched surfaces of $\text{Hg}_{1-x}\text{Cd}_x\text{Te}$ epitaxial islands as-grown at 545 °C on (100) oriented CdTe substrates under reduced (a) and normal (b) gravity conditions after 1.5-hour growth time (at a magnification of $\times 500$).	2-31
Figure 5.	Composition profiles of the constituent elements normal to the surface of a $\text{Hg}_{1-x}\text{Cd}_x\text{Te}$ epitaxial layer as-grown on a (100) CdTe substrate at 545 °C under reduced gravity conditions after 2.5-hour growth time.	2-32
Figure 6.	Spatial composition maps of the as-grown $\text{Hg}_{1-x}\text{Cd}_x\text{Te}$ epitaxial layers grown on (100) CdTe substrates at 545 °C under reduced (flight) gravity and normal (ground test) conditions. The numbers represent the x-values.	2-33
Figure 7.	Optical photomicrographs of the (011) cross sections of $\text{Hg}_{1-x}\text{Cd}_x\text{Te}/(100)$ CdTe epilayer-substrate structures grown at 545 °C under reduced (a) and normal (b) gravity conditions (2.5-hour growth time). The arrow marks the growth interface. The thinner layer below the interface is the interdiffusion zone into the CdTe substrate (dark area). The epitaxial layer is the light-shaded area above the growth interface (at a magnification of $\times 1,000$).	2-34
Figure 8.	Optical photomicrographs of the (011) cross sections of the $\text{Hg}_{1-x}\text{Cd}_x\text{Te}/(100)$ CdTe epilayer-substrate structures grown at 545 °C under reduced (a) and normal (b) gravity conditions (1.5-hour growth time). The arrow marks the growth interface. The thinner layer below the growth interface is the interdiffusion zone into the CdTe substrate (dark area) (at a magnification of $\times 1,000$).	2-34

EXPERIMENT III:

Figure 1.	SEM pictures of zeolite A using TEA as a nucleation control agent.	3-45
Figure 2.	PSDs of zeolite A illustrated in figure 1.	3-45
Figure 3.	Improvements from space research—zeolite A.	3-46
Figure 4.	Particle size distributions of commercial, USML-1, and USML-2 zeolite A crystals.	3-47
Figure 5.	SEM pictures of zeolite A with BIS indicating unreacted gel.	3-47
Figure 6.	PSDs of zeolite A illustrated in figure 5.	3-48

Figure 7.	SEM pictures of zeolite X using TEA as a nucleation control agent.	3-48
Figure 8.	PSDs of zeolite X illustrated in figure 7.	3-49
Figure 9.	SEM pictures of zeolite X using TEA—different formulation.	3-49
Figure 10.	PSDs of zeolite X illustrated in figure 9.	3-50
Figure 11.	Improvements from space research—zeolite X.	3-51
Figure 12.	Particle size distributions of commercial, USML-1, and USML-2 zeolite X crystals.	3-52
Figure 13.	SEM pictures of zeolite X using TEA—different formulation.	3-52
Figure 14.	PSDs of zeolite X illustrated in figure 13.	3-53
Figure 15.	Si/Al ratio by microprobe analysis of zeolite X.	3-53
Figure 16.	Cross sections used in microprobe analysis.	3-54
Figure 17.	SEM pictures of Silicalite from untreated silica gel.	3-54
Figure 18.	PSDs of Silicalite illustrated in figure 17.	3-55
Figure 19.	SEM pictures of Silicalite from heat treated silica gel.	3-55
Figure 20.	PSDs of Silicalite illustrated in figure 19.	3-56
Figure 21.	Teflon™ liners of flight (F7B) and terrestrial (T7B) autoclaves for Silicalite synthesis from heat treated silica gel.	3-56
Figure 22.	SEM pictures of zeolite Beta from silica gel.	3-57
Figure 23.	PSDs of zeolite Beta illustrated in figure 22.	3-57
Figure 24.	TEM pictures of zeolite Beta from silica gel.	3-58
Figure 25.	FTIR analysis of zeolite Beta from silica gel.	3-58
Figure 26.	SEM pictures of zeolite A grown in clear glovebox autoclaves.	3-59
Figure 27.	PSDs of zeolite A illustrated in figure 26.	3-59

EXPERIMENT IV:

Figure 1.	Image Analysis Flow Diagram.	4-100
Figure 2.	A video frame of a drop with a flare at the upper left-hand corner that seriously distorts the drop boundary.	4-101
Figure 3.	The video frame of figure 2 as interpreted by the algorithm. The flare was mistaken as part of the true boundary.	4-102
Figure 4.	Surface deformation results from an unfiltered data set subjected to automated processing.	4-103
Figure 5.	Drop volume for both filtered and unfiltered data sets.	4-104
Figure 6.	Video frame of a drop, corresponding to figure 4 data, that has been filtered.	4-105
Figure 7.	Surface deformation vs. time plot for data, corresponding to figure 4, that has been filtered. Both modes 2 and 4 legendre time series show definite improvement.	4-106
Figure 8.	Surface deformation vs. time plot results from filtered data set using higher frequency components of these data. Both mode 2 and mode 4 oscillations show improvement.	4-107
Figure 9.	R^* versus Ω^* for 100 cSt drops from Session 1. The solid curve is from Brown and Scriven (1980), in which the lower part corresponds to an axisymmetric drop before bifurcation, and the upper part corresponds to the same drop adopting a two-lobed equilibrium shape after bifurcation. The data points on the right correspond to a two-lobed bifurcation perturbed by acoustic flattening. The datapoints on the left represent loss of axisymmetric equilibrium under the influence of rotation. The dashed lines represent the theories in the present work.	4-108
Figure 10.	R^* versus Ω^* for 350 cSt drops from Session 2. The description is similar to that for figure 9.	4-109
Figure 11.	R^* versus Ω^* for 1000 cSt drops from session 3. The 102-percent flattening drop tries, but fails, to bifurcate at $\Omega^* = 0.25$, retains its axisymmetric shape, picks up more angular velocity, and finally loses axisymmetric equilibrium at $\sim \Omega^* = 0.32$. The other drops all bifurcate.	4-110

Figure 12.	Critical rotation rate versus flattening. The drop sizes can be considered to be asymptotically small, acoustically speaking. The cluster on the left end represents two-lobed bifurcation perturbed by flattening. The other data points to the right represent axisymmetric loss of equilibrium under the influence of rotation. The 102-percent drop in figure 11 is highlighted here by an arrow. The dashed lines represent the theories in the present work.	4-111
Figure 13.	Centering of liquid bubble during decaying oscillations, following deployment.	4-112
Figure 14.	Decaying oscillations of liquid bubble, following deployment.	4-113
Figure 15.	Centering of immiscible compound drop during deployment.	4-114
Figure 16.	Centering of rotating-immiscible compound drop during forced oscillations.	4-115
Figure 17.	Experimental time of mode 2 and mode 4 oscillations. Free decay of a low-viscosity 1-cm Glycerin/Water drop. The solid and dashed curves represent the results of the Rayleigh-Lamb linear predictions.	4-116
Figure 18.	The power spectrum of the mode 2 oscillations P_{22} . The existence of superharmonics nf_2 is evident.	4-116
Figure 19.	The power spectrum of the mode 4 oscillations P_{44} . In this case superharmonics, subharmonics, and combination harmonics appear.	4-117
Figure 20.	The cross power spectrum of the mode 2 and 4 oscillations P_{22} . It is interesting to note the existence of the fundamental frequency $1/3f_2$ subharmonic.	4-117
Figure 21.	Relative surface energy is plotted versus time. Note the $2f_2$ modulation of the fundamental frequency.	4-118
Figure 22.	Experimental time series of mode 2 and mode 4 oscillations. Free decay of a highly viscous 2-cm silicone oil drop. Results for fast free decay from USML-2 experiment.	4-119
Figure 23.	The power spectrum of the mode 2 oscillations P_{22} (USML-2 fast decay data).	4-119
Figure 24.	The cross power spectrum of the mode 2 and 4 oscillations P_{24} (USML-2 fast decay data).	4-120
Figure 25.	The power spectrum of the mode 4 oscillations P_{44} (USML-2 fast decay data).	4-120
Figure 26.	Experimental time series of mode 2 oscillations. Forward sweep at 8 V.	4-121
Figure 27.	Experimental time series of mode 2 oscillations. Backward sweep at 8 V amplitude.	4-121

Figure 28.	The PSD of the mode 2 oscillations for forward sweep at 8 V.	4-122
Figure 29.	The CPSD of the mode 2 and 4 oscillations. Backward sweep at 8 V.	4-122
Figure 30.	Experimental time series of mode 2 oscillations. Forward sweep at 12 V amplitude.	4-123
Figure 31.	Experimental time series of mode 2 oscillations. Backward sweep at 12 V amplitude.	4-123
Figure 32.	PSD's for the forward and backward sweep plotted against each other. Note the frequency shift and existence of satellite peaks.	4-124
Figure 33.	The experimental time series of the mode 2 chaotic drop oscillations. The excita- tion amplitude is 12 V.	4-124
Figure 34.	The PSD of the mode 2 oscillations. The excitation frequency is decreasing lin- early with the amplitude of 12 V.	4-125
Figure 35.	The PSD of the mode 4 oscillations. The excitation frequency is decreasing lin- early with the amplitude of 12 V.	4-125
Figure 36.	The CPSD of the mode 2 and 4 oscillations. The excitation frequency is de- creasing linearly with the amplitude of 12 V.	4-126
Figure 37.	Auto-correlation coefficient of the experimental time series of mode 2 oscilla- tions. Excitation amplitude is 12 V.	4-126
Figure 38.	Acoustic torque is observed to be a continuous monotonic function of the gain ratio, as the ratio of [1]:[3] is varied.	4-127
Figure 39.	Time history of specimen motion as derived from experiment videotapes.	4-128
Figure 40.	Angular velocity vs. time showing the specimen's history for the first 200 sec- onds.	4-129
Figure 41.	Acoustic torque measured for spheres of four different diameters as a function of the square of the acoustic pressure per axis.	4-130
Figure 42.	Relationship between acoustic torque applied to specimen and the phase lag be- tween and the x and y components of the acoustic field.	4-131
Figure 43.	Magnitude of torque as a function of the position of specimen in the x, y plane. Cross section of the 3-dimensional surface in the x, -x direction.	4-132

Figure 44.	Relationship between acoustic torque applied to specimen and the position of drop in the x, y plane. Cross section of the 3-dimensional surface in the y, -y direction.	4-133
Figure 45.	Acoustic torque as a function of acoustic pressure for a specimen in the shape of a tall cylinder.	4-134
Figure 46.	Acoustic torque as a function of acoustic pressure for a specimen in the form of a right cylinder ($h \approx r$).	4-135
Figure 47.	Predicted and measured acoustic torque as a function of acoustic pressure for a specimen in the state of a thin disk supported by a fiber of varying stiffness.	4-136

EXPERIMENT V:

Figure 1.	Decay of azimuthal radius for 2.5-cm-diameter aqueous drops with an initial deformation of approximately 20 percent: a) pure water; b) water with 1.4×10^{-4} g/ml Triton X-100 dissolved in the bulk; c) water with 1.0×10^{-5} g/ml Bovine Serum Albumin (BSA) dissolved in the bulk.	5-144
Figure 2.	Two complete cycles of superoscillation of a water drop (6 cm^3) with the surfactant Triton X-100 at the critical micelle concentration. The time in seconds is shown. Also shown is the numerical simulation using the boundary integral method. The time shown with the simulation is non-dimensional. From this data the dynamic surface tension and surface viscosities (shear and dilatational) can be determined. (Apfel group, Yale University.).	5-145

EXPERIMENT VI:

Figure 1.	Various free surface shapes investigated in the STDCE-2.	6-171
Figure 2.	STDCE-2 test chambers module views: (a) exterior, (b) interior.	6-171
Figure 3.	Schematic layout of the STDCE-2.	6-172
Figure 4.	General time line of tests conducted during the STDCE-2. (2.0 cm diameter test container during CT test, $V_r=1$).	6-172
Figure 5.	Streamlines and isotherms with flat free surface. (CF test, $D=2 \text{ cm}$, $Ma=6.4 \times 10^4$, $Ma_Q=8.4 \times 10^3$, $Hr=0.1$, and $Pr=30$).	6-173
Figure 6.	Comparison between computed surface temperature distribution and IR imager data for flat surface CF test.	6-173
Figure 7.	Scaling law for maximum surface velocity in heated region (CF configuration).	6-174

Figure 8.	Scaling law for maximum stream function (CF configuration).	6-174
Figure 9.	Streamlines and isotherms with curved free surface (CF test, $D=2$ cm, $Ma=3.5\times 10^5$, $Ma_Q=3.6\times 10^4$, $Hr=0.1$, $Pr=23$, $Ar=1$, and $Vr=0.59$).	6-175
Figure 10.	Scaling law for maximum stream function with curved free surface (CF configuration).	6-175
Figure 11.	Streamlines and isotherms for steady flow in CT tests ($D=2.0$ cm, $Ar=1$, $Ma=1.1\times 10^5$, $Pr=30.9$).	6-176
Figure 12.	Comparison between computed surface temperature and IR imager data for flat surface CT test.	6-176
Figure 13.	Scaling law for maximum stream function (CT configuration).	6-177
Figure 14.	Qualitative sketch of the observed oscillatory flow field in CT tests.	6-177
Figure 15.	Experimental data for the onset of oscillations in different CT test. (2 cS fluid, $Ar=1$, $Hr=0.1$, $Vr=1.0$).	6-178
Figure 16.	Variation of critical Marangoni number in various CT tests. (2 cS fluid, $Ar=1$, $Hr=0.1$, $Vr=1.0$).	6-178
Figure 17.	S-parameter at the onset of oscillations for flat surface CT tests.	6-179
Figure 18.	Variation of oscillation frequency at the onset of oscillations in CT tests. (2 cS fluid, $Ar=1$, $Hr=0.1$, $Vr=1.0$).	6-179
Figure 19.	Various patterns of the free surface temperature measured by IR imager during oscillatory flow in flat surface CT tests: (a) two-lobed rotating pattern; (b) two-lobed pulsating pattern; (c) three-lobed pulsating pattern.	6-180
Figure 20.	Critical heat fluxes for flat surface CF tests with $Ar=1$	6-181
Figure 21.	Critical Marangoni numbers for flat surface CF tests with $Ar=1$	6-181
Figure 22.	S-parameter for flat surface CF tests with $Ar=1$	6-182
Figure 23.	Dimensional and dimensionless oscillation frequencies near onset of oscillations for flat surface CF tests.	6-182
Figure 24.	Thermograms during oscillations in flat surface CF tests.	6-183
Figure 25.	Critical heat fluxes for various surface shapes (CF tests, $D=2$ cm).	6-183

Figure 26.	Critical heat fluxes under various conditions for $Ar=1$ CF tests.	6-184
Figure 27.	Critical heat fluxes under various conditions for $Ar=0.5$ CF tests.	6-184

EXPERIMENT VII:

Figure 1.	Nested convection cylinders in a rapidly rotating convecting liquid (after <i>Busse</i> , 1983).	7-198
Figure 2.	Schematic cross-section of the geophysical fluid flow cell. The gap contains 0.065 centistoke silicone fluid.	7-199
Figure 3.	Instrument cross-section. The optics provides a Schlieren visualization of convection in the spherical convection cell. A beam splitter diverts the image to both a 16 mm and a video camera.	7-200
Figure 4.	Thermal history at the walls for scenario 145 (4 second basic rotation period, high voltage ramping from 0 to 10 kV). The upper panel shows the inner sphere values at the latitudes shown, while the lower panel illustrates the behavior of the outer sphere at the latitudes shown.	7-201
Figure 5.	Thermal history at the walls for scenario 194 (48 second basic rotation period, high voltage ramping from 0 to 3.5 kV and back down again). The upper panel shows the inner sphere values at the latitudes shown, while the lower panel illustrates the behavior of the outer sphere at the latitudes shown.	7-202
Figure 6.	Regime diagram showing qualitative results for several Rayleigh number ramp up experiments with symmetric heating. Each image is a single snapshot with the south pole at the bottom and the equator at the top. The solid curve shows the onset of banana cell, the dashed the onset of polar wavy convection. Each image corresponds to the dot to its left, in vertical order.	7-203
Figure 7.	Unwrapped convection planforms for scenario 145 (4 second rotation, symmetric heating, 2.16 kV). The top two panels show motions as viewed by "E-W" fringes (left) that are sensitive to longitudinal temperature gradients, and "N-S" fringes (right) that are sensitive to latitudinal gradients. The bottom panel shows radially averaged temperatures from the Miller-Leslie model. Note the general agreement on the structure and equivalence of disturbance longitudinal wavenumber. In all frames the view is from pole (center) to equator (limb) with equal spacing of latitude lines.	7-204

Figure 8.	Unwrapped views (as in fig. 7) of scenario 194 (48 second rotation period, symmetric heating). N-S fringes (sensitive to longitudinal thermal gradients) for the value of voltage shown. The first two images (top left and right) are during the first three hour ramp up, which the bottom (the only stable patterns) is at about hour five. The first image is during the first voltage hold period, the second during the ramp up to 3.5 kV, and the third just after the end of the second voltage hold period.	7-205
Figure 9.	Regime diagram showing computed planforms in the Miller-Leslie model (Fourier decomposition in longitude, grid points in the meridional plane). Boundary conditions, r-dependent gravity, centrifugal acceleration, and geometry as in GFFC.	7-206
Figure 10.	Critical curves from the GFFC experiments. Polar modes become the most unstable for Taylor numbers in excess of about 20,000. The results from computational simulations are shown as points on the figure.	7-207
Figure 11.	(Top) Translation latitudes vs. voltage for 4 second rotation; (Bottom) the model relation when rotation period and voltage are assumed to have the same exponent is shown. This is $\sin(\theta_{predicted}) \approx 270(\tau V)^{-0.85}$, with an average error of 11%. A similar fit to the relation $\sin(\theta_{predicted}) \approx 380(\tau V)^{-1}$ is nearly indistinguishable, with an average error of 12%. However, the scaling in (4) can only collapse the data to within 35% of the identity line.	7-208

EXPERIMENT VIII:

Figure 1.	Plots of the air temperature in the plant chamber and the Shuttle middeck during the USML-2 mission, from launch to landing.	8-216
Figure 2.	Plots of the percent relative humidity of the air in the plant chamber and the Shuttle middeck during the USML-2 mission, from launch to landing.	8-216
Figure 3.	Plots of the carbon dioxide concentration in the air of the plant chamber and the Shuttle middeck during the USML-2 mission, from launch to landing.	8-217

EXPERIMENT IX:

Figure 1.	Concentration of carbon dioxide in the growth unit of the ASTROCULTURE™ unit during 2-3 days and 14-15 days of space flight.	9-227
Figure 2.	Potato tubers produced by the explants after 16 days of growth in space flight (a) and on Earth (b).	9-227
Figure 3.	Starch grains from potato tubers formed in space flight (a) and on the ground (b). ...	9-228

Figure 4.	Percentage of the starch grains by size category formed in potato tubers during space flight and on the ground.	9-228
-----------	--	-------

EXPERIMENT X:

Figure 1.	Parabolic aircraft (NASA's KC-135) and sounding rocket.	10-255
Figure 2.	"Standard configuration" fluids processing apparatus (FPA). The standard configuration FPA contains 1.5 ml of fluid in the C and B chambers and 3.5 ml in the A chamber. Many variations of this standard configuration are possible for accommodating specific experimental objectives.	10-256
Figure 3.	Plant-FPA (P-FPA). The Plant-FPA was modified to allow air exchange between chamber A inside the glass barrel and the outside of the Lexan™ sheath. Both the glass barrel and the Lexan™ sheath have hydrophobic membranes, which allow for air exchange while containing liquids. The Purafil pellets are used to scrub ethylene. This concept has recently been scaled-up to the design of a plant growth chamber (PGBA) which provides a controlled, lighted environment for an approximately 1-cubic-foot plant growth chamber.	10-257
Figure 4.	Manually operated GAP. Shown with crank handle attached for on-orbit activation by a crew member. This version can be stowed either in the GBA-INC or the GBA-AMB.	10-258
Figure 5.	GBA-INC. The GBA-INC consists of a temperature controlled (37 °C) middeck-locker-equivalent replacement module that holds nine GAP's. After unlatching and pulling out the GBA-INC drawer, the incubator lid can be opened to access the nine GAP's stowed within the temperature controlled environment and the optical density measurement apparatus (eight FPA's processed simultaneously).	10-258
Figure 6.	Root curvature response to horizontal gravistimulation. Root tip angle (\pm SD) is plotted over time for horizontally gravistimulated clover seedlings after previous growth under (a) 1 g control, (b) microgravity, and (c) clinorotated conditions. Clinorotated plants did not respond as quickly nor did they reach as great a final angle of curvature as the control or microgravity.	10-259

EXPERIMENT XI:

Figure 1.	(a) A single PCAM cylinder with individual disposable trays with wicks and associated interleaving actuator plates. A total of nine seven-chamber trays are accommodated in each cylinder; (b) illustrates the standard flight arrangement of six PCAM units in STES.	11-273
Figure 2.	A schematic illustrating the basic construction of the PCAM and its mechanism. ...	11-273

Figure 3.	(a) Schematic of the diffusion-controlled crystallization apparatus for microgravity (DCAM). Shown: (1) gel plug, (2) primary reservoir, (3) secondary reservoir, (4) dialysis chamber (button), (5) end cap, (6) vent screws and ports. (b) Machined DCAM ground-based unit. (c) Flight tray assembly of 27 DCAMs. (d) Six DCAM tray assemblies in thermal pouches as loaded for STS-76 <i>Mir</i> increment 2.	11-274
Figure 4.	Crystals of HIV protease complexed with proprietary inhibitor grown aboard USML-2 (STS-73).	11-274
Figure 5.	Crystals of (a) ground-based and (b) USML-2 flight at approximately the same magnification. Pictures provided courtesy of Dr. Jean-Pierre Wery and Eli Lilly and Company.	11-275
Figure 6.	Structure of human antithrombin III. The reactive loop, shown in blue, was never completely visible using data from ground-based crystals. The model was first completed based on samples from STS-67, and the structure is now refined to 2.6 angstroms using crystals grown in microgravity.	11-275
Figure 7.	Crystals of Gro EL Protein/Bacteriophage HK97 Capsid Protein Complex grown in PCAM during USML-2 (STS-73).	11-275
Figure 8.	Ground-based (a) and flight crystals (b) of neurophysin/vasopressin complex grown in PCAM during USML-2 (STS-73).	11-276
Figure 9.	Ground-based (a) and flight crystals (b) of augmenter of liver regeneration protein grown in PCAM on STS-73.	11-276
Figure 10.	Ground-based (a) and flight crystals (b) of L-alanine dehydrogenase protein grown in PCAM on STS-73.	11-276
Figure 11.	Crystal of nucleosome core protein grown in DCAM aboard USML-2 (a). Crystal grown during long duration <i>Mir</i> flight (b). Diffraction limit improved from 3.0 angstroms from Earth-grown crystals to 2.5 angstroms in microgravity. Crystals of the nucleosome core particle grown on <i>Mir</i> were reported to be the largest ever grown by any method (maximum dimension 3 mm).	11-277
Figure 12.	Two crystals of hen egg white lysozyme grown in DCAM via bulk crystallization aboard USML-2 (STS-73). Crystal dimensions: 4 mm (center) and 5 mm (bottom).	11-277

EXPERIMENT XII:

Figure 1.	Protein crystallization facility hardware consisting of four polysulfone bottles, aluminum caps, aluminum containment cylinders, and the side and endplates that attach the assembly to the CRIM.	12-289
-----------	--	--------

Figure 2.	Protein crystal growth glovebox hardware experiment chamber and containment tube. The experiment chamber, molded from polysulfone, contained a growth chamber for a protein droplet up to 50 μ l, surrounded by an annulus which held up to 0.5 ml of reservoir solution.	12-289
Figure 3.	CRIM storage drawer containing crystal growth experiment chambers in containment tubes and solutions for crystallization experiments.	12-290
Figure 4.	Crystal of feline calicivirus grown in PCGG hardware.	12-290
Figure 5.	Square pyramidal crystals, up to 0.4 mm long, produced by Duck Delta II crystalin.	12-291

EXPERIMENT XIII:

Figure 1.	Solute redistribution during solidification with limited liquid diffusion and no convection. Composition profile during steady-state solidification and composition profile after solidification, top. Solute redistribution during solidification with limited liquid diffusion and convection in the melt. Composition profile during steady-state solidification during d , the mass boundary layer and composition profile after solidification, bottom (after Flemings).	13-315
Figure 2.	The effect of convection on the axial and radial segregation in a dilute binary system (after Brown).	13-316
Figure 3.	Schematics of ampoule designs for USML-1 and USML-2 experiments.	13-317
Figure 4.	Schematic of cartridge design for the USML-2 experiment.	13-317
Figure 5.	Schematics of sample/ampoule/cartridge assembly (SACA) relative to the six furnace zones (a) USML-1 fully inserted location during heat up and the start of translation; (b) USML-2 location during heat-up; and (c) USML-2 fully inserted location at the start of translation.	13-317
Figure 6.	Schematic graph of furnace temperature setpoints versus furnace zone for USML-2 ground-based experiments.	13-318
Figure 7.	Sample output of computational model showing the location of the 1511 K isotherm across the layers of the SACA.	13-318
Figure 8.	Graph showing the 1511 K isotherm location relative to the furnace at the centerline of the crystal and at the radial location of the PI thermocouples. The axes are numbered in the coordinate system of the computational model. The location of the gradient zone is marked on the graph for ease of use.	13-319

Figure 9.	USML-2 first flight experiment (flight No. 1) timeline.	13-320
Figure 10.	PI thermocouples versus furnace position during insertion of flight No. 1. The gradient zone extends from 295 to 315 mm in this plot.	13-321
Figure 11.	USML-2 second flight experiment (flight No. 2) timeline.	13-322
Figure 12.	CPID resistance data for flight No. 1.	13-323
Figure 13.	CPID resistance data for flight No. 2.	13-324
Figure 14.	Photomacrograph of the first flight boule.	13-324
Figure 15.	Macrostructure observed on the D-slice from the first flight sample.	13-325
Figure 16.	Photomacrograph of the second flight boule.	13-325
Figure 17.	Macrostructure observed on the D-slice from the second flight sample.	13-325
Figure 18.	Photomacrograph of the first ground truth boule.	13-326
Figure 19.	Macrostructure observed on the D-slice from the first ground truth sample.	13-326
Figure 20.	Photomacrograph of the second ground truth boule.	13-326
Figure 21.	Macrostructure observed on the D-slice from the second ground truth sample.	13-327
Figure 22.	GCEL mission simulation interface shape and deflection.	13-327
Figure 23.	Space flight experiment No. 1 interface shape and deflection.	13-328
Figure 24.	Ground truth experiment No. 1 interface shape and deflection.	13-328
Figure 25.	Ground truth experiment No. 2 interface shape and deflection.	13-329
Figure 26.	Space flight experiment No. 1 demarcation interface shape, position, and maximum deflection.	13-330
Figure 27.	Ground truth experiment No. 1 demarcation interface shape, position, and maximum deflection.	13-331
Figure 28.	Space flight experiment No. 1 growth rate.	13-332
Figure 29.	Ground truth experiment No. 1 growth rate.	13-333

Figure 30.	Ground truth experiment No. 2 growth rate.	13-334
Figure 31.	Dopant distribution and segregation analysis for the GCEL mission simulation ground-based sample.	13-334
Figure 32.	Predictions from numerical model compared to experimental measurements.	13-335

EXPERIMENT XIV:

Figure 1.	IDFT-1 timeline.	14-348
Figure 2.	IDFT-2 timeline.	14-349
Figure 3.	USML-2 CGF attitude.	14-350
Figure 4.	USML-2 gravity-gradient attitude.	14-351
Figure 5.	USML-2 +Z-body solar inertial (+ZSI) attitude.	14-352
Figure 6.	Temperature gradient across solid-melt interface during translation arrest (the open circles represent the location of the six thermocouples).	14-353
Figure 7.	Initial transient growth rate.	14-354
Figure 8.	Growth rate lag behind translation rate.	14-355
Figure 9.	IDFT-1 segregation behavior.	14-356
Figure 10.	Diffusion limited solute redistribution.	14-357
Figure 11.	IDFT-1 initial transient microsegregation behavior.	14-358
Figure 12.	Microphotograph of initial transient (see text for details).	14-359
Figure 13.	IDFT-1 interface shape at start of growth.	14-360
Figure 14.	Convective transport solute redistribution.	14-361
Figure 15.	Microsegregation behavior during CGF to GG transition.	14-362
Figure 16.	Interface shapes before and after CGF to GG transition.	14-363
Figure 17.	IDFT-2 segregation behavior.	14-364

Figure 18.	IDFT-2 microsegregation behavior during translation arrest (the open circles represent growth rate data).	14-365
Figure 19.	Microphotograph of translation arrest region (see text for details).	14-365
Figure 20.	IDFT-2 microsegregation behavior in 1 g environment (the open circles represent growth rate data).	14-366
Figure 21.	Ampoule assembly, exploded view.	14-367

LIST OF TABLES

Table	Title	Page
EXPERIMENT III:		
Table 1.	XRD data comparing flight (F) and terrestrial/control (T) zeolite A samples.	3-39
Table 2.	XRD data comparing flight (F) and terrestrial/control (T) zeolite X samples.	3-40
Table 3.	Comparison of Si/Al ratios and yield of flight (F) and terrestrial/control (T) zeolite Beta crystals.	3-42
EXPERIMENT IV:		
Table 1.	Raw DPM data returned from USML-2 mission.	4-64
EXPERIMENT V:		
Table 1.	Parameter ranges of experiments.	5-140
EXPERIMENT VI:		
Table 1.	Number of CT tests performed with Ar=1.	6-170
Table 2.	Number of CF tests performed with Ar=1.	6-170
Table 3.	Number of CF tests performed with Ar=0.5.	6-170
EXPERIMENT VII:		
Table 1.	Experiment parameters and characteristics of Dow Corning 0.65 centistoke silicone oil.	7-197
EXPERIMENT IX:		
Table 1.	Environmental conditions in the growth chambers of the space flight and of the ground control.	9-224
Table 2.	Growth of tubers produced on explants after 16 days of growth in space flight and on the ground.	9-224

Table 3.	Concentrations of carbohydrates and soluble proteins in potato tubers that developed on explants in space flight and on the ground.	9-225
Table 4.	Activity of enzymes controlling starch synthesis and degradation in potato tubers that developed on explants in space flight and on the ground.	9-226

EXPERIMENT XIII:

Table 1.	Results summary for USML-2 GaAs ground-based samples.	13-313
Table 2.	Results summary for USML-2 GaAs flight and ground-truth samples.	13-314

AUTHOR INDEX

Aibara, S.	12-286
Alexander, J.I.D.	1-3
Anilkumar, A.V.	4-63
Apfel, R.E.	5-139
Bağ, N.	3-37
Berryman, J.	10-231
Betzel, C.	12-286
Bly, J.M.	13-295
Brown, C.S.	9-221
Bula, R.J.	8-211
Carlson, D.	13-295
Carlson, F.M.	1-3
Carter, D.C.	11-263
Chait, A.	13-295
Chattopadhyay	12-286
Chen, X.	5-139
Croonquist, A.P.	5-139
Croxdale, J.G.	9-221
Daidzic, N.	4-63
DeLucas, L.J.	12-281
DiMarzio, D.	1-3

Draeger, N.A.	8-211
Dudley, M.	1-3
Einspahr, H.M.	12-287
Ge, Y.R.	2-19
Gillies, D.C.	1-3
Hart, J.E.	7-187
Hmelo, A.B.	4-63
Holt, R.G.	5-139
Howell, P.L.	12-287
Hutchins, M.A.	2-19
Jankovsky, J.	5-139
Kafalas, J.	13-295
Kaforey, M.K.	13-295
Kamotani, Y.X.	6-149
Ketterling, J.	5-139
Kittelman, S.	7-187
Klaus, D.M.	10-231
Krause, K.	12-287
Larson, D.J.	1-3
Lee, C.P.	4-63
Leslie, F.W.	7-187
Lichtensteiger, M.	14-339
Long, M.	12-286

Luo, M.	12-287
Matthiesen, D.H.	13-295
Miller, T.L.	7-187
Moore, K.	12-286
Ohlsen, D.R.	7-187
Ostrach, S.X.	6-149
Pline, A.D.	6-149
Sacco, A.	3-37
Smith, G.D.	12-287
Sthanam, N.	12-287
Stodieck, L.	10-231
Thomson, J.	12-288
Tian, Y.	5-139
Tibbitts, T.W.	9-221
Trinh, E.H.	5-139
Wang, T.G.	4-63
Warzywoda, J.	3-37
Weber, W.	12-288
Wheeler, R.M.	9-221
Wiedemeier, H.	2-19
Wolfe, R.	10-231
Yetka, R.A.	8-211
Zhou, W.	8-211

ACRONYMS

3-DMA	3-Dimensional Microgravity Accelerometer
APCF	Advanced Protein Crystallization Facility
ARC	NASA Ames Research Center [Moffett Field, CA]
ASC	Astroculture
BNL	Brookhaven National Laboratory [Brookhaven, NY]
BSA	Bovine Serum Albumin
CARB	Center for Advanced Research in Biotechnology [Rockville, MD]
CCD	Charge-Coupled Device
CDOT	Colloidal Disorder-Order Transition
CENG	Centre d'Etudes Nucléaires National de Grenoble [Grenoble, France]
CFD	Computational Fluid Dynamics
CGBA	Commercial Generic Bioprocessing Apparatus
CGF	Crystal Growth Furnace
CMC	Center for Macromolecular Crystallography [UAB]
CMDS	Consortium for Materials Development in Space [UAH]
CMMR	Center for Microgravity and Materials Research [UAH]
CNES	Centre Nationale d'Études Spatiales ["National Center for Space Studies," French Space Agency]
CNRS	Centre National de la Recherche Scientifique [France]
CPCG	Commercial Protein Crystal Growth
CRIM	Commercial Refrigerator/Incubator Module
CSC	Center for Space Commercialization
CSPD	Cross Power Spectral Density
CuK α_1	Copper K α_1 radiation
CVT	Chemical Vapor Transport
DARA	Deutsche Agentur für Raumfahrtangelegenheiten ["German Agency for Space Affairs," German Space Agency]
DCRC	Double Crystal Rocking Curve
DDM	Drop Dynamics Module
DESY	Deutsches Elektronen-Synchrotron [Hamburg, Germany]

DLR	Deutsche Forschungs-und Versuchsanstalt für Luft-und Raumfahrt [German Aerospace Research Establishment, used to be "DFVLR"]
DLS	Dynamic Light Scattering
DPM	Drop Physics Module
EDX	Energy Dispersive X-ray Analysis
EMBL	European Molecular Biology Laboratory [DESY, Hamburg, Germany]
EPD	Etch Pit Density
ESA	European Space Agency
ESTEC	European Space Research and Technology Center
FCC	Fluidized Catalytic Cracking
FO	Functional Objective
FPA	Fluids Processing Apparatus
FSDC	Fiber-Supported Droplet Combustion
FTIR	Fourier Transform Infra-Red
FWHM	Full-Width Half-Maximum
GBX	Glovebox
GBX-ZCG	Zeolite Glovebox Experiment
GCEL	Ground Control Experiments Laboratory [NASA MSFC]
Ge	Germanium
GGFC	Geophysical Fluid Flow Cell
HgCdTe	Mercury Cadmium Telluride
HgI ₂	Mercuric Iodide
HI-PAC	High Packed Digital Television
ICE	Interface Configuration Experiment
IML-1	First International Microgravity Laboratory [STS-42 Shuttle mission, launched in January 1992]
IML-2	Second International Microgravity Laboratory [STS-65 Shuttle mission, launched in July 1994]
IR	Infra Red
ISOVPE	Isothermal Vapor Phase Epitaxy
JPL	Jet Propulsion Laboratory [Pasadena, CA, managed by the California Institute of Technology]
JSC	NASA Johnson Space Center [Houston, TX]

KSC	NASA Kennedy Space Center [Cape Canaveral, FL]
LaRC	NASA Langley Research Center [Hampton, VA]
LeRC	NASA Lewis Research Center [Cleveland, OH]
LMS	Life and Microgravity Spacelab [STS-78 Shuttle mission, launched in June 1996]
LPE	Liquid-Phase Epitaxy
MAWS	Microgravity Acceleration Workstation
MBE	Molecular Beam Epitaxy
MET	Mission Elapsed Time
MOCVD	Molecular Chemical Vapor Disposition
MPES	Mission Peculiar Experiment Support Structure [Shuttle]
MSAD	Microgravity Science and Applications Division [NASA MSFC; also used to be the acronym for an OLMSA division at NASA Headquarters before name was changed to "Microgravity Research Division" (still Code UG)]
MSD	Microgravity Science Division [NASA LeRC]
MSFC	NASA Marshall Space Flight Center [Huntsville, AL]
NASA	National Aeronautics and Space Administration
NIST	National Institute for Standards and Technology [Boulder, CO]
NSLS	National Synchrotron Light Source
NRC	National Research Council
OARE	Orbital Acceleration Research Experiment
OTFE	Oscillatory Thermocapillary Flow Experiment
PCF	Protein Crystallization Facility
PCGG	Protein Crystal Growth Glovebox
PDE	Particle Dispersion Experiment
PI	Principal Investigator
PIMS	Principal Investigator Microgravity Services [NASA LeRC]
PLP	Precision Lattice Parameter
POCC	Payload Operations and Control Center [NASA MSFC]
PR	Photoreflectance
PSD	Particle Size Distribution
PSD	Power Spectral Density
RPI	Rensselaer Polytechnic Institute [Troy, NY]

SACA	Sample/Ampoule Cartridge Assembly
SAMS	Space Acceleration Measurement System
SEM	Scanning Electron Microscope
SMBT	Synchrotron Monochromatic Beam Topography
SPCG	Single-locker Protein Crystal Growth
STABLE	Suppression of Transient Acceleration By Levitation Evaluation
STDCE	Surface Tension Driven Convection Experiment
STES	Single-locker Thermal Enclosure System
STS	Space Transportation System [Shuttle/external tank/solid rocket booster system, also a Shuttle mission designation]
SWBT	Synchrotron White Beam Topography
TBE	Teledyne Brown Engineering
TCS	Triple Crystal Spectroscopy
TEA	Triethanolamine
TEM	Transmission Electron Microscope
UAB	University of Alabama at Birmingham
UAH	University of Alabama in Huntsville
USML-1	First United States Microgravity Laboratory [STS-50 Shuttle mission, launched in June 1992]
USML-2	Second United States Microgravity Laboratory [STS-73 Shuttle mission, launched in October 1995]
VDA	Vapor Diffusion Apparatus
WPI	Worcester Polytechnic Institute [Worcester, MA]
XRD	X-ray Power Diffraction
ZCGG	Zeolite Crystal Growth Glovebox
Zn:CdTe	Zinc Alloyed Cadmium Telluride

KEY WORD INDEX

A

a critical value of free surface deformation parameter	168
acceleration field	152
acoustic boundary layer	89
acoustic flattening	68
acoustic levitation	93
acoustic radiation forces	139
acoustic streaming	90, 93
ADP-glucose pyrophosphorylase	222, 225
adsorbents	37
advection	193
agglomeration	41
aluminosilicates	37
amount of lignin	243
amyloplasts	242
antiorthostatic suspension	238
aspect ratio	162
Astroculture experiment	221
atmospheres of planets	187
Attitude Change	341, 342
Augmenter of Liver Regeneration Protein	269
autoclaves	42
Auxin	244
axial dopant distribution	300
Axial Segregation Analysis	308
axisymmetric shape	69

B

b-convection model	194
Bacterial Growth	248
bifurcation point	68
biophysical/biochemical processes	231
BioServe Space Technologies	231
blood coagulation	267
Bone Marrow Macrophages-Phase II	238
bone mass loss	246
boric oxide	302
Bovine Serum Albumin	144
Bridgman-Stockbarger	3, 5
Bridgman-Stockbarger growth system	300
brine shrimp	235

bubble mode	72
buoyancy convection	5
buoyancy driven modes	188
buoyancy forces	298
Busse-Wang (B&W) torque mechanism	94

C

calcineurin complex	282, 283
Capillary Oscillations	71
carbon dioxide concentrations	223
carbon dioxide conditions	211
carrier concentration	26
carrier mobility	20
catalysts	37
CdTe single crystal	21
cellulase	247
centering mechanism	72
CeReS-18	237
CGF attitude	339
chaos	64
chaotic oscillations	78, 85
characteristic distance	298
chemical homogeneity	5
chemical macrosegregation	8
chemical vapor transport (CVT)	19
chromatin	270
Clinorotation	244, 245
coagulation proteases	267
Collagen binding domain	285, 282
collagenase	247
columnar ("banana cell") modes	192
commercial protein crystal growth (CPCG) experimen	281
commercial refrigerator/incubator module	281
complete convective mixing	296
complete mixing	296
compositional homogeneity	20
compositional microhomogeneity	24
compound drop	72, 71
Computational Model	303, 309, 318
concentration of carbon dioxide in the plant chamber	212
constant flux (CF) configuration	151
constant temperature (CT) configuration	151
container aspect ratio	157
controlled environment plant growth unit	211
convective flow	21

Convective Instability	193
Coriolis forces	187, 193
critical heat flux (Q_{cr})	165
critical Marangoni number	163
critical supersaturation	265
Crystal Growth Furnace	295, 339
crystal-growing techniques	240
crystallization facility	281
Crystallization of Proteins	239
current pulse interface demarcation	302, 339

D

damping of the fluid flow	299
decay constant	140
defect density	8
deformability of the free surface	163
degenerative joint disease	285
degree of supersaturation	37
Demarcation Interface Shapes	307
density gradient vector	21
developmental processes	222
dialysis method	263, 265
dielectric breakdown point	188
dielectric polarization	188
diffusion controlled growth	4, 8, 297, 299, 300, 341
diffusion-controlled crystallization apparatus for	263
diffusion-limited growth	38
diffusion-limited process	263
diffusive mixing	296
direction of growth	243
directional solidification	295
directionally solidified	5
disease process	241
dislocation density	8, 20
dislocations	299
dopant distribution	299
Dopant Distribution Measurements	308
dopant segregation behavior	340
double crystal rocking curve	6
DPM acoustic chamber	64
drop collapse and breakup	85
duck delta II crystallin	282, 285
dynamic surface deformation	155
dynamic surface tension	140
dynamics experiments	63

E

effective gravitational field	301
effective gravity	299
electrodynamic buoyancy	189
electrohydrodynamic flow instability	188
electromagnetic gravity	189
electron microprobe analysis	23
energy dispersive x-ray analysis	5
environment control	214
enzyme efficacy	247
enzymes	225
epidermal growth factor	283
epidermal growth factor receptor	282
epitaxial layers	20
epitaxial processes	4
equilibrium segregation coefficient	296
etch pit densities	23
Ethylene	213, 243
eukaryotes	270
expression of the auxin	244
extent of cell wall deposition	243
extracellular mass transfer processes	248
extracellular mass transport phenomena	248

F

feline calicivirus	282, 284
fibrin degradation	247
fissions	69
Flow Visualization	89
fluid flow	5
Fluids Processing Apparatus	233
Fourier Transform Infra-Red (FTIR) spectra	41
framework	37
free carrier concentration	341
free oscillations	139
free surface deformation	149, 151, 163
free surfaces	305
full width half maximum (FWHM) rocking curve	8
furnace set point temperatures	304
Furnace Translation Rate	308
fused quartz ampoule	302

G

g-jitter	152
GALLIUM-DOPED GERMANIUM	339

Gallium-doped single-crystalline germanium	339, 340
gastroenteritis	284
GBA-Ambient	232
gel phase	37
Gene Expression in Higher Plants	243
Generic Bioprocessing Apparatus—Incubator	232
generic hardware	232
gentamicin	249
Geophysical Fluid Flow Cell	187
Glancing angle x-ray synchrotron topographic analysis	7
Glatzmaier 10 4 model	193
global scale fluid motions	187
global dynamics	188
gradient freeze	6, 304
gradient zone	310
Gravi-response	244
gravistimulation	259
gravitational buoyancy	189
gravitropism	242, 244
gravity	298
gravity gradient	339
gravity perception	242
gravity vector	21
gravity-driven convection	20
Gro EL Protein/Bacteriophage HK97 Capsid Protein C	268
Group Activation Pack	233
growth interface shape	309
growth rate	296, 308

H

Hall effect measurements	306
Hall measurements	26
heat transfer	5
heat transfer rate	158
heater ratio	162
hemispherical annular gap	188
hen egg white lysozyme	271
heparin	267
heteroepitaxial system	19
HgCdTe infrared detectors	4
Hg _{0.8} Cd _{0.2} Te	19
Hg _{1-x} Cd _x Te	19
HgI ₂ transport agent	21
HIV protease	266
Human Antithrombin III	267

hydrostatic pressure	7, 8
hysteresis	64
Hysteresis effect	78

I

Immunocytochemical assays	236
immunosuppressant drugs	283
IMP dehydrogenase	282, 284
influence of buoyancy	167
infrared (IR) imager	152
infrared devices	19
infrared transmission microscope	307
interface demarcation	296, 339
interface demarcation flight test	339
interface demarcation lines	340
Interface Morphology	25
interface position	310
Interface Shapes	307
ion exchangers	37
IR surface mapping	22
islands grown	22
Isothermal Containment Module	232

J

jump	64
Jump phenomena	78

K

kinematic modeling	89
kinematic viscosity	299

L

L-Alanine Dehydrogenase from <i>Bacillus subtilis</i>	269
laminar flow	298
large-amplitude forced drop oscillation	88
lattice parameters	38
lattice-matched substrate	4
Legendre fitting	82
Legendre orthogonal zonal modes	82
Legendre polynomial expansion	64, 82
level of light	213
life support systems	222
light emitting diode (LED)	213
Lindstedt-Poincaré perturbation technique	75
Liquid Encapsulated Czochralski	302

Liquid Shells	72
Liquid-Core Compound Drop	73
liquid-liquid diffusion	263, 265
liver growth factor	269
location and shape of the interface	339
Long-term gravi-response	245
Longitudinal macrosegregation	4
Lysozyme	240, 271, 282, 285

M

magnetic bacteria	247
Magnetic combing	246
Magnetic Combing of Collagen	246
magnetic field strength	301
magnetic viscosity	299
Marangoni effect	142
Marangoni number	157, 160, 162
Marangoni stresses	141
mass transport	20
melt-solid interface	303, 308
meltback interface	306, 341
microdialysis	240
Microgravity processing	5
microgravity test tube	233
microprobe	5
microscopic growth rate	339
microscopic segregation behavior	342
Microsomal triglyceride transfer protein	282, 284
Miller-Leslie	192
minimized residual g-vector	339
mixing process	42
mode coupling	64, 74
mode locked	75
molecule's activity in vivo	240
mycophenolic acid	284

N

n-type conductivity	26
neurophysin	268
Neurophysin II/Vasopressin Complex	268
nickel sphere	188
non-axisymmetric convection	187
non-ionic surfactant	141
Nonlinear drop oscillations	63
nonlinear dynamic behavior	63

nucleation	37
nucleic acid	240
Nucleosome Core Particle	270
Nusselt number	158

O

onset of convection	193
onset of oscillations	152, 162
orthogonal acoustic standing waves	94
oscillatory	151, 298
oscillatory flow	162
oscillatory free decay	74
Oscillatory thermocapillary flows	149
osteoblast cells	236
osteoblast function and structure	236
Osteoporosis	246

P

parabolic aircraft	232
Particle size distributions	38
PBN leaf spring assembly	302
Peclet number	300
petiole	224
petrochemical process industries	37
pharmaceutical development	240
pherulitic agglomerates	40
photoreflectance	5
photosynthesis	223
physiological	222
physiological activity	213
planetary convection	188
plant chamber air temperature	211
plant chamber atmospheric relative humidity	212
Plant Gravity Response	245
plant growth and development	211
plant growth chamber	257
plant hormone	244
plant research	211
plant vitality	223
plasmin	247
Plasmin Enzyme Efficacy	247
plastids	242
Pliolite tracer particles	154
pliolite tracers	72
polar convection	192

poliovirus polymerase	240
polyethylene glycol	265
polyomavirus	239
Potato explants	221
potato tubers	226
Prandtl number	157, 190
Pre-metatarsal Development	245
precipitating agents	265
prograde polar	193
prograde propagating	193
prograde propagating polar disturbances	192
Protein and Nucleic Acid Crystallization	240
protein crystal growth glovebox hardware	281
protein crystallization apparatus for microgravity	263
protein:nucleic acid complexes	240
pyridine nucleotide transhydrogenase	270
pyrolytic boron nitride	302

Q

quadrupole-shape oscillation	141
Qualitative visualization	167
quantitative temperature measurements	167
quantum-confined semiconductors	37

R

rachis	224
radial cooling	6
radial dopant segregation	309
Radial segregation	4, 300
Radial Segregation Analysis	308
radial segregation behavior	341
Raf Kinase	266
rate-limited enzyme	225
Rayleigh number	190, 298
real-time communication	140
recombinant human insulin	283
reduced buoyancy	149
refining	37
refractive index	265
residual convective flow	27
residual g-vector	7
respiration	223
return flow	163
reversible stabilization agent	237
rocking curve widths	4

Ronchi interferometer	152, 155
rotating flows in the Earth's core	187
rotating spherical shells	194
rotating stars and planets	194
rotational bifurcation	68

S

sapphire dome	188
sedimentation	41
seeding interface position	296
Seeding Interface Shape	307, 309
segregation behavior	341
Segregation measurements	296
selenium doped gallium arsenide	295
senescence	223
shear viscosity	141
Silicalite	37
Silicalite synthesis	40
SIMPLER algorithm	157
slosh mode	72
solute distribution	297
solute redistribution	5
sounding rockets	232
Spherically Symmetric Flows	192
Spin-up Time	91
spreading resistance profiling	339, 340, 344
staphylokinase	282, 285
starch accumulation	226
starch phosphorylase	222
starch synthase	222, 225
Starchless Arabidopsis Mutant	242
statocytes	244
Steady thermocapillary flows	160
steady-state growth	297
steady-state growth conditions	309
steady-state regime	21
stratification	188
stream function	60
Stress Ethylene Inhibitors	243
subharmonics	77
substrate	21
superharmonics	77
superoscillations	140
surface deformation parameter (S)	163, 166
surface flow	163

surface shape	156
surface temperature	156
Surface tension Reynolds number Rs	157
surface viscoelastic properties	141
surface viscosities	140
surface viscosity	141
surface-active material	139
surfactants	139
synchrotron monochromatic beam topography	6
synchrotron white beam topography	6

T

T7 RNA Polymerase	269
Taylor number	190
Taylor-Proudman theorem	188
temperature gradient	298, 299
temperature isotherms	309
tetrahedral	37
The aspect ratio β	190
therapeutic applications	241
thermal boundary layer	159
thermal convective flow	298
thermal gradient	5
thermistors	154
Thermocapillary flows	151
thermomechanical stress	1-8
three-lobed pattern	165
three-lobed pulsating patterns	168
time-dependent frequency	140
Topological analysis	65
total hydrolase	222
transient growth conditions	27
transient region	341
transitory convection	194
Translation Arrest	342
transport agent	19
transport of viable cells	237
transport processes	21
trichomonas vaginalis ferredoxin	282, 284
triethanolamine	38
triple crystal spectroscopy	6
Triton X-100	141, 144
tuber formation	222
tubers	211
Tumble Rotation	89

tumble torque	89
turbidity data	234
turbulent	298
turbulent flows	187, 193
twenty-six mer pseudoknot RNA	241
twinning	7
two-lobed pattern	164
two-lobed rotating pattern	168
type-S thermocouples	302

U

U-U dodecamer RNA	240, 241
unicellular	158
uniformity	21
unit cell volumes	38
unit gravity	5

V

vacillatory states	195
van der Pauw Hall effect technique	308
van der Pauw method	26
vapor diffusion apparatus	281
vapor equilibration	263
vertebrate skeleton	236
video images of the explants	223
Viral infection of Mammalian Cells	239
viscoelastic relaxation	77
Viscosity	78
Viscous Drag	91, 93
viscous forces	298
Voids	306
volumetric fill-factor	7
vorticity equations	189

W

wall contact	7
Wisconsin Center for Space Automation and Robotics	211
World Wide Web	141

X

x-ray crystallographic analysis	239
x-ray diffraction Laue	22
x-ray white beam topography	4

Z

zeolite Beta	41
zeolite glovebox experiment	42
zeolites	37
Zeolites A, X, Beta	37
Zn: CdTe	3, 4
zonal bands of Jupiter	187

MISSION INFORMATION

Mission Designation:	STS-73 (72nd Shuttle mission)
Orbiter:	<i>Columbia</i> (18th flight for this Shuttle)
Orbit Inclination:	39.0 degrees
Orbit Altitude:	150 nautical miles (172 statute miles)
Number of Orbits:	255 (6.6 million miles)
Major Payload:	USML-2
Launch:	October 20, 1995 @ 9:53 a.m. EDT
Landing:	November 5, 1995 @ 6:45 a.m. EST at KSC
Mission Duration:	15 days, 21 hours, 53 minutes, 16 seconds (15/21:53:16)
Crew:	
Commander:	Commander Kenneth D. Bowersox, U.S. Navy
Pilot:	Commander Kent V. Rominger, U.S. Navy
Payload Commander:	Kathryn C. Thornton, Ph.D.
Mission Specialist:	Major Catherine G. Coleman, Ph.D., U.S. Air Force
Mission Specialist:	Commander Michael E. Lopez-Alegria, U.S. Navy
Payload Specialist:	Fred W. Leslie, Ph.D., NASA Marshall Space Flight Center
Payload Specialist:	Albert Sacco, Jr., Ph.D., Worcester Polytechnic Institute
Alt. Payload Specialist:	David H. Matthiesen, Ph.D., Case Western Reserve University
Alt. Payload Specialist:	R. Glynn Holt, Ph.D., Yale University

1. INTRODUCTION

1.1 Overview

The Second United States Microgravity Laboratory (USML-2) Space Shuttle mission was launched October 20, 1995, and landed November 5, 1995. The mission lasted 15 days and the Shuttle crew performed extensive microgravity science research during that time. The principal investigators for the mission submitted science reports of their research findings to the mission scientist for USML-2, and those reports were compiled into the USML-2 One Year Report. The purpose of the USML-2 One Year Report is to inform the microgravity science community and the public of the results of the experiments flown on the Shuttle mission.

The USML-2 One Year Report represents the culmination of many years of sustained effort on the part of the investigators, mission management, and support personnel, and is intended not only for the scientific community, but also for general public awareness and education. This mission gave the microgravity science community outstanding research opportunities not only to report and verify results obtained in previous flights, but to perform new experiments which contributed substantially and uniquely to the technological and commercial knowledge of the United States and its international partners. The results obtained and the lessons learned from this and future missions will lead us into a new era of microgravity research, to the Space Station and beyond.

The launch of the Space Shuttle *Columbia* with the USML-2 payload continued the legacy of one of NASA's most successful scientific mission series. Using the knowledge gained from the USML-1 mission, scientists were able to prepare and improve their investigations and experiments by enhancing procedures, refining operations, modifying hardware, and expanding methods for gathering data. The seven-member Shuttle crew performed the USML-2 experiments around the clock in order to maximize the science on orbit, and interacted with scientists on the ground for a perfect example of interactive science in a unique laboratory environment.

The USML-2 mission was dedicated entirely to microgravity research and included 37 investigations in materials science, fluid dynamics, combustion, biotechnology, and technology demonstrations supported by 11 facilities and 3 acceleration measurement systems. Along with investigations that previously flew on USML-1, several new experiment facilities flew on USML-2. The Advanced Protein Crystallization Facility (APCF) was the first facility to use three methods of protein crystal growth: liquid-liquid diffusion, dialysis, and vapor diffusion. The High Packed Digital Television (HI-PAC) Technical Demonstration gave scientists on Earth the ability to view multiple channels of real-time video and to monitor and change experiment parameters as needed. This improved the quality and quantity of downlinked data, thus enhancing science returns. Ground-to-Air Television was first used on the USML-2 mission and allowed the scientists on the ground and the Shuttle crew to talk with and see each other as they discussed science operations. The Geophysical Fluid Flow Cell (GFFC) experiment, which studied how fluids move

in microgravity, first flew on Spacelab-3 in 1985 and was extensively refurbished for this mission. The facilities that measured the microgravity environment added to the success of the mission by providing a complete picture of the Shuttle's acceleration environment and disturbances. The Orbital Acceleration Research Experiment (OARE) provided real-time acceleration data to the science teams. The Microgravity Acceleration Workstation (MAWS) operated closely with OARE, comparing the environment models produced by MAWS with the actual data gathered by OARE. Two other instruments, the Space Acceleration Measurement System (SAMS) and the Three-Dimensional Microgravity Accelerometer (3DMA), collected data throughout the mission. The data was then provided to the experimenters.

The Spacelab Glovebox (GBX) provided by the European Space Agency (ESA) offered investigators the capability to carry out experiments, test science procedures, and develop new technologies in microgravity. It enabled crew members to handle, transfer, and otherwise manipulate experiment hardware and materials in ways that would be impractical in the open Spacelab. In addition, the facility allowed a visual record of experiment operations by means of video and photographic systems. Many investigations benefited from increased crew involvement and video downlink. There were seven separate USML-2 investigations carried out in the Glovebox facility: two of these were in the materials science discipline, two were solution crystal growth investigations, two studied fluid dynamics, and one was a combustion investigation. Details on each are to be found elsewhere in this publication.

The investigations performed on USML-2 brought together a large number of researchers from government, academia, and private industry. Combining the strengths of these communities allowed for more extensive ground-based research, advanced research techniques, improved microgravity experimentation, and a wider distribution of the knowledge gained in the process.

Among the mission highlights and successes:

- The processing of cadmium zinc telluride in the Crystal Growth Furnace (CGF) demonstrated that crystals grown in space without touching the walls of their containers are of markedly higher quality than Earth-grown crystals. This is expected to promote the use of these crystals in critical electronic applications such as radiation detectors, sensors, etc.
- The GFFC experiment sought to better understand the flows in the oceans and atmospheres of planets and stars. The study showed "banded" rotational patterns of flows, like those seen in the atmosphere of Jupiter. These observations are expected to be of great importance in understanding weather patterns and climatic conditions on Earth.
- The protein crystal growth experiment was successful in obtaining antithrombin crystals. This protein, which controls blood coagulation in human plasma, is very difficult to grow in Earth-based laboratories. Its successful growth in space made it possible to further define its molecular model and understand how it works in the human body. This has important implications for medicine.

- In the Drop Physics Module (DPM), the influence of surfactants was examined. It was found that surfactants can change the hydrodynamics of droplets. The findings will lead to new and improved technologies in manufacturing cosmetics and synthetic drugs, in the recovery of oil, and in environmental clean-ups. The behavior of liquid drops was also studied in this facility. It was found that drops subjected to sound waves showed unusual rotation and oscillation patterns. Findings from this study promise improved technologies in the paint, pharmaceutical, and chemical processing industries and a better understanding of rain formation and weather patterns.

KEY USML-2 PERSONNEL

USML-2 Program Scientist: Mark Lee (NASA Headquarters)
 USML-2 Mission Scientist: Marcus Vlasse (NASA Marshall Space Flight Center)
 USML-2 Mission Manager: Paul Gilbert (NASA Marshall Space Flight Center)
 USML-2 Payload Operations Director: Bob Little (NASA Marshall Space Flight Center)
 USML-2 Project Scientist for APCF: Gottfried Wagner (University of Giessen, Germany)
 USML-2 Project Scientist for CGBA: Louis Stodieck (University of Colorado at Boulder)
 USML-2 Project Scientist for CGF: Martin Volz (NASA Marshall Space Flight Center)
 USML-2 Project Scientist for CPCG: Karen Moore (University of Alabama at Birmingham)
 USML-2 Project Scientist for DPM: Arvid Croonquist (Jet Propulsion Laboratory)
 USML-2 Project Scientist for GBX: Don Reiss (NASA Marshall Space Flight Center)
 USML-2 Project Scientist for GFFC: Fred Leslie (NASA Marshall Space Flight Center)
 USML-2 Project Scientist for PIMS: Roshanak Hakimzadeh (NASA Lewis Research Center)
 USML-2 Project Scientist for STDCE: Alex Pline (NASA Lewis Research Center)

EXPERIMENT I.

ORBITAL PROCESSING OF HIGH-QUALITY Zn-ALLOYED CdTe COMPOUND SEMICONDUCTORS

ACKNOWLEDGMENTS

We gratefully acknowledge financial support under NASA Contract NAS8-38147 and NASA Grant 431-0578A. Further, we acknowledge the following State University of New York at Stony Brook personnel: Dr. Jim Quinn, Dr. Lili Zheng, and Balaji Ragothamachar. We also thank Clarkson University personnel: Dr. John Moosebrugger, Dr. Tai-Pei, and Todd Stevens. We would also like to acknowledge technical contributions by Dr. Richard Matyi of the University of Wisconsin-Madison in conducting TPS studies. Finally, we would like to acknowledge the contributions of Andre Berghmans, Dr. Robert Silberstein and Dr. Louis Casagrande of the Northrop Grumman Advanced Technology Development Center for significant contributions to this effort.

EXPERIMENT I. ORBITAL PROCESSING OF HIGH-QUALITY Zn-ALLOYED CdTe COMPOUND SEMICONDUCTORS

D. J. Larson, Jr., and M. Dudley
Materials Science & Engineering Department
State University of New York at Stony Brook
Stony Brook, NY 11794-2275

J.I.D. Alexander*
Center for Microgravity and Materials Research
University of Alabama in Huntsville, Huntsville, AL

F.M. Carlson
Dept. of Mechanical and Industrial Engineering
Clarkson University, Potsdam, NY

D. Gillies
NASA Marshall Space Flight Center
Huntsville, AL

D. DiMarzio
Northrop Grumman Corporation
Bethpage, NY

ABSTRACT

Zinc-alloyed cadmium telluride (Zn:CdTe) crystals were grown in unit gravity and in microgravity for comparative analysis. Two crystals were grown on USML-1/STS-50 in 1992, and two additional crystals were grown on USML-2/STS-73 in 1995. The Crystal Growth Furnace (CGF) in the seeded Bridgman-Stockbarger crystal growth geometry was utilized on both missions. Crystals grown on USML-1/STS-50 were found to have solidified with partial wall contact due to the near-absence of the hydrostatic pressure in microgravity, a residual g-vector that was not axial, and the nonwetting sample/ampoule wetting conditions. Crystals grown on USML-2/STS-73 included: a sample/ampoule identical to the USML-1/STS-73 sample/ampoule, with the addition of a restraining spring to simulate hydrostatic pressure internally, and a tapered ampoule which accomplished 2.2 cm of crystal growth without wall contact.

Infrared transmission of all ground and flight samples was found to be 63–66 percent, very close to the theoretical 66 percent, suggesting good stoichiometric control. Infrared microscopy confirmed that the primary precipitates were Te and their size (1–10 μm) and density suggested that the flight- and ground-base samples experienced similar thermal histories.

* Current address: Department of Mechanical and Aerospace Engineering, Case Western Reserve University, Cleveland, OH

Longitudinal macrosegregation, calculated using scaling analysis, was predicted to be low. Nearly diffusion controlled growth was achieved even in unit gravity and macrosegregation data could be fit with a diffusion controlled model. Radial segregation was monitored and was found to vary with fraction solidified, particularly through the shoulder region, where the sample cross section was varying significantly. It was also disturbed in the flight samples in regions where asymmetric wall contact was noted. In regions where a steady state was established, the radial segregation was invariant within our experimental measurement error.

Flight samples were found to be much higher in structural perfection than samples processed in unit gravity under identical growth conditions. In regions where solidification had occurred without wall contact, the free surfaces evidenced virtually no twinning, although twins appeared in the flight samples in regions of wall contact and were pervasive in the ground samples. These results were confirmed using optical microscopy and synchrotron x-ray white beam topography. Full-width half-maximum rocking curve widths (FWHM), recorded in arc-seconds, were significantly reduced from 20 a-s (1 g) to 9 a-s (μ g) for the best regions of the crystals. The 9 a-s (FWHM) rocking curve value in the unconfined flight samples equals the best value reported terrestrially for this material.

The ground samples exhibited a fully developed (111)[110] dislocation mosaic structure, whereas dislocations within the flight samples were discrete and no mosaic structure was evident. The defect density was quantitatively reduced from 75,000 (1 g) to 800 (μ g) \pm 50 percent. Dislocation etch pit density results were confirmed using transmission synchrotron white beam and monochromated beam topography. The low defect density is thought to have resulted from the near absence of hydrostatic pressure, which allowed the molten boule to solidify with little or no wall contact. This minimized the transfer of hoop stresses during solidification and post-solidification processing.

1. INTRODUCTION

Zn:CdTe is a technologically important member of the family of II-VI compound semiconductors. The most important application of Zn:CdTe is as a lattice-matched substrate for the epitaxial growth of mercury cadmium telluride (HgCdTe) infrared detectors. The requirements for large-area infrared devices have led to increased reliance on epitaxial processes to provide detector-grade material and a concomitant demand for high quality substrates. These substrates are typically grown using modified Bridgman crystal growth techniques.

HgCdTe epilayers are most frequently fabricated using liquid phase epitaxy (LPE). To achieve abrupt device/substrate junctions, however, epitaxial growth of HgCdTe has been driven to lower temperatures using chemical vapor deposition or molecular beam epitaxy techniques. These techniques minimize interdiffusion because they occur at lower temperatures than LPE, but they are much more sensitive to substrate quality, particularly surface quality. In addition, fast diffusion of Hg along dislocation cores has resulted in demands for minimization of extended defects in the substrates as these extended defects are likely to project from the substrate into the epilayer.

It is desirable to lattice-match the substrate and the epitaxial layer at the growth temperature, in order to minimize interfacial strains and dislocation generation, propagation, and/or multiplication at the interface. The lattice-matching substrate of choice is Zn:CdTe. The primary needs for these Zn:CdTe

applications are, therefore, 1) increased structural perfection (reduced defect density) within the bulk crystals and substrates, and 2) uniform lattice parameters (chemical homogeneity) within the substrates, which better match those of the specific HgCdTe composition at the epitaxial growth temperature.

The research objective was thus to investigate the influences of gravitationally-dependent phenomena (hydrostatic and buoyant) on the growth and quality of Zn:CdTe crystals. It was hypothesized that damping gravitationally-dependent buoyancy convection, by processing in microgravity, would substantially enhance chemical homogeneity. Further, it was hypothesized that the near-elimination of hydrostatic pressure would result in a significant reduction in defect density (twins and dislocations) by reducing the thermomechanical stresses experienced in microgravity by the growing and cooling crystals. Microgravity processing thus offered a unique opportunity to advance toward the applications goal of greatly increased structural perfection within bulk crystals of increased chemical homogeneity.

The empirical effort included the development of a unit gravity baseline for quantitative comparison with the microgravity results. This empirical effort was supported by the development of high-fidelity process models of heat transfer, fluid flow and solute redistribution, g-sensitivity, and thermomechanical stress occurring in the sample throughout the melting, solidification, and post-solidification processing. The models were initially used to predict the impact of process and mission parameter variation, supporting the design of critical unit gravity and microgravity experiments. As the models were empiricized, correlation and optimization experiments were conducted. Finally, the models were utilized as a critical element in the interpretation of the flight results and the quantitative comparison of the unit gravity and microgravity results.

2. EXPERIMENTAL TECHNIQUE

The USML-1 and USML-2 samples were processed in the CGF using the seeded Bridgman-Stockbarger method of crystal growth. Bridgman-Stockbarger crystal growth is accomplished by establishing isothermal hot zone (1175 °C) and cold zone (980 °C) temperatures with a uniform thermal gradient (35 °C/cm) in between. After sample insertion, the entire furnace was ramped to the 980 °C cold end temperature "isothermally." The hot zone was subsequently ramped to the 1175 °C hot end temperature, establishing the thermal gradient and melting the bulk of the sample. The furnace was then moved further back on the sample, causing the melt to come in contact with the seed, partially melting the seed crystal and seeding the melt. The seed crystal prescribes the growth orientation of the crystal grown. Having seeded the melt, the furnace is thermally equilibrated, the translation is reversed and the sample is directionally solidified at a constant velocity (1.6 mm/hr) by moving the furnace and thermal gradient down the length of the stationary sample, ampoule, and safety cartridge.

The samples were characterized and the results were quantitatively compared with respect to chemical homogeneity, infrared transmission and structural perfection. Program results were also quantitatively compared with the best results accomplished terrestrially as an external comparison. All samples were double sided chemomechanically polished using a dilute Bromine-Methanol solution.¹

The chemical characterization of samples included: energy dispersive x-ray analysis (EDX), microprobe, and photoreflectance (PR). Electronic characterization included Fourier Transform Infra-Red (FTIR) analysis. Microstructural analysis includes stereo, optical and infrared microscopy. Chemical

etching techniques were used to reveal defect structure and polarity. X-ray structural characterization techniques employed in this study included double crystal rocking curve (DCRC), triple crystal spectroscopy (TCS), precision lattice parameter (PLP), synchrotron white beam topography (SWBT) and synchrotron monochromatic beam topography (SMBT). DCRC, TCS, and PLP measurements were made at the Northrop Grumman Advanced Technology Development Center; additional TCS measurements were made at the University of Wisconsin-Madison, and both the SWBT and SMBT were performed at the National Synchrotron Light Source (NSLS) at Brookhaven National Laboratory (BNL).

3. EXPERIMENTAL PLAN

3.1 Ground

Ground based qualification and developmental tests were conducted in the CGF Ground Control Experiments Laboratory (GCEL) to validate hardware designs for the sample/ampoule, ampoule/cartridge, and the interfaces between these components and instrumentation within the sample/ampoule cartridge assembly (SACA). In addition, timeline compatibility between the entire series of experiments run in series on the CGF on USML-2 was confirmed by an all-up test. Lastly, the test results served to empiricize the process models and optimized the processing parameters for the flight experiment. Figure 1 (a and b) shows the USML-2 ampoule designs. The ampoule design used for the USML-1 flight is essentially the same as that shown in figure 1a, except for the absence of the internal retaining piston and spring.²

The final CGF ground samples, grown under the optimized process conditions, duplicated the anticipated flight conditions and served as "ground truth" samples for quantitative comparison with the flight samples. Since we were fortunate to have the opportunity to run the second (tapered) ampoule, the "ground truth" experiment for this sample was conducted postflight.

3.2 Flight

The USML-2 and USML-1 missions were planned to process one primary sample, with a backup sample available for processing, time permitting. In each case the second flight experiment was successfully conducted, but with a shorter experiment duration. The furnace heat-up profiles and rates, seeding thermal equilibration time, crystal growth thermal profile, and cooling profiles were the same in all experiments. The only difference was the duration of the experiments and therefore the percentage of sample that experienced Bridgman-Stockbarger crystal growth. The secondary samples on both missions were shorter in duration and solidified a larger proportion of the sample under non-plane front growth conditions, initially gradient freeze and subsequently radial cooling. The secondary samples further confirmed the successful seeding technique, {111}B facing the melt, tested the tapered ampoule geometry, and offered additional unique flight material for analysis.

Four crystals were grown in microgravity using the CGF. Two crystals were grown on USML-1/STS-50 in 1992, and two additional crystals were processed on USML-2/STS-73 in 1995. Three of the above crystals were grown using a standard Bridgman-Stockbarger seeded growth configuration. The fourth sample was processed on USML-2 in an identical thermal environment, but the ampoule was designed to maximize the volume of material which solidified without wall contact between the solidifying crystal and the growth ampoule. The latter experiment could only be attempted in microgravity where there is a near-absence of hydrostatic pressure on the bulk liquid.

The temperature/time/position history of the optimized experiment is shown in figure 2. The heat-up rate ($2\text{ }^{\circ}\text{C/min}$), thermal equilibration time (2 hr), solidification velocity (1.6 mm/hr), thermal gradient ($35\text{ }^{\circ}\text{C/cm}$), and cooling rates ($2\text{ }^{\circ}\text{C/min}$), were determined to give the best quality crystals consistent with the available flight time and performance characteristics of the CGF.

4. EXPERIMENTAL RESULTS

Surface evaluation of the USML-1 experiment samples demonstrated that, in the near-absence of hydrostatic pressure, non-wetting liquids separated from the ampoule walls and solidified depending on influences including: volumetric fill-factor, level of constraint, residual g-vector, ampoule geometry and growth conditions. The crystals grown on USML-1 are described fully in reference 2. The USML-2 crystal grown in this geometry, with the addition of a restraining piston and springs, conformed to the ampoule geometry shown as figure 1a. The tapered sample processed on the ground grew a good single crystal which conformed to the ampoule geometry, as shown in figure 3a. The flight sample, however, assumed a far different configuration, which is shown as figure 3b. The region of reduced cross section is entirely single crystalline.

Surface analysis of the tapered flight sample showed that 2.2 cm of material solidified totally without wall contact, and an additional 2.8 cm of crystal solidified with partial (almost total) wall contact. The acceleration of the interface at the onset of furnace cooling froze in a sizeable void, as we had previously noted in the USML-1 samples. Glancing angle x-ray synchrotron topographic analysis of this sample confirmed the absence of twinning in the region without wall contact and the reappearance of twinning as wall contact was reestablished. This is shown in figure 4.

The combined USML-1/USML-2 experimental matrix showed conclusively that wall contact in unit gravity or microgravity served to nucleate numerous twins, and the absence of wall contact in the flight samples virtually eliminated this pervasive defect. This exciting result should be further pursued, since twinning is little understood and its pervasive and deleterious nature is very costly terrestrially.

Surface evaluation of the USML-1/USML-2 cylindrical flight samples revealed surface bubbles that offered some unusual features. Bubbles formed during the directional solidification stages of growth showed a bright metallic surface on the hot side of the bubble and a dull matte finish on the cold side. This was perceived as evidence for vapor transport across the bubble site, after solidification. Bubbles from the radially cooled region of the flight samples evidenced only bright surfaces, with no transport in evidence. This was assumed to be the result of the short time that these bubble sites remained at high temperatures after solidification. Lastly, these bubble sites each revealed a surface facet (in the single crystal regions) or facets (in the polycrystalline regions where more than one grain penetrated the bubble surface). A typical facet is shown as figure 5, and was confirmed by microbeam x-ray analysis to be a $\{111\}$ reflecting plane. This was true of all facets studied. It may be seen that the facet is restricted to a limited angular regime longitudinally and circumferentially, resulting in an oval or circular projected area. This may prove to be the equivalent of the angular relationships that prescribe facet and patch twin formation³ except that the radius of curvature circumferentially is negative, which is not considered in the theory.

Thermal modelling of the USML-1 flight samples suggested that the radial thermal gradient experienced by the flight samples due to the partial loss of wall contact was small, on the order of $3.5\text{ }^{\circ}\text{C/cm}$ in

the vicinity of the solidification temperature. Corresponding predictions of thermomechanical stress suggested that in the absence of stiction at the sample/ampoule wall interface, all stresses should be below the critical resolved shear stress required for plastic deformation. The presence of stiction was predicted to introduce plastic deformation at the sample/wall interface. Plastic deformation in the form of slip bands and dislocations was documented adjacent to the sample/wall interface using x-ray synchrotron topography and etch pit studies, respectively. The defect density diminished as the distance from the wall contact increased, approaching a minimum value at the free surfaces. Residual strain was also imaged and mapped using appropriate x-ray techniques. It was concluded that stiction was present at the sample/ampoule wall interface in these experiments. These results are presented in more detail in reference 2.

DCRC mapping of the wafered samples showed that in the regions grown entirely without wall contact, the full width half maximum (FWHM) rocking curve widths were on the order of 9 arc seconds. This documents a very low level of residual strain, equal to, or better than, the best material grown terrestrially. Further, the precise Gaussian rocking curve fit in the tails of the curves suggested ideally perfect x-ray behavior rather than the commonly experienced ideally imperfect behavior. This suggested the possibility of dynamic x-ray diffraction rather than kinematic diffraction. This possibility was evaluated by transmission SWBT and SMBT. Both techniques imaged highly perfect material, with a low dislocation density and a discrete network of dislocations. Transmission topography using SMBT was not possible in the ground samples and only possible in the best regions of the flight samples, as shown in figure 6. This suggests a lower lattice strain in the flight samples than in the ground samples, confirming the quantitative DCRC results.

The samples were finally exposed to a dislocation etchant and the typical ground and flight dislocation distributions, at the same magnification, are shown as figures 7a (1 g) and figure 7b (μg), respectively. The ground sample showed occasional twinning (straight lines crossing the image) as well as a fully developed dislocation mosaic structure. The flight sample, on the other hand, showed virtually no twins and only discrete dislocations. Quantitatively, the (111)[110] dislocation density is reduced from 800,000 (1 g) to 800 (μg) \pm 50 percent, totally eliminating the cellular (mosaic) structure typical of terrestrial material.

Subsequent evaluation using x-ray triple crystal spectroscopy was undertaken as a further test of the crystal quality and dislocation distribution. The result of this investigation is shown as figure 8. It may be seen that there is a pronounced dynamic diffraction "trunk" that projects vertically, confirming the high crystalline quality (low lattice strain) of the flight material. Further, the limited lateral spreading (mechanical strain) of the data suggests that the dislocations present are uniformly distributed, limited in number and discrete, confirming the microstructural studies.

5. CONCLUSIONS

It was found that in the absence of hydrostatic pressure the liquid separated from the ampoule walls, depending on influences including volumetric fill-factor, level of constraint, residual g-vector, ampoule geometry and growth conditions. The chemical macrosegregation was modest, even on the ground, and diffusion controlled growth was achieved in the flight samples. Radial segregation was within the measurement error, except in regions of geometrical and/or thermal asymmetry.

Regions solidified without wall contact were found to virtually eliminate twinning, suggesting that these pervasive defects are surface nucleated. Further, these regions showed dramatic reductions in (111)[110] dislocation density, from 800,000 (1 g) to 800 (μg) epd \pm 50 percent, resulting from thermomechanical stress reduction within the flight samples grown without wall contact. Regions of partial wall contact showed defect gradients, with high densities on the wall side and low densities on the free surface side. These results are consistent with our high-fidelity thermal and thermomechanical stress models. Additional experiments with respect to twinning and defect reduction are strongly supported by these observations.

REFERENCES

1. Casagrande, L.G.; Larson, D.J. Jr.; DiMarzio, D.; Wu, J.; and Dudley, M.: "*The Growth and Comparison of Large-Diameter, Vertical Bridgman CdZnTe and CdTe,*" J. Crystal Growth, 137, 195-200, 1994
2. NASA Conference Publication 3272, Vol. 1, "Joint Launch + One Year Science Review of USML-1 and USMP-1 with the Microgravity Measurement Group," edited by N. Ramachandran, D.O. Frazier, S.L. Lehoczky, and C.R. Baugher, May 1994.
3. Hurle, D.T.J.: *Journal of Crystal Growth*, 147, 239, 1995.



(a)



(b)

Figure 1. USML-2 Ampoule configurations: (a) cylindrical with liquid constraint; and (b) tapered to maximize growth without wall contact.

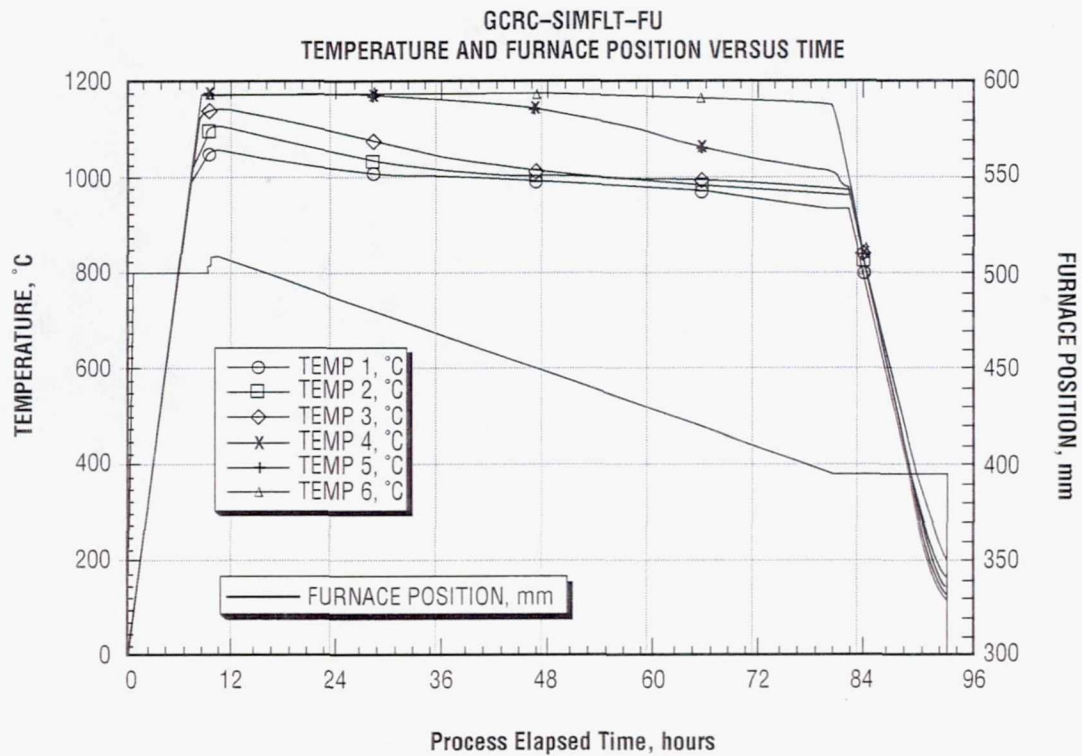


Figure 2. Typical temperature/time/position of the optimized USML-2 primary flight experiment.



(a)



(b)

Figure 3. USML-2 tapered sample configuration after crystal growth: (a) unit gravity; and (b) microgravity

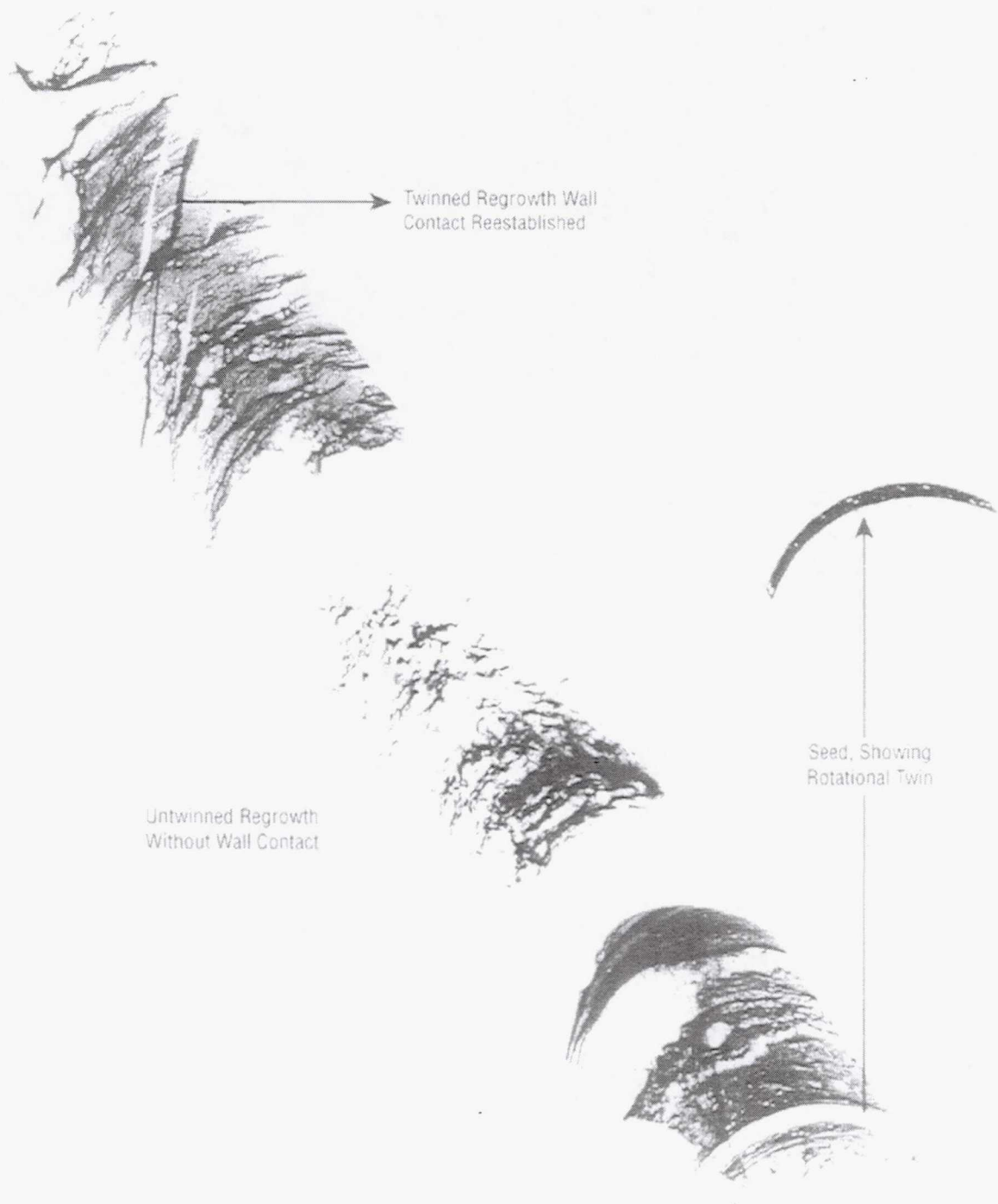


Figure 4. USML-2 SWBT of the tapered microgravity sample surface showing the absence of twins in the region solidified without wall contact and the reappearance of twinning as wall contact is reestablished

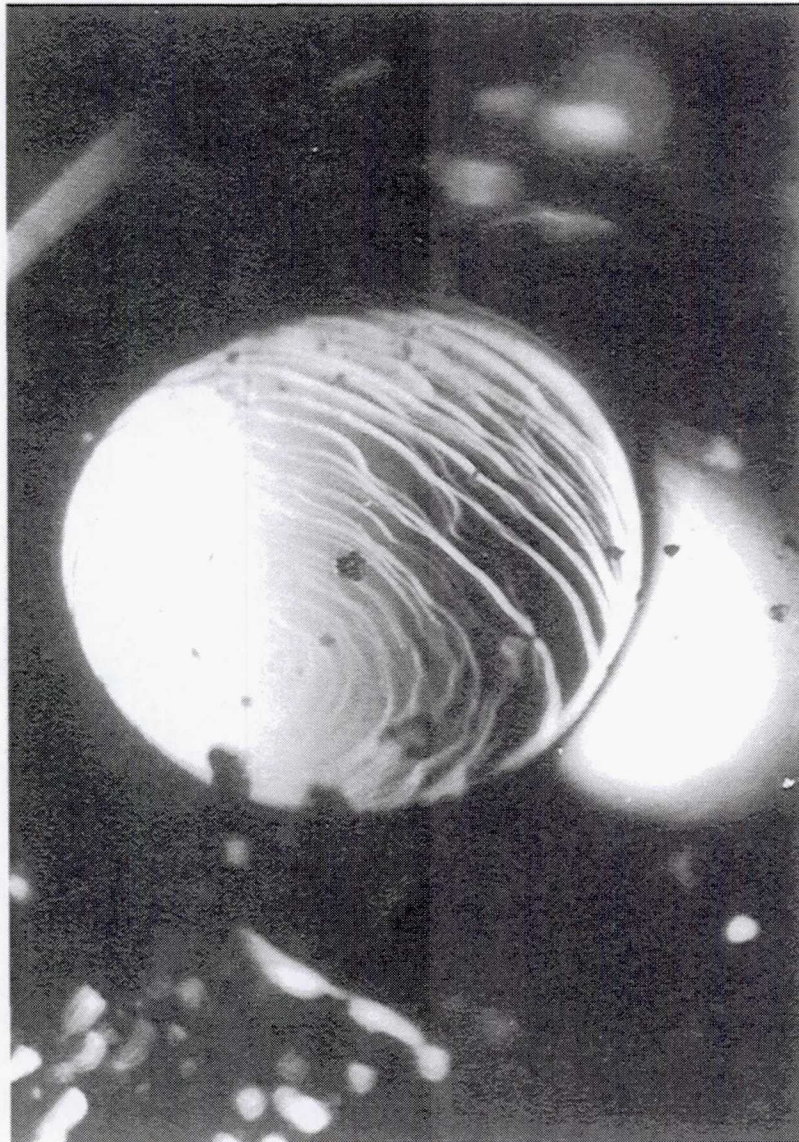


Figure 5. Typical $\{111\}$ facet at bubble surface on surface of USML-2 cylindrical microgravity sample.

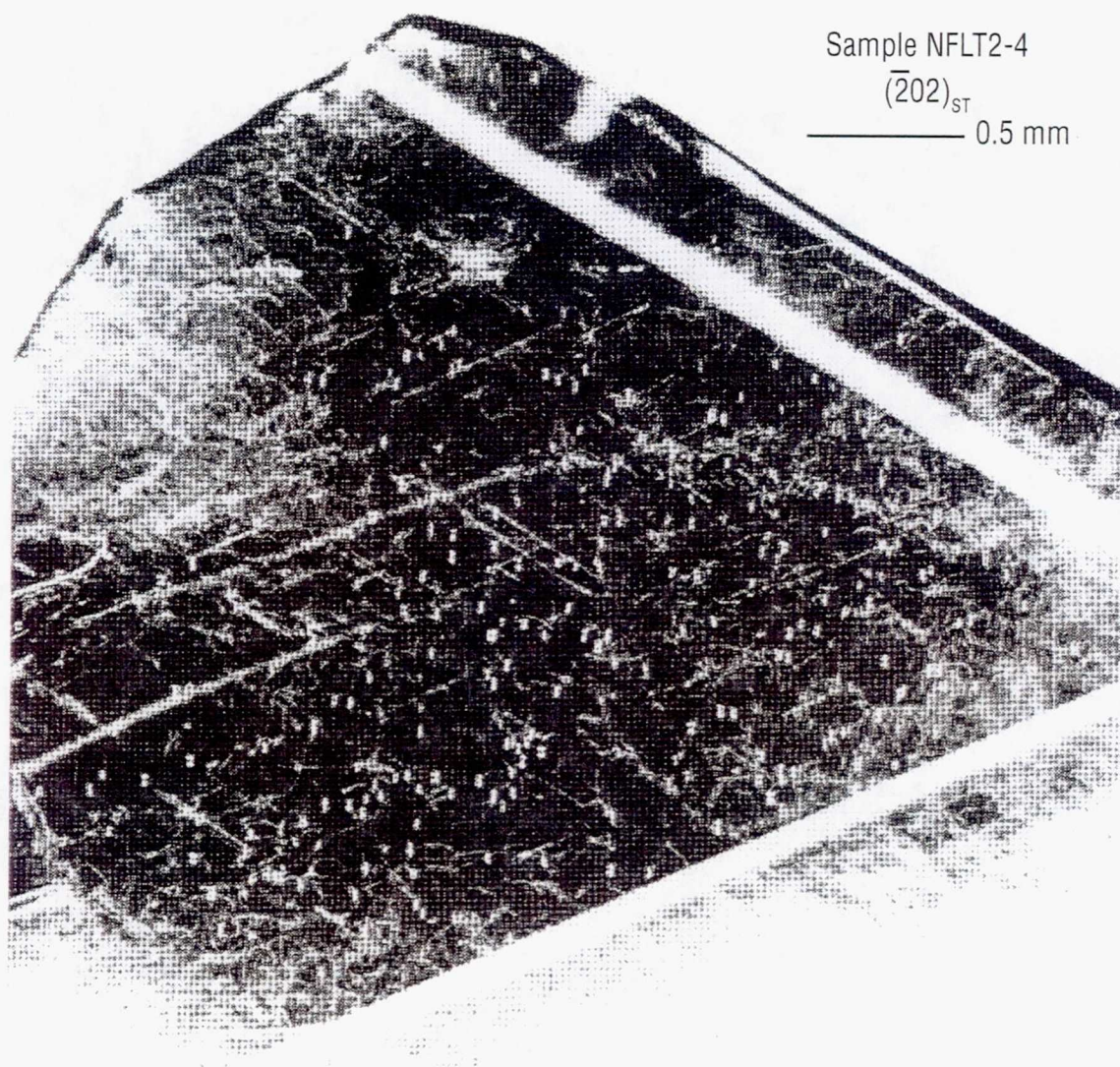


Figure 6. Transmission SMT showing dislocation structure within USML-1 microgravity sample.

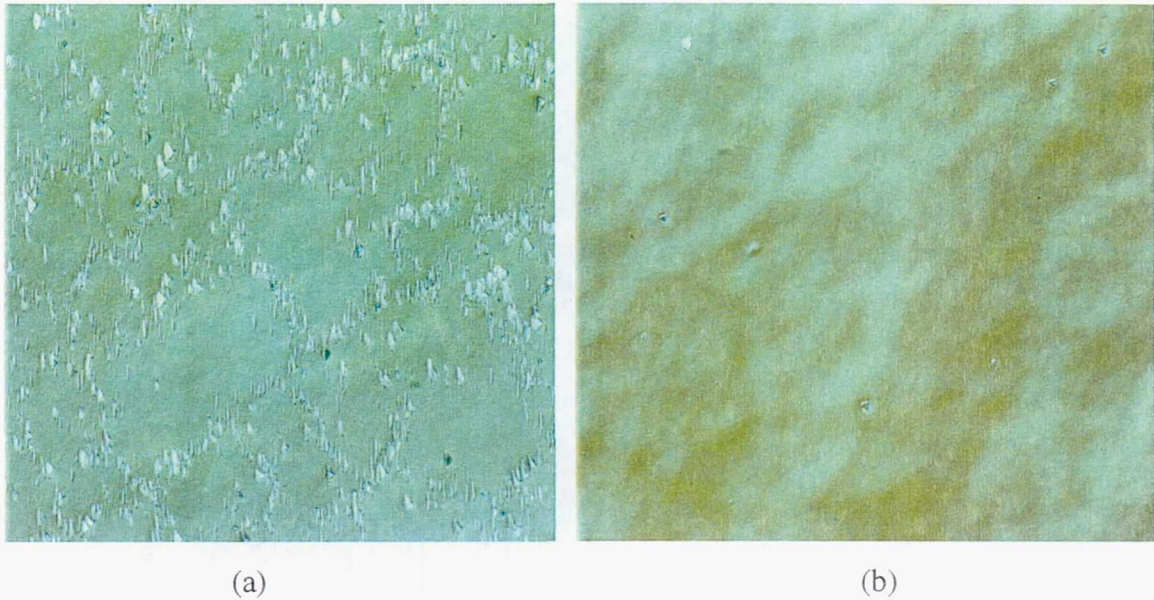


Figure 7. Defect structures typical of USML-1 unit gravity: (a) and microgravity; and (b) samples (original magnification $\times 200$).

- Long-range strain fields from dislocations give rise to diffusely scattered intensity at distances close to a Bragg reflection
- High resolution triple axis diffraction permits the separation of the (kinematic) diffuse scattering due to defects from the (dynamic) perfect crystal bulk diffraction
- Analysis of the 333 reflection from CdZnTe grown on USML-1 shows a roughly symmetric pattern of diffuse intensity, indicating an isotropic distribution of dislocations in the diffracting volume
- Presence of a well-defined crystal truncation rod (or "surface streak") independently indicates a high degree of structural order in the bulk crystal and excellent surface preparation
- No major qualitative differences observed in reciprocal space maps obtained across the wafer, indicating excellent uniformity in CdZnTe grown in microgravity
- High resolution diffraction analysis suggests overall high quality USML-1 CdZnTe

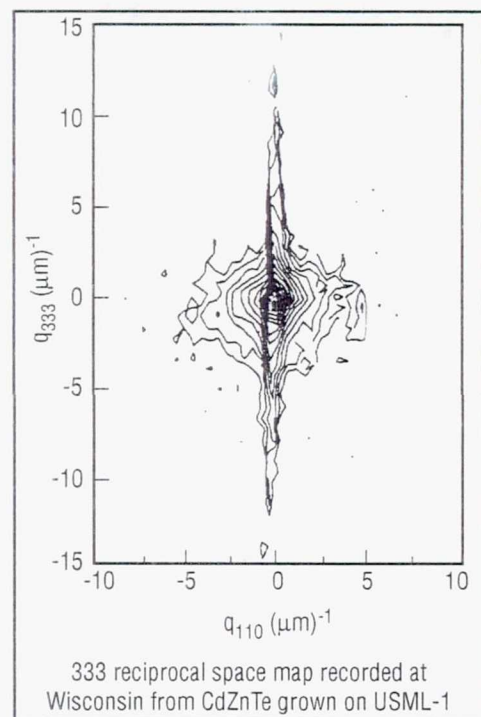


Figure 8. X-ray triple crystal spectrograph of USML-1 flight sample showing low lattice strain and low mechanical strain in the microgravity sample.

EXPERIMENT II.

**VAPOR TRANSPORT CRYSTAL GROWTH OF MERCURY CADMIUM
TELLURIDE IN MICROGRAVITY—USML-2**

ACKNOWLEDGMENTS

The authors would like to thank the astronauts and payload specialists of the USML-2 mission for the performance of the space experiments. We are pleased to acknowledge the support of this work by the National Aeronautics and Space Administration through the Microgravity Science and Applications Division, Washington, DC, and through the Experiments Development Office, George C. Marshall Space Flight Center, Huntsville, Alabama. We would like to thank the technical staff and project officials at MSFC for their valuable support throughout this endeavor, and Drs. M. Volz and Y.G. Sha of the Space Sciences Laboratory for their help with the IR mapping. We would also like to thank Dr. D. Di Marzio of Grumman Corporate Research Center for his help with the rocking curve measurements.

EXPERIMENT II. VAPOR TRANSPORT CRYSTAL GROWTH OF MERCURY CADMIUM TELLURIDE IN MICROGRAVITY—USML-2

H. Wiedemeier, Y.R. Ge, and M.A. Hutchins*

Department of Chemistry
Rensselaer Polytechnic Institute
Troy, NY 12180-3590
Phone: 518-276-8444
Fax: 518-276-8554
E-mail: wiedeh@rpi.edu

ABSTRACT

The new epitaxial growth experiments of $\text{Hg}_{1-x}\text{Cd}_x\text{Te}$ on (100) CdTe substrates by chemical vapor transport (CVT), using HgI_2 as a transport agent, were performed in the transient growth regime of this ternary, heteroepitaxial system at normal and reduced gravity during the USML-2 flight. The surface and interface morphology, the compositional and structural uniformity, and carrier mobility of the epitaxial layer and islands grown in microgravity are measurably improved relative to ground specimens. These observations demonstrate the effects of convective flow on the transport, deposition, and growth processes of this solid-vapor system even in the transient growth regime. The properties of the $\text{Hg}_{1-x}\text{Cd}_x\text{Te}$ layer grown in a microgravity environment compare quite favorably to those of layers obtained by other techniques.

1. INTRODUCTION

The mercury-cadmium-telluride ($\text{Hg}_{1-x}\text{Cd}_x\text{Te}$) alloy system is currently one of the most important semiconductors for infrared devices because its band gap can be varied to cover the entire spectrum from 0.8 to over 30 μm by changing the alloy composition.¹ Various methods have been used to grow single crystals of these compounds.^{2,3} A major problem of the melt growth of $\text{Hg}_{1-x}\text{Cd}_x\text{Te}$ crystals is the high equilibrium pressure of Hg(g) , exceeding 15 atm at the melting temperature of $\text{Hg}_{0.8}\text{Cd}_{0.2}\text{Te}$ ($\sim 700^\circ\text{C}$).⁴ The corresponding partial pressures of Cd(g) and of $\text{Te}_2\text{(g)}$ are several orders of magnitude lower than that of Hg(g) at temperatures between about 500°C and the melting point.⁴ In addition to the effects of natural convection, melt growth of this material is influenced by segregation problems. The drastic differences in partial pressures of the constituent elements would require separate source reservoirs and complex instrumentation for $\text{Hg}_{1-x}\text{Cd}_x\text{Te}$ growth by sublimation techniques. Other methods such as Molecular Beam Epitaxy (MBE), Molecular Chemical Vapor Deposition (MOCVD), and Liquid Phase Epitaxy (LPE) require also rather complex facilities.

Chemical vapor transport (CVT), using mercuric iodide (HgI_2) as a transport agent, is presently the only method which offers the advantage of growing single crystals of $\text{Hg}_{1-x}\text{Cd}_x\text{Te}$ at relatively low temperatures (below 550°C) employing a single source material of predetermined composition. In addition,

*Current address: Lockheed Martin IR Imaging Systems, 2 Forbes Road, Lexington, MA 02173

the use of a closed ampoule eliminates *a priori* forced convection. The chemical reactions^{5, 6} of the $\text{Hg}_{1-x}\text{Cd}_x\text{Te-HgI}_2$ system, the mass transport rates⁵⁻⁸, the composition of the grown $\text{Hg}_{1-x}\text{Cd}_x\text{Te}$ crystals⁹, as well as the growth of bulk crystals⁵ and epitaxial layers^{10, 11} by the CVT method, have been studied in our laboratory. The earlier investigations demonstrated the effects of gravity-driven convection on the mass flux of this system, and revealed the influences of even small convective contributions on the chemical and structural microhomogeneity of the grown crystals.⁵ The earlier exploratory studies showed the feasibility of the CVT technique for the epitaxial growth of $\text{Hg}_{1-x}\text{Cd}_x\text{Te}$ on CdTe substrates.^{10, 11} Further studies showed the effects of growth temperature and of transport agent (HgI_2) pressure on the layer morphology and composition for different substrate orientations.¹² Epitaxial growth of $\text{Hg}_{1-x}\text{Cd}_x\text{Te}$ on (100) CdTe yields smoother surfaces, which are desirable for device fabrication. The desired epilayer composition can be obtained by properly adjusting the source composition, the growth temperature, and the HgI_2 transport agent pressure.¹³

The above investigations demonstrate that bulk crystals and epitaxial layers of $\text{Hg}_{1-x}\text{Cd}_x\text{Te}$ can be grown by chemical vapor transport in closed ampoules. They also indicate the sensitivity of this vapor transport system to possibly even minute convective flow under vertical, stabilizing conditions. Our earlier mass transport and crystal growth experiments of binary Ge-chalcogenides in microgravity employing the chemical^{14, 15} and physical^{16, 17} vapor transport methods demonstrated, for the first time, the feasibility of these techniques for space flight experiments. The observation of unexpectedly greater mass transport rates under CVT conditions^{14, 15} than estimated for microgravity provided new insight into the transport phenomena of these complex multicomponent, multireaction systems.¹⁸ In all cases,¹⁴⁻¹⁷ larger single crystals of improved crystallinity were grown in microgravity.

Based on the above investigations of metal-chalcogenides on ground and in microgravity, epitaxial growth experiments of $\text{Hg}_{1-x}\text{Cd}_x\text{Te}$ on (100) CdTe using the CVT method were conducted on ground and during the USML-1 flight.¹⁹ The results of these earlier experiments¹⁹ demonstrated considerably improved morphology of the as-grown surfaces, compositional homogeneity, single crystallinity, and carrier mobility of the epitaxial layers grown in microgravity relative to layers grown on ground. In particular, the (011) cross sections of the $\text{Hg}_{1-x}\text{Cd}_x\text{Te}/(100)$ CdTe structure showed that the substrate-layer interfaces obtained in microgravity¹⁹ had significantly lower etch pit densities than those of ground-control¹⁹ and of other, independently grown samples.²⁰ Relative to the ground samples, there is an almost "seamless" transition from the substrates to the epitaxial layers grown in microgravity.¹⁹ These differences demonstrate the effects of convective flow on the transport and deposition processes of this solid-vapor transport system under steady-state growth conditions. The improved interface morphology suggests that the effects of inherent lattice mismatch, of other substrate, and of growth defects on the interface and layer morphology are enhanced by gravity-driven convective flow.

Because of the importance of the interface structure for layer growth, detailed investigations of the growth properties of $\text{Hg}_{1-x}\text{Cd}_x\text{Te}$ islands²¹ and films²² on (100) CdTe substrates were performed in our laboratory. The prolonged growth of individual islands and their properties could, in part, be related to the defect structure of the CdTe substrates.²¹ The morphological evolution of $\text{Hg}_{1-x}\text{Cd}_x\text{Te}$ films²² and the transition from three-dimensional islands to two-dimensional layers are consistent with the Stranski-Krastanov growth mode. The observations of these studies²⁰⁻²² demonstrate that the morphology, dislocation density, growth rate, and compositional uniformity of the epitaxial layers, islands, and growth interfaces are time dependent in the transient growth regime of this $\text{Hg}_{1-x}\text{Cd}_x\text{Te}/(100)$ CdTe heterojunction

system. As indicated above, the morphology of the growth interfaces observed during these studies²⁰⁻²² is distinctly different from that obtained under microgravity conditions.¹⁹ In order to further explore the relationship between convective flow and transport processes at or near the growth interface, new growth experiments of $\text{Hg}_{1-x}\text{Cd}_x\text{Te}$ on (100) CdTe using the CVT method were performed during the second flight of the United States Microgravity Laboratory (USML-2).

The present work is concerned with the development, performance, and evaluation of the new microgravity experiments. The primary focus of the USML-2 experiments is on the observation and measurement of any microgravity effects on the uniformity of $\text{Hg}_{1-x}\text{Cd}_x\text{Te}$ epitaxial growth under transient growth conditions, during which the compositional and structural properties of this material change with growth time. The USML-1¹⁹ experimental conditions were well within the steady-state regime. The development of the USML-2 growth conditions in terms of film thickness and characterization were supported by the above ground-based studies.²⁰⁻²²

2. EXPERIMENTAL PROCEDURES

2.1 Materials Synthesis

The composition of the $\text{Hg}_{1-x}\text{Cd}_x\text{Te}$ source material, the pressure of the HgI_2 transport agent, and the temperature profile were selected to optimize the growth conditions for the flight experiments and to maintain continuity with the USML-1 experiments. Based on the earlier studies,^{12, 13, 19} a source composition of $\text{Hg}_{0.4}\text{Cd}_{0.6}\text{Te}$, a HgI_2 pressure of about 0.01 atm, and source and growth temperatures of about 595 °C and 545 °C, respectively, were preselected. The synthesis of $\text{Hg}_{0.4}\text{Cd}_{0.6}\text{Te}$ and the purification of the chemical transport agent HgI_2 are described earlier.¹³

Commercially available CdTe single crystal wafers ($\rho=80-100 \text{ W}\cdot\text{cm}$) of (100) orientation were used as substrates for the epitaxial growth. The substrates were about 1.5-mm thick and 14.5 mm in diameter. The growth sides were chemically polished by the supplier, and chemically etched immediately before loading in this laboratory.

2.2 Ampoule Design and Preparation

The detailed description of the design, preparation, loading, and sealing of the double-ampoule-sample assembly used for the epitaxial growth experiments has been discussed previously.¹²

2.3 Growth Conditions

The transient growth experiments in our laboratory were performed in a vertical, stabilizing orientation, i.e., the density gradient vector is parallel to the gravity vector (hot on top). The growth furnace, the temperature profile along the ampoule, and the experimental procedures were discussed earlier.^{12, 13} For the ground control (GCEL) and microgravity experiments, the ampoule-sample assembly was enclosed in a metal cartridge, and instrumented with six K-type thermocouples along the outside wall of the ampoule at the source, substrate, and intermediate locations. The GCEL experiments were performed in the same crystal growth furnace, under the same conditions as discussed earlier.¹⁹ For the GCEL tests, experiments in our laboratory, and flight experiments in the CGF, about 1 gram $\text{Hg}_{0.4}\text{Cd}_{0.6}\text{Te}$ source material and

0.01 atm HgI_2 (at growth temperature) were used. To improve the thermal conductivity, a 0.7-mm-thick polished sapphire disc was placed between the substrate and the flat end of the ampoule. The nominal source and growth temperatures were 595 °C and 545 °C, respectively, and the growth times for the flight experiments (RPI2-1 and RPI2-2) were 2.5 and 1.5 hours, respectively. At the beginning of the growth period of the first flight sample (RPI2-1, 2.5 hours), an unprogrammed drop in the growth temperature of about 5–7 °C occurred. This was corrected within about 7 minutes, whereupon the experiment proceeded normally. The mechanical and structural integrity and the proper location of the thermocouples of the ampoule-cartridge assembly were confirmed before and after the GCEL and flight experiments by x-ray transmission photographs.

2.4 Characterization

In accordance with the earlier ground^{12, 13, 20–22} and space¹⁹ experiments, the GCEL and flight samples were characterized using optical and scanning electron microscopy (SEM), x-ray diffraction Laue, WDS, chemical etching techniques, IR surface mapping, x-ray diffraction rocking curves, and electrical measurements. For a comparative analysis, typical results of the ground control experiments are compared with the epitaxial layer and islands grown under microgravity conditions.

3. OBJECTIVES OF THE USML-2 EXPERIMENTS

The primary objectives of the USML-2 experiments were to observe microgravity effects on the epitaxial growth at an early state. This was not possible during the USML-1 mission because of the annealing of the layer during subsequent growth. Therefore, the epitaxial growth times of the USML-2 experiments were considerably shorter (2.5 and 1.5 hours) than those of the earlier mission (8.1 and 6.4 hours). The shorter growth times were selected to observe any annealing effects, and to possibly “bracket” the transition from island to layer growth.

The specific objectives include the observation and measurement of microgravity effects on—

- The transient behavior and morphology of the epitaxial layer and growth islands;
- The compositional and structural microhomogeneity of the layer and islands;
- The growth interface morphology of layers and islands;
- The propagation of “birth” defects from the interface into the layer; and on
- The properties of space-grown epitaxial layers and islands.

The assessment and evaluation of the above effects is based on a direct comparison between microgravity and ground-based test experiments under otherwise identical conditions.

4. RESULTS TO DATE AND DISCUSSION

4.1 Morphology of Epitaxial Layer and Islands

Both the epitaxial layer and islands grown during the USML-2 flight are high quality single crystals. The surface morphology of the as-grown epitaxial layer in microgravity (fig. 1a) is significantly smoother and flatter, relative to the best surface area of a ground test sample (fig. 1b). The more typical ground test

samples have irregular step-terrace structures with step heights less than about 5 mm and widths ranging from 50 to 200 mm. The steps and terraces of the space-grown layer and island surfaces are less than 1 mm in height. These differences reveal the effects of microgravity on the mass flow and deposition processes near the solid-vapor interface under transient growth conditions, and are comparable to those observed for considerably longer growth periods during the USML-1 flight.¹⁹

As shown earlier,¹⁹ the surface morphology of the previous¹⁹ and present space-grown layers compare quite favorably to $\text{Hg}_{1-x}\text{Cd}_x\text{Te}$ layers grown by other vapor phase methods. The etch pit densities (employing etchants of previous studies^{12, 13}) of the as-grown flight sample are about $5 \times 10^4 \text{ cm}^{-2}$, compared to our ground samples of about 10^5 – 10^6 cm^{-2} (fig. 2). EPD values reported in the literature for LPE²³ and MOCVD^{24, 25} growth of $\text{Hg}_{1-x}\text{Cd}_x\text{Te}$ on buffer layer structures range from 10^5 cm^{-2} to the upper 10^7 cm^{-2} , at lower growth temperatures than employed in this work. Employing the ISOVPE method at 550°C ²⁶ yielded EPD values of 10^4 to the upper 10^5 cm^{-2} .

The growth morphology for the short-term (1.5 hour) experiments in microgravity and on ground (fig. 3) shows similar island-type growth. However, a closer inspection of many individual islands reveals very well developed as-grown faces and facets of the $\text{Hg}_{1-x}\text{Cd}_x\text{Te}$ islands obtained in microgravity compared to numerous ground samples. Typical etch pit densities (fig. 4) of the space-grown islands are lower ($5 \times 10^4 \text{ cm}^{-2}$) than those of the ground samples (10^6 cm^{-2}).

The transition time from three-dimensional islands to two-dimensional layer growth is between 1.5 and 2.5 hours for the two microgravity experiments and for several GCEL test experiments. The transition time observed during independent studies in our laboratory for this system is about 1 hour.²² The difference in transition times between the latter²² and the present experiments can be explained by the lower temperature gradient dT/dx ($\sim 7^\circ\text{C cm}^{-1}$) at the growth interface employed in our laboratory²² as compared to that of the Crystal Growth Furnace (CGF) ($\sim 20^\circ\text{C cm}^{-1}$). The lower temperature gradient enhances the mobility of condensed species on the growth surface. This enables the faster growth of individual islands parallel to the (100) surface, and, thus, the faster coalescence of islands to form a layer.

4.2 Compositional Uniformity

Based on infrared (IR) spectroscopy, the overall compositions of the GCEL and space-grown islands (1.5 hour) and layer (2.5-hour growth time) of the present work are in very good agreement with the corresponding compositions of independent ground-based investigations.²² In combination with the analogous results for the previous USML-1 flight experiments¹⁹ (6.4 and 8.1-hour growth time), the data clearly reveal the transient nature of the present flight experiments. Considering the sensitivity of the growth composition with respect to very small changes in experimental parameters,¹³ the present and previous¹⁹ composition results obtained in microgravity are in excellent agreement with the time dependence of the other²² studies. This shows that the inherent transient behavior of the system is gravity independent.

Based on electron microprobe analysis, the depth composition profile perpendicular to the (100) growth face of the epitaxial layer (2.5 hour) grown in microgravity (fig. 5) shows that a nearly uniform composition of about $\text{Hg}_{0.8}\text{Cd}_{0.2}\text{Te}$ over a distance of about 5 mm can be obtained for this growth time by the CVT technique. Because of the shorter growth time, the width of the interdiffusion region is smaller than that for longer growth times.¹⁹

A more detailed view of the compositional microhomogeneity is obtained by IR spectroscopy measurements employing a beam diameter of 0.8 mm. The spatial composition maps after 2.5-hour growth of the flight and ground-control samples (fig. 6) show measurable differences. The composition uniformity of the former ($Dx/x \approx 5$ percent) is considerably better than that of the latter ($Dx/x \approx 12$ percent) for the major portion of the surface. The differences between the space ($Dx/x \approx 1.5$ percent) and ground-grown ($Dx/x \approx 10$ percent) islands (1.5-hour growth time) are even more pronounced. These quantitative differences over 10^{-1} mm distances under transient growth conditions demonstrate the sensitivity of this ternary system to nonuniformities in the fluid flow and concentration of nutrient species, owing to the effects of convection. The above-mentioned initial drop of the substrate temperature for the 2.5-hour growth flight sample probably affected the microhomogeneity in the central portion of the layer less than around the periphery. The absence of any such temperature fluctuations for the 1.5-hour flight sample and for the GCEL experiments strongly emphasizes the compositional improvement observed in microgravity for the 2.5-hour sample. These improvements of the compositional microhomogeneity of the flight samples under present transient (time-dependent) growth conditions are similar to those obtained for much longer growth periods and after steady-state conditions have been achieved of the USML-1 experiments.¹⁹ Based on a comparison of the earlier work¹⁹ with the literature, the earlier¹⁹ and presently observed compositional uniformities of the space-grown layers compare quite favorably to those obtained by other techniques on ground.¹⁹

4.3 Crystallinity of Epitaxial Layer and Islands

The epitaxial growth of the layers and islands parallel to the (100) orientation of the CdTe substrate was confirmed by x-ray diffraction Laue photographs. The size and shape of the diffraction spots also indicated single crystallinity of both the ground and space samples. A double-crystal x-ray diffraction monochromator (beam diameter 1 mm), the (400) diffraction plane, and $\text{CuK}\alpha_1$ radiation were used to determine rocking curves at various locations of the as-grown epitaxial layer and islands.

The inherent transient nature of the present growth experiments adds to the formation of local variations in the crystallinity of the epitaxial layers and islands. The appearances of double peaks in several rocking curves of different ground samples reflect the compositional nonuniformities and the possible existence of subgrain boundaries in these samples. Under these conditions it is more meaningful to represent the structural uniformity in terms of DF/F , where F is FWHM (full width at half maximum) and F the average of the FWHM values of the sample. Numerical values of DF/F for the 2.5-hour and 1.5-hour growth time flight samples are 14 percent and 7 percent, respectively. The corresponding quantities of the ground-based samples range from about 45 percent to 36 percent. These data clearly show the improved crystallinity of the space-grown layer and islands. Considering the possible influence of the temperature disturbance for the 2.5-hour space experiment, the uniformity of this ternary system obtained in microgravity and under transient conditions is quite remarkable. The observed trend of the DF/F values demonstrates the effects of microgravity on the crystallinity of this inherently complex, ternary, heterojunction structure even under transient growth conditions. A detailed discussion of the crystallinity of epitaxial layers grown from the vapor phase, reported in the literature, under more favorable conditions with respect to inherent defects (lattice mismatch), as discussed above, shows a range of FWHM values from about 200–600 arcsec (except for MBE).¹⁹ Based on the literature and on the fact that the compositional and structural uniformity measurements of the present work were performed on as-grown, untreated surfaces, the results obtained in this work for the space and ground experiments are very good.

4.4 Interface Morphology of Epitaxial Layer and Islands

Earlier investigations of the (011) cross section of the $\text{Hg}_{1-x}\text{Cd}_x\text{Te}/(100)$ CdTe structure yielded important information about the effects of the interface morphology on subsequent layer growth.²⁰ As shown in figure 7, the etched (011) cross sections of the $\text{Hg}_{1-x}\text{Cd}_x\text{Te}/(100)$ CdTe layer-substrate interfaces obtained after 2.5-hour growth in microgravity and in GCEL experiments on ground reveal significant differences in the dislocation densities of the growth interfaces. The EPD of the space-grown layer interface (fig. 7a) is much lower than that of the ground (fig. 7b) sample. The etched growth interface of the latter is a continuous groove of overlapping etch pits (fig. 7b). These observations strongly suggest that the effects of inherent lattice mismatch and of substrate surface defects on the interface morphology are affected by convective flow at or near the growth surface. It is justified to conclude that the combined effects also influence the formation and propagation of growth defects. These findings under transient growth conditions are similar to those of the earlier experiments¹⁹ for longer growth times (steady-state conditions), during which a nearly "seamless" transition from the substrate to the epitaxial layers grown in microgravity was observed.¹⁹ These new results also show that any annealing effects on the interface morphology during subsequent growth (USML-1¹⁹) are small.

Observations of the growth interfaces of the epitaxial islands grown in microgravity and on ground (fig. 8) yielded similar results. The etch pit densities of the space-grown interfaces are significantly lower (fig. 8a) than those of ground samples where the interfaces again are continuous grooves of overlapping etch pits (fig. 8b and reference 20). Also, the $\text{Hg}_{1-x}\text{Cd}_x\text{Te}$ islands grown in microgravity have very well-defined growth faces and facets (fig. 8a).

The proposed enhancement of the effects of inherent substrate-layer defects, and of the associated formation and propagation of growth defects by convective flow is strongly supported by the combined observations of the present and previous works.^{19, 20} The present work for considerably shorter-growth periods (transient growth conditions) also suggests that the interaction between fluid flow and the growing surface occurs from the very beginning of growth. Lattice matched substrates, buffer layers, and interdiffusion processes are well-known practices to minimize the effects of inherent defects. The combined results of the present and previous¹⁹ investigations show that the adverse interference of convective flow with layer growth cannot be excluded even for the above-mentioned techniques.

4.5 Growth Rates of the Epitaxial Layers

The average growth rates of the ground- and space-grown epitaxial layers are about 8 and 10 mm/hour, respectively, after 2.5 hours of growth. The differences between these and that of independent transient experiments²² is still being investigated. It possibly could be due to the considerably larger axial temperature gradient, dT/dx , at the substrate surface of the present work (CGF) of about $20^\circ\text{C}\cdot\text{cm}^{-1}$ compared to about $7^\circ\text{C}\cdot\text{cm}^{-1}$ employed in our laboratory.²² In addition, the sensitivity of the growth rate with respect to small variations in the transport agent pressure¹³ could also have contributed to this difference. The slightly higher growth rate in microgravity than on ground in the present work could be affected by the above temporary drop in the growth temperature in the beginning of the 2.5-hour growth period in microgravity. The higher growth rates of the present work relative to those of the USML-1¹⁹ experiments are explained by the transient nature of the present experiments.

The combined growth rates of the present and previously¹⁹ grown epitaxial layers on ground and in microgravity reveal the transient regime of the $\text{Hg}_{1-x}\text{Cd}_x\text{Te}/(100)\text{ CdTe-HgI}_2$ vapor transport system. The overall trend of the present and earlier¹⁹ growth rates as a function of time is in good agreement with that of independent studies.²²

4.6 Electrical Properties of Ground and Space-Grown Epitaxial Layers and Islands

Electrical measurements on the as-grown epitaxial layers and islands are performed using the van der Pauw method and Indium for ohmic contacts. The islands are interconnected electrically by the diffusion layer below the original growth interface.²⁰ The relative contributions of the diffusion layer and islands to the measured conductivity are not well understood. For the evaluation of the Hall measurements (of the islands), different thicknesses of the conducting layer and islands are used, which affects the calculated carrier concentration, but leaves the computed mobility essentially unchanged. The average carrier mobility of the epitaxial layer (2.5-hour growth time) and islands (1.5-hour growth) obtained in microgravity is about $7 \cdot 10^3 \text{ (cm}^2 \cdot \text{V}^{-1} \cdot \text{s}^{-1})$. The corresponding average of the GCEL samples is about $3.5 \cdot 10^3 \text{ (cm}^2 \cdot \text{V}^{-1} \cdot \text{s}^{-1})$. Measurements on postflight GCEL samples, subjected to the identical temperature-timeline as employed in microgravity (including the initial temperature drop of the 2.5-hour growth experiment), clearly show a considerably reduced mobility of the latter sample relative to that grown without the temperature variation. This demonstrates that the above difference in mobilities between space and ground samples should be even larger. This comparison emphasizes the considerable improvement in crystallinity of the epitaxial growth in microgravity relative to that on ground.

The n-type conductivity and carrier concentration of all samples are due to the incorporation of a transport agent (iodine) into the grown layers and islands. The carrier concentrations of the ground-control and flight samples are of the order of $10^{17} \text{ (cm}^{-3})$ similar to those of the earlier USML-1 experiments¹⁹ using considerably longer growth periods. The iodine concentration in the layer and islands under present experimental conditions is estimated to be about 10^{-2} percent, well below the detection limits of the electron microprobe analysis.

In the present work, the carrier concentrations of all ground samples apparently are greater than those of the space-grown layer and islands. This observation is being further investigated.

The differences in the single crystallinity and growth morphology observed for the 2.5-hour samples grown under microgravity and ground-based conditions suggest that convective flow on ground amplifies any effects of the initial temperature disturbance. This interpretation represents an extension of that proposed for the differences in interface morphology observed in the present and previous¹⁹ work (between ground- and space-grown layers), namely, the enhancement of the effects of inherent defects on growth morphology by convective flow. The combined observations suggest that the effects of any growth and/or flow disturbances are apparently increased under ground-based convective flow conditions.

Although the growth conditions of the USML-2 experiments are within the transient regime, the carrier mobilities of the present epitaxial layers (and islands) are quite comparable to those obtained for the much longer growth times of the USML-1¹⁹ experiments. Based on a comparison of the earlier¹⁹ results with the electrical properties of $\text{Hg}_{1-x}\text{Cd}_x\text{Te}$ grown by other vapor phase methods,¹⁹ the present mobilities compare quite favorably to the literature data.

5.0 SUMMARY AND CONCLUSIONS

The comparative analysis of the $\text{Hg}_{1-x}\text{Cd}_x\text{Te}$ epitaxial layers and islands grown on (100) CdTe substrates under normal and microgravity conditions yielded important results.

1. The inherent overall transient properties of this system are not affected by gravity. However, there are measurable convection effects on the morphology and crystallinity of the material.
2. The as-grown surfaces of the layer and islands obtained in microgravity are considerably smoother relative to those of ground samples.
3. The improvement of the compositional uniformity of the space-grown layer and islands demonstrates the effects of convection on composition profiles near the growing surface on ground.
4. The crystallinity and structural uniformity of the flight samples are improved relative to ground-control specimens.
5. The electrical properties of the space-grown samples are improved compared to those of ground samples.
6. The growth interfaces of the space-grown samples have considerably lower dislocation densities than those of the ground-control specimens.

These observations demonstrate that even under transient growth conditions the mass flow and deposition processes are more uniform in microgravity than on ground. They also confirm the existence of residual convective flow under vertical, stabilizing conditions and its effects on the transport and deposition processes at or near the growing surface of this vapor-solid growth system.

The combined results of the present and previous investigations of this system strongly support the conclusion that the effects of inherent defects on the growth interface and growth morphology are amplified by convective flow. In addition, flow disturbances, as a result of a temperature fluctuation, appear to be less harmful to crystalline properties of samples grown in microgravity than on ground. These new observations contribute to a better understanding of the interactions between interface processes and fluid flow.

REFERENCES

1. Kruse, P.W.: *Semiconductors and Semimetals*, 18, eds. R.K. Willardson and A.C. Beer, Academic Press, New York, 1, 1981.
2. Schmit, J.L.: *J. Crystal Growth*, 65, 249, 1983.
3. Herman, M.A.; and Pessa, M.: *J. Appl. Phys.*, 57, 2671, 1985.
4. Tung, T.; Golonka, L.; and Brebrick, R.F.: *J. Electrochem. Soc.*, 128, 451, 1981.
5. Wiedemeier, H.; and Chandra, D.: *Z. Anorg. Allg. Chem.*, 488, 137, 1982.
6. Wiedemeier, H.; and Uzpurvis, A.E.: *Anorg. Allg. Chem.*, 510, 199, 1984.
7. Chandra, D.; and Wiedemeier, H.: *Anorg. Allg. Chem.*, 545, 98, 1987.
8. Wiedemeier, H.; and Chandra, D.: *Anorg. Allg. Chem.*, 545, 109, 1987.
9. Wiedemeier, H.; and Palosz, W.: *J. Crystal Growth*, 96, 933, 1989.
10. Wiedemeier, H.; and Uzpurvis, A.E.: *J. Electrochem. Soc.*, 130, 252, 1983.
11. Wiedemeier, H.; Uzpurvis, A.E.; and Wang, D.C.: *J. Crystal. Growth*, 65, 474, 1983.
12. Wiedemeier, H.; and Sha, Y.G.: *J. Electron. Mater.*, 21, 563, 1992.
13. Sha, Y.G.; and Wiedemeier, H.: *J. Electron. Mater.*, 21, 613, 1992.
14. Wiedemeier, H.; Klaessig, F.C.; Irene, E.I.; and Wey, S.J.: *J. Crystal Growth*, 31, 36, 1975.
15. Wiedemeier, H.; Sadeek, H.; Klaessig, F.C.; Norek, M.; and Santandrea, R.: *J. Electrochem. Soc.*, 124, 1095, 1977.
16. Wiedemeier, H.; Trivedi, S.B.; Zhong, X.R.; and Whiteside, R.C.: *J. Electrochem. Soc.*, 133, 1015, 1986.
17. Wiedemeier, H.; and Trivedi, S.B.: *Naturwissenschaften*, 73, 376, 1986.
18. Palosz, W.; and Wiedemeier, H.: *J. Crystal Growth*, 89, 242, 1988.
19. Wiedemeier, H.; Ge, Y.-R.; Hutchins, M.A.; and Sha, Y.G.: *J. Crystal Growth*, 146, 610, 1995.

20. Ge, Y.-R.; and Wiedemeier, H.: *J. Electron. Mater.*, 23, 1221, 1994.
21. Ge, Y.-R.; and Wiedemeier, H.: *J. Electron. Mater.*, 25, 1067, 1996.
22. Wiedemeier, H; and Ge, Y.-R.: *J. Electron. Mater.*, 25, 1072, 1996.
23. Johnston, S.; Blazejewski, E.; Bajaj, J.; Chen, J.S.; Bubulac, L.; and Williams, G.: *J. Vac. Sci. Techn.*, B9, 1661, 1991.
24. Korenstein, R.; Hallock, P.; and MacLeod, B.: *J. Vac. Sci. Techn.*, B9, 1630, 1991.
25. Sugiyama, I.; Hobbs, A.; Saito, T.; Veda, O.; Shinohara, K.; and Takigawa, H.: *J. Crystal Growth*, 117, 161, 1992.
26. Lee, S.B.; Magel, L.K.; Tang, M.F.S.; and Stevenson, D.A.: *J. Vac. Sci. Techn.*, A8, 1098, 1990.

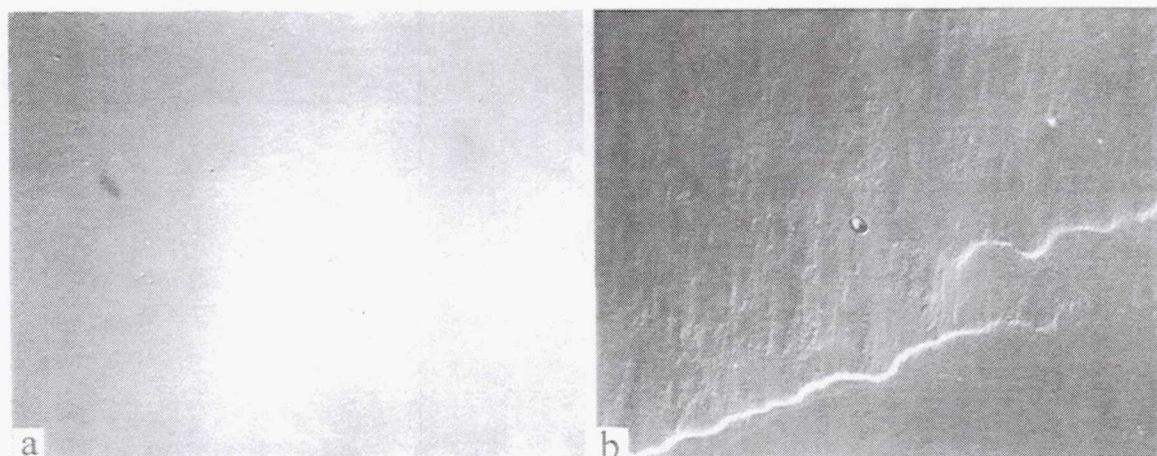


Figure 1. Optical photomicrographs of $\text{Hg}_{1-x}\text{Cd}_x\text{Te}$ epitaxial layers as-grown at 545°C on (100) oriented CdTe substrates under reduced (a) and normal (b) gravity conditions after 2.5-hour growth time (at a magnification of $\times 200$).

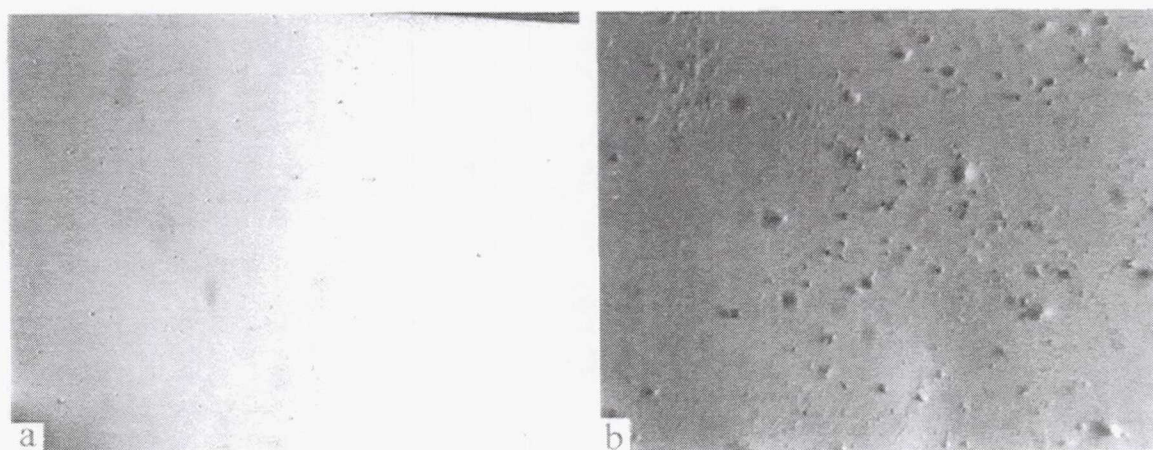


Figure 2. Optical photomicrographs of chemically etched $\text{Hg}_{1-x}\text{Cd}_x\text{Te}$ epitaxial layers as-grown at 545°C on (100) oriented CdTe substrates under reduced (a) and normal (b) gravity conditions after 2.5-hour growth time (at a magnification of $\times 500$).

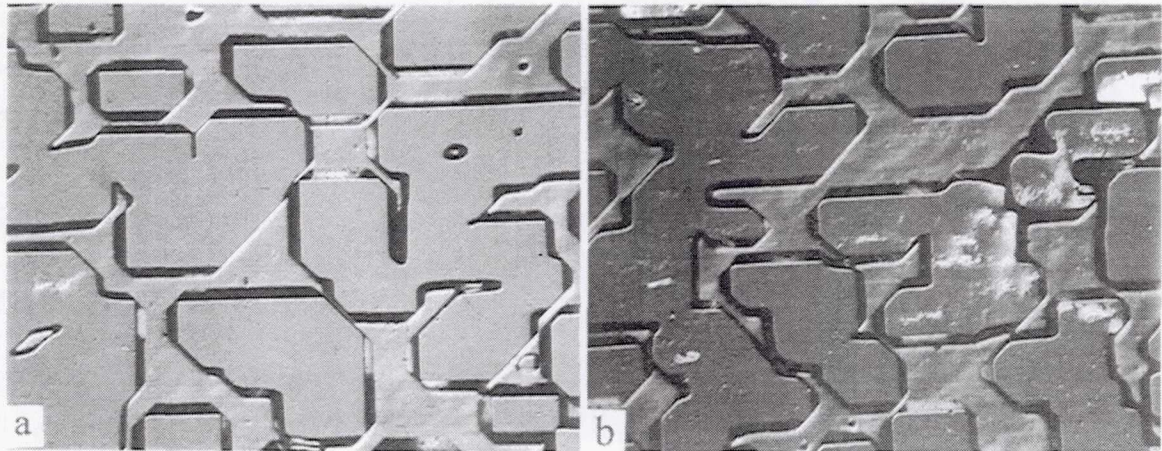


Figure 3. Optical photomicrographs of $\text{Hg}_{1-x}\text{Cd}_x\text{Te}$ epitaxial islands as-grown at 545°C on (100) oriented CdTe substrates under reduced (a) and normal (b) gravity conditions after 1.5-hour growth time (at a magnification of $\times 200$).

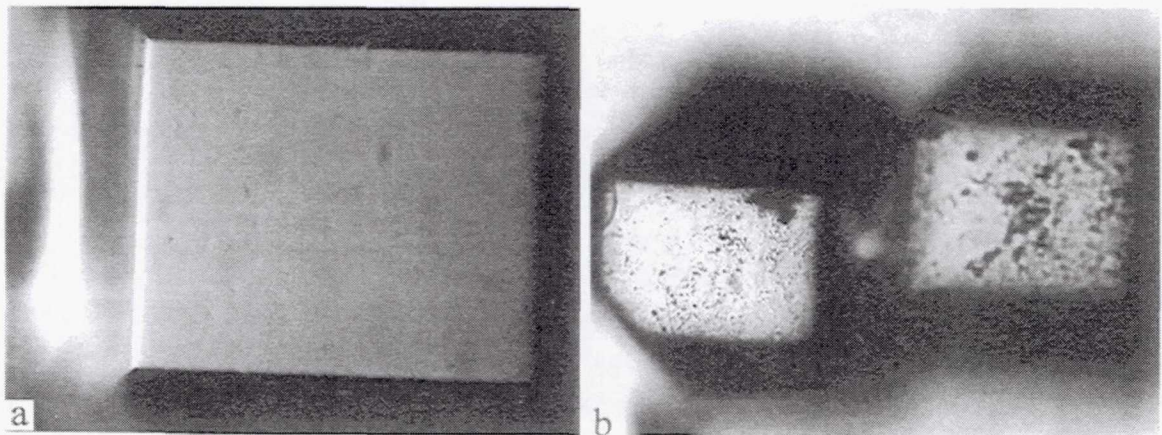


Figure 4. Optical photomicrographs of chemically etched surfaces of $\text{Hg}_{1-x}\text{Cd}_x\text{Te}$ epitaxial islands as-grown at 545°C on (100) oriented CdTe substrates under reduced (a) and normal (b) gravity conditions after 1.5-hour growth time (at a magnification of $\times 500$).

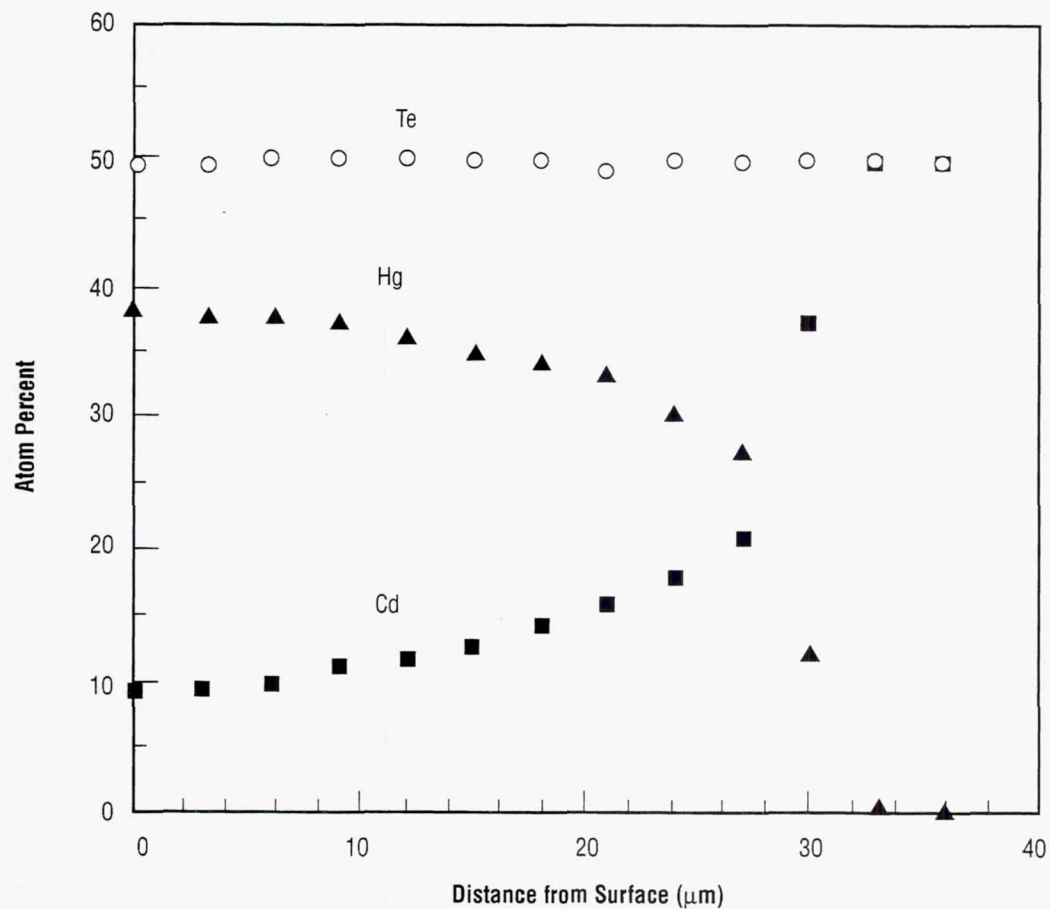


Figure 5. Composition profiles of the constituent elements normal to the surface of a $\text{Hg}_{1-x}\text{Cd}_x\text{Te}$ epitaxial layer as-grown on a (100) CdTe substrate at 545 °C under reduced gravity conditions after 2.5-hour growth time.

$\text{Hg}_{1-x}\text{Cd}_x\text{Te}$
Spatial Composition Maps

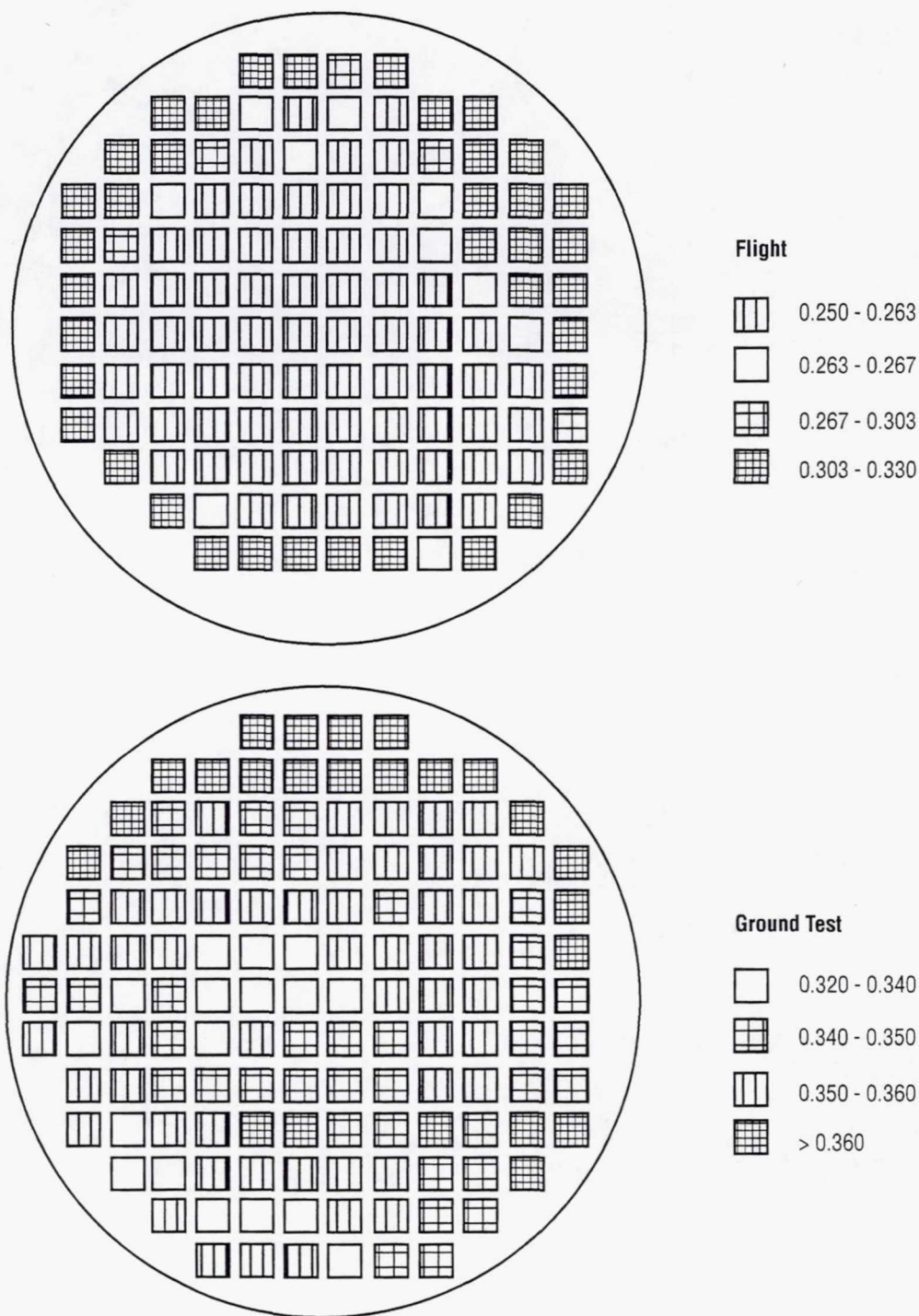


Figure 6. Spatial composition maps of the as-grown $\text{Hg}_{1-x}\text{Cd}_x\text{Te}$ epitaxial layers grown on (100) CdTe substrates at 545 °C under reduced (flight) gravity and normal (ground test) conditions. The numbers represent the x-values.

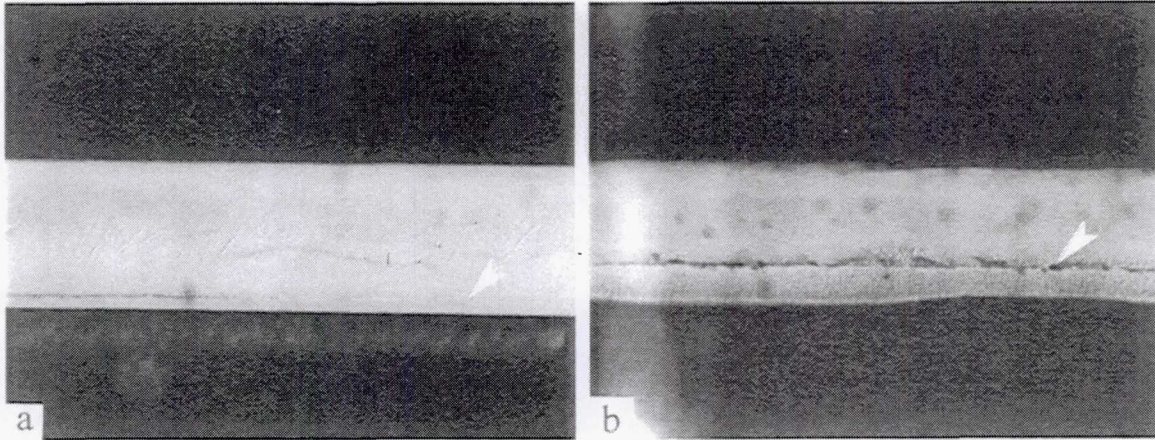


Figure 7. Optical photomicrographs of the (011) cross sections of $\text{Hg}_{1-x}\text{Cd}_x\text{Te}/(100)$ CdTe epilayer-substrate structures grown at 545 °C under reduced (a) and normal (b) gravity conditions (2.5-hour growth time). The arrow marks the growth interface. The thinner layer below the interface is the interdiffusion zone into the CdTe substrate (dark area). The epitaxial layer is the light-shaded area above the growth interface (at a magnification of $\times 1,000$).

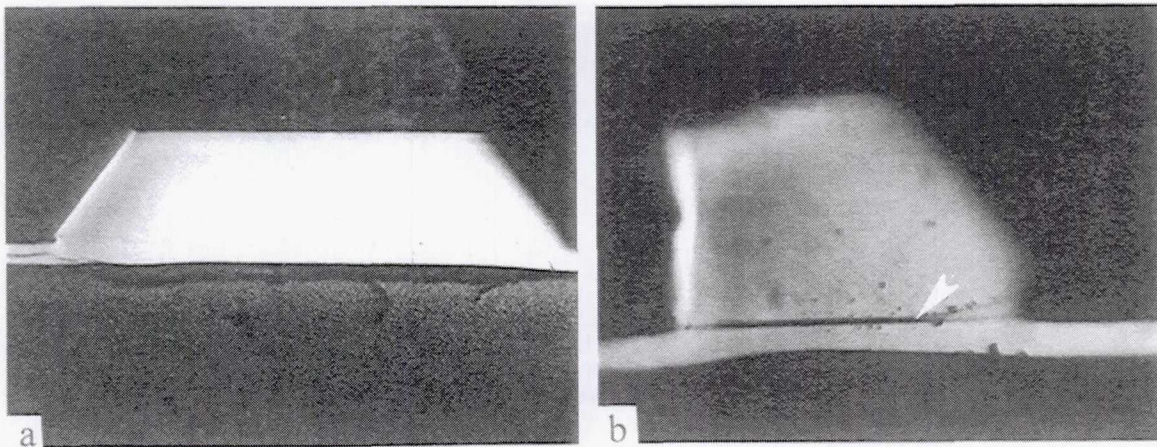


Figure 8. Optical photomicrographs of the (011) cross sections of the $\text{Hg}_{1-x}\text{Cd}_x\text{Te}/(100)$ CdTe epiisland substrate structures grown at 545 °C under reduced (a) and normal (b) gravity conditions (1.5-hour growth time). The arrow marks the growth interface. The thinner layer below the growth interface is the interdiffusion zone into the CdTe substrate (dark area) (at a magnification of $\times 1,000$).

EXPERIMENT III.

ZEOLITE CRYSTAL GROWTH IN MICROGRAVITY—THE USML-2 MISSION

ACKNOWLEDGMENTS

The authors acknowledge NASA for funding. Thanks are extended to the crew of STS-73, especially Kathryn Thornton and Catherine Coleman for a great job in orbit. In addition thanks are extended to Lisa McCauley of Battelle for her support, and Jack Ferraro and the ZCG assembly crew at KSC—Ipek Guray, Teran L. Sacco, Michelle Marceau, and Robert Whitmore.

EXPERIMENT III. ZEOLITE CRYSTAL GROWTH IN MICROGRAVITY—THE USML-2 MISSION

Nurcan Baç, Juliusz Warzywoda and Albert Sacco Jr.

Chemical Engineering Department

Worcester Polytechnic Institute

Worcester, MA 01609

ABSTRACT

The extensive use of zeolites and their impact on the world's economy leads to many efforts to characterize their structure, and to improve the knowledge base for nucleation and growth of these crystals. The Zeolite Crystal Growth (ZCG) experiment on USML-2 aims to enhance the understanding of nucleation and growth of zeolite crystals while attempting to provide a means of controlling the defect concentration in microgravity. Zeolites A, X, Beta, and Silicalite were grown during the 16-day USML-2 mission. The solutions where the nucleation event was controlled yielded larger and more uniform crystals of better morphology and purity than their terrestrial/control counterparts. Space-grown Beta crystals were free of line defects while terrestrial/controls had substantial defects.

1. INTRODUCTION

Zeolites are crystalline aluminosilicates. These materials have an open framework based on an extensive three-dimensional network of oxygen ions. Situated within the tetrahedral sites formed by the oxygen can be either an Al^{+3} or Si^{+4} ion. This unique structure has proven to be extremely effective in processing materials at the molecular level and in turn, zeolites formed the backbone of chemical and petrochemical process industries. The extensive use of zeolites in refining (gasoline production by fluidized catalytic cracking (FCC)), petrochemical processing, laundry detergents, agriculture, and environmental cleanup as catalysts, adsorbents, and ion exchangers caused the market to mushroom in the mid-1980's reaching worldwide sales of about 2 billion dollars. The existing markets for zeolites are expected to grow at a rate of 3-4 percent through 2000.¹

Continued growth for zeolites includes cultivating markets beyond petroleum refining and detergents. New applications for these molecularly selective materials are in areas such as selective membranes, chemical sensors, molecular electronics, quantum-confined semiconductors and zeolite-polymer composites. These new applications are expected to have an impact on novel technological developments.

The importance of zeolites has driven extensive efforts to characterize their structures and understand their nucleation and growth mechanisms. These efforts aim to produce "custom-made" zeolites tailored for a desired application. To date, nucleation mechanisms and growth are not well understood for many of the systems involved. In most cases, the problem is compounded with the presence of a gel phase which controls the degree of supersaturation. This gel also undergoes a continuous polymerization type

reaction during nucleation and growth. Currently, there is no available technology to grow large, crystallographically perfect zeolites in high yield. The microgravity environment on board the Space Shuttle in low-Earth orbit provides a unique environment (around 10^{-4} – 10^{-6} g) for zeolite crystal growth. This environment virtually eliminates settling and convection, enhances diffusion-limited growth and reduces collision breeding. These benefits led to several attempts to grow larger and structurally improved zeolites in space²⁻⁵ providing mixed results in literature. The previous attempts of Sacco et. al indicated that larger zeolite crystals with fewer defects can be synthesized in microgravity.⁶ Investigating zeolite crystal growth in microgravity enhances the understanding in nucleation and growth mechanisms. This also attempts to control the defect structure in zeolites.

2. RESULTS

2.1 Zeolite A

Figures 1 and 2 show typical results from zeolite A synthesis using the nucleation control agent triethanolamine (TEA). Scanning Electron Microscope (SEM) photomicrographs in figure 1 indicate that largest flight zeolite A crystals (85- μ m cubes) are 70 percent larger in linear dimension than the largest terrestrial zeolite A crystals with sizes up to 50 μ m. This linear size increase corresponds to about 190-percent increase in the surface area, and a 390-percent increase in the volume of the zeolite A crystal. Particle size distributions (PSD's) of these flight and terrestrial products shown in figure 2 are in agreement with the SEM photomicrographs and indicate that a considerable population of large zeolite A crystals exist in the flight sample. The shape of PSD is different for flight and terrestrial samples, indicating different nucleation and/or growth history for these samples. It should be noted that the sizes of zeolite A crystals grown during USML-2 and their terrestrial counterparts show a substantial improvement over commercial zeolite A products and previous USML-1 flight results. Our increased zeolite crystallization knowledge through space flight allowed us to produce terrestrial zeolite A crystals during USML-2 that are equal or larger in size than those produced during the USML-1 flight.

Figure 3 shows the improvements in zeolite A crystallization with SEM photomicrographs of commercial, USML-1, and USML-2 crystals at the same magnification. The large zeolite A crystals (~85 μ m) in the USML-2 product are about 42 times greater than the commercial crystals (~2 μ m). This corresponds to a volume increase of about 77,000 times for the flight crystals over the commercial crystals. Figure 4 illustrates the PSD's for the samples shown in figure 3. Figures 5 and 6 show typical results from zeolite A synthesis using nucleation control agent 2,2-Bis(hydroxymethyl)-2,2',2''-nitrilotriethanol (BIS). Figure 6 shows that flight crystals are 40–60 percent larger than terrestrial/control crystals, and indicate the presence of an amorphous phase in addition to zeolite A crystals in the flight sample. The amorphous phase corresponds to unreacted species which, given enough time at reaction temperature, will allow the flight sample to grow even larger. The corresponding terrestrial sample is free from unreacted amorphous material. These differences indicate the possibility of slower crystallization rates of zeolite A in microgravity. PSD's for these samples shown in figure 6 confirm size differences between flight and terrestrial/control samples seen in figure 5, and clearly indicate the presence of an amorphous material in flight sample manifested as a second peak centered around 5 μ m. Table 1 shows the comparison of lattice parameters for flight and terrestrial/control samples in a typical zeolite A experiment. As illustrated, the lattice parameters and, thus, the unit cell volumes for the flight samples, were frequently smaller than for the terrestrial counterparts. This is consistent with fewer lattice defects in the structure, and is consistent with similar results for Spacehab-1 and USML-1.

Table 1. XRD data comparing flight (F) and terrestrial/control (T) zeolite A samples.

Sample	a(Å)	Volume (Å ³)
F (TEA)	12.27±0.01	1848.97
T (TEA)	12.29±0.00	1857.10
F (BIS)	12.30±0.00	1863.23
T (BIS)	12.31±0.00	1866.82

2.2 Zeolite X

Figures 7 and 8 show typical results from zeolite X formulations using nucleation control agent TEA. SEM photomicrographs (fig. 7) indicate that largest flight zeolite X crystals (octahedra with side ~215 μm) are about 35 percent larger in linear dimension than the largest terrestrial/control zeolite X crystals with side ~160 μm . This linear size increase corresponds to about an 81-percent increase in the surface area, and about a 143-percent increase in the volume of the zeolite X crystal. The increases in surface area and volume are significant for certain applications, such as incorporating semiconductors into cages in the zeolite.

The PSDs of these flight and terrestrial/control samples, shown in figure 8, are in agreement with the SEM photomicrographs and confirm a significant shift to larger sizes for crystals grown in microgravity. Other formulations using less TEA resulted in similar 30–40 percent increase of linear dimension of flight zeolite X crystals in comparison to their terrestrial/control counterparts. SEM photomicrographs and PSDs for other formulations are shown in figures 9 and 10, respectively.

Both scanning electron microscopy and particle size analysis show that a substantially larger product is obtained in microgravity. SEM photomicrographs indicate that flight crystals are predominantly pure, while the terrestrial/control samples have considerable amounts of zeolite A and clusters of zeolite R and P impurity phases. The presence of impurities is also indicated in the PSDs in figure 10 showing bimodal distributions for the control samples. X-ray powder diffraction (XRD) analysis confirmed the presence of impurities indicated by SEM and PSDs. XRD patterns for crystals grown in space exhibit sharp peaks indicating a very pure product consisting of large single crystals. The terrestrial samples have considerable peak broadening of additional peaks due to polycrystalline impurities.

Figure 11 illustrates the improvements in zeolite X crystallization with SEM photomicrographs of commercial, USML-1, and USML-2 crystals at the same magnification. The particle size of the zeolite X product of USML-2 is about 107 times larger than the commercial product. This corresponds to a volume increase of about 1.24 million times for the flight crystals over the commercial product. Figure 12 shows PSDs of the products depicted in figure 11. Figure 12 indicates a substantial increase of the size of the USML-2 product in comparison to USML-1 and commercial zeolite X.

Figures 13 and 14 show results from another zeolite X formulation using the nucleation control agent TEA. SEM photomicrographs in figure 13 and PSDs in figure 14 indicate that the flight zeolite X product contains a zeolite A impurity; however, the flight zeolite X crystal size increase over its terrestrial/control counterpart is about 70 percent (120 μm flight versus 70- μm control). These results are very similar to USML-1 results obtained with a similar formulation.⁷

Figure 15 shows the results of a microprobe analysis of the hexagonal cross sections of a flight sample and its control (fig. 16). The results indicate the distribution of Al in both samples. The increase of Si/Al ratio from the center to the exterior of the crystals suggests depletion of Al in the reaction mixture in agreement with the fact that Al is a limiting reagent in zeolite X synthesis.⁸ As shown in figure 15 the Si/Al ratio is higher for the flight sample than for the terrestrial counterpart, consistent with USML-1 results showing average Si/Al ratios larger in flight samples than in their terrestrial/control counterparts. Also, the Si/Al ratio of the flight material appears to be more uniform throughout the center of the crystal. Table 2 shows the comparison of lattice parameters for flight and terrestrial sample shown in figure 15. As illustrated, the lattice parameters and, thus, the unit cell volumes for the flight sample, are smaller than for the terrestrial counterpart, which is consistent with its lower Al content.

Table 2. XRD data comparing flight (F) and terrestrial/control (T) zeolite X samples.

Sample	a(Å)	ESD	Volume (Å ³)
F	24.849	0.002	15343.25
T	24.855	0.0009	15354.41

2.3 Silicalite

Figures 17 and 18 illustrate typical results from the Silicalite synthesis using untreated silica gel (without nucleation control). SEM photomicrographs shown in figure 17 indicate clearly that the intergrown disk morphology of Silicalite crystals grown in microgravity is different from the morphology of Silicalite crystals grown in 1 g, which crystallized in the form of spherulitic agglomerates.

Although the morphologies are very different for crystals synthesized in microgravity and 1 g environments, XRD patterns for these products, indicate that they are both pure Silicalite. The PSDs for the products corresponding to figure 17 are given in figure 18. Figure 18 shows that the PSDs of Silicalite crystals grown in μ g are distinctly shifted to larger geometrical diameters in comparison to PSDs of Silicalite crystals grown in 1 g. These results illustrate that when one compares the nucleation and crystal growth processes for Silicalite grown in microgravity and 1g environment, the microgravity effect yields larger crystals with a different (better) morphology.

A heat treatment of silica gel granules in air at sufficiently high temperatures prior to their use in syntheses (resulting in the decrease of effective surface area of silica source available to dissolution) is an effective method of reducing nucleation of Mordenite crystals.⁹ Nucleation control of Silicalite was accomplished by heat treating silica gel at 700 °C for 20 hours prior to use in syntheses. Specific surface area of heat treated silica gel decreased from 750 to 320 m²/g. Figure 19 shows the SEM photomicrographs of Silicalite crystals grown from heat treated silica in microgravity and 1g. PSDs for the products corresponding to figure 19 are given in figure 20.

Comparison of SEM photomicrographs shown in figures 17 and 19 indicates a change of morphology of terrestrial crystals from spherulitic agglomerates obtained using untreated silica gel, to intergrown disks obtained using heat treated silica gel. Change of morphology (combined with distinct size shift of PSDs to larger geometric diameters for crystals grown using heat treated silica gel in comparison to crystals grown using untreated silica gel) indicates the reduction of nucleation of Silicalite crystals by using a

heat treated silica source. Similar morphologies and size of flight crystals grown using untreated silica gel (no nucleation control) and terrestrial/control crystals grown using heat treated silica gel (reduction of nucleation rate), shown in figures 17, 18, 19, and 20, indicate that the microgravity environment resulted in reduction of the nucleation rate of flight crystals. Flight crystals grown from heat treated silica gel show the same intergrown disks morphology as their terrestrial counterparts (nucleation rate is reduced in both cases). However, they appear to be predominantly individual crystals or assemblies of a few crystals while the terrestrial crystals are predominantly in groups of larger agglomerates. The effects of these terrestrial/control agglomerates are seen in the PSDs shown in figure 20. The observation of larger PSDs for the terrestrial case is due to agglomerates in this case. The product grown in microgravity is free of large agglomerates, resulting in smaller PSDs. However, when comparing the flight/heat treated silica gel and flight/untreated silica gel samples, the heat treated samples are 52 percent larger.

The effect of agglomeration and sedimentation in the terrestrial samples was examined by cutting the Teflon™ liners used in synthesis of Silicalite in μg and 1 g along the longitudinal axis. Figure 21 shows typical appearance of internal walls of the Teflon™ liners used to grow terrestrial and flight crystals. The effect of sedimentation in the terrestrial samples is obvious. Part of the product in the terrestrial autoclaves is in the form of a scale, or cake, attached to the internal wall of the Teflon™. This region is circled to show the terrestrial agglomerates in figure 21. However, the autoclave for the Silicalite samples grown in μg has a clean and smooth surface with no crystals, scale, or agglomerates attached. This shows the clear advantage of crystal growth in microgravity where absence of settling results in containerless processing.

2.4 Zeolite Beta

XRD patterns of products obtained from the zeolite Beta synthesis using untreated silica gel (no nucleation control) are typical for zeolite Beta¹⁰ and show that the material is an intergrowth of two or three polymorphs. SEM photomicrographs and PSDs of these products shown in figures 22 and 23 do not show significant differences in either morphology or size between the terrestrial and flight samples of zeolite Beta. Both products crystallized in the form of polycrystalline round or slightly elongated aggregates 0.25–1.5 μm in geometric diameter.

Although SEM pictures and particle size distributions look similar, transmission electron microscope (TEM) photomicrographs of the same samples given in figure 24 clearly indicate that zeolite Beta grown in μg is structurally more perfect while the terrestrial sample has considerable line defects.

Fourier Transform Infra-Red (FTIR) spectra of the same samples are shown in figure 25. Intensity of a band at 3,750 cm^{-1} for flight sample is lower than for its terrestrial counterpart. This band is due to terminal hydroxyl group from the surface or at a defect site, and, therefore, a more intense band at 3,750 cm^{-1} for the terrestrial sample may indicate more defect sites in the terrestrial sample, consistent with TEM results.

The Si/Al ratios determined by SEM/Energy Dispersive X-ray Analysis (EDX) (which is a semi-quantitative technique with an accuracy ~ 20 percent) indicate a higher Al content in flight samples than in its terrestrial/control counterpart, as shown in table 3. Yield of zeolite Beta is also higher in flight than in the terrestrial/control sample, as seen in table 3.

Table 3. Comparison of Si/Al ratios and yield of flight (F) and terrestrial/control (T) zeolite Beta crystals.

Sample	Si/Al	Yield(g)
F (untreated silica source)	5.8	0.759
T (untreated silica source)	7.6	0.670
F (silica source heat treated at 850 °C)	7.1	0.820
T (silica source heat treated at 850 °C)	7.8	0.650

Morphology, PSDs, and the purity of zeolite Beta synthesized using silica gel heat treated at 850 °C prior to use in syntheses, are the same for crystals grown in microgravity and 1 g. However, flight crystals were formed in higher yield and with higher Al content, as shown in table 3. These results cannot be attributed to formation of impurity phases because XRD patterns for both products are the same.

The flight zeolite Beta product synthesized using another silica source was in loose powder form, similarly to all flight and terrestrial/control zeolite Beta products grown from silica gel in both untreated and heat treated forms. The terrestrial zeolite Beta product grown using this other silica source, however, showed two distinct forms: a loose powder (herein referred to as "powder") and agglomerated solid chunks (referred to as "chunk"). These two different terrestrial forms were analyzed separately. X-ray data indicate that the space zeolite Beta sample contained a very small amount of Chabazite and Faujasite impurities while the powder portion of the terrestrial sample contained a large amount of Faujasite impurity in addition to very small amounts of Chabazite impurity. XRD did not reveal Faujasite in the chunk portion of the terrestrial sample. PSDs of flight and two terrestrial portions of zeolite Beta samples were very similar to PSDs of samples grown using silica gel. The reason for the presence of Faujasite in the flight sample and in the loose portion of the terrestrial sample is unclear at this time, but may be due to local nonhomogeneous mixing pockets in the autoclaves.

2.5 Zeolite Glovebox Experiment (GBX-ZCG)

The zeolite glovebox experiment was used to establish mixing procedures for the zeolite solutions to be processed in the ZCG facility. The results from the glovebox experiment using clear autoclaves illustrated that real-time observation of the mixing process is necessary to ensure gel uniformity without excessive shear. Bubble formation, inherent in the mixing process, was minimized with real-time observations including spinning the autoclaves if necessary.

In addition to establishing mixing protocols for the ZCG experiment, four GBX autoclaves contained reaction mixtures developed to produce zeolite A at low temperature. These were mounted on the outside surface of the ZCG furnace for crystal growth at 40 °C. No nucleation control agent was used in this synthesis in order to achieve 100 percent crystallinity of product at the end of synthesis. Visual observation of the progress of crystallization occurring in microgravity was therefore achieved for the first time. Visual observations verified the hypothesis that during synthesis gel will not settle and crystals will remain suspended in the reaction mixture. Figures 26 and 27 show the comparison of flight and terrestrial results from the zeolite A synthesis carried out at 40 °C. As shown in figure 26 the results from an on-orbit experiment do not differ significantly from terrestrial duplicate, although PSDs of flight samples appear to be shifted slightly towards larger sizes, as illustrated in figure 27. Similar results were observed for zeolite A synthesis with no nucleation control during USML-1.

3. CONCLUSIONS

Flight zeolite A samples show enhanced size of the largest crystals in comparison to terrestrial/control counterparts. In addition, amorphous material is present in many flight zeolite A samples grown in the presence of BIS. This indicates that fewer crystals nucleated in flight samples and the crystallization (conversion of amorphous gel into crystalline product) process took longer to complete in microgravity than in 1 g. Smaller unit cell volumes of flight samples in comparison to terrestrial samples appear to suggest fewer lattice defects in their structure.

Flight zeolite X samples are substantially larger in size in comparison to terrestrial/control counterparts. This indicates that fewer crystals nucleated in flight samples. The size increase varies between 30–70 percent, depending on the type of formulation. Zeolite X crystals with sizes up to 215 μm were obtained. Flight crystals have higher Si/Al ratios than their terrestrial counterparts and are more uniform.

Silicalite crystals grown from silica gel heat treated at 700 °C yielded larger crystals with intergrown disks morphology. This morphology is different in comparison to crystals synthesized from untreated silica gel, which grew as spherulitic agglomerates. This is due to reduced nucleation of Silicalite caused by slower dissolution rates of heat treated silica gel in comparison with untreated silica gel caused by its decreased specific surface area. Almost no agglomeration is observed in flight samples due to lack (or reduction) of settling of silica gel substrate and/or Silicalite product.

The results of zeolite Beta synthesis show that flight samples have better morphology and less structural defects in comparison to terrestrial/control samples. The silica source used in syntheses affected the quality, purity, and morphology of the final product. Yield and Al content in zeolite Beta obtained using untreated and heat treated silica gel was higher for flight than for terrestrial samples. Different silica sources resulted in large amounts of Faujasite impurity present in flight zeolite Beta samples while terrestrial samples had substantially lower Faujasite content. These results again illustrate the differences between nucleation and growth processes occurring in microgravity and 1 g environments.

REFERENCES

1. *Chemical Week*, 35, June 5, 1996.
2. Pennisi, E.: "Shuttle Surprise—Zeolites Form Odd Rods," *Science News*, 140, 22, 1992.
3. Schmidt, W.: CASIMIR-1 Mission, Final Report, Into Space, 1992.
4. Sano, T.; Mizukami, F.; Kawamura, M.; Takaya, H.; Mouri, T.; Inaoka, W.; Toida, Y.; Watanabe, M.; and Toyoda, K.: "Crystallization of ZSM-5 Zeolite Under Microgravity," *Zeolites*, 12, 801, 1992.
5. Sacco, A., Jr.; Thompson, R.W.; Dixon, A.G.: "Microgravity Processing of Zeolites in Space," Int. SAMPE Conference, 18, 330, 1986.
6. Sand, L.B.; Sacco, A., Jr.; Thompson, R.W.; and Dixon, A.G.: "Large Zeolite Crystals Their Potential Growth in Space," *Zeolites*, 7, 387, 1987.
7. Sacco A., Jr.; Baç, N.; Coker, E.N.; Dixon, A.G.; Warzywoda, J.; and Thompson, R.W.: "The Growth of Zeolites A, X, and Mordenite in Space," Joint L+1 Year Science Review of USML-1 and USMP-1, NASA Conference Publication 3272, May 1994.
8. Breck, D.W.: *Zeolite Molecular Sieves*, J. Wiley, New York, 1974.
9. Warzywoda, J.; Dixon, A.G.; Thompson, R.W.; and Sacco, A., Jr.: "Synthesis and Control of Large Mordenite Crystals Using Porous Silica Substrates," *J. Mater. Chem.*, 5, 985, 1995.
10. Newsam, J.M.; Tseang, M.M.; Koetsier, N.T.; and de Gruyter, C.B.: "Structural Characterization of Zeolite Beta," *Proc. R. Soc. Lond. A*420, 375, 1988.

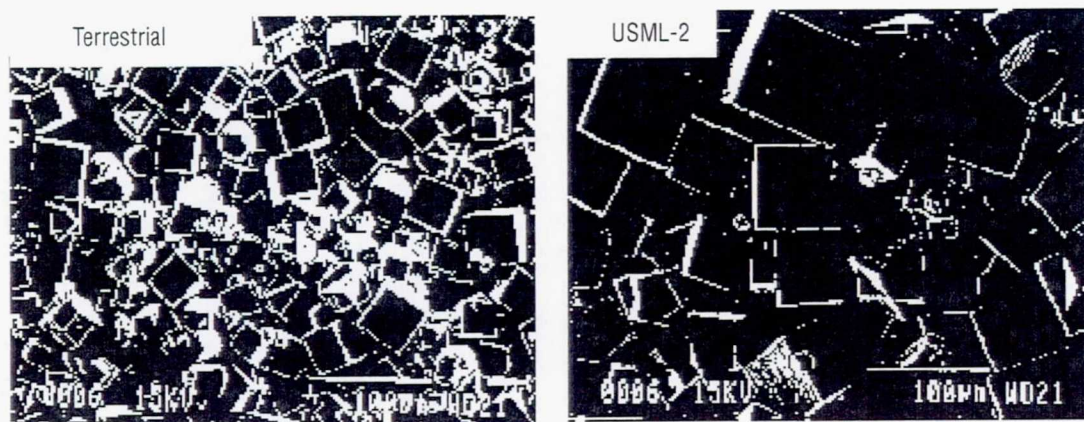


Figure 1. SEM pictures of zeolite A using TEA as a nucleation control agent.

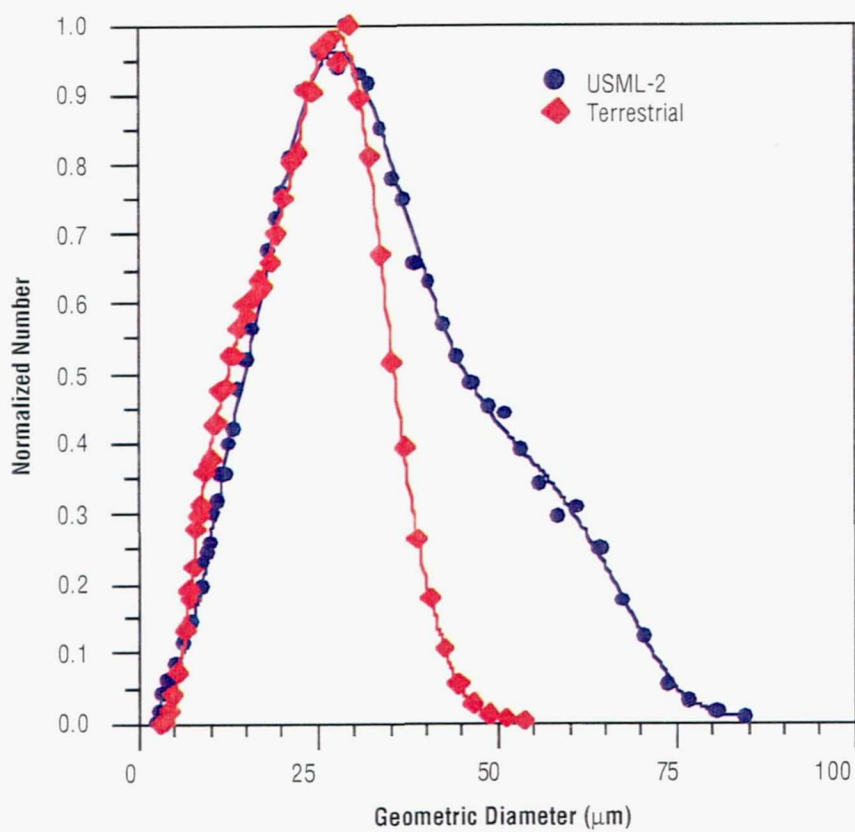


Figure 2. PSDs of zeolite A illustrated in figure 1.

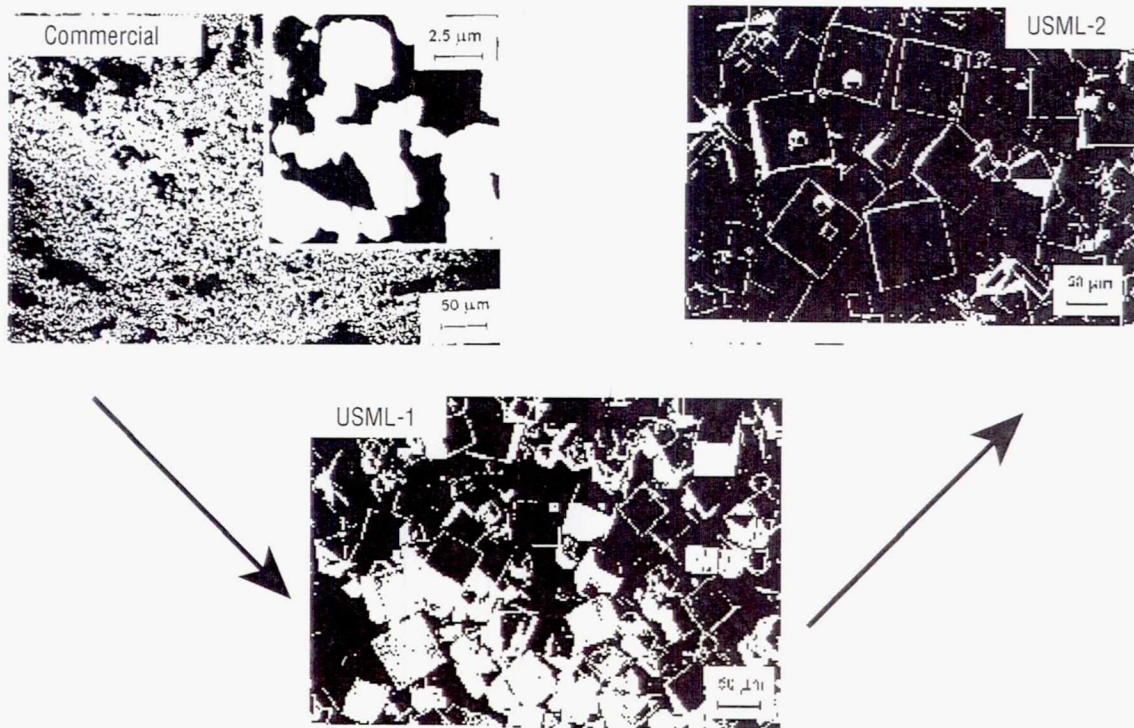


Figure 3. Improvements from space research—zeolite A.

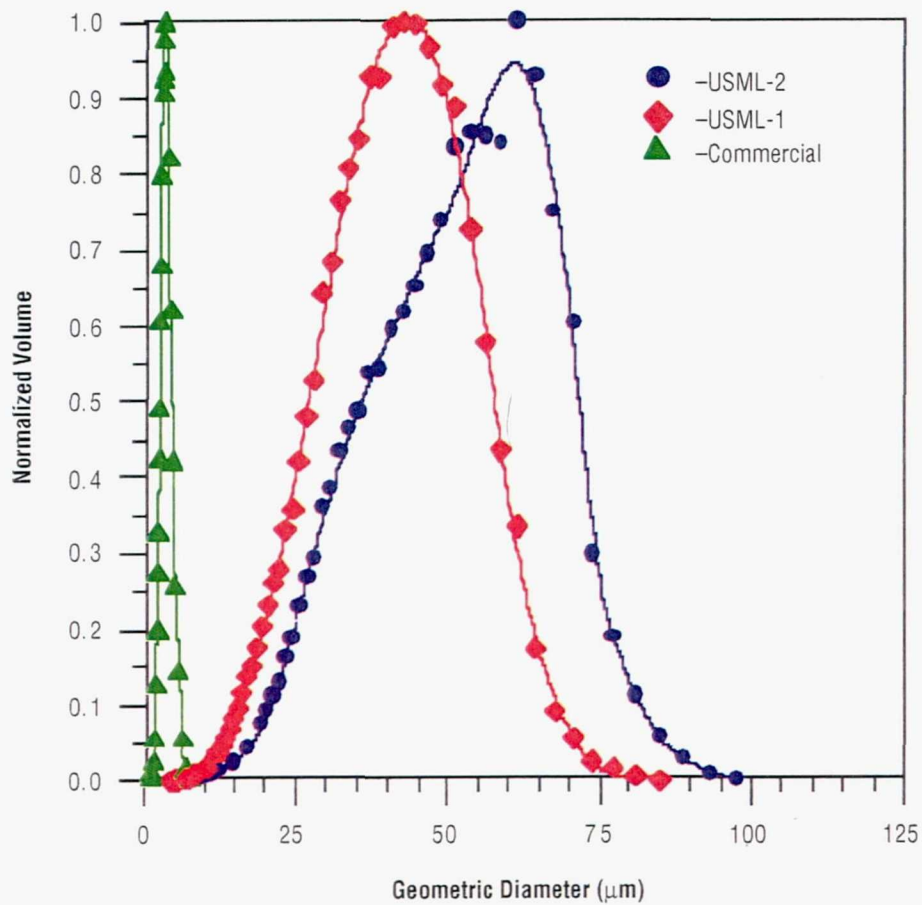


Figure 4. Particle size distributions of commercial, USML-1, and USML-2 zeolite A crystals.

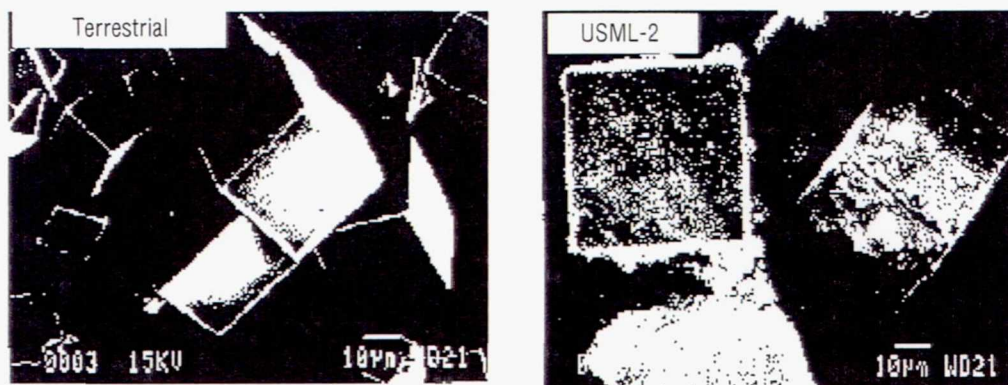


Figure 5. SEM pictures of zeolite A with BIS indicating unreacted gel.

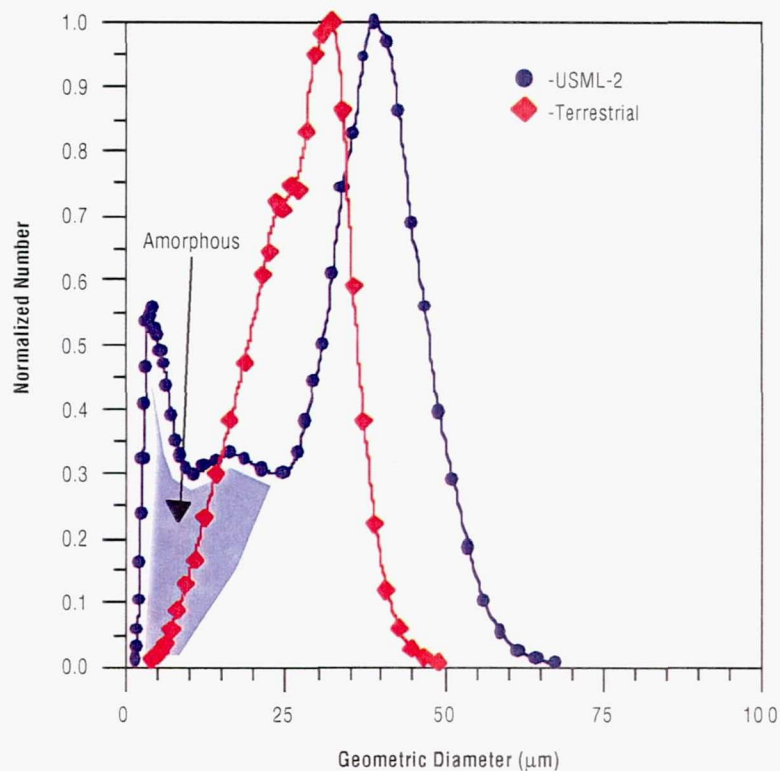


Figure 6. PSDs of zeolite A illustrated in figure 5.

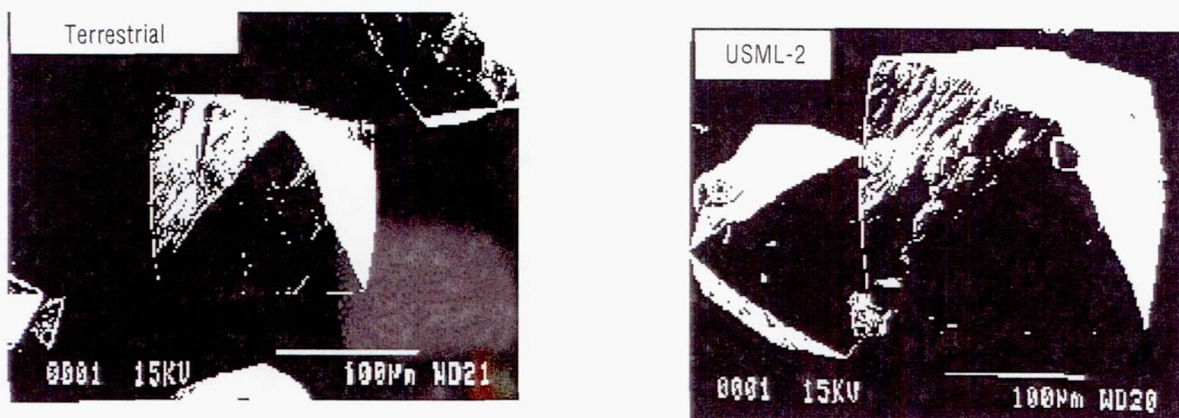


Figure 7. SEM pictures of zeolite X using TEA as a nucleation control agent.

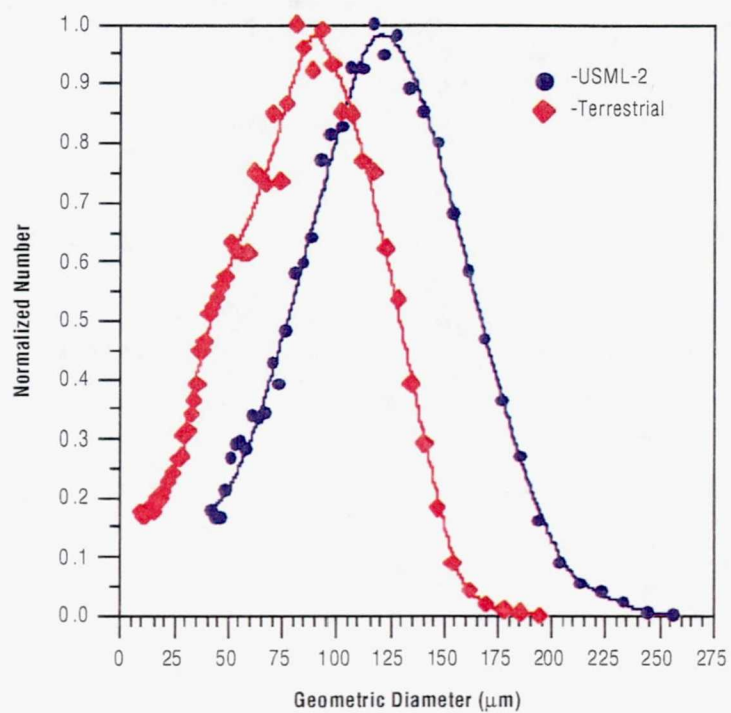


Figure 8. PSDs of zeolite X illustrated in figure 7.

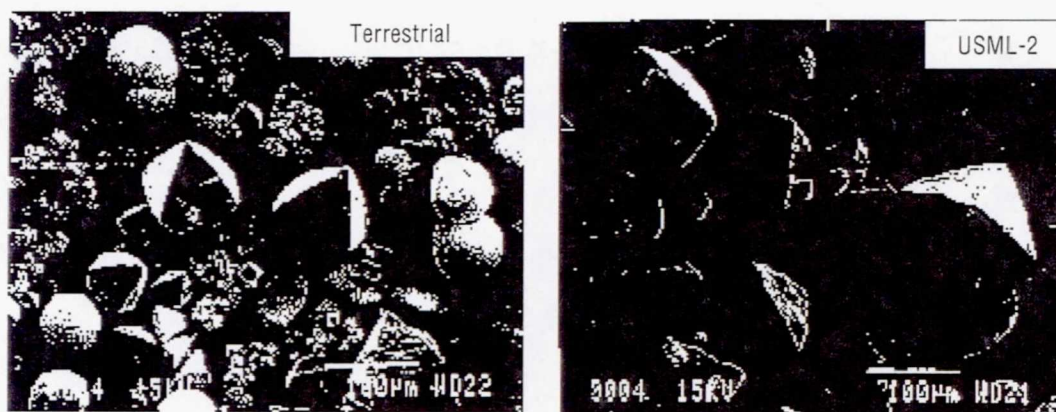


Figure 9. SEM pictures of zeolite X using TEA—different formulation.

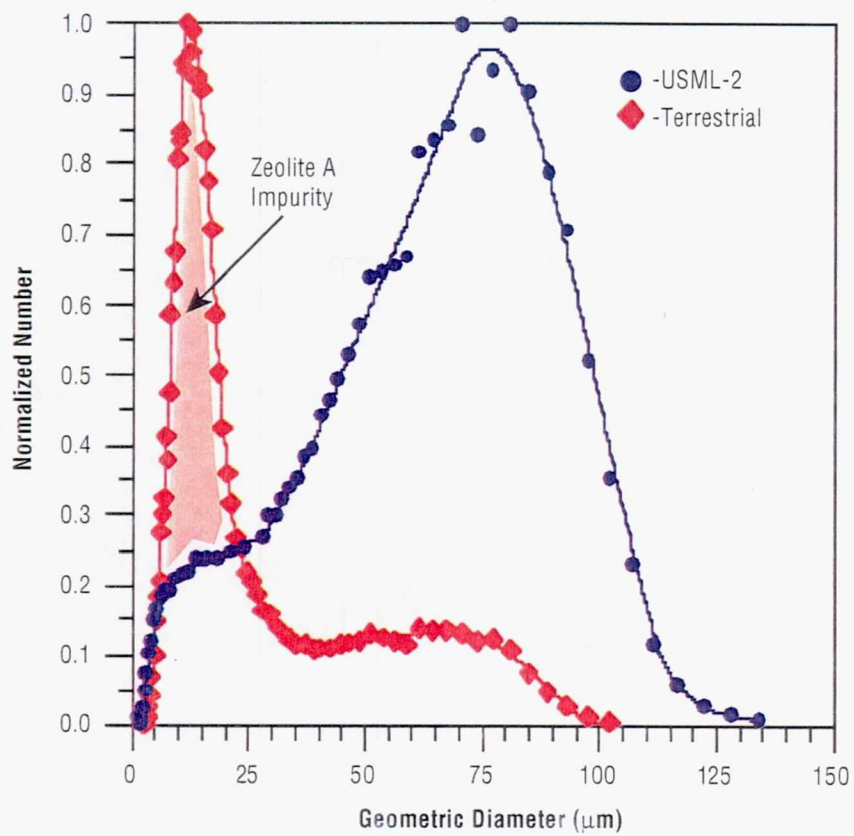


Figure 10. PSDs of zeolite X illustrated in figure 9.

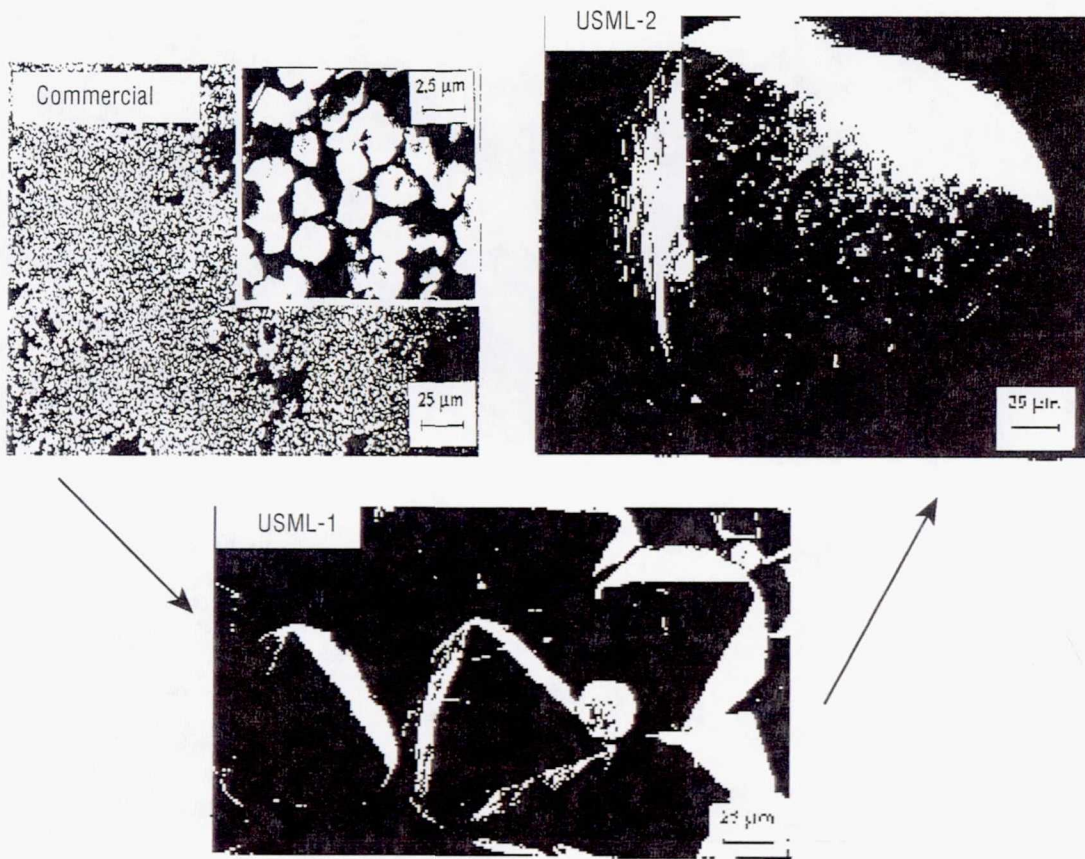


Figure 11. Improvements from space research—zeolite X.

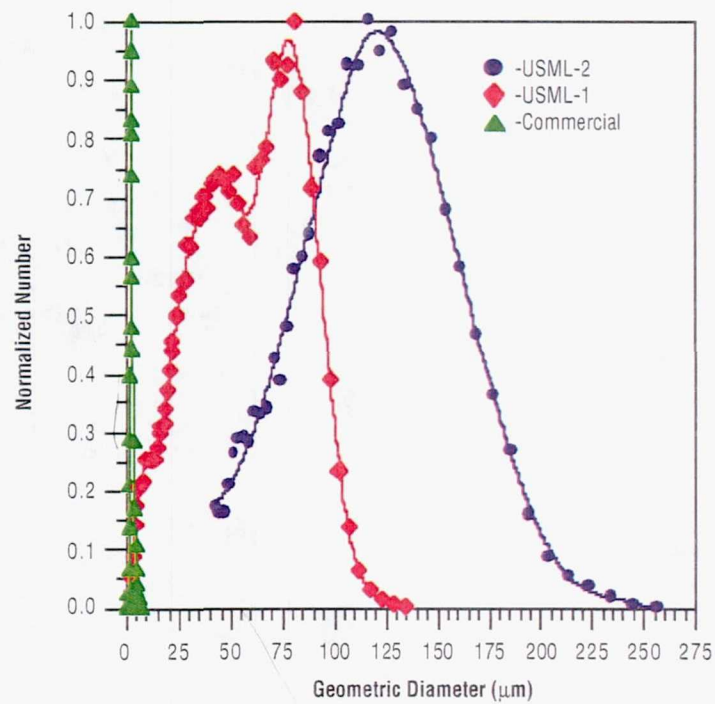


Figure 12. Particle size distributions of commercial, USML-1, and USML-2 zeolite X crystals.

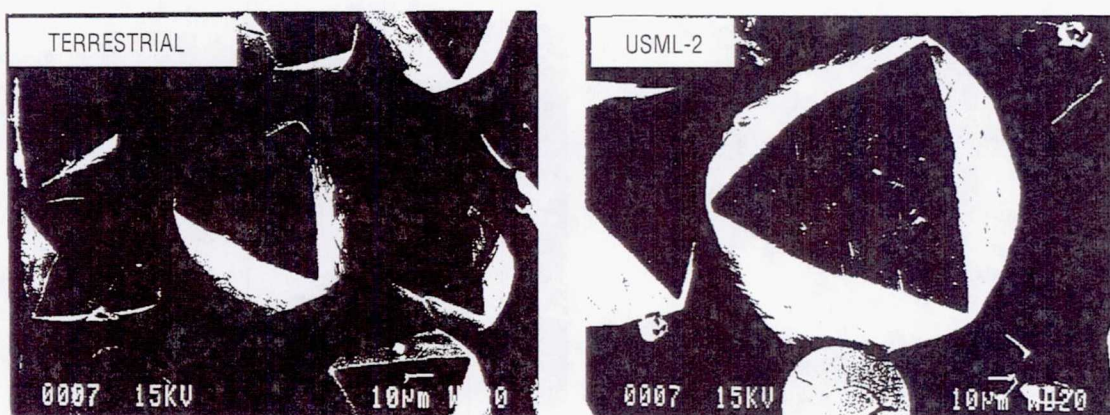


Figure 13. SEM pictures of zeolite X using TEA—different formulation.

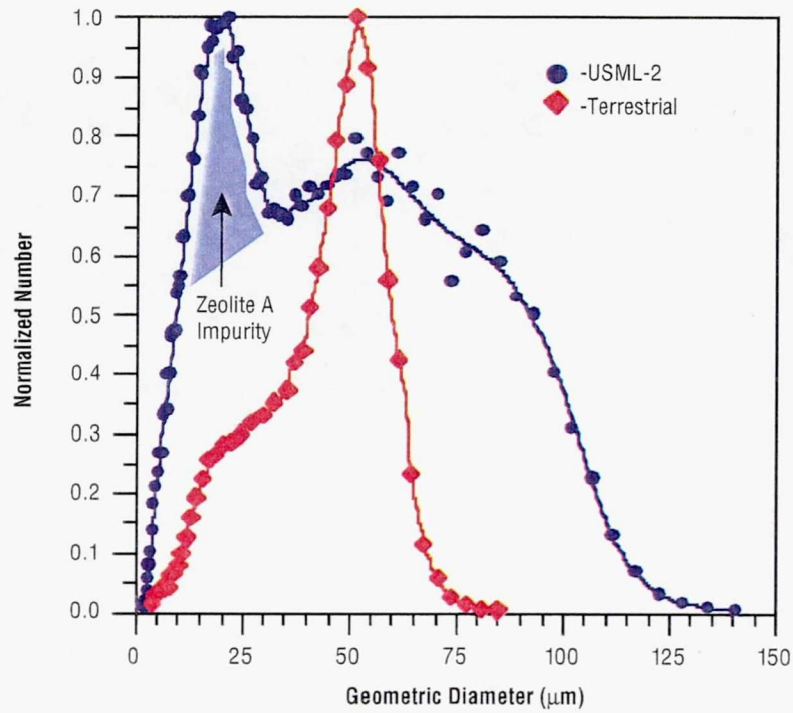


Figure 14. PSDs of zeolite X illustrated in figure 13.

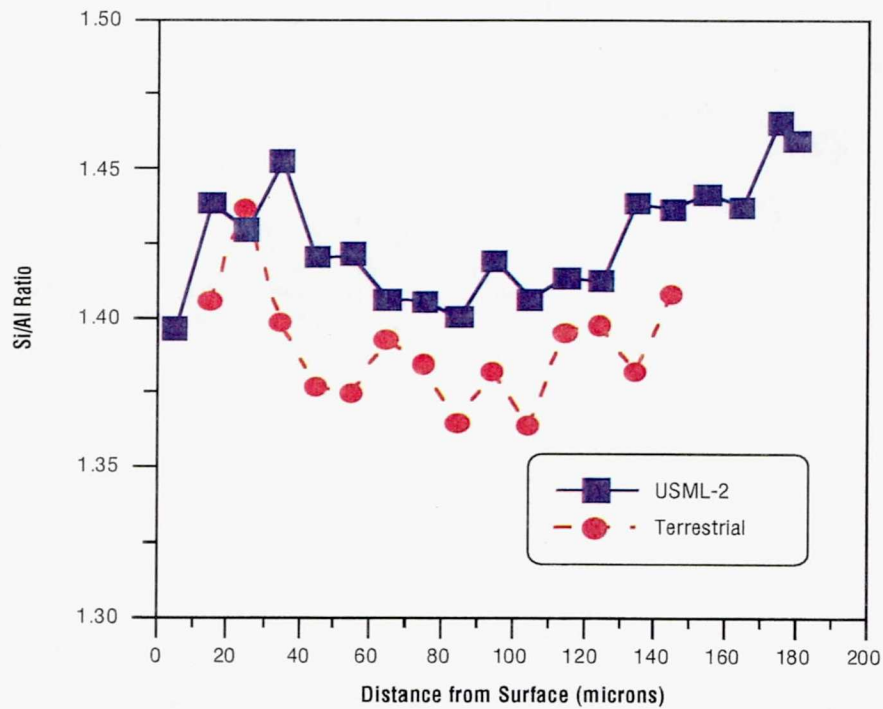


Figure 15. Si/Al ratio by microprobe analysis of zeolite X.

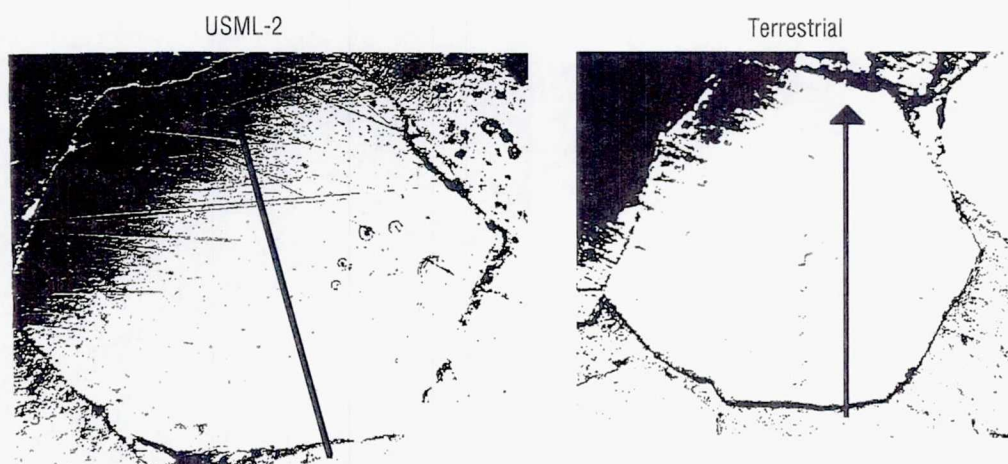


Figure 16. Cross sections used in microprobe analysis.

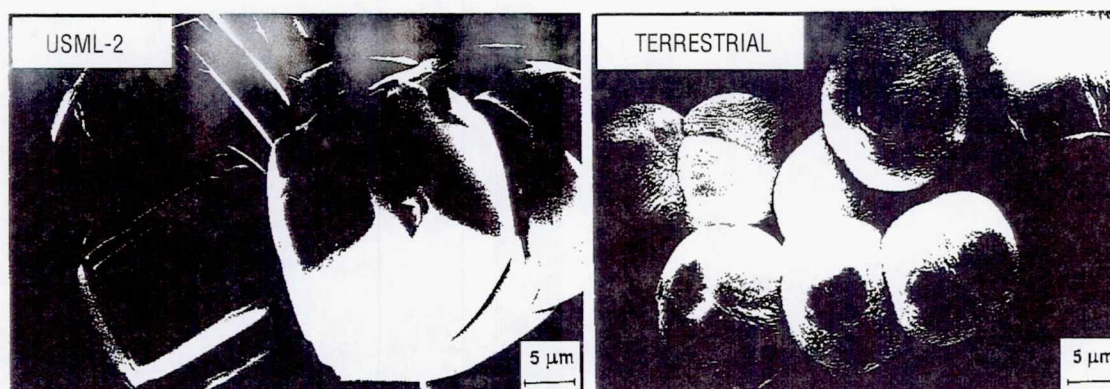


Figure 17. SEM pictures of Silicalite from untreated silica gel.

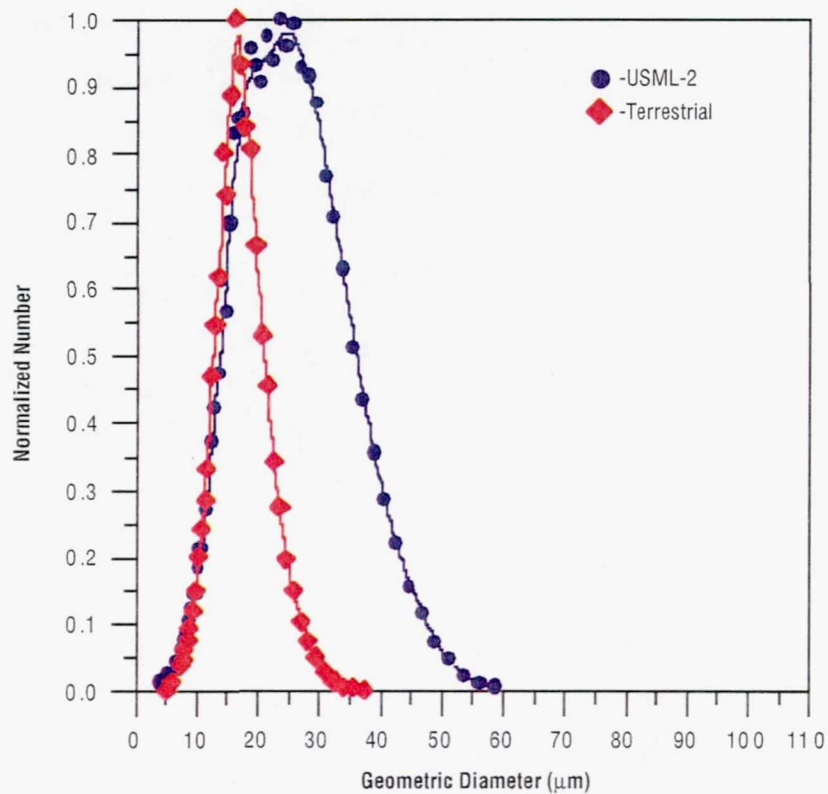


Figure 18. PSDs of Silicalite illustrated in figure 17.

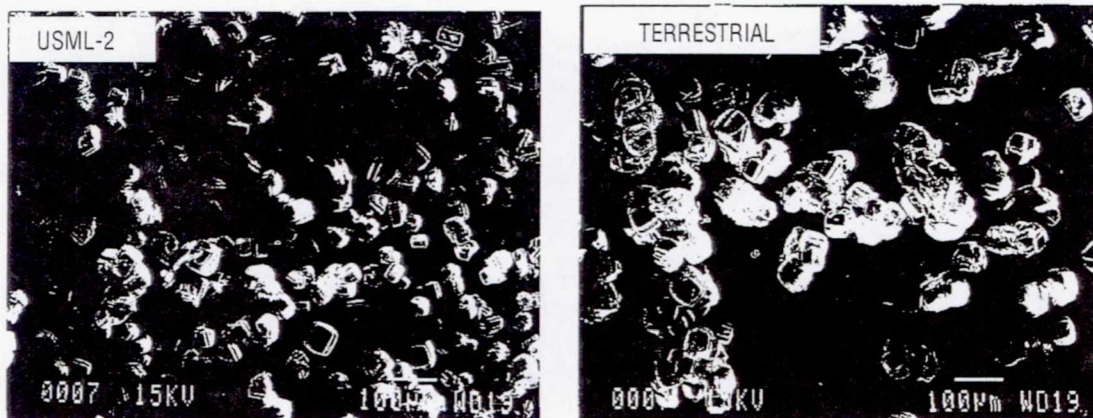


Figure 19. SEM pictures of Silicalite from heat treated silica gel.

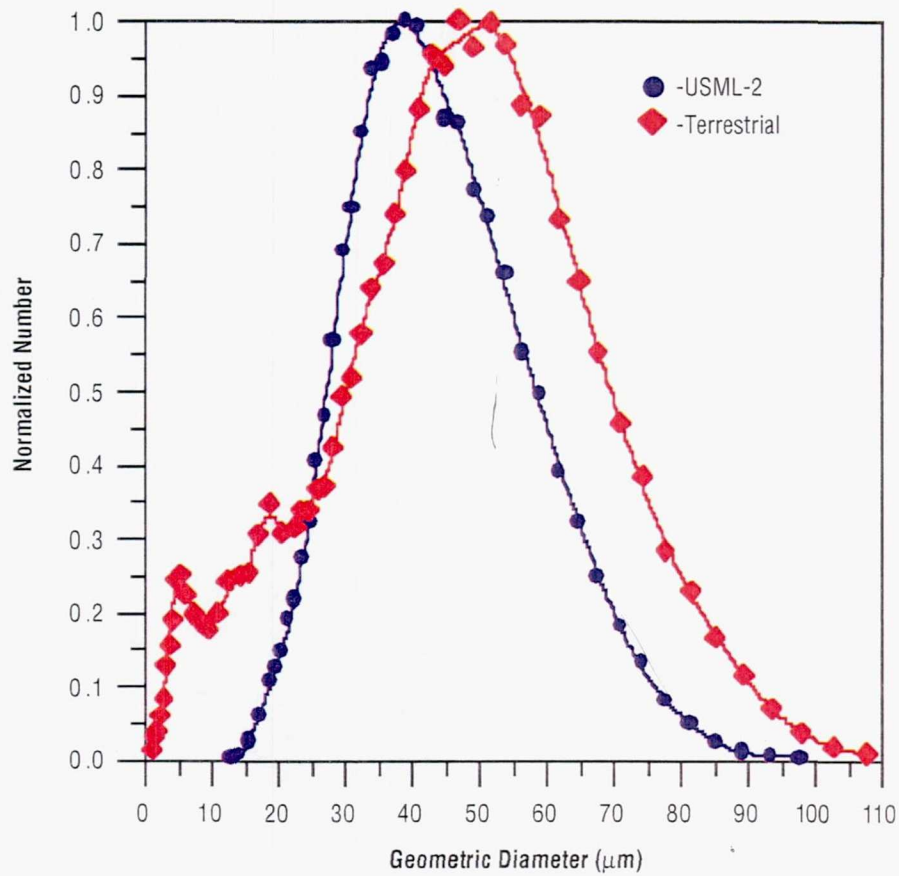


Figure 20. PSDs of Silicalite illustrated in figure 19.

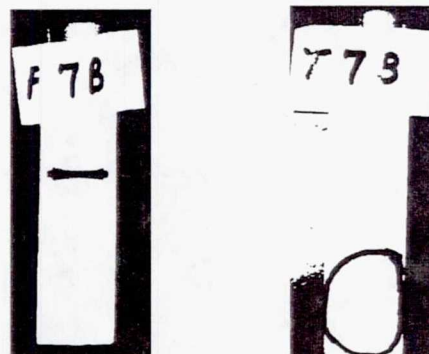


Figure 21. Teflon™ liners of flight (F7B) and terrestrial (T7B) autoclaves for Silicalite synthesis from heat treated silica gel.

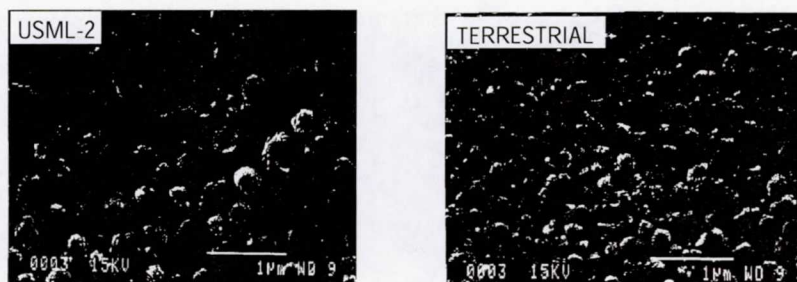


Figure 22. SEM pictures of zeolite Beta from silica gel.

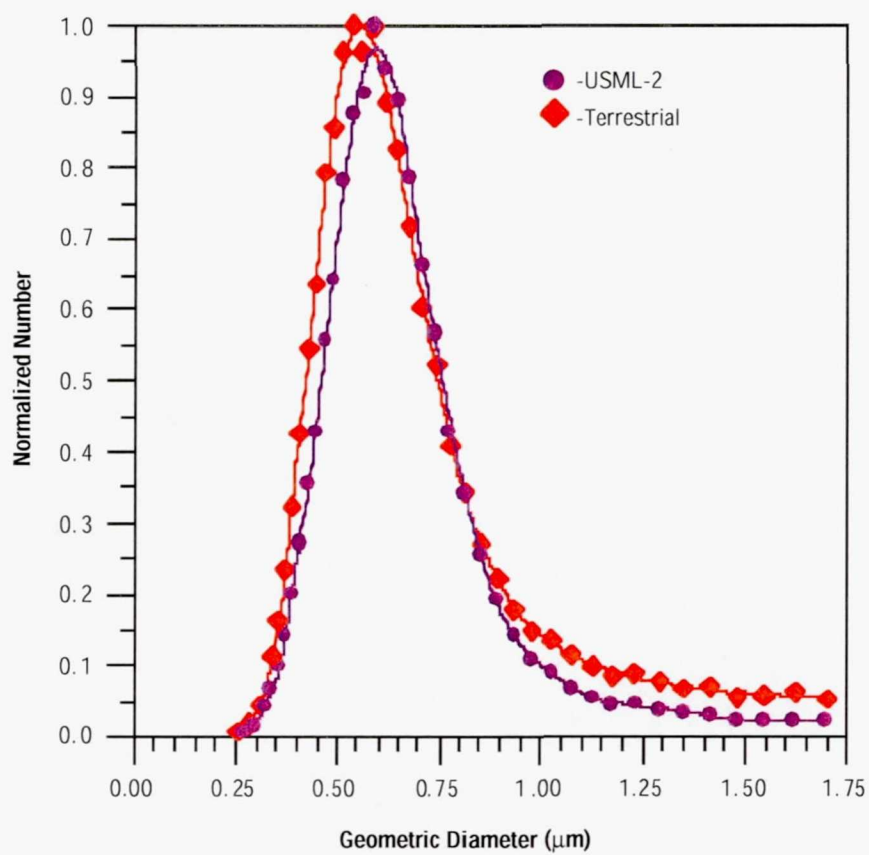


Figure 23. PSDs of zeolite Beta illustrated in figure 22.

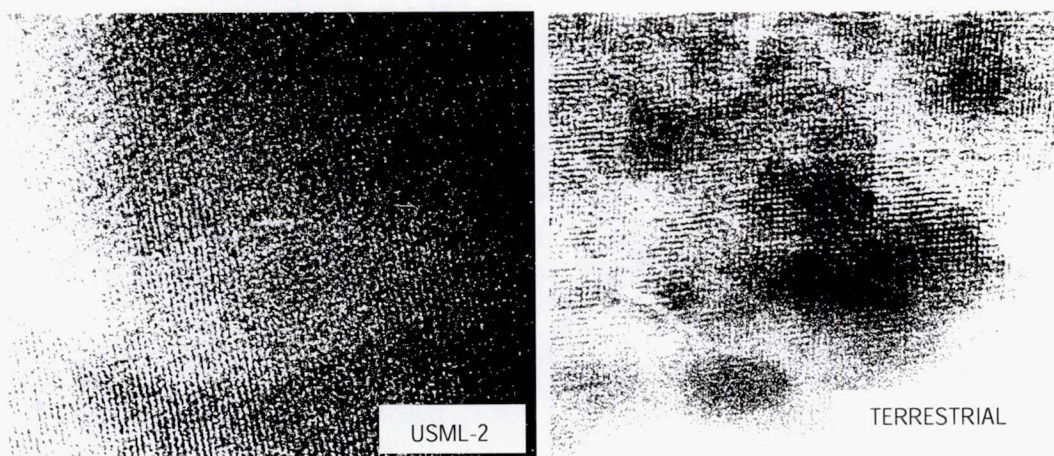


Figure 24. TEM pictures of zeolite Beta from silica gel.

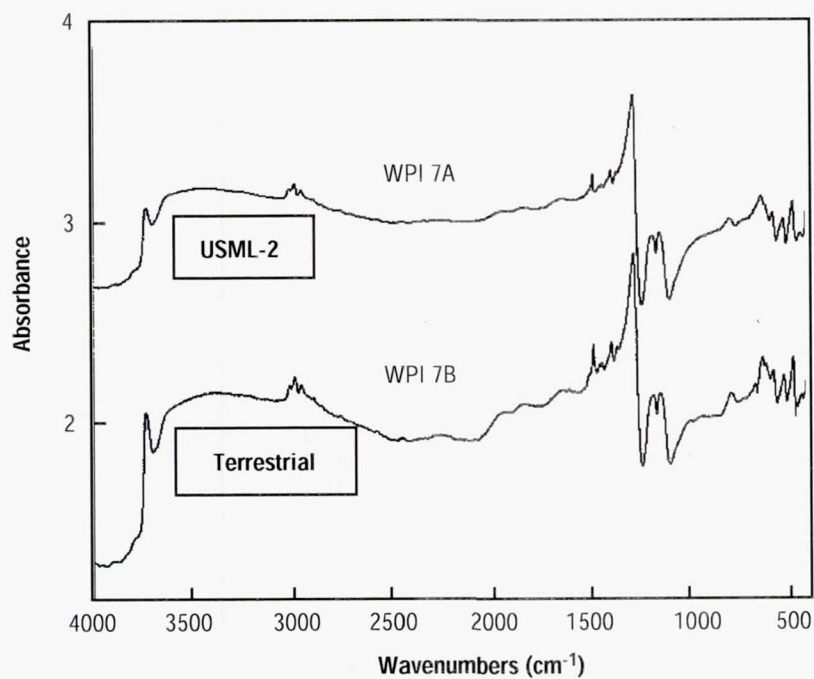


Figure 25. FTIR analysis of zeolite Beta from silica gel

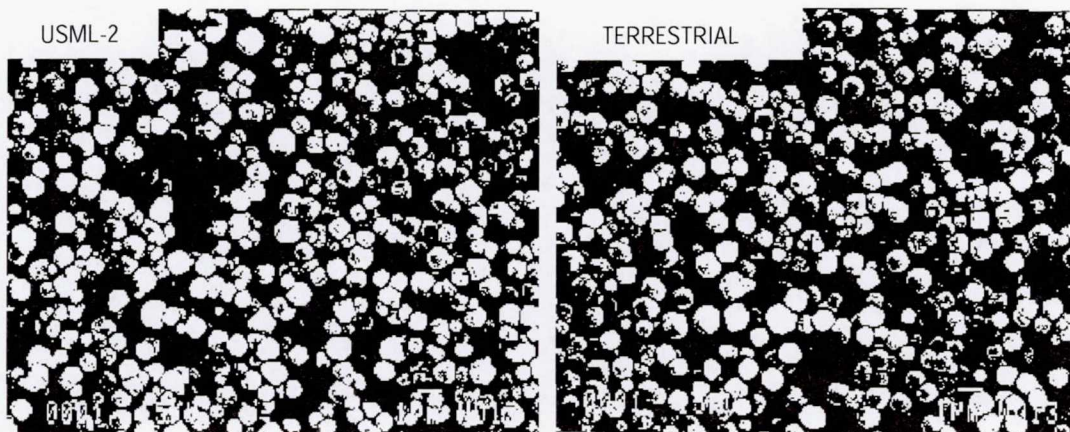


Figure 26. SEM pictures of zeolite A grown in clear glovebox autoclaves.

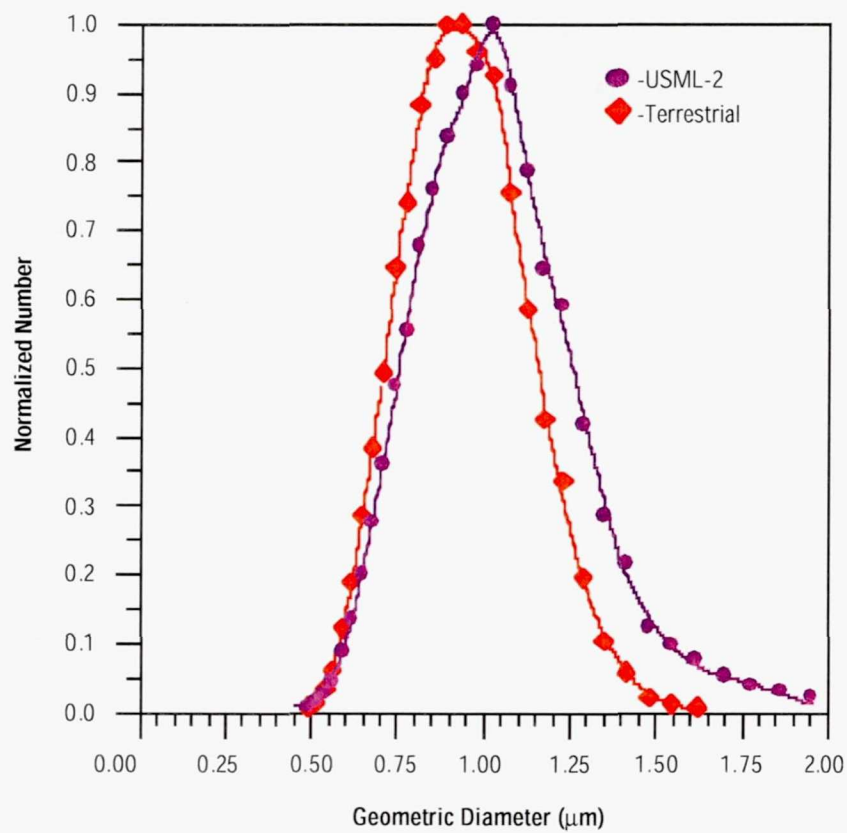


Figure 27. PSDs of zeolite A illustrated in figure 26.

Page intentionally left blank

EXPERIMENT IV.

USML-2 DROP DYNAMICS EXPERIMENT

Page intentionally left blank

EXPERIMENT IV: USML-2 DROP DYNAMICS EXPERIMENT

T.G. Wang, A.V. Anilkumar, C.P. Lee, A.B. Hmelo, and N. Daidzic

Center for Microgravity Research and Applications
Vanderbilt University
Nashville, Tennessee

1. INTRODUCTION

The drop dynamics experiments utilized the unique zero-g environment provided by space flight to investigate the nonlinear dynamic behavior of free drops. These experiments are natural candidates for implementation in a manned space flight. Astronauts volunteered their own free time to conduct additional experimental runs, making the experiments successful. The USML-2 flight was aimed at completing the experimental series originally scheduled for USML-1, which were not completed because of hardware malfunction. The past experience helped us in designing the USML-2 experiments, taking into account the limitations of the experimental hardware. It also prepared us to anticipate extensive data reduction and processing activities.

The USML-2 experiments had three primary objectives:

- 1) Equilibrium shapes of liquid drops under the effects of rotation and acoustic flattening: The USML-2 experiments showed that a rotating liquid drop bifurcates into two-lobed shapes at a lower angular velocity if it is flattened. We have conducted a systematic study of the flattening effects on rotation bifurcation.
- 2) Core-centering of compound drops in capillary oscillations: The USML-1 experiments showed the effect of oscillations on core-centering. In USML-2 we pushed the experimental parameters into regions unexplored by theory.
- 3) Nonlinear drop oscillations:
 - a) Mode coupling: In this experiment we have observed energy transfer between the oscillation modes.
 - b) Hysteresis and jump: We have observed weak softening hysteresis effects in our experiments. This can be described by Duffing-like sets of equations.
 - c) Chaotic drop oscillations: Chaotic oscillations of a drop driven by multi-frequency excitation has been observed. Detailed analysis is underway.

2. DPM VIDEO DATA REDUCTION

ABSTRACT/OBJECTIVE

In order to extract the greatest possible scientific return from Drop Physics Module (DPM) experiments, advanced data reduction techniques have been employed for the purpose of improving the signal to noise and measuring both the shape and the shape evolution of oscillating drops. This extended abstract describes the hardware and software that implements our approach to this task.

2.1 Background/Justification

Raw DPM data returned from USML-2 amounts to 5 million video frames. As shown in table 1, this represents a $600 \times$ increase over the data delivered during USML-1. We have developed automated and semiautomated data processing capabilities to handle the sheer volume of data available.

Table 1. Raw DPM data returned from USML-2 mission.

	USML-1	USML-2
Total # Frames	4,000,000	5,000,000
# Useful Frames	200,000	500,000
# Frames Analyzed	10,000	50,000
Data Extracted per Frame	12 bytes	1.4 kB
Total Data Extracted	120 kB	70 mB

Our concern has been to describe the detailed shape, and shape evolution, of approximately spherical drops, undergoing small amplitude oscillation and rotation, moving about some mean position within the DPM acoustic chamber, in an environment of uneven lighting. In order to test our hypotheses of mode coupling, jump, hysteresis, and chaos, we require the complete 3-dimensional topology of the drop as a function of time. Once we have reduced the description of the drop boundary to a time series of relevant coefficients, many other data may be derived as a product of subsequent analysis. Our present task is to discuss the protocol for generating the shape time series.

In the general case, a complete description of the 3-dimensional shape of a drop would require a synchronized photographic record of infinite views of the specimen. In practice, only two orthogonal views are available for data collection. It is for this reason that the experiments were carefully planned to satisfy the requirements of axisymmetry. For data that satisfy this requirement, a complete 3-dimensional description of the drop may be obtained in a view that is orthogonal to the symmetry axis of the drop. Axisymmetry is confirmed prior to data analysis by examining the specimen in two orthogonal views, such as x and z .

We choose to express the drop shape as a Legendre polynomial expansion. Legendre polynomials provide the natural solution to problems involving the Laplace equation, such as those describing potential flow. Not only does the Legendre polynomial provide the best approximation of the drop shape, it is the only unique solution to the problem of best fit (least squares). Any axisymmetric simply connected shape can be expanded as a Legendre series, consisting of the sum of an infinite series of trigonometric terms,

each weighted with a Fourier-Legendre coefficient, equation (2.1):

$$r(\vartheta) = \sum_{n=0}^{\infty} \varepsilon_n P_n(\cos \vartheta) \quad (2.1)$$

where ε_n represents the Legendre coefficient of order n and P_n are the Legendre polynomials:

$$P_0 = 1$$

$$P_1(\cos \vartheta) = \cos \vartheta$$

$$P_2(\cos \vartheta) = \frac{1}{2}(3 \cos^2 \vartheta - 1)$$

and so on.

In practice, we sum a limited number of terms which through their superposition approximates the shape we are examining, as discussed below. The problem of describing the shape of an axisymmetric drop is reduced to one of specifying a set of coefficients that characterize the approximating polynomial. When performed on a frame by frame basis, we then have a record of both the spatial and temporal variation of the drop shape. From an analysis of these coefficients we can identify the temporal interaction amplitudes of the various modes.

2.2 Experiment

2.2.1 Hardware

DPM footage is supplied in the form of SVHS video tapes. Data analysis can be performed at one of three temporal resolutions. For data with a temporal resolution of 1/30 sec, the video source is a Sanyo GVR-950 SVHS VCR. For data with a temporal resolution of 1/60 sec, a Panasonic AG 7350 SVHS VCR is used. Data from cine film are converted to a video frame rate of 30 frames per sec. Depending on the exposure conditions, this data may be available in a range of resolutions from 1/30 to 1/400 sec. Data analysis software is implemented on a Macintosh Quadra 900. Image acquisition is accomplished using a Data Translation QuickCapture DT2255 video frame buffer.

2.2.2 Software Modules

Boundary recognition is performed in software using a program developed by Dr. Tian Yuren of Yale University. Minor improvements and modifications have been added to the original code to make the program compatible with Vanderbilt hardware and objectives. Some of these modifications, such as batch file processing, will be mentioned below. The software runs in the MacRail 8.2 software environment. Topological analysis of oscillating drops is performed on a Pentium computer using the Legendre expansion coefficients from video processing.

2.2.3 Criteria for Automated Versus Batch File Processing

The image analysis algorithm is provided in figure 1. Initially a user must test the quality of the video data based on a trial run of the processing software on a segment of video data. Frames are read into buffer memory and processed sequentially. The VCR is advanced by a user-specified number of frames per cycle under control of the computer. Once the frame has been stored in the graphics buffer, the image is interrogated pixel by pixel. The drop boundary is identified by specifying threshold values of gray level and gradient that characterize the drop boundary, over and above the noise in the vicinity of the boundary. Adjacent boundary points satisfying the threshold conditions are subsequently identified.

However, the trial run may show that the drop boundary may not be of sufficient contrast for reliable discrimination. An underlying assumption of the edge detection routine is that the shape being sought is a simply connected figure. This assumption is satisfied by the physical drop; however, the drop image on video presents other challenges, which we will refer to as (1) background noise, (2) hot spots and streaks, and (3) low contrast edges.

For example, in the case of cine film converted to video, drop images from USML-1 were impressed on a complicated or "busy" background featuring gray levels and image gradients comparable to the drop itself. This background is attributable to defocussed DPM components, such as optical window cutouts. In the case of USML-2 footage, significant noise in the form of a fog or haze has been noticed in the background. The gray level of a pixel from the noise significantly exceeds the average gray level on the drop boundary. In the case of noise, the background must be removed from the video frame before the edge sensing algorithms may operate reliably.

Hot spots are attributable to DPM light sources, and lead to flares that seriously distort the drop boundary. Finally, the visible drop boundary may appear incomplete as a result of an interplay of lighting and difficult reflection conditions, especially for drops that depart significantly from the spherical shape. In these cases the automated processing routines can report corrupted data files as the programs interpret these artifacts of illumination or background as true drop boundaries. Additional filtering of the images must be performed to recover data that the computer may not recognize. The human eye is very good at judging the continuity of drop boundaries in cases where the illumination artifacts are not severe. For example, in figure 2, an experienced investigator can judge which parts of the image are artifact and where the true boundary exists. The computer program will interpret the flare as part of the true boundary, as in figure 3. In these cases, off-line graphical editors are used to filter the image and to remove inappropriate artifacts from the drop background. In no case is more than 10 percent of the circumference of the drop image repaired. Images not satisfying this criteria are rejected for data reduction. The filtered frame is then placed in a batch file on hard disk for shape analysis. In figure 6 we demonstrate the result of one such repair, as discussed below. We have chosen this approach of human edge recognition as a practical alternative to writing a rules-based algorithm for machine edge recognition. This allows us to extract the available data in the shortest amount of time.

2.2.4 Determination of the Legendre Coefficients

Assuming that the source data is of sufficient quality, frames are read into buffer memory and processed sequentially. Three-hundred and sixty equiangular edge determinations are performed for each

frame allowing a precise evaluation of drop shape. The coordinates of the 360 points are reported as $x'y'$ pairs corresponding to locations in the pixel buffer that correspond to boundary positions. These 360 points are written sequentially to a file on hard disk for further processing. The VCR is advanced one frame per cycle under control of the computer.

Legendre analysis is performed in a polar coordinate system. The $x'y'$ coordinates of the drop boundary as determined from the computer buffer are taken as the starting points of the calculation. The first step in processing is to find the centroid of the shape defined by the drop boundary. All $x'y'$ coordinates are then adjusted to locate the centroid at the origin of coordinates. The 360 $x'y'$ pairs are then converted to polar coordinates r and ϑ .

By nature of the levitation conditions, drops often have their axis aligned to within 5° of vertical. In the event a small correction of drop orientation is required, the program has the capability to align major and minor axes with the coordinate axes. To avoid large rotations that would result from attempts to align drops of near spherical shape, the maximum rotation is limited to 3° . Data requiring larger adjustments are rejected. Following adjustment of the drop orientation, the shape is examined to determine the degree of asymmetry in the view. This is done by comparing the radius of the specimen at the $\vartheta=0^\circ, 90^\circ, 180^\circ$, and 270° degree positions. If the shape is not axisymmetric the data is rejected.

Data are further filtered by averaging each half of the drop boundary. Legendre coefficients for the filtered boundary are then evaluated numerically according to equation (2.2):

$$\varepsilon_n = \frac{2n+1}{2} \sum_{i=1}^{180} r(\vartheta_i) P_n(\cos \vartheta_i) \sin \vartheta_i \Delta \vartheta \quad (2.2)$$

where (r, ϑ) are the polar coordinates of the drop boundary, and $\Delta \vartheta$ is the angular increment between boundary points, in this case 1° . Legendre coefficients are evaluated to order 12, sufficient to recover the empirical drop boundary with <1-percent error.

This error is evaluated by expressing the computational drop shape as a Legendre series expansion as indicated in equation (2.1). For 360 values of (r, ϑ) beginning at zero, a difference is taken between the computational and empirical radius of the corresponding drop. If the rms value of the sum of these 360 differences is >1 percent, a flag is set and the data is rejected. In practice, the Legendre expansions recovered the drop shape to better than 0.5 percent.

2.3. Results and Discussion

As a practical illustration of these techniques we will illustrate data from the free decay of a compressed 100 cSt silicone oil drop from FO 9. The video data source is Spacelab video tape. This drop was initially compressed to a large value of W/L and then released by turning off all acoustics. Free decay to the spherical shape occurs within 3 sec, during which time it translated along the z -axis for a distance of 5 cm. Video frames relevant to this experiment were captured to hard disk and filtered for batch processing. In figure 2 we show one frame that contains a typical lighting defect. The computer program readily follows the lighting flare as a true boundary, as seen in figure 3. Misinterpreted drop boundaries have serious

implications for subsequent data analysis. Figures 4 and 5 display results from unfiltered data subjected to the automated processing, before filtering. In figure 4 we see that although the software can track the drop as it translates in the field of view, the time series for the ε_2 and ε_4 Legendre coefficients display irregularities and noise, attributable to inaccurate boundary detection. Figure 5 shows a plot of drop volume, as a function of time, for both the filtered and unfiltered data sets. Figure 5 clearly shows that the image filtering has recovered the drop volume compared to the unfiltered condition. This improvement is possible after repairing minor defects to the drop boundary, recovering data that would otherwise be lost. In figure 6 we show an example of a single frame, corresponding to figure 4, that has been filtered. The lighting flare has been removed, allowing the drop boundary to be detected unambiguously. Figure 7, corresponding to figure 4, illustrates the improvements in mode 2 and mode 4 Legendre time series that result from filtering.

The best temporal resolution is obtained at the highest frame rates. Video data are available on a field-by-field basis, and provide an opportunity to examine higher frequency components of the data. The entire free decay sequence was filtered on a field-by-field basis at 1/60 sec resolution. The results for the ε_2 and ε_4 shown in figure 8 illustrate the improved signal to noise that video data reduction techniques have provided.

3. EQUILIBRIUM OF LIQUID DROPS UNDER THE EFFECTS OF ROTATION AND ACOUSTIC FLATTENING: RESULTS FROM USML-2 EXPERIMENTS IN SPACE

3.1 Objective

Previous experiments¹ showed that a rotating liquid drop bifurcates into a two-lobed shape at a lower critical angular velocity if it is flattened acoustically by the levitating sound field. In this work, we undertake a systematic experimental study of the effect of acoustic flattening on the rotational bifurcation of a liquid drop. We also look into the complementary effect of rotation on the equilibrium of a drop drastically flattened by acoustics. Theoretical models are developed for the two effects and then woven into a unified picture. The first effect is about neutral equilibrium while the second is about loss of equilibrium, neither of them involving instability.

3.2 Justification

The question is, how does flattening affect bifurcation? A better understanding of this and related phenomena can contribute to the noncontact techniques for measuring surface tensions.² But a ground-based experiment³ cannot clearly answer this question. According to a remark by Wang et al. (1994),⁴ gravity, though small compared with surface tension in the case of small drops, can tip the delicate balance between rotation and surface tension near the bifurcation point. Consequently the drop tends to be spread more horizontally and to become asymmetrical about its equatorial plane as a result of gravity, leading to biased results. This accounts for the difference between the space-based data of Wang et al. (1994)⁴ and the ground-based data of Biswas et al. (1991).³ Furthermore, there are always the spatial and temporal limitations in a ground-based study that can be overcome in the microgravity environment of space. The study of the shift in the bifurcation point due to acoustic flattening was one of the objectives of the USML-2 flight experiments.

3.3 Experiments

The experiments were conducted using Dow Corning 200 series silicone oils, with drops of volumes from 1 to 3 cm³, and viscosities 100 cSt, 350 cSt and 1000 cSt. Each drop was acoustically flattened before an acoustic torque was imposed to spin up the drop to and beyond bifurcation. The sound pressure levels were kept constant during the spin-up, essentially unaffected by the presence of the small drop. Flattening is measured by $(a/b - 1) \times 100$ percent, where a and b are respectively the equatorial and polar radii of the drop. The experiments were performed in three sessions corresponding to the three values of viscosity. In each run, the initially flattened drop was spun up until one of the following two things happened. The drop can bifurcate from an axisymmetric shape into a two-lobed equilibrium shape, which, upon further spin-up, eventually becomes unstable and fissions into two drops.^{5,6} The drop can also retain its axisymmetric shape as it becomes more flattened, until it loses equilibrium, expands horizontally, and shatters.⁷⁻¹⁰

Let ρ and σ be the density and surface tension of the liquid, and R_0 be the spherical radius of the drop rotating with an angular velocity Ω . The size of the drop is specified by $\alpha = kR_0$, where k is the wavenumber of the sound wave that vibrates along the axis of symmetry of the drop. The quadrupole oscillation frequency of the drop¹¹ is given by $\omega_0 = (8\sigma / \rho R_0^3)^{1/2}$. Let the normalized rotation rate be $\Omega^* = \Omega / \omega_0$. Let R^* be the maximum equatorial radius R scaled by R_0 , for either two-lobed bifurcation or axisymmetric loss of equilibrium. One way to present the evolution of a drop is to plot R^* versus the normalized rotation rate Ω^* , for a given initial flattening.

In figures 9-11, we show such plots for the three viscosities. For reference purposes, we have also drawn the (solid) theoretical curve describing the deformation of an initially spherical drop due to rotation alone.^{5,6} The curve goes from left to right, representing the deformed but axisymmetric equilibrium shape of the drop. It turns upward and backward at the critical rotation rate $\Omega_c^* = 0.56$, leading to the familiar bifurcation branch for the two-lobed equilibrium shape of the drop.⁶ For a flattened drop, the axisymmetric part of the curve shifts upward from its counterpart in the reference curve, as the initial flattening increases. The curve similarly turns backward and upward from the axisymmetric curve, at a critical rotation rate depending on the initial flattening. But the nature of the transition also depends on the following.

The experimental data are classified into two clusters: the one on the right side leads to two-lobed bifurcation, while the one on the left side leads to axisymmetric loss of equilibrium. From the cluster on the right side, it is clear that the critical rotation rate for bifurcation decreases with initial flattening. For the cluster on the left side, where the drops suffer from greater initial flattening, there is no bifurcation: a drop simply loses equilibrium beyond the critical rotation rate. The curve that branches out from the axisymmetric curve represents not equilibrium, but the dynamic process of horizontal expansion due to the acoustic suction stress at the equator of the drop,⁷⁻¹⁰ with a little help from the centrifugal force due to the rotation. A special feature in figure 11 is the behavior of the 102-percent flattening drop. The drop lies between the regime where it bifurcates and that regime where it loses axisymmetric equilibrium. At the rotation rate of ~ 0.25 , it tries but fails to bifurcate, and loses equilibrium at a higher rotation rate.

The results are summarized in figure 12, where we plot the data, from both USML-1 and USML-2, in the form of critical rotation rate versus initial acoustic flattening. The points stand for drops of different sizes, but the drops are small enough such that the asymptotical limit $\alpha \rightarrow 0$ can be considered. The cluster of data on the left represents a two-lobed bifurcation perturbed by acoustic flattening. Those further to the right side represent loss of axisymmetric equilibrium under the influence of rotation.

3.4 Theories

There are two theoretical problems: the perturbation of two-lobed bifurcation by acoustic flattening, and the perturbation of the acoustically flattened drop by rotation. The formulation for the first problem can be summarized by

$$\delta E = \delta E_s + \delta E_r + \delta E_a = 0 \quad (3.1)$$

where δE_s and δE_r are the variations of the surface and rotational energies respectively, at constant angular momentum, due to a two-lobed shape perturbation, δE_a is the work done by the acoustic radiation pressure due to the deformation, and δE is the total variation in energy. The variations are all second-order in the shape perturbation amplitude ε . The result is:

$$\frac{\Delta \Omega^*}{\Omega_c^*} = -\frac{4}{7} \left(\frac{a}{b} - 1 \right) \quad (3.2)$$

where Ω_c^* is the critical rotation rate for the two-lobed bifurcation, and $\Delta \Omega^*$ is the shift in its value due to acoustics.

For the second problem, the formulation is given by Lee et al. (1994),⁹ using a boundary integral technique, but including rotation in the Young-Laplace equation:

$$\sigma \nabla \cdot \mathbf{n} = P_1 - P_a + \frac{1}{2} \rho \Omega^2 r^2 \quad (3.3)$$

where \mathbf{n} is the normal unit vector pointing out of the drop surface, P_1 is the hydrostatic pressure inside the drop, P_a is the acoustic radiation pressure on the drop surface, and r is the radial distance in cylindrical coordinates. Let the acoustic Bond number be $B_a = A^2 R_0 / \sigma \rho_0 c_0^2$, where A is the sound amplitude, and ρ_0 and c_0 are the density and speed of sound of air, respectively. For small α , if there is no rotation, B_a rises from zero to a peak $B_{a,c}$ when plotted versus R^* from 1 to R_c^* of about 1.45.⁹ With rotation, we have found in this study that:

$$\frac{\Delta B_a}{B_{a,c}} = -CB_r \quad (3.4)$$

where ΔB_a is the shift in $B_{a,c}$ due to rotation, C is approximately constant at 0.21, and $B_r = \rho \Omega^2 R_0^3 / \sigma$ is the rotational Bond number, while R_c^* is essentially unchanged.

3.5 Results

The results of the two problems can be translated into R^* versus the critical rotation rate. They are superimposed on the experimental data in figures 9-11. The horizontal dashed line on the left represents the critical value of R^* at which the drop at large acoustic deformation loses axisymmetric equilibrium due to rotation. The critical R^* here is independent of the rotation rate. The dashed curve coming out of the unperturbed two-lobed bifurcation point on the right represents the critical rotation rate and the corresponding R^* at two-lobed bifurcation involving rotation. It can be seen that the theoretical predictions are in good agreement with the data. The theoretical results can also be translated into the shift in the critical rotation rate versus initial acoustic deformation just like equation (3.2). They are superimposed on the experimental data in figure 12. Again, the agreement is good.

3.6 Conclusion

Previous experiments¹ showed that acoustic flattening lowers the two-lobed bifurcation point of a rotating drop. In this work, we have conducted systematic experimental and theoretical studies of the effect of acoustic flattening on rotational bifurcation, which is about neutral stability. We have also considered the other extreme regime of the effect of rotation on the equilibrium of an acoustically drastically flattened drop, which is about loss of equilibrium. Theoretical models have been developed for the two effects and then put together to explain the whole situation. The theoretical results agree well with the experiments.

In summary, we have explored a situation in which a regime of neutral stability overlaps with a regime in which equilibrium is on the verge of collapsing, in the context of a rotating drop subjected to acoustic flattening. The situation is comparable to that of a ball sitting in neutral stability near the edge of a flat table. The behavior of a "confused" borderline case like the 102-percent drop in figure 11 might be worthy of further study.

4. CORE-CENTERING OF COMPOUND DROPS IN CAPILLARY OSCILLATIONS: OBSERVATIONS ON USML-2 EXPERIMENTS IN SPACE

ABSTRACT

Experiments on liquid shells and liquid-core compound drops were conducted with large shell-core volume ratio drops (>4) using the DPM on the USML-2 mission. It was observed that the drop inner and outer interfaces became concentric during the capillary oscillations. These oscillations were either the freely decaying type, that occurred following the deployment of the drops, or they were externally forced by the acoustic fields. The results of core-centering should push theoretical computations beyond the regimes currently possible and also enhance the preliminary results available from USML-1.¹

4.1 Justification and Background

A compound drop¹² consists of a fluid drop enclosed inside another liquid drop. The inner drop, the outer drop, and the external medium are called the core, shell, and host, respectively. When the core is a gas bubble, the compound drop is referred to as a *liquid shell*. In our studies, we are only interested in air as the host medium, and its dynamics can be neglected compared with that of the drop. A compound drop exhibits two types of oscillations due to the surface tensions on its inner and outer interfaces: 1) the lower frequency slosh mode in which the two interfaces move opposite to each other; and 2) the higher frequency bubble mode in which they move in the same direction as each other.¹³

In the absence of gravity, the core can sit anywhere inside the shell. From the experiments on USML-1, it has been demonstrated that the core goes towards the center of the drop, for both the liquid-core compound drop and the liquid shell, when the drop oscillates. From a theoretical point of view, in the linear regime, the core is still neutrally stable anywhere inside the shell. Taking into account the nonlinearity, the centering mechanism for an inviscid liquid shell has been studied in the thin shell limit¹⁴ and for the finite shell thickness.¹⁵ The two theories are formulated completely differently, but their essential results agree with each other. Their main conclusion is that in the presence of a pure mode of capillary oscillation, the bubble of the liquid shell undergoes a slow translational oscillation inside the shell, with a frequency that is proportional to the amplitude of the capillary oscillation. Theoretical results for liquid shell centering are available for drop-core volume ratios up to 3, whereas the current experiments push this to volume ratios up to 8.

Whereas with the USML-1 experiments we demonstrated the mechanism of centering in the regions handled by theory, with USML-2 the objective was to push the experimental parameters into regions unexplored by theory.

4.2 Experiments

The experiments were conducted on the DPM using acoustic fields for positioning and manipulating the drops. Two types of compound drops were deployed: 1) water shells, and 2) silicone oil, water-glycerol immiscible compound drops. The data were recovered from two scenarios: 1) during drop deployment, and 2) during forced oscillations of the drops. All data analysis has been conducted using standard video available at 30 frames and 60 fields per sec.

4.3 Results and Discussion

4.3.1 Liquid Shells

The deployed drop had a volume of $4.0 \pm 0.1 \text{ cm}^3$, consisting of 3.5 cm^3 of water and 0.5 cm^3 of air. The average operating temperature was 27°C . The water contained some pliolite tracers ($50 \mu\text{m}$, Goodyear Chemical Co.) for monitoring any uncontrolled rotation of the drop.

Following deployment, the liquid bubble executes $n=2$ bubble mode oscillations, with decaying amplitude, at a frequency of around 15 Hz. In the process of these oscillations, the air core is centered. Figure 13 shows the bubble position as a function of time. The levitating field is switched on following deployment, and the sole effect of this is to propel the air bubble away from the edge, along the deployment axis. Owing to the ongoing capillary oscillations of the bubble, along the deployment axis, the bubble retraces its path, after a delay, and is eventually centered. The characteristic slow oscillation signature, reminiscent of centering, can be seen in figure 13. This signature is uncontaminated by the picking up of the uncontrolled rotation by the drop because the latter occurs at a slightly later time scale. The slow oscillation signature has a frequency of around 1.1 radians per second. For this radius ratio R^* of 0.5, there are no theoretical predictions to compare the magnitude of the slow oscillation frequency. Figure 14 shows the decaying oscillations of the liquid shell following deployment. The shape oscillation amplitude " ϵ " during centering ($\epsilon = (L'/W' - b'/a') \times 100$ percent; L' and W' are the height and width of the drop in the maximum prolate shape, and b' and a' represent the equilibrium minor and major axes of the drop) was very small, an average of about 1.5 percent. Once the core was centered, it did not go off center easily.

4.3.2 Liquid-Core Compound Drop

The deployed drop had a volume of $2.5 \pm 0.05 \text{ cm}^3$, with 2.0 cm^3 of silicone oil shell and 0.5 cm^3 of water/glycerine core. The core and shell viscosities were matched to be about 2 cSt. The shell contained pliolite tracers, and the water/glycerine core contained green food coloring (0.5 percent by volume). The tracers were used for monitoring any uncontrolled rotation of the drop. The dye helped to make the inner interface more visible.

Following deployment the drop had a cigar shape, with both the drop and core aligned along the deployment axis (see inset fig. 15). The free decay of this shape to a spherical shape, via slosh-mode capillary oscillations, provides an interesting study of the uniaxial motion of the core (fig. 15). Here, the core is centered in about five oscillation cycles.

In a second experiment, oscillations were forced on this drop by modulating the acoustic field. These experiments were done with the drop rotating, and thereby the centering force competed with the centrifugal force. Results showed that the coupling of the oscillations in the bubble mode were weak, and no centering could be effected in the bubble mode. On the contrary, the compound drop could be driven to large amplitudes in the slosh mode and centering could be effected. Figure 16 follows the core's radial position as the rotating compound drop was driven into slosh-mode oscillations. The drop was initially rotating at 0.15 rps, along the oscillation axis. The modulation frequency was swept from 1.8 to 2.7 Hz in 200 seconds, through the $n=2$ slosh mode of the compound drop. Centering occurred in the first 10 sec, where the frequency is essentially about 1.8 Hz. The amplitude during the first 10 sec was $\epsilon \sim 0.35$. In the context of a rotating drop, the core took a spiral route to the center. The centering time (cycles) was much longer here compared to the nonrotating case (fig. 15), because the centering force was competing with the centrifugal force and that tended to push the core to the periphery.

4.4 Concluding Remarks

Experiments on liquid shells and liquid-core compound drops were conducted with large shell-core volume ratio drops (>4), using the DPM on the USML-2 mission. These oscillations were either the freely

decaying type that occur following the deployment of the drops, or they were externally forced by the acoustic fields. Both the liquid shells and the liquid core compound drops were found to center following initiation of capillary oscillations. The results on core-centering should push theoretical computations beyond the regimes currently possible, and also enhance the preliminary results available from USML-1.¹

5. MODE COUPLING AND NONLINEAR DROP OSCILLATIONS

ABSTRACT

Free oscillations of levitated drops were performed in the USML-2 reduced-gravity environment using the DPM chamber. Different liquid drops with large variations in thermophysical properties were used. The oscillatory free decay was observed. The time series and the spectral analysis have confirmed the existence of various nonlinear phenomena. Mode coupling (i.e., energy transfer between the oscillation modes) was clearly observed and confirmed. The mode coupling phenomena, which in general includes mode excitation, quenching, mode locking, and other exclusively nonlinear properties, is the result of the structural nonlinearity given by the surface deformation and the kinetic nonlinearity expressed through the nonlinear inertial matrix in the Lagrangian or the Hamiltonian formulation.

5.1 Background

In contrast with the case of systems having a single degree of freedom, which has only a single natural resonance frequency and a single mode of motion, a n -degree-of-freedom system has n natural frequencies $f_1, f_2, f_3, \dots, f_n$ and n corresponding natural modes.¹⁶ New physical phenomena occur in the free oscillations of a system, some of whose frequencies are commensurable or nearly commensurable; that is, there exist positive or negative integers $m_1, m_2, m_3, \dots, m_n$ such that

$$m_1 \cdot f_1 + m_2 \cdot f_2 + m_3 \cdot f_3 + \dots + m_n \cdot f_n \approx 0$$

When such conditions exist we speak of internal resonance, and the natural modes of the multi-degree-of-freedom system are involved in so-called mode coupling and energy transfer between the modes.¹⁶ In addition, if the system—having finite degrees of freedom—is gyroscopic and possesses an internal resonance, then its free nonlinear oscillations may be unbounded with time even though its free linear-free oscillations are bounded.

Because the drops have commensurable oscillation pairs in modes 2 and 4, and then in modes 5 and 8, it is very important to investigate the existence of the internal resonance, mode coupling, and the nonlinear oscillation energy transfer between the modes. This also has very important practical implications because it may accordingly lead to drop breakup in free oscillation systems. The mode coupling will be even more visible in the forced oscillation systems.

Trinh and Wang (1982)¹⁷ were the first to measure large-amplitude drop oscillations. They measured a soft nonlinearity in the frequency change due to amplitude and equilibrium static distortions. They also studied internal flow patterns during small and large droplet oscillations. Despite its importance, an

entire century passed between Rayleigh's analytical formulation of small-amplitude oscillations of inviscid droplets and the theoretical solution of Tsamopoulos and Brown (1983)¹⁸ for inviscid, moderate-amplitude droplet oscillations. This system of equations was solved with the help of the singular Lindstedt-Poincaré perturbation technique. After a tedious and time-consuming perturbation analysis using the symbolic algebra computation code MACSYMA, the authors determined the softening-spring nonlinear effect (i.e., a resonance frequency decreases with the square of the oscillation amplitude). Natarajan and Brown (1987)¹⁹ used the preaveraging Lagrangian variational principle. They found a nongeneric cubic resonance between the second and the fourth inviscid oscillatory modes which leads to quasi-periodic oscillation. The authors also derived the amplitude equations, which describe the generic cubic resonance caused by the spatial degeneracy of the eigenfrequencies of the (linear) normal modes. Lundgren and Mansour (1988)²⁰ numerically studied large-amplitude droplet oscillations in zero gravity with weak viscosity effects (irrotational approximation) with a boundary-integral method. They found that small viscosities have a relatively large effect on resonant mode coupling and can sometimes trigger the instability rather than damping it. Basaran (1992)²¹ used a full-viscous, arbitrary-amplitude, numerical scheme based on Galerkin's finite-element, implicit predictor-corrector and Newton's method for solving the resulting system of nonlinear algebraic equations; this showed that both oscillation frequency and viscous damping are time- and amplitude-dependent functions. Basaran approved conjecture that viscosity might have a larger significance than was anticipated in Lundgren and Mansour's "low-viscosity" computations. Unfortunately, Basaran did not perform spectral analysis of his computed time series so that no frequency information was available.

Möhring and Ravindran (1993)²² used the variational (Lagrangian) principle to investigate nonlinear axisymmetric oscillations of a drop in another incompressible inviscid fluid. They modified the variational approach to account for an external enforced oscillation. The special focus of their study was the investigation of the "mode locked" states (i.e., states where the drop oscillates with the external force frequency). Becker, Hiller and Kowalewski (1994)²³ used the mode expansion technique and variational principle of Gauss. They obtained a system of ordinary differential equations which includes all nonlinear and viscous terms. Their computation confirmed results of Lundgren and Mansour and Basaran. The general conclusion is that viscosity plays a decisive role in mode coupling phenomena. Recently, Becker, Brosa, and Kowalewski (1994)²⁴ proposed a method of reducing large and complex full-viscous numerical methods into a simple but, nevertheless, realistic model of nonlinear viscous droplet oscillations. They examined the applicability of the irrotational approximation for low-viscosity liquids and obtained good agreement with experiments and large-scale computational models. Their model is based on the variational principle, and the results were analyzed in phase space. Wang, Anilkumar, and Lee (1996)²⁵ have used the USML-1 experimental results and basically confirmed the Tsamopoulos and Brown (1983)¹⁸ theory for inviscid, moderate-amplitude drop oscillations. However, the authors were mainly concerned with the intermediate and final stage of free drop oscillations. The first region of large drop oscillations, where the mode coupling takes place, was not investigated.

The importance of various nonlinear phenomena in atomization has been recognized recently by Daidzic (1995a, 1995b)^{26, 27} and Daidzic, Wang, and Stadler (1995).²⁸ In a series of experiments and theoretical investigations performed by Daidzic, the mode coupling and nonlinear energy transfer phenomena have been identified. However, in order to verify the theoretical investigations a very clean experiment was needed. This was provided by the USML-1 and USML-2 experiments.

5.2 Experiment

The free oscillations experiment was performed in the DPM chamber during the USML-1 and USML-2 missions. Liquid drops of various thermophysical properties and the diameter size of approximately 2 cm (4 cm^3) were suspended and stabilized in an acoustic well of an ultrasonic levitator. Sound pressure level was then slowly increased and a drop was subsequently deformed in an oblate equilibrium shape.

After all the parameters were stabilized in a chamber, the acoustic radiation pressure (and the levitation) was instantly turned off. Due to the boundary and initial conditions a drop started to oscillate, trading its potential energy for the kinetic energy and vice versa. Because of the finite liquid viscosity, the oscillations ultimately died out and a drop drifted from the camera focal point due to the residual acceleration.

Drop oscillations were captured with the high-speed film camera and a CCD electronic camera. In both cases the top and side views were taken. It was then possible to verify the assumption that the oscillations have to be axially symmetric. And they were! The sampling rate of the high-speed camera was 400 Hz. The sampling rate of the CCD camera was 60 Hz. Field analysis instead of CCD frame image analysis was used for better temporal resolution, and the Nyquist sampling criterion was used in the case when the CCD camera was used instead of the high-speed camera. The individual images were first frozen and then cleaned, filtered, and smoothed. This was necessary in order to achieve high spatial resolution (SNR) and to remove protuberances and disturbances caused by the illumination. Images were then again checked for axial symmetry and volume conservation.

Such preprocessed images were then fitted with the Legendre polynomials, and the Fourier coefficients were estimated. Those coefficients have a direct physical meaning because they represent the mode amplitudes. Processing the individual images, it was possible to obtain the time series of drop oscillations for each mode. Depending on the deformation size, up to 18 Legendre orthogonal zonal modes were detected. This was also necessary to keep track of the volume conservation and to ensure that the volume remained constant. Since 360 points were taken over the circumference, the Legendre fitting was statistically very stable and, consequently, the small localized errors in boundary recognition were insignificant. One of the virtues of the Legendre polynomial expansion is its capability to actually recover some missing points on the interface. This, in conjunction with the discrete Fourier transform filtering, resulted in very smooth and extremely accurate shape recognition.

The time series of the surface modes enabled the estimation of the complete drop topology. Parameters such as drop volume, drop cross-section area, superficial area, circumference, surface energy, mean drop size, volume conservation coefficient, etc., were all obtained at once. All these parameters have proven to be indispensable tools in understanding the drop nonlinear oscillation dynamics.

The spectral analysis of the time series was performed as the next step. The results of spectral analysis have shown the fine details of the mode coupling and energy transfer between the modes. The

Welch periodogram with the Hamming windowing and the Cooley-Tukey (decimation-in-time) fast Fourier transform of the discrete time series was obtained for the power spectral density (PSD) calculations. The same technique was used for the estimation of the cross power spectral density (CPSD) function.

5.3 Results and Discussion

Many useful results were extracted from the image processing, time series and spectral analysis. Let us first look at some results from the USML-1 free decay experiment. The 4 cm³, 65/35 glycerin/water drop was released from the initial static deformation containing both second and fourth Legendre zonal initial deformation. Time series of the mode 2 and mode 4 oscillations are shown in figure 17. Also the Rayleigh-Lamb linear prediction was plotted with solid and dashed lines. Periodic amplification of the mode 4 oscillations is coming from the internal interaction with the mode 2 oscillations. Since the oscillations are truly free, such periodic amplifications can be only explained by some sort of internal mode excitations. In figure 18, the PSD of the second mode oscillations is shown. The appearance of higher order harmonics is clearly evident. In figure 19, the PSD of the fourth mode oscillations is shown. The mode 4 resonance frequency is around 9.5 Hz. Note the appearance of the subharmonics and harmonics of the second fundamental oscillations. In figure 20, the mode 2 and mode 4 CPSD is shown. The CPSD function represents the transfer or the coherence function of the system. Therefore, one might see the CPSD function as the filter function uncovering the internal oscillation energy transfer in the frequency domain. This process is similar to turbulent energy transfer. From the distinctive, sharp, and clean peaks one can easily identify the regions and the frequencies most responsible for the internal interactions. Note the curious appearance of the mode 2 one-third subharmonic resonance. This implies the existence of the subharmonic internal mode excitations. In figure 21, the relative surface area and/or incremental surface energy is presented. The first harmonic modulation of the basically second mode oscillations of the surface energy is the product of the nonstationary energy interactions between the modes and between the kinetic and the potential energy itself. In figure 22, the free-decay time history of a USML-2 drop is shown. This was a 1 cm (\approx 4 cm³) silicone oil drop released from the oblate equilibrium shape. The viscosity of a drop is 100 cSt, the density is 962 kg/m³, and the surface tension is 0.0209 N/m (dyn/cm). When released from the initial deformed state, the drop undergoes only one oscillation and then aperiodically slowly relaxes to the equilibrium shape. We are assuming that the viscoelastic relaxation is responsible for the very slow relaxation toward the spherical shape. \dot{U} for such small surface distortions become so small that they cannot drive shape oscillations and resist viscoelastic interface properties.

Mode 2 and mode 4 oscillations are presented simultaneously as in the case of the USML-1 experiment. Mode 4 oscillation decay is very fast and shows the same qualitative behavior as in the low-viscosity USML-1 experiment. As anticipated, the viscosity plays a great role in mode coupling. When the viscosity is large enough the internal interactions become insignificant. In figure 23, the power spectrum of the mode 2 oscillations is presented. The resonance frequency is somewhere around 2.4 Hz. The second harmonic and the fourth oscillation mode are barely visibly in the second peak. In figure 24, the CPSD of the mode 2 and mode 4 oscillations is presented. Very similar nonlinear interactions as those presented in figure 20 are also present for this highly viscous drop. However, keep in mind that the initial distortion was substantial and despite the high viscous dissipation, the mode coupling is still present. This fact is clearly once again supported with the PSD of the mode 4 oscillations presented in figure 25. Once again, one can see the existence of the mode 4 fundamental frequency accompanied by the mode 2 fundamental frequency (and mode 4 one-third subharmonic) and other superharmonics, subharmonics and combinational resonances.

5.4 Concluding Remarks

Experiments on free oscillating drops have confirmed the existence of mode coupling. Mode coupling appears as the result of the third-order nonlinearity in the surface amplitude. In general, free decay oscillations as well as forced oscillations can be divided into three main regions:

- Strong nonlinearity ($\propto \epsilon^3$) with mode coupling (i.e., energy transfer between the oscillation modes).
- Weak to moderate nonlinearity ($\propto \epsilon^2$) with nonlinear normal modes. This region is well described with the Tsamopoulos and Brown nonlinear perturbation theory.
- Linear or small-amplitude oscillations ($\propto \epsilon$) described with normal modes. Rayleigh-Lamb linear theory predicts well the oscillation dynamics in this region.

Mode coupling is the result of the structural nonlinearity given by the surface deformation and supported with the kinetic nonlinearity expressed through the nonlinear inertial matrix in the Lagrangian or Hamiltonian.

Viscosity plays one of the major roles in the mode coupling phenomena and internal energy interactions. The magnitude of the initial amplitude is responsible for the subsequent nonlinear interactions. Very large initial deformations could easily lead to chaotic oscillations. This is particularly important for low-viscosity drops such as water. In this case internal energy redistributions could even lead to drop breakup.

5.5 What Is Still Missing?

In order to fully understand complicated nonlinear interactions it is indispensable to develop a mathematical/theoretical model for strong nonlinear oscillations. This model will go beyond the Tsamopoulos and Brown (1983)¹⁸ mathematical model of inviscid small to moderate drop oscillations. The Tsamopoulos and Brown model is not capable of modeling the internal resonances, mode coupling and nonstationary oscillation energy transfers. A new model should be capable of going to very large deformations which would include transition to chaotic oscillations and drop breakup.

6. HYSTERESIS AND JUMP PHENOMENA IN DROP OSCILLATIONS

ABSTRACT

Forced oscillations of levitated drops were performed in the USML-2 reduced-gravity environment using the DPM chamber. The Hysteresis effect and the Jump phenomena for a 4 cm³ water drop were investigated. The excitation amplitudes were 4, 8, and 12 V respectively. The temporal and frequency

responses of oscillating drops on linearly changing frequency excitations were observed. The sweep rate was chosen carefully in order to prevent unwanted nonstationary sweep effects. The time series and the spectral analysis have confirmed the existence of Hysteresis which ultimately leads to the multivalued amplitudes and the very curious Jump phenomena. In the case of drops, we measured lower frequencies for larger oscillation amplitudes. This relaxation phenomena is a so called softening effect. The width of the Hysteresis and the Jump amplitude increases with the excitation amplitude.

6.1 Background

Axisymmetric (zonal) drop oscillations are described with:

$$r(\theta, t) = R_0 \cdot \alpha(\varepsilon_n; t) \left[1 + \sum_{n=1}^{n=N} \varepsilon_n(t) \cdot P_n(\cos \theta) \right]$$

where R_0 is the radius of the equivalent spherical drop having the same volume. $\alpha(\varepsilon_n; t)$ is the volume conservation coefficient assuring that volume remains constant during oscillations. Finally, $\varepsilon_n(t)$ is a dimensionless axisymmetric amplitude of oscillations.

Nonlinear equations describing decoupled (no mode coupling) low-viscosity (irrotational approximation) fixed-volume driven drop shape oscillations for each mode n separately yields:

$$\frac{d^2 \varepsilon_n}{dt^2} + 2\delta_n \frac{d\varepsilon_n}{dt} + \sum_{i=1}^{i=M} \beta_i \varepsilon_n^i = F \cos(\Omega t + \varphi) \quad (n = 2, 3, 4, \dots, N)$$

The effect of the nonlinear inertia matrix was neglected in this formulation. Depending on the sign and the magnitude of each stiffness coefficient β_i , nonlinear drop oscillations may be hard or soft. Note that $\beta_1 = \omega_0^2$ is the natural (linear resonance) oscillation frequency squared.

The equation of motion describing the discrete oscillation modes of drops is strikingly similar to the well-known Duffing equation which, however, has only cubic nonlinearities:

$$\frac{d^2 \varepsilon_n}{dt^2} + 2\delta_n \frac{d\varepsilon_n}{dt} + \omega_0^2 \varepsilon_n + \beta_3 \varepsilon_n^3 = F \cos(\Omega t + \varphi) \quad (n = 2, 3, 4, \dots, N)$$

Duffing nonlinear oscillators may experience both a hard and a soft nonlinearity depending on the sign of β_3 .

Hard nonlinearity describes the increase in the oscillation frequency with the increase in the oscillation amplitude. This corresponds to larger restoring surface forces as the deformation increases. Soft nonlinearity represents a decrease of the oscillation frequency with an increasing oscillation amplitude.

Therefore, the restoring surface forces decrease as the deformation increases.

Equilibrium oscillation shape (oblate-biased or prolate-biased), in general, affects the stiffness coefficients β_i (and even more the inertia matrix). Accordingly, for the oblate-biased oscillation, one may expect hard nonlinearity and for the prolate-biased oscillation, the soft nonlinearity should occur.

The Sweep experiment may be mathematically described with the time varying excitation:

$$\frac{d^2 \varepsilon_n}{dt^2} + 2\delta_n \frac{d\varepsilon_n}{dt} + \sum_{i=1}^{i=M} \beta_i \varepsilon_n^i = F \cos[(\Omega + \psi_n t) \cdot t] \quad (n = 2, 3, 4, \dots, N) .$$

The Sweep experiment enables investigations of the type of nonlinearity (hard or soft), Hysteresis and accompanying Jump phenomena, and mode splitting. Initial observations have indeed shown the existence of Hysteresis, Jump phenomena, and the mode splitting.

The Multifrequency experiment was used particularly in the chaos experiment. The process of excitation can be formally written as:

$$\frac{d^2 \varepsilon_n}{dt^2} + 2\delta_n \frac{d\varepsilon_n}{dt} + \omega_0^2 \varepsilon_n + \beta_2 \varepsilon_n^2 + \beta_3 \varepsilon_n^3 + \beta_4 \varepsilon_n^4 + \dots = F_1 \cos(\Omega_1 t + \varphi_1) + F_2 \cos(\Omega_2 t + \varphi_2) .$$

In $\Omega_1/\Omega_2 \neq m$ where m is an integer, then the quasi-periodic oscillations appear. Such oscillations are described as having an attractor in a form of n -dimensional torus. If the excitation amplitudes F_1 and F_2 exceed some threshold values the chaotic oscillations will result. Those thresholds are much higher in the case of the single-frequency excitation.

Let us now solve a conservative null equation for single mode drop-free oscillations (which includes both the quadratic and cubic nonlinearities):

$$\ddot{x} + \omega_0^2 x + \varepsilon \beta_2 x^2 + \varepsilon^2 \beta_3 x^3 = 0 , \quad (6.1)$$

with the initial conditions $x(0) = A$ and $\dot{x}(0) = 0$. This model also represents a good approximation of the USML-1 free decay experiment. In order to obtain a uniform periodic solution we will use the Lindstedt-Poincaré singular perturbation method or the method of strained parameters. The fundamental idea in this technique is based on the fact that nonlinearities alter the frequency from the linear one ω_0 to $\omega(\varepsilon)$. To account for this change we write:

$$x(t) = x_0(t) + \varepsilon x_1(t) + \varepsilon^2 x_2(t) + \dots \quad (6.2)$$

$$\omega^2 = \omega_0^2 + \varepsilon \alpha_1 + \varepsilon^2 \alpha_2 + \dots , \quad (6.3)$$

where α 's are constants to be determined in order to prevent the appearance of secular (resonant) terms. It is very important to note that the Lindstedt-Poincaré singular perturbation method forces a solution to be strictly periodic and therefore is only applicable to periodic nonlinear oscillations. It also explicitly prohibits the existence of the internal resonance and the mode coupling. After very lengthy and tedious symbolic computation which was much facilitated with the help of the MAPLE symbolic language, one obtains:

$$x(t) = -\left(\frac{\varepsilon A^2 \beta_2}{2\omega^2} + \frac{\varepsilon^2 A^3 \beta_2^2}{3\omega^4}\right) + \left(A + \frac{\varepsilon A^2 \beta_2}{3\omega^2} - \frac{\varepsilon^2 A^3 \beta_3}{32\omega^4} + \frac{29\varepsilon^2 A^3 \beta_2^2}{144\omega^4}\right) \cos \omega t +$$

$$\left(\frac{\varepsilon A^2 \beta_2}{6\omega^2} + \frac{\varepsilon^2 A^3 \beta_2^2}{9\omega^4}\right) \cos 2\omega t + \left(\frac{\varepsilon^2 A^3 \beta_2^2}{48\omega^4} + \frac{\varepsilon^2 A^3 \beta_3}{32\omega^4}\right) \cos 3\omega t + O(\varepsilon^3)$$

$$\omega \approx \omega_0 \left(1 + \frac{3\varepsilon^2 A^2 \beta_3}{8\omega_0^2} - \frac{5\varepsilon^2 A^2 \beta_2^2}{12\omega_0^4}\right)$$

An immediate consequence may be drawn from the frequency change. Namely, it can experience softening or hardening effects depending on the factors β_2 , β_3 , and the linear eigenfrequency ω_0

$$\begin{aligned} \beta_3 &= \frac{10}{9} \beta_2^2 \omega_0^{-2} & \omega &= \omega_0 & \text{no bending} \\ \beta_3 &> \frac{10}{9} \beta_2^2 \omega_0^{-2} & \omega &> \omega_0 & \text{hard spring} \\ \beta_3 &< \frac{10}{9} \beta_2^2 \omega_0^{-2} & \omega &< \omega_0 & \text{soft spring} \end{aligned}$$

The equality $\beta_3 = \frac{10}{9} \beta_2^2 \omega_0^{-2}$ represents a bifurcation point in the frequency response curve. Substituting β coefficients for the second mode drop oscillation, we conclude that a drop always experiences softening nonlinearity (as it was calculated by Tsamopoulos and Brown (1983)).¹⁸ Now when we have shown the origin of the frequency curve bending it is easy to understand why and how the Hysteresis appears. The Jump phenomena is now also the normal consequence of the Hysteresis.

Though the Hysteresis and the Jump phenomena were observed earlier in some mechanical systems, they were rarely anticipated and/or identified in the fluid systems. As far as drop dynamics is concerned, it was first in the works of Daidzic (1995a, 1995b)^{26, 27} that the Hysteresis and the Jump were experimentally and theoretically identified.

6.2 Experiment

The drop-forced oscillation experiment with linearly increasing (positive sweep) and decreasing (negative sweep) excitation was performed in the DPM chamber during the USML-2 experiment. Water drops of ~ 1 cm in radius were suspended and stabilized in an acoustic well of an ultrasonic levitator. Sound pressure level was then slowly increased to a predetermined level (4, 8, or 12 V) and a drop was

subsequently deformed in an oblate equilibrium shape. After these preparations, the forward (positive) sweep started with the sweep rate of ~ 5 mHz/s. The exact procedure was that the frequency range (lower and higher frequency end) was determined first, and the total time for the run was then estimated so that the sweep rate fulfilled quasi-stationary conditions. Negative sweeps were performed in the same manner. Here, the signal generator started with the higher excitation frequency, and then quasi-stationary and linearly decreased the excitation frequency to the lower end limit.

Drop shape oscillations were captured with the CCD electronic camera. The top and side views of the oscillating drops were recorded. It was then possible then to verify the axial symmetry of the oscillations. The sampling rate of the CCD camera is 60 Hz. The CCD frame image analysis (30 frames/sec) has been used to give a Nyquist sampling rate of only 15 Hz. This means that the higher oscillations in the system could not be detected, and if they do exist in the system they would be aliased or spilled over to the low-frequency range, thus making the spectral analysis incorrect.

The individual images were first frozen and then cleaned, filtered, and smoothed. This was necessary in order to achieve high spatial resolution (high SNR ratio) and to remove protuberances and disturbances caused by the illumination. Then images were again checked for the axial symmetry and volume conservation.

Such preprocessed images were fitted with the Legendre polynomials and the Fourier coefficients were estimated. Those coefficients have a direct physical meaning because they represent the mode amplitudes. Processing the individual images, it was possible to obtain the time series of drop oscillations for each mode. Depending on the deformation size, up to 18 Legendre orthogonal zonal modes were estimated. This was also necessary to keep track of the volume conservation and to make sure the volume remained constant. Since 360 points were taken over the circumference, the Legendre fitting was statistically very stable and, consequently, the small localized errors in boundary recognition were insignificant. One of the virtues of the Legendre polynomial expansion is its capability to actually recover some missing points on the interface. This, in conjunction with the discrete Fourier transform filtering, resulted in very smooth and extremely accurate shape recognition.

The time series of the surface modes enabled the estimation of the complete drop topology. The parameters such as drop volume, drop cross-section area, superficial area, circumference, surface energy, mean drop size, volume conservation coefficient, etc. were all obtained at once. All these parameters have proven to be indispensable tools in understanding the drop nonlinear oscillation dynamics.

The spectral analysis of the time series was performed as the next step. The Welch periodogram with the Hamming windowing and the Cooley-Tukey (decimation-in-time) fast Fourier transform algorithm (for the quick and inexpensive discrete Fourier transformation calculations of the discrete time series) were used for the PSD calculations. The same technique was used for the estimation of the CPSD function.

The Hysteresis and Jump phenomena in nonlinear forced oscillations of liquid drops were discovered first in the works of Daidzic (1995a and 1995b).^{26, 27}

6.3 Results and Discussion

The Hysteresis effect is the result of the resonance frequency curve bending toward lower or higher frequencies. The Hysteresis actually represents two domains of attraction. The importance of Hysteresis is also that it implies appearance of bifurcations and the subsequent oscillation memory loss leading to chaotic oscillations.

Many useful results were extracted from the image processing, time series and spectral analysis. In figure 26, the time series of mode 2 oscillations for the linearly swept 8 V acoustic drive is presented. The oscillation amplitude increases as the sweep frequency approaches Jump frequency. The oscillations then become chaotic, and, as the excitation frequency slowly increases, drop oscillations become regular again although at a higher amplitude (not shown here). The frequency where the forward positive amplitude Jump starts is at the higher end of the Hysteresis. It also implies that we have a frequency response curve bending to the left (soft nonlinearity). In figure 27, the oscillation time series is shown for the 8 V acoustic excitation and for the negative sweep (decreasing frequency). The first region of large amplitude oscillations is not shown here. After the frequency at the lower end of the Hysteresis is reached, the drop oscillations undergo quasi-periodic and chaotic oscillations. As the frequency is reduced further the oscillations become regular again and follow the forward sweep inbound frequency response curve now outbound. The Hysteresis width in the case of 8 V acoustic excitation was estimated to be 0.28 Hz. In figure 28, the frequency response for the forward sweep excitation is presented. Since the sampling rate was not high enough, the aliasing effect occurred in the lower frequency region.

In figure 29, the CPSD of the second and fourth oscillation modes for the 8 V excitation is presented. The CPSD clearly shows the mode coupling which was also expected due to the large oscillation amplitudes and particularly during the Jump.

In figure 30, the forward sweep time series of mode 2 oscillations for the linearly swept 12 V acoustic drive is presented. In figure 31, the backward sweep time series of mode 2 oscillations for the linearly swept 12 V acoustic drive is presented. Basically, the same phenomena was observed as in the case of 8 V sweep. However, the Jump phenomenon was more pronounced since the difference in amplitudes is larger. The width of the Hysteresis was estimated at 0.35 Hz (i.e., increasing). The Jump was very violent, inducing multi-mode, chaotic, and asymmetric oscillations. As soon as the sweep passed the critical region the oscillations stabilized. In figure 32, the frequency responses for the positive and negative sweeps at 12 V are presented. Note the lower "resonant" frequency for the forward sweep and its lower amplitude (power). This is, of course, natural since the forward sweep for the softening system falls in the low amplitude and the lower frequency region. The frequency response curve for the backward sweep is broader and with more power. The reason why is given above.

6.4 Concluding Remarks

Using the forward and backward sweeps around the natural resonance frequencies, we have confirmed the existence of the Hysteresis and the Jump phenomena. It was found that the Hysteresis width and

the amplitude variation depend on the excitation-response amplitude. The larger the oscillation amplitude, the larger the Hysteresis width and the amplitude jump. It was also found that the frequency response curve is bent toward lower frequencies (i.e., exercising the softening effect). During the amplitude Jump, drops have undergone complex oscillations. Higher order and subharmonic modes were excited and chaotic oscillations have resulted in some cases. This is in agreement with our hypothesis that the Hysteresis and the amplitude Jump initiate bifurcations which may consequently lead to chaotic oscillations. Some general conclusions may be drawn from the preliminary analysis of the experimental results:

1. The softening Hysteresis was observed for the given oscillatory system.
2. Jump phenomena were observed during the linear frequency sweeps. Such Jumps are the result of the Hysteresis effect and the associated amplitude multi-valueness.
3. Amplitude Jumps resulted in complex quasi-periodic and chaotic oscillations.
4. Nonlinear drop oscillations may be well described with a Duffing-like set of ordinary differential oscillations. Basic nonlinearity comes from the restoring surface forces, nonlinear inertia matrix, and mode coupling.

6.5 What Is Still Missing?

In order to understand the complicated nonlinear nature of forced oscillations and their implications, it is necessary to develop an appropriate mathematical/theoretical model.

A theoretical model, based on the Hamiltonian principle and the Lagrangian equations, which is already in development phase will be applied. The existing discrete model of drop oscillations will be expanded in order to include, for the solid-body drop rotation, electrostatic energy of a surface charge for both good and poor conducting liquids, higher-order viscous irrotational approximation, and multifrequency excitation. The expression for the potential energy will be improved in order to account for the uniformly convergent expansions in terms of deformation amplitudes up to the point of breakup. The nonlinear terms in the stiffness, inertial, and dissipation matrix will also be included.

For small to moderate oscillation amplitudes it will be possible to apply the singular perturbation analysis and analytically solve the coupling of the second and the fourth oscillation modes. These results will first be verified with the existing theoretical findings. The model will then be refined with the existing confident experimental results in order to assure for the asymptotic regularity.

Besides the theoretical investigations, new experiments are needed where the bifurcations and amplitude jumps would be followed more precisely. A new model should be capable of going to very large deformations which would include transition to chaotic oscillations and drop breakup. The results will also be presented as the Phase-Space and the State-Space portraits. In addition, the stroboscopic processing of the Phase-Space (i.e., the Poincaré sections or maps) will be evaluated. Such analysis gives a qualitative picture of nonlinearity and the existence of strange attractors. The rate of chaos induced by bifurcations will be estimated by calculating the fractal or noninteger (Hausdorff) dimension of the strange attractors.

Further, Kolmogorov entropy (i.e., Liapunov exponents) will be calculated from the measured time series describing the bifurcation points and loss of memory from the initial state. Those parameters will be hard evidence of the Hysteresis, bifurcations, jumps, and the chaotic oscillations.

7. CHAOTIC DROP OSCILLATIONS

ABSTRACT

Forced nonlinear and chaotic oscillations of levitated drops were performed in the USML-2 reduced-gravity environment using the DPM chamber. The onset, transition, and fully developed chaotic oscillations were observed during the forced oscillation experiment. The transition from the pure harmonic to quasi-periodic and finally to chaotic oscillations was investigated. Multi-frequency and single-frequency excitation drives were used in order to excite and stimulate chaotic oscillations. In the case of the single-frequency excitation, the excitation threshold is disproportionally higher than in the case of the multi-frequency oscillations. The time series analysis and the spectral analysis have confirmed the existence of various nonlinear phenomena and particularly of the chaotic oscillations. The chaotic oscillations are the product of the memory loss (supersensitive on the initial conditions and a violation of the weak causality principle) and are the fundamental feature of nonlinear systems. Chaotic oscillations are far from being irregular in the true sense. Chaotic oscillations possess internal superstructure which is described by fractal geometry and strange attractors and has to be thoroughly investigated for drop dynamics.

7.1 Background

The phenomenon of deterministic chaos has been investigated for the last three decades. However, there is still a widely held misconception that chaotic oscillations mean irregular oscillations. This is simply not true. What might look irregular to us on the large scale does not need to be true for the small scale. This is exactly what is happening in chaotic oscillations. Despite their gross irregularities, the chaotic oscillations in fact follow a fine superstructure which can be observed in the phase space. Strong determinism states that equal inputs produce equal results. On the other hand, weak determinism states that similar inputs should produce similar results. When the assumptions of weak determinism are violated, we talk about supersensitivity on the initial conditions. This is what deterministic chaos is about. Subsequent oscillation history is impossible to predict, even though the problem is completely deterministic. The problem actually arises from our practical inability to estimate the initial conditions with such accuracy that the oscillations can be predicted for any time in the future.

Why is chaos so important for drops? Well, the answer is very straightforward. From the pure academic point of view it is, of course, very interesting to investigate the chaotic oscillations on such a unique fluid shape with a closed surface, such as a drop. However, more important are two phenomena which are directly connected to the chaotic oscillations of drops. They are drop breakup and drop evaporation.

Due to mode coupling which is further intensified and stimulated during chaotic oscillations, the oscillation energy can and will be transferred to other surface modes, which could subsequently lead to amplification of the oscillations and finally to drop collapse and breakup.

Drop evaporation and combustion increase with the oscillation amplitude, frequency, and surface area. These parameters are intensified and maximized during chaotic oscillations. So, logically, we want to excite the chaotic oscillations in order to improve heat and mass transfer. However, sometimes we want to prevent chaotic drop oscillations. Regardless of our needs, we first have to fully understand the nature of chaotic oscillations in order to use its properties to our advantage. This is by no means an easy task.

As far as drop oscillations are concerned, there is a very limited volume of previous work. Becker, Brosa, and Kowalewski (1994)²⁴ have worked on the reconstruction of the dynamic equations of motion from the measured time series of drop shape oscillations. They were able to recover the inertia, dissipation, and stiffness coefficients from the experimental time series by assuming the order of the nonlinear ordinary differential equations of motion. They have also examined their results in the phase space and have used the Poincaré sections. The importance of chaotic oscillations has been recently recognized by Daidzic (1995a, 1995b).^{26,27} In a series of experiments and theoretical and computational investigations, the chaotic oscillations have been identified and quantified. It was found in this study that chaotic oscillations can be easily excited if the multi-frequency driving forces are used instead of a single-frequency excitation. The explanation for this phenomenon is in the internal energy redistribution and multi-mode excitation which more easily triggers the quasi-periodic and chaotic oscillations.

7.2 Experiment

The chaotic oscillations experiment was performed in the DPM chamber during the USML-2 mission. Liquid drops of ~ 2 cm in diameter (4 cm^3) were suspended and stabilized in an acoustic well of an ultrasonic levitator. The Sound Pressure Level (SPL) was then adjusted in order to minimize the static distortions and to prevent any rotation of the drops.

Drop oscillations were captured with a high-speed film camera and a CCD electronic camera. In both cases the top and side views of an oscillating drop were taken. Doing so, it was possible to verify the hypothesis on axial symmetric drop oscillations. The sampling rate of the high-speed camera was 400 Hz.

The individual images were first frozen and then cleaned, filtered, and smoothed. This was necessary in order to achieve the high spatial resolution (better SNR ratio) and to remove protuberances and disturbances caused by the illumination. Images were then checked again for axial symmetry and volume conservation.

Such preprocessed images were fitted with the Legendre polynomials, and the Fourier-Legendre coefficients were estimated. The coefficients have a direct physical meaning because they represent the surface mode amplitudes. Processing the individual images, it was possible to obtain the time series of drop oscillations for each mode. Depending on the deformation size, up to 18 Legendre orthogonal zonal modes were detected. It was necessary to keep the track of the volume conservation and to make sure that the volume remained constant. The standard deviation and asymmetry parameters were also obtained for the purpose of accurate image processing. Since 360 surface points were taken over the drop circumference, the Legendre fitting was statistically very stable, and consequently the small localized errors in boundary recognition were filtered. One of the special virtues of the Legendre polynomial expansion is its capability to actually recover some missing points on the interface. This, in conjunction with the discrete Fourier transform filtering, resulted in very smooth and extremely accurate shape recognition.

The time series of the surface modes enabled the estimation of the complete drop topology. The parameters such as drop volume, drop cross-section area, superficial area, circumference, surface energy, mean drop size, volume conservation coefficient, etc., were all obtained at once. All these parameters have proven to be indispensable tools in understanding the drop nonlinear oscillation dynamics.

The spectral analysis of the time series was performed as the next step. The spectral analysis is capable of showing the fine details of the mode coupling and energy transfer between the modes. The Welch periodogram with the Hamming windowing and the Cooley-Tukey (decimation-in-time) fast Fourier transform of the discrete time series was obtained for the PSD calculations. The same technique was used for the estimation of the CPSD function.

7.3 Results and Discussion

In figure 33, the time series of the chaotic drop oscillations is presented. The experimental time series was extracted from the mode 2 drop oscillations. Amplifications and attenuations of the oscillation amplitudes are the direct result of the well-developed mode coupling and energy exchange between the modes. The results of spectral analysis are presented in figures 34–36. Spectral analysis was used in order to identify resonance peaks and decompose drop oscillations into modes. In figure 34, the PSD of the mode 2 oscillation time series is presented. The resonance peak is at ~ 3 Hz. Note the existence of many satellite peaks. In addition, the PSD is not quasi-stationary with several distinctive peaks, but is broad-banded and continuous. Due to aliasing some of the high-frequency oscillations are spilled into the low-frequency region.

In figure 35, the PSD of the mode 4 nonlinear drop oscillations is shown. One can easily recognize three fundamental regions. These are around the fundamental mode 2 resonance frequency or 3 Hz. This is also the absolute peak. The second peak is around 6 Hz, which is the first superharmonic of the fundamental frequency. The third region is the mode 4 resonance frequency and also the mode 2 second superharmonic frequency. However, it is extremely difficult to identify all the regions since so many subharmonic, superharmonic, combination, and other types of resonances are taking place simultaneously. This shows only that the chaotic oscillations are complicated, however, not that they are completely intractable.

In figure 36, the CPSD of the mode 2 and mode 4 oscillations is presented. This result identifies the frequency domain regions where the oscillation energy exchange takes place. The energy transfer is the fundamental property of some multi-degree-of-freedom systems. A necessary condition for the internal energy transfer to take place is that the internal resonance must exist. Internal resonance appears when two or more modes are exactly or nearly commensurable. This is exactly the picture that we have in drop oscillations. It is a well known fact in drop dynamics that the mode 2 and mode 4 oscillations are commensurate with the ratio of 3 for linear cases and close to 3 for nonlinear oscillations.

In figure 37, the auto-correlation function of the mode 2 oscillations is shown. This autocorrelation shows rapid decay toward zero correlation which means that the drop does not remember its initial state. This fact, together with the broad spectrum, is the definite clue in detecting chaotic oscillations. The time constant in which this rapid decay to zero increases is actually related to the Liapunov exponents. However, at this stage of the investigation we were still unable to determine this relation.

7.4 Concluding Remarks

The preliminary analysis of the several large-amplitude forced drop oscillation experiments has indicated the existence of chaotic drop oscillations. From the qualitative analysis, which included time series, power spectrum, and the autocorrelation, the occurrence of chaos was positively identified. In the case of the single-frequency excitation the driving force threshold is disproportionally higher than in the case of the multi-frequency oscillations. Several conclusions can be drawn from the initial studies on nonlinear and chaotic drop oscillations:

- Large-amplitude (nonlinear) droplet oscillations are an excellent example of a nonlinear dynamic system. All the nonlinear properties observed in some mechanical systems can also be demonstrated for drop oscillations.
- Droplet oscillations are non-isochron (amplitude-dependent frequency).
- A curious one-way energy transfer between the modes exists. That means that the oscillation energy spills from odd-to-even modes spontaneously. On the other hand, the rate of energy transfer from even-to-odd modes is an order of magnitude lower.
- Forced droplet oscillations over a long period of time are unpredictable. The reason for that is the passage through several bifurcations (Hysteresis and Jump) and the onset of chaos.

7.5 What Is Still Missing?

In order to fully understand the complicated nature of chaotic oscillations it is indispensable to work on the development of a mathematical/theoretical model. Due to some unique features of drops (fluid particles with finite surface area) it is possible that some new properties of chaotic oscillations may be found as well. This means that the drops do not necessarily have to undergo some of the known scenarios of bifurcations and routes to chaos. The theoretical dynamic equations of motion should then be compared to dynamic equations obtained by reconstruction from the experimental time series techniques.

Therefore, new experiments in reduced gravity are needed. Such experiments have to account for the non-axisymmetric drop oscillations. During the transition to chaotic oscillations, and later during the fully developed chaotic oscillations, the axial symmetry of the oscillations will be lost. The shape of the liquid drop can then only be characterized with the tesseral spherical surface harmonics. In order to achieve that goal a 3-dimensional image processing is necessary. This can be accomplished by a holocamera or by using laser scattering techniques. Of course, the shape of a drop must remain as a simple connected domain.

This work was partially supported by NASA under contract NAS-7918/JPL-958314.

8. THE MECHANISM OF TUMBLE ROTATION

ABSTRACT/OBJECTIVE

Drop stability is an important prerequisite to performing precision experiments on free drops in a microgravity environment. Based on our previous experience during USML-1, we were concerned that we had a good understanding of the sources of unwanted drop rotation. We have considered the tumble phenomena from four vantage points: (1) flow visualization in a high fidelity DPM chamber to observe the interaction of acoustic streaming with specimens; (2) ground-based mechanical measurements, using a torsion pendulum to determine the magnitude of the torques generated by streaming patterns occurring during nominal flight operations; (3) some modeling that supports the magnitude of our torque measurements; and finally, (4) an analysis of the USML-2 drop dynamics experiment that establishes the magnitude of the tumble torque that was experienced by a free drop during normal operations. As a result of these investigations we have developed a good understanding of the origins of tumble rotation in the DPM, and used this understanding to improve specimen stability during the mission.

8.1 Background/Justification

During USML-1, several experiments were influenced by an unexplained tendency of the specimen to rotate about an axis that was aligned predominantly along the y axis of the DPM. In an effort to stabilize the drops, several methods, including flattening, and imposing a z axis rotation, complicated the interpretation of the results of several experiments. In cooperation with JPL, we undertook an effort to find the origin of these torques, and performed a large number of measurements using a sensitive torsion pendulum to quantify the torque and establish its functional dependence on DPM operating parameters. Our efforts were directed along four paths: flow visualization; direct mechanical measurement; kinematic modeling of drop motion; and finally, an analysis of one dedicated experiment that was performed during the mission to verify our understanding of this phenomenon.

8.1.1 Flow Visualization in a High Fidelity DPM Chamber

One goal of this investigation was to image the effect of the DPM acoustic environment on the flow field near the surface of the specimen. We performed experiments on a high-fidelity model of the DPM that was built at Vanderbilt. Two domains were of particular interest. First, the global circulation of fluid around the specimen would illustrate in a macroscopic way the general streaming behavior. Second, and more importantly, we were interested in the acoustic boundary layer. It is in this region that the viscous torques are actually transmitted to the specimen.

We have developed a methodology to visualize flow patterns within the DPM acoustic positioning chamber, and have demonstrated this technique by applying it to the analysis of well understood acoustic streaming conditions in a DDM-like chamber. We used this technique to investigate the physical basis of the structured streaming that accompanies the tumbling rotation phenomenon observed during USML-1 and USML-2. In this study we demonstrated that the magnitude of the tumbling torque does respond to adjustment of the operating conditions, in a way that suggests that quartz wind from the drivers may play an important part in the origin of the phenomenon.

The flow pattern inside the chamber is seeded using smoke particles. After several tests, common household incense was found to produce the required particle size and density for good imaging. A laser sheet was used to probe the 3-dimensional flow pattern and to provide a sense of the component of the overall flow on 2-dimensional sections. The laser light was introduced through the chamber viewports. Flow patterns were imaged by CCD television cameras and recorded on video tape. The video images were analyzed by metrology software based on a Macintosh computer. The actual circulation in the chamber is a complicated 3-dimensional pattern. Our optical system revealed the components of this circulation on transverse sections, providing an approximation to the 3-dimensional flow field.

The acoustic streaming at the specimen influences global flow patterns. Since the chamber is essentially a closed volume, streaming away from the specimen forces a return flow. This return flow closes a loop which is observed as a vortex on the tumbling planes.

The results of our investigation provide the framework for advancing the problem of the potential vortex interaction with the viscous boundary layer. The results provide the experimental data base needed to confirm the theoretical description of the flow field by Riley (1992)²⁹ and others.

8.1.2 Mechanical Measurement of the Magnitude of the Tumble Torque

The magnitude of the tumble torque was characterized by observing the displacement of a calibrated torsion pendulum that was introduced to the interior of the flight chamber. Spheres of various diameters were suspended from thin fibers and their angular position measured optically using a CCD camera and image analysis software based on a Macintosh computer.

Due to the preflight configuration of the DPM mechanical assembly, only the y-axis of tumble torque was characterized prior to launch. We were unable to make any measurements for the x-axis. The dependence of the tumble torque on the distribution of acoustic energy between the [1] and [3] drivers was investigated. The [1] and [3] drivers are of interest because they are contained in the xz plane, the one perpendicular to the rotation axis that was observed during the USML-1 mission. Our hypothesis was that these were the drivers that would be most effective in controlling the torque about the y-axis.

In figure 38, as the ratio of [1]:[3] is varied, the torque is observed to be a continuous monotonic function of the gain ratio. We see that it is possible to achieve zero torque for a particular axis if the acoustic energy is shared properly among the relevant drivers. We note that it is often necessary to deviate from the acoustically balanced condition to achieve the zero torque. This is due to peculiarities of the quartz wind phenomenon associated with individual drivers.

8.1.3 Estimated torque due to structured streaming.

As an estimate of the torque attributable to viscosity, we consider the approximate solution of boundary layer equations governing the flow around a sphere rotating in a medium of otherwise undisturbed fluid (Howarth, 1951).³⁰ The surface shear stress and hence the torque due to the rotation of the sphere is given approximately by:

$$\tau_{r\theta} = 0.5 \varepsilon a \omega \left[\frac{vV}{x} \right]^{\frac{1}{2}} = 0.5 \rho a \sqrt{v \omega^3} \quad (8.1)$$

where $2a$ is the diameter of the sphere. ε is the density of the surrounding air, v is the kinematic viscosity of the fluid, ω is the angular velocity of the fluid about the axis of the sphere, V is a characteristic particle velocity (approximated as $x\omega$), and x is the radial distance from the rotation axis. The shear stress produces a drag force that is constant at every point on the surface of the sphere. The torque is found by integrating this force over the surface:

$$T_{r\theta} = \int_{\phi} 2\pi a^3 (\tau_{r\theta}) \sin \phi d\phi = 2\pi a^4 \rho \sqrt{v \omega^3} \quad (8.2)$$

If we assume as typical values $v = 1 \times 10^{-2} \text{ cm}^2/\text{sec}$ for air, $a = 1.27 \text{ cm}$ and a value of $2\pi \text{ rad/sec}$ for the angular velocity of the streaming pattern, near the high end of the experimentally observed streaming velocities (indicated by the arrow in the figure), we find that the torque = 0.03 dyne-cm after conversion to cgs units. This is about 2 percent of the value of the torque that is impressed upon a specimen according to the Busse-Wang model at a SPL of 145 dB per axis. This torque has the correct order of magnitude to account for tumbling rotation, as demonstrated by the following spin-up calculation.

8.1.4 Estimation of the Spin-up Time for a Drop Due to Viscous Drag.

We use a simple model to calculate the spin-up time of the drop. We have shown that the torque acting on a sphere can be expressed by equations (8.1) and (8.2). Combining these two expressions we find that the torque on the specimen can be expressed as a constant A times a function of the angular velocity of the surrounding fluid:

$$T_r = Af(\omega) \quad (8.3)$$

We know from elementary mechanics that a free body subject to a constant torque experiences a constant angular acceleration:

$$T_r = I\alpha \quad (8.4)$$

where I is the mass moment of inertia of a body of mass m , and α is the angular acceleration. The mass moment of inertia of a spherical drop is given as:

$$I = \frac{2}{5} ma^2 \quad (8.5)$$

Therefore:

$$\alpha = \frac{T}{I} = \frac{Af(\omega)}{I} \quad (8.6)$$

An expression for the instantaneous angular velocity ω of the drop is:

$$\omega = \omega_0 + \alpha t \quad (8.7)$$

where ω_0 is the initial angular velocity at $t = 0$. Assuming the drop is initially at rest, then we express the spin up time t as the time required for the drop to accelerate to the terminal angular velocity, that of the surrounding fluid:

$$t = \frac{\omega}{\alpha} = \frac{\omega I}{Af(\omega)} \cong \frac{I}{A\sqrt{\omega}} \quad (8.8)$$

Drops in high-velocity streaming patterns reach a high terminal velocity in nearly the same time as drops in low velocity streaming patterns. The torques are different in the two cases, but so are the resultant accelerations.

Using values for the density of water = 1 gm/cm³, a 1-in. diameter for the dimension, we find that the spin-up time is 59.4 seconds. This is the correct order of magnitude for the spin-up times observed during the USML-1 mission. This result supports the hypothesis that the observed acoustic streaming may be related to the tumbling torque.

8.2 Experiment

During the USML-2 mission, tumble rotation was observed about the x -axis of the DPM. We report on an experiment that we conducted as part of FO 6 during USML-2. This experiment occurred at MET 03:05:04:00. Upon deployment of a 4-cm³ water drop, a tumble along the x -axis was observed. (x -axis tumble dominated the USML-2 mission as opposed to the y -axis tumble observed during USML-1.) The nominal operating conditions following drop deployment were acoustic pressures of 145 dB for the x -, y -, and z -axes, 25 percent nominal gain ratio for each of the z drivers, and a phase modulation frequency of 15 Hz. Subsequent dynamic behavior of the drop is presented in figure 39.

8.3 Results/Discussion

At Time = 0 seconds, a counter torque was applied to the drop by commanding the z_2 driver to a gain ratio of 70 percent. The goal was to provide a stationary drop with no rotation or linear translations. By comparison with pendulum measurements performed on our DPM chamber at Vanderbilt, this should have resulted in a counter torque applied in a direction to decelerate the motion of the drop. We were unable to perform torque measurements about the x -axis on the flight hardware prior to the flight. We expected an applied torque in the range 0.05–0.10 dyne-cm based on our torque measurements about the y -axis with an allowance for individual differences between drivers, and for how effectively they promote acoustic streaming during operations.

The time history of specimen motion as reduced from Spacelab video tapes is shown in figure 39. Data points shown are those that were measured during periods of pure x -axis rotation. During this experiment, the specimen may have been disturbed by other acoustic forces that were applied in an attempt to gain control of the rotation. This resulted in several periods of multi-axis rotation, as labeled on the figure. The counter torque was maintained continuously for the first 200 sec of the experiment, after which the z_2 gain ratio was reduced so as to find the point of zero net torque. As revealed in the figure, the specimen decelerates, undergoes an ill-defined motion as it approaches zero velocity, and then picks up a rotation in the opposite sense, again about the x -axis.

In figure 40 we show only the first 200 seconds of the specimen's history. The deceleration that is obtained by measuring the slope of the velocity vs. time curve is -0.068 sec^{-2} . If we consider the drop as a solid body and use the moment of inertia for a drop of the deployed size, shape, and density, we can determine the torque that was responsible for the deceleration. This is found to be $0.10 \pm 0.01 \text{ dyne-cm}$, in good agreement with our ground-based measurements.

8.4 Conclusions

- 1) Specimens positioned in the DPM experience torques that arise from the organized circulation of air inside the acoustic chamber. The origin of this circulation appears to be acoustic streaming.
- 2) The torques that act on specimens are small, as determined by direct ground-based measurements using torsion pendulums. We hypothesize that the tumble torque is attributable to a viscous drag of air over the surface of the specimen.
- 3) The angular acceleration of free drops, analyzed as part of well controlled experiments during USML-2, suggests a torque of the same magnitude as those measured by torsion pendulums, to well within experimental error. In this case, we have considered only spherical specimens undergoing pure x -axis rotation.
- 4) Simple models assuming viscous drag account for both the magnitude of the torques and the acceleration of the free drop.
- 5) We feel this is strong experimental evidence establishing this mechanism of uncontrolled rotation.

9. AN EXPERIMENTAL INVESTIGATION OF THE TORQUE GENERATED BY ORTHOGONAL ACOUSTIC WAVES

ABSTRACT / OBJECTIVE

The acoustic levitation of small liquid samples is often accompanied by instabilities, such as uncontrolled rotation (Allen 1947³¹, Gammel et al. 1988³²). In this paper, we discuss this phenomenon with reference to the Drop Physics Module (DPM). During the First United States Microgravity Laboratory (USML-1) mission, some of the experiments that were performed in the DPM were hampered by

uncontrolled rotation of the specimens about an unintended axis. This axis was observed to be nearly parallel to the y -axis of the chamber. In-order to generate the greatest scientific return during USML-2, it was important to understand the origin of this phenomenon and its influence on the behavior of free drops. One of our approaches has been to verify our understanding of the Busse-Wang torque mechanism.

The goal of this investigation was to test the predictions of Busse and Wang by direct measurement of the torque in a resonant acoustic chamber for a number of axisymmetric specimens of varying size, shape, and position. The following parameters were tested: size (r_o), P^2 dependence, phase angle (ωt_0) and location (x_o, y_o) within the chamber. Measurements were made by observing the displacement of a torsion pendulum that was introduced to the interior of the chamber. Spheres of various diameters were suspended from thin fibers and their angular position measured optically using a CCD camera and image analysis software based on a Macintosh computer.

9.1 Background / Justification

Busse and Wang (1981)³³ have presented a detailed theory that predicts the acoustic torque generated by orthogonal acoustic standing waves on a sphere, cylinder, or flat disk located at the center of a rectangular acoustic chamber. This torque has been employed in many terrestrial and reduced-gravity experiments, such as in investigations of drop fission (Wang, 1994³⁴).

Equation (9.1) presents the mathematical form of the theory. In the case of a sphere, the magnitude of the torque under ideal conditions can be expressed as follows:

$$T = 3 / 2 \ell_{\eta} A \left(\frac{P_x P_y}{2 \rho c^2} \right) \sin \omega t_0 \quad (9.1)$$

where ℓ_{η} is the viscous length, A is the surface area of the specimen, P_x and P_y are the pressure amplitudes of the x and y acoustic waves, ρ is the density of air, c is the speed of sound in air, and the term ωt_0 is the phase angle between the x and y waves. Thus, according to theory, the torque that a specimen will experience depends largely on the amplitudes of the pressure waves, and only weakly on the exact dimensions of the acoustic cavity. Any chamber at resonance that is driven in such a way as to provide a certain P_x and P_y will deliver the same torque to a specimen at the center of the chamber. Here r_o is the characteristic radius of the sphere, and k is the wave number of the acoustic wave at resonance.

9.2 Experiment

The current torque measurements have been performed in a DDM-like torque measurement chamber of 6×6×5 in. internal dimension, outfitted with two JBL drivers. Measurements have been made in the case of spheres, right circular cylinders, and thin circular disks.

All torque measurements were made at chamber resonance (1126 Hz) at the center of the chamber ($x=7.26$ cm, $y=7.26$ cm, $z=6.35$ cm), except in the case of the position parameter experiment described below. The microphone was mounted in a corner position to record the P_x and P_y pressure maximums.

Great care was taken in calibration of the microphone, balance of the P_x and P_y pressures, and calibration of the acoustic phase shift. The acoustic phase shift for all torque measurements was set to 90° , except for the phase parameter series as noted below. Frequency shifts that arise as a result of volume exclusion effects for large specimens, as well as the frequency shift experienced in the non-linear high dB range, were detected and corrected.

9.3 Results / Discussion

9.3.1 The Results for Spheres.

The results for spheres were very successful. Theory was tested against a number of spheres as a function of diameter. In figure 41 we plot the acoustic torque measured for spheres of four different diameters as a function of the square of the acoustic pressure per axis (in cgs units).

Generally, the torque on the sphere is found to increase dramatically with increasing radius and increasing SPL. Even spheres up to 5.08 cm in diameter ($r_0 k = 0.53$) showed no significant deviation from theory, up to a pressure of 162 dB.

9.3.2 As a Function of Phase Angle.

Busse-Wang theory suggests a trigonometric relationship between the magnitude of the torque applied to a specimen and the phase lag between the x and y components of the acoustic field. In figure 42 we show some results for two spheres. Starting from a phase difference of 90° (maximum torque) we reduced the phase angle between x and y in increments. There is a good correspondence between theory and data, confirming the phase component of the Busse-Wang theory.

9.3.3 As a Function of Position.

The top z face of the chamber was mounted on a xy translation mechanism that enabled us to position the specimen to any intended position within the acoustic chamber. This mechanism was utilized in the preparation of the 2-dimensional torque distribution maps.

B&W found that the magnitude of the torque should vary with position on the xy plane as follows:

$$T = \Phi \ell \eta A \left(\frac{P_x P_y}{2 \rho c^2} \right) \sin \omega t_0 \cos(kx_0) \cos(ky_0) \quad (9.2)$$

where x_0 and y_0 correspond to the displacement of the specimen from the center of the chamber.

The first results shown are for the torque distribution experienced by a 7/8 in. diameter sphere on the centermost xy plane of the chamber. The agreement with theory is perhaps better illustrated in cross sections of the 3-dimensional surface above. In figures 43 and 44, we present sections of the data along the $(x, -x)$ and $(y, -y)$ directions.

9.3.4 Tall Circular Cylinders

We further tested Busse and Wang's theory by measuring the torque on a tall cylinder of height h and radius r ($h \gg r$) for which the cylinder wall contribution clearly dominates the end faces, modelled as a disk-like feature.

This idea was tested by examining the torque on a 2.54 cm (1 in.) diameter cylinder 9.65 cm (3.8 in.) tall. In this case the entire cylinder specimen was suspended inside the closed acoustic chamber at the end of a fiber. The weight of the specimen was sufficient to pull the fiber taut. In figure 45 we see that Busse and Wang's cylinder prediction adequately accounts for the observed torque, and provides a confirmation of the theory in the case of cylinders. Similar results have been reported (Wang, 1976³⁵) in a previous investigation in which a cylinder penetrated the top and bottom surface of the acoustic chamber. In that investigation, no contribution to the torque from the end faces of the specimen was possible, and the theoretical magnitude of the torque was confirmed.

9.3.5 Right Circular Cylinders of Intermediate Thickness

We have examined somewhat shorter cylinders satisfying the relation ($h \approx r$). In this case the entire cylinder specimen was suspended inside the closed acoustic chamber at the end of a fiber. The weight of the specimen was sufficient to pull the fiber taut. We expect that since a right circular cylinder has both a cylindrical wall and two end faces that we might measure a contribution to the torque from both of these sources. In this experiment a 5.08-cm (2 in.) diameter cylinder 0.56 cm (7/32 in.) tall was examined in the acoustic chamber. In figure 46 we compare the torque expected from a pure cylinder of height $h = 0.56$ cm, to torque data corresponding to the specimen. We see that the measured torque exceeds the torque predicted from a pure cylindrical wall, by a small amount. We interpret this additional increment over the predicted value to be a contribution from the circular end faces of the right circular cylinder.

9.3.6 Thin Disks

Busse and Wang originally modelled the theory for the disk on a mathematically thin sample, one without measurable thickness. Clearly, real specimens must have some thickness. An attempt was made to rigorously satisfy the requirements of Busse and Wang by using the thinnest available disk as a specimen. A thin mica disk, 0.0127 cm (0.032 in.) thick, and 2.54 cm (1 in.) diameter, was mounted on a fiber that was threaded through the top and bottom surfaces of the acoustic chamber. Since the specimen was essentially massless, special precautions were taken to insure that the fiber was taut and straight, in order to satisfy the assumptions of the torsion pendulum theory. The fiber was held taut by applying weights to the lower half. The apparatus was arranged so that the fiber would be supported by two fixed points, one at the top and the other at the bottom. The weighing system was designed to apply a constant force during the experiment, and to allow adjustment to new values of fiber tension between experiments. By changing the tension in the fiber between experiments, we were able to vary its stiffness. Using fibers of different stiffness allowed us to make several independent measurements of torque using different springs.

In figure 47 we see that as the fiber's stiffness changed, varying its spring constant, the data, in the form of torque as a function of pressure, were reproducible. This is as we expect if we are measuring an independent physical torque. This result indicates that a significant discrepancy exists between the predicted and measured values of acoustic torque in the case of the thin disk. This discrepancy cannot be attributed to a cylindrical wall contribution to the measured torque, as the surface area in the wall is negligible in the present case. We suggest that scattering effects from the sharp edges at the circumference of the disk surfaces are not properly accounted for in the current theory.

In their earlier paper, Wang and Kanber (1978³⁶) had proposed a phenomenological approach to estimate the torque that a thin disk should experience under the conditions we have investigated. The form of their expression is compatible with that given in equation (9.1), using a shape factor with a value of unity. In figure 47 we plot their prediction of torque as a function of P^2 , and find that the fit to the current experimental results is reasonable.

9.4 Conclusions

We have investigated the predictions of Busse and Wang by measuring the torque experienced by axisymmetric specimens of different geometries as a function of pressure, phase angle, location within an acoustic chamber, as well as the shape. For all shapes, we have confirmed the pressure, phase angle, and position dependence of the theoretical prediction. In the case of tall cylinders ($h \gg r$) the experiment agrees with the prediction for a pure cylinder. However, as the thickness of the cylinder approaches the radius ($h \approx r$) deviations from theory are observed, the measured torques exceeding the predicted magnitudes by some small amount. In the case of thin disks ($h \ll r$) the observed torque exceeds expected value by a large factor, possibly indicating that the torque mechanism is something other than that assumed by Busse and Wang. In fact, the predictions of a previous theory of Wang and Kanber appears to be an adequate fit to the current results for a thin disk. Additional work will be required to resolve this discrepancy between the observed and expected value of the torque in the case of a thin disk.

REFERENCES

1. Wang, T.G.; Anilkumar, A.V.; Lee, C.P.; and Lin, K.C.: *J. Fluid Mech.*, 276, 389–403, 1994.
2. Elleman, D.D.; Wang, T.G.; Trinh, E.H.; and Croonquist, A.P.: NASA Tech Brief, NPO–15839, 1985.
3. Biswas, A.; Leung, E.W.; and Trinh, E.H.: *J. Acoust. Soc. Am.*, 90, 1502–1507, 1991.
4. Wang, T.G.; Anilkumar, A.V.; Lee, C.P.; and Lin, K.C.: *J. Colloid Interf. Sci.*, 165, 19–30, 1994.
5. Chandrasekhar, S.: *Proc. R. Soc. Lond. A.*, 286, 1–26, 1965.
6. Brown, R.A.; and Scriven, L.E.: *Proc. R. Soc. Lond. A*, 371, 331–357, 1980.
7. Lee, C.P.; Anilkumar, A.V.; and Wang, T.G.: *Phys. Fluids A*, 3, 2497–2515, 1991.
8. Anilkumar, A.V.; Lee, C.P.; and Wang, T.G.: *Phys. Fluids A*, 5, 2763–2774, 1993.
9. Lee, C.P.; Anilkumar, A.V.; and Wang, T.G.: *Phys. Fluids*, 6, 3554–3566, 1994.
10. Shi, W.T.; and Apfel, R.E.: *Phys. Fluids*, 7, 2601–2607, 1995.
11. Lamb, H.: *Hydrodynamics*, 6th ea., Dover Publ., 1945.
12. Johnson, R.E.; and Sadhal, S.S.: *Ann. Rev. Fluid Mech.*, 17, 289, 1985.
13. Saffren, M.; Elleman, D.D.; and Rhim, W.K.: *Proc. 2nd Int'l Coll. on Drops and Bubbles*, Monterey, California, November 1981, D.H. Le Croisette, ed., p 7, Jet Propulsion Laboratory, Caltech, Pasadena, California (JPL Publication # 82–7), 1982.
14. Lee, C.P.; and Wang, T.G.: *J. Fluid. Mech.*, 188, 411, 1988.
15. Pelekasis, N.A.; Tsamopoulos, J.A.; and Manolis, G.D.: *J. Fluid Mech.*, 230, 541, 1991.
16. Nayfeh, A.H.; and Mook, D.T.: *Nonlinear Oscillations*, John Wiley & Sons, New York, 1979.
17. Trinh, E.H.; and Wang, T.G.: *J. Fluid Mech.*, 122, 315–338, 1982.
18. Tsamopoulos, J.A.; and Brown, R.A.: *J. Fluid Mech.*, 127, 519–537, 1983.
19. Natarajan, R.; and Brown, R.A.: *J. Fluid Mech.*, 183, 1987.

20. Lundgren, T.S.; and Mansour, N.N.: *J. Fluid Mech.*, 194, 479–510, 1988.
21. Basaran, O.A.: *J. Fluid Mech.*, 241, 169–198, 1992.
22. Möhring, W.; and Knipfer, A.: *Physica D*, 64, 404, 1993.
23. Becker, E.; Hiller, W.J.; and Kowalewski, T.A.: *J. Fluid Mech.*, 258, 191, 1994.
24. Becker, E.; Brosa, U.; and Kowalewski, T.A.: *Comp. Assn. Mech. Eng. Sci.*, 1, 1, 1994.
25. Wang, T.G.; Anilkumar, A.V.; and Lee, C.P.: *J. Fluid Mech.*, 308, 1–14, 1996.
26. Daidzic, N.E.: *Proc. 2nd Int. Conf. on Multiphase Flow*, April 3–7, 1995, Kyoto, Japan, 1995a.
27. Daidzic, N.E.: D. Sc. Thesis, Univ. of Erlangen-Nurnberg, Erlangen, July 1995b.
28. Daidzic, N.E.; Wang, T.G.; and Stadler, R.: *Proc. 1st World Congress on Ultrasonics*, Berlin, Sept. 3–7, 1995.
29. Riley, N.: *J. Engrg. Math.*, 26, 71, 1992.
30. Howarth, L.: *Philos. Mag.*, 42, 1308, 1951.
31. Allen, D.N. de G.: *Nature*, 160, 509, 1947.
32. Gammel, P.M.; Croonquist, A.P.; and Wang, T.G.: *J. Acoust. Soc. Am.*, 83, 496, 1988.
33. Busse, F.H. and Wang, T.G.: *J. Acoust. Soc. Am.*, 69, 1634, 1981.
34. Wang, T.G.; Anilkumar, A.V.; Lee, C.P.; and Lin, K.C.: *J. Fluid Mech.*, 276, 389, 1994.
35. Wang, T.G.: “Acoustics in Space,” *Proceedings of the International School of Physics “Enrico Fermi,”* edited by D. Sette, North-Holland, Amsterdam, 1976.
36. Wang, T.G. and Kanber, H.: *J. Acoust. Soc. Am., Suppl. 1*, 64, 514, 1978.

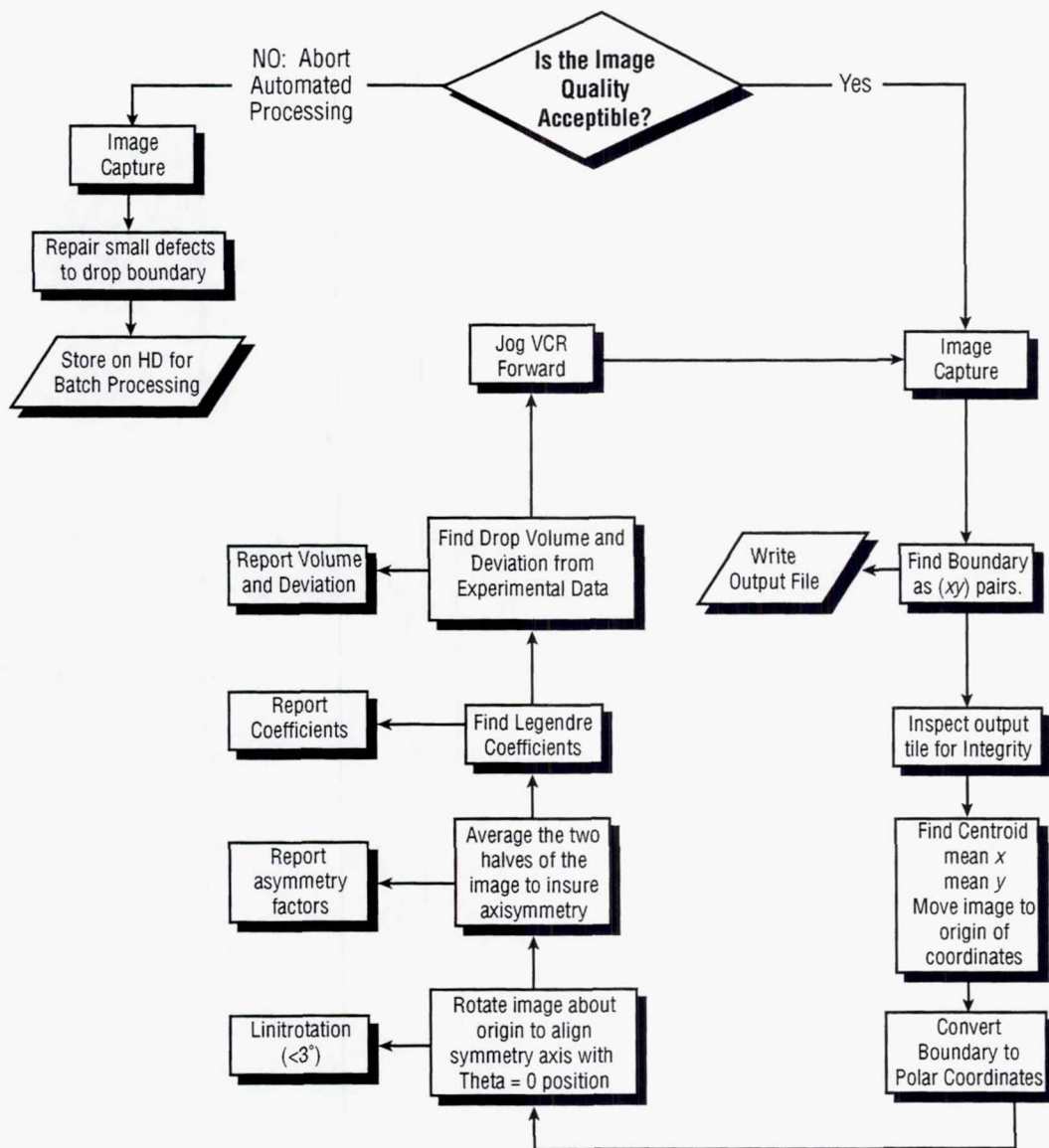


Figure 1. Image Analysis Flow Diagram

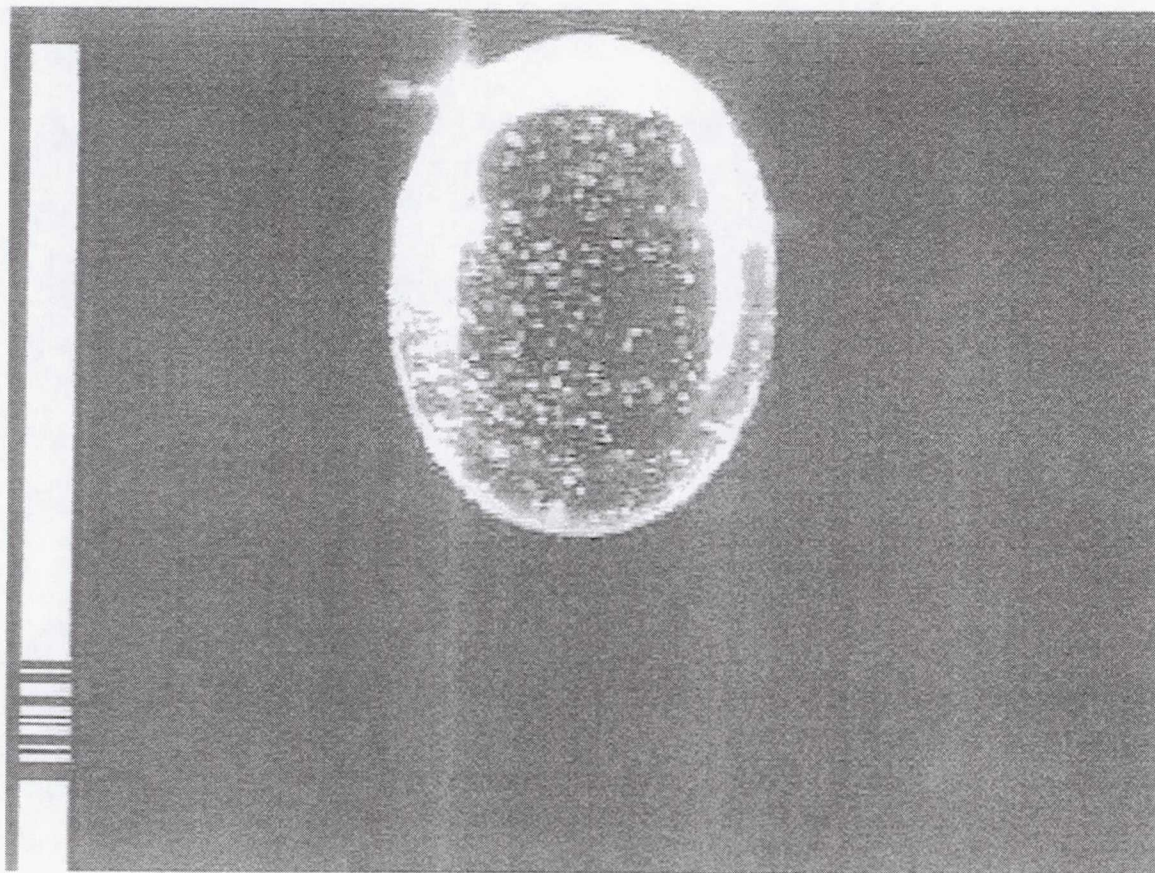


Figure 2. A video frame of a drop with a flare at the upper left-hand corner that seriously distorts the drop boundary.

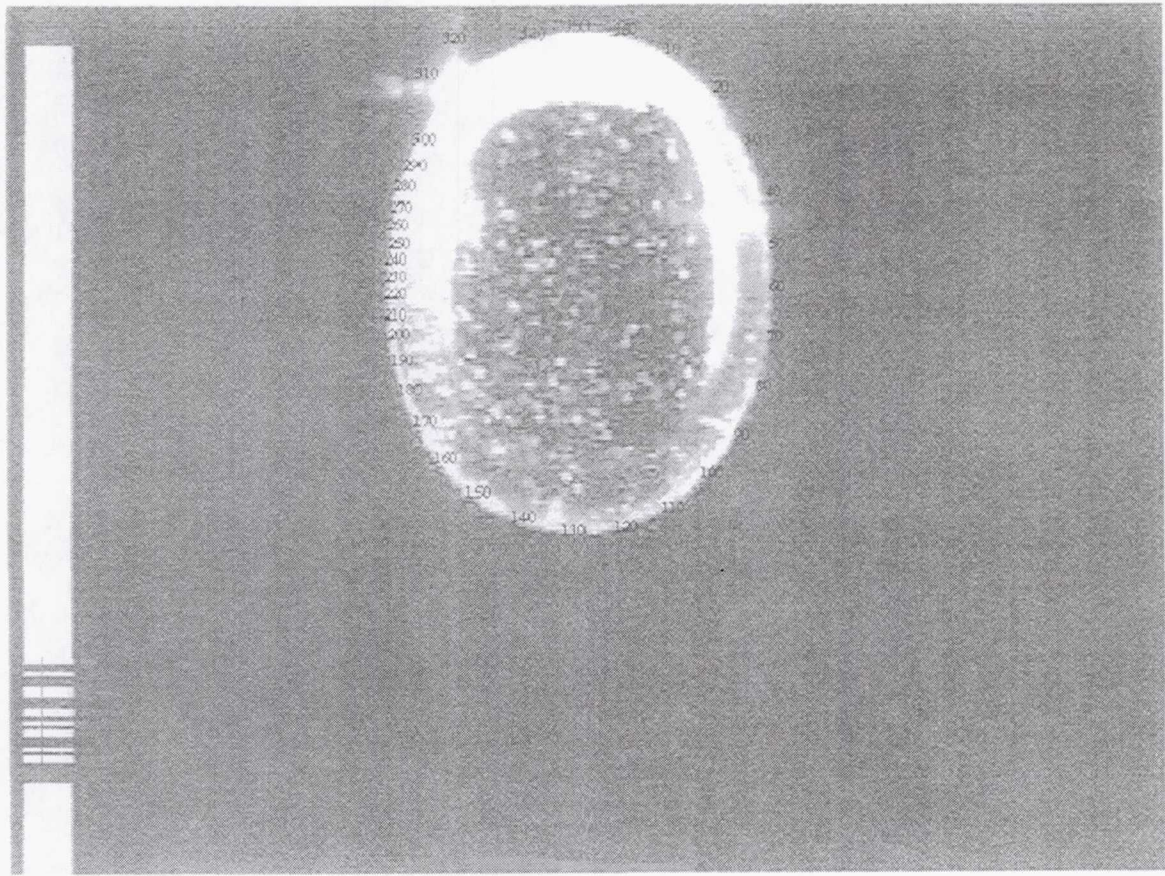


Figure 3. The video frame of figure 2 as interpreted by the algorithm. The flare was mistaken as part of the true boundary.

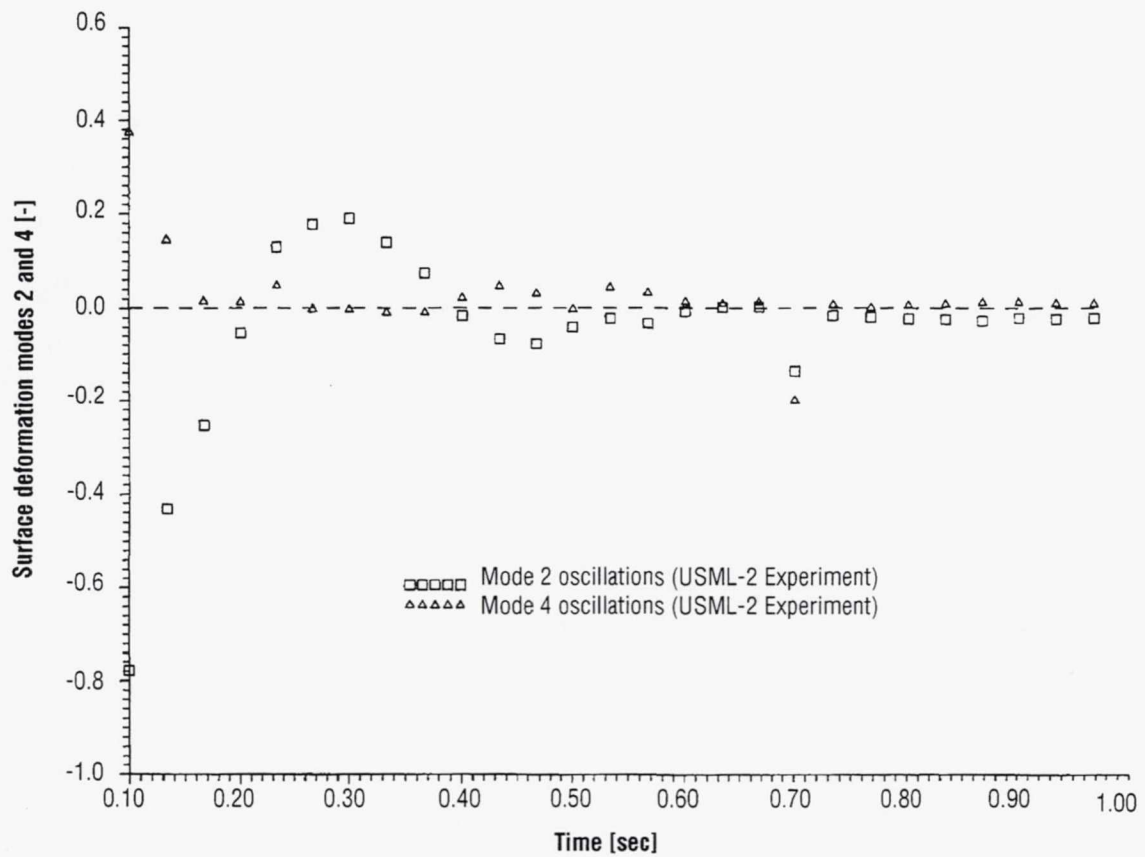


Figure 4. Surface deformation results from an unfiltered data set subjected to automated processing.

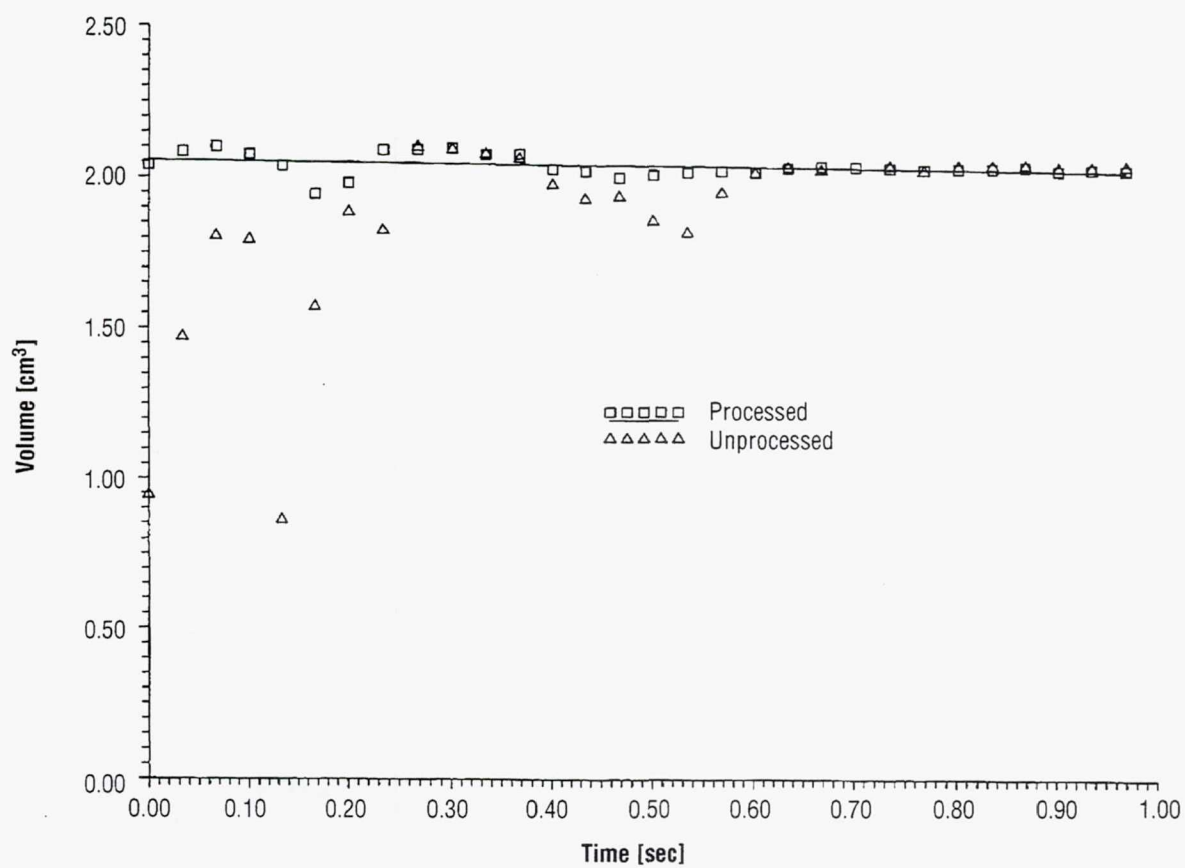


Figure 5. Drop volume for both filtered and unfiltered data sets.

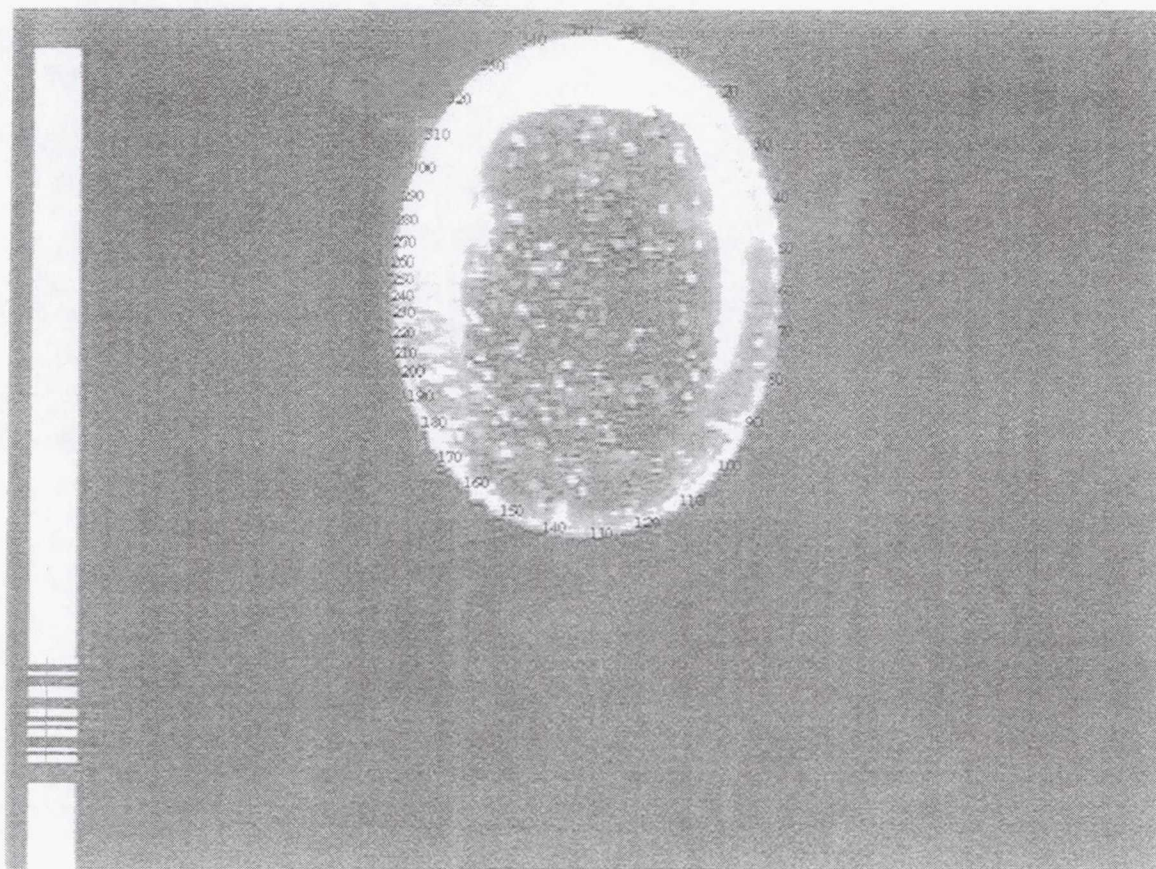


Figure 6. Video frame of a drop, corresponding to figure 4 data, that has been filtered.

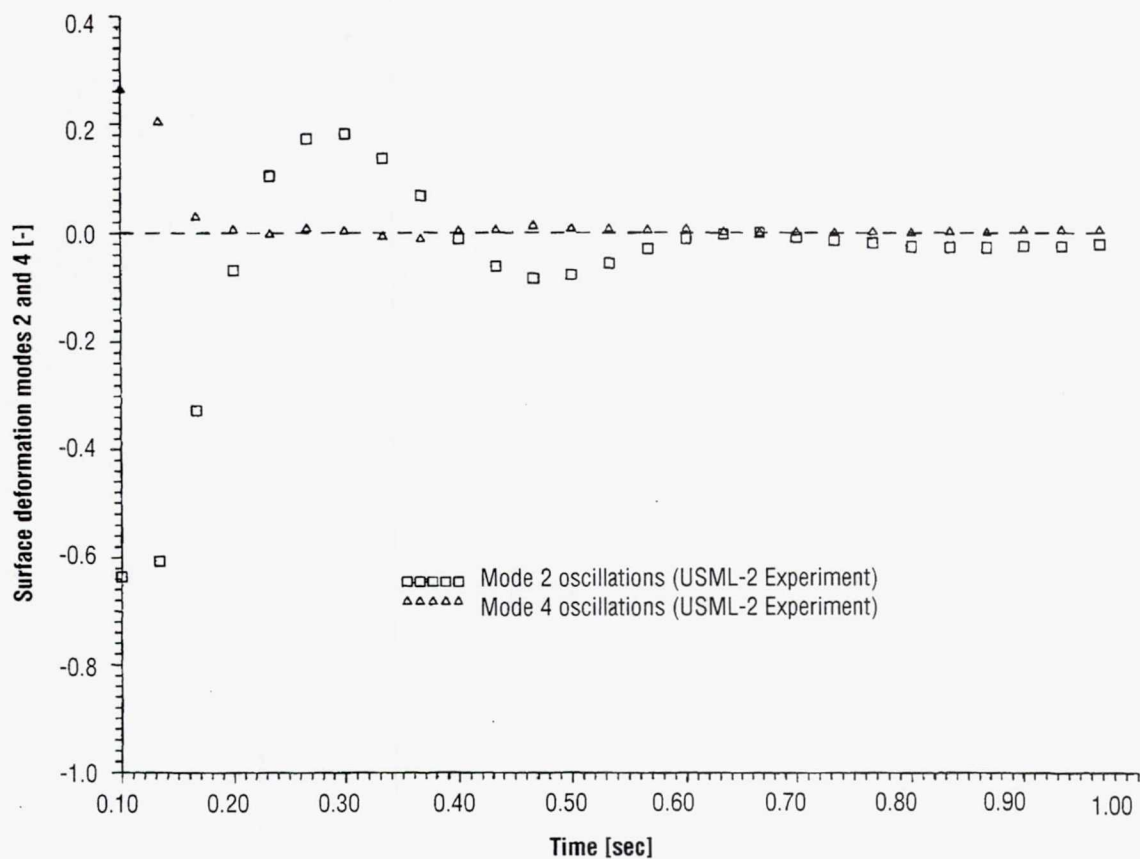


Figure 7. Surface deformation vs. time plot for data, corresponding to figure 4, that has been filtered. Both modes 2 and 4 Legendre time series show definite improvement.

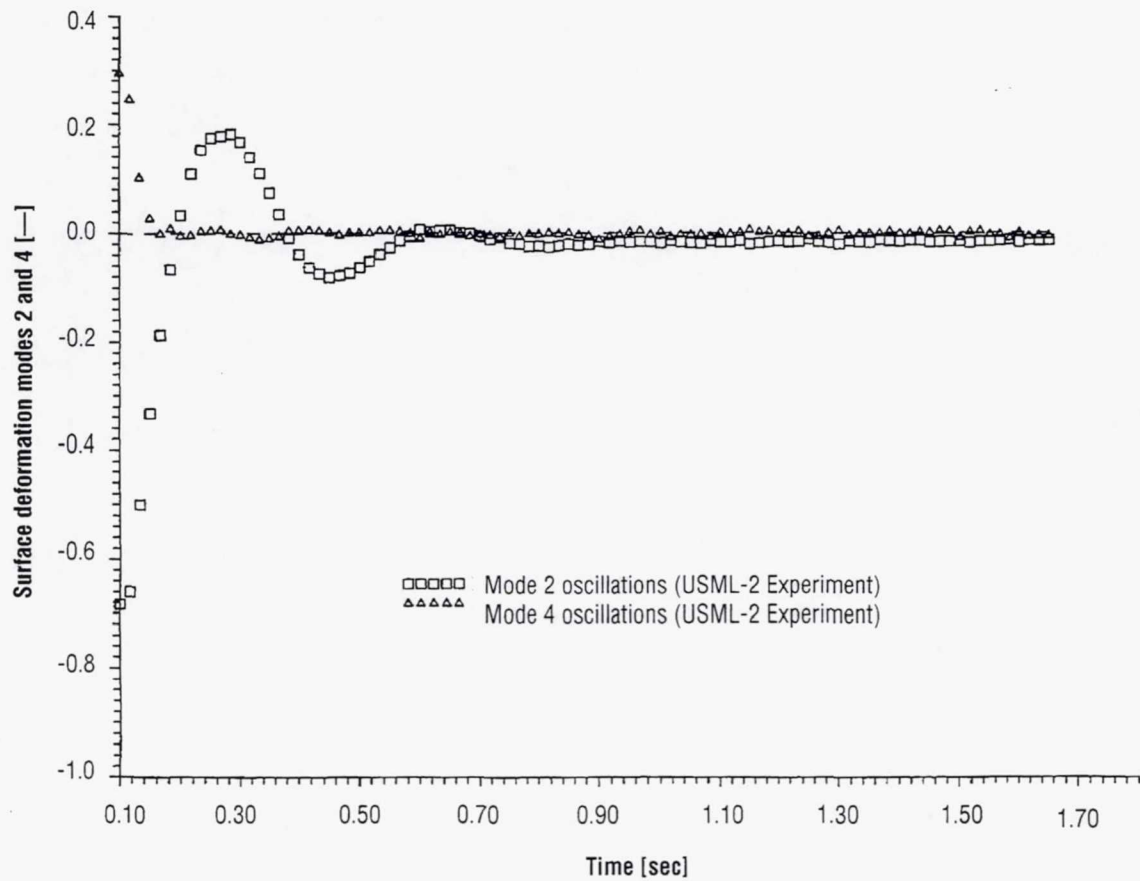


Figure 8. Surface deformation vs. time plot results from filtered data set using higher frequency components of these data. Both mode 2 and mode 4 oscillations show improvement.

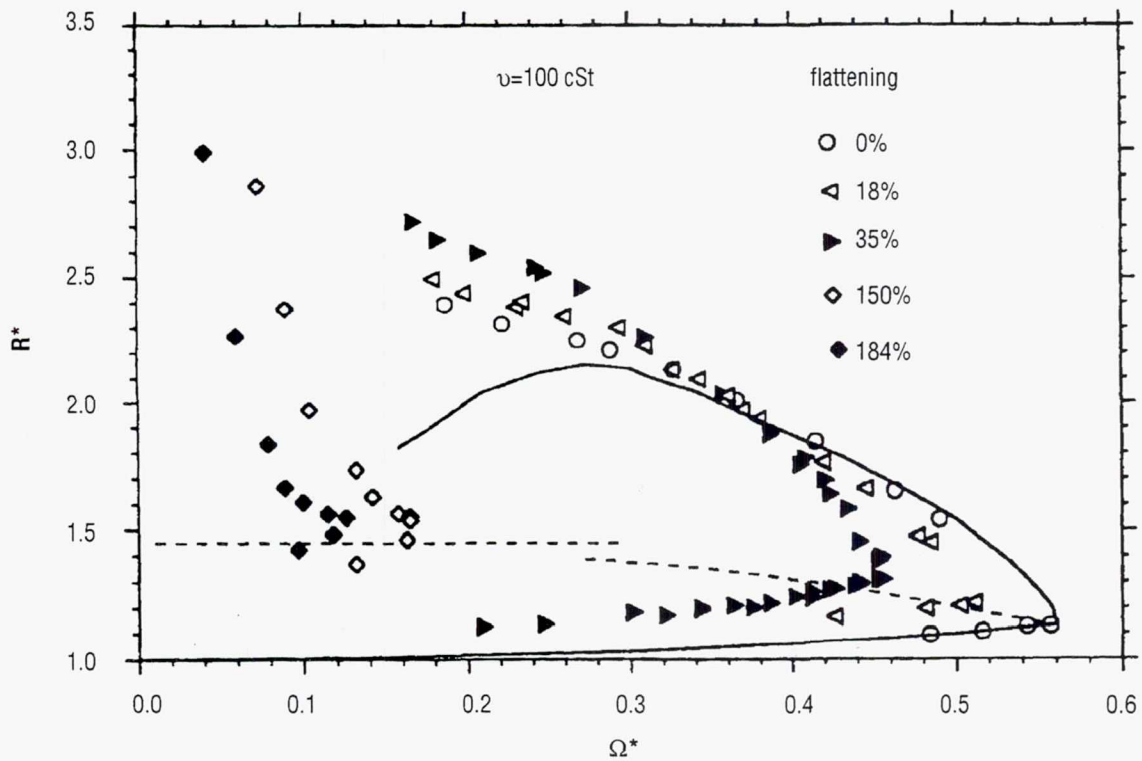


Figure 9. R^* versus Ω^* for 100 cSt drops from Session 1. The solid curve is from Brown and Scriven (1980), in which the lower part corresponds to an axisymmetric drop before bifurcation, and the upper part corresponds to the same drop adopting a two-lobed equilibrium shape after bifurcation. The data points on the right correspond to a two-lobed bifurcation perturbed by acoustic flattening. The data points on the left represent loss of axisymmetric equilibrium under the influence of rotation. The dashed lines represent the theories in the present work.

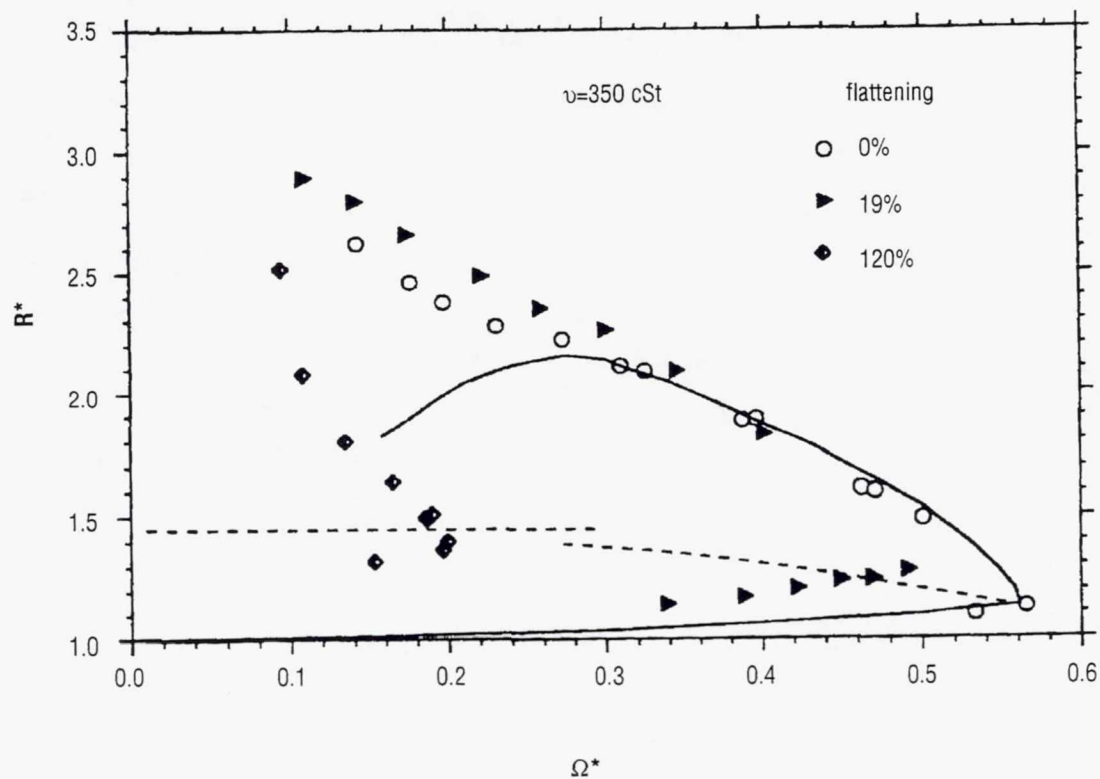


Figure 10. R^* versus Ω^* for 350 cSt drops from Session 2. The description is similar to that for figure 9.

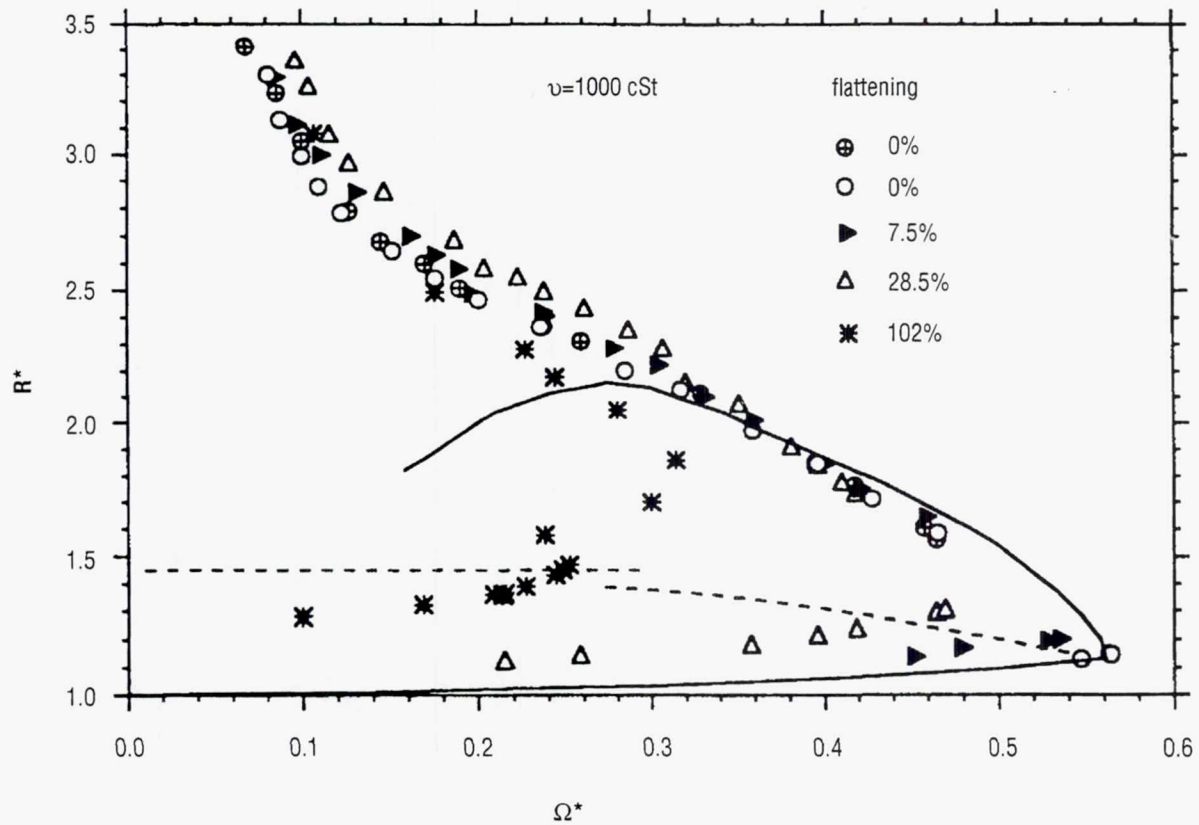


Figure 11. R^* versus Ω^* for 1000 cSt drops from session 3. The 102 percent flattening drop tries, but fails, to bifurcate at $\Omega^* = 0.25$, retains its axisymmetric shape, picks up more angular velocity, and finally loses axisymmetric equilibrium at $\sim \Omega^* = 0.32$. The other drops all bifurcate.

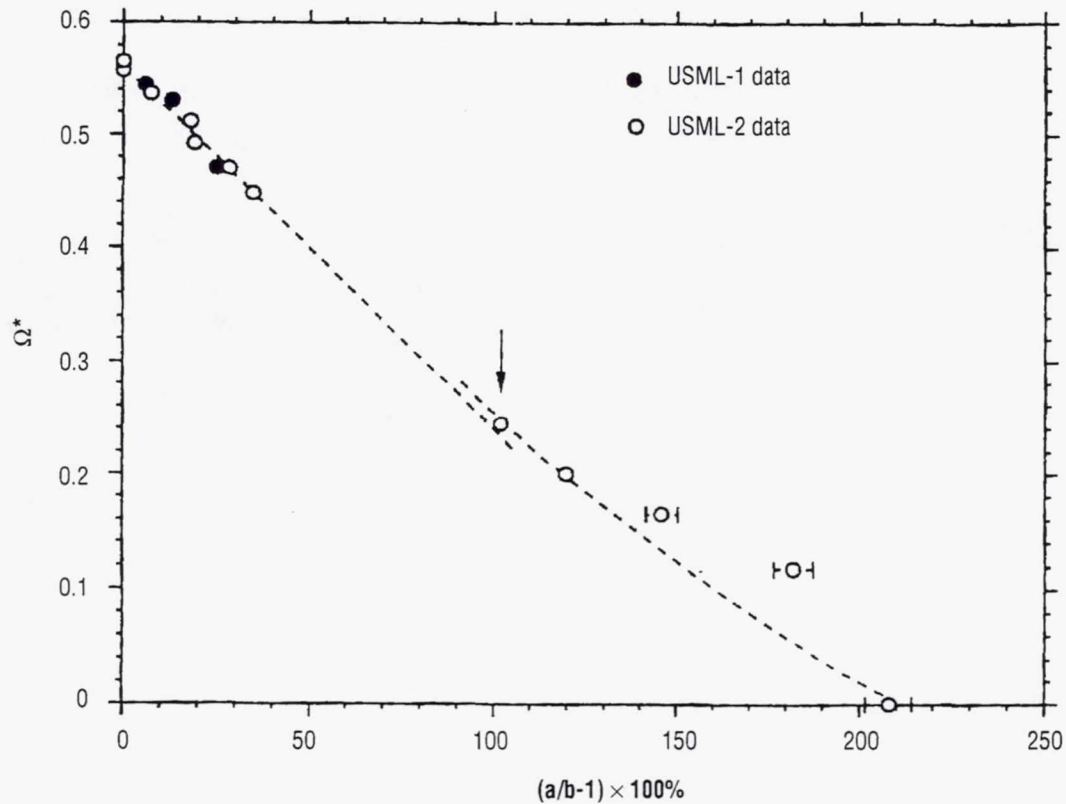


Figure 12. Critical rotation rate versus flattening. The drop sizes can be considered to be asymptotically small, acoustically speaking. The cluster on the left end represents two-lobed bifurcation perturbed by flattening. The other data points to the right represent axisymmetric loss of equilibrium under the influence of rotation. The 102 percent drop in figure 11 is highlighted here by an arrow. The dashed lines represent the theories in the present work.

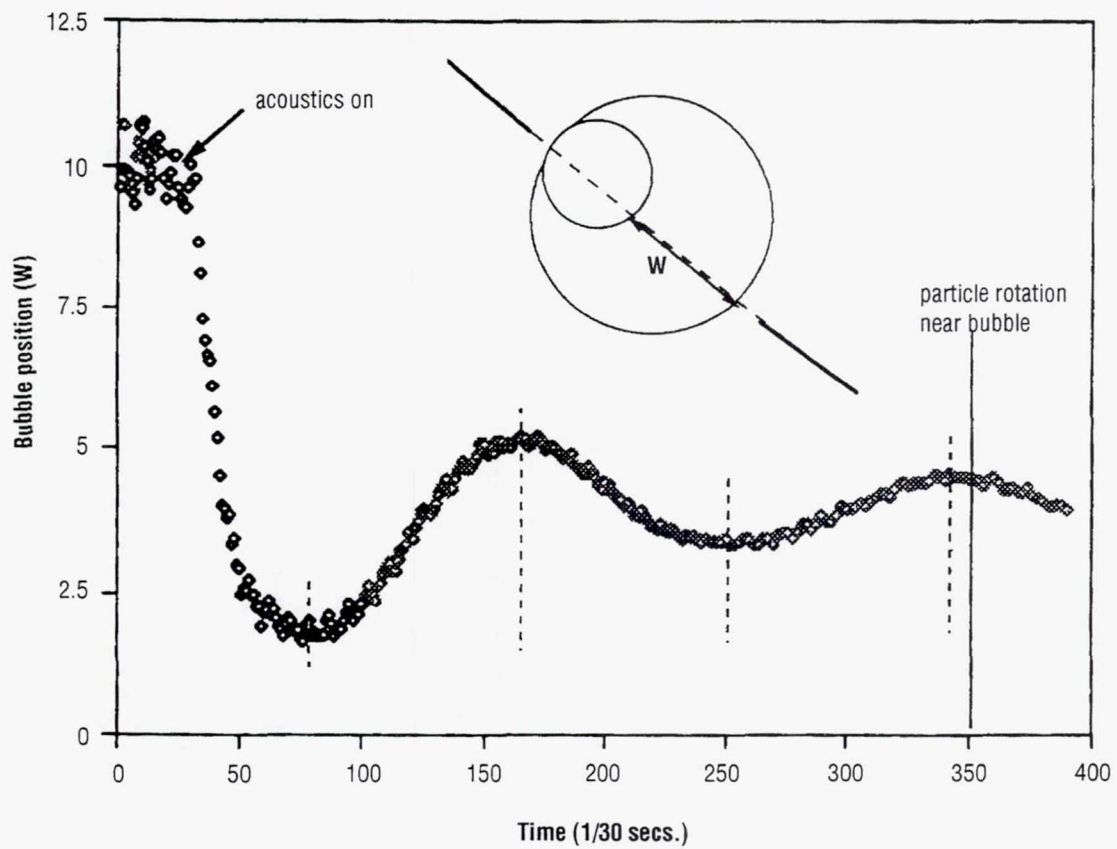


Figure 13. Centering of liquid bubble during decaying oscillations following deployment.

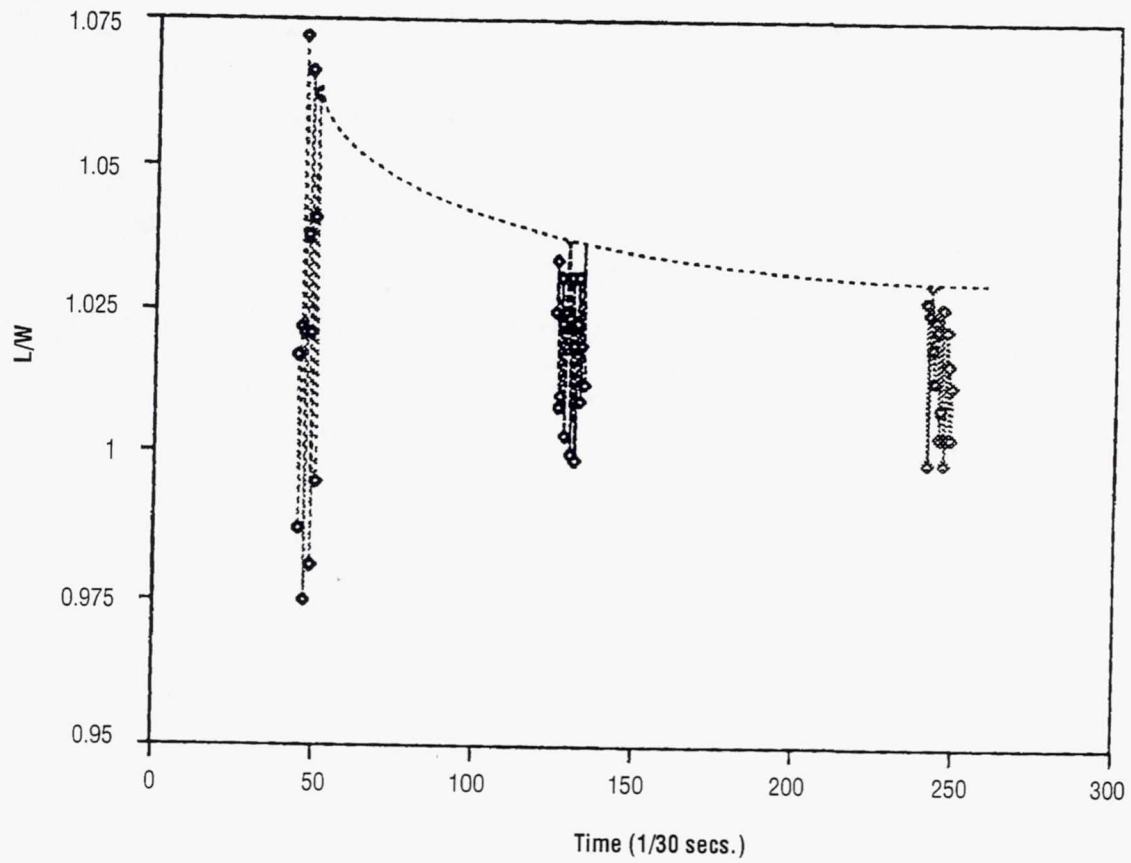


Figure 14. Decaying oscillations of liquid bubble following deployment.

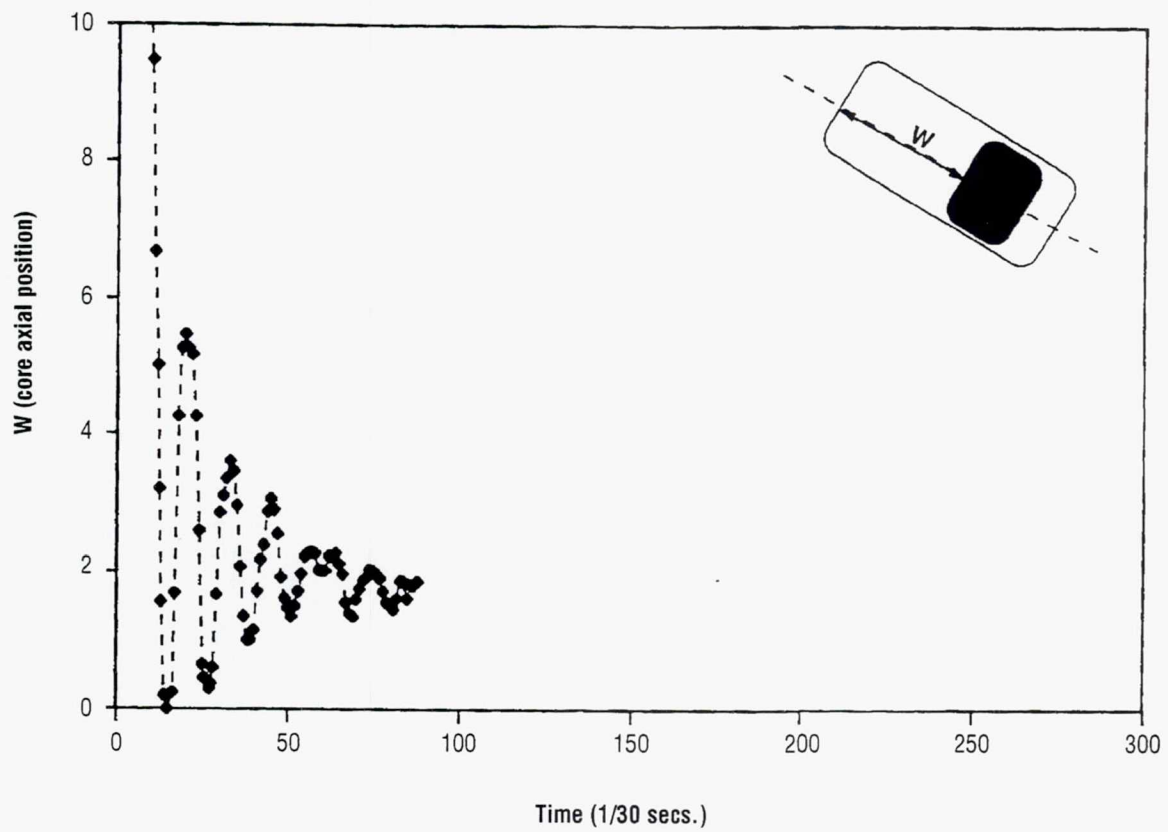


Figure 15. Centering of immiscible compound drop during deployment.

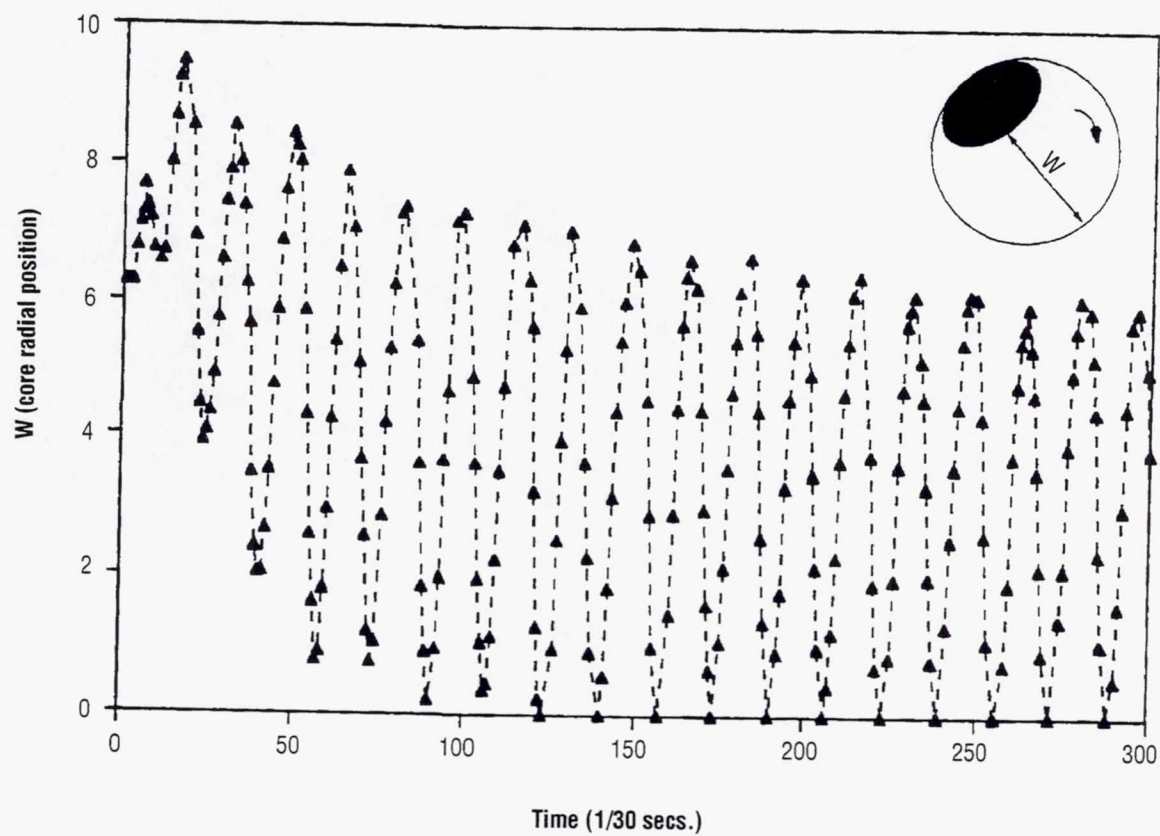


Figure 16. Centering of rotating-immiscible compound drop during forced oscillations.

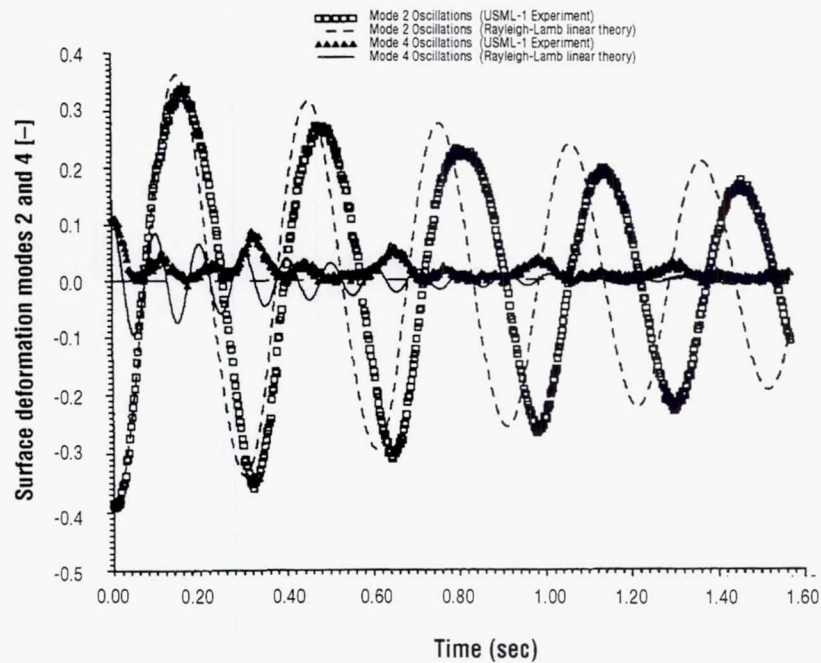


Figure 17. Experimental time series of mode 2 and mode 4 oscillations. Free decay of a low-viscosity 1 cm Glycerin/Water drop. The solid and dashed curves represent the results of the Rayleigh-Lamb linear predictions.

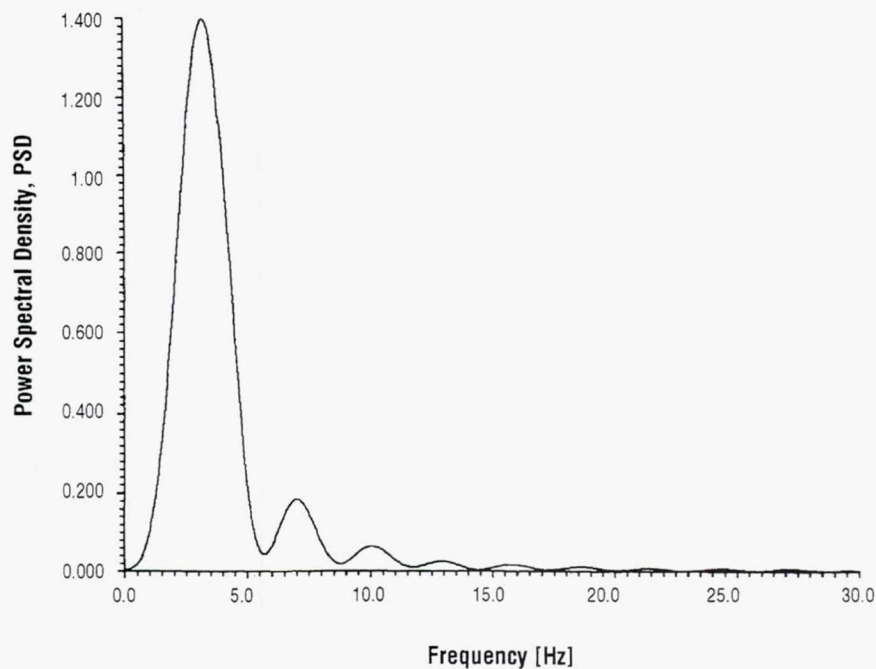


Figure 18. The power spectrum of the mode 2 oscillations P_{22} . The existence of superharmonics nf_2 is evident.

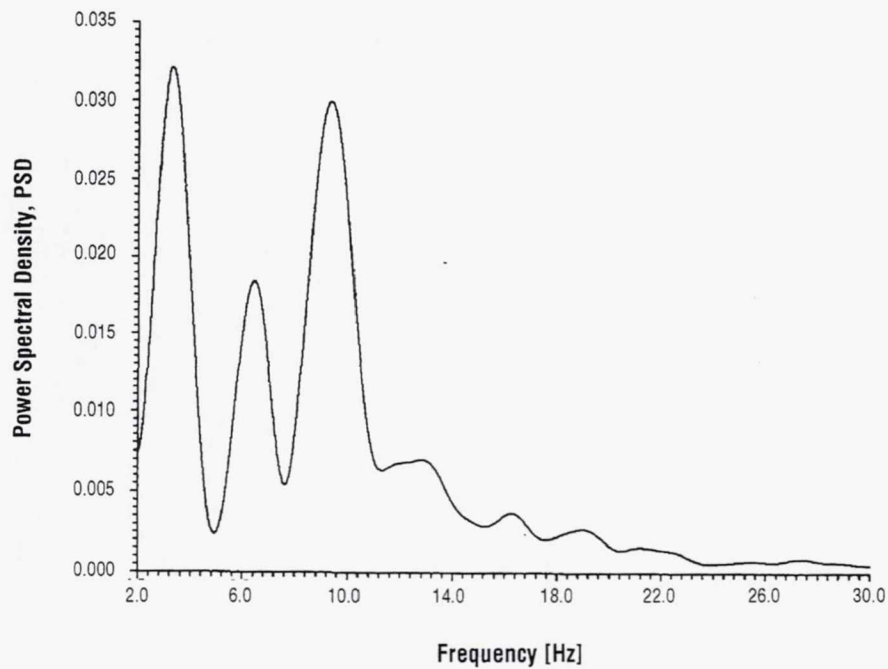


Figure 19. The power spectrum of the mode 4 oscillations P_{44} . In this case superharmonics, subharmonics and combination harmonics appear.

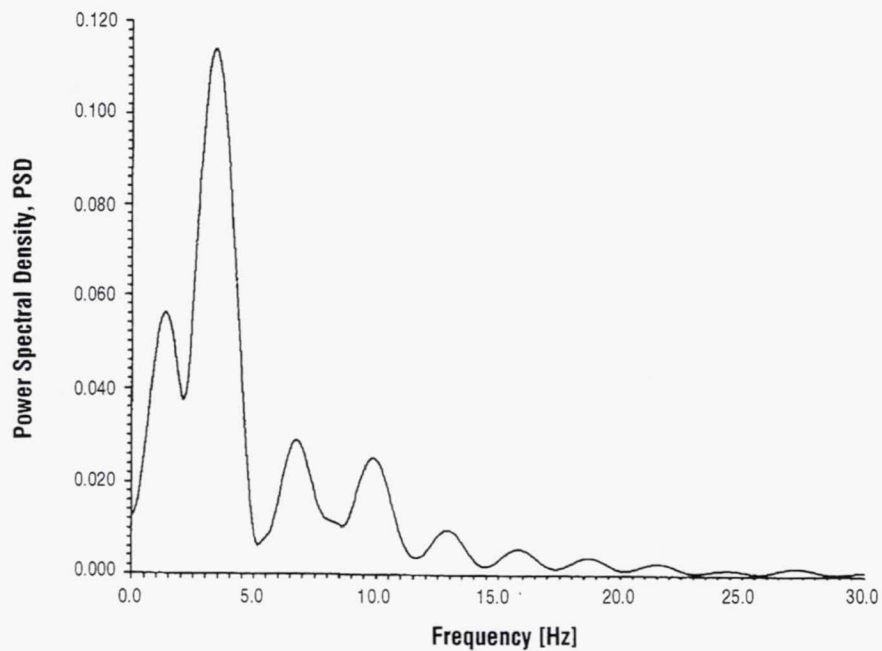


Figure 20. The cross power spectrum of the mode 2 and 4 oscillations P_{24} . It is interesting to note the existence of the fundamental frequency $1/3 f_2$ subharmonic.

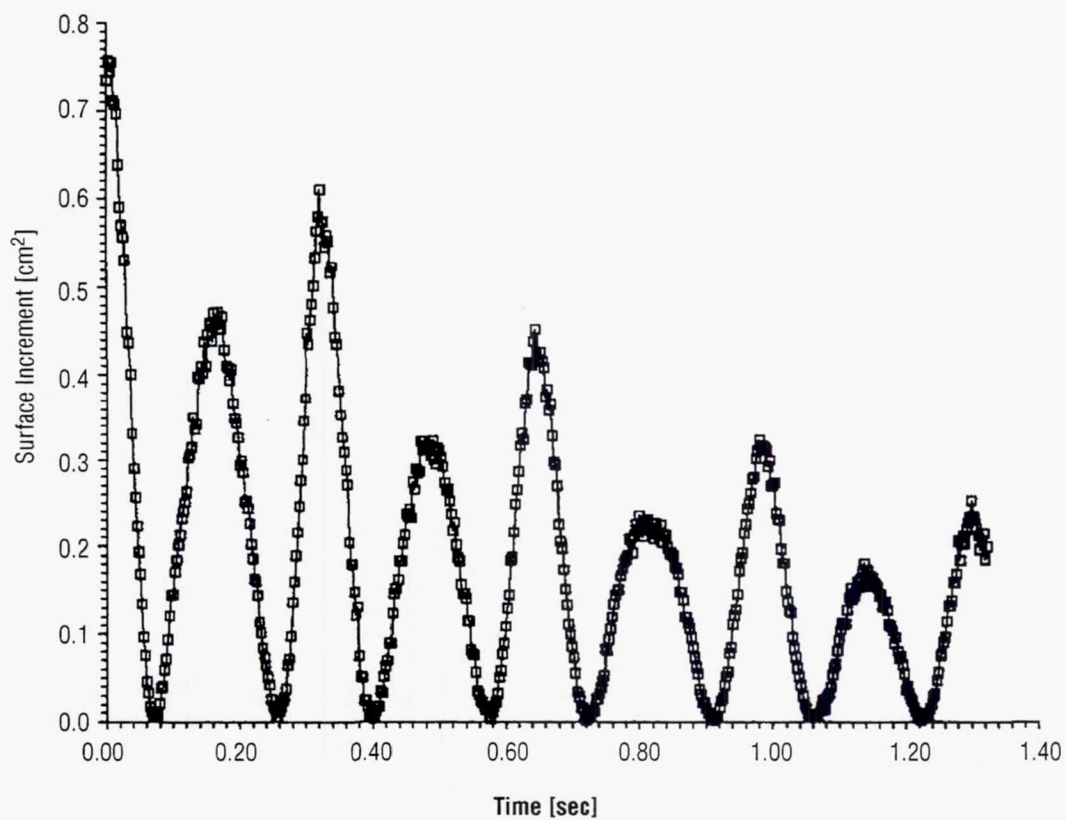


Figure 21. Relative surface energy is plotted versus time. Note the $2f_2$ modulation of the fundamental frequency.

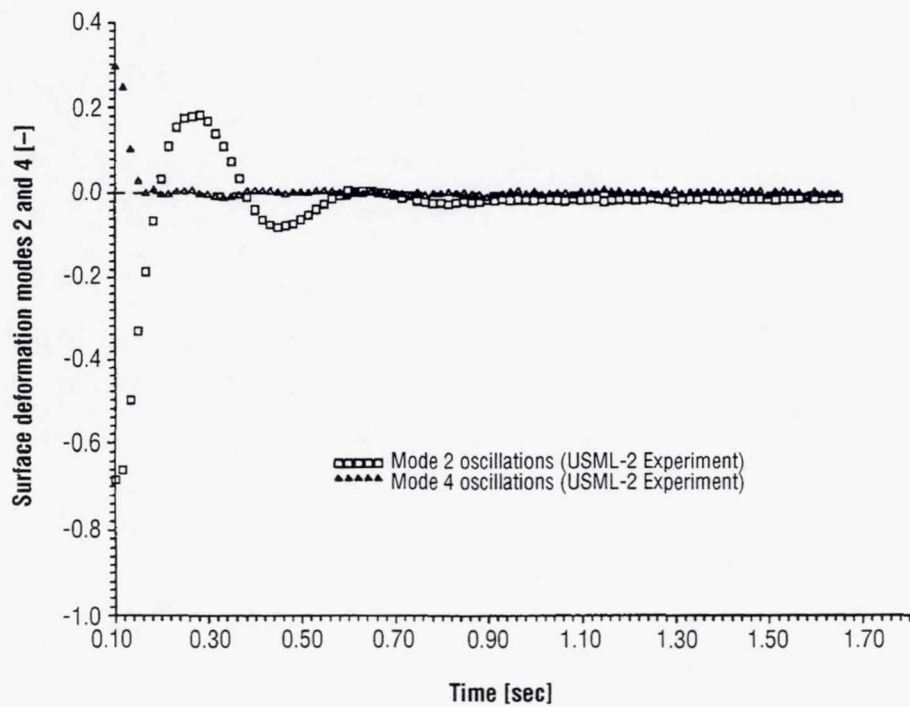


Figure 22. Experimental time series of mode 2 and mode 4 oscillations. Free decay of a highly viscous 2 cm silicone oil drop. Results for fast free decay from USML-2 experiment.

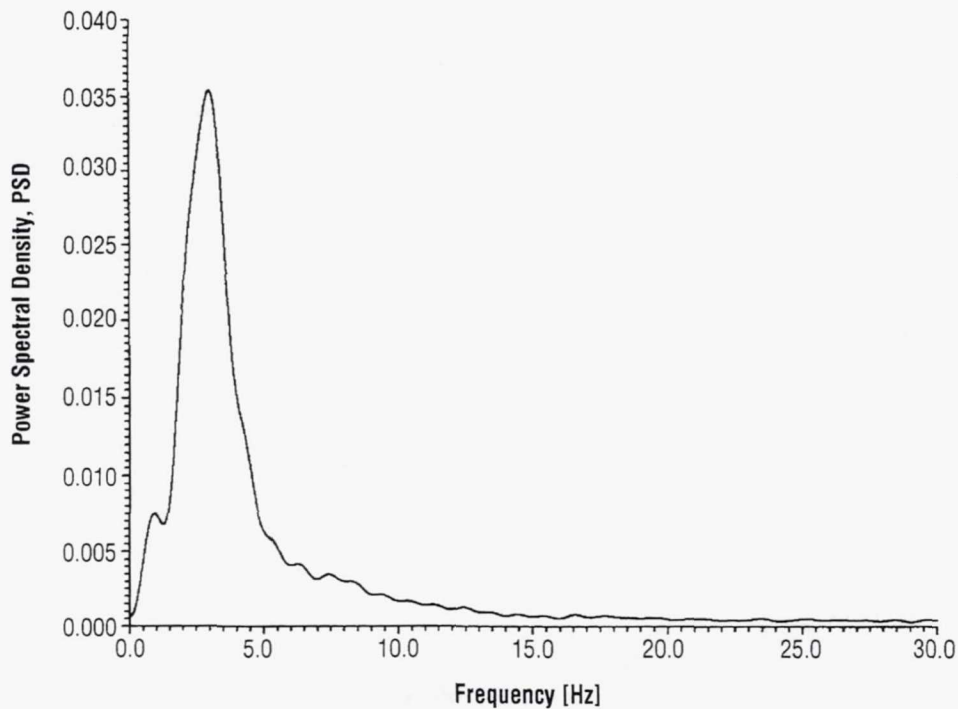


Figure 23. The power spectrum of the mode 2 oscillations P_{22} (USML-2 fast decay data).

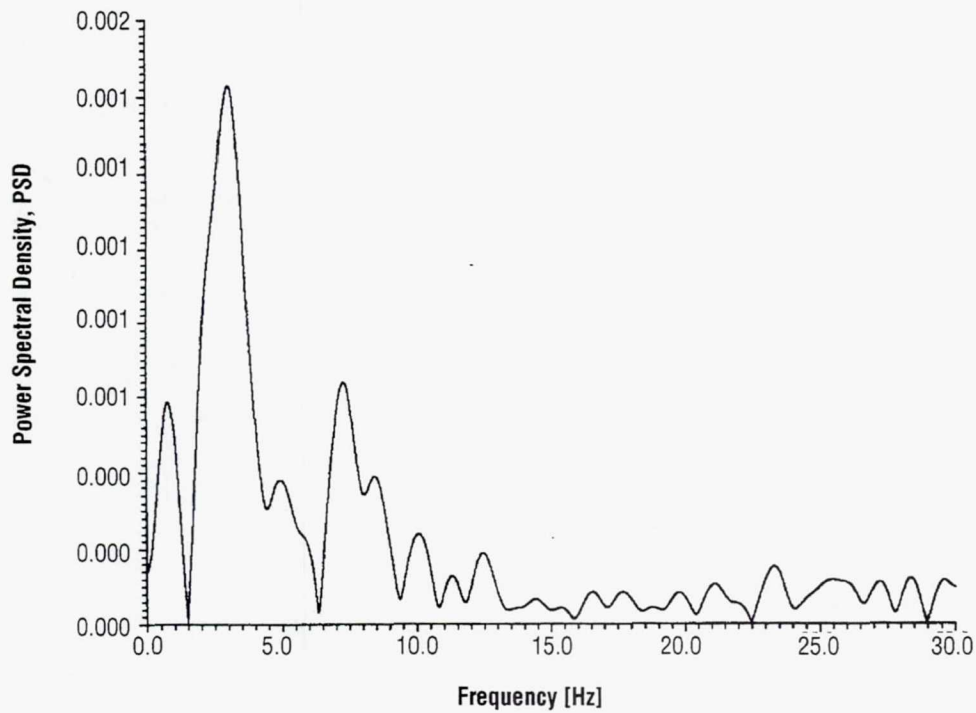


Figure 24. The cross power spectrum of the mode 2 and 4 oscillations P_{24} (USML-2 fast decay data).

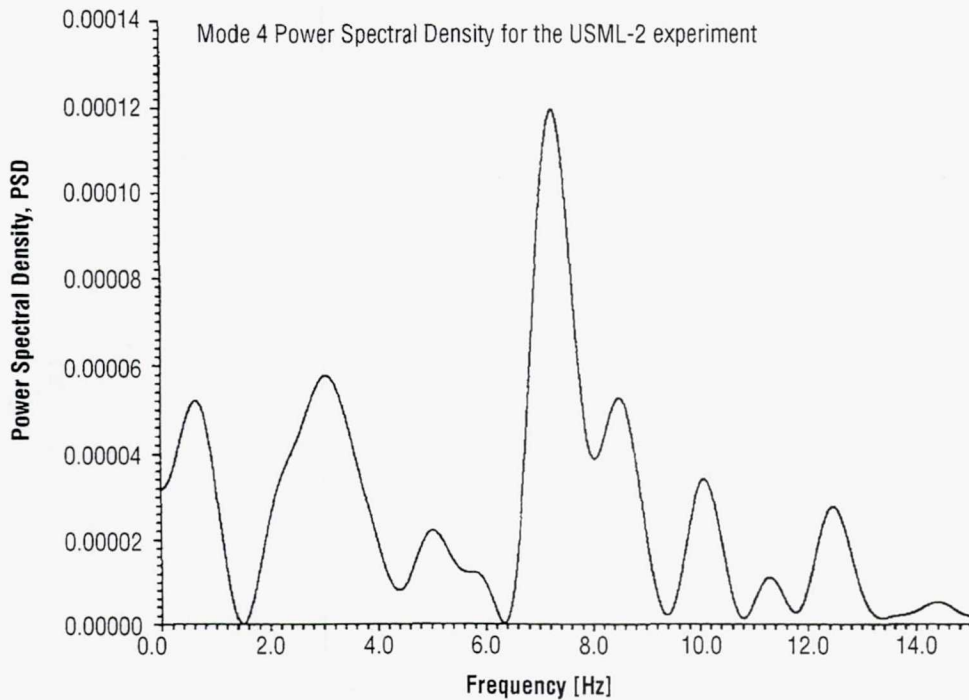


Figure 25. The power spectrum of the mode 4 oscillations P_{44} (USML-2 fast decay data).

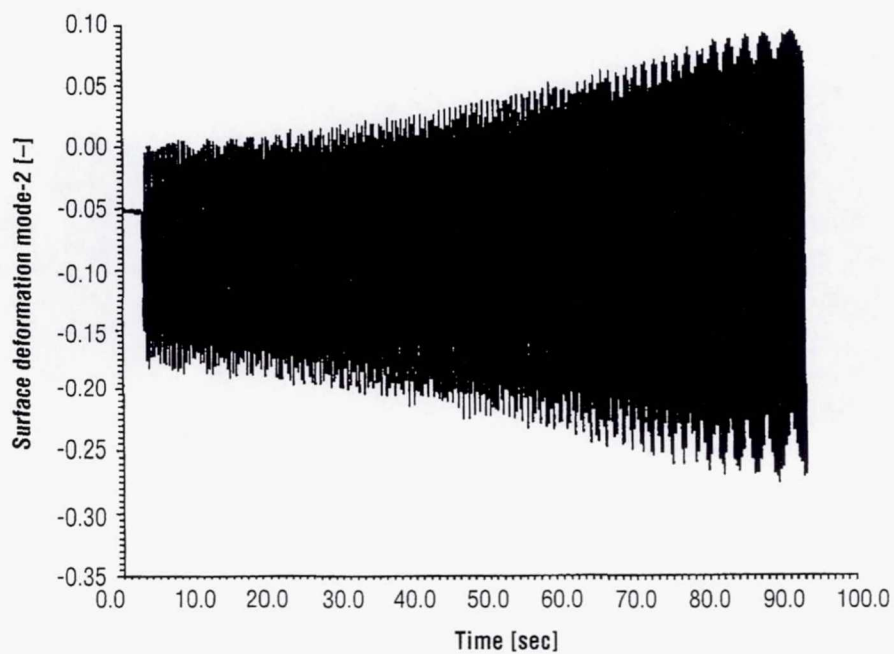


Figure 26. Experimental time series of mode 2 oscillations. Forward sweep at 8 V.

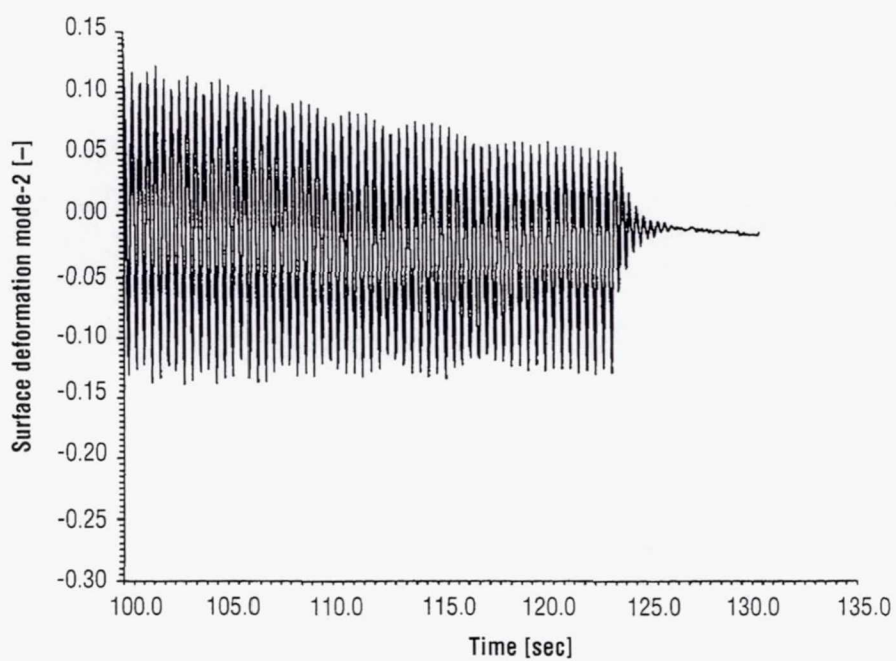


Figure 27. Experimental time series of mode 2 oscillations. Backward sweep at 8 V amplitude.

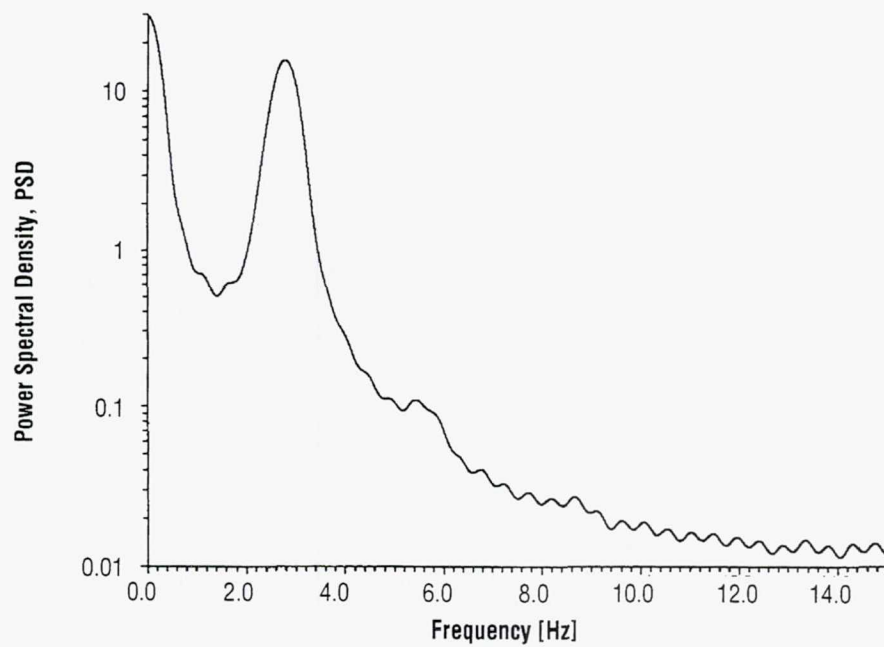


Figure 28. The PSD of the mode 2 oscillations for forward sweep at 8 V.

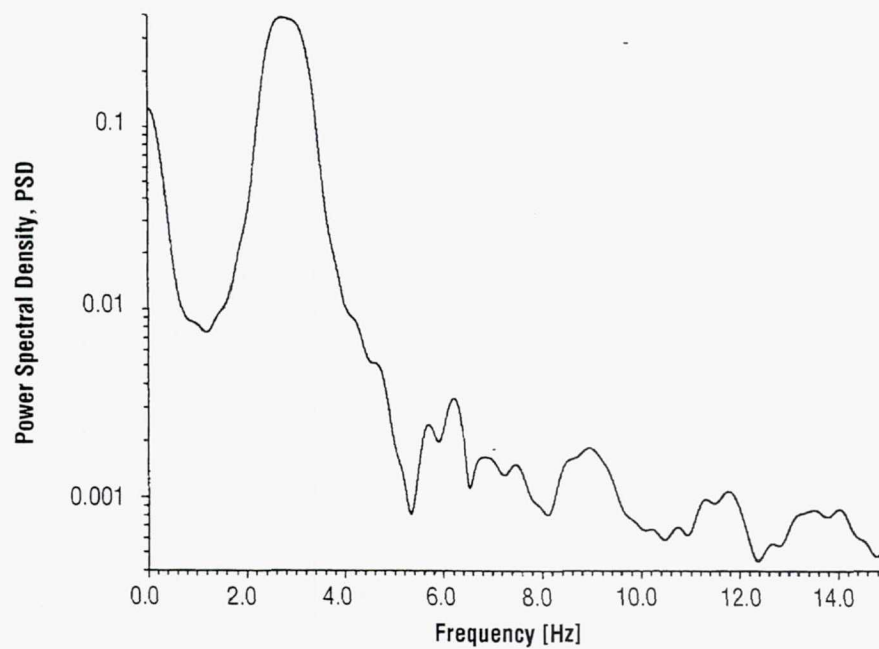


Figure 29. The CPSD of the mode 2 and 4 oscillations. Backward sweep at 8 V.

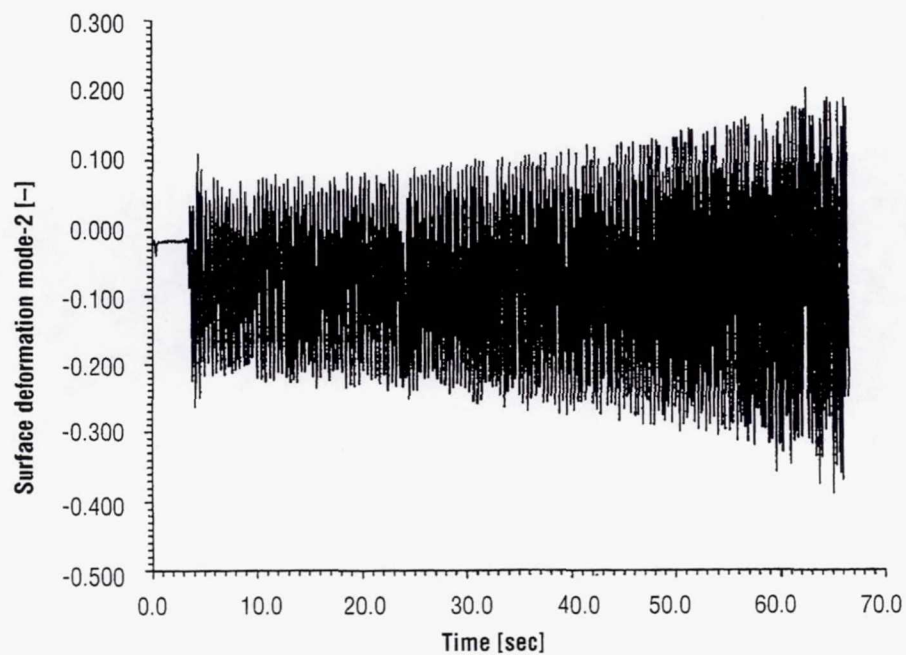


Figure 30. Experimental time series of mode 2 oscillations. Forward sweep at 12 V amplitude.

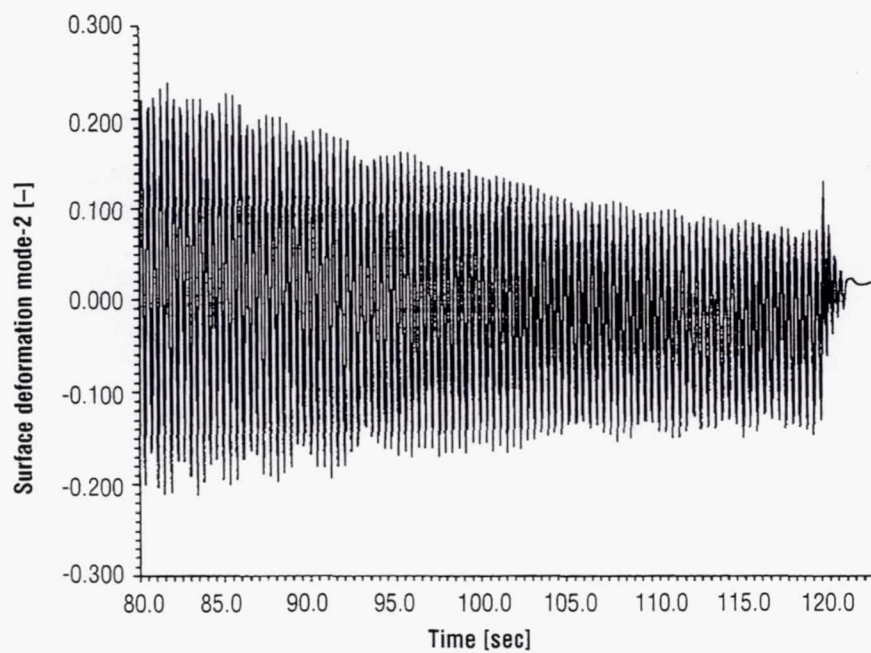


Figure 31. Experimental time series of mode 2 oscillations. Backward sweep at 12 V amplitude.

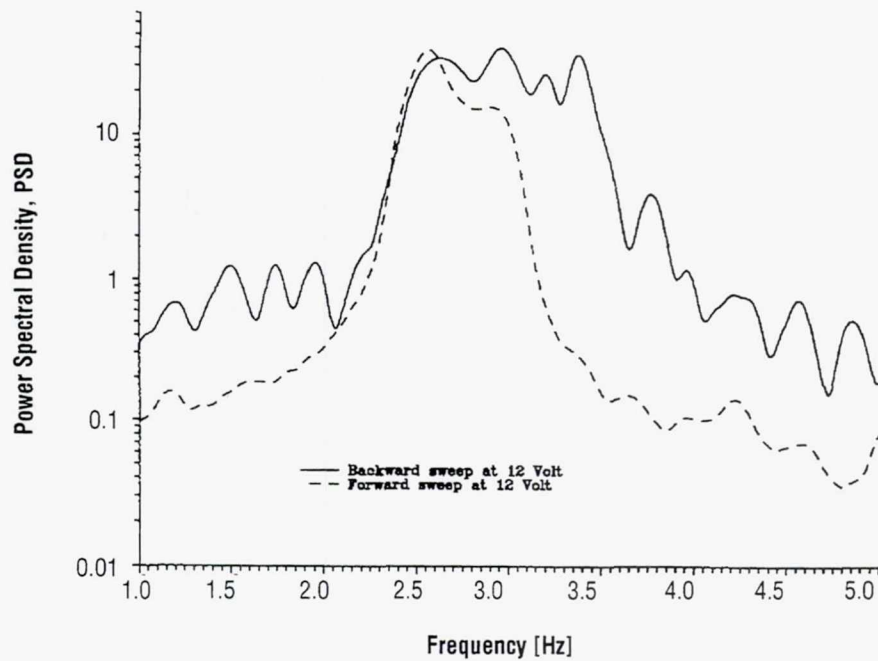


Figure 32. PSD's for the forward and backward sweep plotted against each other. Note the frequency shift and existence of satellite peaks.

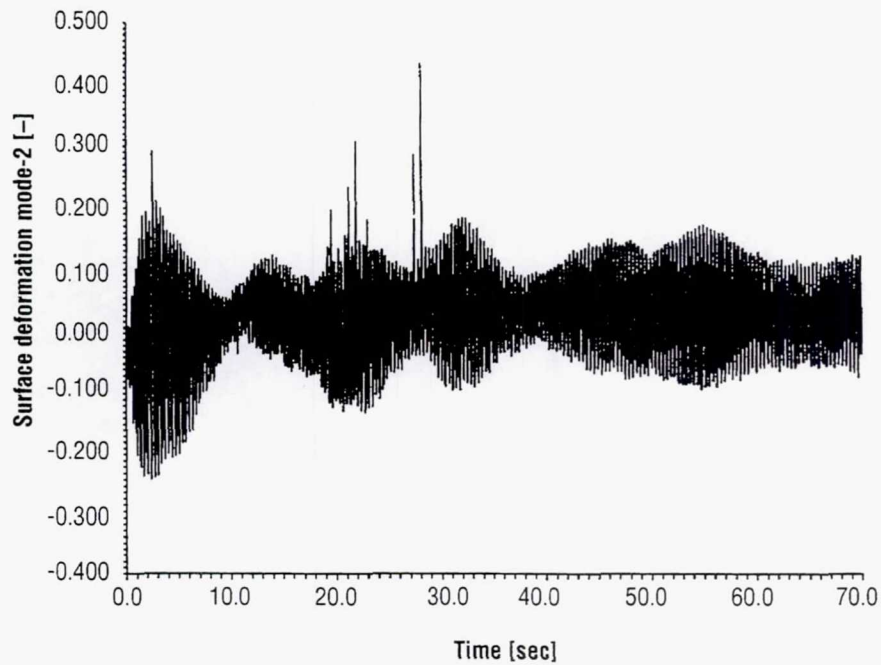


Figure 33. The experimental time series of the mode 2 chaotic drop oscillations. The excitation amplitude is 12 V.

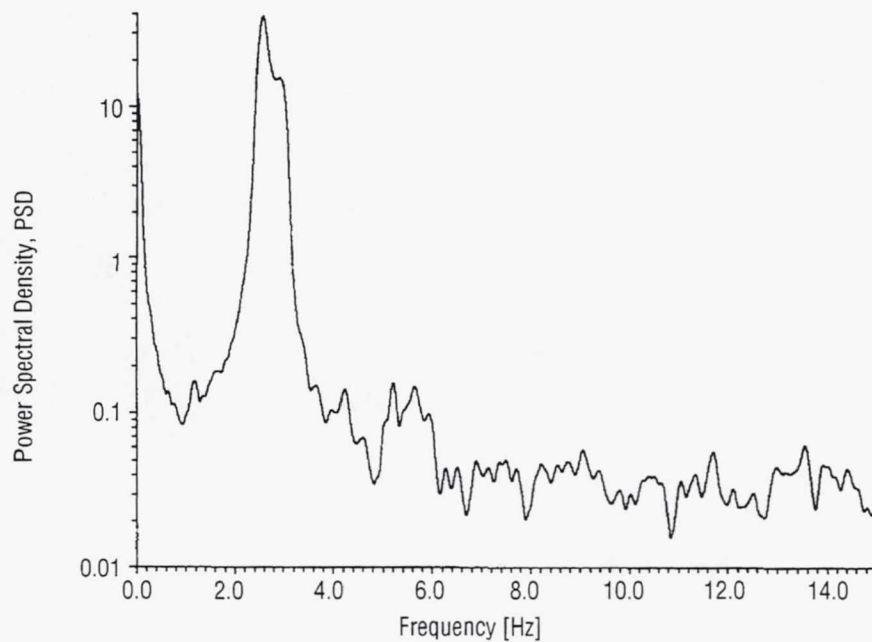


Figure 34. The PSD of the mode 2 oscillations. The excitation frequency is decreasing linearly with the amplitude of 12 V.

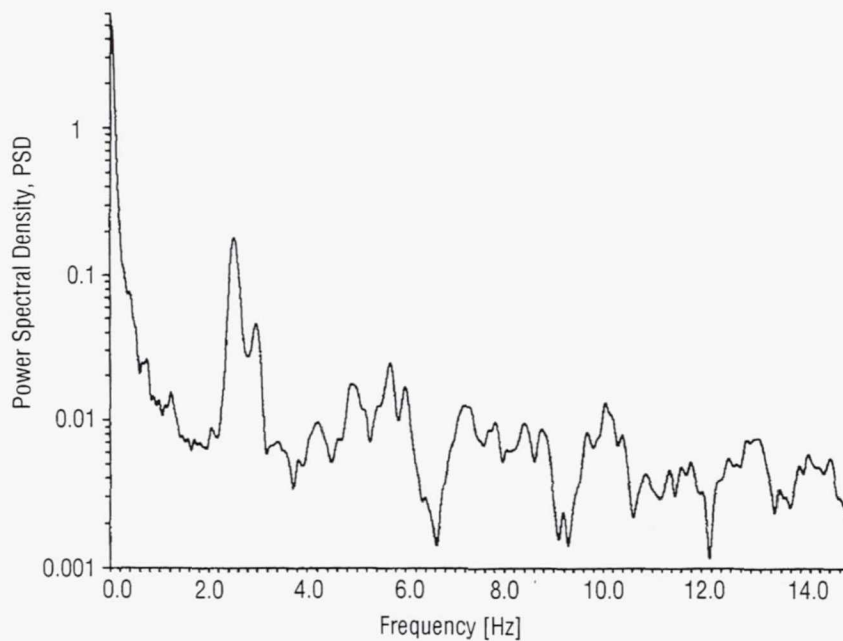


Figure 35. The PSD of the mode 4 oscillations. The excitation frequency is decreasing linearly with the amplitude of 12 V.

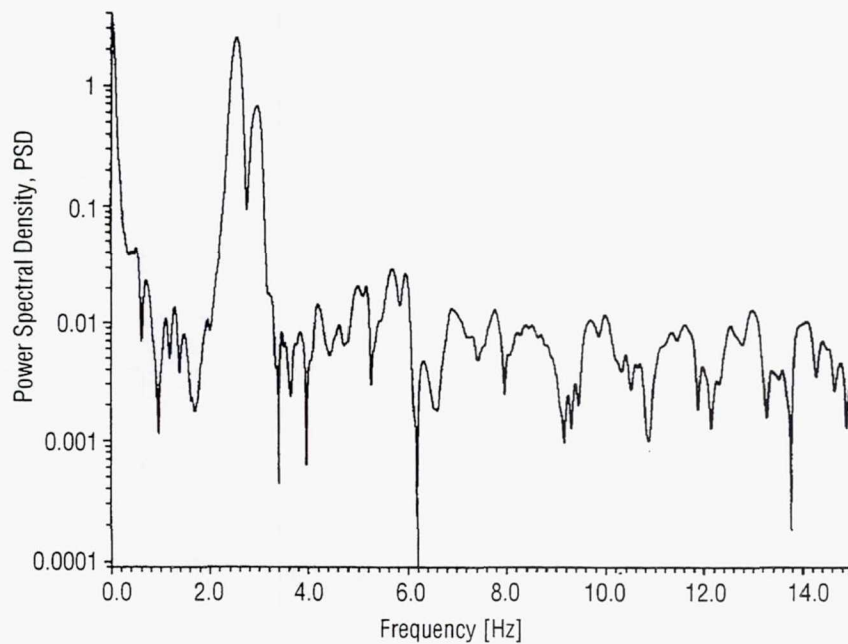


Figure 36. The CPSD of the mode 2 and 4 oscillations. The excitation frequency is decreasing linearly with the amplitude of 12 V.

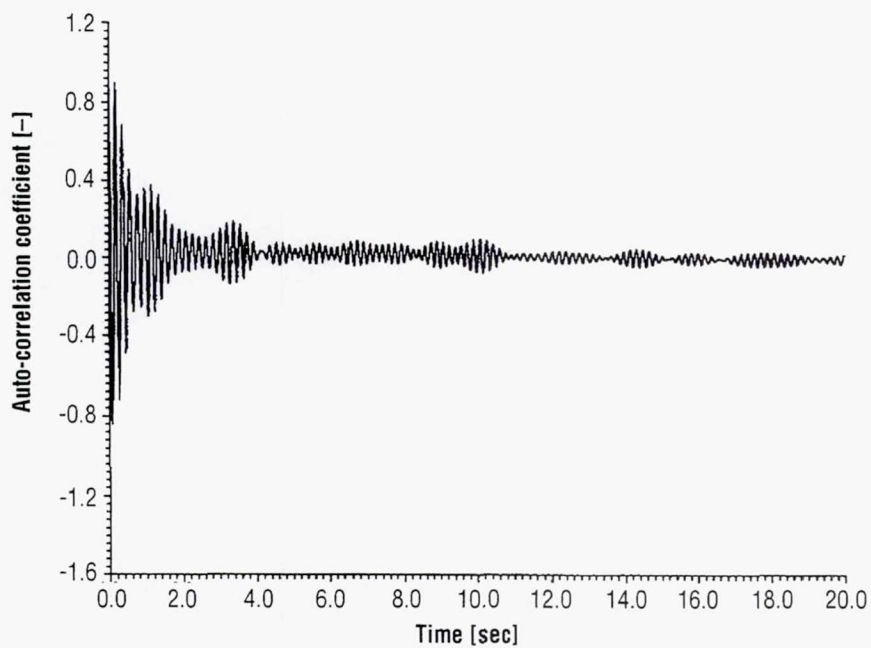


Figure 37. Auto-correlation coefficient of the experimental time series of mode 2 oscillations. Excitation amplitude is 12 V.

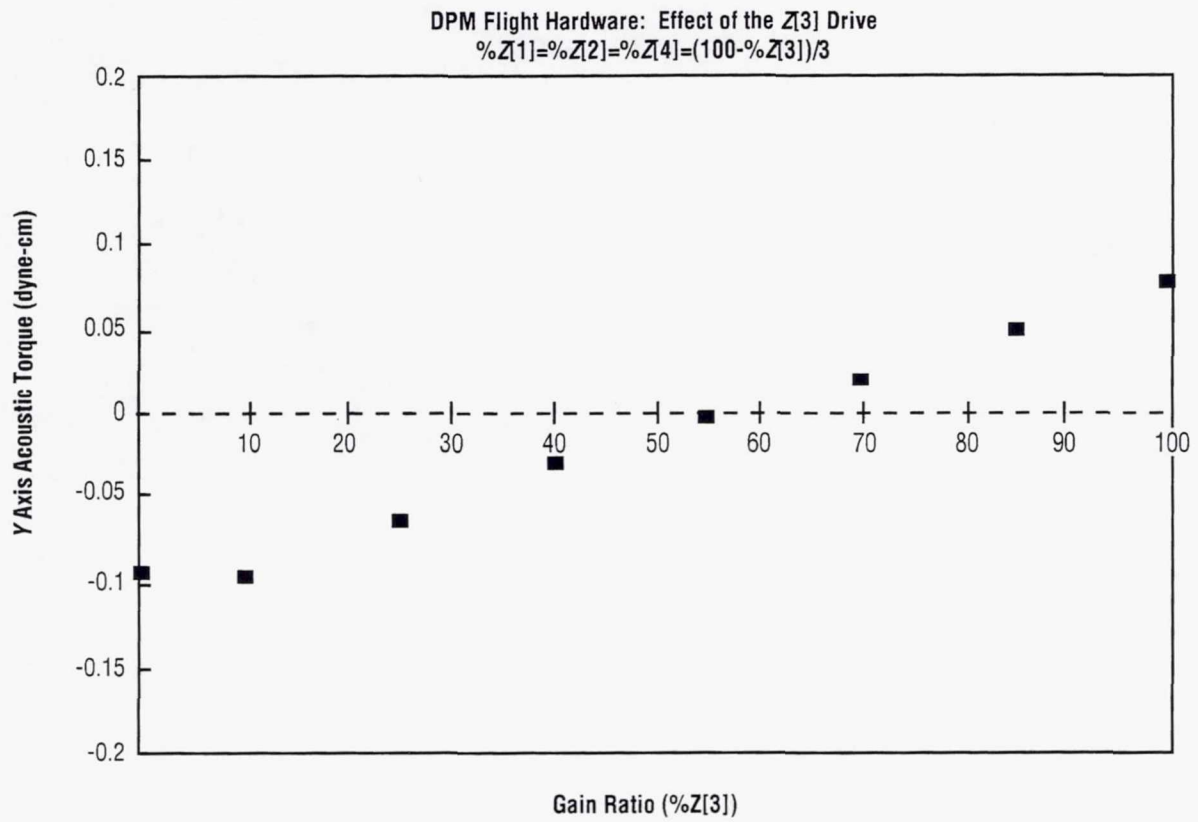


Figure 38. Acoustic torque is observed to be a continuous monotonic function of the gain ratio, as the ratio of [1]:[3] is varied.

Control of X Axis Tumble Rotation

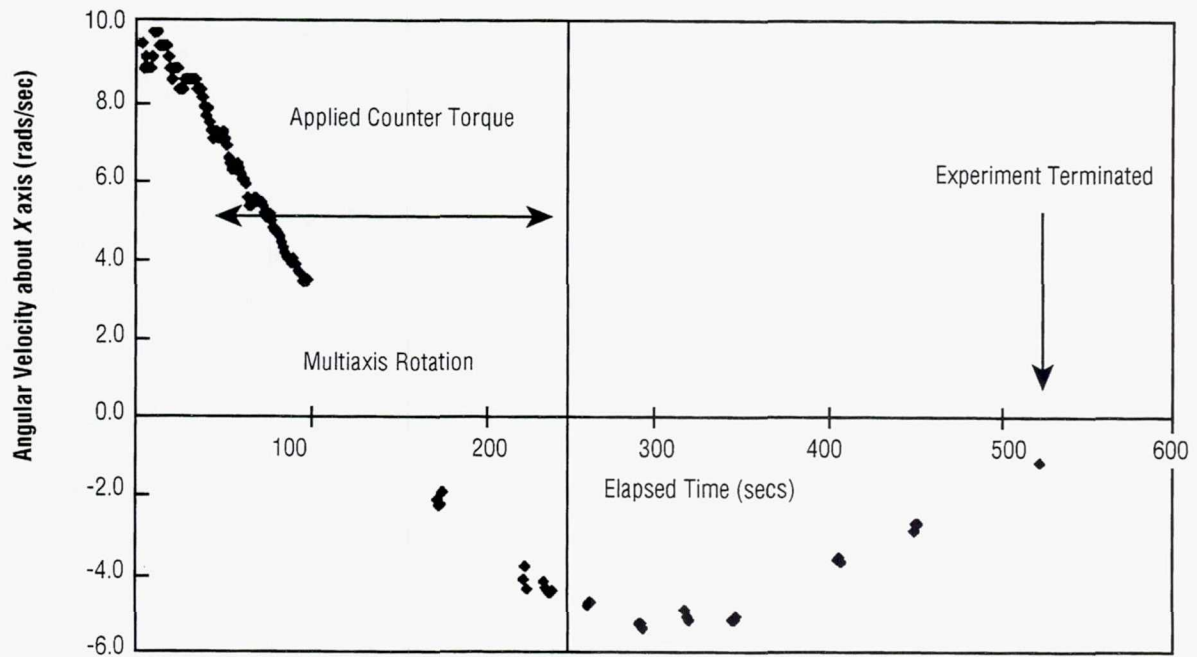


Figure 39. Time history of specimen motion as derived from experiment videotapes.

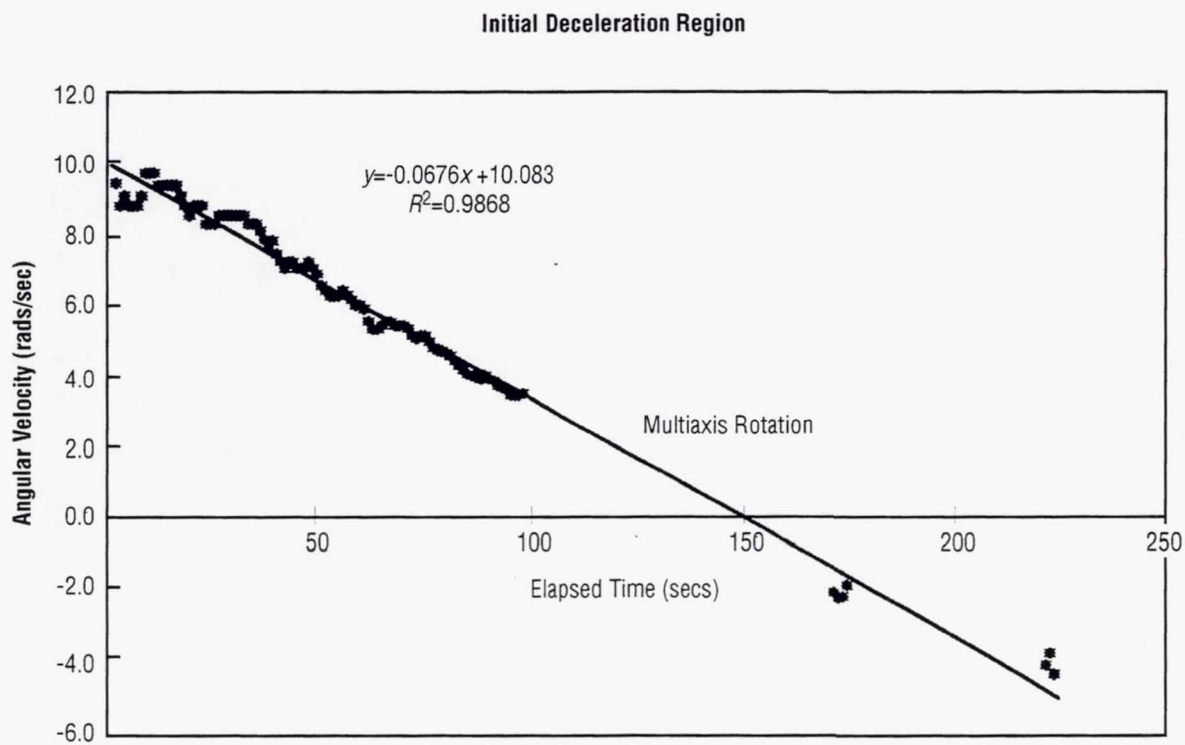


Figure 40. Angular velocity vs. time showing the specimen's history for the first 200 seconds.

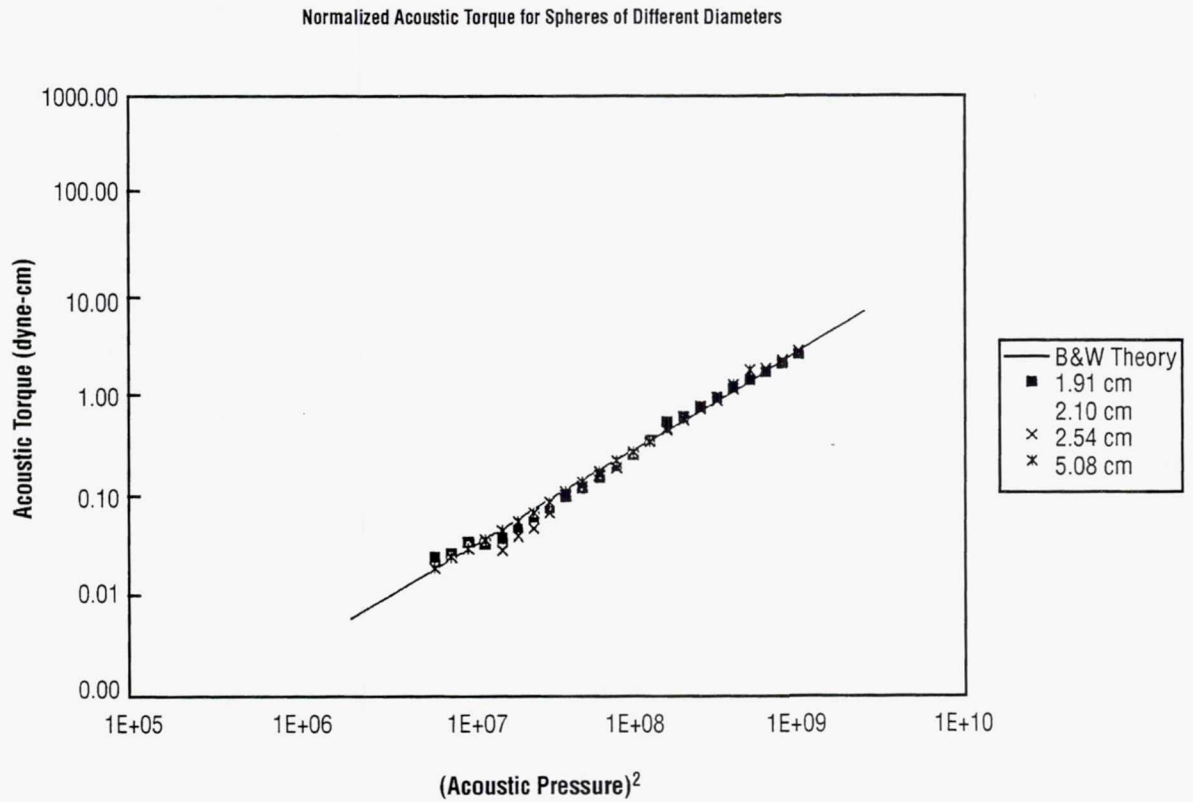


Figure 41. Acoustic torque measured for spheres of four different diameters as a function of the square of the acoustic pressure per axis.

Acoustic Torque as a Function of Phase Angle for Spheres of Different Diameters

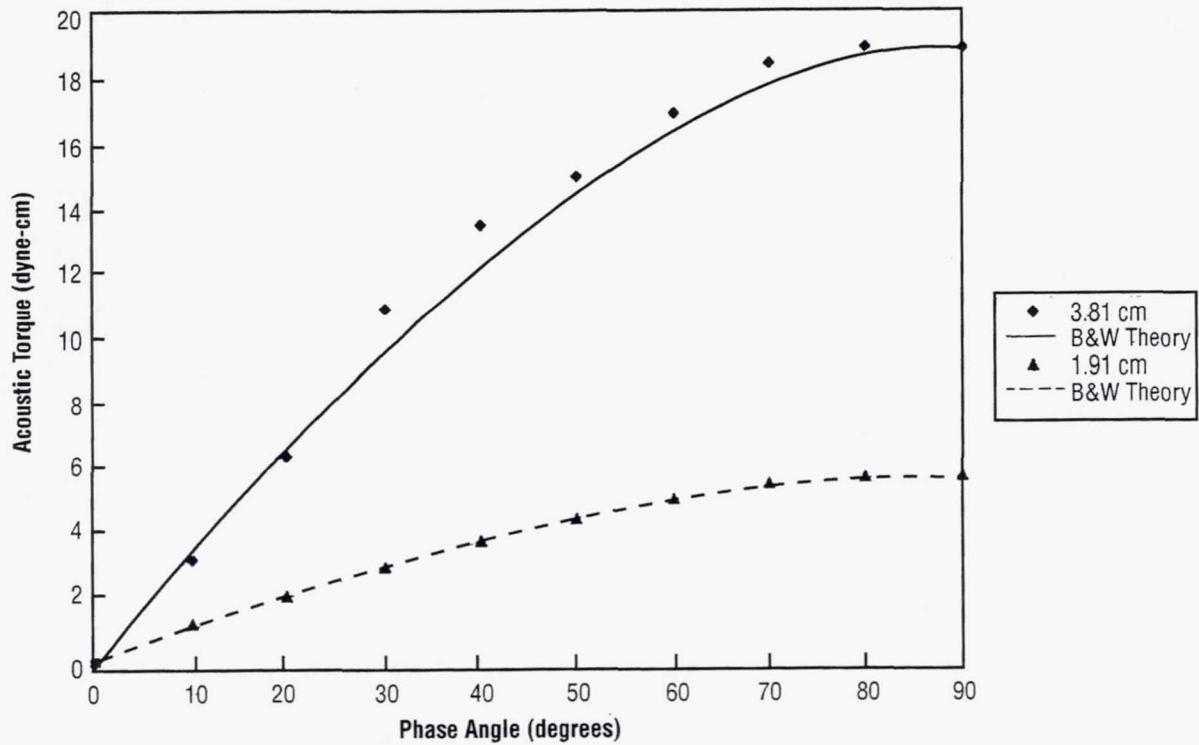


Figure 42. Relationship between acoustic torque applied to specimen and the phase lag between the x and y components of the acoustic field.

Variation of the Acoustic Torque
Along the $X, -X$ Direction

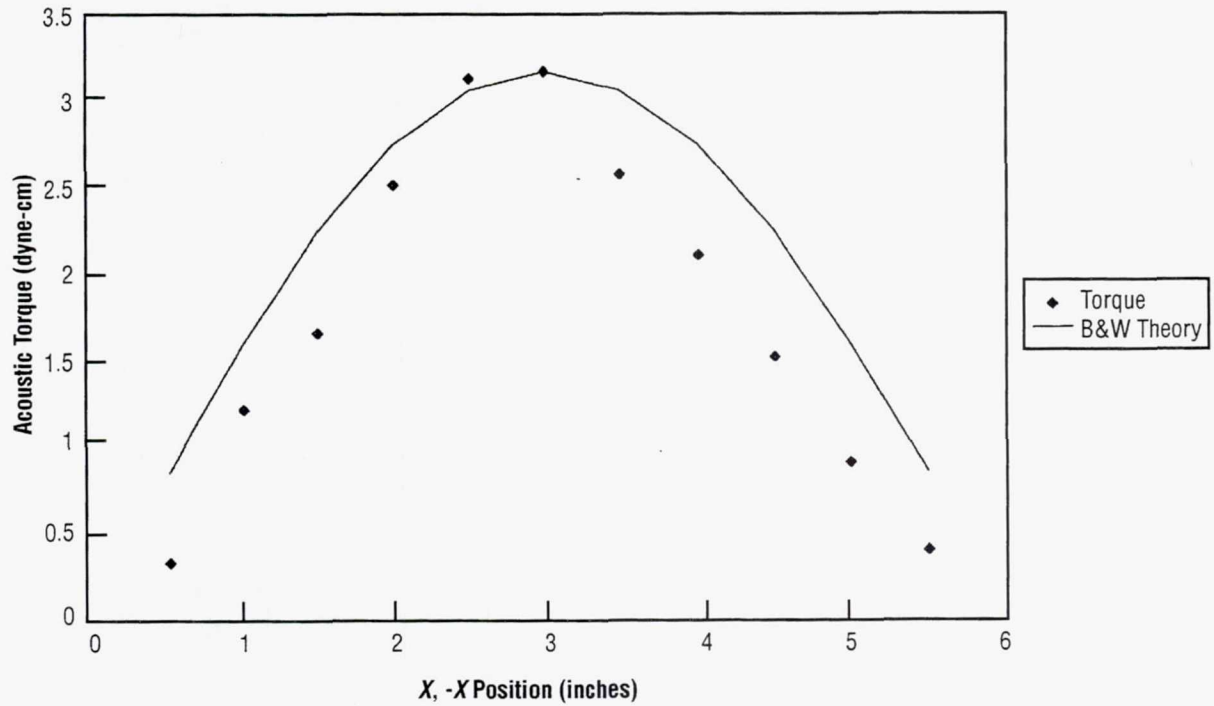


Figure 43. Magnitude of torque as a function of the position of specimen in the xy plane. Cross section of the 3-dimensional surface in the $x, -x$ direction.

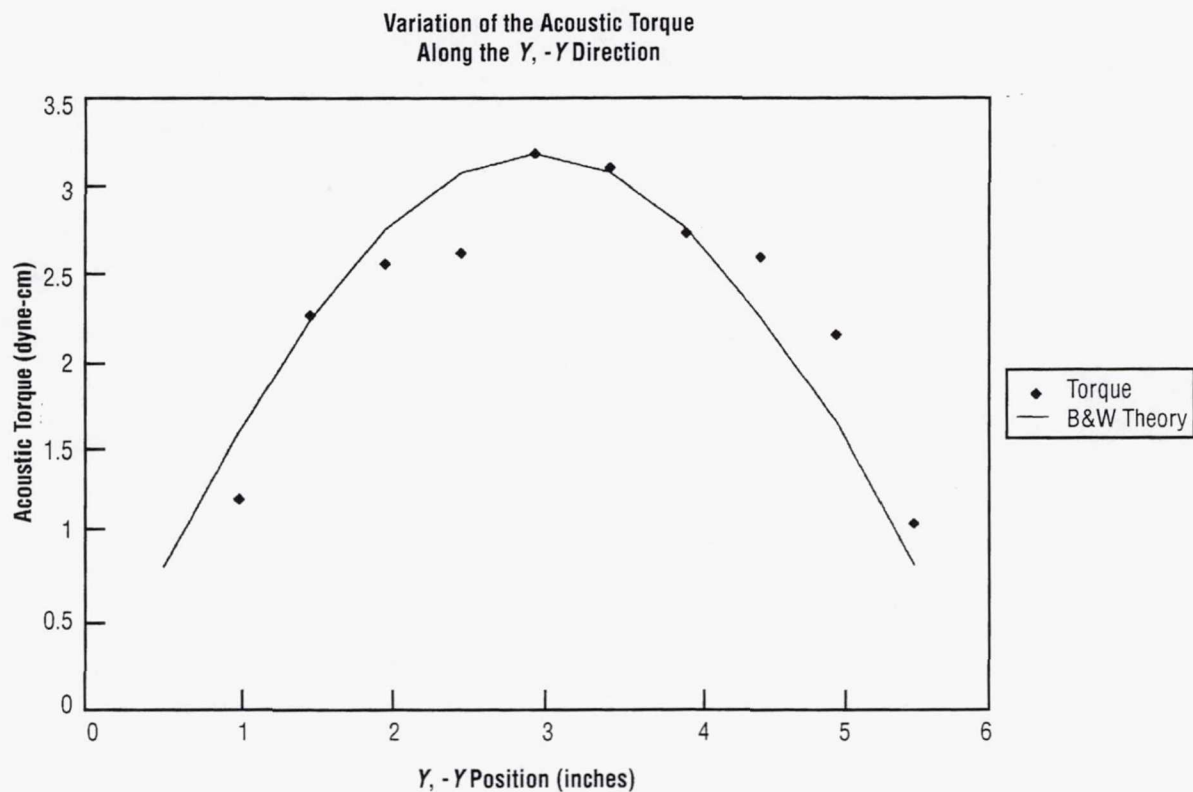


Figure 44. Relationship between acoustic torque applied to specimen and the position of drop in the xy plane. Cross section of the 3-dimensional surface in the $y, -y$ direction.

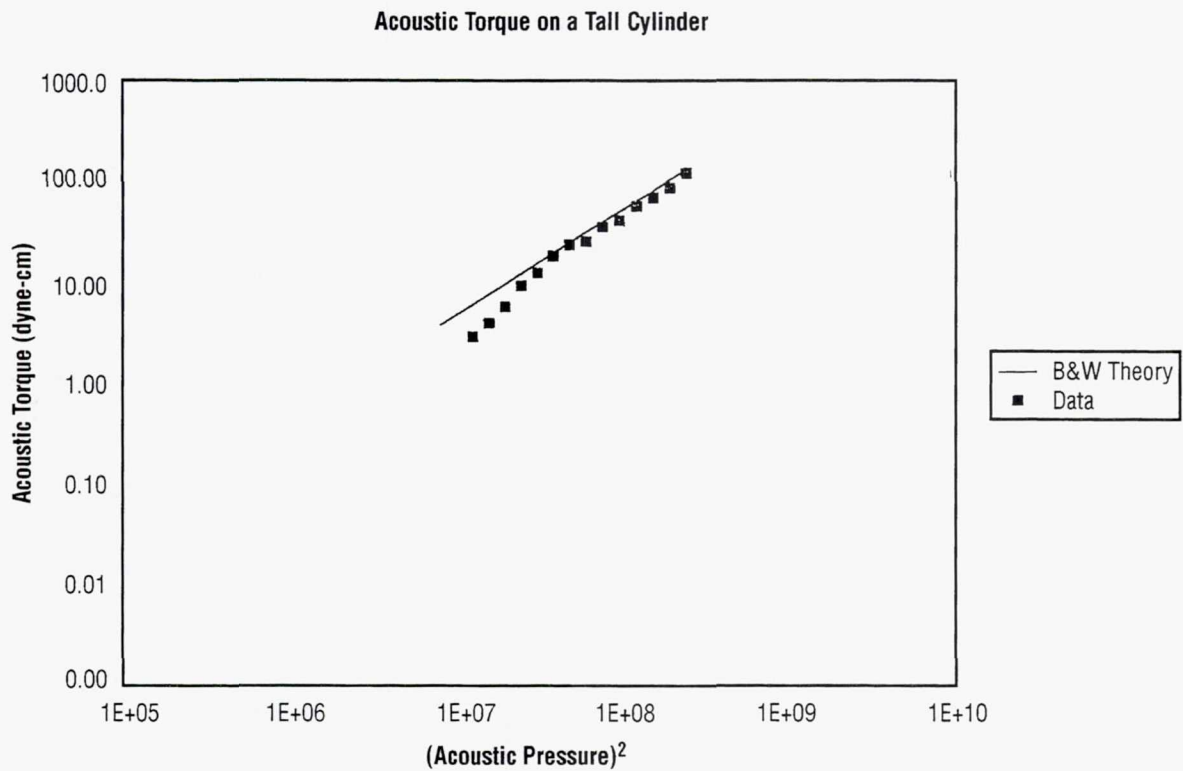


Figure 45. Acoustic torque as a function of acoustic pressure for a specimen in the shape of a tall cylinder.

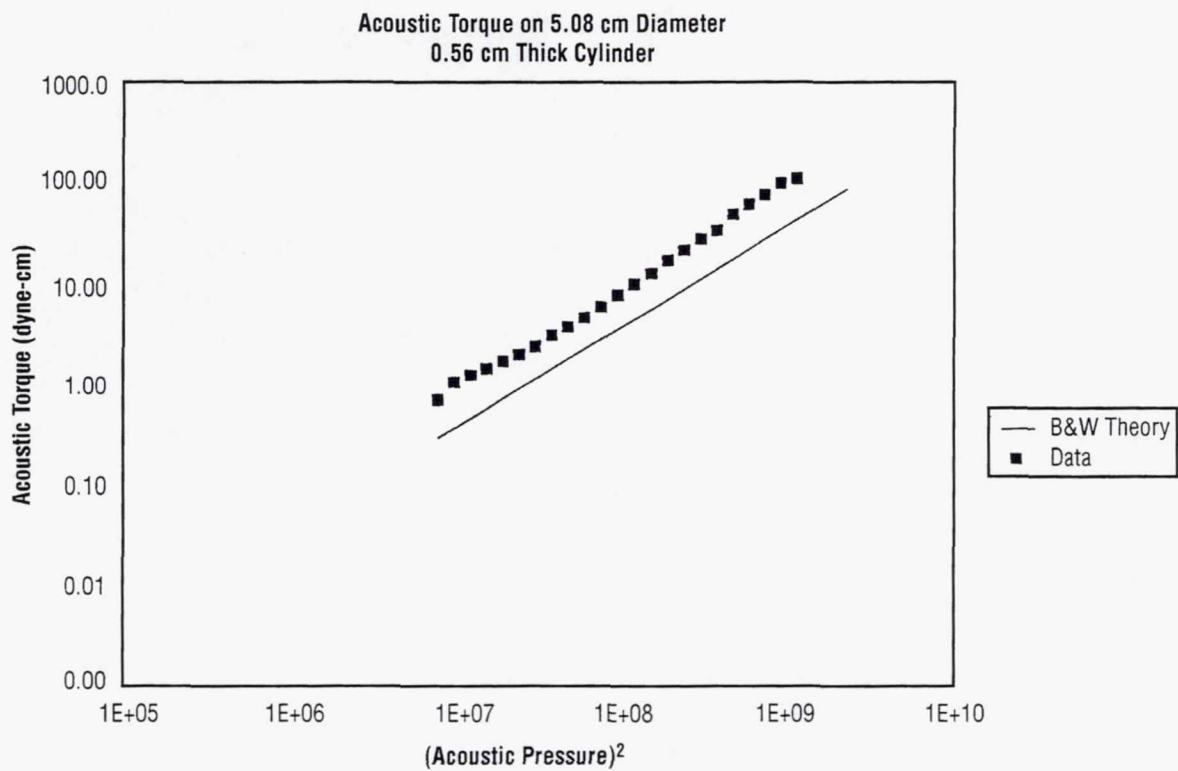


Figure 46. Acoustic torque as a function of acoustic pressure for a specimen in the form of a right cylinder ($h \approx r$).

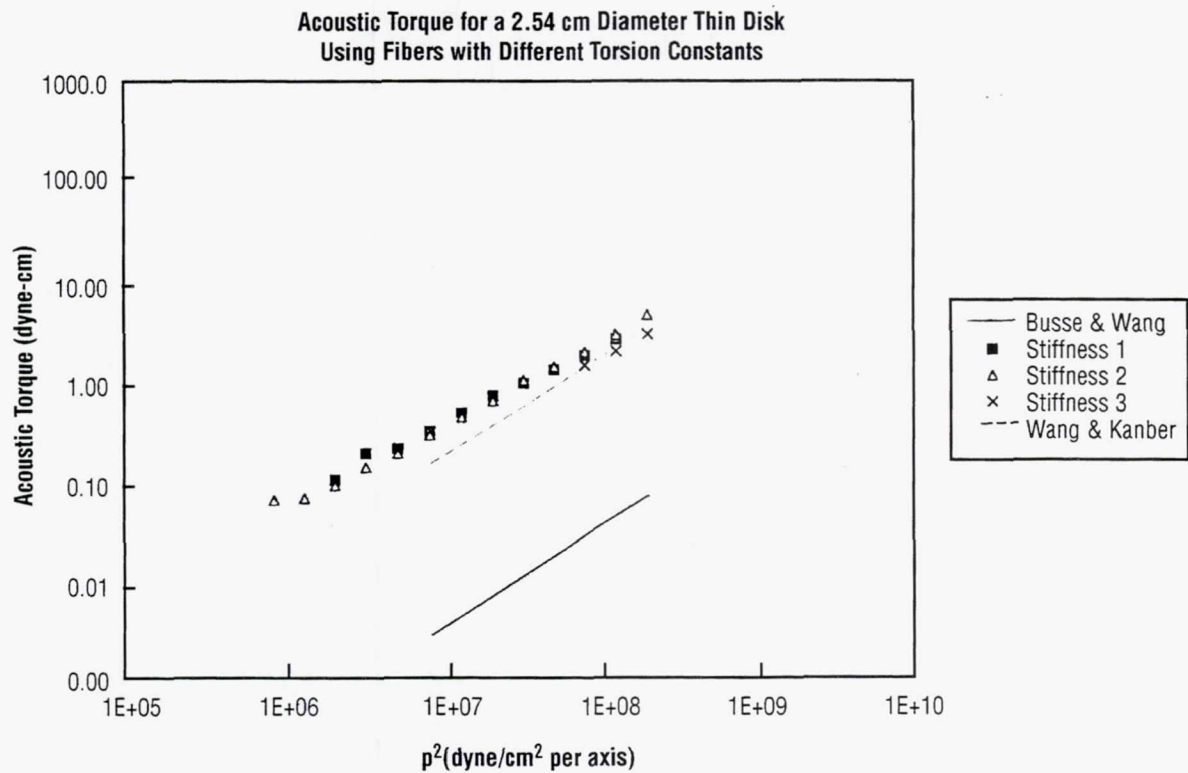


Figure 47. Predicted and measured acoustic torque as a function of acoustic pressure for a specimen in the shape of a thin disk supported by a fiber of varying stiffness.

EXPERIMENT V

SCIENCE AND TECHNOLOGY OF SURFACE CONTROLLED OSCILLATIONS: REPORT ON USML-2 RESULTS

Page intentionally left blank

EXPERIMENT V: SCIENCE AND TECHNOLOGY OF SURFACE CONTROLLED OSCILLATIONS: REPORT ON USML-2 RESULTS

**Robert E. Apfel (P.I.), Yuren Tian, Ph.D., Joseph Jankovsky, Xiaohui Chen
and Jeffrey Ketterling**

Yale University
P.O. Box 208286
New Haven, CT 06520
Phone: 203-432-4346
Fax: 203-432-7654
E-mail: robert.apfel@yale.edu

Arvid Croonquist and Eugene Trinh

Jet Propulsion Laboratory
4800 Oak Grove Drive
Pasadena, CA 91109
Phone: 818-354-7125
Fax: 818-393-5039
E-mail: etrinh@voyager.jpl.nasa.gov

R. Glynn Holt

Boston University
Dept. of Aerospace and Mechanical Engineering
110 Cummington Street
Boston, MA 02215
Phone: 617-353-9594
Fax: 617-353-5866
E-mail: rgholt@acs-mail.bu.edu

ABSTRACT/INTRODUCTION

Minuscule amounts (e.g., 1 part in 10,000) of a surface-active material in a liquid can drastically affect the surface behavior of the liquid, influencing how the material flows and mixes with other liquid and solid materials. In many respects, the science of surfactants has been empirical, with trial and error dominating over the ability to predict how surfactant type and concentration influence surface behavior. A program for the modeling of surfactant behavior has been established at Yale. This program combines experimental work performed both on the ground and in space, and theoretical and numerical modeling. By levitating a drop of liquid in air, away from solid container surfaces, and by manipulating the drop with acoustic radiation forces, we have been able to establish idealized conditions for surface behavior studies. The primary experiments involve the study of the free oscillations of initially deformed drops. In STS-73, the USML-2 mission of the Space Shuttle, we performed the following measurements: 1) the oscillation of

a spherical drop in its quadrupole mode, 2) the oscillation of a drop about a deformed (oblate) shape, 3) the slow static squeezing of the drop from spherical to nearly flat, and 4) the superoscillations of drops when the radiation forces maintaining the drop in a flattened state are suddenly reduced. Analytic and numerical studies have enabled us to understand the physics of these oscillations and to extract material properties such as the dynamic surface tension and the surface viscosities (shear and dilatational). The relation to ground-based studies is essential, because the knowledge and understanding gleaned from our space studies enable us to interpret ground-based data.

1. SPACE-BASED EXPERIMENTS

The Drop Physics Module (DPM-2) facility, which was used in USML-2 to perform our tests, was designed by the Jet Propulsion Laboratory, in conjunction with the science teams at Yale and Vanderbilt, and built by Loral Corporation's Electro-Optical Sensors Division. The test section of the DPM facility is an air-filled acoustic resonator at ambient (atmospheric) pressure with inner dimensions (x , y , and z) of 12.4 cm, 12.4 cm, and 15.2 cm, respectively. Four custom high-amplitude, titanium-dome acoustic loudspeakers are used to drive the (100) x mode, (010) y mode, (001) z mode, typically at 1350, 1350, and 1130 Hz, respectively. A pair of stepper-motor-controlled injectors are used to inject and retrieve drops, ranging from 1–14 cc in our experiments.

The payload crew scientists onboard *Columbia* operated the DPM via an interactive software interface, supported on the ground by the payload operations team of the Marshall Space Flight Center (Huntsville, AL) and the DPM science team. Almost continuous real-time communication between the Spacelab team and the ground team via voice, telemetry, and video enabled results to be immediately evaluated, allowing for parameter adjustments over the course of the experiments which could not be defined before the mission.

From that oscillation data both the time-dependent frequency of oscillation and decay constant can be retrieved. Special drop handling techniques, both planned and improvised, were an essential element in retrieving "good" data. The axisymmetric character, along with the idealized spherical shape made possible by microgravity, makes data analysis straightforward.

During the Yale experiments with the DPM, we observed 101 oscillation sequences of drops of pure water or solutions of either of two surfactant materials, as illustrated by the following table.

Table 1. Parameter ranges of experiments.

Surfactant Concentrations			Number of Oscillation Events		
Surfactant Material	Number of different concentrations	Concentrations	Liquid	Number of Drops	Number of Events
Triton X-100	7	0.02, 0.05, 0.1, 0.25 0.5, 1.0, 2.0 CMC	Water	5	12
			Triton X-100	12	42
BSA	4	0.1, 0.5, 1.0, 2.0 CMC	BSA	10	47
			TOTAL	27	101

2. OSCILLATIONS ABOUT A SPHERICAL SHAPE

A deployed drop is nearly spherical in shape. By increasing the amplitude of the z mode, we could squeeze the drop until its aspect ratio was about 1.3. Releasing the deforming force then resulted in the nearly quadrupole-shape oscillation. The decay of such an oscillation depends both on the shear viscosity of the bulk liquid and the surface viscosity (shear and dilatational) produced by the presence of surfactant. By fitting the decay, we can determine the frequency and decay constant, which are both approximately constant for relatively low-amplitude oscillations.

Two different surfactants produced qualitatively different results. For the Triton X-100, which possesses short diffusion/sorption times, the damping was relatively low (one about 1.7 that of pure water) owing to the fact that the dissolved surfactant rapidly moved between the bulk and surface, keeping the surface concentration constant (i.e., the Marangoni stresses were very small). By contrast, Bovine Serum Albumin (BSA) is a slow sorber, and therefore the Marangoni stresses are significant, leading to a damping constant nearly 15 times that of water. These differences are illustrated in Figure 1.¹

The data on frequency and damping constants can be used to extract surface properties using the formalism developed by Tian, et al.²

3. SUPEROSCILLATIONS OF DROPS

In the course of the USML-2 experiments, unprecedented maximal shape oscillations of large, surfactant-bearing water drops were observed. Reviewed below is a particular drop sequence for which we have performed extensive analysis.³

A 6.6 cm^3 drop (2.33 cm diameter) water drop contained the non-ionic surfactant Triton X-100, which is commonly used in detergents and mixing agents. The chemical formula is $\text{CH}_3\text{C}(\text{CH}_3)_2\text{CH}_2\text{C}(\text{CH}_3)_2\text{C}_6\text{H}_4\text{E}_{(n)}\text{OH}$, where $\text{E}=\text{OCH}_2\text{CH}_2$, and ranges from 9 to 10. It was saturated in the water at the critical micelle concentration (CMC)—that is, the concentration beyond which small aggregates of the material will form in the bulk of the liquid and negligible lowering of the surface tension will occur. The CMC for Triton is a minuscule $1.4 \times 10^{-4} \text{ g/ml}$, at which the approximate static surface tension of this aqueous solution is 0.03 Newtons/m (less than half that of pure water). It is thus readily apparent why these types of materials are of interest to scientists and engineers—tiny concentrations leave bulk properties unchanged but result in marked surface viscoelastic properties, and thus alter the surface and bulk motion dramatically. The development of rational models of the behavior of surfactants is the ultimate goal of this research.³

Figure 2 shows a drop that was slowly squeezed so that in the z -view the circular outline grew and the x -view appeared initially as a narrow ellipse of aspect ratio of 4.5. Two complete cycles are shown here, both in x and z views, although the complete video shows about 20 cycles (in about 17 seconds) before the oscillation reverts to the lowest energy quadrupole mode. A World Wide Web animated video sequence can

be found at <<http://www.yale.edu/engineering/faculty/vitae/apfel-data/drop.mpg>>. The cigar-shaped image of the eighth frame has an aspect ratio approaching 3, which, in the parlance of nuclear modeling is called "hyperdeformed,"⁴ and is just short of the condition for drop fission.

The oscillation in figure 2 is beyond the reach of analysis via methods based on small-amplitude motion, found in references 1 and 2. In an initial attempt to determine how closely the dynamics adhered to pure fluid motion, we have performed numerical computations of the evolution of the shape of greatly deformed drops using the boundary integral method. With the simulated data, we can get the damping constants, frequencies, decomposed oscillation modes, and surfactant distribution at the drop surface.

Because the surfactants influence the drop oscillation significantly, without altering the shear viscosity of the bulk phase, we need to consider the "Marangoni effect"—due to surface tension gradients—as well as the surface elasticity, surface dilatational viscosity and surface shear viscosity.^{5 6 7 8 9} Lamb¹⁰ has shown that viscosity produces a thin weak vortical layer at the free surface resulting in viscous damping of deep water waves. Lamb¹⁰ and Batchelor¹¹ have illustrated that dissipation is mainly in the irrotational part of the flow, not in the vortical layer. With the assumptions of a very thin vortical layer and the weak shear viscosity of the bulk phase, Lundgren¹² and Shi^{13 14} have employed the boundary-integral method to study the nonlinear oscillations of large, axially symmetric liquid drops. With the same theoretical analysis, but now including surfactants, we also get the result that the dissipation is mainly in the irrotational part of the flow. Therefore, we can continue to take advantage of the boundary integral method.

From an analysis of the data in figure 2, comparing theory and experiment frame by frame, we were able to deduce a surface tension of 33 dynes/cm (slightly higher than the static value) and surface dilatational viscosity and shear viscosity of 0.20 sp and 0.10 sp, respectively. In the near future, we shall also provide numerical results for BSA-laden drops, but in this case the concentration of surfactant along the surface will not be assumed to be constant.

4. CONCLUDING REMARKS

We can thus see that such an extremely nonlinear motion as that recorded in figure 2 is a wellspring of new information. Only with a proper model of surfactant behavior will a one-to-one correspondence between observation and prediction be possible, if at all. The maximal oscillation data set therefore becomes a standard of comparison for surfactant models. It can also be related to work with much smaller drops (and higher oscillation frequencies) performed at 1 g, so that the models can be tested over at least two orders of magnitude in the relevant time constants of the process.¹⁵

Finally, it should be noted that the observed maximal oscillations may provide insights into similar processes occurring in other sciences and at vastly different scales, such as the behavior of hyperdeformed atomic nuclei or the explosion of stars. Moreover, the images of these oscillations may be viewed by some as aesthetically pleasing, reinforcing connections between motivations underlying those who contribute in science and in art.

REFERENCES

1. Holt, R.G.; Tian, Y.; Jankovsky, J.; and Apfel, R.E.: "Surface-Controlled Drop Oscillations in Space," *J. Acoust. Soc. Am.*, in press.
2. Tian, Y.; Holt, R.G.; and Apfel, R.E.: "Investigations of Liquid Surface Rheology of Surfactant Solutions by Droplet Shape Oscillations: Theory," *Phys. Fluids* 7, 2938–2949, 1995.
3. Apfel, R.E., et al.: "Free Oscillations and Surfactant Studies of Superdeformed Drops in Microgravity," *Phys. Rev. Lett.*, in press.
4. Schwarzschild, B.: in "Search and Discovery" section of *Physics Today*, 48, 17–19, 1995.
5. Marangoni, C.G.M.: "Über die Ausbreitung der Tropfen einer Flüssigkeit auf der Oberfluche einer Anderen," *Ann. Physik. (Poggendorff)*, 3, 337–354, 1872.
6. Sternling, C.G.; and Scriven, L.E.: "Interfacial Turbulence: Hydrodynamic Instability and the Marangoni Effect," *AIChE*, 5, 514–523, 1959.
7. Scriven, L.E.: "Dynamics of a Fluid Interface," *Chem. Eng. Sci.*, 12, 98–108, 1960.
8. Scriven, L.E.; and Sterling, C.V.: "On Cellular Convection Driven by Surface-Tension Gradients: Effect of Mean Surface Tension and Surface Viscosity," *J. Fluid Mech.*, 19, 321–340, 1964.
9. Boussinesq, M.J.: "The Application of the Formula for Surface Viscosity to the Surface of a Slowly Falling Droplet in the Midst of a Large Unlimited Amount of Fluid Which Is at Rest and Possesses a Smaller Specific Gravity," *Ann. Chim. Phys.*, 29, 357, 1913b.
10. Lamb, H.: *Hydrodynamics*, 6th edn. Cambridge University Press, 1932.
11. Batchelor, G.K.: *An Introduction to Fluid Dynamics*, Cambridge University Press, 1967.
12. Lundgren, T.S.; and Mansour, N.N.: "Oscillation of Drops in Zero Gravity With Weak Viscous Effects," *J. Fluid Mech.*, 194, 479–510, 1988.
13. Shi, W.T.; and Apfel, R.E.: "Oscillation of a Deformed Liquid in an Acoustic Field," *Phys. Fluids*, 7, 1545–1551, 1995.
14. Shi, W.T.; and Apfel, R.E.: "Instability of a Deformed Liquid Drop in an Acoustic Field," *Phys. Fluids*, 7, 2601–2607, 1995.
15. Tian, Y.; Holt, R.G.; and Apfel, R.E.: "Investigations of Liquid Surface Rheology of Surfactant Solutions by Droplet Shape Oscillations: Experiments," in press.

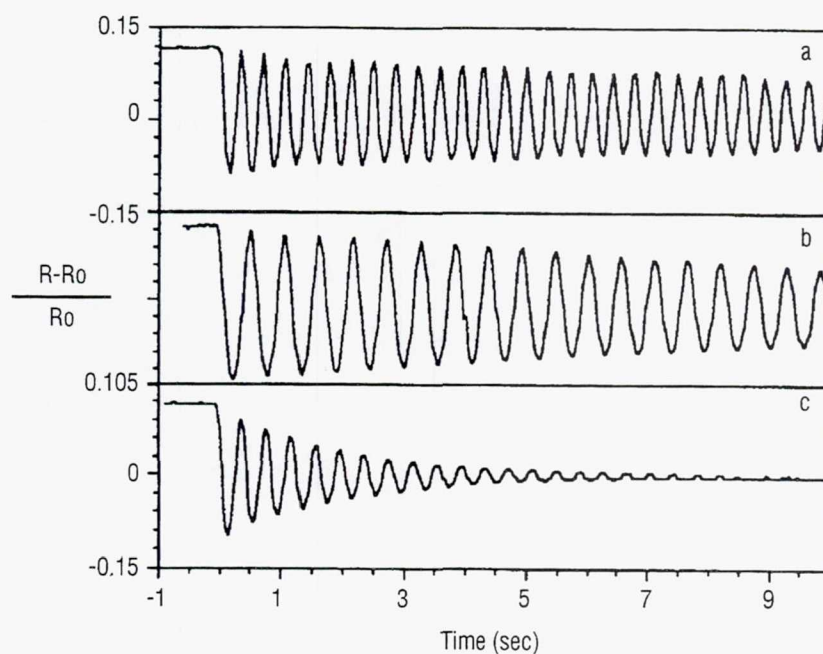


Figure 1. Decay of the azimuthal radius for 2.5 cm diameter aqueous drops with an initial deformation of approximately 20 percent: a) pure water; b) water with 1.4×10^{-4} g/ml Triton X-100 dissolved in the bulk; c) water with 1.0×10^{-5} g/ml Bovine Serum Albumin (BSA) dissolved in the bulk.

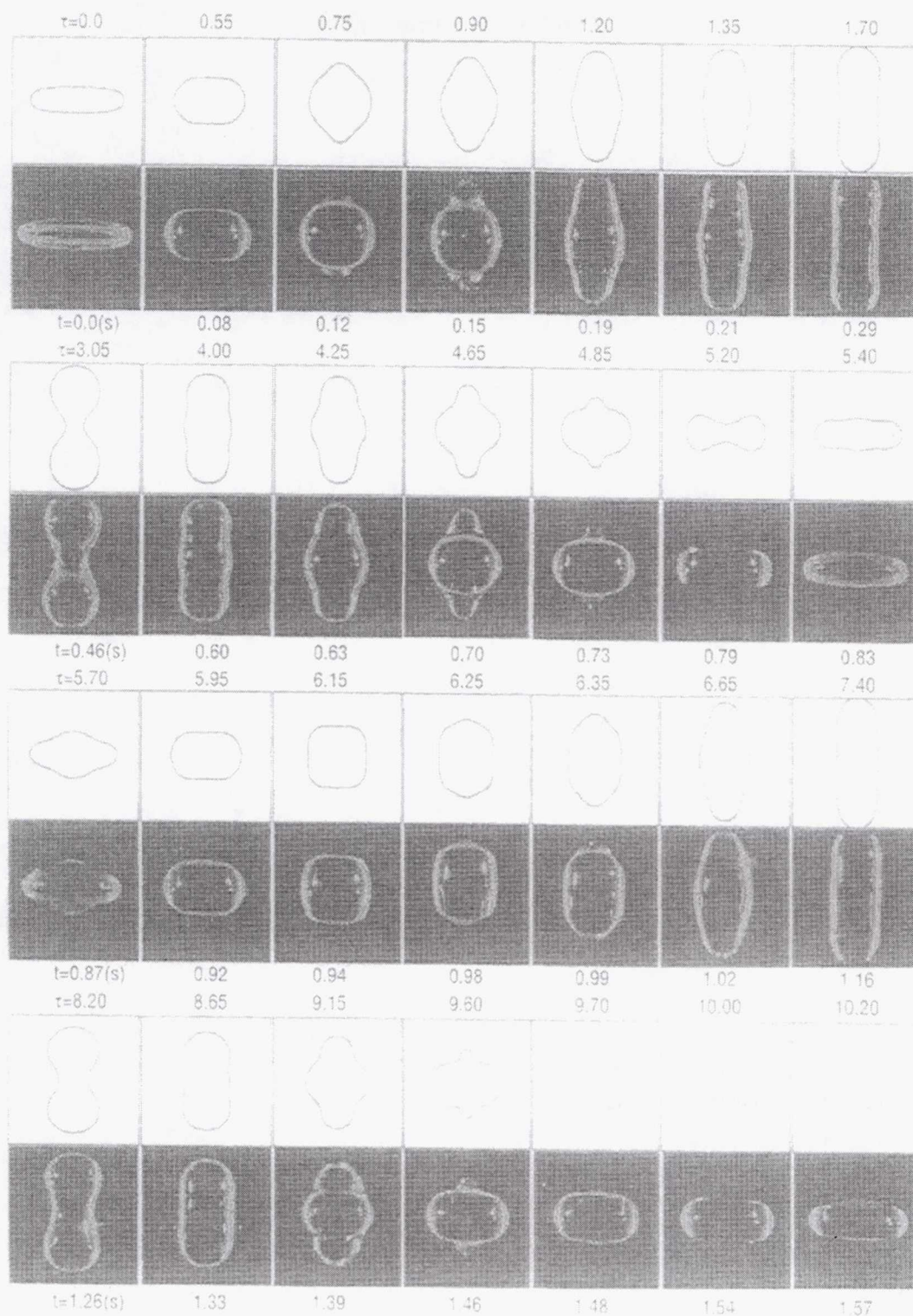


Figure 2. Two complete cycles of superoscillation of a water drop (6 cm^3) with the surfactant Triton X-100 at the critical micelle concentration. The time in seconds is shown. Also shown is the numerical simulation using the boundary integral method. The time shown with the simulation is non-dimensional. From this data the dynamic surface tension and surface viscosities (shear and dilatational) can be determined. (Apfel group, Yale University.)

Page intentionally left blank

EXPERIMENT VI.

SURFACE TENSION DRIVEN CONVECTION EXPERIMENT-2 (STDCE-2)

ACKNOWLEDGMENTS

The authors would like to thank many people, especially the NASA Lewis Research Center engineering and operations teams, who worked hard to make the STDCE-2 a successful experiment. Special thanks to the payload crew of the USML-2, Drs. Fred Leslie, Kathy Thornton, Cady Coleman, and Al Sacco, who conducted the tests expertly to obtain excellent data. The authors also wish to thank Dr. J. Masud for his help in the data analysis and in the preparation of this report. The work done at Case Western Reserve University is supported by NASA under grant NAG3-1568.

EXPERIMENT V1. SURFACE TENSION DRIVEN CONVECTION EXPERIMENT-2 (STDCE-2)

Simon Ostrach

Department of Mechanical and Aerospace Engineering
Case Western Reserve University
Cleveland, OH 44106
Phone: 216-368-2942
Fax: 216-368-6445
E-mail: sxo3@po.cwru.edu

Yasuhiro Kamotani

Department of Mechanical and Aerospace Engineering
Case Western Reserve University
Cleveland, OH 44106

Alexander D. Pline

Code UG
NASA Headquarters
Washington, DC 20546

ABSTRACT

Results are reported from the Second Surface Tension Driven Convection Experiment (STDCE-2) performed aboard the Second United States Microgravity Laboratory (USML-2), which flew as Space Shuttle mission STS-73 and launched on October 20, 1995. Oscillatory thermocapillary flows were investigated in open cylindrical containers filled with 2 centistokes kinematic viscosity ($Pr = 27$ at 25°C) silicone oil. Two different heating modes were investigated in detail. The main objectives of the experiments were to determine the onset of oscillatory thermocapillary flow under highly reduced buoyancy and gravity conditions and to study the important features of the oscillatory flow. The onset conditions were determined in three different size containers (1.2-, 2-, and 3-cm diameter) and for various free surface shapes (flat and curved). Numerical and scaling analyses were also performed to understand the basic steady flows. The analysis shows that the main flow is viscous-dominated near the onset of oscillations. The onset conditions determined in the present experiments together with our earlier ground-based data show that one could not describe the oscillation phenomenon if the fluid free surface is assumed to be rigid. Therefore, a parameter representing free surface deformation was derived, and the data are shown to be correlated well by that parameter. The oscillation patterns and frequencies are also presented.

NOMENCLATURE

Ar	= container aspect ratio, H/R
a	= absorption length of CO_2 laser by test fluid
C_p	= specific heat at constant pressure
D	= test container inner diameter
f	= oscillation frequency
f^*	= dimensionless oscillation frequency defined by Eq. (13)
H	= container depth
H_r	= relative heating zone size, R_h/R
k	= thermal conductivity
Ma	= Marangoni number, $\sigma_T \Delta T R / \mu \alpha$
Ma_{cr}	= critical Marangoni number
Ma_Q	= Marangoni number based on Q , $(\sigma_T Q / k \mu \alpha)^{2/3}$
$(Ma_Q)_{cr}$	= critical Ma_Q for onset of oscillations
Pr	= Prandtl number evaluated at temperature $(T_H + T_C)/2$, ν/α
Pr_C	= Prandtl number evaluated at temperature T_C
Q	= total heat input
Q_{cr}	= critical heat flux for onset of oscillations
r	= radial coordinate
R	= container radius
R_h	= heating zone radius (CF tests) or heater radius (CT tests)
$R\sigma$	= surface tension Reynolds number, Ma/Pr
$R\sigma^*$	= surface tension Reynolds number based on R_h , $\sigma_T \Delta T R_h / \mu \nu$
S	= S-parameter, δ_s / δ_{TS}
T	= temperature
T_C	= side (cold) wall temperature
T_H	= free surface temperature at center (CF tests) or the heater temperature (CT tests)
U_b	= velocity of bulk flow
U_o	= maximum velocity in heated region
U_o^*	= dimensionless U_o , $\mu U_o / \sigma_T \Delta T$
Vr	= ratio of total fluid volume to that for flat surface
z	= axial coordinate
α	= thermal diffusivity
ΔT	= overall temperature difference, $T_H - T_C$
ΔT_b	= temperature difference for bulk flow
ΔT_{cr}	= critical temperature difference
δ_s	= free surface deformation at onset of oscillations
δ_{TS}	= thermal boundary layer thickness
δ_v	= velocity boundary layer thickness
μ	= fluid dynamic viscosity
ν	= fluid kinematic viscosity
ρ	= fluid density
σ	= surface tension
σ_T	= temperature coefficient of surface tension
Ψ_{max}	= maximum stream function

1. INTRODUCTION

Thermocapillary flows are known to become oscillatory (time-periodic), but how and when they become oscillatory in containers of unit-order aspect ratio are not yet fully understood. The present work is a part of our continuous effort to obtain a better understanding of the phenomenon. Our past work on the subject, as well as related studies by other investigators, have been reviewed.^{1, 2} Thermocapillary flow experiments in normal gravity are limited to a narrow parametric range in order to minimize gravity and buoyancy effects, which is an important reason for our lack of full understanding of the oscillation phenomenon. One important unanswered question is what role, if any, free surface deformation plays in the oscillation mechanism. For that reason we performed thermocapillary flow experiments, called the Surface Tension Driven Convection Experiment-2 (STDCE-2), aboard the USML-2 Spacelab in 1995. The main objectives of the experiments were to investigate oscillatory thermocapillary flows in microgravity and to clarify the importance of free surface deformation in such flows.

In the STDCE-2, steady and oscillatory thermocapillary flows were generated in cylindrical containers by employing two heating modes. A CO₂ laser with adjustable power and beam diameter was used in the constant flux (CF) configuration to heat the free surface. The other configuration investigated in the STDCE-2 was the constant temperature (CT) configuration in which a submerged cylindrical cartridge heater placed at the symmetry (axial) axis of the test container heated the fluid. Both heating modes cause nonuniform temperature distributions on the free surface which generates thermocapillary flow. The experiments were conducted over a wide range of conditions, and a large amount of data was acquired in the STDCE-2. The data are still being analyzed. The data analyzed so far are presented and discussed herein.

2. DESCRIPTION OF EXPERIMENTS

2.1 Hardware Design Parameters

The science objectives for the STDCE-2 called for an investigation of the onset conditions and nature of oscillatory flows under a variety of test conditions and configurations, including a study of the effect of heating mode, heating rate, surface heat flux distribution, container size and static free surface shape on the oscillations. Analysis of the 38 tests conducted during the STDCE-1 agreed well with numerical models developed to predict the fluid dynamics of steady thermocapillary flows.^{1, 2} In order to study the oscillation phenomenon in thermocapillary flows and to test our model of the oscillation mechanism in the STDCE-2, cylindrical test cells of various sizes (1.2, 2.0 and 3.0 cm diameter test cells), each with a nominal aspect ratio of one (radius=depth), were chosen. Silicone oil with kinematic viscosity of 2 centistokes was selected for use in the STDCE-2. Due to its very low surface energy, this fluid also resisted surface contamination, an important factor in surface tension experiments. Tracer particles were mixed into the fluid to enable visualization of the velocity field during testing.

To study the effects of heating mode, heating rate, and surface heat flux distribution on the fluid motion, two heating systems were used during experimentation. In the CF heating mode the laser power level and laser spot size could be varied to study the effects of heat input and surface heat flux distribution on the flow field. In the CT mode the cartridge heater power could be varied to study the effect of internal

heat input and heater-to-external wall temperature gradients on the flow field. For each heating mode (CT or CF) and each test cell size (1.2, 2.0 or 3.0 cm diameter), a matrix of tests were performed which are discussed later. Therefore, a total of six interchangeable test chamber modules (three CT and three CF test cells) were required to conduct the full range of tests for the STDCE-2.

The static free surface shape of the test fluid was a variable in the STDCE-2 test matrix. Each test module contained an oil delivery system which allowed the oil in the module's test cell to be filled to various levels. The rim of the test cell had a sharp "pinning" edge coated with a barrier coating (3M FC-723) which prevented the oil from flowing out of the cell in microgravity. A specific free surface shape could thereby be established for a test by adjusting the level of oil in the test cell. Flat free surfaces were set by filling the oil to the pinning edge of the test cell. Concave free surfaces were set by underfilling the test cell and, conversely, convex free surfaces were set by overfilling. The free surface shapes in the STDCE-2 are shown in figure 1.

The primary objectives of the STDCE-2 were to investigate the conditions for the onset of oscillations under various test conditions and to validate our physical model which suggests that the oscillation phenomenon is a result of the three-way coupling among the velocity field, the temperature field and the deformation of the fluid free surface. In order to accomplish this, several quantities needed to be measured, including: 1) the temperature distribution along the free surface of the fluid, 2) the temperature at several points within the bulk fluid and along the walls, 3) the velocity field in the bulk fluid, 4) the shape and motion of the free fluid surface and 5) g-jitter and the acceleration field at the experiment site. Precision diagnostic instruments, including an infrared (IR) imager with a three-position zoom telescope and a Ronchi interferometer, were used for quantitative measurements of the temperature and deformation of the free surface. Visualization of the flow field in each test cell also provided a qualitative picture of the flow field during experimentation and enabled the behavior of the fluid to be monitored when filling the test cell.

2.2 Module Configuration

Each test chamber module consisted of an upper housing, a test section, a lower housing and an oil reservoir, as shown in figure 2. The test chamber modules were stowed during launch and installed on orbit by a crew member. Precision alignment of the module at a fixed location on an optics bench (also called the "chamber bracket") in the experiment package was achieved upon module installation. After module installation, electrical and water connections were made and a thermistor positioning shaft was installed, enabling the position of a movable thermistor to be set by the crew from the front panel.

The upper housing contained three windows for optical access (i.e., for flow visualization, free surface deformation measurement and infrared imaging). A tombstone-shaped zinc selenide (ZnSe) window (also called the "beam combiner" window) sealed the top of the test chamber module and enabled surface heating with a CO₂ laser, infrared temperature measurement, and free surface deformation measurements to be performed. Optical coatings were optimized to provide maximum transmission on all optical surfaces. An inner, reflective surface on the beam combiner window also enabled illumination of the test cell with collimated light for measurement of the free fluid surface deformations and camera viewing for visualization of the flow field. A small side window in the module upper housing enabled camera viewing for flow visualization of the test fluid in the test cell. The upper housing of the test chamber module could be removed by a crew member to clean up oil spills and/or insert disks to change the aspect ratio of the test cell. The general layout of the STDCE-2 is shown in figure 3.

2.3 Test Section

The test section of each module consisted of a high thermal conductivity, cylindrical, water-cooled copper test chamber wall with water cooled channels, a Teflon™ bottom, a movable thermistor, a central cartridge heater (for CT modules), an oil fill port, and a floor thermistor all held in place by an aluminum backing plate and bolts and sealed with an O-ring. Teflon™ was selected as a material for the bottom of the test cell because it was thermally insulating. A thin, ceramic (Macor™) insert was epoxied into the Teflon™ bottom and painted black to minimize stray, reflected light for flow visualization.

2.4 Water Cooling

The test sections were designed so that the side walls could be maintained at a nearly uniform temperature. A water pump driven by a 24-VDC motor circulated water in a closed loop from a 1-gallon reservoir through the coolant circuit to control the wall temperature of the test section. A counterflow, shell and tube heat exchanger in this reservoir used Spacelab water to regulate the STDCE-2 water temperature. Dripless quick disconnect couplings connected the test chamber modules to the water cooling system.

2.5 Oil Delivery

Each test chamber module included a reservoir (43-ml capacity) containing a mixture of oil and 70-micron Pliolite tracer particles. The reservoir was designed in a closed loop with the test section to deliver oil to the test cell. The crew used a handwheel to translate a piston in the reservoir to manually fill and withdraw oil from the test cell. A diaphragm installed on the face of each piston absorbed volumetric changes in the oil (due to temperature variations experienced prior to use) to prevent leakage of the oil from the system. Flow visualization during testing required a uniform dispersion of tracer particles in the oil. Because of pre-mission settling of the tracer particles, a small ball bearing was placed in the reservoir to provide manual mixing via gentle shaking of the module assembly.

2.6 Thermistors

Temperatures were measured using thermistors positioned at various locations within and at the boundaries of the test cell. Side wall temperature was monitored at three locations, as shown in figure 3. The temperature at the bottom of the test cell was monitored by the floor thermistor (mounted flush with the Teflon™ bottom). In addition, the ambient air temperature was measured above the test cell. Bulk fluid temperature was measured using a movable thermistor which perforated the Teflon™ chamber bottom at the mid radial location ($r/R = 0.5$) and was translated by a thermistor crank external to the module. The movable thermistor could be precisely positioned parallel (± 0.1 mm) to the axis of the test cell. A fiber optic borescope in the experiment package enabled the crew to view a mechanical gauge on the module to position the thermistor. All temperature measurements for the STDCE-2 were accurate within ± 0.1 °C with a response time of 0.1 seconds.

2.7 Cartridge Heaters

For the CT modules, a submerged, cylindrical electrical resistance heater (centered in the test cell) was used to heat the oil. These cartridge heaters were one-tenth the diameter (1.2, 2.0 and 3.0 mm) of the test chamber and extended the depth of the test cell from the pinning edge plane. The top edge of the heater was designed so that a well-defined, circular contact line with the test fluid could be obtained. Three thermistors were embedded in the heater's shell, at the locations shown in figure 3. Temperature uniformity along the heater shell was ± 3 percent of the temperature difference between the heater shell and the chamber wall. A control system for the cartridge heater was used to adjust heater output (from 0 to 3.5 W for the 1.2 CT chamber, 0 to 6 W for the 2-cm CT chamber and 0 to 10 W for the 3.0-cm CT chamber) in 0.01-W increments. Since the thermistors imbedded inside the heater were some distance away from the liquid free surface (pinning edge at the top of the heater), the heater temperature based on this measurement tended to be higher than the heater outside surface temperature at the top edge. In order to compensate for this, a ground-based calibration was done for all the test containers to relate the heater thermistor output to the actual temperature at the heater top edge.

2.8 Disk Inserts

Cylindrical TeflonTM inserts, which were designed to be installed on orbit into the test cell of each module to reduce its aspect ratio to 0.5 (height=half of the radius), were also utilized for some STDCE-2 CF tests. Removal of the module upper housing on orbit was required by the crew to install the disks.

2.9 Flow Visualization

A flow visualization system illuminated suspended 70-micrometer tracer particles (Pliolite) in the test fluid to provide a qualitative record of the bulk flow. In addition, this system was used extensively to monitor the flow for the onset of oscillations and the fluid behavior while filling the test cell. The system consisted of a CCD camera, two turning mirrors, pre-adjusted to accommodate the required viewing angle, and a laser diode light source (30-mW rated output, 690 nm). Three CCD cameras were used, each with a lens preset to focus on a given test cell size. The camera/lens assemblies were changed prior to installing different test modules. The laser diode output was collimated and used for illumination for both flow visualization and free surface deformation measurement.

2.10 Surface Temperature Measurement

A scanning IR imaging system operating in the 8–14 micrometer wavelength range was used to detect radiated emissions to determine the thermal signature along the fluid free surface. The imager was identical to that used in the STDCE-1, and thus a detailed description can be found in the literature.^{3,4} A zoom telescope was fitted externally to the imager to properly focus to the three test cell sizes.

2.11 Free Surface Deformation Measurement

New to the STDCE-2 was a Ronchi interferometer, designed to measure the dynamic surface deformation during the experiment. In this novel implementation of the Ronchi test, a collimated beam, reflected off the sample surface—in this case a dynamically deforming fluid surface—was focused through a grating en route to the detector. Distortions in the reflected wavefront caused by surface deformations resulted in variations in the shadow patterns produced as the waveform passed through a grating. The detector recorded a Ronchigram in which the shadow pattern was superimposed on the image of the fluid surface. Pattern variations and surface slope information were related to the surface deformation. Further details regarding this system can be found in the paper by Stahl and Stultz.⁵ Since the Ronchi data are still being analyzed, they are not included in this report.

2.12 Surface Heating

The RF-excited CO₂ laser was reflown on the STDCE-2 to heat the fluid surface during the CF tests at powers from 0.2 to 5.0 W, in 0.01-W increments, with all the energy absorbed within 0.2 mm of the surface. The optics were modified to produce heating zone sizes between 0.6–6 mm at the free surface for both curved and flat surface shapes. In addition, an optical isolator was included in the system to prevent back reflections into the CO₂ laser which could have caused instability of the laser output.

3. EXPERIMENTAL TECHNIQUE

The hardware configuration process, prior to starting a set of tests, began by installing the appropriate optics for the upcoming tests (flow visualization camera/optics and Ronchi magnification optics). The desired test module was installed after gentle shaking to mix the flow visualization particles in the fluid reservoir. Following a power-up sequence, the experiment parameters were set either by the crew or via ground commanding. These included filling the chamber to a specified level, initial heater setpoint, CO₂ laser beam diameter (CF tests), initial internal thermistor location and initial Ronchi interferometer grating style/location. During this time experiment status and temperature data were being displayed on the ground.

At this point there was a pause in the operations to allow the hardware and test chamber/fluid to reach thermal equilibrium. Often, this pause was used as a buffer to align the experiment start with the most complete communications coverage. A test commenced by energizing the heater at the initial setpoint. The onboard video cassette recorders were started just prior to this step. These conditions were held until the experiment again reached equilibrium, with a steady, two-dimensional flow established. During this steady-state period, the Ronchi interferometer and IR imager were optimized to gather data on the steady-state surface deformations and surface temperature. The Ronchi interferometer was optimized by changing the type of grating (linear, crossed, circular and radial) to give different slope components, the line frequency (0.5–2.5 lines per millimeter) to vary sensitivity and the spatial sampling by varying the location in the optical path. These changes were made by the crew (generally at their judgment) by interchanging gratings in slide mounts in the optical path through the grating access door in the experiment package.

A typical time sequence for a CT test is shown in figure 4. The first objective in the experiment was to find the transition point from steady to oscillatory flow. This objective was achieved by increasing the power in a stepwise manner at user determined intervals, until the transition from steady to oscillatory flow was reached. The intervals were chosen to allow the flow to again become steady at each power level and were on the order of 2–3 minutes each. The diagnostics (IR imager/Ronchi system) were set to their most sensitive settings to allow the earliest identification of the onset. During the equilibration periods, the flight and ground crews observed the flows to identify the onset of oscillatory flow while communicating in real time via the voice link. Once the onset was reached, this ramp sequence was repeated in smaller steps to more precisely determine the transition point. After the study of onset of oscillations, the heater power was increased to higher levels to investigate pronounced oscillations.

The second objective was to measure dynamically the surface temperature and surface shape as well as qualitatively to view the flow structure during oscillatory flow. In order to achieve this objective the heater power level was increased substantially to produce “pronounced” oscillatory flow. This was done to facilitate the measurement process as the oscillation levels (temperature, surface shape and flow structure variations with time) were small at the transition point. Again the diagnostics were optimized to provide the best measurements.

For the tests with aspect ratio reduced to 0.5, the test modules were opened and inserts were placed in the test cell to decrease the depth of the chamber.

4. EXPERIMENTAL DATA

During the USML-2 mission, 55 tests were conducted, yielding greater than 100 percent of the science objectives. A significant result was that oscillatory flow was observed in nearly all the tests conducted. Tables 1, 2, and 3 list the complete set of tests conducted as a function of test cell diameter, free surface shape and heating beam diameter (CF tests). These tests yielded 112 Hi-8 video tapes (about 200 hours) from the Ronchi, IR imager and flow visualizations systems as well as 97 megabytes of digital data.

5. RANGES OF PARAMETERS

5.1 CF Tests

As discussed in our earlier work,¹² the important dimensionless parameters for steady thermocapillary flows in the present experimental configuration with a flat free surface are: Marangoni number (Ma), Prandtl number (Pr), container aspect ratio (Ar), and relative heating zone size or heater ratio (Hr). Surface tension Reynolds number $R\sigma$ is related to Ma and Pr as $R\sigma = Ma/Pr$. In addition, the relative fluid volume (Vr) is important in the curved surface tests and its value for each shape is given in figure 1. The heat loss from the free surface is due to radiation and the forced convection induced by the free surface motion. Based on the numerical analysis to be discussed later, the heat loss from the free surface relative to the total heat transfer rate is estimated to be about 3 percent so that it is not a major factor in the present experiments. The mean absorption length of CO_2 laser by the test fluid has been determined to be $a = 0.06$ mm. The ratio a/R_b ranges from 0.02 to 0.2 in the present experiment. The effect of this parameter will be discussed later.

Forty-two tests were performed in the CF mode. The parametric ranges of those CF tests were: $Ma < 6 \times 10^4$, $Pr = 22-32$, and $Hr = 0.05, 0.1$, and 0.2 . Thirty-two tests were conducted with $Ar = 1$. In the other 10 tests a cylindrical plastic disc was inserted at the bottom of each test chamber to reduce its aspect ratio to 0.5 as discussed earlier. The fluid viscosity in the above Pr is evaluated at the mean temperature, $(T_H + T_C)/2$, where T_H is the free surface temperature at the center. The above Ma is based on ΔT , which is convenient because Ma is defined similarly in other configurations. Later, an Ma based on Q will also be introduced.

5.2 CT Tests

The relevant dimensionless parameters for thermocapillary flow in the CT configuration, with negligible gravity, insignificant heat loss and nondeformable free surface, are the same as those in the CF tests discussed above. Ar and Hr in the 13 CT tests were fixed at 1.0 and 0.1, respectively. The values of Pr and Ma in the CT tests were $Pr=26-31$ and $Ma \leq 1.7 \times 10^5$.

6. NUMERICAL ANALYSIS

6.1 CT Configuration

The numerical analysis is done only for steady flows and is based on the SIMPLER algorithm.⁶ The same numerical program has been used and validated in our past work on thermocapillary flows.^{12,7} For the steady analysis, the free surface is assumed to be flat and nondeformable and the fluid viscosity and surface tension vary with temperature. Both the heater and container side walls are kept at uniform temperatures T_H and T_C , respectively, and the bottom wall is assumed to be thermally insulating. Radiative and convective heat loss from the free surface is taken into account in the analysis. The velocity and stream function are nondimensionalized by $\sigma_T \Delta T / \mu$ and $\sigma_T \Delta T R H / \mu$, respectively, and the temperature is nondimensionalized as $(T - T_C) / \Delta T$. The coordinate system used in the present analysis is defined in figure 1. A nonuniform grid system is employed with meshes graded towards the heater and container walls in the r direction and towards the free surface in the z direction to accurately capture the thermal boundary layers. For the conditions of $Ma = 1.3 \times 10^5$ (close to the largest value for the steady flow in the CT flat surface tests), the values of dimensionless maximum stream function computed with three different grids, 46×40 ($r \times z$), 58×51 , and 80×60 with the smallest radial mesh sizes next to the heater of 0.001, 0.0005, and 0.0002, respectively, are 9.11×10^{-4} , 9.17×10^{-4} , and 9.17×10^{-4} , respectively. The values of dimensionless heat transfer rate, Nusselt number, are 4.92, 4.91, and 4.90, respectively. Therefore, the 58×51 grid is used in the present analysis.

6.2 CF Configuration

The scheme for the flat surface tests is based on the SIMPLER algorithm described above. A non-uniform grid system is employed with the smallest meshes next to the free surface and also next to the cold wall. For the conditions of $Ma = 4.3 \times 10^4$ (close to the largest value for the steady flow in the CF tests), $Hr = 0.2$, and $Ar = 1$, the values of $k \Delta T R_H / Q$ (dimensionless ΔT) computed with three different grids, 37×31 ($r \times z$), 46×40 , and 67×60 with the smallest axial mesh sizes next to the free surface of 0.003, 0.001, and 0.0005, respectively, are 0.0114, 0.0110, and 0.0110, respectively. The computed maximum stream functions are 0.00221, 0.00218, and 0.00217, respectively. Therefore, the 46×40 grid is used in the present analysis.

In the case of curved free surfaces the computational domain is transformed into a rectangular domain by a coordinate transformation. The velocity and temperature fields are solved by a time-marching, finite-difference scheme (Kamotani and Platt).⁸ The grid system is similar to the one used for flat surface. For the conditions of $Ma=2.4 \times 10^5$, $Vr=0.59$ (deep concave surface), and $Ar=1$ in the CF configuration, the values of $k\Delta TR_H/Q$ computed with three different grids, 37×31 , 46×40 , and 67×60 with the smallest axial mesh sizes next to the free surface of 0.006, 0.005, and 0.003, respectively, are 0.00573, 0.00576, 0.00575, respectively. The computed maximum stream functions are 0.00155, 0.00110, and 0.00110, respectively. Therefore, the 46×40 grid is used in the present analysis of CF curved surface tests.

7. BASIC FLOW FIELDS

7.1 CF Tests

The basic steady flow fields are discussed based on numerical and scaling analysis. Typical streamlines and isotherms with flat free surfaces are shown in figure 5. The main flow structure is unicellular, which agrees with our experimental observations. The flow structure is similar to those we investigated in detail in microgravity with a larger container (10 cm dia.) and with a more viscous fluid (10 centistokes silicone oil).¹² One important feature of the thermal field is that there exists a very thin thermal boundary layer along the free surface because Ma is large, and the bulk fluid outside the boundary layer is relatively cool. Since the fluid near the free surface is mainly heated, the free surface temperature distribution and the flow field are established quickly after the start of heating. For example, for the conditions of $D=3$ cm, $Ma=7.1 \times 10^4$, $Hr=0.1$, and $Ar=1$, if the initial fluid temperature is equal to the side wall temperature, it will take less than 10 seconds after the start of heating for the maximum stream function to attain 95 percent of its steady-state value, according to the present numerical simulation. The fact that the flow becomes nearly steady in several seconds is consistent with our flow observation.

The free surface temperature was measured by the IR imager in the STDCE-2. In figure 6 the computed surface temperature distribution is compared with the imager data. They agree well except near the heated region where the imager data are slightly lower than the computed value because of the thin thermal boundary layer.

According to Kamotani et al.,⁹ if both velocity and temperature boundary layers exist in the heated region in the case of flat surface tests, the dimensionless maximum velocity in the region (U_o^*) should scale with $(R\sigma^*)^{-1/3}$, where $R\sigma^*$ is the surface tension Reynolds number based on R_h and ΔT . The computed maximum velocities shown in figure 7 indeed follow that scaling law near the onset of oscillations in the STDCE-2 tests ($R\sigma^*>280$). In our earlier ground-based experiments with smaller containers, $R\sigma^*$ was larger than 160 (for the tests with 2 centistokes silicone oil), so both boundary layers existed also. The flow and temperature fields in the heated region are influenced by the CO_2 laser absorption length a . For a given Q the maximum surface temperature (or ΔT) decreases with increasing a/R_h , as more fluid volume is heated by the laser. For example, for the conditions of $D=2.0$ cm, $R_h=0.1$ cm ($Hr=0.1$), and $Q=0.15$ W, the values of ΔT will change from 14.7 to 9.6 °C when a/R_h is varied from 0.02 to 0.2 (the range of a/R_h in the STDCE-2 tests). Therefore, ΔT represents the thermocapillary driving force more accurately than Q in the heated region (the scaling law of fig. 7 would not be obtained if Q is used).

Since the mass flux out of the heated region is confined to the thin boundary layer, its total mass flux is relatively small compared to that of the bulk flow. The bulk flow is driven mainly by the surface temperature gradient outside the heated region. The characteristic temperature drop in the bulk flow (ΔT_b) can be estimated as follows. The laser heat absorbed in the heated region is convected from that region to the cold wall through a thermal boundary layer along the free surface, which gives the following relation,

$$Q \sim \rho C_p U_b \Delta T_b \delta_{TS} R \quad (1)$$

where δ_{TS} is the thermal boundary layer thickness along the free surface and is estimated as

$$\delta_{TS} \sim \left(\frac{\alpha R}{U_b} \right)^{1/2} \quad (2)$$

Equation (1) is independent of the heating zone diameter (and the laser absorption length), because all the heat from the laser goes into δ_{TS} regardless of the diameter. As mentioned above, the center of the unicellular motion moves in the increasing r -direction with increasing $R\sigma^*$, but its axial position is nearly fixed (at about $z/H=0.8$) in the parametric range of the present study. Therefore, assuming that the overall axial extent of the bulk flow scales with the container dimension (or the bulk flow is viscous-dominated), the shear stress balance at the free surface gives for $Ar=1$

$$U_b \sim \frac{\sigma_T \Delta T_b}{\mu} \quad (3)$$

Since the bulk flow region occupies a much larger volume than the heated region, the maximum stream function is considered to be determined by the bulk flow so that $\psi_{\max} \sim U_b R^2$ for $Ar=1$. Then from equations (1) to (3) one obtains

$$\frac{\psi_{\max}}{\alpha R} \sim \left(\frac{\sigma_T Q}{k \mu \alpha} \right)^{2/3} \quad (4)$$

By means of equations (1)–(3) the right side of equations (4) can be expressed in terms of the Marangoni number based on ΔT_b and R , called Ma_Q herein,

$$Ma_Q = \frac{\sigma_T \Delta T_b R}{\mu \alpha} = \left(\frac{\sigma_T Q}{k \mu \alpha} \right)^{2/3} \quad (5)$$

The scaling law, equation (4), is compared with the numerical results in figure 8. The numerical results are obtained for a range of Ma_Q up to near the maximum value for steady flow found experimentally. The scaling law agrees very well with the computed results.

The Reynolds number of the bulk flow can be estimated as $U_b R / \nu \sim \psi_{\max} / \nu R$, which is about 3 for $Ma_Q = 10^4$ (the largest Ma_Q in fig. 8) and $Pr = 30$. Therefore, the bulk flow Reynolds number is not large enough to have a boundary-layer type flow. The ratio of the volume flux out of the heated region ($U_o \delta_v R_h$ where δ_v is the velocity boundary layer thickness) to the bulk flow volume flux ($U_b R^2$) can be expressed as $(R\sigma^*)^{1/3} Pr Hr / Ma_Q$. The ratio is less than 1 percent near the onset of oscillations in the flat surface tests. Therefore, all the assumptions made in the above analysis are consistent with the results. In summary, the bulk flow driven by ΔT_b dominates the overall flow, it is viscous-dominated, and is not influenced by the heating zone diameter in the parametric ranges of the present experiments. For that reason, we use Ma_Q to characterize the flow in the following discussion.

Typical streamlines and isotherms with deeply concave free surface are shown in figure 9. The flow structure is unicellular and a thin thermal boundary layer exists along the free surface. Steady thermocapillary flows with various curved free surfaces have been investigated in detail in our earlier space experiments.^{1, 2, 10} Compared to the flat surface case, steady flow with a curved free surface is slower under the same conditions, because the overall flow passage is narrower when the surface is concave. The computed maximum stream function is shown in figure 10 as a function of Ma_Q up to near the maximum value for steady flow found experimentally. Above about $Ma_Q = 10^4$ the dimensionless maximum stream function is a linear function of Ma_Q and it is nearly independent of Hr (less than 10 percent difference between $Hr = 0.05$ and $Hr = 0.2$). Therefore, one can conclude that whether the free surface is flat or curved, the main flow is viscous-dominated near the onset of oscillations. Comparing figures 8 and 10 one sees that for a given Q (or Ma_Q) the flow is slower with highly concave surface: at $Ma_Q = 10^4$, for example, $\psi_{\max} / \alpha R$ is about 100 for the flat surface compared to about 60 for the deep concave surface.

7.2 CT Tests

A set of typical computed streamlines and isotherms for steady flow in a fixed radial (r - z) plane are presented in figure 11. The flow field is unicellular (called the flow cell herein) with rapid outward flow from the heater to the cold wall along the free surface and a return flow towards the heater in the bulk. Strong fluid motion occupies almost all of the test section, which is in contrast to the situation in 1 g where buoyancy induced stratification (important in large test containers)⁷ restricts the strong thermocapillary flow to a region nearer to the free surface. Convection along the free surface and return flow towards the heater causes thin thermal boundary layers along the free surface and along the heater, which are typical of thermocapillary flows of high Pr liquids at relatively high Ma . It is also noted from figure 11 that within the flow cell, the temperature is relatively uniform owing to strong convection, which limits large temperature variations in the liquid to small regions close to the heater and the cold wall.

In order to see the accuracy of the steady surface temperature distribution measured by the IR imager, some comparisons with computed surface temperature profiles are made. Figure 12 shows the computed and measured radial surface temperature distributions for two test containers during steady flow. It can be seen that generally the computed and measured surface temperature profiles are in agreement. Similar to the interior of the liquid, large temperature variations on the free surface occur in the vicinity of the heater and the cold wall with a large region of relatively small temperature variation in between.

Because large surface temperature variations occur in very small regions, a thermocapillary driving force in those regions is not effective in driving the entire flow. Thus the surface temperature distribution

outside those regions is more important. Consequently, the driving force for the whole flow is relatively weak, so the flow remains viscous-dominated even when $R\sigma$ is large, as shown below.

Equations (1) through (4) are still valid in the CT configuration. However, the quantity Q (the total heat flux from the heater to the fluid) is not measured in the CT tests but ΔT is. Q can be related to ΔT by analyzing the heat transfer at the heater. Based on that analysis it can be shown that the Nusselt number scales as

$$Nu \sim Ma_Q^{1/4} \quad (6)$$

for a given Ar and Hr . By definition,

$$Nu = Q/k\Delta TR \quad (7)$$

for a given Ar and Hr . By eliminating Nu from equations (6) and (7) one derives the relationship between Q and ΔT . From that one obtains $Ma_Q \sim Ma^{4/5}$, so that Eq. (4) can be written in terms of Ma as

$$\frac{\Psi_{\max}}{\alpha R} \sim Ma^{4/5} \quad (8)$$

Equation (8) is compared with the numerical results in figure 13. As seen in the figure, the scaling law, which is obtained based on viscous-dominated flow, agrees with the computed results in the parametric range of the present experiment.

As seen above, the bulk flows are viscous-dominated near the onset of oscillations in all the situations investigated. That fact is important because it implies that the oscillation phenomenon is not caused by a hydrodynamic instability where inertia forces play an important role.

8. OSCILLATORY FLOW

8.1 CT Tests

It is known from our previous studies^{7,11} in the CT configuration that once ΔT is increased beyond a certain value (called the ΔT_{cr} herein), the flow field becomes oscillatory with corresponding time periodic variations in the temperature field. The onset of oscillatory flow disturbs the axial symmetry of the flow and temperature fields which then become three-dimensional. In the STDCE-2, transition of steady thermocapillary flow to oscillatory flow was observed in almost all the tests carried out. The observed oscillatory motion in all the tests in the STDCE-2 was similar in nature and is sketched in figure 14. In oscillatory flow, the fluid particles moved back and forth in the azimuthal direction with the frequency of oscillations as they circulated in the flow cell. In addition to the oscillatory motion in the azimuthal direction, a very slow rotation of the whole flow field was also observed. The time period of this rotation was much larger than the time period of the oscillatory motion in the azimuthal direction. In a fixed radial (r - z) plane, the flow is observed to go through periods of strong and weak motion during one oscillatory cycle. The observed oscillatory flow field is similar to that described by Kamotani et al.^{7,11} in 1 g tests, which shows that the oscillatory flow observed in the 1 g tests is thermocapillary in nature and is discussed further later.

The onset of oscillatory flow is signified by ΔT_{cr} which is shown in figure 15 for various test containers with flat free surface. 1 g data from Kamotani et al.⁷ for the CT configuration (same fluid and Hr as in the STDCE-2) are also included to increase the range so as to make the trend clear. It can be seen that for the test containers with a diameter around 1.2 cm, the onset of oscillations in 1 g and microgravity occur at a similar ΔT_{cr} . The small difference in ΔT_{cr} noticeable from figure 15 is due to a somewhat different cold wall temperature in the 1 g⁷ (~25 °C) and microgravity (~15 °C) experiments, which results in slightly higher viscosity in the microgravity tests for the same fluid. For the test containers with 1.2-cm diameter, in addition to the similarity in the observed oscillatory flow field stated earlier, the oscillation frequency and the IR image of the free surface were also similar in the 1 g⁷ and microgravity tests. This clearly shows that for the 1.2-cm-diameter test container, buoyancy does not influence the onset of oscillations. Therefore, one can conclude that the onset of oscillations in test containers with diameters smaller than 1.2 cm is not affected by buoyancy in normal gravity as the influence of buoyancy is reduced with decreasing test container dimensions. From figure 15 it can be seen that ΔT_{cr} decreases with increasing test section size, which is consistent with our previous study.⁷

In order to determine the criteria for the onset of oscillations, it is appropriate to look at the problem in a nondimensional manner. The important factors which could influence the onset of oscillations in the absence of buoyancy are: the Marangoni number (Ma), the fluid (Pr), the heater ratio (Hr), the aspect ratio (Ar), heat loss from the free surface (Biot number) and the deformability of the free surface (capillary number). In the present experiments, the heat loss from the free surface is estimated numerically and is found to be insignificant (less than 3 percent of the total heat transfer) for the conditions near the onset of oscillations. Therefore, if the free surface is assumed to be nondeformable, then the conditions of the experiment are determined by Pr , Ar , Hr and Ma . In the present experiments Ar and Hr are fixed and Pr is nearly constant in all the tests; therefore, the only variable parameter is Ma . Consequently, the onset of oscillations should be characterized by a critical Marangoni number (Ma_{cr}). In order to see the behavior of Ma_{cr} in the present and in our 1 g experiments,⁷ the data in figure 15 are nondimensionalized in terms of Ma_{cr} and plotted in figure 16 against the test container diameter to differentiate among various tests. From figure 16 it is clearly seen that for different tests with similar Pr , Ar and Hr , the value of Ma_{cr} changes almost fourfold over the range of the experiments. This shows that Ma_{cr} is not a sufficient parameter to characterize the onset of oscillations in the CT configuration. The same conclusion was obtained in our previous work^{7,12} in the CT and other configurations. It is clear then that some other factor needs to be included in the analysis. Since buoyancy and heat loss from the free surface are insignificant, the only important factor is the deformability of the free surface. Based on our extensive experimental and theoretical work on the oscillation phenomenon, we believe that the additional aspect is free surface deformation. The detailed theoretical basis for oscillatory thermocapillary flows in the so-called half-zone configuration is given by Kamotani and Ostrach.¹³ The same concept is applied to the present configuration in the following discussion. It is convenient to divide the flow field into two—surface flow along the free surface toward the cold wall and return flow in the interior toward the heated region. The surface flow is driven by thermocapillarity and the return flow is due to the pressure field caused by the surface flow. Consider a transient situation where the surface flow is somewhat changed for some reason. The return flow does not respond to that change immediately, because the surface flow must deform the free surface shape first to modify the pressure field. Such a small delay could cause a large change in the flow field, if the free surface deformation alters the thermal boundary layer thickness along the free surface significantly.

The free surface deformation of interest, δ_s , can be estimated as follows. It delays the return flow response by δ_s/U_b , and after that time the pressure gradient becomes large enough for the response to occur, which can be written mathematically as

$$\rho \frac{U_b}{\delta_s / U_b} \sim \sigma \frac{\delta_s}{R^2} \frac{1}{R} \quad (9)$$

Equation (9) is a balance of the unsteady term and pressure gradient in the momentum equation. Based on the scaling analysis discussed above, it can be shown that near the heater the thermal boundary layer thickness along the free surface is given as

$$\frac{\delta_{TS}}{R} \sim Ma^{-1/5} \quad (10)$$

Our concept of oscillation mechanism is that the driving force could be altered appreciably if the above surface deformation is comparable with the thermal boundary layer thickness, which could lead to oscillatory flow (Kamotani and Ostrach).¹³ Therefore, we define a surface deformation parameter (S) as the ratio of δ_s to δ_{TS} . From equations (8), (9) and (10) one then obtains

$$S = \frac{\delta_s}{\delta_{TS}} \sim \left(\frac{\rho \alpha^2}{\sigma R} \right)^{1/2} Ma \quad (11)$$

Oscillations should appear when S is larger than a certain value. According to the above concept both Ma and S are important in characterizing the onset of oscillations. For that reason the critical conditions are plotted in terms of Ma and S in figure 17. As seen in figure 17, all our data can be correlated well by S and in the parameteric range of the present study the flow becomes oscillatory when S is larger than about 15.

The oscillation frequency near the onset of oscillations is shown in figure 18. The oscillation frequency decreases with increasing test container diameter. As discussed by Kamotani et al.,⁷ the oscillation period depends upon the time scale for the flow to recirculate in the torriodal cell, so that as the container size gets larger, the period of recirculation increases which results in smaller frequency of oscillation. Since the period of recirculation of the flow is a function of the imposed ΔT , therefore the oscillation frequency was measured near ΔT_{cr} (within 10 percent) in all the tests including the 1 g tests by Kamotani et al.⁷

The IR imager provided real-time thermal images of the free surface during steady and oscillatory flow. In steady flow IR images provided good quantitative data as discussed earlier. During oscillatory flow, the IR images were also very useful in giving an insight into what was happening during oscillations. During steady flow the IR pattern of the free surface was axisymmetric, which changed into different transitional, nonaxisymmetric, patterns before settling down to an elliptic rotating pattern at the onset of oscillations. Upon further increase in the imposed ΔT , the IR patterns assumed various other shapes depending upon the test container under investigation. The details regarding the oscillatory IR patterns of the free surface are discussed next for the three test containers.

Figure 19 shows the various IR patterns (isotherms) of the free surface observed for the three test containers during oscillations in the flat free surface tests. Figure 19a shows the IR pattern observed just after the onset of oscillations in all three test containers. The axial symmetry of the steady flow IR pattern breaks down into an elliptic (oblong) pattern, called the two-lobed pattern herein, which rotates about the axial (z) axis. This pattern suggests that at a given time, convection along the free surface is strong in two diametrically opposed directions indicated by the elongated isotherms, corresponding to the active period in those directions. Similarly, relatively weak convection along the free surface occurs in directions normal to the elongations, corresponding to weak periods in those directions. Therefore, one rotation of the pattern produces two temperature peaks and valleys at a fixed location so that the period of temperature oscillation is one half of the rotational period of the pattern. The only difference between the three test containers during the two-lobed rotating pattern was in the period of rotation as reflected in the frequency of temperature oscillations shown in figure 18. For the 1.2- and 2.0-cm diameter test containers, at a higher ΔT , the two-lobed rotating IR pattern changed into a two-lobed pulsating pattern shown in figure 19b. At the start of the oscillation cycle, the elliptic pattern extends radially outward in diametrically opposed directions. After reaching a peak, it then recedes inwards, subsequently extending radially outward again in diametrically opposed directions but this time normal to the first elongation. Thus, the oscillation cycle consists of two pulsations of the two-lobed pattern. During the two pulsations, the temperature at a fixed location at the surface goes through one peak and valley; therefore the oscillation frequency in this case is one-half of the pulsation frequency. The elongations of the isotherms signify stronger convection (active period) similar to the rotating two-lobed pattern discussed earlier. The two-lobed pulsating pattern was not observed for the 3.0-cm diameter test container.

In the 2.0- and 3.0-cm diameter test containers, at a significantly higher ΔT , the IR oscillation pattern was observed to transition into a three-lobed pulsating pattern shown in figure 19c. In this pattern, the active regions (elongations of isotherms/strong convection) were in three equally spaced azimuthal directions (three-lobed pattern) while the three weak regions (weaker convection) were between the active regions. At the start of an oscillation cycle, the active regions extended radially outward in three equally (azimuthal) spaced lines (directions). After reaching a peak, the active regions receded inward along the same lines. Subsequently, the active regions again extended outward in three equally spaced lines, but this time these lines were between (azimuthally) the first elongations. After reaching a peak in the new directions, the three active regions receded along the same lines to complete the oscillation cycle. Thus, the oscillation cycle consists of two pulsations of the three-lobed IR pattern. The two pulsations of the pattern correspond to one temperature peak and valley at a fixed location on the free surface; therefore, the temperature oscillation frequency is one-half of the IR pattern pulsation frequency, similar to the two-lobed pulsating pattern described earlier. The three-lobed pulsating pattern was not observed in the 1.2-cm diameter test container.

The IR images of the free surface temperature distribution during oscillatory flow (fig. 19) show that the two-lobed rotating pattern persists at the onset of oscillations for all the test containers in the STDCE-2. For all the ground-based tests shown in figures 15 and 16, the IR pattern at the onset of oscillations was also a two-lobed rotating type.⁷ Therefore, at the onset, it is seen that a single (common) mode of oscillation occurs in all microgravity (present) and simulated microgravity experiments⁷ in the CT configuration.

For tests with concave free surface ($Vr=0.81$), the onset of oscillations occurs at a higher ΔT_{cr} than for the flat surface tests. A part of the reason for this is that with a concave free surface, the flow is observed to be slower for the same ΔT . At present, we have not derived an S -parameter for curved free surface, so more time is needed to complete the data analysis.

8.2 CF Tests

When the flow was steady, the tracer particles were observed to recirculate in fixed radial planes and the IR images were axisymmetric. However, beyond a certain Q the flow became oscillatory. The oscillatory flow was found to be very similar to that described for the CT mode. The heat input at the onset of oscillations is called the critical heat flux (Q_{cr}). The critical heat fluxes measured in the flat surface tests with $Ar=1$ are presented in figure 20, together with the data taken in our ground-based tests with smaller containers filled with the same fluid (Lee et al.).¹⁴ The flow was found to be already weakly oscillating at the minimum power of the CO_2 laser for the 1.2 cm container, so that the critical heat flux could not be determined for that container. As seen in figure 20, the trend of the space data is consistent with that of the ground data: Q_{cr} increases with increasing D . As discussed earlier, the data taken in the CT tests show that the critical temperature difference for the 1.2 cm container measured in the STDCE-2 was close to that measured in 1 g with a similar sized container, which means that buoyancy has a negligible effect on the onset in our ground tests with small containers ($D \leq 1.2$ cm). According to figure 20, Q_{cr} seems to depend slightly on Hr but the effect of Hr is within the experimental error.

The whole flow field changes during oscillations, which suggests that the oscillations are associated mainly with the bulk flow. Therefore, we compute $(Ma_Q)_{cr}$ based on Q_{cr} according to Equation (5). Viscosity in Ma_Q is evaluated at the side wall temperature because the bulk fluid is close to that temperature (fig. 5). The Prandtl number associated with Ma_Q is also evaluated at T_c and is called Pr_c . The value of Pr_c is nearly constant in the STDCE-2 tests, equal to about 33, as the cold wall temperature was nearly constant. The result is given in figure 21, which does not include the 1.2 cm data. As in our past work, we plot $(Ma_Q)_{cr}$ against D . If $(Ma_Q)_{cr}$ were the only parameter to specify the onset of oscillations, it should not vary with D . Figure 21 shows clearly that, as we found also in various experiments under different conditions, the Marangoni number alone cannot specify the onset. As in the CT case we introduce a surface deformation parameter, S , as follows.

The transient surface deformation is given by equation (9). In the CF mode a thin thermal boundary appears along the free surface, as discussed earlier. The boundary layer thickness is given by equation (2). Then, if the deformation is comparable with the thermal boundary layer thickness, the driving force could be altered significantly. Therefore, we define S as the ratio of those two quantities,

$$S = \frac{\delta_s}{\delta_{TS}} \sim \left(\frac{\rho U_b^3 R^2}{\sigma \alpha} \right)^{1/2} \sim \left(\frac{\rho \alpha^2}{\sigma R} \right)^{1/2} Ma_Q^{3/2} \quad (12)$$

Oscillations should appear beyond a certain value of S . The data in figure 21 are replotted in figure 22, where S is plotted against Ma_Q . It is clear that Ma_Q is an important parameter, because the oscillations are a convection phenomenon, but in the parametric ranges of the STDCE-2 and our ground tests the S -parameter is the limiting parameter.

The frequency of oscillations near the onset of oscillations is shown in figure 23. The frequency decreases with increasing D . The frequency is not a strong function of Hr , which again suggests that the oscillations are caused by the bulk flow. The IR images during oscillations, which will be shown later, suggest that the period of oscillations is determined by the time of convection across the container. Therefore, the oscillation frequency is nondimensionalized as

$$f^* = \frac{f}{U_b / R} = \left(\frac{fR^2}{\alpha} \right) / Ma_Q \quad (13)$$

The result is also presented in figure 23 which shows that the oscillation period indeed scales with the time of convection of the bulk flow. The effect of Hr on the frequency is within the experimental error.

The isotherms obtained from the IR images during one cycle of oscillations are given in figure 24. Since the IR imager cannot accurately resolve the surface temperature near the heated region, as discussed above, figure 24 is meant to show only qualitative pattern changes during oscillations. When the flow is steady, the isotherms were axisymmetric. When the flow became oscillatory, the pattern became elongated, with the elongation direction changing alternately between two nearly perpendicular directions (fig. 24). The pattern remained the same with increasing Q , unlike in the CT tests where different patterns were observed for significantly different ΔT . With those pattern changes in one cycle of oscillations, the free surface temperature along a given radial direction becomes alternately high and low, which is caused by alternately strong and weak convection along the free surface. In our concept of oscillations the surface flow changes in that way because the surface flow and the return flow are not balanced at any given time due to the aforementioned time delay associated with free surface deformation.

Since large curved free surfaces can be obtained only in microgravity, the oscillatory flow data obtained in the STDCE-2 with curved surfaces are quite unique. The onset of oscillations was similar to that found in the flat surface tests. The values of Q_{cr} measured for various free surfaces with the 2-cm container are presented in figure 25. In the case of convex free surface the flow was found to be oscillating with the minimum laser power. As figure 25 shows, Q_{cr} increases with increasingly concave free surface. A part of the reason for the increase is that the overall flow becomes slower with increasingly concave surface, as shown above. For the deep concave surface Q_{cr} increases slightly with decreasing Hr .

The values of Q_{cr} for concave surfaces are given in figure 26. At present, we have not derived a S -parameter for curved free surface, so the data for curved surfaces are presented in dimensional form. As seen in figure 26, Q_{cr} increases with increasing container diameter, which is true also in the flat surface tests (fig. 20) but the dependence of Q_{cr} on diameter becomes stronger with increasingly concave surface.

In the CF configuration, a few tests were done with $Ar=0.5$ as well. The values of Q_{cr} for these tests are presented in figure 27. Q_{cr} increases with container size as well as with concave free surface shape. This variation of Q_{cr} for $Ar=0.5$ is similar to that shown in figures 20, 25 and 26 for $Ar=1$. The closer proximity of the bottom wall to the free surface with $Ar=0.5$ slows down the flow due to increased viscous effects, thus increasing Q_{cr} needed for the onset of oscillations.

9. CONCLUSIONS

The data taken during the STDCE-2 experiment conducted aboard USML-2 Spacelab in 1995 and analyzed so far are presented and discussed. The thermocapillary flow was generated in a cylindrical container by using two different heating modes. Three test containers with 1.2-, 2.0- and 3.0-cm diameters were used. Qualitative visualization of the flow field was made and quantitative temperature measurements by thermistors were taken. The entire free surface temperature field was measured by an IR imager. Free surface deformation measurements were also made for steady and oscillatory flows. The experimental hardware performed according to specifications with no loss of data.

9.1 CT Tests

The flows were generated by a cylindrical cartridge heater ($Hr=0.1$) in open cylindrical containers filled with two centistokes kinematic viscosity silicone oil. The steady thermocapillary flow was observed to change to an oscillatory state at a critical temperature difference between the heater and the cold wall. The onset of oscillations in the 1.2-cm diameter test container coincided with the onset of oscillations observed with the identical test container in our 1 g tests⁷ which showed the negligible influence of buoyancy on the onset of oscillations in this size container and smaller. The data show that the onset of oscillations over a wide range of experiments (including simulated microgravity data) is not characterized by Ma_{cr} alone. Based on our idea of the oscillation mechanism, a critical value of free surface deformation parameter (S -parameter) describes the onset of oscillation in microgravity. The measured oscillation frequency reduces with increasing test container size indicating its relationship with the recirculation of flow in the torroidal thermocapillary cell.

The IR images (isotherms) of the free surface during oscillatory flow revealed various oscillatory patterns. At the onset of oscillatory flow, a two-lobed rotating pattern was observed in all test sections. Subsequent increases in the imposed temperature difference (ΔT) resulted in two-lobed pulsating and three-lobed pulsating patterns which were specific to certain test containers. However, all the oscillatory IR patterns reveal regions of strong (active period) and weak (weak period) convection along the free surface at different stages of the oscillation cycle.

9.2 CF Tests

The flows were generated by CO_2 laser heating and became oscillatory beyond the critical heat fluxes. The effects of free surface shape, container size, heating zone size and aspect ratio on the oscillation phenomenon were investigated. The critical heat flux increases with increasing container diameter, which is consistent with our ground-based data taken with smaller containers. The effect of heating zone size on the critical flux is relatively small. The Marangoni number alone cannot specify the onset of oscillations, requiring an additional parameter to describe the oscillations. Numerical analysis of the basic flow shows that it is viscous-dominated near the onset of oscillations. Therefore, a surface deformation parameter (S -parameter) was derived for the viscous bulk flow. The experimental data show that the flow becomes

oscillatory when S is larger than about 130. The oscillation period increases with increasing container diameter and scales with the time of convection in the bulk flow. Pulsating thermograms were observed during oscillations. The critical heat flux increased with increasingly concave free surface shape and reducing aspect ratio.

Some data, including the Ronchi data, are still being analyzed. In the end we want to relate the surface temperature, flow field and free surface deformation during oscillations to prove our concept of oscillations which is based on a three-way coupling among those quantities.

REFERENCES

1. Kamotani, Y.; Ostrach, S.; and Pline, A.: "Analysis of Velocity Data Taken in Surface Tension Driven Convection Experiment in Microgravity," *Physics of Fluids*, 6, No. 11, 3601–3609, 1994.
2. Kamotani, Y.; Ostrach, S.; and Pline, A.: "A Thermocapillary Convection Experiment in Microgravity," *Journal of Heat Transfer*, 117, 611–618, 1995.
3. Pline, A.; Jacobson, T.; Kamotani, Y.; and Ostrach, S.: "Surface Tension Driven Convection Experiment," Paper AIAA-93-4312, AIAA Space Programs and Technology Conference and Exhibit, Huntsville, AL, September 21–23, 1993.
4. Pline, A.; and Butcher, R.: "Spacelab Qualified Infrared Imager for Microgravity Science Experiments," *SPIE*, 1313, Thermosense XII, 250–258, 1990.
5. Stahl, H.; and Stultz, K.: "Free-Surface Deformation Measurements," *AIAA Paper 97-0778*, presented at the 35th AIAA Aerospace Sciences Meeting and Exhibit, Reno, NV, January 1997.
6. Patankar, S.V.: *Numerical Heat Transfer and Fluid Flow*, McGraw-Hill, New York, 1980.
7. Kamotani, Y.; Masud, J.; and Pline, A.: "Oscillatory Convection Due to Combined Buoyancy and Thermocapillarity," *J. Thermophysics & Heat Transfer*, 10, No. 1, 102–108, 1996.
8. Kamotani, Y.; and Platt, J.: "Effects of Free Surface Shape on Combined Thermocapillary and Natural Convection," *Journal of Thermophysics and Heat Transfer*, 6, 721–726, 1992.
9. Kamotani, Y.; Chang, A.; and Ostrach, S.: "Effects of Heating Mode on Steady Axisymmetric Thermocapillary Flows in Microgravity," *Journal of Heat Transfer*, 118, 191–197, 1996.
10. Ostrach, S.; and Kamotani, Y.: "Surface Tension Driven Convection Experiment (STDCE)," NASA Contractor Report 198476, June 1996.
11. Kamotani, Y.; Lee, J.H.; Ostrach, S.; and Pline, A.: "An Experimental Study of Oscillatory Thermocapillary Convection in Cylindrical Containers," *Physics of Fluids A*, 4, No. 5, 955–962, 1992.

12. Masud, J.; Kamotani, Y.; and Ostrach, S.: "Oscillatory Thermocapillary Flow in Cylindrical Columns of High Prandtl Number Fluids," *J. Thermophysics and Heat Transfer*, 11, No. 1, 105–111, 1997.
13. Kamotani, Y.; and Ostrach, S.: "Theoretical Analysis of Thermocapillary Flow in Cylindrical Columns of High Prandtl Number Fluids," submitted to *Journal of Heat Transfer*, 1996.
14. Lee, J.H.; Ostrach, S.; and Kamotani, Y.: "A Study of Oscillatory Thermocapillary Convection in Circular Containers with CO₂ Laser Heating," Report EMAE/TR-94-213, Department of Mechanical and Aerospace Engineering, Case Western Reserve University, Cleveland, OH, 1994.

Table 1. Number of CT tests performed with $Ar=1$.

Test Cell Diameter (cm)	Free Surface Shape		
	Flat ($Vr=1.0$)	SC ($Vr=0.817$)	DC ($Vr=0.563$)
1.2	2*	2*	1*
2.0	2*	2*	1*
3.0	1*	2*	1*

SC=shallow concave, DC=deep concave, *=originally planned test matrix

Table 2. Number of CF tests performed with $Ar=1$.

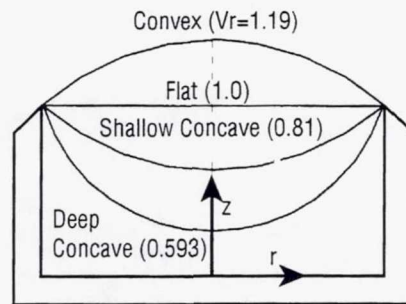
Test Cell Diameter (cm)	Beam Diameter (cm)	Free Surface Shape			
		Flat ($VR=1.0$)	SC ($Vr=0.81$)	DC ($Vr=0.59$)	CVX ($Vr=1.19$)
1.2	0.06	*	1*	1*	
	0.12	1*	1*	1*	
	0.24	1*	1*	1*	
	0.4	1			
2.0	0.1	1*	1*	1*	1*
	0.2	1*	1*	1*	1*
	0.4	1*	1*	1*	1*
	0.6				1
3.0	0.15	1*	1*	1*	
	0.3	3*	1*	*	
	0.6	1*	1*	1*	

SC=shallow concave, DC=deep concave, CVX=convex, *=original test matrix

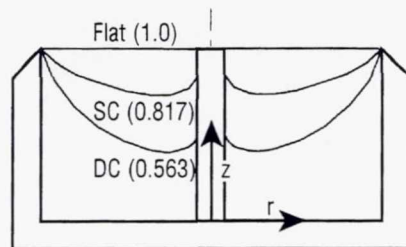
Table 3. Number of CF tests performed with $Ar=0.5$.

Test Cell Diameter (cm)	Beam Diameter (cm)	Free Surface Shape			
		Flat	SC	DC	CVX
1.2	0.06	1	1		
	0.24	1	1		
2.0	0.2	1	1		
3.0	0.15		1		
	0.3	1	1		
	0.6		1		

SC=shallow concave, DC=deep concave, CVX=convex, *=original test matrix



CF Test Containers



SC= shallow concave, DC=deep concave

CT Test Containers

Figure 1. Various free surface shapes investigated in the STDCE-2.

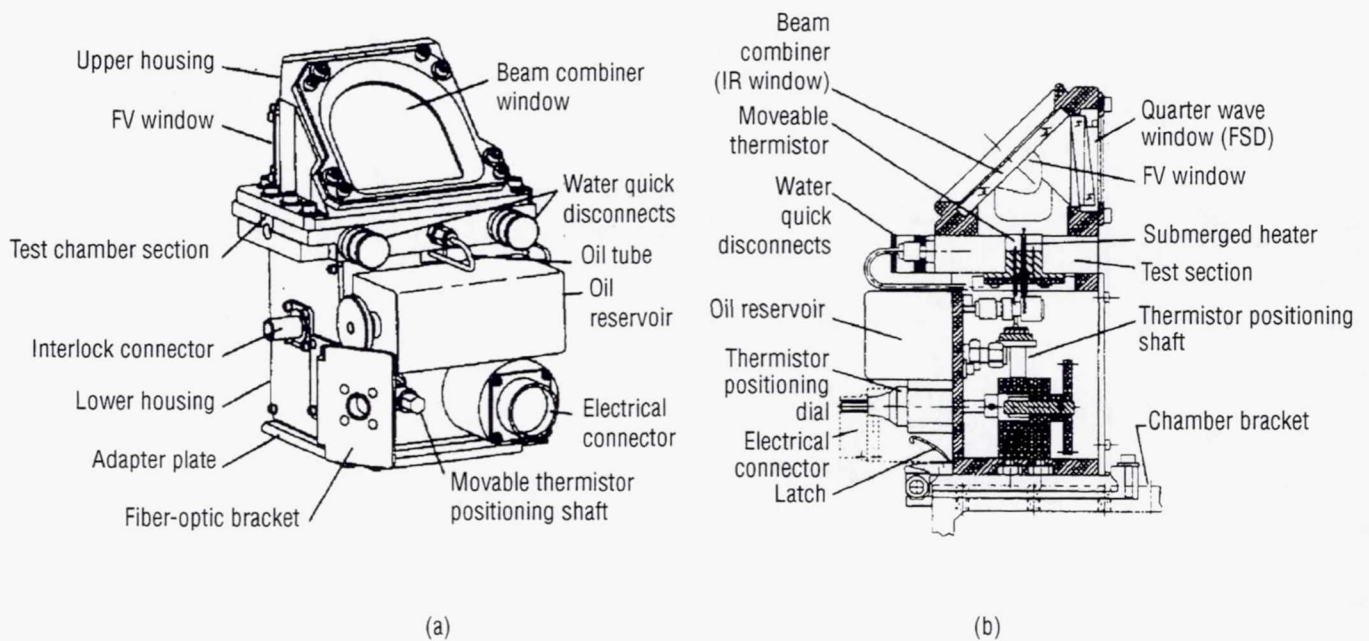


Figure 2. STDCE-2 test chambers module views: (a) exterior, (b) interior.

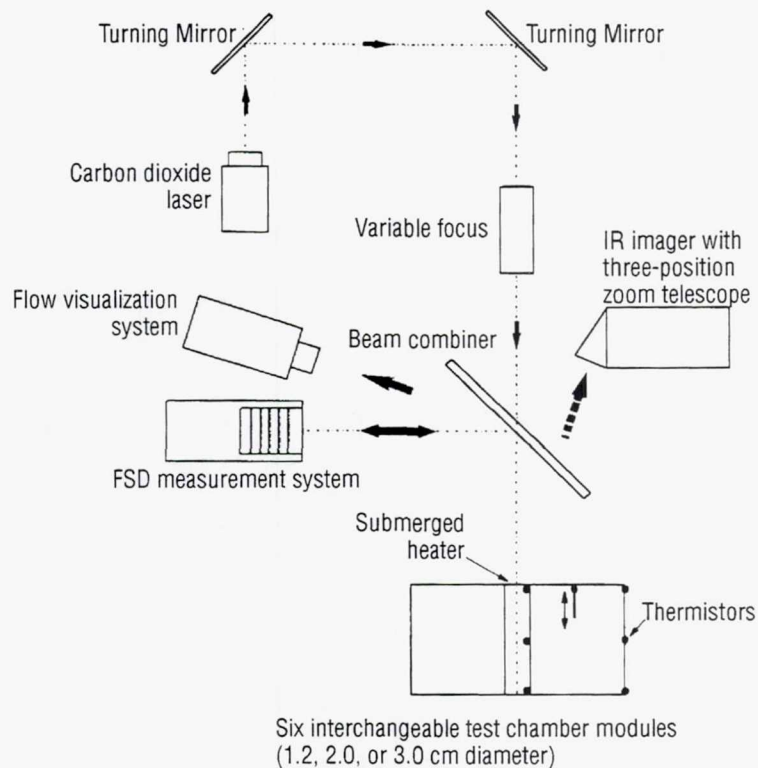


Figure 3. Schematic layout of the STDCE-2.

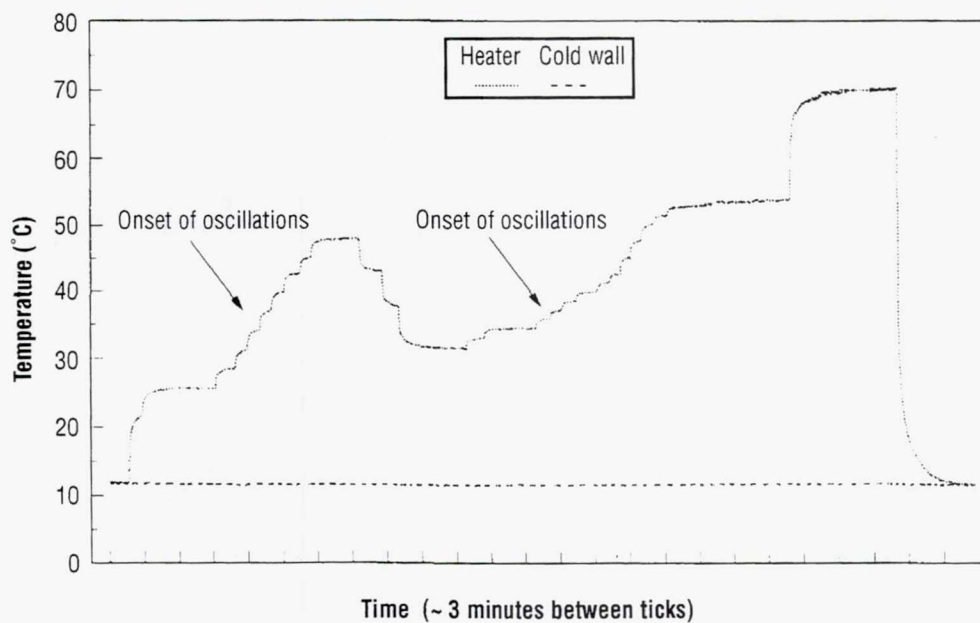


Figure 4. General time line of tests conducted during the STDCE-2.
(2.0 cm diameter test container during CT test, $V_r=1$)

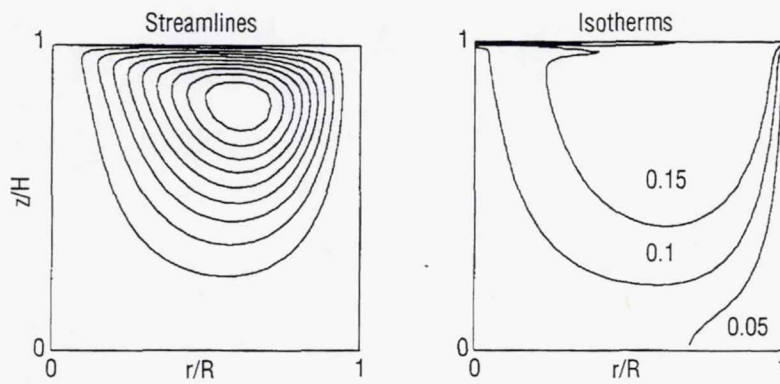


Figure 5. Streamlines and isotherms with flat free surface. (CF test, $D=2$ cm, $Ma=6.4 \times 10^4$, $Ma_Q=8.4 \times 10^3$, $Hr=0.1$, and $Pr=30$)

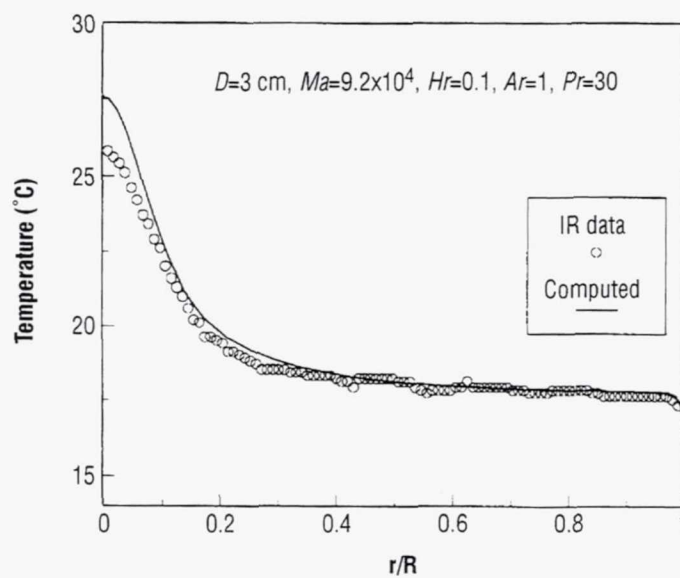


Figure 6. Comparison between computed surface temperature distribution and IR imager data for flat surface CF test.

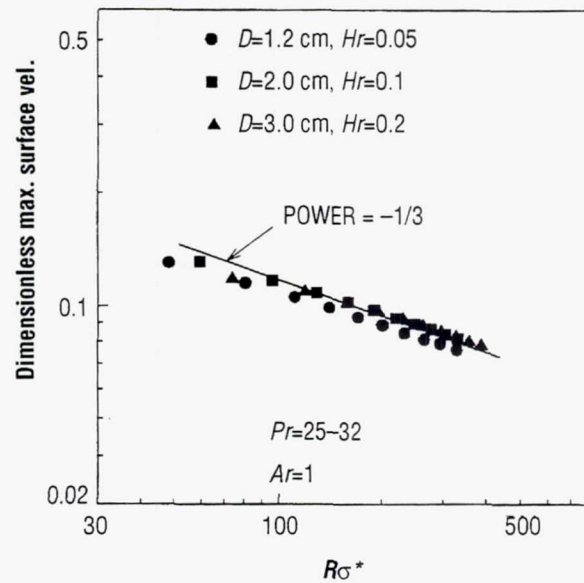


Figure 7. Scaling law for maximum surface velocity in heated region (CF configuration).

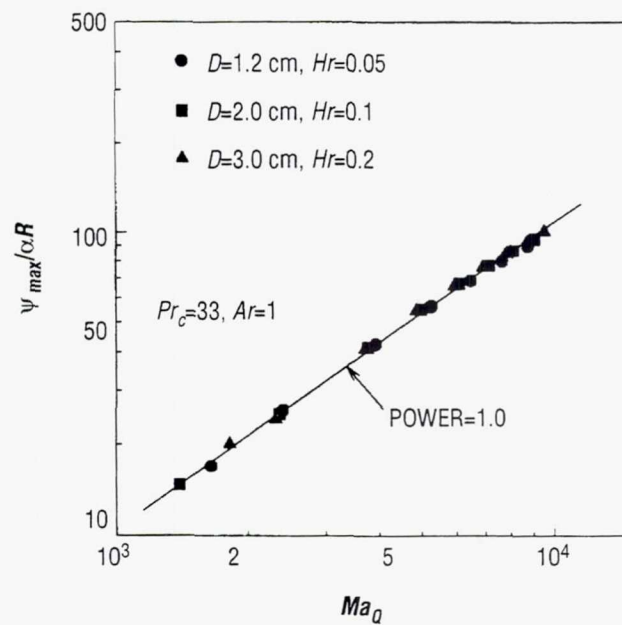


Figure 8. Scaling law for maximum stream function (CF configuration).

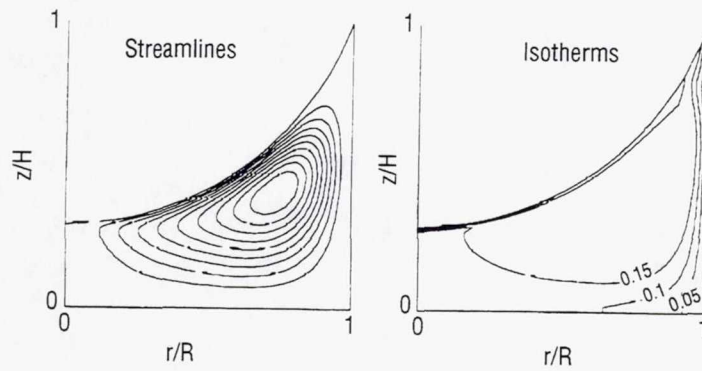


Figure 9. Streamlines and isotherms with curved free surface (CF test, $D=2$ cm, $Ma=3.5\times 10^5$, $Ma_Q=3.6\times 10^4$, $Hr=0.1$, $Pr=23$, $Ar=1$, and $Vr=0.59$).

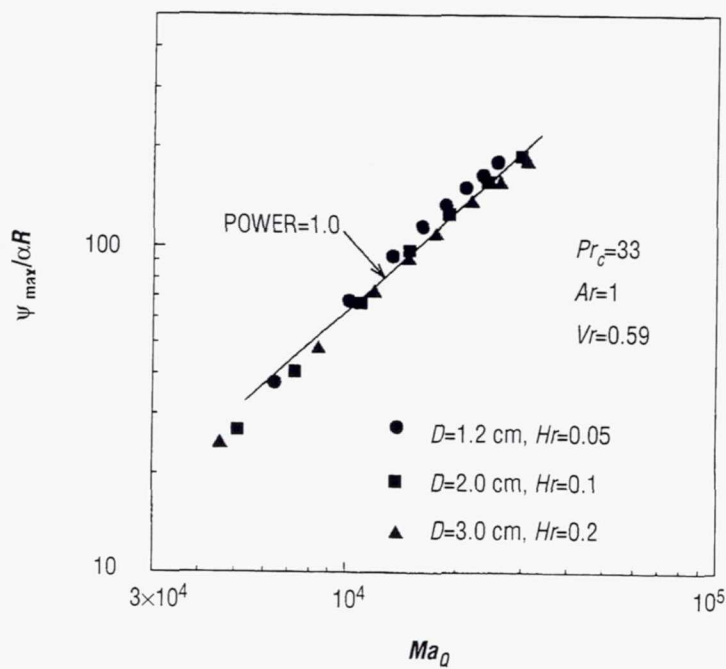


Figure 10. Scaling law for maximum stream function with curved free surface (CF configuration).

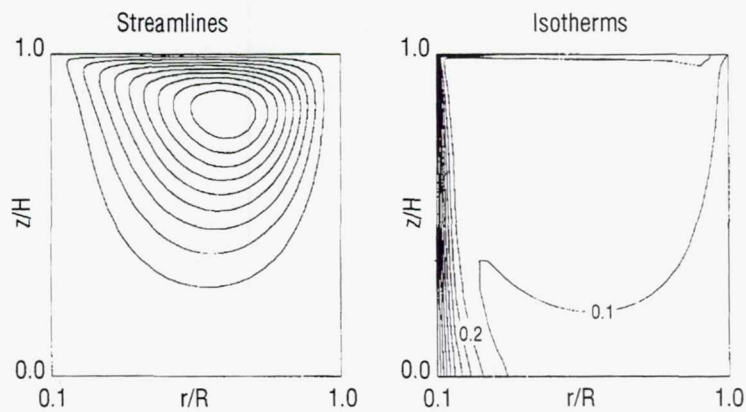


Figure 11. Streamlines and isotherms for steady flow in CT tests ($D=2.0$ cm, $Ar=1$, $Ma=1.1 \times 10^5$, $Pr=30.9$).

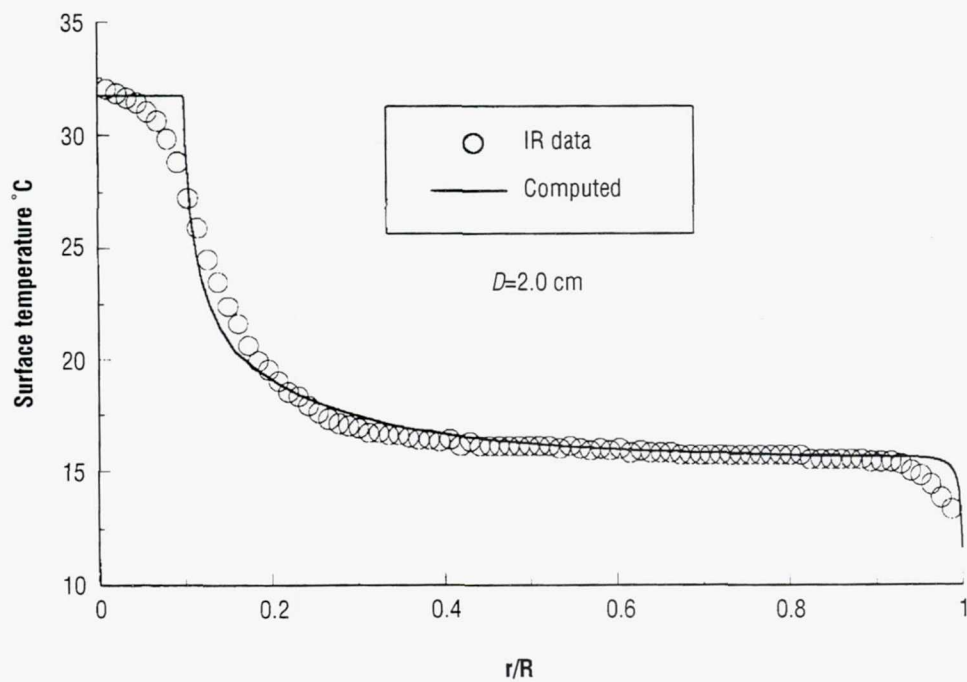


Figure 12. Comparison between computed surface temperature and IR imager data for flat surface CT test.

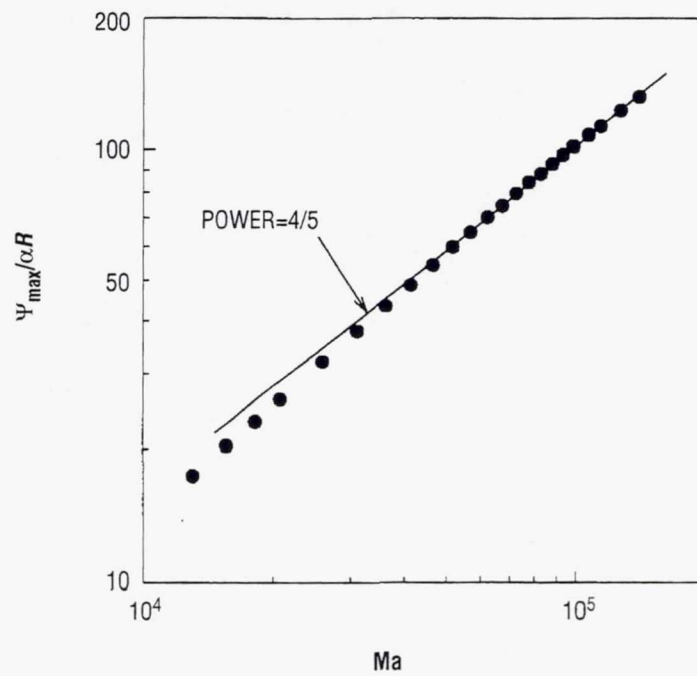


Figure 13. Scaling law for maximum stream function (CT configuration).

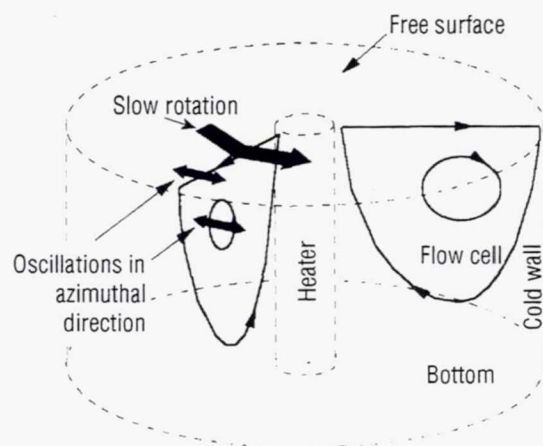


Figure 14. Qualitative sketch of the observed oscillatory flow field in CT tests.

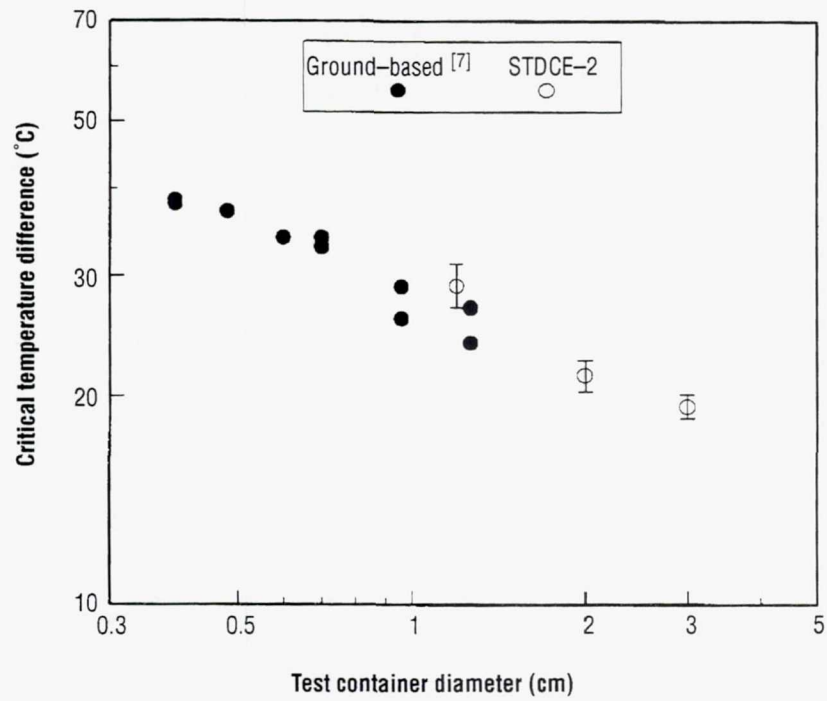


Figure 15. Experimental data for the onset of oscillations in different CT test.
(2 cS fluid, $Ar=1$, $Hr=0.1$, $Vr=1.0$).

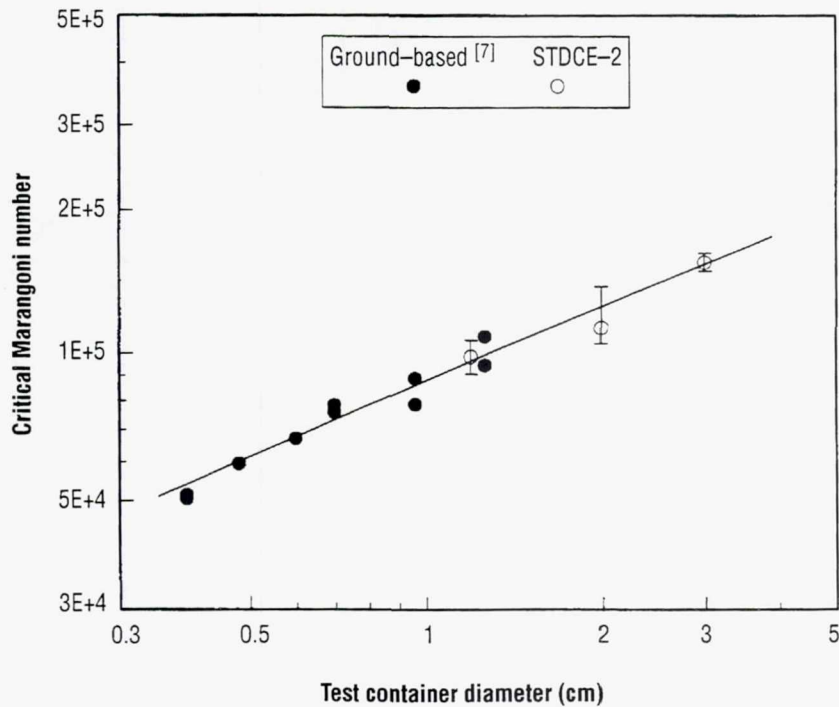


Figure 16. Variation of critical Marangoni number in various CT tests.
(2 cS fluid, $Ar=1$, $Hr=0.1$, $Vr=1.0$).

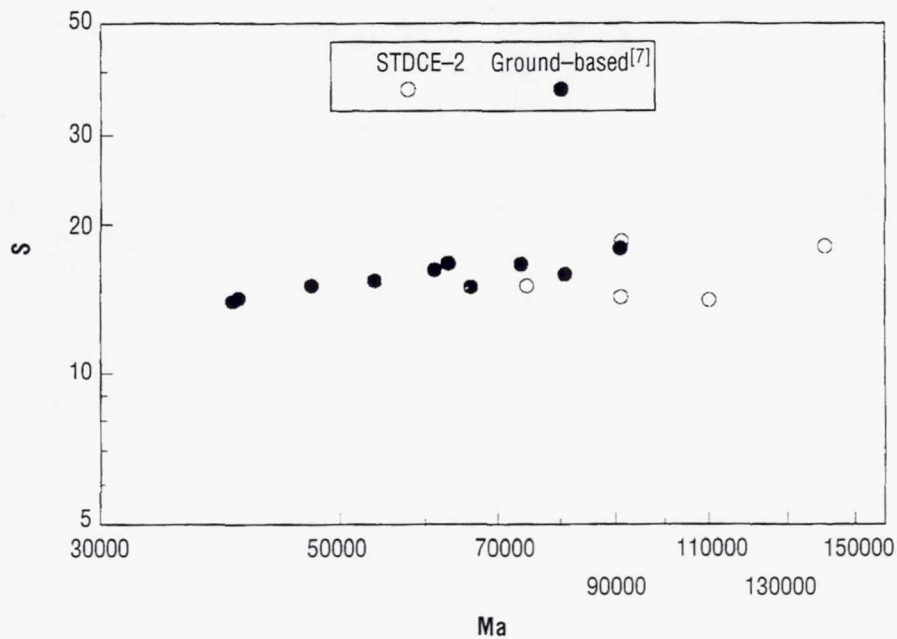


Figure 17. S-parameter at the onset of oscillations for flat surface CT tests.

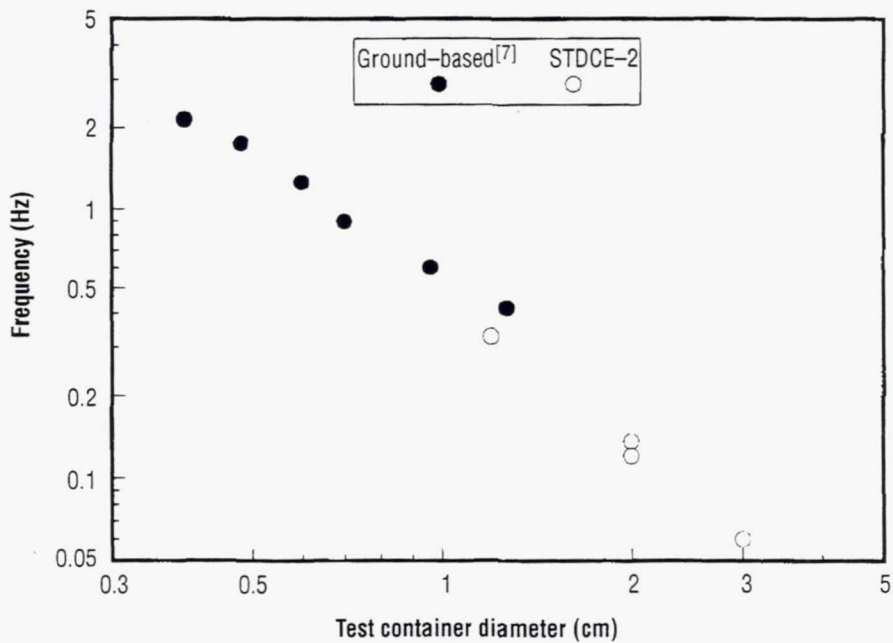


Figure 18. Variation of oscillation frequency at the onset of oscillations in CT tests.
(2 cS fluid, $Ar=1$, $Hr=0.1$, $Vr=1.0$)

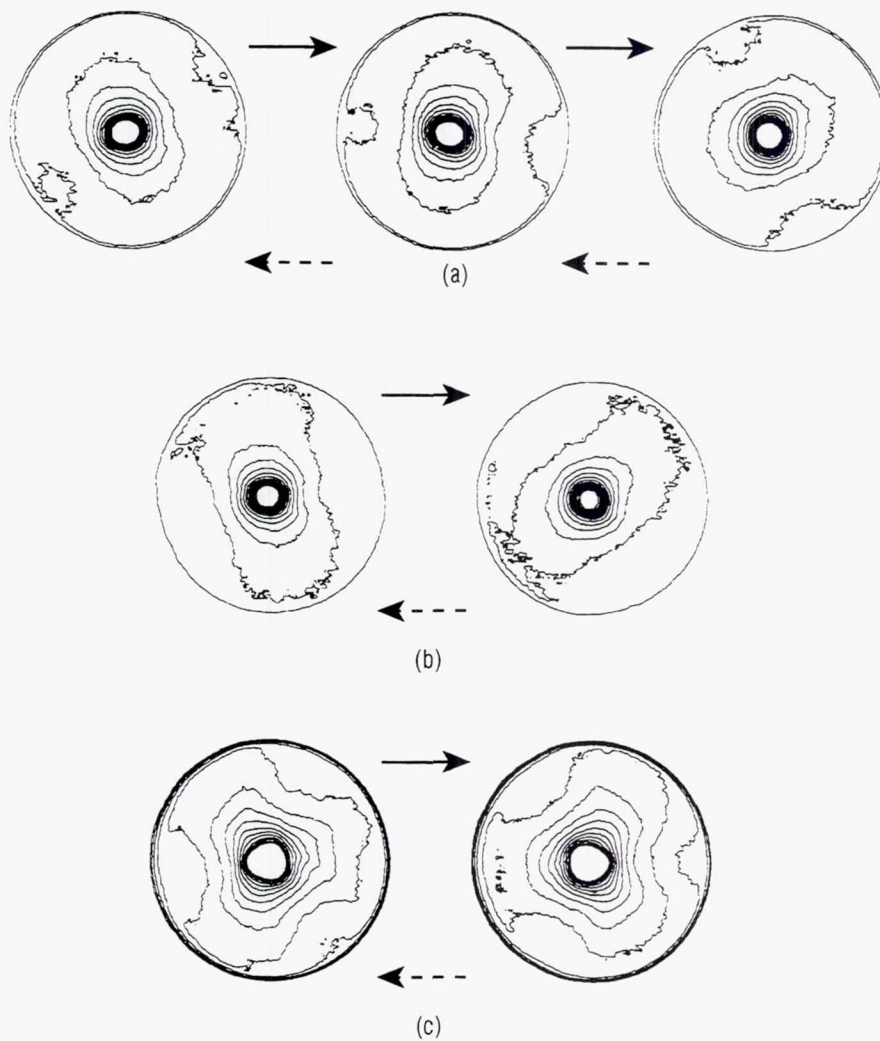


Figure 19. Various patterns of the free surface temperature measured by IR imager during oscillatory flow in flat surface CT tests: (a) two-lobed rotating pattern; (b) two-lobed pulsating pattern; (c) three-lobed pulsating pattern.

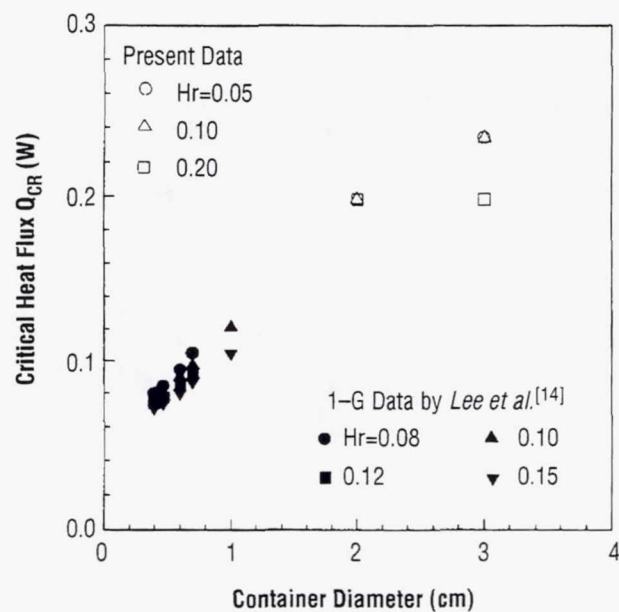


Figure 20. Critical heat fluxes for flat surface CF tests with $Ar=1$.

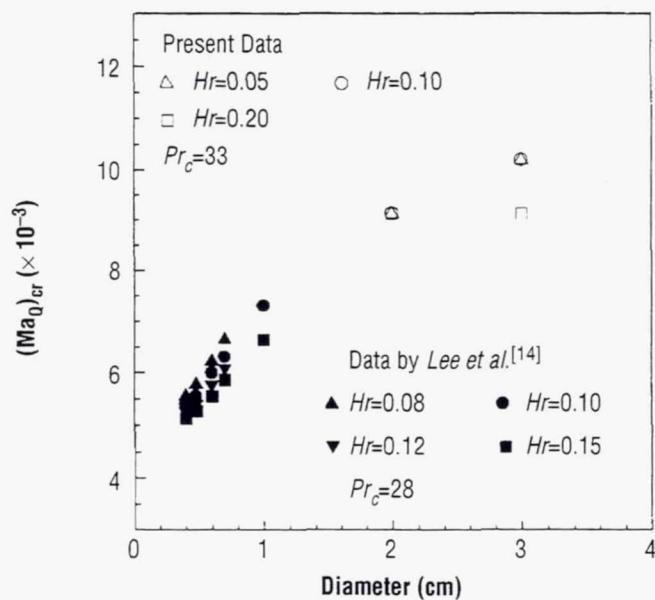


Figure 21. Critical Marangoni numbers for flat surface CF tests with $Ar=1$.

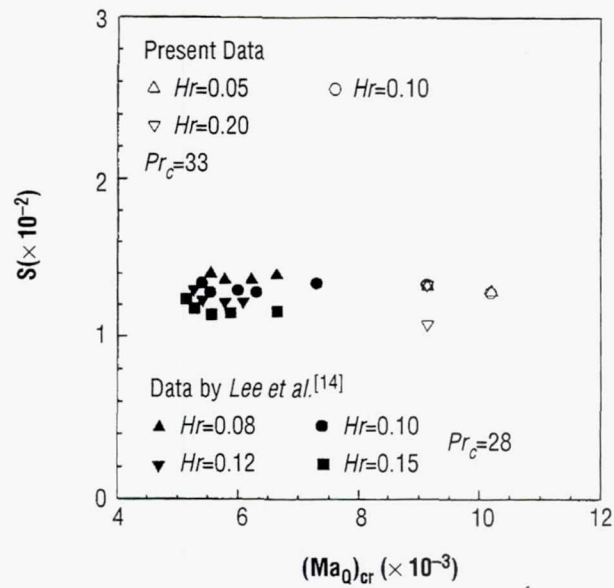


Figure 22. S-parameter for flat surface CF tests with $Ar=1$.

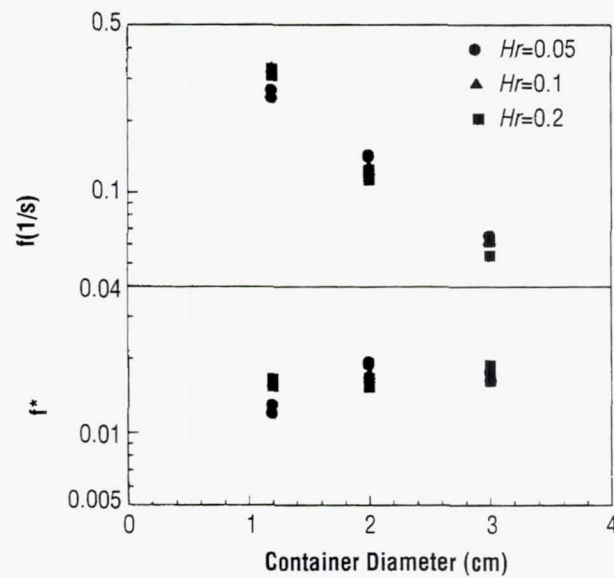


Figure 23. Dimensional and dimensionless oscillation frequencies near onset of oscillations for flat surface CF tests.

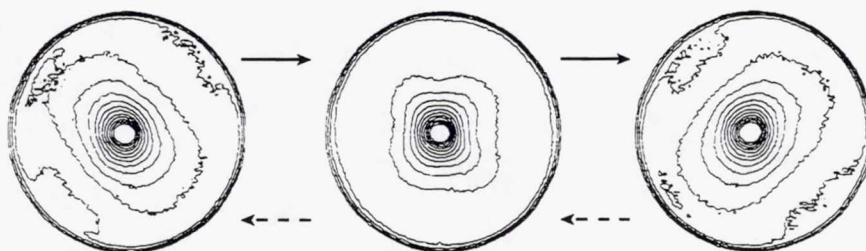


Figure 24. Thermograms during oscillations in flat surface CF tests.

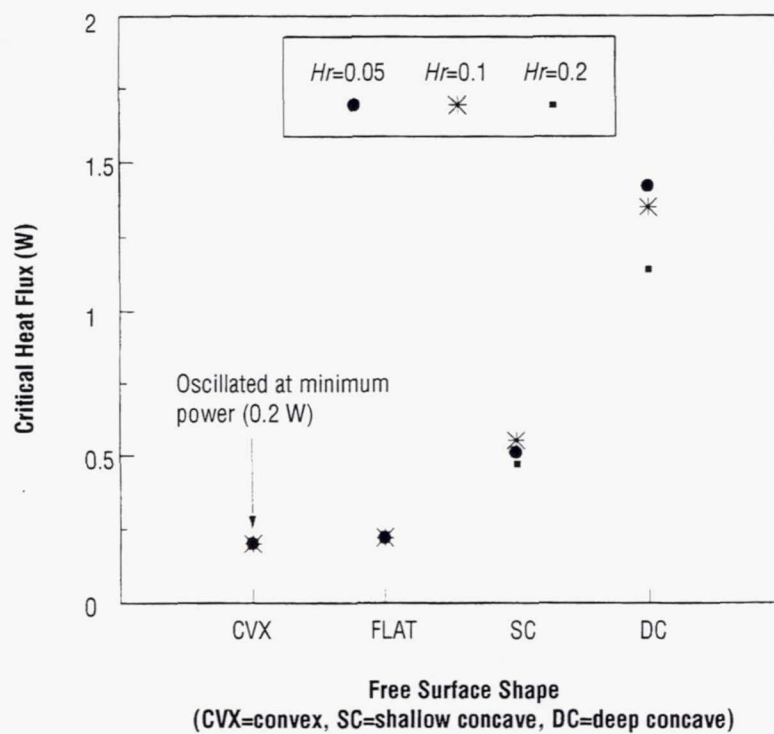


Figure 25. Critical heat fluxes for various surface shapes (CF test, $D=2$ cm).

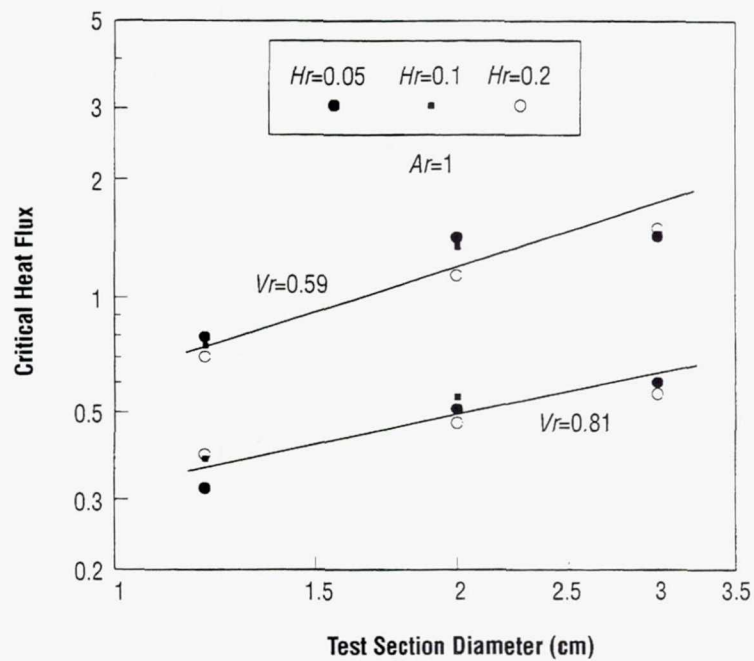


Figure 26. Critical heat fluxes under various conditions for $Ar=1$ CF tests.

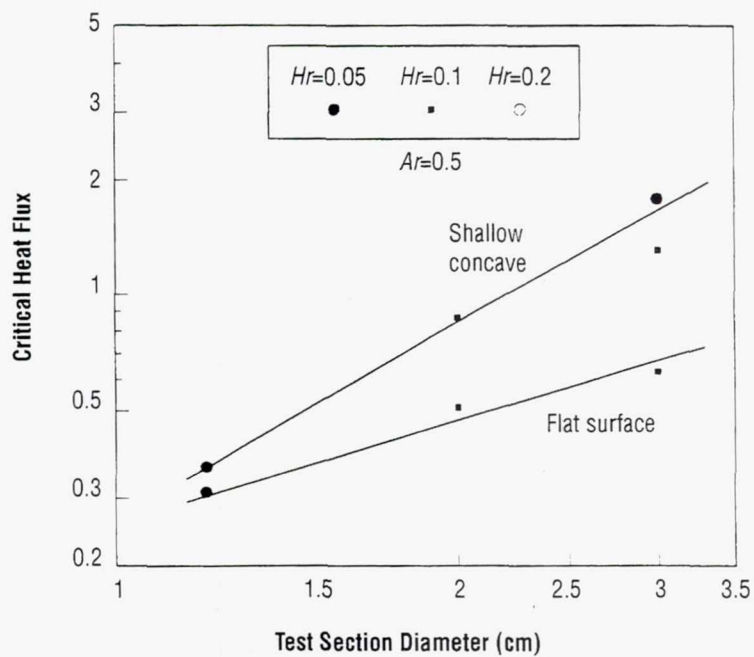


Figure 27. Critical heat fluxes under various conditions for $Ar=0.5$ CF tests.

EXPERIMENT VII.

THE GEOPHYSICAL FLUID FLOW CELL EXPERIMENT ON USML-2

ACKNOWLEDGMENTS

The authors thank the Microgravity Sciences and Applications Division of NASA for support of the GFFC flight experiment and the analysis of the unique data set obtained on USML-2. We are also grateful to Gary Glatzmaier, of Los Alamos National Laboratory, who supplied previews of their computational results for this publication.

EXPERIMENT VII: THE GEOPHYSICAL FLUID FLOW CELL EXPERIMENT ON USML-2

John E. Hart

Department of Astrophysical, Planetary and Atmospheric Sciences
Program in Atmospheric and Oceanic Sciences
University of Colorado, Boulder, Colorado 80309-0311
Phone: 303-492-4248
E-mail: hart@tack.Colorado.EDU

Daniel R. Ohlsen and Scott Kittelman

Program in Atmospheric and Oceanic Sciences
University of Colorado, Boulder, Colorado 80309-0311

Fred W. Leslie and Timothy L. Miller

Space Sciences Laboratory
Marshall Space Flight Center, MSFC, Alabama 35812

ABSTRACT

The Geophysical Fluid Flow Cell (GFFC) experiment performed visualizations of thermal convection in a rotating differentially heated spherical shell of fluid. In these experiments dielectric polarization forces are used to generate a radially directed buoyancy force. This enables the laboratory simulation of a number of geophysically and astrophysically important situations in which sphericity and rotation both impose strong constraints on global scale fluid motions. During USML-2 a large set of experiments with spherically symmetric heating were carried out. These enabled the determination of critical points for the transition to various forms of non-axisymmetric convection and, for highly turbulent flows, the transition latitudes separating the different modes of motion. This paper presents a first analysis of these experiments as well as data on the general performance of the instrument during the USML-2 flight.

1. INTRODUCTION

Large-scale motions of the atmospheres of planets and in the convection zones of rotating stars are strongly constrained by rotation, under the action of Coriolis forces, and gravity, which is manifest in the buoyancy forces that drive thermal circulations. The resulting flow structures are often surprising and continue to baffle scientists seeking fundamental understanding of such phenomena as the zonal bands of Jupiter, the origin of extremely high winds in the tropics and subtropics of Jupiter, Saturn and Neptune, the persistent differential rotation of the Sun, the complex patterns of convection in the slowly-rotating mantle of the Earth, and the rapidly rotating flows in the Earth's core that are thought to generate the Earth's magnetic field.

Several idealized theories have been offered as explanations for some of these phenomena. Busse^{1,2,3} considers that Coriolis forces-associated with planetary rotation dominate the large-scale (global) dynamics on the major planets. He hypothesized that motions in planetary atmospheres are constrained by the Taylor-Proudman theorem, which states that winds should be invariant along the axis of rotation for sufficiently high planetary rotation. His idea is sketched in figure 1. The axial invariance leads to a set of nested cylinders with convection occurring as columnar pipes inside the cylinders. Nonlinear interactions of individual convection columns can lead to large scale "zonal" winds (i.e., winds that are invariant with changes in longitude). The theories of Busse presume that the Taylor-Proudman theorem applies. However, this constraint is known to break down when stratification or turbulence (e.g., small-eddy viscosity) is strong enough. The precise nature of the breakdown of axial invariance due to turbulence is not known. A major goal of the USML-2 experiments was to observe the parameter-space dependence of this process for comparison with scaling theory and computational simulations.

2. THE PRINCIPLE OF THE GFFC

The microgravity laboratory allows the study of fundamental physical processes that are masked or overpowered by gravitational influences in the terrestrial laboratory. One such physical force in dielectric liquids is that due to imposed electric fields. In a thermally stratified fluid, the dielectric polarization force is small compared to gravitational thermally induced buoyancy unless the field strengths and dielectric constant are unrealistically large (e.g., the electric field is well above the dielectric breakdown point). Therefore microgravity is required. The GFFC is an instrument based on electrohydrodynamic flow instability in a spherical annular geometry. It can be shown that for the particular electrodynamic system we use, the dominant flow instability is directly analogous to the buoyancy driven modes in rotating spherical shells. Thus observations of the evolution of the electrohydrodynamic instabilities, and their dependence on rotation rates and other parameters, show us how normal buoyant fluids should behave in the presence of heating and radial gravity.

Detailed descriptions of the GFFC experiment have appeared previously^{4,5,6} so only a brief overview is given here. Figure 2 shows a cross section of the working cell. A dielectric silicone oil is contained in a hemispherical annular gap between a nickel sphere and a sapphire dome. The gap $d = R_o - R_i$ is about 1 cm (see table 1). By using servo-controlled heaters imbedded in the inner sphere, and at the pole and equator of the outer sphere, various temperature distributions can be set up on the two surfaces bounding the working fluid. These are denoted $T_i(\theta)$ and $T_o(\theta)$ respectively, where θ is the latitude. The simplest applied heating occurs when T_o and T_i are constant with $T_i > T_o$. This latitudinally invariant convectively unstable heating distribution corresponds, for example, to astrophysically motivated simulations of stellar convection where nuclear burning at the core leads to a spherically symmetric destabilization of the convection layer. Latitudinally varying heating relates to planetary convection situations where the differential heating from the Sun either dominates or significantly affects the circulation in the fluid. Cases with a hotter pole or a hotter equator are both of interest. The latter has obvious connections to terrestrial planets like the Earth, but the geophysically relevant distribution of boundary temperature depends on how, in the case of planetary atmospheres, solar radiation is deposited with altitude.

A large alternating voltage, V_o , is imposed across the working fluid (a transparent but electrically conducting coating of Indium is applied to the inner surface of the sapphire dome for this purpose). The

hemispherical annular gap shown in figure 2 is continued below the equator to form a spherical capacitor. The large voltage (up to 10 kilovolts rms) gives rise to a substantial electric field in the fluid. There then occur both electromagnetic and gravitational buoyancy forces in the fluid which are given by

$$\vec{F} = q\vec{E} - \frac{1}{2}E^2\nabla\epsilon + \frac{1}{2}\nabla\left\{E^2\rho\frac{D\epsilon}{D\rho}\right\} - \bar{g}\rho, \quad (1)$$

where q is the free-charge density, $E(r,t)$ the instantaneous electric field which is a function of radius r and time t , ρ the fluid density, ϵ the dielectric permittivity, and g the gravitational acceleration. E^2 is the dot product of the electric field vector.

The use of an alternating potential with a frequency large compared to the charge relaxation time for the silicone oil working fluid leads to a negligible contribution from the first term on the right side of equation (1). Because the oil is incompressible and divergence free, the flows are governed by vorticity equations. Thus the dynamically relevant forces are those which survive after taking the curl of equation (1). Namely,

$$\nabla \times \vec{F} = \rho_o \alpha \nabla T \times \nabla \phi + \epsilon_o \frac{\gamma}{2} \nabla T \times \nabla E^2, \quad (2)$$

where we have substituted the equations of state $\rho = \rho_o(1 - \alpha T)$ and $\epsilon = \epsilon_o(1 - \gamma T)$ for the density ρ and the permittivity ϵ as a function of the temperature T . Here α is the coefficient of thermal expansion and γ is the dependence of the dielectric constant on temperature. ϕ is the geopotential associated with whatever real gravity is present. Equation (2) shows that E^2 plays the same role as the geopotential in the dynamics.

Because $E^2 = \vec{E} \cdot \vec{E}$ has a time-average part that goes like r^{-4} , ∇E^2 is a radial vector decreasing like r^{-5} . For the narrow gap used in the experiment the difference between r^{-2} and r^{-5} is relatively insignificant. However, because ϵ is quite small for nonpolar fluids that can withstand a large applied potential, the electrodynamic buoyancy torques resulting from the curl of the polarization forces is small compared with terrestrial gravity. This smallness of the electrohydrodynamic polarization force is the main reason for placing the GFFC experiment in a microgravity environment. For example, table 1 gives typical values for the various parameters in the GFFC experiment. As shown in Hart et al.,⁴ the effective electromagnetic gravity is

$$g_{em} = 2\epsilon_o \frac{V^2 \beta^2 R_o^5}{(1 + \beta)d^3 \rho r^5},$$

where r is the radius and β is the ratio of the gap width d to the inner radius. Using a maximum voltage of 10 kilovolts and the values in table 1, it can be seen that the effective gravity is about 0.13 g's or less at the outer boundary, decreasing as V is lowered.

3. PREVIOUS TERRESTRIAL EXPERIMENTS IN RELATION TO GFFC

Previous laboratory studies of convection have been constrained to rotating layers between parallel plates oriented perpendicular to gravity.⁷ This is because when rotating shells are used, terrestrial gravity is no longer everywhere perpendicular to spherical surfaces so that symmetry with respect to geopotential is

lost and anomalous motions are generated. Even so, laboratory experiments in planar layers of rotating fluids have previously played a significant role in geophysical fluid dynamics. However, because terrestrial gravity and rotation are parallel in these experiments, only dynamics relevant to the polar regions of planetary atmospheres are addressed. Indeed it has long been a goal of fluid dynamicists to warp gravity in such a way as to allow a continuous variation of the angle between rotation and gravity vectors as is found in atmospheres and oceans of global extent. Prior to the GFFC this was only possible in a fluid of constant density, or in fluids with a very limited representation of thermal stratification. For example, Hart⁸ studied β -plane dynamics for two immiscible fluid layers in which the aforementioned angle varies from one side of the experiment to the other.

4. CONTROL PARAMETERS AND EXPERIMENT PROCEDURES

There are four fundamental dimensionless parameters for the GFFC. The Prandtl number (the ratio of kinematic viscosity to thermal diffusivity) is fixed at 8.4. The aspect ratio β is fixed at 2.65. The Taylor number $Ta \equiv 4\Omega^2 d^4 / \nu^2 = 2.43 \times 10^6 / \tau^2$ (where τ is the rotation period of the cell) measure the effects of rotation relative to viscosity. The period ranged from 2 to 255 seconds. The Rayleigh number $Ra = g_{em} \gamma \Delta T d^3 / \kappa \nu = 218.4 \nabla T V^2$, where ∇T is the applied radial temperature difference (degrees C) and V is the applied voltage in kilovolts, measures the relative effects of buoyancy and diffusion. The temperature differences were typically about 15 degrees while the applied voltages ranged from 0 to 10 kV. In addition to these nondimensional numbers relating the magnitudes of the experimental controls, there is also the prescribed distribution of temperatures on the inner and outer spheres. These scale with ∇T , but with spherically symmetric thermal boundary conditions no additional information is required to specify the system.

Figure 3 shows a schematic of the GFFC instrument as flown on USML-2. The cell is mounted on a turntable containing devices to regulate the temperature on the spherical shells. Visualization of the electrohydrodynamical buoyancy modes is obtained remotely, as any probes will perturb the desired spherical symmetry of the electric field and would find themselves in a very hostile electromagnetic environment. An aspheric lens assembly projects a Ronchi ruling onto the inner sphere. This is reflected back upon the ruled grid itself and the resulting image is then photographed on 16-mm film. Upon traversing the working fluid, light rays are bent due to index of refraction fluctuations in the silicone oil that are in turn caused by temperature variations in latitude or longitude. Thus the film records images which depict radially averaged horizontal temperature gradients in the fluid. These reveal patterns of convection which arise under various external conditions: rotation rate Ω , applied gravity (i.e., V), and heating distribution. During the filming, experiment performance data are recorded in digital (both decimal and binary) form on each frame. After the mission these data were read by a digital image acquisition system on the ground after the film is processed. The images of the convection cell were also recorded by a video camera. This video image includes four pieces of information concerning the experiment parameters. This is a very small fraction of the parameter and performance data recorded on the 16-mm film. Thus the film was the primary data storage medium for refined analysis after the flight, but the video system allowed for interactive experiments to be carried out during the USML-2 mission.

The generic experiment procedure was:

1. Fix the external parameters of the experimental run. These are the rotation rate Ω , the photography protocols, and the boundary temperature distributions.
2. After an initial setup, begin taking 16-mm photographs through the backfocus Schlieren system. The frame rate was about 1 per rotation of the cell at high rotation rates ($\Omega > 1$ radian per sec.), making it possible to reconstruct a long time series of images to look for periodicities, aperiodicity, etc.
3. Repeat with the new Ra (obtained by ramping or jumping the applied voltage V).
4. After a range of Ra 's are explored at fixed Ω , T_i , and T_o , move on to cases with different rotation rates and heating distributions. Each Ra ramp experiment lasted 6 hours. In all, thirty 6-hour runs were made.

4. INSTRUMENT PERFORMANCE

During the USML-2 mission the downlinked astronaut monitoring information suggested there was a problem with the thermal controller. The actual temperatures obtained on the spheres did not match the commanded values very well. The binary LED data on the film, after using the postflight thermal calibration curves, confirmed this. Figures 4 and 5 illustrate the history of boundary temperatures for two 6-hour runs. Both runs have horizontally uniform commanded temperatures of 25 (outer sphere) and 40 (inner sphere) degrees. Because of calibration shifts (possibly during launch), the controller thought the outer sphere was too hot, and reacted by cooling it too much. However, during the run, as convection transferred heat from the inner to the outer sphere, the instrument cooler could not keep up and the inner sphere drifted upwards. Also notable is the nonuniformity of inner sphere temperature, approaching 10 percent of the applied gradient.

The astronaut monitoring of the instrument panel suggested that experiments which commanded large imposed latitudinal temperature differences (with latitudinal variations as large or larger than the requested radial variation) were in thermal error by order one amounts. In these cases, use of the postflight calibration indicated better performance than expected from the real-time monitoring data sent down during the flight, but still with considerable (30 percent) differences from the commands. This means that it will likely be necessary to use the detailed thermal data taken from the film to build useful interpretive computational models of the GFFC results because one cannot rely on the assumption that the commanded temperatures actually were attained during the USML-2 runs. Unfortunately the film camera failed during run 19 (out of 30), so that it is impossible to get detailed quantitative results from the last 11 experiments because precise data on the thermal boundary conditions are not available for these runs. However, the downlinked video provides some qualitative information on flow states.

5. RESULTS FOR SPHERICALLY SYMMETRIC HEATING

Runs 1 through 19 concentrated on the issue of the evolution of convection with spherically symmetric heating. Of these 19 runs, for which full 16-mm film data were obtained, only runs 2 and 19 had commanded nonsymmetric (i.e., latitudinally varying) thermal boundary conditions.

Figure 6 summarizes several of these spherically symmetric runs by showing individual snapshots of the convection on the parameter plane of the experiments. $H=0$ denotes spherically symmetric heating. Each image shows the equivalent of an astronomer's telescopic view of a star with the south pole at the bottom and the equator at the top. For high Taylor number (low rotation period, e.g., 2 seconds) the convection initiates as prograde propagating polar disturbances, followed closely, as Ra is increased, by north-south oriented columnar ("banana cell") modes (compare to fig. 1).

The GFFC camera can be set to take a sequence of images each 45 degrees in longitude. If the motion is not evolving too fast in time, it is possible to take a set of eight of these telescopic views, unwrap the peculiar birds-eye geometry, and merge the images into a full hemispheric (equal latitude line) projection. Figure 7 illustrates one example of this processing technique for a state with both propagating banana cell disturbances and nonperiodic polar waves. A computational simulation of this state by Miller and Leslie is included for comparison. At weak-to-moderate supercriticality the comparison between simulation and experiment is reasonably good.

As Ra moves higher so that the motions become turbulent, the polar convection eats northwards into the banana cell regime, basically eliminating the presence of axially symmetric elements in the motion. As the period of rotation is increased, the convection states become more complicated. The separation of polar and banana cells decreases and the eradication of banana cells with increasing Ra is more rapid.

At very low Taylor number (long period of rotation) the convection is more transitory and patterns are less well defined. However, some runs showed evidence for persistent states with relatively simple geometry. Figure 8 shows some examples from a run with a 48-second period. The voltage was commanded to ramp quickly to 1.5 kV, hold there, then run up to 3.5 kV and back down to hold at 1.5 kV again. During the first 4 hours of the run, the states (fig. 8a, 8b) were irregular in time and space. However, the system finally settled down into a persistent wavenumber two propagating eddy (fig. 8c). One possible conclusion is that the system exhibits hysteresis (e.g., fig. 8a and 8c are two fundamentally different states that are possible at essentially the same parameter setting). However, because the flows near figure 8a are not periodic, while figure 8c is, another interpretation is simply that it takes many hours for the fluid system to equilibrate and the images in figure 8a and 8b have not reached statistical equilibrium.

5.1 Computational Simulation of Spherically Symmetric Flows

Figure 9 shows a regime diagram obtained from a 3D computational "Miller-Leslie" model (a variant of that described by Miller, et al.⁹), using 30 radial points, 62 latitudinal points and 45 longitudinal wavenumbers. The model boundary conditions correspond to the experiment, except that purely symmetric temperatures (e.g., averaging fig. 4 in latitude) were used. At high Taylor number the states are similar with prograde propagating polar modes coming in first as Ra is increased, and clear indication of banana cells in the mid-latitudes and tropics. The states at low Taylor number appear to be more stable (less transitory) than in the experiments. Multiple states (or hysteretic behavior) were found in the simulations. For example there are two qualitatively different but persistent states of motion at $Ta = 1000$, $Ra = 20,000$. In general, the simulations using this model do a good job at describing the motions at high Ta and low-to-moderate Ra , but seem to give overly simple states at low Ta . At low Ta the onset of convection occurs at a lower Ra , and the supercriticality at a fixed voltage (3 kV, for example) is much higher so that there may

be resolution problems in some of the low Ta runs. Also, at this time it is not known how sensitive the computed flows are to modest latitudinal variations in the boundary temperatures.

5.2 The Onset of Convective Instability

A new camera action protocol, implemented on the USML-2 flight that gives a closely spaced time series of images at a fixed longitude permits an accurate determination of the onset of convection (i.e., the fundamental horizontal symmetry breaking instability). Figure 10 shows the observed onset points. As illustrated in figures 6 and 7, there are two types of modes, prograde polar and prograde propagating banana cells, the latter having strong north-south alignment. The experimental curves represent fits through data from nine runs at different rotation rates. At high Ta polar modes come in first as Ra is raised, while at lower Ta the banana cells onset first.

Onset data can be compared with predictions of computational simulation, and this provides a useful validation of the latter because the weak motions associated with the instability tests most of the terms in the model while not requiring enormous 3D resolution. Figure 10 shows that the Miller-Leslie model comes quite close to the experimental result for the 4-second period, although the separation between polar and banana modes is smaller than observed and the onset points are slightly higher. More simulations that include a fit to the actual (not smoothed) thermal boundary conditions are planned. The Glatzmaier^{10,4} model has higher resolution, but because it is a pseudo-spectral code, it does not implement the rigid boundary condition of the GFFC present at the equator (fig. 2). The tips of the banana cells should generate Ekman layers along the equatorial barrier, and should be more damped in the presence of this wall. Thus it is not too surprising that the Glatzmaier model predicts that banana cells should arise first, at a lower Ra .

5.3 Transition Latitudes for Turbulent Flows

A very important result from the GFFC experiments, obtained by combining data from the 18 runs done with symmetric heating, is an estimate of the parametric conditions required to observe axial (banana cell) convection in highly nonlinear and turbulent flow. Such results cannot be obtained computationally over the entire range of the GFFC parameter values. What is the latitudinal limit for banana (axially aligned) structures in the flows? If this critical latitude shrinks to zero, then the object will not have a banana cell regime. If the results from the experiments conform to an asymptotic scaling relation, then it might be possible to use the GFFC results to predict whether or not a rotating star or planet will have aligned giant cells in its atmosphere. Figure 10 shows data for one rotation rate. As the voltage increases the banana cell domain shrinks towards the equator. For $V > 8$ kilovolts, the basic planetary rotation is too weak to align the motion in the north-south direction.

Attempts to derive a scaling in this complex geometry typically involve some perhaps tenuous assumptions, but the GFFC results can be used as an independent check. One simple idea is that the transition boundary is related to the existence of more constrained geostrophic convection equatorward of a transition latitude θ , and we take θ to be the latitude at which the convection has unit Rossby number. The Rossby number measures the relative strengths of advection and Coriolis forces and is given by $R_o = U / 2\Omega \sin(\theta)d$ where U is a characteristic convection velocity. If we take the convection velocity to

be estimated by buoyancy-induced free fall, then $U \approx \sqrt{g_{em} \gamma \Delta T d}$ and setting the Rossby number equal to 1 gives the scaling relation (for fixed Prandtl number):

$$\sin(\theta) \propto R_a^{-1/2} T_a^{1/2} \propto (\tau V)^{-1}. \quad (3)$$

An alternative model, using estimates of U from the numerical β -convection model of Brummell and Hart¹¹ that includes local boundary curvature in the dynamics, gives a somewhat different scaling:

$$\sin(\theta) \propto R_a^{-3/4} T_a^{15/24} \propto V^{-3/2} \tau^{-5/4}. \quad (4)$$

In the second result the transition latitude falls faster with V because in the Brummell-Hart free slip β -convection model, the motions develop high speed jets by mean flow instability. The zonal flows dominate the convection and the high velocities associated with these jets lead to a prediction that unit Rossby number is reached sooner.

Figure 11 shows that the data are consistent with the simple thermal Rossby number scaling. The data are not consistent with the β -convection scaling. This is in concert with the observation from GFFC that no high-speed jets (which would be associated with anomalous disturbance propagation rates) were observed. Also, the β -convection model predicts vacillatory states involved with mean flow instability. Such periodic pattern pulsation states were not seen in the USML-2 GFFC results. Thus full sphericity seems to detract from the potential for strong jet formation. This result needs to be tempered by the possibility that the GFFC experiments, conducted with a Prandtl number of 8.4, may not accurately predict what might happen in a low Prandtl flow, or in atmospheres with forcing parameters well outside the GFFC experimental range. If, however, the Prandtl number dependence turns out to be weak (as checked, perhaps, by computational simulation), the scaling (3) may allow determination of the flow regimes to be expected in rotating stars and planets where the applied temperature difference (or supercriticality) is known. Unfortunately whereas (3) is independent of diffusion parameters (a plus!), if one must use observations of emitted heat flux in order to estimate the Rayleigh number (through a Nusselt number scaling), this then reintroduces the thermal diffusivity into the scaling. Future work in the application of such scaling relations as (3) and (4) to astrophysical situations will determine whether or not the obstacle of having only a poor knowledge of small-eddy diffusivity is significant.

6. CONCLUSIONS

The GFFC experiments on USML-2 returned an extensive data set on the nature of convection in rotating spherical shells with nearly horizontally symmetric applied thermal boundary conditions. The main results extracted to date are as follows:

- 1) Good agreement between computational simulations of the onset of instability and the experiments;
- 2) Observation of much more complicated and transitory convection at low rotation than found in the models;

- 3) Lack of experimental evidence for vacillatory states and states with high speed zonal jets as predicted in some pre-mission theories and models; and
- 4) Approximate verification of a simple scaling law for the existence of columnar convective turbulence in highly stressed shells.

Future analyses and comparisons with models will focus on how weak latitudinal variation in boundary temperatures may influence the dynamics, whether or not simulations with higher resolution can recover some of the low rotation GFFC results, and on further characterizations of the important high Rayleigh number turbulent states observed in rotating spherical shells.

REFERENCES

1. Busse, F.H.: "Thermal Instabilities in Rotating Systems," *J. Fluid Mech.*, 44, 441–460, 1970.
2. Busse, F.H.: "Differential Rotating in Stellar Convection Zones II," *Astron. and Astrophys.*, 28, 27–37, 1973.
3. Busse, F.H.: "A Model of Mean Zonal Flows in the Major Planets," *Geophys. and Astrophys. Fluid Dyn.*, 23, 153–174, 1983.
4. Hart, J.E.; Glatzmaier, G.A.; and Toomre, J.: "Space-Laboratory and Numerical Simulations of Thermal Convection in a Rotating Hemispherical Shell With Radial Gravity," *J. Fluid Mech.*, 173, 519–544, 1986a.
5. Hart, J.E.; Toomre, J.; Deane, A.; Hurlburt, N.E.; Glatzmaier, G.A.; Fichtl, G.H.; Leslie, F.; Fowles, W.W.; and Gilman, P.A.: "Laboratory Experiments on Planetary and Stellar Convection Performed on Spacelab 3," *Science*, 223, 61–64, 1986b.
6. Hart, J.E.: "Microgravity Laboratory Simulations of Planetary and Stellar Circulations," *Microgravity Science and Technology*, 3, 143–147, 1990.
7. Rossby, H.T.: "A Study of Benard Convection With and Without Rotation," *J. Fluid Mech.*, 36, 309–335, 1969.
8. Hart, J.E.: "A Laboratory Study of Baroclinic Instability," *Geophys. & Astrophys. Fluid Dynamics*, 3, 181–209, 1972.
9. Miller, T.L.; Lu, H.I.; and Butler, K.A.: "A Fully Nonlinear, Mixed Spectra and Finite-Difference Model for Thermally Driven, Rotating Flows," *J. Comp. Physics*, 101, 265–275, 1992.
10. Glatzmaier, G.A.: "Numerical Simulations of Stellar Convective Dynamos. I. The Model and Method," *J. Comp. Phys.*, 55, 461–484, 1983.
11. Brummell, N.; and Hart, J.E.: "High Rayleigh Number β -Convection," *Geophys. and Astrophys. Fluid Dynamics*, 68, 85–114, 1992.

Table 1. Experiment parameters and characteristics of Dow Corning 0.65 centistoke silicone oil.

Nominal Fluid Properties (Dow Corning 0.65 cs 200 fluid)		
Ambient density	$\bar{\rho}$	760 kg/m ³
Expansivity	α	$1.34 \times 10^{-3} \text{ }^{\circ}\text{C}^{-1}$
Kinematic viscosity	ν	$6.5 \times 10^{-7} \text{ m}^2/\text{s}$
Thermal diffusivity	κ	$7.7 \times 10^{-8} \text{ m}^2/\text{s}$
Ambient permittivity	$\bar{\epsilon}$	$2.5\epsilon_0$
Vacuum permittivity	ϵ_0	$8.90 \times 10^{-12} \text{ farad/m}$
Dielectric variability	γ	$1.29 \times 10^{-3} \text{ }^{\circ}\text{C}^{-1}$
Conductivity	σ	10^{-12} mho/m
Heat capacity	c	$1.7 \times 10^3 \text{ joules/kg }^{\circ}\text{C}$
Dissipation loss factor	ϕ	$\approx 4 \times 10^{-5}$
Nominal Experiment Parameters		
Rotation rate	Ω	0–3 rad/s
Radial temp. difference	ΔT_r	0–25 $^{\circ}\text{C}$
Voltage (r.m.s.)	V	0–10 kV
Voltage frequency	ω	300 Hz
Inner radius	R_i	2.402 cm
Outer radius	R_o	3.300 cm
Gap	d	0.908 cm
Aspect ratio	$\beta = R/d$	2.65
Prandtl number	Pr	8.4

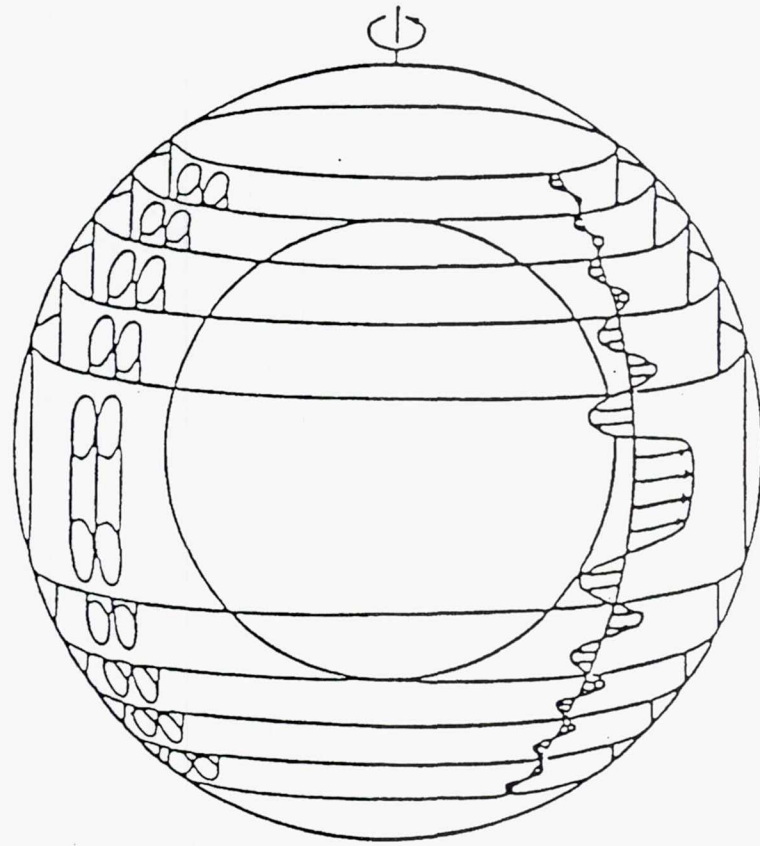


Figure 1. Nested convection cylinders in a rapidly rotating convecting liquid (after *Busse*, 1983).

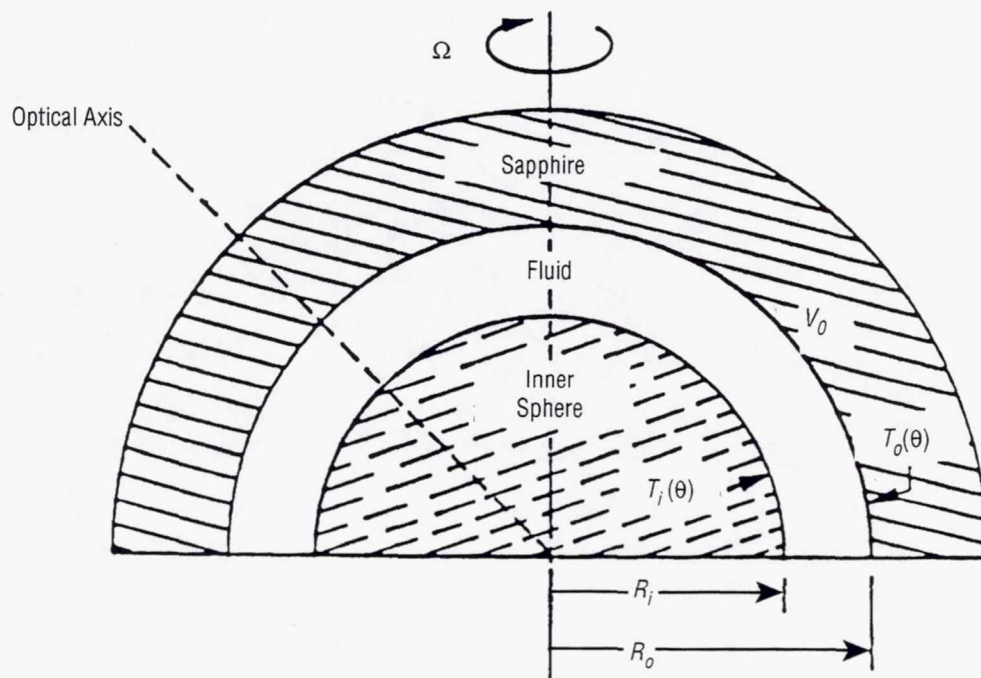


Figure 2. Schematic cross-section of the geophysical fluid flow cell. The gap contains 0.065 centistoke silicone fluid.

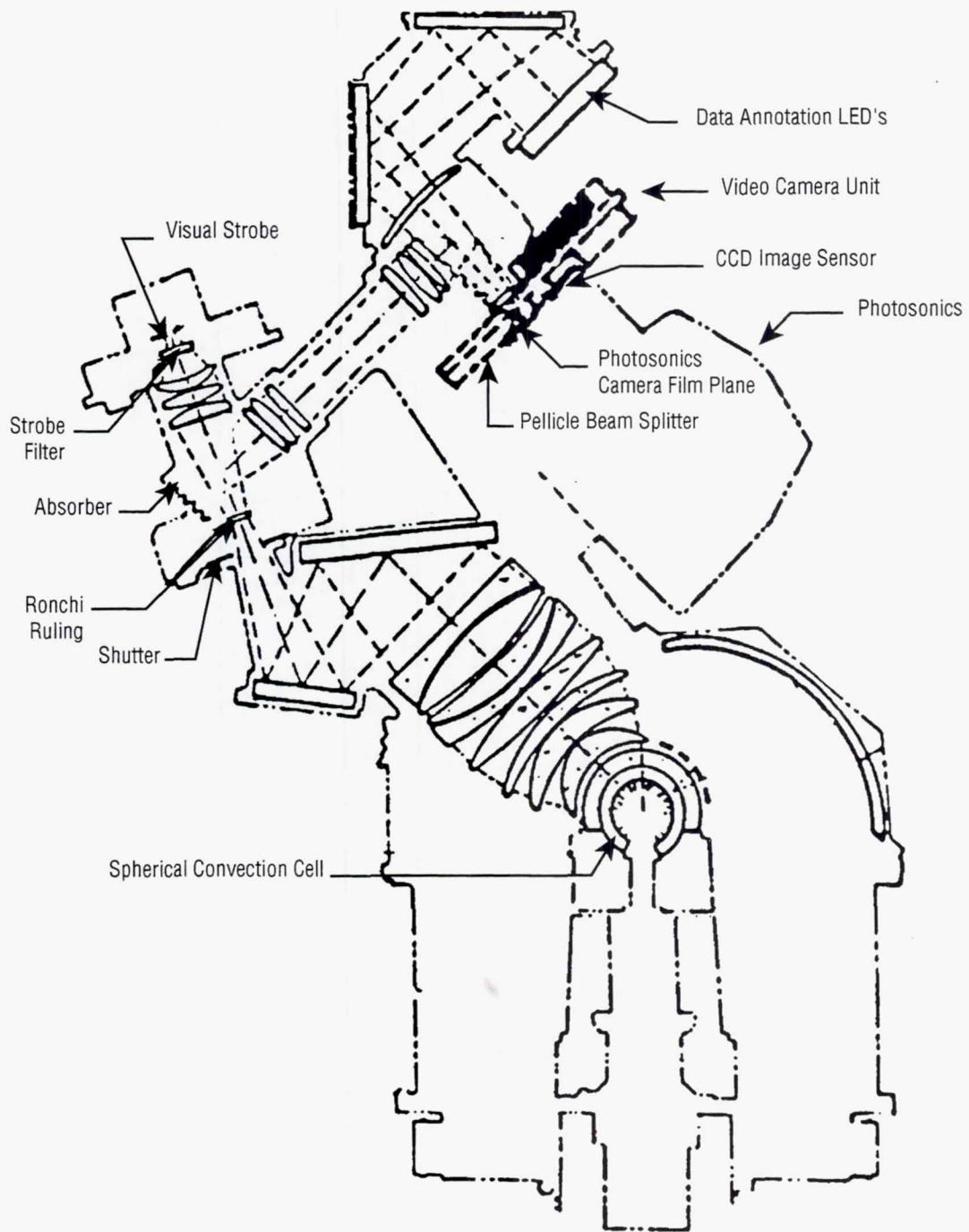


Figure 3. Instrument cross-section. The optics provides a Schlieren visualization of convection in the spherical convection cell. A beam splitter diverts the image to both a 16 mm and a video camera.

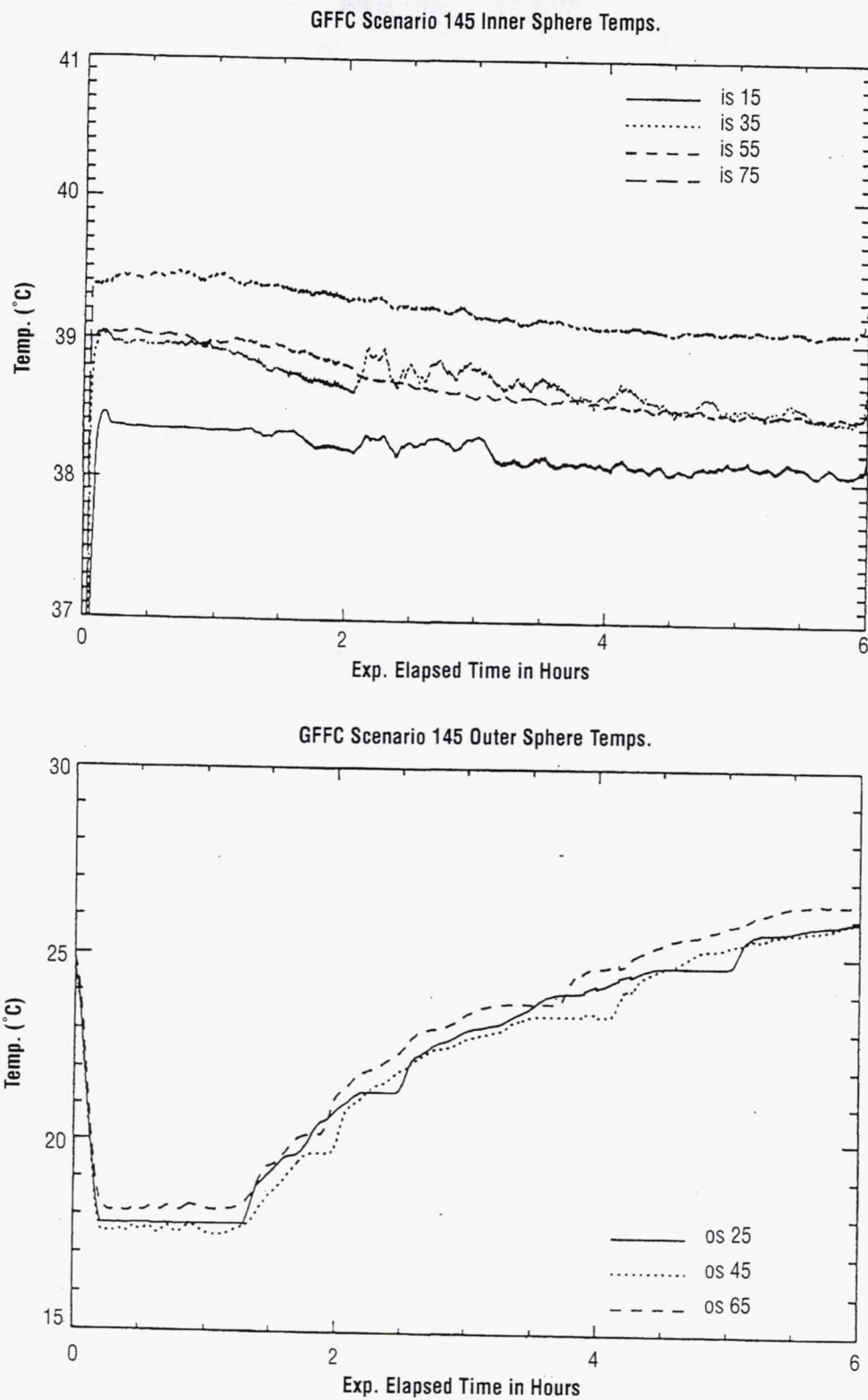


Figure 4. Thermal history at the walls for scenario 145 (4 second basic rotation period, high voltage ramping from 0 to 10 kV). The upper panel shows the inner sphere values at the latitudes shown, while the lower panel illustrates the behavior of the outer sphere at the latitudes shown.

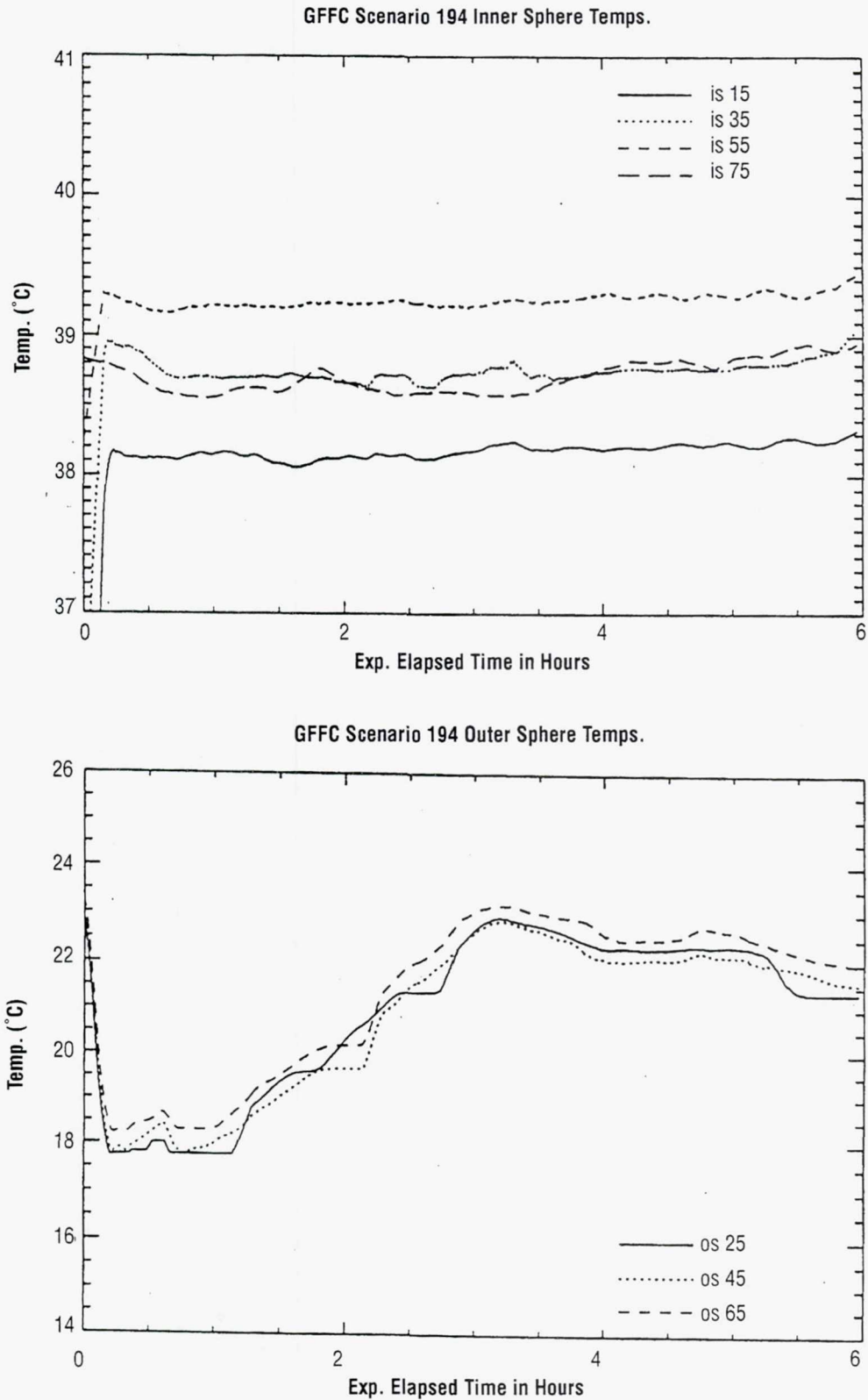


Figure 5. Thermal history at the walls for scenario 194 (48 second basic rotation period, high voltage ramping from 0 to 3.5 kV and back down again). The upper panel shows the inner sphere values at the latitudes shown, while the lower panel illustrates the behavior of the outer sphere at the latitudes shown.

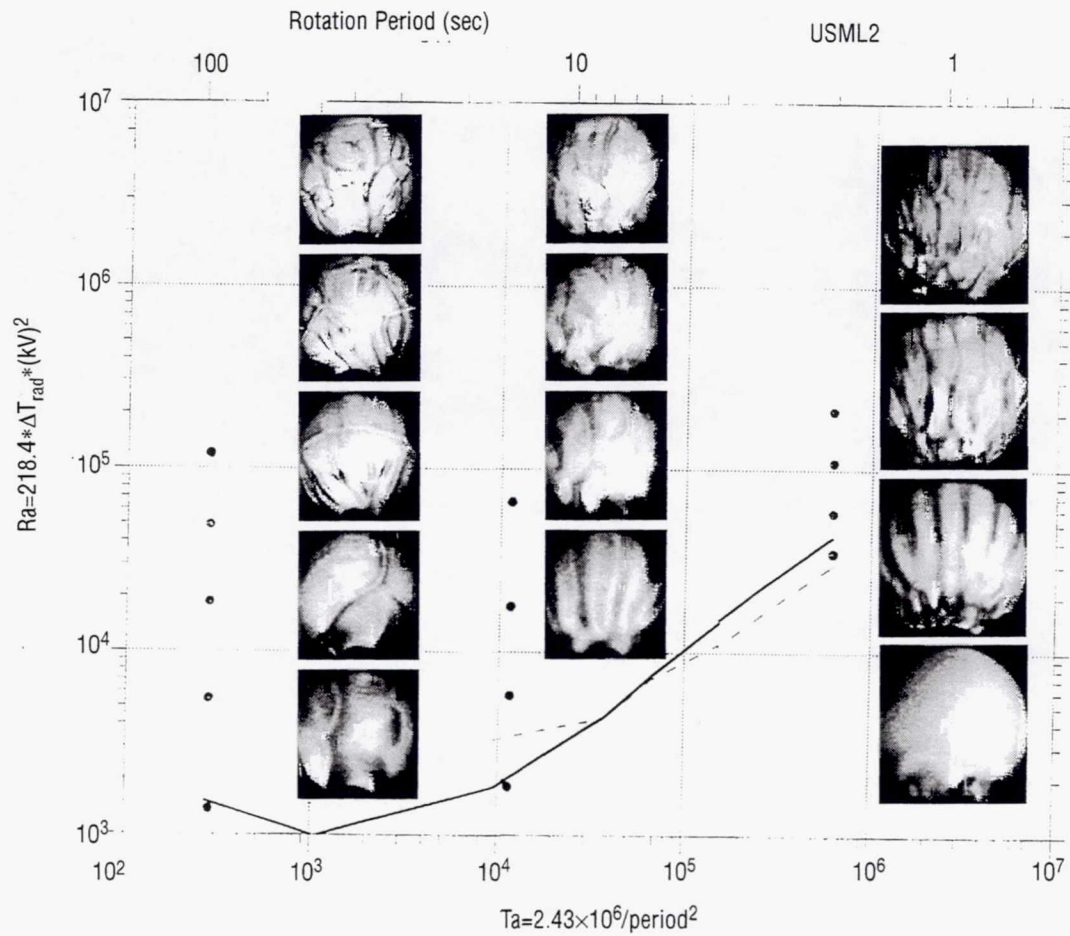
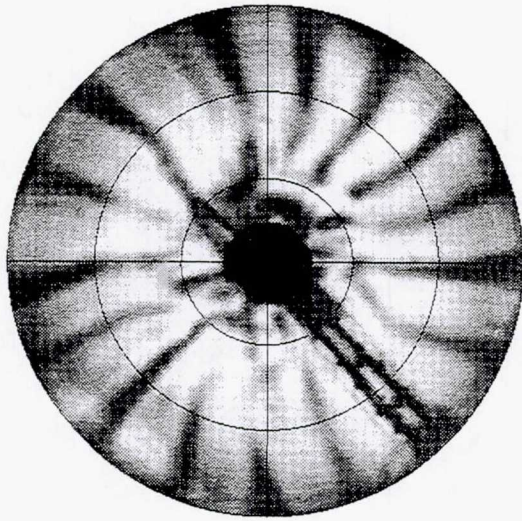
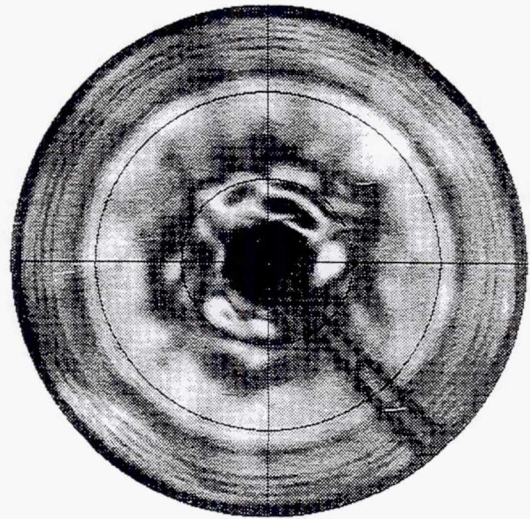


Figure 6. Regime diagram showing qualitative results for several Rayleigh number ramp up experiments with symmetric heating. Each image is a single snapshot with the south pole at the bottom and the equator at the top. The solid curve shows the onset of banana cell, the dashed the onset of polar wavy convection. Each image corresponds to the dot to its left, in vertical order.



kV:2.16000



kV:2.16000

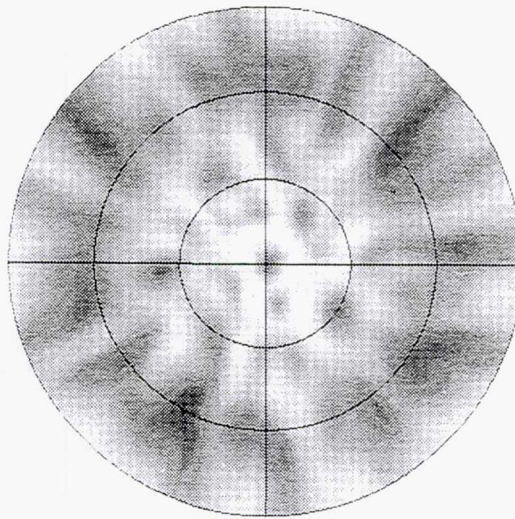
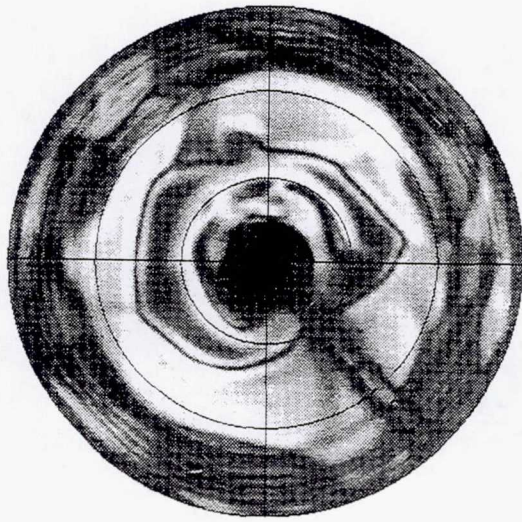
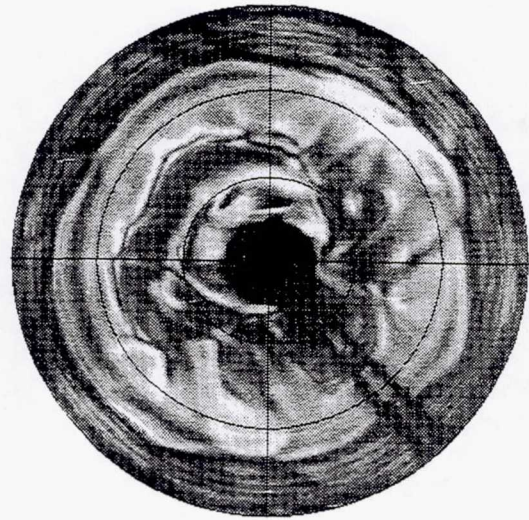


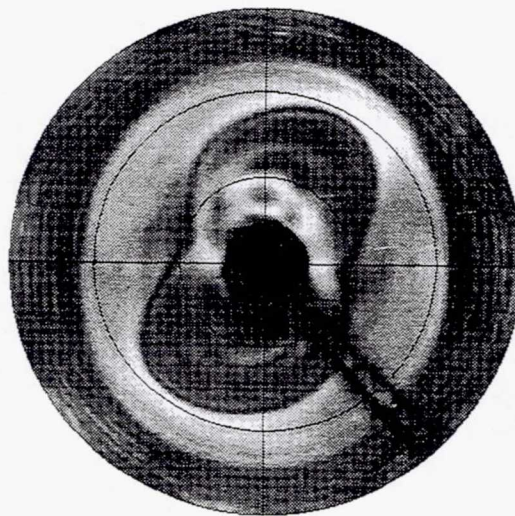
Figure 7. Unwrapped convection planforms for scenario 145 (4-second rotation, symmetric heating, 2.16 kV). The top two panels show motions as viewed by “E–W” fringes (left) that are sensitive to longitudinal temperature gradients, and “N–S” fringes (right) that are sensitive to latitudinal gradients. The bottom panel shows radially averaged temperatures from the Miller–Leslie model. Note the general agreement on structure and equivalence of disturbance longitudinal wavenumber. In all frames the view from pole (center) to equator (limb) with equal spacing of latitude lines.



kV:1.46000



kV:3.16000



kV:1.26000

Figure 8. Unwrapped views (as in fig. 7) of scenario 194 (48 second rotation period, symmetric heating). N-S fringes (sensitive to longitudinal thermal gradients) for the values of voltage shown. The first two images (top left and right) are during the first three hour ramp up, while the bottom (the only stable patterns) is at about hour five. The first image is during the first voltage hold period, the second during the ramp up to 3.5 kV, and the third just after the end of the second voltage hold period.

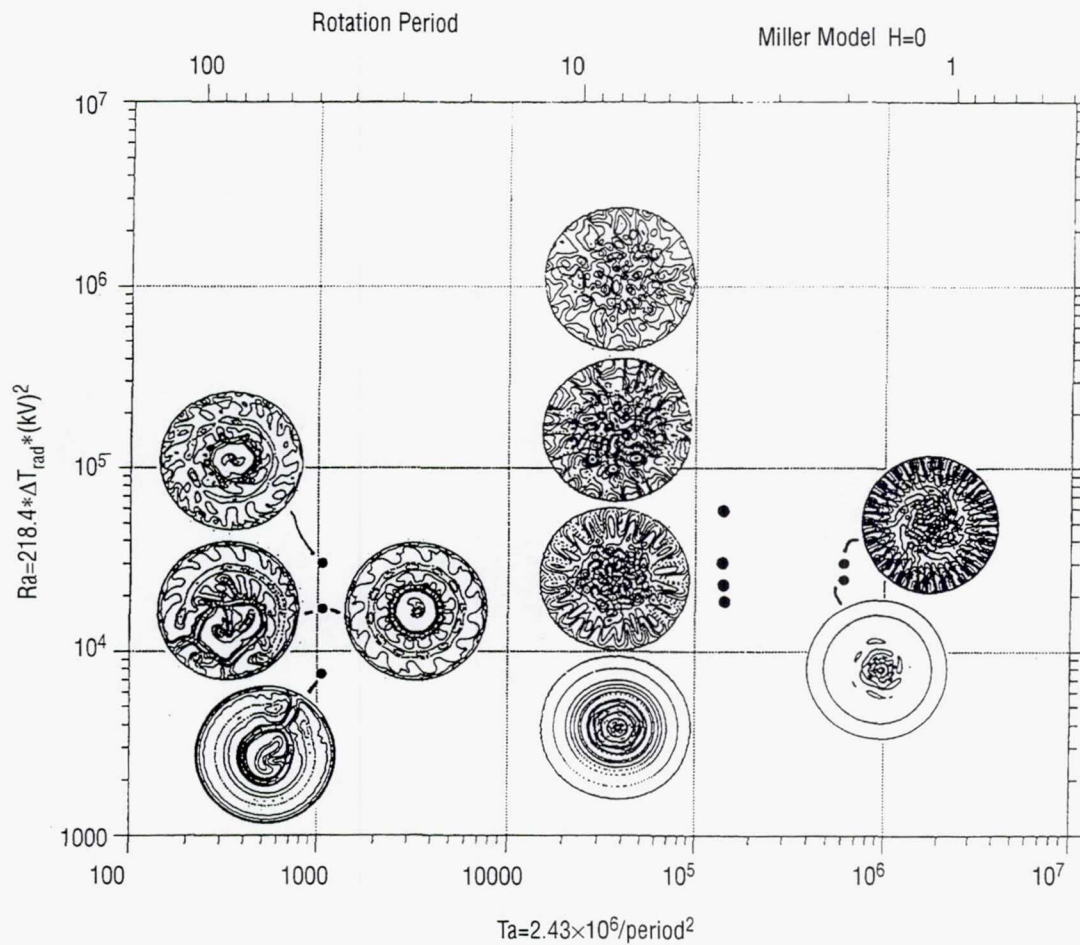


Figure 9. Regime diagram showing computed planforms in the Miller-Leslie model (Fourier decomposition in longitude, grid points in the meridional plane). Boundary conditions, r -dependent gravity, centrifugal acceleration, and geometry as in GFFC.

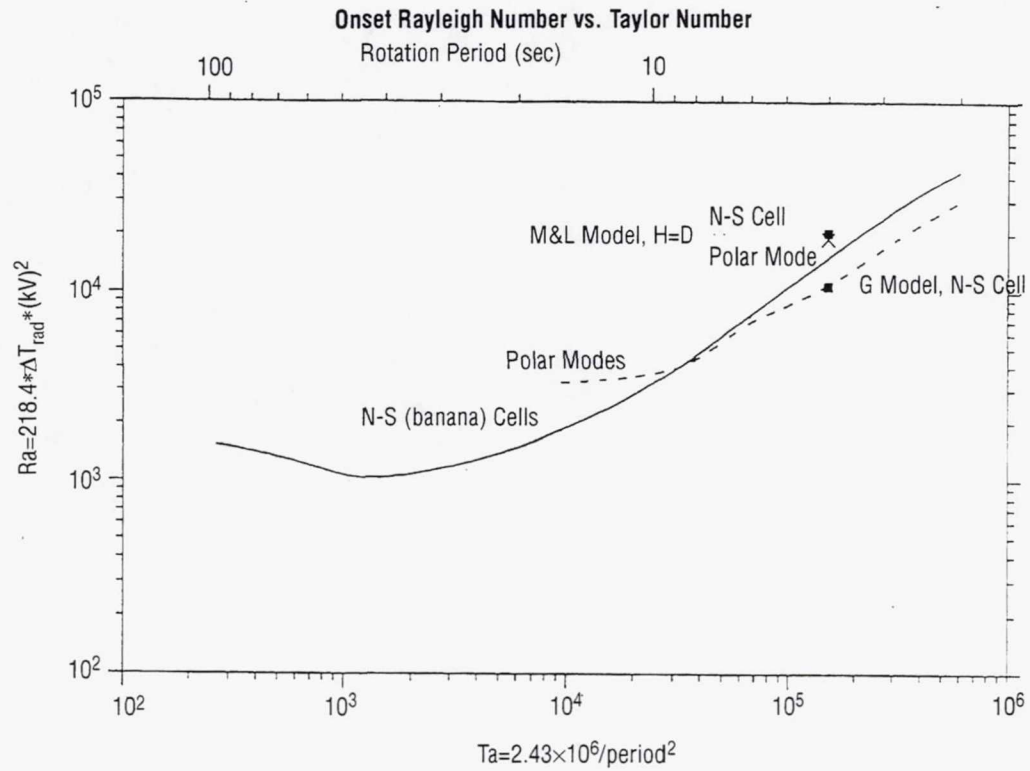


Figure 10. Critical curves from the GFFC experiments. Polar modes become the most unstable for Taylor numbers in excess of about 20,000. The results from computational simulations are shown as points on the figure.

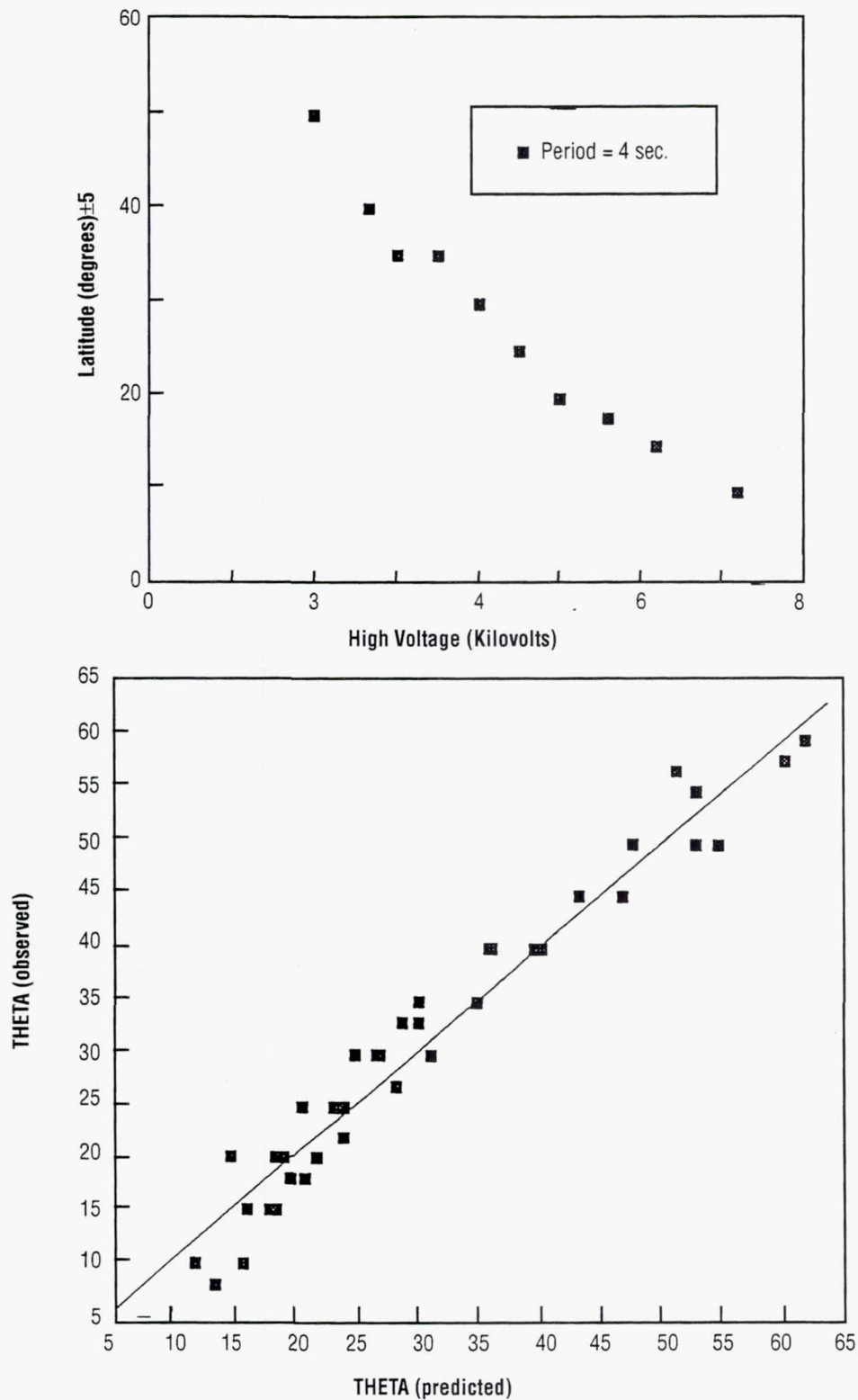


Figure 11. (Top) Translation latitudes vs. voltage for 4 second rotation; (Bottom) the model relation when rotation period and voltage are assumed to have the same exponent is shown. This is $\sin(\theta_{\text{predicted}}) \approx 270 (\tau V)^{-0.85}$, with an average error of 11%. A similar fit to the relation $\sin(\theta_{\text{predicted}}) \approx 380 (\tau V)^{-1}$ is nearly indistinguishable, with an average error of 12%. However, the scaling in (4) can only collapse the data to within 35% of the identity line.

EXPERIMENT VIII.

**ENVIRONMENTAL CONDITIONS IN THE ASTROCULTURE™
PLANT CHAMBER DURING THE USML-2 MISSION**

ACKNOWLEDGMENTS

This work was supported in part by NASA under Grant NAGW-975. The authors also wish to acknowledge the contributions of the other WCSAR staff, undergraduate students, staff of Quantum Devices, Inc., Barneveld, WI, and the crew of STS-73 for their important role in the success of this flight experiment.

EXPERIMENT VIII. ENVIRONMENTAL CONDITIONS IN THE ASTROCULTURE™ PLANT CHAMBER DURING THE USML-2 MISSION

R.J. Bula, Weijia Zhou, R.A. Yetka, and N.A. Draeger

Wisconsin Center for Space Automation and Robotics

College of Engineering

University of Wisconsin-Madison

Madison, WI 53706-1691

Phone: 608-262-5526

Fax: 608-262-9458

E-mail: bula@engr.wisc.edu

1. INTRODUCTION

Conducting plant research to assess the impact of microgravity on plant growth and development requires a plant chamber that has the capability to control other environmental parameters involved in plant growth and development. The environmental control in a space-based plant chamber must be equivalent to that available in such facilities used for terrestrial plant research. Additionally, plants are very sensitive to a number of atmospheric gaseous materials. Thus, the atmosphere of a plant chamber must be isolated from the space vehicle atmosphere, and the plant growth unit should have the capability to remove any such deleterious materials that may impact plant growth and development.

The Wisconsin Center for Space Automation and Robotics (WCSAR), University of Wisconsin-Madison, has developed a totally enclosed controlled environment plant growth unit.¹ The flight unit was used to support the ASTROCULTURE™ experiment conducted during the USML-2 mission. The experiment had two major objectives: 1) Provide further validation of the flight unit to control the experiment-defined environmental parameters in the plant chamber, and 2) support a plant experiment to assess the capability of potato plant material to produce tubers in microgravity. This paper describes the temperature, humidity, and carbon dioxide conditions of the plant chamber during the mission, from launch to landing. Another paper will present the plant response data.

2. PLANT CHAMBER AIR TEMPERATURE

A plot of the plant chamber's air temperature during the mission—based on point sampling every 10 minutes—is shown in figure 1. For comparison purposes, the air temperature of the middeck area of the shuttle is included. Air temperature for the plant experiment was defined as $21\text{ }^{\circ}\text{C} \pm 2\text{ }^{\circ}\text{C}$. The air temperature data during the first 9 days of the mission were for the most part at the desired set point of $21\text{ }^{\circ}\text{C}$. During this period, air temperatures reached $23\text{ }^{\circ}\text{C}$ for short and intermittent periods of time. It is not clear why such air temperature deviations occurred. From day 9 until landing, air temperatures fluctuated considerably, reaching $25\text{ }^{\circ}\text{C}$ at times. One explanation for these observed temperature conditions is that the air intake vents of the flight unit became covered with material that impeded the amount of air flow into the

interior of the flight unit. Since transfer of heat from the chamber air to the air in the interior of the flight unit is achieved by passing cabin air over the radiators of the thermoelectric components of the temperature control subsystem, a high level of air flow is essential. Restriction of the air flow resulting from accumulation of material on the air vents results in degradation of the temperature control capabilities of the flight unit. This situation could account for the deviations from the set point of the recorded chamber air temperatures during the latter part of the mission.

3. PLANT CHAMBER ATMOSPHERIC RELATIVE HUMIDITY

A plot of the percent relative humidity of the plant chamber's air during the mission—based on point sampling every 10 minutes—is shown in figure 2. For comparison purposes, the percent relative humidity of the air in the Shuttle's middeck is included. Percent relative humidity for the plant experiment was defined as 75 percent \pm 5 percent. The recorded values for percent relative humidity in the plant chamber ranged from 78 to 83 percent. No set-point deviation pattern was noted. This suggests that the humidity was controlled within the experiment defined condition. The fact that the data varied around 80 percent rather than 75 percent likely results from a sensor calibration effect rather than because of a lack of control capability. Another indication of the humidity control subsystem to effectively control the humidity level in the plant chamber is shown by the wide difference in humidity of the middeck area and that in the plant chamber. Likewise, the deviations from the set point of the humidity in the plant chamber were not related to the changes in the humidity of the air in the middeck.

4. CONCENTRATION OF CARBON DIOXIDE IN THE PLANT CHAMBER AIR

A plot of the concentration of carbon dioxide in the plant chamber's atmosphere during the mission—based on point sampling every 10 minutes—is shown in figure 3. For comparison purposes, the concentration of the carbon dioxide in the air of the Shuttle's middeck is included. The experiment requirement for carbon dioxide concentration of the air in the plant chamber was $500 \mu\text{mol}\cdot\text{mol}^{-1} \pm 50 \mu\text{mol}\cdot\text{mol}^{-1}$ during the 12-hour light period. The experiment requirement did not specify a concentration of carbon dioxide in the plant chamber air during the 12-hour dark period. Pure carbon dioxide was injected into the air of the plant chamber if the sensed concentration was below the set point concentration. The data show that the carbon dioxide concentration was in the range of 400 to $500 \mu\text{mol}\cdot\text{mol}^{-1}$ during the 12-hour period when the lights were on and the plant material was photosynthetically active (during the first 10 days). The recorded data of concentrations during the light period are slightly lower than the experiment defined concentration range of 450 to $550 \mu\text{mol}\cdot\text{mol}^{-1}$. The recorded deviations from the experimental set-point may be related to the way the pure carbon dioxide gas was added to the plant chamber or to the calibration of the analyzer. In any event, the recorded concentration deviations are insignificant from a general plant response standpoint. After the 10th day of the mission, the plant material began to senesce and as would be expected this condition negatively impacted the rate of photosynthesis. Consequently, the concentration of carbon dioxide in the plant chamber air did not go below $2000 \mu\text{mol}\cdot\text{mol}^{-1}$ during any portion of the light period during the last 5 days of the mission.

The flight unit did not contain any provisions for removal of the carbon dioxide from the air in the plant chamber when the concentration exceeded the set point. During the dark period the plant material released carbon dioxide via respiration. Thus, the concentration of carbon dioxide in the plant chamber air increased gradually to a level approaching $4000 \mu\text{mol}\cdot\text{mol}^{-1}$ towards the end of the 12-hour dark period.

However, the high concentration of carbon dioxide was reduced to the set-point concentration within 4 hours after the light period started and the plant material became photosynthetically active. An interesting aspect is that even though the plant material exhibited decreased photosynthetic activity during the last 5 days of the mission, the rate of respiration appeared to not be reduced as evidenced by the high concentrations of carbon dioxide in the plant chamber air during that period of the mission.

The carbon dioxide concentration data show that the carbon dioxide control subsystem was able to maintain the experiment-defined concentration during the light period when the plant material was absorbing carbon dioxide. These data also verify that the plant chamber was effectively isolated from the cabin or middeck atmosphere as indicated by the vast differences between the concentration of carbon dioxide in the plant chamber air and the middeck air. Changes in concentration of carbon dioxide in the air of the plant chamber were totally different from changes in concentration of carbon dioxide in the air of the middeck area. Also, the recorded concentrations of carbon dioxide in the air of the middeck area for the most part ranged from 3200 to 4400 $\mu\text{mol}\cdot\text{mol}^{-1}$. These data compare to periods of low concentrations (400 to 500) and peak concentrations for short time periods of 3600 to 4000 $\mu\text{mol}\cdot\text{mol}^{-1}$ in the plant chamber.

5. OTHER ENVIRONMENTAL PARAMETERS

Although temperature, humidity, and concentration of carbon dioxide in a plant chamber's air represent important environmental variables that must be controlled in any plant environmental physiology experiment, several other environmental conditions are critical to the success of such research. These include providing an adequate level of light with the required spectral characteristics for the experiment-defined photoperiod and elimination of gaseous materials from the plant chamber atmosphere that may have a negative impact on plant growth and development.

The lighting system used in the ASTROCULTURE™ flight unit during the USML-2 mission was a light emitting diode (LED) unit that provided photons in the red and blue regions of the spectrum. The LED light unit consisted of a monolithic array of LED chips mounted on a thermally conductive substrate that in turn was mated on a metal heat sink. Cabin air was moved over this, maintaining the temperature of the light unit near cabin ambient temperature.^{2,3} The experiment defined light level was 150 $\mu\text{mol}\cdot\text{m}^{-2}\cdot\text{s}^{-1}$ and a photoperiod of 12 hours (lights were on for 12 hours and off for 12 hours). Since the light levels recorded during the entire mission were at the specified intensity and for the 12-hour photoperiod, these data are not shown.

Ethylene is an important gaseous contaminant of an enclosed plant chamber because plants release this compound as a normal physiological activity. Provisions must be made to assure that the concentration of ethylene in the atmosphere of an enclosed plant chamber does not exceed 50 $\mu\text{mol}\cdot\text{mol}^{-1}$ (50 ppb) since concentrations above this level negatively impact plant growth and development. The ASTROCULTURE™ flight unit was equipped with a nonconsumable photocatalytic ethylene oxidation unit. The ethylene removal unit contains a small UV emitting lamp encased in a modified titanium dioxide material that serves as a catalyst for the UV radiation to oxidize the ethylene to carbon dioxide and water.⁴ This unit may also be capable of oxidizing other volatile organic contaminants that may be present in the plant chamber atmosphere. Samples of the plant chamber air were taken three times during the mission for postmission analyses. Ethylene concentration of these samples did not exceed the level considered deleterious to plant growth.

6. CONCLUSIONS

The ASTROCULTURE™ flight unit used to support a plant experiment during the USML-2 mission provided a controlled environment comparable to that available for terrestrial plant environmental physiology research. The critical environmental parameters were controlled within the experiment defined levels. The ability of the ASTROCULTURE™ flight unit to provide the quality of environment control recorded during this mission was due to several unique controlled environment technologies developed by the Wisconsin Center for Space Automation and Robotics and used in this flight unit.

REFERENCES

1. Duffie, N.A.; Zhou, W.; Morrow, R.C.; Bula, R.J.; Tibbitts, T.W.; Wranovsky, S.R.; and Macaulay, P.D.: SAE Technical Paper Series, Paper No. 951627, 1995.
2. Ignatius, R.W.; and Martin, T.S.: U.S. Patent No. 5, 278, 432, 1994.
3. Bula, R.J.; Tennessen, D.J.; Morrow, R.C.; and Tibbitts, T.W.: In *NASA Conference Publication CP-3309*, 255-268, 1994.
4. Bula, R.J.; and Ignatius, R.W.: In *Proceedings of the International Symposium on Plant Production in Closed Ecosystems*, Narita, Japan, August 1996.

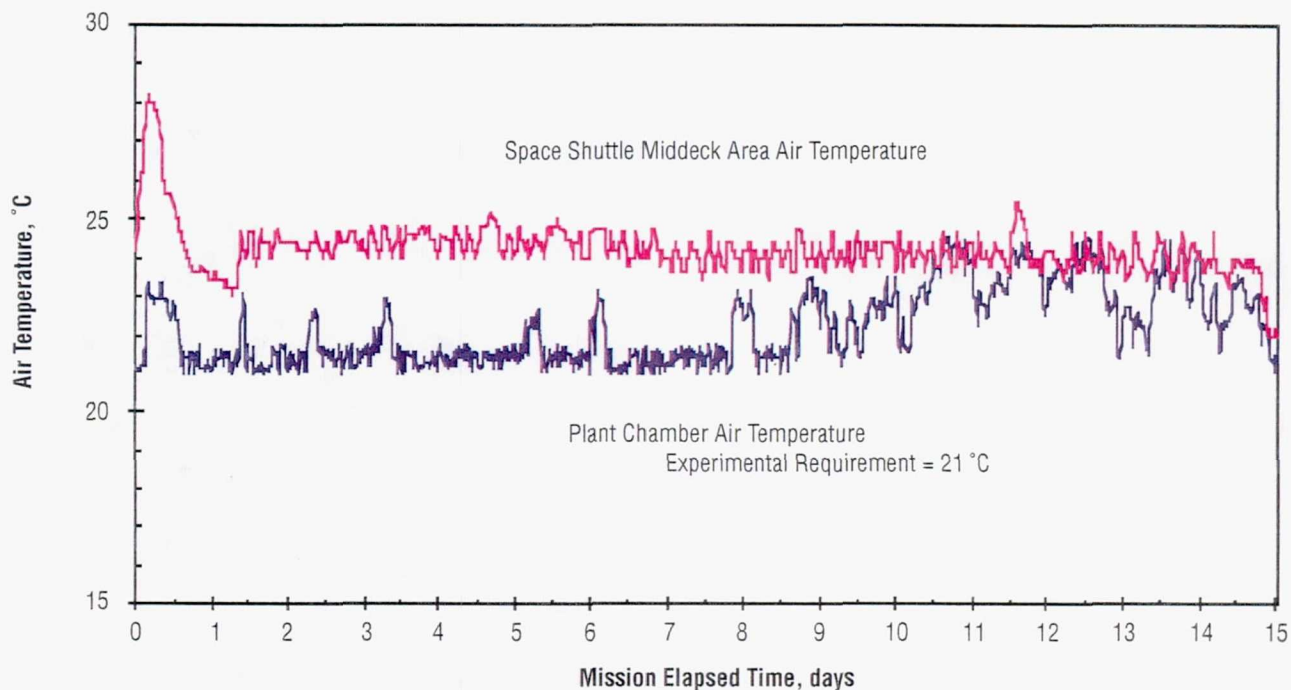


Figure 1. Plots of the air temperature in the plant chamber and the Shuttle middeck during the USML-2 mission, from launch to landing.

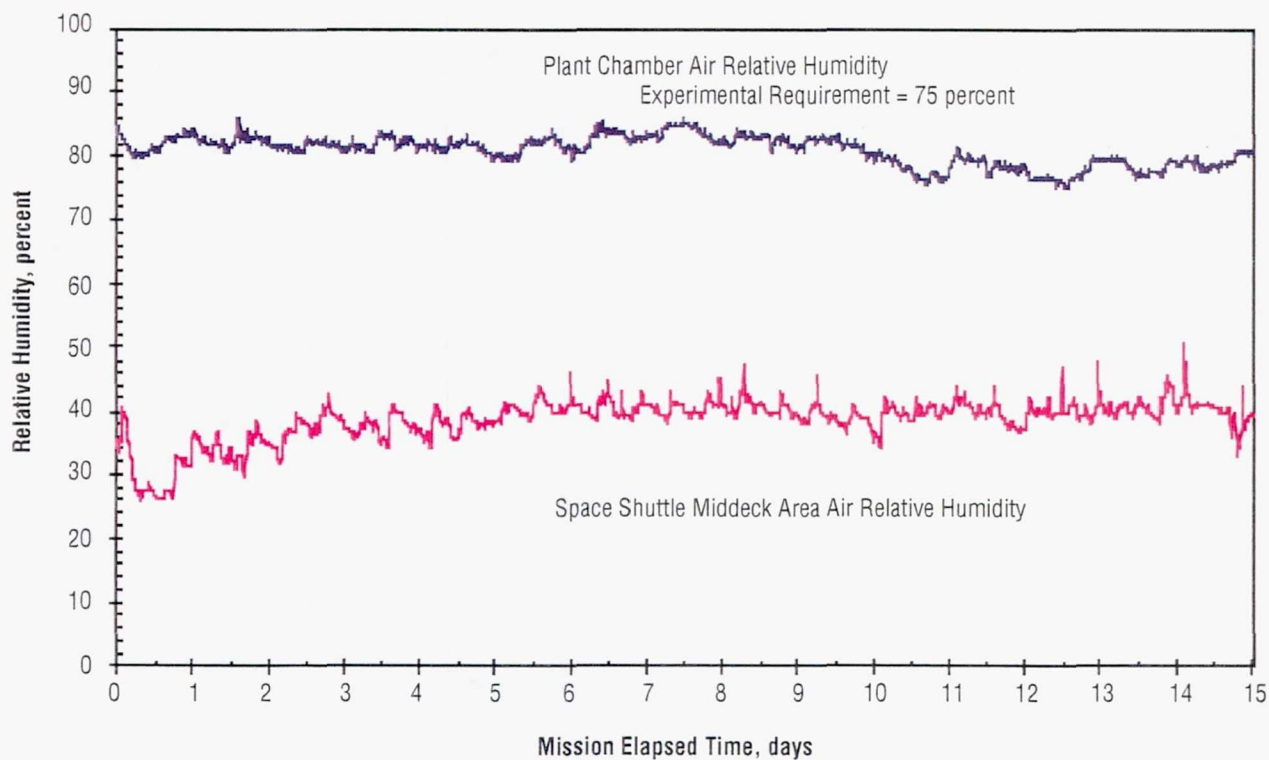


Figure 2. Plots of the percent relative humidity of the air in the plant chamber and Shuttle middeck during the USML-2 mission, from launch to landing.

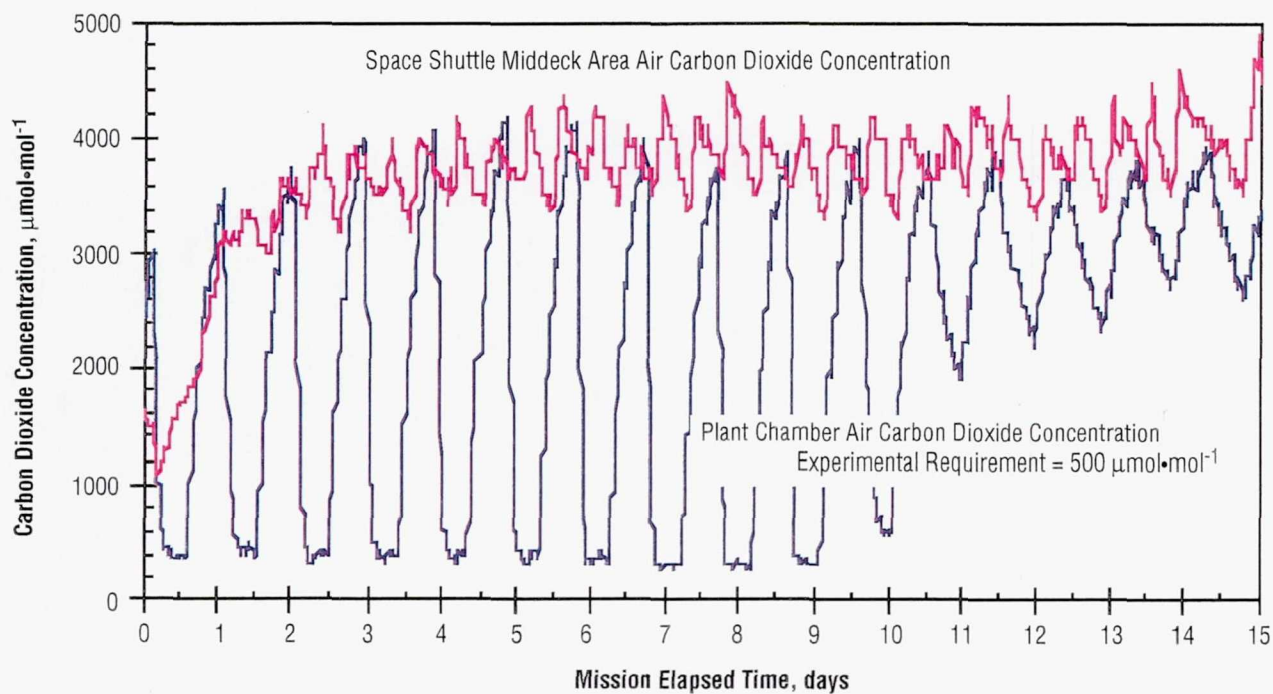


Figure 3. Plots of the carbon dioxide concentration in the air of the plant chamber and the Shuttle middeck during the USML-2 mission, from launch to landing.

Page intentionally left blank

EXPERIMENT IX.

**ASTROCULTURE: GROWTH AND STARCH
ACCUMULATION OF POTATO TUBER**

ACKNOWLEDGMENTS

Many individuals were instrumental in the success of this experiment. The authors particularly thank University of Wisconsin-Madison researchers Martha Cook and Thomas Frank; and Kennedy Space Center researchers Gregory Goins, Monica Sanwo, Neil Yorio, Barbara Peterson, and David Chapman. The research was supported by the College of Agricultural and Life Sciences, University of Wisconsin-Madison, NASA Grant NAGW-4022, and NASA contract NAS10-12180 to Dynamac Corporation.

EXPERIMENT IX. ASTROCULTURE: GROWTH AND STARCH ACCUMULATION OF POTATO TUBER

Theodore W. Tibbitts
Dept. of Horticulture
Univ. of Wisconsin
Madison, WI 53706
Phone: 608-262-1816
Fax: 608-262-4743
E-mail: twt@facstaff.wisc.edu

Christopher S. Brown
Dynamac Corp.
Durham, NC 27713
Phone: 919-544-642
Fax: 919-544-6755
E-mail: christopher_brown@ncsu.edu

Judith G. Croxdale
Dept. of Botany
Univ. of Wisconsin
Madison, WI 53706
Phone: 608-262-2743
Fax: 608-262-7509
E-mail: croxdale@facstaff.wisc.edu

Raymond M. Wheeler
NASA
Kennedy Space Center, FL 32899
Phone: 407-853-5142
Fax: 407-853-4165
E-mail: wheelerr@bonsmtp.ksc.nasa.gov

ABSTRACT

Potato explants (leaf, small stem section, and axillary bud) flown on STS-73 developed tubers of 1.5 cm diameter and 1.7 g mass during the 16-day period of space flight. The experiment was undertaken in the ASTROCULTURE™ experiment package under controlled temperature, humidity, lighting, and carbon dioxide concentrations. The tubers that formed in the explant system under microgravity had the same gross morphology, the same anatomical configuration of cells and tissues, and the same sizes, shapes, and surface character of starch granules as tubers formed in a 1 g environment. The total accumulation of

starch and other energy containing compounds was similar in space flight and ground control tubers. Enzyme activity of starch synthase, starch phosphorylase, and total hydrolase was similar in space flight and ground controls, but activity of ADP-glucose pyrophosphorylase was reduced in the space flight tuber tissue. This experiment documented that potatoes will metabolize and accumulate starch as effectively in space flight as on the ground. Thus, this data provides the potential for effective utilization of potatoes in life support systems of space bases.

1. INTRODUCTION

The ASTROCULTURE™-05 plant experiment was undertaken to establish the effectiveness of potato explants to form tubers and to metabolize and accumulate starch during spaceflight. This process is of critical importance to utilizing plants for providing energy-rich foods in life support systems in future space bases. This study also was of particular importance to plant physiologists because previous experiments with other plant species in space, and some ground-based studies, have documented reduced starch accumulation when plants are subjected to real or simulated microgravity.

Each potato explant used in this study consisted of a leaf, its axillary bud, and a small stem segment harvested from mother plants which had grown in controlled environments on the ground. Tubers formed from the axillary bud in the days immediately after harvest from the mother plants. These explants provided a model system for the study of the physiological and developmental processes that occur during tuber formation in the short period of a Shuttle flight.

2. METHODOLOGY

Potato (*Solanum tuberosum* cv. Norland) mother plants were grown from in-vitro propagated plantlets, beginning 6 weeks before launch. Plants were grown at 21 °C, 80 percent RH, 150 $\mu\text{mol m}^{-2} \text{s}^{-1}$ photosynthetic photon flux (PPF) for a 12-hr photoperiod and approximately 350 ppm CO_2 in a walk-in plant growth chamber at the Kennedy Space Center (KSC). Five explants for flight were harvested from the 7th and 8th leaves of the mother plants, counting basipetally from the youngest leaf that was 1 cm in length. Each explant consisted of a leaf, axillary bud, and small section of stem. Since more leaf tissue was present than could be accommodated in the plant chamber, the lamina was trimmed to fit by cutting off leaflet tips. The stem and lower petiole region of each explant was placed into a tray filled with moistened arcillite (calcined clay particles). Light-tight flexible gaskets were placed around the petiole of each explant and opaque acrylic plates were secured over the base of the explants and arcillite for their containment during space flight.

The group of explants was then secured within the small controlled environment chamber of the ASTROCULTURE™ growth unit detailed in the cooperative hardware evaluation experiment. This flight package was programmed to maintain the plant chamber at 21 °C, 80 percent RH, and a minimum of 50 ppm CO_2 . Above the plant chamber was an array of red and blue LED's to provide 150 $\mu\text{mol m}^{-2} \text{s}^{-1}$ PPF for a 12-hr light period. Water was delivered to the arcillite-containing plant tray by porous tubes and a negative pressure system.

Six hours after loading the explants, the ASTROCULTURE™ unit was installed into the middeck of the Space Shuttle *Columbia* and the unit powered to initiate the programmed environmental conditions. The Shuttle launch occurred 22 hours after power up and 28 hours after loading the explants into the package. Details of the precise experimental conditions over the course of the 16-day study are provided in the hardware experimental report prepared by Bula et al. Of particular importance for this study were, 1) the downlinking every 2 days of video images of the explants, and 2) the daily downlinking of carbon dioxide concentrations within the chamber, both of which provided information on the physiological vigor and activity of the explants.

The above protocol also was followed for baseline control studies conducted in a controlled environment facility (Biotron) at Madison, Wisconsin, one month following the flight. Care was taken to insure that ground control mother plants, grown at KSC, were the same age from transplanting as the plants used for the flight. The temperature, humidity, and carbon dioxide concentrations of the middeck during the 16-day flight period were duplicated as closely as possible in the controlled environment room of the Biotron. Explants were harvested from mother plants 12 hours before loading into the ASTROCULTURE™ flight unit and held at $5^{\circ}\text{C} \pm 2^{\circ}\text{C}$ for this period in small cold storage units over ice. This provided time to carry the explants from KSC to Madison. (The flight explants were also harvested 12 hours before loading into the ASTROCULTURE™ unit and held in the same storage units in a cold room at $5^{\circ}\text{C} \pm 2^{\circ}\text{C}$.)

3. RESULTS

3.1 In Flight

The downlinking of video images demonstrated good plant vitality during the first 12 days of the mission followed by senescence of the leaves. This same pattern of plant vitality was documented by the downlinked carbon dioxide data from the plant chamber, which showed low levels (~500 ppm) of carbon dioxide during the light period (due to photosynthetic CO_2 uptake) followed by high levels (~3,000 ppm) each dark period (due to respiratory CO_2 output) during the first 12 days (fig. 1). After 12 days, the carbon dioxide changes over light—dark periods were slower and reduced in magnitude as photosynthesis and respiration slowed.

The environmental conditions maintained in the experiment package during the space flight and ground control are shown in table 1. Similar temperature (22°C) and humidity conditions (80 percent) were maintained for both the flight and ground controls. Some variations in carbon dioxide concentrations did occur between flight and ground controls; however, it is felt that this difference was not significant to the maintenance and development of the explants.

Table 1. Environmental conditions in the growth chambers of the space flight and of the ground control.

Environmental Parameter	Set Point	Space Flight			Ground Control		
		Ave*	Max**	Min**	Ave*	Max**	Min**
Temperature (°C)	21	22.1	23.9	21.2	22.0	23.9	20.6
Relative Humidity (%)	80	81.3	88.0	76.6	78.2	81.4	75.5
Carbon Dioxide (ppm)	500	2308	4100	350	2102	5758	204

* Average conditions for the 16-day period.

** Maximum and minimum average conditions for 12-hour period.

3.2 Postflight

The package was recovered from the Space Shuttle Columbia within 4 hours after touchdown at KSC and explant harvests completed within 6 hours after touchdown. Explants were photographed, then tubers were measured and prepared for anatomical and biochemical analysis. Tissue was placed in a formalin-based fixative for anatomical studies and frozen in liquid nitrogen for biochemical analysis.

The size and shape of the space-formed tubers were similar to ground control tubers (fig. 2). Periderm color was similar.

All explants showed signs of senescence (chlorosis and/or necrosis) of laminar tissue and the death of the leaf rachis basipetally, but all explants had turgid petioles and stems. The space-grown explant that formed the smallest tuber had green laminar tissue in the terminal leaflet and one of the first pair of leaflets. The entire rachis and petiole of this explant were turgid and dark green in contrast to the other four explants. It had been found in baseline studies that tubers produced from explants of different development age can vary, and this leaf with the small tuber was slightly younger developmentally, based on its leaf position and leaf length. Tubers formed under conditions of microgravity had the same diameter and weight as those formed on Earth (table 2).

Table 2. Growth of tubers produced on explants after 16 days of growth in space flight and on the ground.

Space Flight		Ground Control	
Diameter (cm)	Mass (g)	Diameter (cm)	Mass (g)
1.5±0.8	1.69±0.34	1.5±0.1	1.51±0.28

* The small tuber developed on one explant in space flight is not included in this data.

For space flight n=4, for ground control n=5. Values ± SD.

Tuber tissues were found in the same geometric arrays, with interior cells arranged in a honeycomb pattern and the tissues at the surface comprised of cell layers with cells of a layer stacked directly on top of those of the previous layer. Cell wall thickness in space flight tubers varied, some cells with thin walls (60 to 90 nm in thickness) and other cells with thick walls (147 to 440 nm). In contrast the thickness of cell walls in ground grown tubers was more uniform (175 to 440 nm in thickness).

The number of layers in the periderm was the same as in ground grown tubers, and there was neither starch nor protein in this tissue. Instead, starch and protein were found exclusively in the interior cells in both the space flight and in the ground control tubers.

Starch grains had comparable shapes, similar smooth surfaces, and a size range that was the same as those in ground controls (fig. 3).

The distribution of grains into size categories differed in tubers developed under space flight conditions compared to those formed on the ground. A greater percentage of grains were found in the smaller size classes in space flight than were found in Earth-grown tubers (fig. 4). The aspect ratio (length/width) of the grains formed in space was not different from that of ground-control tuber grains.

Protein crystals were found in tissues of the tubers developing both in space flight and on the ground. No obvious differences in crystal size, or distribution within the tuber, were evident.

The biochemical analysis of the tuber tissues did not document any large differences in tissues developed in space flight compared to the ground controls. The starch, sucrose, glucose, and soluble protein concentrations in the tubers of flight and ground controls were similar (table 3). Although there were some differences, the standard deviation of values was quite large and thus no significance can be placed on the small differences.

Table 3. Concentrations of carbohydrates and soluble proteins in potato tubers that developed on explants in space flight and on the ground.

Constituent (%)	Space Flight *	Ground Control
Starch	43.4±13.4	40.1±12.3
Sucrose	0.9±0.1	0.7±0.2
Glucose	0.2±0.1	0.1±0.0
Soluble protein	12.6±1.2	11.5±0.9

* Values represent the means of 4 replicates ± SD on a dry weight basis.

Activities of enzymes controlling starch formation in plant tissues were similar between flight and ground control tubers with one notable exception (table 4). ADP-glucose pyrophosphorylase, a rate-limited enzyme in starch synthesis, had significantly reduced activity in the space flight tubers compared to the ground controls. However, another enzyme involved in starch synthesis, starch synthase, showed simi-

lar activity in tubers developed in space flight compared to the ground. Two enzymes involved in starch degradation, starch phosphorylase and total hydrolase, showed similar activities in tubers from space flight and from the ground (table 4).

Table 4. Activity of enzymes controlling starch synthesis and degradation in potato tubers that developed on explants in space flight and on the ground.

Enzyme nmol (gfw • min) ⁻¹	Space Flight	Ground Control
ADP-glucose pyrophosphorylase	8.7±1.9	16.2±2.5
Starch synthase	71.0±10.5	73.0±2.5
Starch phosphorylase	8.3±0.5	9.3±1.2
Total hydrolase	48.1±9.0**	39.0±3.6**

* Values represent the means of 4 replicates ± SD on a dry weight basis.

** μmol (gfw • min)⁻¹

Thus, although the activity of the ADP-glucose pyrophosphorylase was reduced, this had no significant influence upon the total quantity of starch accumulated in the tubers, which was similar between the space flight and ground explants (table 3). This decrease in activity of the ADP-glucose pyrophosphorylase is consistent with research with other plant issues, which has documented reductions in activity of this enzyme in space flight and in simulated microgravity experiments on the ground.

4. CONCLUSIONS

This study has documented that starch accumulation occurred effectively in potato tubers in the space flight environment. The tubers formed in the explant system under microgravity had the same gross morphology, the same anatomical configuration of cells and tissues, and the same sizes, shapes, and surface character of starch granules as tubers formed in a 1 g environment. Space flight did not alter these fundamental features of tuber differentiation. The total accumulation of starch and other energy containing compounds was similar in space flight and ground control tubers. However, the reduced activity of the one critical starch synthetic enzyme, ADP-glucose pyrophosphorylase, deserves further study and evaluation with other crop plants that are being considered for food production in life support systems for long-term space bases.

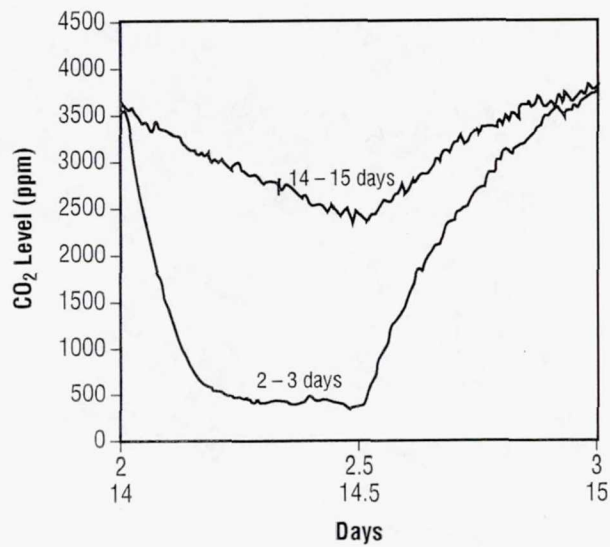


Figure 1. Concentration of carbon dioxide in the growth unit of the ASTROCULTURE™ unit during 2–3 days and 14–15 days of space flight.



Figure 2. Potato tubers produced by the explants after 16 days of growth in space flight (A) and on Earth (B).

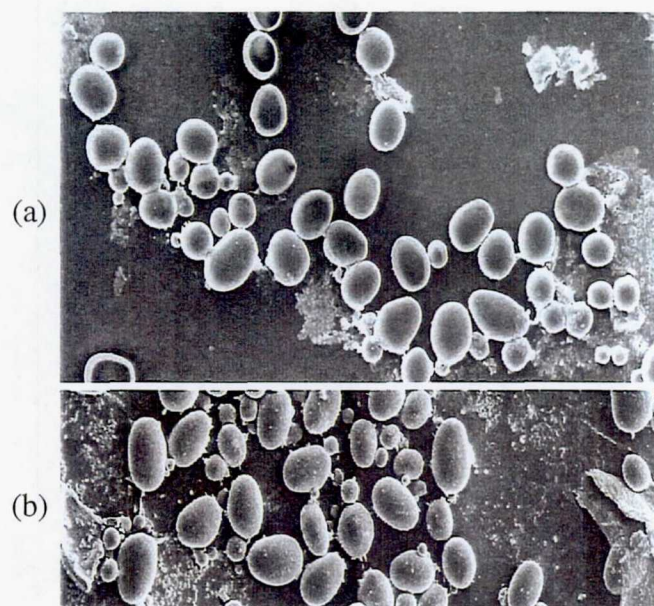


Figure 3. Starch grains from potato tubers formed in space flight (a) and on the ground (b).

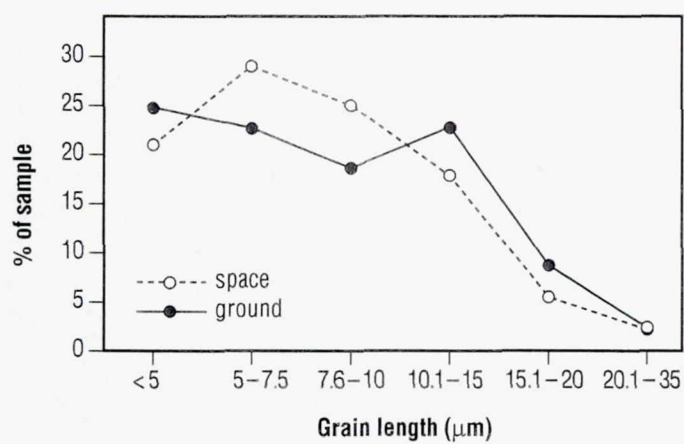


Figure 4. Percentage of the starch grains by size category formed in potato tubers during space flight and on the ground.

EXPERIMENT X.

**USML-2/STS-73 ONE-YEAR POST-FLIGHT SUMMARY OF THE COMMERCIAL
GENERIC BIOPROCESSING APPARATUS (CGBA) PAYLOAD**

Page intentionally left blank

**EXPERIMENT X. USML-2/STS-73 ONE-YEAR POST-FLIGHT SUMMARY
OF THE COMMERCIAL GENERIC BIOPROCESSING
APPARATUS (CGBA) PAYLOAD**

Dr. Louis S. Stodieck

Center for Bioserve Technologies
University of Colorado at Boulder
Campus Box 429
Boulder, CO 80309-0429
Phone: 303-492-1005
Fax: 303-492-8883
E-mail: louis.stodieck@colorado.edu

John Berryman, Contact

BioServe Space—CU
Aerospace Engineering Sciences
Campus Box 429
Boulder, CO 80309-0429
Phone: 303-492-1005
Fax: 303-492-8883
E-mail: berrymaj@spot.colorado.edu

Rachelle Wolfe, Contact

BioServe Space Technologies—KSU
Division of Biology
Ackert Hall, Kansas State University
Manhattan, KS 66506
Phone: 913-532-6705
Fax: 913-776-5273
E-mail: rwolfe@ksu.ksu.edu

BioServe Web Site—<http://www.colorado.edu/engineering/BioServe/>

1. INTRODUCTION

1.1 BioServe Space Technologies—An Overview

BioServe Space Technologies is a NASA Center for Space Commercialization (CSC) located jointly at the University of Colorado in Boulder, CO, and Kansas State University in Manhattan, KS. Dr. George Morgenthau (CU) is BioServe's center director and Dr. Terry Johnson (KSU) is the Center's chief scientist.

The primary mission of BioServe is to facilitate commercial use of the unique environment of space, primarily that of microgravity, in the field of life sciences. Space flight provides a unique test-bed for developing new technologies/products with ultimate terrestrial benefit. The space environment can be used to understand, accelerate, or retard biophysical/biochemical processes, to create new biological products or to improve existing ones, via process-oriented applied research. In other words, the investigations focus on how the space environment can be used as a commercially viable "tool" that will eventually provide a "value added" factor to a commercial product or process.

BioServe focuses on research in three main project areas: 1) biomedical/pharmaceutical, 2) bioprocessing/biotechnology, and 3) agricultural/environmental. Previous space flight investigations sponsored by BioServe can be broadly categorized to include studies on small whole organisms/invertebrates, plants, microorganisms, mammalian cells, viruses, biomaterials, bones, crystal growth, human physiology, and other related topics. In general, reduced gravity, often referred to as weightlessness, and the space environment have been shown to alter one or more aspects associated with each of the above categories. Ongoing research is directed towards identifying the underlying causes of the altered outcomes and exploring the potential of related commercial applications.

Support of commercial space life science research in the three designated project areas described above is provided through BioServe personnel's multidisciplinary space flight research experience, payload planning expertise, space flight operations management, and the capability to provide flight certified hardware. This provides a service for clients that otherwise could not feasibly perform space flight research. The process consists of the following fundamental steps:

- BioServe adopted the philosophy of using "generic" hardware designs to enable a wide variety of pilot studies to be accomplished in a common apparatus. This strategy allows a "next step" approach to be taken in the sense that specialized payloads can be consequently designed to further support promising initial findings. For example, seedling experiments which were initially performed in our test tube-like device, the Fluids Processing Apparatus (FPA) evolved into a full-scale Plant Growth Chamber (PGBA) that recently flew on STS-77 and is currently manifested on STS-83. Reasonable upgrades to Shuttle hardware capabilities can be implemented to reflect client needs, with special emphasis on changes that may enable more effective approaches to desired market segments when the *International Space Station* (ISS) becomes operational.
- BioServe has designed and flown a variety of hardware on numerous carriers including NASA's KC-135 parabolic aircraft, sounding rockets (fig.1), the Space Shuttle and the *Mir* space station. For additional information on the flight program or experimental findings, please direct inquiries to one of the above points of contact, or visit our Web site at the address given above.

2. DESCRIPTION OF HARDWARE AND OPERATIONS

2.1 Commercial Generic Bioprocessing Apparatus (CGBA)

The CGBA payload consists of three types of locker replacement units referred to as the 1) Generic Bioprocessing Apparatus—Incubator (GBA-INC), 2) GBA-Isothermal Containment Module (GBA-ICM), and 3) the GBA-Ambient (GBA-AMB). Each can be accommodated in the Space Shuttle middeck, Spacelab,

SPACEHAB or the *Mir* space station. All three lockers provide stowage for experimental samples contained in test tube-like devices. Additionally, the GBA-INC and GBA-ICM provide thermal control. The individual components associated with the CGBA payload complement that flew on STS-73/USML-2 (GBA-INC and GBA-AMB) are described and illustrated as follows.

2.2 Fluids Processing Apparatus (FPA)

The FPA is the fundamental workhorse of the payload (fig. 2). It is essentially a "microgravity test tube" which allows controlled, sequential on-orbit mixing of two or three fluids. The fluids are contained inside a glass barrel (ID 13.5 mm). The glass barrel can process up to a total 6.5 ml of liquid in the standard configuration. The glass barrel is contained within a Lexan™ sheath. The fluids are initially kept isolated from each other by rubber septa. The glass and septa are autoclavable. The septa are moved by depressing a plunger mechanism. A bypass in the glass barrel allows the mixing of the fluid into the adjacent chamber. The samples can be mixed sequentially on orbit by depressing the plunger manually or by motor drive in the Auto-GAP design. The glass and rubber septa components provide the first level of containment and the Lexan™ sheath provides the second level. The Lexan™ sheath is leak tested using a water submersion/vacuum technique to a 5 psid differential pressure to ensure integrity.

Variations of the standard FPA configuration include a Gas-Exchange FPA (GE-FPA) and a Plant-FPA (P-FPA) shown in figure 3. The GE-FPA uses a PTFE membrane to contain the fluid while allowing passive diffusion of gases between the sample and the entire volume of the outer level of containment (GAP—described below). The P-FPA provides a means of scrubbing ethylene from the closed atmosphere (see fig. 3). Various inserts are also used to facilitate protein crystal growth experiments. The different designs address specific experimental requirements such as providing larger habitats (insects) or allowing gas exchange to increase the available amount of oxygen/carbon dioxide. On their initial flight, STS-50, the FPA's were individually activated by astronauts. In the current design, eight FPA's are now contained inside a Group Activation Pack (GAP—fig. 4) for simultaneous processing.

2.3 Group Activation Pack (GAP)

The GAP allows for the simultaneous activation of eight FPA's and provides an additional level of containment for hazardous fluids (see fig. 4). During flight, the GAP's are either stowed inside the GBA-INC, GBA-ICM or in ambient temperature stowage lockers. Astronauts activate all eight FPA's simultaneously by attaching a hand crank to the GAP, or in the case of the Auto-GAP design, a motor drive is used. The GAP's can be opened during flight to remove individual FPA's for video/35-mm film recording or for monitoring the FPA's in the optical density measurement device inside the GBA-INC module.

2.4 Generic Bioprocessing Apparatus (GBA)

The GBA-Incubator (GBA-INC) replaces a standard middeck locker (fig. 5). It provides a temperature-controlled volume for nine GAP's (37 °C), data acquisition and control electronics, and optical density measurement capabilities (565 nm) for up to eight FPA's at a time. Experimental samples are contained inside GAP's. Each GAP contains eight FPA's. The GBA locker and its samples can be loaded as late as 16 hours prior to launch to maximize viability of the biological samples.

If GAP's are flown in ambient stowage lockers only (using either the GAP or the GAP-II components), the payload is referred to as the GBA-Ambient (GBA-AMB).

A third version of GBA, called the GBA-Isothermal Containment Module (GBA-ICM), was evolved. This unit flew for the first time on STS-77, and more recently resided on the Russian space station *Mir* for 4 months during the NASA *Mir* increment 3. The GBA-ICM provides temperature control and fully autonomous initiation and termination of eight GAP-II's.

2.5 STS-73/USML-2 CGBA Payload Complement and Summary of Operations

2.5.1 CGBA Hardware and Operations

The CGBA components flown on board the STS-73/USML-2 mission consisted of 264 total experiment samples contained in FPA's. Of the 264 FPA's, 72 were maintained in a GBA-INC at 37 °C, and the remaining 192 samples were stowed at ambient temperature (GBA-AMB). One-hundred forty-four of the samples were prepared and stowed on board the Spacelab module approximately two months prior to the original launch date. The remaining 120 samples were prepared at the Kennedy Space Center and turned over for integration into Columbia's middeck approximately 24 hours before launch. Final preparations were performed as planned without significant difficulty; however, several experiments required the use of backup samples due to the numerous launch delays this mission experienced.

Following launch, payload operations were supported around-the-clock by BioServe personnel in the Life Science Support Facility (Hangar L) at Cape Canaveral, FL. Backup support was provided by BioServe personnel at a remote site situated at the University of Colorado in Boulder. Information and data obtained in real time by on-call BioServe personnel were disseminated to appropriate investigators at their respective test sites. Using such information, investigators were able to perform simultaneous matched ground controls.

From both operations and sample return perspectives, the payload was successful. All but one GAP were activated and terminated according to the schedules laid out by the investigators and mission support personnel. For one GAP inadvertently initiated too early, samples were still obtained with only a slight loss of science. Minor anomalies did occur during operations of a few of the FPA's but there were no significant overall impacts. The science return was compromised in 32 FPA's, or 12 percent of the total number. Of these 32 FPA's, 24 samples were impacted due to the combination of early stowage and the numerous launch delays. Eight sample losses were attributable to incomplete activation of a time critical experiment. The remaining 232 FPA's were operated successfully to yield data and samples for analysis.

During the mission, 16 of the FPA's were placed (8 at a time) in the optical density measuring device within the GBA for collection of turbidity data. These data provided an indication of the rate at which the biological processes occurred which could be compared with the matched ground controls upon completion of the mission. Video and photography operations were performed for three experiments over three photo sessions equally spaced throughout the mission. Photos and video recordings have been reviewed by the principal investigators (PI's) for important data regarding the behavior of samples in microgravity.

Within 3 hours of landing at KSC, the GBA-INC locker, and the six GAP's located in the ambient middeck locker were removed from the orbiter and transported to Hangar L for deintegration. The 18 GAP's located in the Spacelab module were removed and transported to Hangar L for deintegration at approximately 6 hours after landing. Experiments requiring timely postflight processing (such as fixation, photography and behavioral gravity-related studies) were performed by PI's at Hangar L. All samples were photographed and packaged for return to the various PI's laboratories for analysis.

3. CATEGORIZED SUMMARY OF EXPERIMENT RESULTS AND CONCLUSIONS

3.1 Whole Organisms

3.1.1 Brine Shrimp Development

PI: Spooner, B.

This experiment is part of an ongoing series of research into the effects of space flight on the development of brine shrimp (*Artemia franciscana*). Little information is available on the requirements of gravity in animal developmental biology. The constraints of space flight (launch delays, mission duration, infrequent access) contribute to the difficulty of obtaining the pertinent data. Developmentally arrested brine shrimp can be used to overcome many of the obstacles. Dehydrated, encysted embryos are stable and unaffected by launch delays and embryonic development. Hatching and substantial larvae development can be initiated on orbit through the addition of an NaCl solution to the dry cysts.

The STS-73 flight was a continuing series of investigations into the development of brine shrimp. The data obtained from this mission corroborated prior results. In general, the development appears to be accelerated in the weightless environment. Successive larval instars (or stages) interrupted by molts occurred in space. Naupliar larvae possessed the singular naupliar eye, and development of the lateral pair of adult eyes took place. Transmission electron microscopy (TEM) revealed extensive differentiation, including skeletal muscle and gut endoderm, as well as the eye tissues. These initial studies demonstrated that extensive degrees of development can take place in microgravity. Flight and ground brine shrimp do not differ significantly with respect to hatching rates of larval morphology at the scanning and TEM levels. However, in three different experiments on two different flights, involving a total of 232 larvae that developed in space, a highly significant difference in degree of development was observed to occur in space relative to matched ground controls. By as early as 2.25 days after reactivation, the space flight brine shrimp growth was accelerated by a full instar over their comparable ground controls.

The commercial applications targeted by this study include the use of brine shrimp in toxicological assessment performed to evaluate toxins in food and the environment as well as providing a model to determine the potency of anesthetics and drugs. Furthermore, understanding what caused the accelerated development might have terrestrial applications for improving aquaculture yields, as more protein can be produced in a shorter amount of time. Brine shrimp are used all over the world as a protein source for humans and livestock.

3.2 Mammalian Cells

3.2.1 Growth of Embryonic Chick Calvariae Osteoblasts Attached to Type-I Collagen

PI: Kacena, M.

3.2.1.1 Background. Space flight exploration and associated experiments have shown that human bones experience a loss in density during initial unloading, primarily due to demineralization. This research project attempts to examine the effect of reduced force on the vertebrate skeleton by studying osteoblast function and structure in low gravity and the role played by integrins in bone deposition. Cultured chicken calvarial osteoblasts are cultured under static 1 g in the laboratory and space flight. Electron microscopy of the cells and resulting matrix will identify changes in osteoblast function and structure. Immunocytochemical assays will investigate differences in protein concentrations, focusing on integrin expression.

3.2.1.2 Results. Because of multiple launch delays, the primary osteoblast cells were unhealthy and samples did not yield much information. For STS-77, some main results (analysis is ongoing) include an apparent increase in cells in laboratory cultures over space-flown cultures. It also seems that more bone matrix is being produced in the ground control culture.

3.2.1.3 Follow-on. This experiment was repeated on STS-77. In addition, clinostat experiments were performed as were experiments with various coverslips. The cells were much healthier for the STS-77 flight and analysis as seen by scanning electron microscopy and transmission electron microscopy. Immunocytochemical assays are currently in progress.

3.2.1.4 Commercial Implications. Discovering the differences between osteoblast cells grown on Earth and in space have both space-related and terrestrial implications. Because astronauts lose bone in space flight, it is critical to understand how the loss occurs (by what mechanism). This research attempts to understand this by looking at differences in the concentration of proteins secreted by the osteoblasts, analyzing changes in cell shape, and examining the integrin pattern expression (integrins are thought to be responsible, to some extent, for the transmission of mechanical signals). Understanding how the bone loss occurs as a result of microgravity will lend insight to specific countermeasures that are directed toward the cause of the loss, not just a symptom. Similarly, several terrestrial bone diseases resemble (in one way or another) the bone loss that astronauts experience. If the mechanism behind the loss can be understood in the "accelerated loss condition" (space flight), that knowledge can then be applied to appropriate terrestrial diseases, such as osteoporosis or osteopenia.

3.2.2 The Reversibility of Cell Stabilization Induced by a Novel Cell Growth Regulator

PI's: Johnson, Terry C. and Fattaey, Heideh K.

3.2.2.1 Background. The transport of living mammalian cell culture lines and tissues, in a stabilized and nonproliferating state, has relevance for both terrestrial and space applications. Delays in transport of cells in a nonstabilized condition can lead to a loss of cell viability and/or provide selection pressure for cell survival that can alter the nature of the final cell population. This is a particular problem with cell populations destined for experimental studies in the microgravity environment. Continued cell proliferation, or

lack of cell stabilization, during delays in Shuttle or rocket launches can easily lead to increased cell concentrations that endanger the planned microgravity experiments. An even greater problem is envisioned for experimental cell populations destined for study on Space Station. Both launch and docking delays, as well as the intervals before deployment of the cultures may negate many cell and tissue experimental protocols designed for biological and biomedical studies on Space Station. In addition, a means to stabilize experimental cell and tissue cultures that have been used on Space Station prior to their transport back to Earth, and without the cytotoxic influences of cryopreservation or chemical fixation, will require the use of an effective and reversible stabilization agent.

3.2.2.2 Earlier Missions. CeReS-18 holds promise as a stabilization agent to restrain cell proliferation during transport in both terrestrial and reduced gravity environments. Previous experiments have shown that CeReS-18 can hold a wide array of mammalian cell lines in cell cycle arrest for several days. Results gained from previous missions, i.e., STS-50, STS-54, and STS-57, showed that cell cycle arrest was mediated in the microgravity environment and that the inhibitory activity was comparable, if not identical, to that measured at unit gravity.

3.2.2.3 Specific Goals for STS-73 Mission Experiment. The study was designed to assess the possibility that CeReS-18 could stabilize cell populations during their transport from KSU to KSC, and maintain the cell cycle arrest during launch preparation until the cultures reached the microgravity environment and a research study conducted in space. In addition, the tests involved the possibility that a simple dilution of the CeReS-18 to below inhibitory levels could reverse the inhibition and reinitiate cell proliferation in flight.

3.2.2.4 Summary of Findings. The study illustrated a successful application of the inhibitor in stabilizing cell populations, from the site of preparation until at least 2 to 3 days later, when the cultures reached an initiation point in space. Furthermore, a simple dilution of CeReS-18, by the introduction of fresh culture medium, resulted in a reactivation of cell proliferation. After reversal, the cell population regained cell cycling and maintained a generation time in reduced gravity that was similar to that measured on Earth. Furthermore, a continued incubation of the cells with CeReS-18 resulted in the stabilization of the cell population in reduced gravity for at least a week.

3.2.2.5 Commercial Applications. The studies simply would not have been possible without access to microgravity. The technical approach was shown to be possible by the success of the study. We believe that essentially all researchers who focus on cell biology studies in microgravity will be a potential market. A terrestrial market already exists for the transport of viable cells, for biomedical and related studies, to laboratories throughout the world.

The potential of CeReS-18 to arrest a wide array of cell lines, obtained from a diverse range of species including mammalian, avian, and insect cells provides a novel means to stabilize experimental cultures during transport and launch delays, as well as operational procedures associated with transport of experimental cultures to Space Station. In addition, an inhibitor like CeReS-18 that reversibly arrests cell cycling in a site specific manner has numerous applications as a cytologic reagent to study cell, genetic, and molecular processes in terrestrial laboratories associated with either basic research or clinical studies. Finally, the ability of CeReS-18 to efficiently arrest the proliferation of transformed and highly malignant cell populations holds promise for biomedical applications.

We believe that the space research requirements are totally consistent with the potential benefits associated with the product.

This project was supported with cash funding from Lockheed-Martin, SynchroCell, Inc., the KSU Research Foundation, and the Center for Basic Cancer Research. In addition, in-kind support was provided by these and other agencies.

3.2.3 Development, Growth and Activation of Bone Marrow Macrophages-Phase II

PI: Chapes, Stephen Keith Ph.D., M.P.H.

3.2.3.1 Background. Bone marrow macrophage development is inhibited in vivo by space flight or by antiorthostatic suspension. Inhibition of macrophage development and function can have severe consequences on health and immunological function. Experiments on STS-57, STS-60, STS-62 and STS-63 found that bone marrow macrophage differentiation in liquid culture was significantly inhibited by space flight; however, growth was significantly enhanced. Furthermore, experiments from STS-69 demonstrated that bone marrow macrophage colony formation was enhanced during space flight.

In addition, experiments on STS-37 and STS-43 found that space flight altered bone marrow macrophage secretion of cytokines. The experiments for STS-73 were designed to expand on these studies and to test whether the transcription of receptor proteins or cytokines is altered by space flight. We also attempted to confirm that space flight enhanced macrophage colony formation in an agar culture system compared to ground controls.

3.2.3.2 Methods

- Experiment 1 (B6MP102 cells attached to beads)-The continuous bone marrow macrophage cell line B6MP102 was used in these experiments. B6MP102 cells were attached to cytodex 3 beads and cultured in 2.8 ml of Dulbecco's modified Eagle's Medium. Cells were exposed to fresh medium or medium including 12.5 mg/ml lipopolysaccharide. After 18 hours the experiment was terminated by the addition of guanidinium HCL. RNA was purified from the samples after FPA recovery. Cells were analyzed for their transcription of TNF and other cytokine genes.
- Experiment 2 (Bone marrow macrophage growth in soft agar)-Freshly harvested bone marrow cells were isolated from the marrow of C3HeB/FeJ mice. Marrow cells were resuspended in 1.5 ml of soft agar containing medium and macrophage colony stimulating factor and the FPA's were plugged with gas exchange septa. The FPA's were gassed in an 8 percent CO₂ incubator for >8 hours and the FPA's were sealed with conventional septa leaving >5 ml of an air atmosphere with an 8 percent CO₂ concentration. The FPA's were stored at 37 °C during flight, and colony formation was quantitated upon FPA recovery.

3.2.3.3 Results

- Experiment 1—The FPA's were stored in an ambient temperature GAP during the flight of STS-73. This GAP was terminated at the designated time, the samples were recovered, and RNA was purified from the samples. Several ground control FPA's were not terminated correctly. Therefore, we did not have enough control RNA to make valid comparisons. Alternative data analyses are planned for these samples and will be conducted in the future.

- Experiment 2—The FPA's demonstrated good colony formation using the soft-agar technique. We scored 76 ± 6 (mean SEM) colonies per FPA flown in space versus 98 ± 6 colonies in ground controls maintained in Florida. In addition, cells in soft agar secreted $2,280 \pm 279$ ng/ml of soft agar when flown in space compared to $1,730 \pm 390$ ng/ml soft agar of Florida ground controls.

3.2.3.4 Conclusions. These experiments confirmed the data from STS-69 which demonstrated that soft-agar bone marrow cultures analogous to those in conventional lab settings could be done. However, we also found that marrow colony formation was depressed by space flight. This contrasts the data obtained from STS-69. The trend for enhanced IL-6 secretion also contrasts the results of STS-69. However, the methodology to assay IL-6 was changed from that used to assay for IL-6 in STS-69. It is possible that the contrasting results between STS-69 and STS-73 are due to the differences in flight lengths. It is possible that a 16-day flight allowed for overgrowth and death of colonies that would have been quantitated at day 8 (length of STS-69 flight), and the 16-day flight was more satisfactory to slower forming colonies. Additional ground-based experiments are planned to test this hypothesis. STS-73 was also plagued by several delays. Unfortunately, our poorest bone marrow cell preparation eventually flew. We think that earlier loads, that had to be scrubbed, were better cultures as assessed by the eventual colony formation that was seen. Therefore, the quality of the cell preparation may have also influenced the final data.

3.3 Viruses

3.3.1 Viral infection of Mammalian Cells

PI: Consigli, R.

The purpose of the STS-73 flight experiment was to determine if microgravity affected the ability of a virus to infect mammalian cells. The virus used was the polyomavirus, a small DNA virus that has the capability to infect murine (mouse) cultured 3T6 cells. Unfortunately, due to the numerous launch delays that STS-73 experienced, the cultured cells experienced adverse conditions and did not remain sufficiently viable. Postflight analyses indicated that infection was proceeding in microgravity; however, it was not possible to determine whether the infection capability was improved or reduced in microgravity.

3.4 Crystal Growth

3.4.1 Crystallization of Proteins in Microgravity for High Resolution Structural Basis for Drug Design

PI: Shoham, G.

3.4.1.1 Background. A new field of structure-based drug design has recently been established, where both academic institutes and pharmaceutical companies are increasing their efforts to utilize structural information of important biological macromolecules. This will enable them to intelligently and rationally produce medicinally effective agents. Such high resolution structural data is available today only through x-ray crystallographic analysis, especially for medium and large proteins. Nevertheless, crystal structure analysis of proteins is still handicapped today by lack of systematic and efficient methods for obtaining high quality crystals which are suitable for such studies at the molecular level. Crystallization of proteins in microgravity has been recently proposed as one of the approaches that will improve the efficiency of protein crystallization and the quality of the resulting crystals. However, except for a few specific cases,

such superiority of microgravity crystallization has not yet been firmly established and/or applied for practical day-to-day crystal growth.

3.4.1.2 Goals. The experiment conducted onboard the STS-73 mission is the first in a series of experiments targeted with the goal of better understanding, increased efficiency and more dynamic control of protein crystallization in microgravity. The specific goal of the STS-73 experiment was to crystallize two model proteins by a flight adaptation of the microdialysis lab techniques in the currently available FPA hardware of BioServe.

3.4.1.3 Results. Most (~80 percent) of the microdialysis crystallization experiments on the Space Shuttle resulted in protein crystals which are suitable for high resolution analysis. Although not larger in size, the quality of these crystals was proven to be significantly better than their Earth-grown counterparts, as evaluated by the resolution of the x-ray diffraction, the mosaicity of the crystals and their stability in x-ray radiation. Additional analyses are ongoing at Brookhaven National Labs.

3.4.1.4 Commercial Applications. The results demonstrate that the microdialysis approach is suitable for both comparative crystallization studies in environments of different gravitation values, as well as for the improvement of the diffraction quality of reasonably diffracting protein crystals. These findings can now be used for follow-on experiments in these series, where a wider family of proteins will be examined and more control will be introduced to the dialysis crystallization process. Commercial applications are mostly in the field of protein crystallization itself as discussed in the background above.

3.4.2 Protein and Nucleic Acid Crystallization

PI's: Todd, P. and Sportiello, M.

3.4.2.1 Background. Crystals grown from proteins and/or nucleic acids, if of sufficient quality, can be used to determine the three-dimensional structure of the biomolecules. Knowledge of this structure can provide information leading to understanding of the molecule's activity in vivo and development of pharmaceuticals designed to be effective in the treatment of disease. Our experiments seek to develop and test new techniques to grow these crystals—techniques that are designed to maximize the chance of obtaining the high-quality crystals necessary for eventual pharmaceutical development. In addition, crystals grown in low gravity are often of higher quality than those grown on Earth, thereby providing more structural information and, down the line, more effective pharmaceuticals.

3.4.2.2 Previous Experiments. We have grown protein and nucleic acid crystals in BioServe hardware (FPA's) on seven previous Space Shuttle flights (STS-50, STS-54, STS-57, STS-60, STS-62, STS-63, and STS-69). Experiments were performed to investigate a variety of crystal-growing techniques (batch, osmotic dewatering, step osmotic dewatering, dialysis diffusion, and step dialysis diffusion) and hardware (large and small crystallization inserts placed in the FPA's), and both protein and nucleic acids were used on these flights. We were successful in growing crystals of protein (lysozyme and poliovirus polymerase), nucleic acid (U-U dodecamer RNA), and protein:nucleic acid complexes (telomere binding protein: DNA oligomer complex, gene 32 protein:ss DNA complex). These successes helped provide validation of the utility of the hardware used for crystallization, incrementally led to improvements in techniques and hardware, and provided information on the conditions for successful growth of protein and nucleic acid crystals in space. Intrinsically of interest in the field of health sciences were the successes in growing crystals of the

protein:DNA complexes, as these complexes are involved in such processes as cancer and aging, and the successful growth of poliovirus polymerase crystals.

3.4.2.3 STS-73 Goals. Our goals for our STS-73 experiments included building upon our earlier successes and growing even better crystals of the U-U dodecamer RNA, the telomere binding protein:DNA complex, and poliovirus polymerase than we had grown on previous Shuttle flights, growing crystals of molecules that we had not successfully crystallized in low gravity previously (e.g., the twenty-six mer pseudoknot, an RNA developed by NeXstar that inhibits HIV reverse transcriptase), and continued evaluation of the various pieces of crystallization hardware and the techniques used for crystal growth.

3.4.2.4 STS-73 Results. We were successful in crystallizing only one of the six biomolecules that we attempted to crystallize in space; this one success was with the 26-mer pseudoknot RNA. The five molecules that we were not successful in crystallizing included three molecules that we had successfully crystallized on previous Space Shuttle flights (the U-U dodecamer RNA, the telomere binding protein:DNA complex, and poliovirus polymerase). The major cause of the overall lack of success seemed to be the effect of the many launch delays on the sensitive and labile biological molecules that we were attempting to crystallize. Typically, our experiments require activation of the crystallization process soon after loading in order to avoid degradation of our molecules. The launch delays prolonged the period between loading and activation.

3.4.2.5 Commercial Relevance. It has been documented that crystals grown in low gravity are often more highly ordered than those grown at 1 g. These better quality, space-grown crystals can, upon analysis, often provide more detailed information on the structure of the protein and/or nucleic acid molecules being crystallized. BioServe has developed specialized hardware in which crystals have been grown in low gravity by a variety of traditional and new techniques.

Pharmaceutical companies, which are a significant part of the U.S. economy, are very interested in determining the three-dimensional structure of macromolecules that have therapeutic applications or that are involved in a disease process. The ability to use specific crystallization techniques, the lessons learned from basic crystallization experiments in low gravity, and the structures derived from crystals of the specific macromolecules of interest are all quite valuable to pharmaceutical companies.

Knowledge of the three-dimensional structure of molecules of interest can lead to development of new pharmaceuticals to treat diseases. If crystallization experiments performed in low gravity provide high enough quality crystals, effective pharmaceuticals may be produced.

IDEA Scientific has received a SBIR award and will contract with BioServe to support space crystallization experiments. BioServe also has an agreement in place with Amgen to collaborate with BioServe on low-gravity crystallization experiments.

3.5 Plants

3.5.1 Plastid Distribution in Columella Cells of a Starchless Arabidopsis Mutant Grown in Microgravity

PI: Guikema, J.

3.5.1.1 Background. Roots of higher plants reorient relative to the gravity vector by the process of gravitropism. Columella cells of the root cap have been proposed as the site of gravity perception and contain starch-filled plastids whose positioning may influence the gravitropic curvature. In support of that, a TC7 Arabidopsis mutant (TC7) has been characterized and shown to have starchless plastids and a reduced gravitropic response.

3.5.1.2 Summary of Findings From Previous Space Flight Experiments. We have shown that root growth (as well as ethylene production) was enhanced in microgravity. In addition, cellular ultrastructure, particularly that of columella cells, is affected by microgravity, possibly because of a cytoskeletal rearrangement. We have also found that calcium was redistributed in sweet clover columella cells developed in microgravity, suggesting a role of calcium as a second messenger in gravity perception.

3.5.1.3 Specific Experimental Goals for the STS-73 Mission Experiment. The microgravity environment of space flight, obtained through the NASA Space Shuttle program, provides an opportunity to examine the effects of plastid density on organelle distribution in the absence of unit gravity. In this experiment, we have examined the distribution of the amyloplasts in columella cells of a starchless Arabidopsis mutant (TC7) and the wild type strain.

3.5.1.4 Summary of Findings From STS-73. Computer image analysis of columella cells revealed that plastids of the mutant grown in microgravity were mostly found in the middle of the cell, whereas amyloplasts of the wild-type were in majority located at the top of the cell. Therefore, these data suggest a different plastid positioning mechanism for mutant and wild-type in the absence of gravity.

3.5.1.5 Commercial Criteria. Microgravity effects on plant growth, including the direction of growth, the extent of cell wall deposition, amount of lignin deposited in the cell wall matrix, and the partitioning of carbohydrate between lipid and starch, will have profound effects on bioregenerative life support.

These fundamental processes are critical for food and fiber production in the U.S., and basic knowledge of these processes will impact our abilities to develop sustainable production systems that are economically and environmentally sound.

Starch has been a useful component in novel production items, such as biodegradable materials, as well as an important food component. The free fall conditions of Shuttle-based space flight provide a unique test-bed for monitoring microgravity effects on starch localization, quality, quantity, and intracellular impact by production of stress ethylene.

3.5.2 Effects of Stress Ethylene Inhibitors on Sweet Clover

PI: Guikema, J.

3.5.2.1 Background. The enclosed environment of the FPA permits buildup of gasses such as ethylene, which may impact plant growth and development, and which may mask important findings. This research further explores ethylene responses.

3.5.2.2 Summary of Previous Results. Previous work, both from our laboratory and from others, has shown that microgravity influences the amount of ethylene produced by seedlings. The specific response, however, seems to be plant specific. This is an interesting speculation. Enhanced ethylene was observed for such plants as soybean. However on STS-57, we showed that there was less ethylene produced by sweet clover at 69 and 141 hours post-hydration in space than in ground controls. Greater levels of carbon dioxide were observed in space, as was an increase in overall plant length. Greater ethylene production was also observed with wild-type *Arabidopsis* during STS-69. Interestingly, mutations influencing starch biosynthesis induced high ethylene production, at levels identical to wild-type space flight values, in ground controls, clinorotated controls, and in space flight.

3.5.2.3 Goals for STS-73. To examine the effects of ethylene biosynthesis inhibitors on the space-induced increase in ethylene synthesis in sweet clover.

3.5.2.4 Results From STS-73. Inhibitors such as AOA inhibited ethylene synthesis in both space flight and in ground controls.

3.5.2.5 Commercial Criteria. Microgravity effects on plant growth, including the direction of growth, the extent of cell wall deposition, amount of lignin deposited in the cell wall matrix, and the partitioning of carbohydrate between lipid and starch, will have profound effects on bioregenerative life support.

These fundamental processes are critical for food and fiber production in the U.S., and basic knowledge of these processes will impact our abilities to develop sustainable production systems that are economically and environmentally sound.

Starch has been a useful component in novel production items, such as biodegradable materials, as well as an important food component. The free fall conditions of Shuttle-based space flight provide a unique test-bed for monitoring microgravity effects on starch localization, quality, quantity, and intracellular impact by production of stress ethylene.

3.5.3 Effects of Microgravity on Gene Expression in Higher Plants

PI: Li, Y.

3.5.3.1 Summary of Findings Prior to STS-73. We observed the expression of two auxin regulated genes were enhanced in the space-grown seedlings.

3.5.3.2 Goals for the STS-73 Mission Experiment. To confirm the effects of microgravity on the expression of the auxin regulated genes in higher plants.

3.5.3.3 Summary of findings from STS-73. We confirmed the expression of the auxin-regulated genes is indeed enhanced in the space-grown seedlings.

3.5.3.4 Commercial Applications. Auxin is an important plant hormone influencing almost every aspect of plant growth and developmental processes. An altered tissue's sensitivity to auxin or changes in auxin contents normally cause dramatic effects on plant growth rates. Many changes, such as reduced root growth, have been observed in space grown plants. Our research should improve the understanding of the effects of microgravity and gravity on plant growth at the physiological and molecular levels, which is an important step toward commercial application of space using plants as bioreactors for pharmaceutical products. It will also aid in the development of bioregenerative life support systems to support crews in extra-terrestrial environments. Weyerhaeuser Company has provided some funds to our research project, and Nunhems Zaden BV in Holland will soon provide financial support to our project.

3.5.4 Clover (*Trifolium repens*) Gravi-response After Space Flight or Clinorotation

PI: Smith, J.D.

3.5.4.1 Abstract. In order to survive, plants need to know up from down. Within hours, germinating seedlings turn roots downward and shoots upward regardless of their initial orientation. This process, called gravitropism, has been studied extensively on Earth, but questions regarding exactly how the force of gravity is turned into a biochemical signal still remain. In space, where gravity's influences are very small, the specialized gravity sensing cells in plants (the statocytes) appear different than that in comparative cells of Earth-grown plants. These cellular changes, in turn, affect the greater processes of gravity-dependent plant growth and may also affect the production of essential nutrients or secondary metabolites of pharmaceutical value. In this study, the gravity response of clover seedlings is compared to Earth-grown controls and seedlings grown on a slow-rotating two-axis clinostat. The BioServe FPA provides an excellent environment for short-term, low-cost plant growth experiments in space. We have successfully characterized the long-term effects on gravity response in white clover under nominal, low-gravity, and clinorotated conditions. The physiological differences we have observed for clover correlate well to those previously found for other species flown in space and subjected to slow clinorotation. However, for the characterization of short-term changes in gravity sensitivity, faster experiment turnaround after landing or new hardware modifications will be necessary.

3.5.4.2 Introduction. Today, many of the underlying cellular mechanisms governing gravitropism are well known.^{1,2,3} However, only with the relatively recent development of space flight and opportunities to grow and observe plants in space has it been possible to ask the question: Is gravity simply an orientation cue, or have plants evolved to require gravity for proper growth and development?

Higher plants have been grown from seed to seed in microgravity aboard orbital space platforms^{4,5} but a number of differences, including altered growth rates, carbohydrate production, lignin formation, and gravity perception and response have been noted for various species under various conditions.^{6,7} Unfortunately, the high cost and inaccessibility of experimental biology in space have made it difficult for researchers to gain sufficient access to space to repeat critical experiments and perform adequate follow-up studies. As a result, it is still unclear how plant growth and development are changed by the absence of gravitational cues.

3.5.4.3 Plant Gravity Response After Space Flight and Clinorotation. To test the gravity sensitivity of clover seedlings after prolonged space flight, 30 seeds aboard Shuttle mission STS-73 were grown for 96 hours in microgravity and then returned to Earth viable for subsequent bending response measurements. Plants were removed from FPA's as soon as possible following landing (about 5 hours after the Shuttle touched down) and placed horizontally on 1 percent agar plates (Sigma Chemical Corp.). Time lapse photographs were taken over a 10-hour period. Angle and length measurements were made from color photographs using a SummaSketch scanning board and Sigma Scan scanning software (Jandel Inc.). Clinostat and stationary 1 g control seedlings were treated identically to flight seedlings. The average root tip angle is shown for each gravity treatment in figure 6. There was no significant difference between bending responses of 1 g control and microgravity grown seedlings. However, clinorotated seedlings did not respond well to gravity after 96 hours of constant rotation.

Long-term gravi-response is affected by prolonged clinorotation but not space flight. The curvature response of clover seedlings after 96 hours of clinorotation is significantly reduced when compared to 1 g control plants. We believe this result is directly related to our observations of root cap deterioration in 72-hour clinorotated plants (previously observed in an STS-63 experiment). Plants with damaged root caps must rebuild the proper gravity sensing system in order to sense and respond to gravity. No significant difference was found between the gravity curvature of space flight and 1 g control plants. Based on histology, seedlings flown in space had intact root caps. Presumably, the intact/functioning root cap enabled them to respond to gravity as quickly as 1 g controls. In contrast, some researchers have observed that lentil seedlings grown in space over-respond to an applied gravity stimulus.^{8,9} Because of the long duration between Shuttle landing and the gravity stimulation experiment, our study could only distinguish between long-term effects on the gravitropic system. Short-term transient effects that plants could repair within 6 hours could not be detected with this method. Future research will focus on the isolation of short-term changes in the sensitivity of plants to gravitational cues after return to Earth and how those changes affect secondary metabolite production. If plant sensitivity to gravity is changed in space, the production of pharmaceutically valuable metabolites may not occur, except after the application of a gravitational acceleration.

3.6 Biomaterials/Bones

3.6.1 Pre-metatarsal Development and Mineralization

PI's: Klement, B. and Spooner, B.

3.6.1.1 Background. Space flight is known to cause bone mass loss in animals and humans. This condition is of particular concern to the health of astronauts exposed to reduced gravity conditions for long durations, such as will become routine on the *International Space Station* and will be even more severe for a manned mission to Mars. Previous research on humans and animals has begun to elucidate the mechanisms of this bone material loss; however, much work remains to be done. Studying the skeletal system in animals and humans is complicated by the numerous other physiological changes occurring such as muscle atrophy, immune suppression, blood volume shifts and reductions, etc. Studying developing skeletal tissue isolated in vitro offers the opportunity to directly study the effects of unloading without the complications of other physiological changes. Though such a model may not fully characterize bone responses in vivo, important insight into localized effects of gravity on bone tissue may be derived. The following experiment was performed to evaluate the effects of reduced gravity on pre-metatarsal derived from embryonic mice and allowed to develop in culture.

3.6.1.2 Methods. Pre-metatarsal tissue from embryonic mice at 13 days gestation were removed and placed on special inserts permitting gas exchange and then covered with Matrigel. Chambers A, B and C of the FPA's contained BGJb culture medium. Chambers B and C contained ^{45}Ca , to monitor Ca incorporation into the potentially mineralized extracellular matrix. All pre-metatarsals were fixed after landing. Analyses of tissues consisted of measuring lengths, staining for mineral content and assaying ^{45}Ca incorporation in both flight and matched ground-control pre-metatarsal tissues.

3.6.1.3 Results. Previous research using standard FPA's that did not permit gas exchange showed that pre-metatarsal tissue exposed to space flight had significantly greater mineralization relative to tissue grown on the ground. This result was surprising given the known effect of space flight to cause reduced bone mass in intact animals. In contrast however, tissues derived in the same manner and flown on STS-73 were found to have the same level of mineral content as ground tissues. These experiments were performed using FPA's modified to allow gas diffusion into the culture chamber (GE-FPA's) which allows for greater O_2 availability and for removal of CO_2 .

Even though STS-73 tissues revealed comparable levels of mineralization, ^{45}Ca uptake indicated lower uptake of Ca in flight pre-metatarsals. This result is consistent with the normal physiological response of bone to respond to loading stresses with greater Ca incorporation. Analyses are continuing to better understand the relationship of Ca uptake and overall mineralization and tissue development. Ongoing ground experiments and future flight experiments are expected to further characterize the effects of gravity on the pre-metatarsal model system.

3.6.1.4 Commercial Relevance. Osteoporosis is a serious bone disorder that affects many millions of people in the U.S. and over a billion people worldwide. Similar to space flight, this condition is characterized by bone mass loss resulting in porous, weak bones that can more easily break. Many elderly people suffer broken hips and falls which can often result in health complications leading to death.

This research is attempting to explore the link between the accelerated effects of space flight and this debilitating disease. Novel pharmaceutical countermeasures provided by BioServe affiliates (including Chiron) may be used to prevent reduced gravity-induced bone mass loss and possibly help prevent osteoporosis. These experiments, along with other BioServe experiments being done on whole animals, may lead to a greater understanding of how these drugs function and may lead to more rapid FDA approval and availability to the public.

3.6.2 Magnetic Combing of Collagen

PI: Doyle, John

3.6.2.1 Background. Implantable-grade collagen is difficult to produce in vitro because collagen normally formed by standard polymerization techniques is not organized at the fiber level. However, when collagen is formed in microgravity and combed with fixed magnetic bacteria under the influence of a magnetic field, collagen more closely resembling collagen produced by the body is formed.

Magnetic combing of collagen has been achieved on previous space flights (STS-57, STS-63). Using both photography and electron microscopy, it was determined that magnetic combing positively affected the collagen matrix produced. Ground controls and other ground experiments supported these results.

3.6.2.2 Goals for STS-73. The experimental objectives were two-fold: confirm the results of the two previous missions on which this experiment flew (STS-57, STS-63) and test other variables controlling polymerization, specifically pH of assembly buffer and concentration of magnetic bacteria. Twelve separate experiments were distributed between two GAP's. This minimized space requirements while maximizing experimental data gathering possibilities. The GAP's were shared with other experiments.

3.6.2.3 Results. Due to numerous delays in the launch of STS-73, three reloads of the experiment were required. On the third reload, spacers were left out of the C chamber of the FPA. This delayed initiation of the experiment from day 0 to day 5 of the mission. During the delay, the collagen self-polymerized and thus no magnetic combing was possible.

Fortunately, results from STS-77 were much more encouraging. Magnetic bacteria drawn by a magnetic field through a polymerizing collagen matrix positively affected the collagen matrix. Collagen also polymerized in a larger area than plugs of collagen that had polymerized on the ground. Previous data from STS-57 and STS-63 were confirmed.

3.6.2.4 Commercial Potential. This experiment has tremendous commercial potential. It has a wide market appeal in the areas of artificial organ, limb, tendon, and bone growth. Potentially, it could appeal to cosmetic applications as well. Through this research, it is hoped that the technology will evolve to artificially produce such materials as skin, tendon, bone, heart valves, et al., thus improving the quality of life for all people.

3.6.3 Examination of Plasmin Enzyme Efficacy in Microgravity

PI: Bateman, Ted

The fibrin degradation experiment performed on STS-73 was the culmination of three experiments examining enzyme efficacy in microgravity. These enzymes are plasmin, collagenase, and cellulase which digest fibrin, collagen, and cellulose, respectively.

The fibrin/plasmin results from STS-73, and other Shuttle experiments (STS-63, STS-69, STS-77), are very similar to those of the other two enzyme models. Enzymes degrade proteins faster in microgravity than in a 1 g environment. The fibrin and collagen experiments showed a greater enzyme efficacy in microgravity than both clinostat (tumbled mixing) and 1 g. (Simske and Luttgies: "Effect of Microgravity on Collagenase Deproteinization and EDTA Decalcification of Bone Fragments," *Micrograv. Sci. and Tech.*, 3, 266-269, 1994.)

During the 2 to 3 days the fibrin gels were allowed to degrade, the plasmin was 30 to 50 percent more efficient, respectively, in microgravity than on the ground. Clinostat proved to be 15 to 25 percent more effective.

The combination of these three experiments gives strong evidence that enzyme efficacy is enhanced in the microgravity environment of space. Though efficacy can be increased in an alternate ground model, it cannot match that which occurs in space. Though a specific company did not sponsor these experiments, this has an impact on potential materials manufacturing of intricate protein structures essential for human tissue reconstruction. A paper with the combined results of fibrin and cellulase will be submitted to *J. Biomedical Materials Res.* this spring.

3.7 Microorganisms

3.7.1 A Summary of Research on Bacterial Growth in Suspension Cultures, on Semisolid Agar and Biofilm Development

PI's: Klaus, D., Kacena, M. and Manfredi, B.

3.7.1.1 Introduction. Microorganisms have been shown by a variety of researchers to undergo altered growth behavior when cultured in a space flight environment. Relative to matched ground controls, increased final population density and decreased antibiotic effectiveness in space are two of the more predominant findings reported to occur. The underlying mechanisms causing the changes remain largely unknown, however. The goal of this ongoing series of experiments is to further the understanding of what specific factor(s) is (are) responsible for the observed changes by studying several facets of bacterial growth in an attempt to isolate particular variables. One fundamental endeavor has been an attempt to compare *E. coli* growth in suspension cultures to that cultured on semisolid agar under otherwise comparable experimental conditions. This approach was aimed at determining what role bulk fluid effects play in bringing about the metabolic changes. This phenomenon is typically referred to as an "indirect" effect of weightlessness. That is, gravity is suspected to alter the extracellular mass transfer processes such that the cell is exposed to altered conditions in its immediate surrounding microenvironment, or is indirectly affected by weightlessness. Bacterial metabolism is highly dependent on environmental parameters and the interactions between the cell and its bulk fluid depend primarily on diffusion and sedimentation to transfer mass across the boundary layer. Sedimentation is gravity dependent while diffusion is not; therefore, the net mass transport into and out of the cell's boundary layer will be altered in the absence of gravity and, as a consequence of the changes in its surroundings, the cell will exhibit an altered metabolic response. By comparing the behavior of cells that are suspended in a fluid medium to that of cells attached to a semisolid agar medium, the effects due to bulk fluid can be further ascertained. A third component of this investigative series deals with biofilm formation. The formation process has been analyzed from the perspective of how gravity might influence each specific step from initial growth in solution, to contact probability, to reversible attachment, and finally, irreversible attachment and subsequent growth of the biofilm.

3.7.1.2 Results. The findings from STS-73 for the *E. coli* suspension culture experiment corroborated data from previous research. Since only four samples were flown for this experiment, it was limited to establishing reproducibility of prior results. Namely, the in-flight optical density monitoring capability showed that the lag phase ended on the order of 5 hours sooner than matched ground controls and post-flight microscopy counts indicated that final cell population was increased by 29 percent ($p < 0.001$, t-test) in flight. This is in agreement with earlier findings conducted with the same hardware and strain of bacteria. In all cases, the *E. coli* strain used (ATCC 4157) was largely nonmotile, as swimming action would complicate the analysis aimed at elucidating the individual contributions of diffusion and sedimentation.

The semisolid agar experiment had two components. First, the effect on growth kinetics and second, the effectiveness of the antibiotic gentamicin in inhibiting growth. Both aspects, growth and inhibition, are dependent on fundamentally similar extracellular mass transport phenomena for uptake of nutrients or drugs. Therefore, the underlying aspects associated with the individual findings can be combined to form a larger picture of how gravity influences the cells. The findings showed that *E. coli* cultures grown in flight on agar for 24 to 27 hours experienced a heightened growth compared to matched, simultaneous

ground controls. However, addition of gentamicin to the agar inhibited bacterial growth to the same extent in space as on the ground, and cell viability after gentamicin treatment did not change in flight. Therefore, while the existence of a decrease in antibiotic effectiveness in suspension cultures remains unexplained, the increased growth characteristics observed in both, suspension and agar cultures, adds information to the central focus on how extracellular mass transport phenomena affect cellular metabolism.

The biofilm experiment on STS-73 was unfortunately found to have contaminated medium. The samples were reloaded several times due to the numerous launch delays. However, it was determined that bacterial cells from a mixed culture irreversibly attach to surfaces in low gravity.

The intended goal of this experiment was to determine if the initial steps in biofilm formation are altered in low gravity, more specifically, to determine if cells irreversibly attach to a substratum forming a biofilm. The study has subsequently been repeated on STS-77 and the data again indicate that cells do irreversibly attach to surfaces in low gravity. Furthermore, the attachment process was similar in the flight and ground controls, although the flight surfaces had larger biofilms, most likely due to the lack of shear forces acting on the film in the low-gravity environment.

3.7.1.3 Commercial Applications. This series of investigations into the fundamental behavior of microbes in a weightless environment has been undertaken with the ultimate goal of applying the knowledge gained to explore the potential for enhancing the process of microbial pharmaceutical production. To this effect, more recent flight experiments were performed in collaboration with a pharmaceutical research company in which the production of the antibiotics monorden by the fungus *Humicola fuscoatra* and actinomycin-D by *Streptomyces antibioticus* was investigated. Preliminary data from the first investigation conducted on STS-77 indicated that monorden production was increased by up to 190 percent ($p < 0.001$, t-test) relative to matched ground controls which had comparable amounts of fungal dry mass. The more recent actinomycin-D experiment is still being analyzed. Initial observations showed that an increase in sporulation occurred in the space cultures.

The significance of these findings is currently under discussion and "next steps" in the collaborative effort are being considered. The initial pilot studies were performed in FPA's which do not provide optimal conditions for the production process. In following BioServe's basic philosophical approach, the next step is likely to involve designing and flying a more specialized device to further investigate what caused the process to increase so significantly. The ultimate application may involve cost feasible processing on a space platform or a means of enhancing terrestrial processing as a result of the unique knowledge gained in the novel environment of weightlessness. With the ever increasing appearances of drug resistance in pathogenic microbes, the space flight environment provides a unique environment in which the efficacy of drugs can be studied as well as the possibility of producing novel pharmaceuticals such that the microbes may not be able to respond using their normal paths of resistance.

REFERENCES (As cited in this report)

1. Moore, R.; and Evans, M.L.: "How Roots Perceive and Respond to Gravity," *Amer. J. Bot.*, 73, 574–587, 1986.
2. Sack, F.D.: "Plant Gravity Sensing," *International Reviews of Cytology*, 127, 193–252, 1991.
3. Konings, H.: "Gravitropism of Roots: An Evaluation of Progress During the Last Three Decades," *Acta Bot. Neerl.*, 44, 195–223, 1995.
4. Halstead, T.W.; and Dutcher, R.F.: "Plants in Space," *Annual Review of Plant Physiology*, 38, 317–346, 1987.
5. Steward, F.C.; Krikorian, A.D.; Levine, H.G.; and Bidwell, R.G.S.: "Development and Growth in Space: Chapter Eight," In *Plant Physiology: A Treatise; Volume Ten: Growth and Development*, Academic Press Inc., San Diego, pp. 491–571, 1991.
6. Cowles, J.R.; Scheld, H.W.; Lemay, R.; and Peterson, C.: "Growth and Lignification in Seedlings Exposed to Eight Days of Microgravity," *Annals of Botany*, 54, 33–48, 1984.
7. Brown, C.S.; and Piastuch, W.C.: "Starch Metabolism in Germinating Soybean Cotyledons is Sensitive to Clinorotation and Centrifugation," *Plant, Cell and Environment*, 17, 341–344, 1994.
8. Lorenzi, G.; and Perbal, G.: "Root Growth and Statocyte Polarity in Lentil Seedling Roots Grown in Microgravity or on a Slowly Rotating Clinostat," *Physiol. Plant.*, 78, 532–537, 1990.
9. Perbal, G.; and Driss-Ecole, D.: "Sensitivity to Gravistimulus of Lentil Seedling Roots Grown in Space During the IML–1 Mission of SpaceLab," *Physiol. Plant.*, 90, 313–318, 1994.

CATEGORIZED BIBLIOGRAPHY

This bibliography is categorized in the same manner as the experiment result and conclusion section above. It contains a select set of publications from the experiments flown on STS–73/USML–2. Because many of these experiments are part of ongoing research, the bibliography also includes related articles from previous missions and in some cases publications stemming from data obtained from more recent flights.

EXPERIMENT 3.1 Whole Organisms

1. Abbot, M.K.; Hilgenfeld, R.B.; and Dennel, R.E.: "Drosophila melanogaster as a Model System for Assessing Development Under Conditions of Microgravity," *Trans. Kansas Acad. of Sci.*, 95, 70–75, 1992.
2. Rosowski, J.R.; Gouthro, M.A.; Schmidt, K.K.; Klement, B.J.; and Spooner, B.S.: "Effect of Microgravity and Hypergravity on Embryo Axis Alignment During Postcystment Embryogenesis in *Artemia franciscana*," *J. Crustacean Biology*, 15(4), 625–632, 1995.
3. Spooner, B.S.; Debell, L.K.; Armbrust, L.; Guikema, J.A.; Metcalf, J.A.; and Paulsen, A.: "Embryogenesis, Hatching and Larval Development of *Artemia* During Orbital Space Flight," *Adv. Space Res.*, 14, No. 8, (8)229–(8)238, 1994.
4. Spooner, B.S.; Metcalf, J.; DeBell, L.; Paulsen, A.; Noren, W.; and Guikema, J.A.: "Development of Brine Shrimp *Artemia* is Accelerated During Space Flight," *J. Experimental Zoology*, 269, 253–262, 1994.

EXPERIMENT 3.2 Mammalian Cells

1. Armstrong, J.W.; Gerren, R.A.; and Chapes, S.K.: "The Effect of Space and Parabolic Flight on Macrophage Hematopoiesis and Function," *Experimental Cell Research*, 216, 160–168, 1995.
2. Betz, N.A.; Fattaey, H.K.; Westhoff, B.A.; Paulsen, A.Q.; and Johnson, T.C.: "CeReS-18, A Novel Cell Surface Sialoglycopeptide, Induces Cell Cycle Arrest and Apoptosis in a Calcium-Sensitive Manner," *Breast Canc. Res. and Treat.*, 1996 in press.
3. Betz, N.A.; Fattaey, H.K.; and Johnson, T.C.: "Growth Inhibition of BALB/c Mouse Keratinocytes by TGF- β and CeReS-18 Appear to Act Through Distinct Mechanisms," *Exper. Cell Res.*, 277, 47–54, 1996.
4. Chapes, S.K.; Morrison, D.R.; Guikema, J.A.; Lewis, M.L.; and Spooner, B.S.: "Cytokine Secretion by Immune Cells in Space," *J. Leuk. Biol.*, 52, 104–110, 1992.
5. Chapes, S.K.; Mastro, A.M.; Sonnenfield, G.S.; and Berry, W.D.: "Antiorthostatic Suspension as a Model for the Effects of Space Flight on the Immune System," *J. Leuk. Biol.*, 1993, in press.
6. Chapes, S.K.; Woods, K.M.; and Armstrong, J.W.: "Ground-Based Experiments Complement Microgravity Flight Opportunities in the Investigation of the Effects of Space Flight on the Immune Response: Is Protein Kinase C Gravity Sensitive?" *Trans. Kans. Acad. Sci.*, 96, 74–79, 1993.
7. Chapes, S.K.; Morrison, D.R.; Guikema, J.A.; Lewis, M.L.; and Spooner, B.S.: "Production and Action of Cytokines in Space," *Adv. Space Res.*, 14 (8), 5–9, 1994.
8. Chapes, S.K.; and Forsman, A.D.: "Shuttle Flight Influences Macrophage Colony Formation," *Gravitational and Space Biol.*, 10, 33, 1996.
9. Fattaey, H.K.; Betz, N.A.; Westhoff, B.A.; Moos, P.J.; and Johnson, T.C.: "Inhibition of Hormone and Growth Factor Responsive and Resistant Human Breast Cancer Cells by CeReS-18, a Cell Regulatory Sialoglycopeptide," *Breast Canc. Res. and Treat.*, 1996, in press.
10. Johnson, T.C.: "Negative Regulators of Cell Proliferation," *Pharmac. Ther.*, 62, 247–265, 1994.
11. Johnson, T.C.; and Fattaey, H.K.: "Applications for CeReS-18, a Novel Cell Growth Inhibitor, for the Stabilization of Cell Populations in the Microgravity Environment," *Amer. Soc. for Gravitat. and Space Biol. Bull.*, 10, 29, 1996.
12. Kopydlowski, K.M.; McVey, D.S.; Woods, C.M.; Iandolo, J.J.; and Chapes, S.K.: "Effects of Antiorthostatic Suspension and Corticosterone on Macrophage and Spleen Cell Function," *J. Leuk. Biol.*, 52, 202–208, 1992.
13. Moos, P.J.; Fattaey, H.K.; and Johnson, T.C.: "Cell Proliferation Inhibition in Reduced Gravity," *Experimental Cell Research*, 213, 458–462, 1994.
14. Todd, P.: Gravity and the Mammalian Cell. In *Physical Forces and the Mammalian Cell*, edited by Frangos, J. and Ives, C., Acad. Press, NY, pp. 347–381, 1992.
15. Woods, K.M.; and Chapes, S.K.: "Abrogation of TNF-Mediated Cytotoxicity by Space Flight Involves Protein Kinase C," *Experimental Cell Research*, 211, 171–174, 1994.

EXPERIMENT 3.3 Viruses

1. Burton, K.S.; and Consigli, R.A.: "Methylation of the Polyomavirus Major Capsid Protein VP1," *Virus Research*, 40, 141–147, 1996.
2. Chang, D.; Haynes, II, J.I.; Brady, J.N.; and Consigli, R.A.: "Identification of a Nuclear Localization Sequence in the Polyomavirus Capsid Protein VP2¹," *Virology*, 191, 978–983, 1992.
3. Chang, D.; Cai, X.; and Consigli, R.A.: "Characterization of the DNA Binding Properties of Polyomavirus Capsid Proteins," *J. Virol.*, 61, 69–74, 1993.

4. Chang, D.; Haynes, II, J.I.; Brady, J.N.; and Consigli, R.A.: "Identification of Amino Acid Sequences in the Polyomavirus Capsid Proteins That Serve as Nuclear Localization Signals," *Trans. Kans. Acad. Sci.*, 96, 35–39, 1993.
5. Chang, D.; Paulsen, A.; Johnson, T.C.; and Consigli, R.A.: "Virus Protein Assembly in Microgravity," *Adv. Space Res.*, 13, 251–257, 1993.
6. Funk, C.J.; and Consigli, R.A.: "Evidence for Zinc Binding by Two Structural Proteins of the Plodia interpunctella Granulosis Virus," *J. Virol.*, 66, 3168–3171, 1992.
7. Haynes II, J.I.; Chang, D.; and Consigli, R.A.: "Mutations in the Putative Calcium Binding Domain of Polyomavirus VP1 Affect Capsid Assembly," *J. Virol.*, 67, 2486–2495, 1993.

EXPERIMENT 3.4 Crystal Growth

1. Todd, P.; Sikdar, S.K.; and Walker, C.: "Application of Osmotic Dewatering to the Controlled Crystallization of Biological Macromolecules and Organic Compounds," *Journal of Crystal Growth*, 110, 283–292, 1991.
2. Lee, C.; Sportiello, M.G.; Cape, S.P.; Ferree, S.; Todd, P.; Kundrot, C.E.; Lietzke, S.; and Barnes, C.: "Characterization and Application of Osmotic Dewatering to the Crystallization of Oligonucleotides," *Biotechnology Progress*, 12(2), 1997, in press.

EXPERIMENT 3.5 Plants

1. Campbell, J.; Pecaut, M.; and Luttgies, M.: "Prevalence and Arrangement of Lignified Vascular Elements in 6-day-old Alfalfa (*Medicago sativa* L.) Seedlings Raised in Reduced Gravity," *J. Plant Physiol.*, 149, 539–547, 1996.
2. Gallegos, G.L.; Hilaire, E.M.; Peterson, B.V.; Brown, C.S.; and Guikema, J.A.: "Effects of Microgravity and Clinorotation on Stress Ethylene Production in Two Starchless Mutants of *Arabidopsis thaliana*," *Journal of Gravitational Physiology*, 2(1), 153–154, 1995.
3. Gallegos, G.L.; Odom, W.R.; and Guikema, J.A.: "Effect of Microgravity on Stress Ethylene and Carbon Dioxide Production in Sweet Clover (*Melilotus alba* L.)," *Journal of Gravitational Physiology*, 2(1), 155–156, 1995.
4. Gallegos, G. L.; Peterson, B. V.; Brown, C. S.; and Guikema, J. A.: "Effects of Stress Ethylene Inhibitors on Sweet Clover (*Melilotus alba* L) Seedling Growth in Microgravity," *Journal of Gravitational Physiology*, 2(1), 151–152, 1995.
5. Guikema, J.A.; Debell, L.; Paulsen, A.Q.; Spooner, B.; and Wong, P.P.: "Clover Development During Spaceflight: A Model System," *Advanced Space Research*, 14, 173–176, 1993.
6. Hilaire, E.; Brown, C.S.; and Guikema, J.A.: "Clinorotation Affects Soybean Seedling Morphology," *Journal of Gravitational Physiology*, 2(1), 149–150, 1995.
7. Hilaire, E.; Paulsen, A.Q.; Brown, C.S.; and Guikema, J.A.: "Cortical Microtubules in Sweet Clover Columella Cells Developed in Microgravity," *Plant Cell Physiology*, 36(7), 1387–1392, 1995.
8. Hilaire, E.; Paulsen, A.Q.; Brown, C.S.; and Guikema, J.A.: "Effects of Clinorotation and Microgravity on Sweet Clover Columella Cells Treated with Cytochalasin D," *Physiologia Plantarum*, 95, 267–273, 1995.
9. Hilaire, E.; Paulsen, A.Q.; Brown, C.S.; and Guikema, J.A.: "Microgravity and Clinorotation Cause Redistribution of Free Calcium in Sweet Clover Columella Cells," *Plant and Cell Physiology*, 36(5), 831–837, 1995.

10. Hoehn, A.: "Effects of Gravity and Light on Plant Growth and Performance in Normal and Reduced Gravity," Doctoral Thesis, University of Colorado, Aerospace Engineering Sciences, 1993.
11. Todd, P.: "Mechanical Analysis of Statolith Action in Roots and Rhizoids," *Advances in Space Research*, 14(8), 121–124, 1994.
12. Moore, R.; and Evans, M.L.: "How Roots Perceive and Respond to Gravity," *Amer. J. Bot.*, 73, 574–587, 1986.
13. Sack, F.D.: "Plant Gravity Sensing," *International Reviews of Cytology*, 127, 193–252, 1991.
14. Konings, H.: "Gravitropism of Roots: An Evaluation of Progress During the Last Three Decades," *Acta Bot. Neerl.*, 44, 195–223, 1995.
15. Halstead, T.W.; and Dutcher, R.F.: "Plants in Space," *Annual Review of Plant Physiology*, 38, 317–346, 1987.
16. Steward, F.C.; Krikorian, A.D.; Levine, H.G.; and Bidwell, R.G.S.: "Development and Growth in Space: Chapter Eight," In *Plant Physiology: A Treatise*; Volume Ten: Growth and Development, Academic Press Inc., San Diego, pp. 491–571, 1991.
17. Cowles, J.R.; Scheld, H.W.; Lemay, R.; and Peterson, C.: "Growth and Lignification in Seedlings Exposed to Eight Days of Microgravity," *Annals of Botany*, 54, 33–48, 1984.
18. Brown, C.S.; and Piastuch, W.C.: "Starch Metabolism in Germinating Soybean Cotyledons is Sensitive to Clinorotation and Centrifugation," *Plant, Cell and Environment*, 17, 341–344, 1994.
19. Lorenzi, G.; and Perbal, G.: "Root Growth and Statocyte Polarity in Lentil Seedling Roots Grown in Microgravity or on a Slowly Rotating Clinostat," *Physiol. Plant.*, 78, 532–537, 1990.
20. Perbal, G.; and Driss-Ecole, D.: "Sensitivity to Gravistimulus of Lentil Seedling Roots Grown in Space During the IML–1 Mission of SpaceLab," *Physiol. Plant.*, 90, 313–318, 1994.

EXPERIMENT 3.6 Biomaterials/Bones

1. Armstrong, J.W.; Nelson, K.A.; Simske, S.J.; Luttges, M.W.; Iandolo, J.J.; and Chapes, S.K.: "Skeletal Unloading Causes Organ-Specific Changes in Immune Cell Responses," *J. Appl. Physiol.*, 1993, in press.
2. Armstrong, J.W.; Balch, S.; and Chapes, S.K.: "Interleukin-2 Therapy Reverses Some Immunosuppressive Effects of Skeletal Unloading," *American Physiological Society*, 77(2), 584–589, 1994.
3. Klement, B.J.; and Spooner, B.S.: "Utilization of Microgravity Bioreactors for Differentiation of Mammalian Skeletal Tissue," *J. Cell. Biochem.*, 51, 252–256, 1993.
4. Nunes, C.R.; Roedersheimer, M.T.; Simske, S.J.; and Luttges, M.W.: "Effect of Microgravity, Temperature, and Concentration on Fibrin and Collagen Assembly," *Microgravity Sci. Technol.*, VIII/2, 125–130, 1995.
5. Roedersheimer, M.T.; Bateman, T.A.; and Simske, S.J.: "Effect of Gravity and Diffusion Interface Proximity on the Morphology of Collagen Gels," *Journal of Biomedical Materials Research*, 1996.
6. Roedersheimer, M.T.; Nunes, C.R.; and Simske, S.J.: "Collagenase Digestion of Bone Fragments in Microgravity," *Biotechnology and Bioengineering*, 50, 211–216, 1996.
7. Simske, S.J.; Greenburg, A.R.; and Luttges, M.W.: "Tail Suspension Induced Osteopenia in Mouse Femora: An Animal Model for Microgravity Exposure," *Journal of Materials Science: Materials in Medicine*, 2, 43–50, 1991.
8. Simske, S.J.; Wachtel, H.; and Luttges, M.W.: "Effect of Localized Pulsed Electromagnetic Fields on Tail-Suspension Osteopenia in Growing Mice," *Bioelectromagnetics*, 12, 101–116, 1991.

9. Simske, S.J.; Greenburg, A.R.; and Luttges, M.W.: "Effects of Suspension-Induced Osteopenia on the Mechanical Behavior of Mouse Long Bones," *Journal of Materials Science: Materials in Medicine*, 2(1), 43, 1991.
10. Simske, S.J.; Guerra, K.M.; Greenburg, A.R.; and Luttges, M.W.: "The Physical and Mechanical Effect of Suspension-Induced Osteopenia on Mouse Long Bones," *J. Biomechanics*, 25 (5), 489–499, 1992.
11. Simske, S.J.; Luttges, M.W.; and Allen, K.A.: "Effect of Oral Calcium and Calcium + Fluoride Treatments on Mouse Bone Properties During Suspension," *Biomimetics*, 1, 311–327, 1993.
12. Simske, S.J.; Broz, J.J.; Fleet, M.L.; Schmeister, T.A.; Gayles, E.C.; and Luttges, M.W.: "Contribution of Dietary and Loading Changes to the Effects of Suspension on Mouse Femora," *Journal of Experimental Zoology*, 269, 277–285, 1994.
13. Simske, S.J.; and Luttges, M.W.: "Effect of Microgravity on Collagenase Deproteinization and EDTA Decalcification of Bone Fragments," *Microgravity Sci. Technol.*, VII/3, 266–269, 1994.
14. Simske, S.J.; Schmeister, T.A.; Fleet, M.L.; Broz, J.J.; Gayles, E.C.; and Luttges, M.W.: "An Experimental Model for Combined Neural, Muscular, and Skeletal Degeneration," *Journal of Neuromusculoskeletal System*, 2 (3), 116–123, 1994.
15. Simske, S.J.; Luttges, M.W.; Allen, K.A.; and Gayles, E.C.: "The Role of Sex and Genotype on Antiorthostatic Suspension Effects on the Mouse Peripheral Skeleton," *Aviation, Space and Environmental Medicine*, 123–133, February, 1994.
16. Simske, S.J.; and Sachdeva, R.: "Cranial Bone Apposition and Ingrowth in a Porous Nickel-Titanium Implant," *Journal of Biomedical Materials Research*, 29, 527–533, 1995.
17. Simske, S.J.; Broz, J.J.; and Luttges, M.W.: "Effect of Suspension on Mouse Bone Microhardness," *Journal of Material Science: Materials in Medicine*, 6, 486–491, 1995.
18. Simske, S.J.; and Luttges, M.W.: "Suspension Osteopenia in Mice: Whole Body Electromagnetic Field Effects," *Bioelectromagnetics*, 16, 152–159, 1995.

EXPERIMENT 3.7 Microorganisms

1. Klaus, D.M.; Simske, S.J.; Todd, P.; and Stodieck, L.S.: "Investigation of Space Flight Effects on Escherichia coli and a Proposed Model of Underlying Physical Mechanisms," *Microbiology*, 143, Part 2, 449–455, 1997.
2. Klaus, D.M.; Luttges, M.W.; and Stodieck, L.S.: "Investigation of Space Flight Effects on Escherichia coli Growth," 24th International Conference on Environmental Systems, Proceedings, SAE Technical Paper Series 941260, 1994.
3. Klaus, D.M.: "Effects of Space Flight on the Growth and Development of Escherichia coli," Ph.D. Thesis, University of Colorado, Boulder, 1994.
4. Manfredi, B.: "Effects of Space Flight on the Growth and Development of Escherichia coli and Bacillus subtilis in Liquid Suspension and of Pseudomonas aeruginosa Biofilm," M.S. Thesis, University of Colorado, Boulder, 1996.
5. Marchin, G.L.; Silverstein, J.; and Brion, G.M.: "Effect of Microgravity on Escherichia coli and MS-2 Bacteriophage Disinfection by Iodinated Resin," *Acta Astronautica*, 1995, in press.
6. Sterrett, K.S.; Luttges, M.W.; Simske, S.J.; Edelen, C.L.; and Patino, H.: "A Study of Saccharomyces uvarum Fermentation in a Microgravity Environment," *Technical Quarterly*, 33 (1), 33–38, 1996.
7. Urban, J.E.; Gerren, R.; and Zoelle, J.: "Effects of Microgravity on the Binding of Acetylsalicylic Acid by Rhizobium leguminosarum by Trifolii," *Acta Astronautica*, 36 (2), 129–133, 1995.

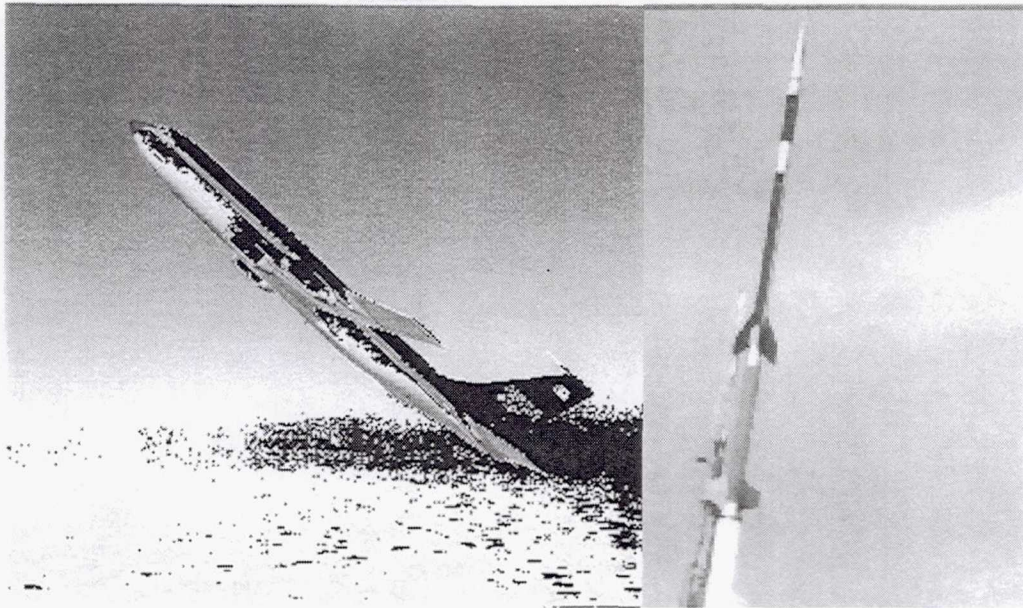
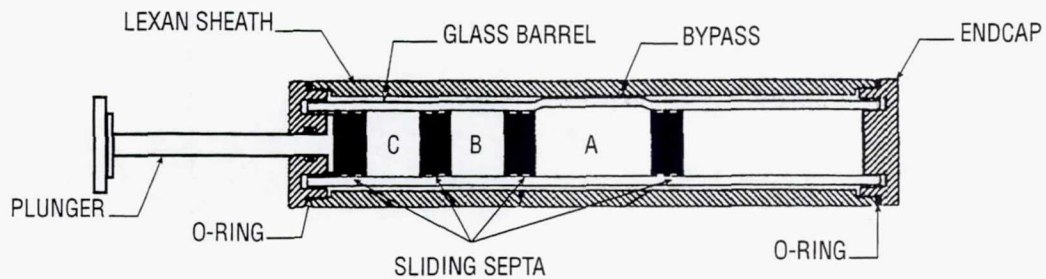


Figure 1. Parabolic aircraft (NASA's KC-135) and sounding rocket.



CHAMBER A – PRECURSOR MATERIAL
 CHAMBER B – INITIATION FLUID
 CHAMBER C – TERMINATION FLUID

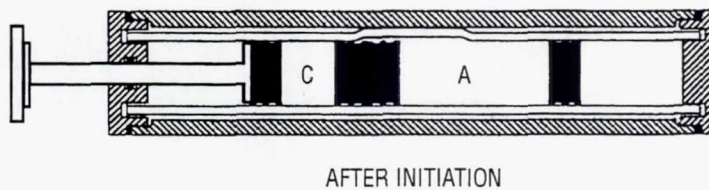
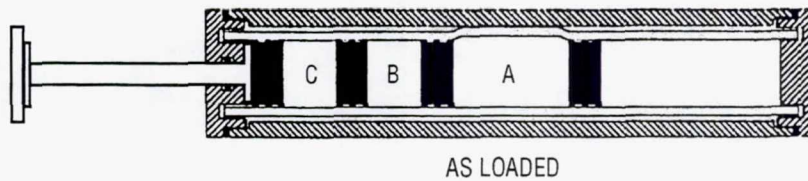
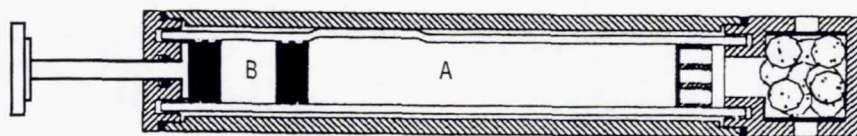
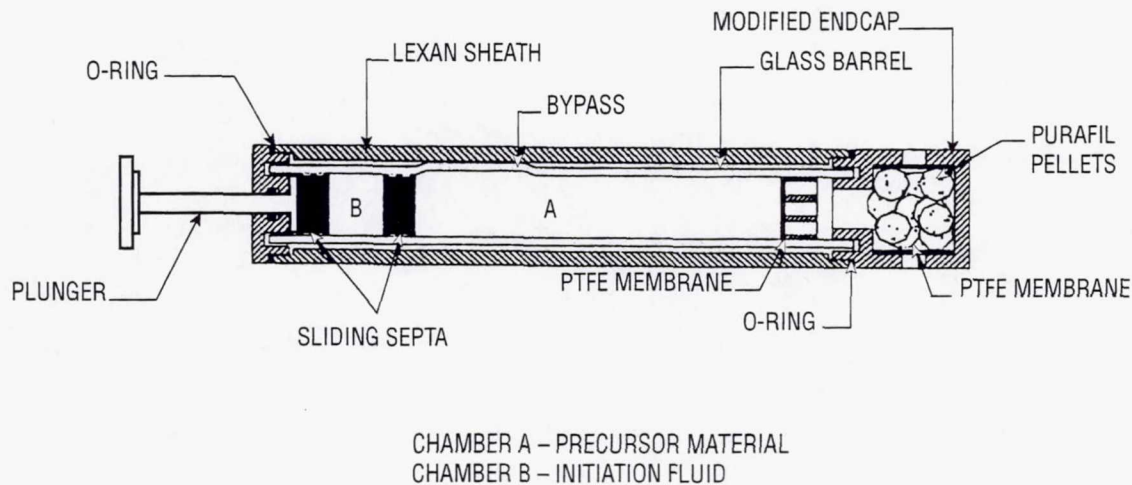
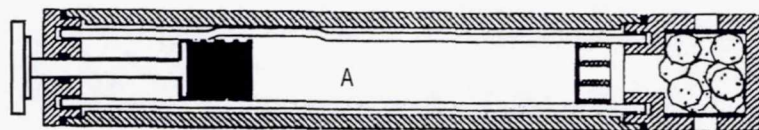


Figure 2. "Standard configuration" fluids processing apparatus (FPA). The standard configuration FPA contains 1.5 ml of fluid in the C and B chambers and 3.5 ml in the A chamber. Many variations of this standard configuration are possible for accommodating specific experimental objectives.



AS LOADED



AFTER INITIATION

Figure 3. Plant-FPA (P-FPA). The Plant-FPA was modified to allow air exchange between chamber A inside the glass barrel and the outside of the Lexan™ sheath. Both the glass barrel and the Lexan™ sheath have hydrophobic membranes, which allow for air exchange while containing liquids. The Purafil pellets are used to scrub ethylene. This concept has recently been scaled-up to the design of a plant growth chamber (PGBA) which provides a controlled, lighted environment for an approximately 1-cubic-foot plant growth chamber.

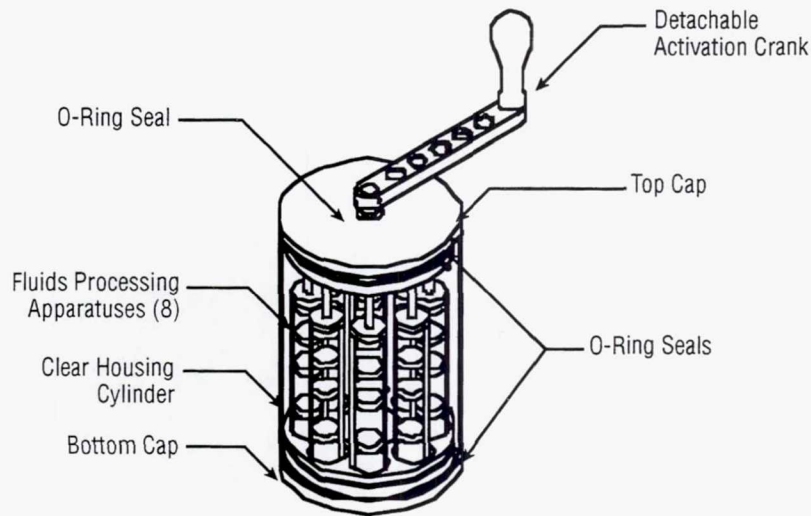


Figure 4. Manually operated GAP. Shown with crank handle attached for on-orbit activation by a crew member. This version can be stowed either in the GBA-INC or the GBA-AMB.

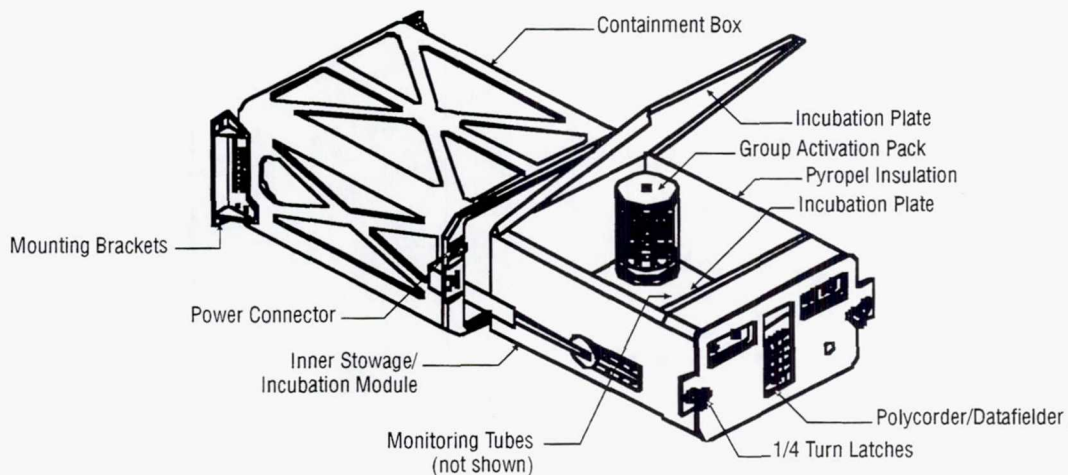


Figure 5. GBA-INC. The GBA-INC consists of a temperature controlled (37°C) middeck-locker-equivalent replacement module that holds nine GAP's. After unlatching and pulling out the GBA-INC drawer, the incubator lid can be opened to access the nine GAP's stowed within the temperature controlled environment and the optical density measurement apparatus (eight FPA's processed simultaneously).

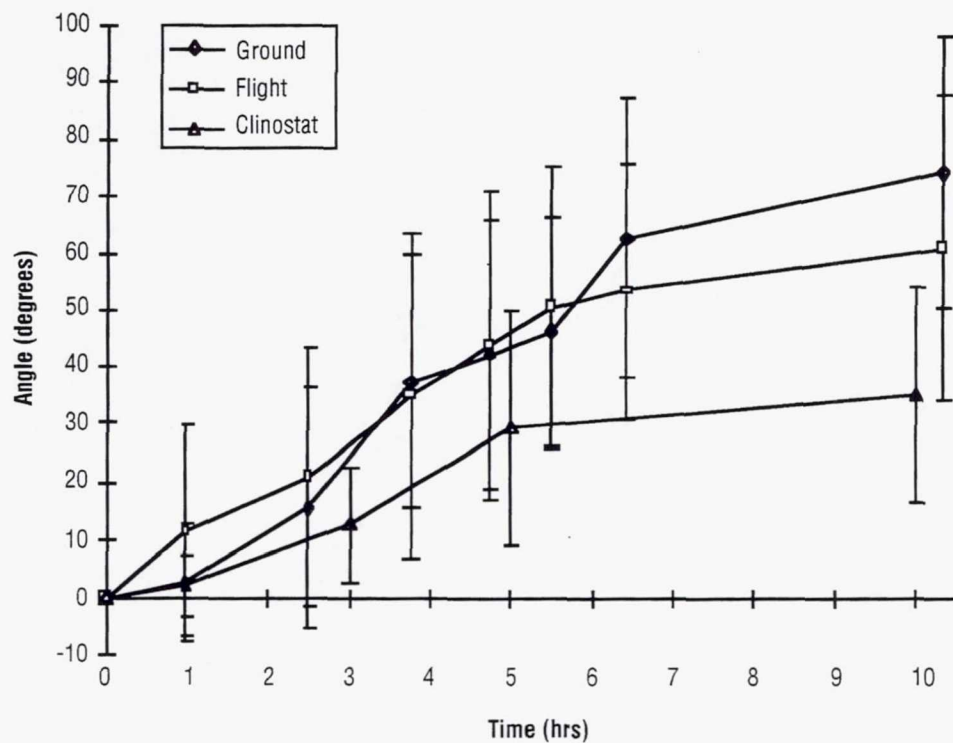


Figure 6. Root curvature response to horizontal gravistimulation. Root tip angle (\pm SD) is plotted over time for horizontally gravistimulated clover seedlings after previous growth under (a) 1 g control, (b) microgravity, and (c) clinorotated conditions. Clinorotated plants did not respond as quickly nor did they reach as great a final angle of curvature as the control or the one grown in microgravity.

Page intentionally left blank

EXPERIMENT XI.

PROTEIN CRYSTAL GROWTH IN MICROGRAVITY: PCAM AND DCAM

Page intentionally left blank

EXPERIMENT XI. PROTEIN CRYSTAL GROWTH IN MICROGRAVITY: PCAM AND DCAM

Daniel C. Carter

New Century Pharmaceuticals, Inc.

895 Martin Road

Huntsville, AL 35824

Phone: 256-461-0024

Fax: 256-461-4224

1. INTRODUCTION

The advent of protein crystal growth in microgravity began with the early experiments of Littke¹ over a decade ago and has progressed into an extensive series of flight experiments which now involve numerous international academic and industrial investigations. The original premise of utilizing microgravity for crystal growth was put forth by a number of scientific groups during the late Apollo and Skylab era of space flight and based on the understanding that in the free-fall environment of an orbiting spacecraft, solution crystal growth would proceed in the absence of convection as a diffusion-limited process, thereby producing materials of greater crystalline perfection. Indeed, for protein crystal growth there are now numerous examples of such improvements.²⁻⁹ While these experiments have been performed in parallel with studies of the fundamental processes involved, the principal application has been in the production of protein crystals with improved diffraction quality allowing, in many cases, for the determination and refinement of atomic structures to higher resolution than previously obtainable by ground-based methods. The methods employed principally have encompassed the techniques most routinely used, namely, vapor equilibration or liquid-liquid diffusion.

This research is part of a series of protein crystallization experiments in microgravity aimed at the design and construction of an improved microgravity protein crystal growth facility. Two new facility hardwares, the protein crystallization apparatus for microgravity (PCAM) and diffusion-controlled crystallization apparatus for microgravity (DCAM), were designed and subsequently manifested in 1995. PCAM facility hardware had its maiden flight early in 1995 on STS-63 and ended the year with a large complement of experiments on USML-2. In addition to PCAM, DCAM was developed with an aim at taking advantage of long duration crystallization experiments available on *Mir* and the *International Space Station*. DCAM utilizes the dialysis method and counter-diffusion to provide variable control of the approach to critical supersaturation for each individual experiment. USML-2 provided the verification of the DCAM facility and approach; this hardware is now currently active on *Mir*. A large flight co-investigator group with representatives from government, industry, and academia has been established for the PCAM and DCAM experiment series. Access to the facility is operated in a manner encouraging international involvement from scientists representing industry, academic, and government laboratories.

The principal aims of these facilities were to:

1. Establish a protein crystal growth facility which would provide greatly increased experiment and co-investigator capacity in order to increase the odds of obtaining significantly improved protein crystals for application in the atomic structure determination, thereby increasing the overall science return from each mission.
2. Investigate the disposable interface concept in the development of microgravity hardware for reduced cost and improvements in logistics and handling.
3. Utilize the facility to delineate factors contributing to the effect of microgravity on the growth and quality of protein crystals.
4. Emphasize application to problems of fundamental importance in science and/or of projects with important humanitarian impact.

2. PCAM FACILITY HARDWARE

A design which met all of the requirements was rapidly produced, manufactured (fig. 1), and tested.¹⁰ The hardware consisted of an injected molded Lexan tray containing seven vapor-equilibration chambers based on an accepted and widely-used commercial tray for ground-based applications. The trays are sealed with a silicon rubber tape. A series of nine trays are disposed in a cylinder (fig. 2) with an interleaving actuator. Turning the actuator knob several revolutions to a fixed stop activates or deactivates all nine trays simultaneously. Consequently, each cylinder contains 63 individual experiments for a total of 378 in a standard single locker thermal enclosure system (STES) unit, or 504 in a padded locker without temperature control. This provided a middeck locker experiment capacity from 6 to 8 times that available in the older vapor diffusion apparatus (VDA) hardware. Some of the design advantages are synopsized below:

1. Disposable interface allows for rapid *in situ* evaluation of results during postflight analysis and postflight distribution. This is extremely important since a number of co-investigators have noted that their crystals are damaged during postflight removal from more elaborate hardware. PCAM allows the individual co-investigator to take the crystals back to their respective laboratories where familiar equipment and surroundings facilitate the proper handling of the samples for diffraction studies.
2. The interface is disposable, inexpensive, and allows for unprecedented capabilities in logistics and handling.
3. Cryogenic storage of experiments is allowed through hardware design. Trays were engineered to fit into existing flight dewars available through Johnson Space Center. Previously we determined that these trays could be stored without detriment for over 18 months at -150°C .

4. Each cylindrical unit contains hand-operated locking and pinning mechanisms to allow for disassembly in microgravity. This was a design feature necessary for any future glovebox interactive experiment opportunities which might be available on Spacelab, *Mir*, or the *International Space Station*.
5. Facility operation requires limited crew involvement and skill. Units can be operated as hand-held or easily adapted to automation.
6. The unprecedented experiment capacity allows each co-investigator numerous experiments, increasing the odds of achieving favorable conditions in microgravity and the total science return.

3. DCAM FACILITY HARDWARE

DCAM was developed to accommodate the dialysis method of growing protein crystals in microgravity by uniquely taking advantage of liquid-liquid diffusion to control the approach to critical supersaturation.¹¹ Previously, using vapor diffusion, it was demonstrated that a slower approach to supersaturation would result in fewer and larger crystals. Each DCAM is comprised of a central housing with two chambers separated by a gel impregnated "fuse" (fig. 3). The fuse acts as a diffusion-limited barrier between the two reservoirs. Selection of proper fuse length and diameter provides passive control of the equilibration rate and thus approach to critical supersaturation. Twenty-seven individual DCAMs are assembled onto a tray for a total of 81 in a STES.

4. USML-2 EXPERIMENT RESULTS SUMMARY

4.1 Equilibration Experiments

An opportunity of stowage for eight small hand-held versions of the facility hardware on USML-2 allowed for an experiment to determine the differences in vapor equilibration rates in the hardware in microgravity versus terrestrial conditions. This is important for two reasons: (1) characterization of the hardware performance in microgravity for proper selection of crystallization conditions in microgravity, and (2) characterization of all variables which might be attributed to affect the quality of crystals in microgravity versus terrestrial conditions.

A range of representative precipitating agents and concentrations were selected and loaded identically into each of the trays in the eight cylinders. Once in microgravity, all eight cylinders were activated to begin the equilibration. During approximately 24-to-48 hour intervals at the crews' convenience, a single cylinder was deactivated. Thus, a profile of the equilibration rates could be determined by measuring the refractive index of each sample/chamber during postflight analysis. While the results suggest that important differences in equilibration rates do exist, particularly for larger molecular weight precipitants such as polyethylene glycol, no conclusions have been drawn because of significant scatter in the data.

5. SELECTED MICROGRAVITY RESULTS PRODUCED FROM GUEST INVESTIGATORS

5.1 Project: HIV Protease Complexed with Inhibitor

Investigators

Dr. Chong Hwan Chang

Dr. Paul J. Ala

DuPont Merck Pharmaceutical Company

5.1.1 Objective

The objective of this research is to improve the quality of the crystals for increased resolution to aid in the design of an inhibitor against HIV. The structure of the HIV protease complexed with an inhibitor has been utilized to design *de novo* inhibitors and improve the potency of current inhibitors (rational drug design) (fig.4). The most effective AIDS therapeutics have been designed by this approach.

5.1.2 Results

- A complete diffraction data set has been collected from a selected crystal. Diffraction data exhibit superior R-factors in shells of resolution and overall.
- Enhanced I/sig. I ratios and improved resolution.
- Increase in resolution of approximately 0.3 angstroms.
- Refinement of the drug complex is in progress to evaluate any improvements in the resulting electron density.
- Highest quality and largest crystal of this protein complex yet obtained.
- An additional observation was that the crystals did not show significant decay under x-ray exposure; this is a marked difference from the terrestrial samples.

5.2 Project: Raf Kinase

Investigators

Dr. Jean-Pierre Wery

Dr. David Clawson

Eli Lilly & Company

5.2.1 Objective

The objective of this project is to determine the 3-dimensional structure of the N-terminal regulatory domain of Raf Kinase. Cancer oncogene product/drug target Raf Kinase is a Ser/Thr kinase involved in the signal transduction cascade that originates with a receptor at the surface, due to binding of a growth hormone, etc.

5.2.2 Results

Crystals of Raf Kinase were the largest ever produced (fig. 5), approximately an order of magnitude larger in a single dimension. Crystals were previously not large enough to pursue the structure. Analysis is in progress. This is potentially an extremely important example of "enabling" microgravity research.

5.3 Project: Human Antithrombin III

Investigator

Dr. Mark R. Wardell

Department of Haematology

University of Cambridge/U.K.

Present Address:

Department of Biochemistry and Molecular Biophysics

Washington University in St. Louis

School of Medicine

St. Louis, MO

5.3.1 Objective

The objective of this experiment is to improve crystal quality to obtain higher resolution data to aid in the design of antithrombin therapeutics. Antithrombin is a member of the serpin family of serine protease inhibitors which are larger than the other inhibitor families and characterized by the remarkable flexibility of their relatively long reactive center loops. Antithrombin has 432 amino acids organized into nine helices and three β -sheets with three disulfide bonds and four N-linked oligosaccharide chains. Its physiological function is to control blood coagulation in human plasma. It does this by forming inhibitory complexes with thrombin and other coagulation proteases in a process greatly accelerated by heparin. Its importance is underscored by the occurrence of severe thrombotic disorders including deep vein thrombosis, pulmonary embolism, and cerebral infarction in subjects with antithrombin mutations that result in either decreased plasma levels or aberrant inhibitory function. Antithrombin is also commonly given as supplementation therapy in patients suffering the thrombotic crises of the shock syndromes.^{12, 13}

5.3.2 Results

On an earlier Shuttle flight PCAM produced crystals superior to any previously grown by any method. This has resulted in the ability to fit and refine regions of the atomic model not previously seen in the structure (fig. 6) solved with early Earth-grown crystals. In particular, a portion of the reactive loop, and areas of the heparin binding site, were seen for the first time. Newly observed hydrogen bonds between heparin binding residues and the body of the molecule have given the first indication of the switching on of inhibitory activity in antithrombin by heparin. Additionally, crystals of this protein complexed with effectors were sought from this mission to study the molecule's chemistry. Unfortunately, because of the series of long delays, this very fragile protein did not crystallize well after the third reload (documented by loading team). However, crystals were produced and analysis is in progress. This is a beautiful example of "enabling" microgravity research on an extremely important, medically significant protein.

5.4 Project: Gro EL Protein/Bacteriophage HK97 Capsid Protein Complex

Investigator
Dr. John Rosenberg
Dept. of Crystallography
University of Pittsburgh

5.4.1 Objective

This work focuses on improving the diffraction quality of the crystals in order to aid in structural determination.

5.4.2 Results

Large crystals were grown (fig. 7). Seed crystals produced from this mission produced the highest quality diffraction data yet obtained.

5.5 Project: Neurophysin II/Vasopressin Complex

Investigators
Dr. John Rose and Dr. B.C. Wang
Dept. of Biochemistry and Molecular Biology
University of Georgia

5.5.1 Objective

The objective of this work is to improve the diffraction quality of the crystals in order to aid in structural determination. The hormone vasopressin is synthesized and packaged in the posterior pituitary as a prohormone with its carrier neurophysin. Vasopressin, which has long been associated with cardiovascular function, has recently been shown together with the related hormone oxytocin to help orchestrate social and sexual relationships. Knowledge of this structure could provide information for basic understanding of human relationships, mental illness, and endocrinology.

5.5.2 Results

This is the largest crystal of neurophysin/vasopressin complex grown to date by any method (fig. 8). Crystals also appear superior in optical perfection. An analysis has been performed by the University of Georgia and details are forthcoming.

5.6 Project: T7 RNA Polymerase

Investigators

Dr. John Rose and Dr. B.C. Wang

Dept. of Biochemistry and Molecular Biology

University of Georgia

5.6.1. Objective

This work centers on improving diffraction quality of the crystals in order to aid in structural determination. T7 RNA polymerase is an enzyme responsible for reading the DNA code and translating it into RNA. The RNA is then used to make proteins which are necessary for cells to function. This structure will add to our knowledge of how life functions at its most minute level.

5.6.2 Status

Our supply was exhausted during USML-2's extensive launch delays.

5.7 Project: Augmenter of Liver Regeneration Protein

Investigators

Dr. John Rose and Dr. B.C. Wang

Dept. of Biochemistry and Molecular Biology

University of Georgia

5.7.1. Objective

This work centers on improving the diffraction quality of the crystals in order to aid in structural determination. This is a new liver growth factor which promotes liver regeneration after it is damaged or injured. The crystal structure of ALR will provide a road map for other researchers to use in better understanding the biochemical and physiological properties of this new class of growth factors and may open the door for new ways to treat liver diseases or make liver transplants more successful.

5.7.2 Results

Large crystals with dramatically improved optical perfection were obtained (fig. 9). No additional information has been reported at this time.

5.8 Project: L-Alanine Dehydrogenase from *Bacillus subtilis*

Investigator

Dr. Jean-Paul Declercq

Laboratoire de Chimie Physique et de Cristallographie

Université Catholique de Louvain/Belgium

5.8.1 Objective

This project aims to improve the diffraction quality of the crystals in order to aid in structural determination. L-alanine dehydrogenase catalyzes the reversible oxidative deamination of L-alanine to pyruvate and ammonium. This enzyme doesn't seem to share sequence similarity with other amino acid dehydrogenases whose three-dimensional structures are known, but seems to be structurally related to the transmembrane proton translocating pump, pyridine nucleotide transhydrogenase. The three-dimensional crystal structure will allow a better understanding of the catalytic reaction and of the enzymologic and structural relationships between these proteins.

5.8.2 Results

We produced the largest crystals of L-alanine dehydrogenase ever grown (fig.10), a new morphology and space group. Unfortunately, only two crystals of this size were available. Tests on the synchrotron elucidated the space group but did not provide the desired resolution. However, Dr. Declercq remains extremely interested in pursuing this further, as his terrestrial crystals are otherwise too small to study.

6. SELECTED DCAM MICROGRAVITY RESULTS PRODUCED FROM GUEST INVESTIGATORS

6.1. Project: Nucleosome Core Particle

Investigators

Dr. Gerard J. Bunick

Mr. Joel Harp

Structural Biology Program/Biology Division

Oak Ridge National Laboratory

6.1.1 Objective

The focus of this research is to grow larger, better quality crystals to aid in structure determination. The nucleosome is the fundamental structural unit of chromatin. It is the basis for organization within the genome by compaction of DNA within the nucleus of the cell, making selected regions of chromosomes available for transcription and replication. Nucleosomes represent a protein-DNA complex found in all eukaryotes which has been considered nonspecific with regard to the DNA sequence and nonregulatory in function. We now know that certain DNA's, such as the human alpha-satellite DNA used here, contain subtle sequence characteristics that allow the core histones to bind in a specific phase on the sequence. We also know that nucleosomes have important roles in the regulation of gene expression, particularly in the expression of genes transcribed by RNA polymerase III. The nucleosome core particle has been defined on the basis of protection of DNA from nuclease attack. The nucleosome core particle consists of two units each of the core histones; H4, H3, H2A and H2B, along with approximately 146 base pairs of double helical DNA wound in about 1.7 left-handed, superhelical turns about the histone core with a total molecular weight of 206 kDa.

6.1.2 Results

Because of the experiment location in the lab module, we were unable to access the DCAM units for an additional reload. Consequently, most of the nucleosome core particle crystals were produced on the launch pad. However, in a few experiments where the equilibration profiles were set for extended times, a large crystal of new morphology (fig. 11) was produced in microgravity. This is clearly a larger and more desirable crystal form for the structure determination. Diffraction data have been collected at Brookhaven National Synchrotron Light Source. Data have now been collected to significantly higher resolution than anything previously obtained.

6.2 Project: Lysozyme

Investigator

Dr. Daniel C. Carter

Biophysics and Advanced Materials Branch

Marshall Space Flight Center

6.2.1 Objective

Our objective is to study the effects of microgravity conditions on crystal growth through ground-based comparison. Lysozyme protein crystals were also grown (fig.12) to analyze equilibration and nucleation properties of the DCAM hardware.

6.2.2 Results

- Control of nucleation and size were demonstrated.
- Hardware performance was verified.
- Controlled diffusion produced the largest crystal ever grown by the principal investigator of the tetragonal form of hen egg white lysozyme.

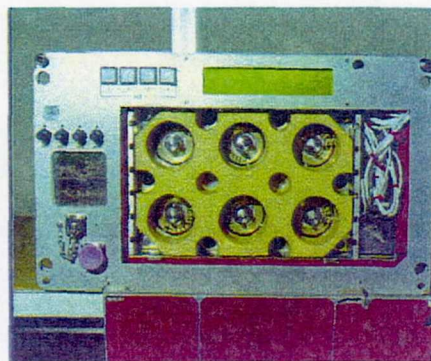
REFERENCES

1. Littke, W.; and John, C.: *Science*, 225, 203, 1984.
2. DeLucas, L.J.; Suddath, F.L.; Snyder, R.S.; Naumann, R.; Broom, M.B.; Pusey, M.; Yost, V.; Herren, B.; Carter, D.C.; Nelson, B.; Meehan, E.J.; McPherson, A.; and Bugg, C.E.: *J. Crystal Growth*, 76, 681, 1986.
3. DeLucas, L.J.; Smith, C.D.; Smith, H.W.; Senadhi, V.-K.; Ealick, S.E.; Carter, D.C.; Snyder, R.S.; Weber, P.C.; Salemme, F.R.; Ohlendorf, D.H.; Einspahr, H.M.; Koszelak, L.L.S.; Taylor, G.; Stammers, D.; Powell, K.; Darby, G.; and Bugg, C.E.: *Science*, 246, 651, 1989.
4. DeLucas, L.J.; Smith, C.D.; Carter, D.C.; Snyder, R.S.; McPherson, A.; Koszelak, S.; and Bugg, C.E.: *J. Crystal Growth*, 109, 12, 1991.
5. DeLucas, L.J.; Smith, C.D.; Smith, H.W.; Senadhi, V.-K.; Ealick, S.E.; Carter, D.C.; Snyder, R.S.; Weber, P.C.; Salemme, F.R.; Ohlendorf, D.H.; Einspahr, H.M.; Clancy, L.L.; Navia, M.A.; McKeever, B.M.; Nagabhushan, T.L.; Nelson, G.; McPherson, A.; Koszelak, S.; Taylor, G.; Stammers, D.; Powell, K.; Darby, G.; and Bugg, C.E.: *J. Crystal Growth*, 110, 302, 1991.
6. DeLucas, L.J.; Moore, K.M.; Bray, T.L.; Rosenblum, W.M.; Einspahr, H.M.; Clancy, L.L.; Rao, G.S.J.; Harris, B.G.; Munson, S.H.; Finzel, B.C.; and Bugg, C.E.: *J. Phys. D: Appl. Phys.*, 26, B100, 1993.
7. Day, J.; and McPherson, A.: *Protein Science*, 1, 1254, 1992.
8. McPherson, A.: *J. Phys. D: Appl. Phys.*, 26, B104, 1993.
9. Littke, W.; and John, C.: *J. Crystal Growth*, 76, 663, 1986.
10. Carter, D.C.; and Dowling, T.: U.S. Patent Pending (1996).
11. Carter, D.C.: U.S. Patent Issuing (1997).
12. Skinner, R.; Abrahams, J.-P.; Whisstock, J.C.; Lesk, A.M.; Carrell, R.W.; and Wardell, M.R.: "The 2.6 Å Structure of Antithrombin Indicates a Conformational Change at the Heparin Binding Site," *J. Mol. Biol.*, in press, 1997.
13. Wardell, M.R.; Skinner, R.; Carter, D.C.; Twigg, P.D.; and Abrahams, J.-P.: "Improved Diffraction of Antithrombin Crystals Grown in Microgravity," *Acta Crystallographica*, in press, 1997.

Note: Several manuscripts describing the results from USML-2 and other flight experiments in PCAM and DCAM are in preparation.



(a)



(b)

Figure 1. (a) A single PCAM cylinder with individual disposable trays with wicks and associated interleaving actuator plates. A total of nine 7-chamber trays are accommodated in each cylinder; (b) illustrates the standard flight arrangement of six PCAM units in an STES.

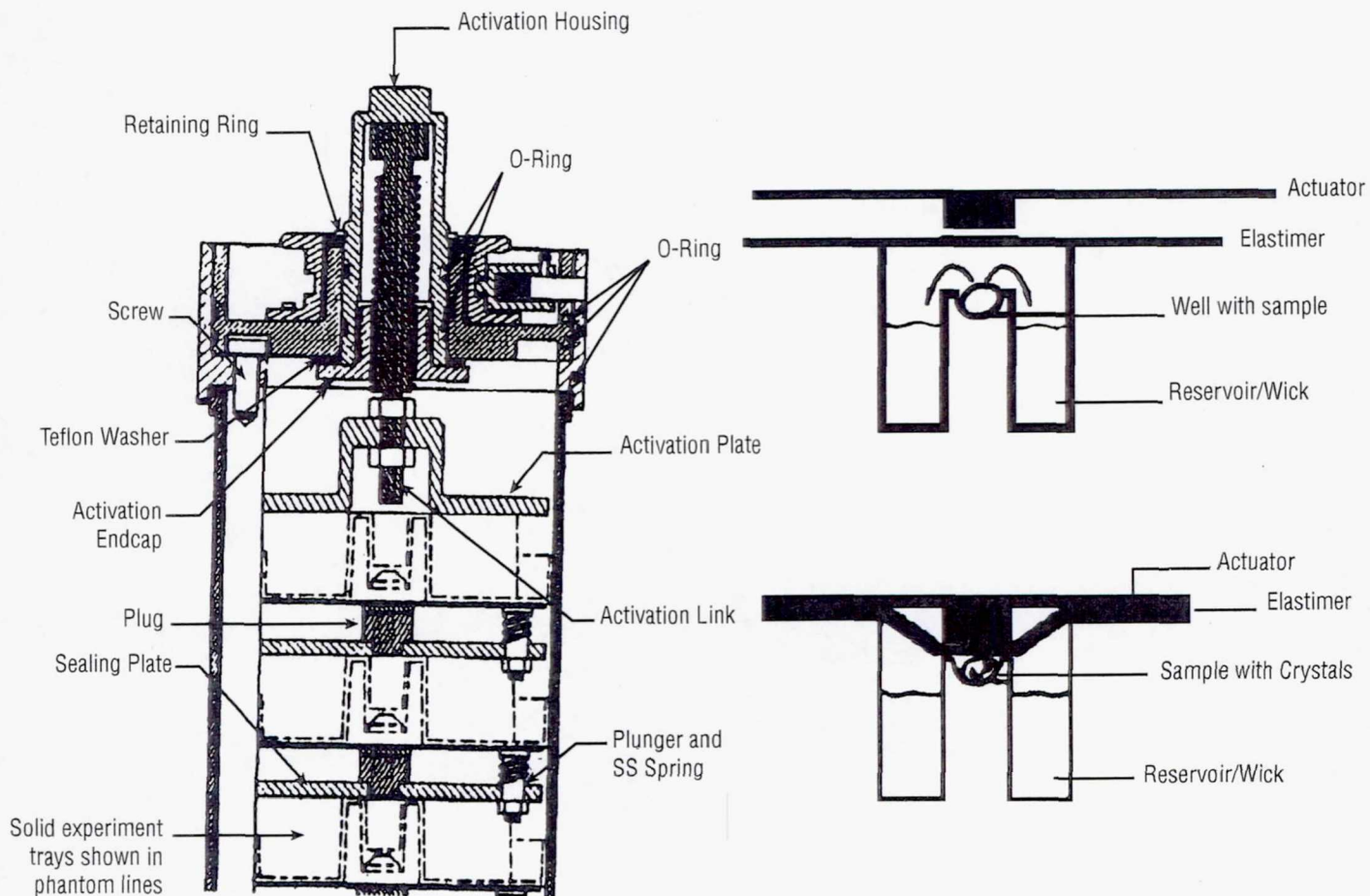


Figure 2. A schematic illustrating the basic construction of the PCAM and its mechanism.

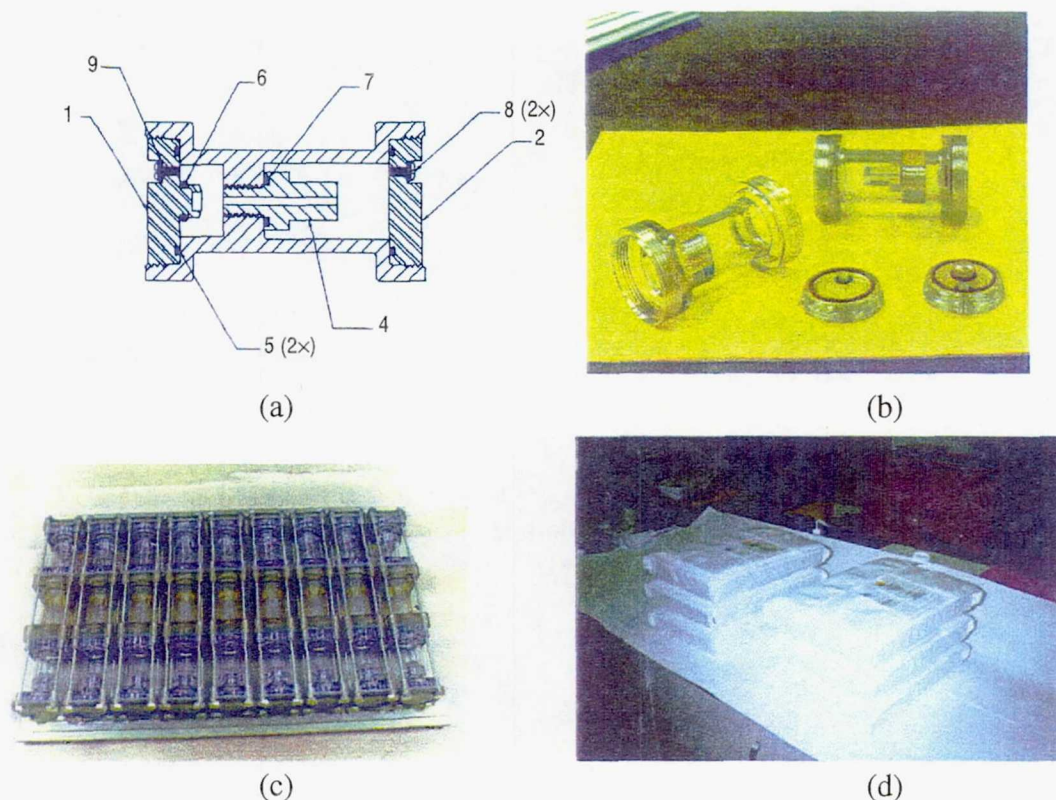


Figure 3. (a) Schematic of the diffusion-controlled crystallization apparatus for microgravity (DCAM). Shown: (1) gel plug, (2) primary reservoir, (3) secondary reservoir, (4) dialysis chamber (button), (5) end cap, (6) vent screws and ports. (b) Machined DCAM ground-based unit. (c) Flight tray assembly of 27 DCAM's. (d) Six DCAM tray assemblies in thermal pouches as loaded for STS-76 *Mir* increment 2.

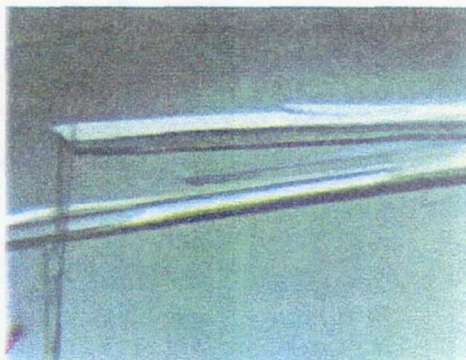


Figure 4. Crystals of HIV protease complexed with proprietary inhibitor grown aboard USML-2 (STS-73).

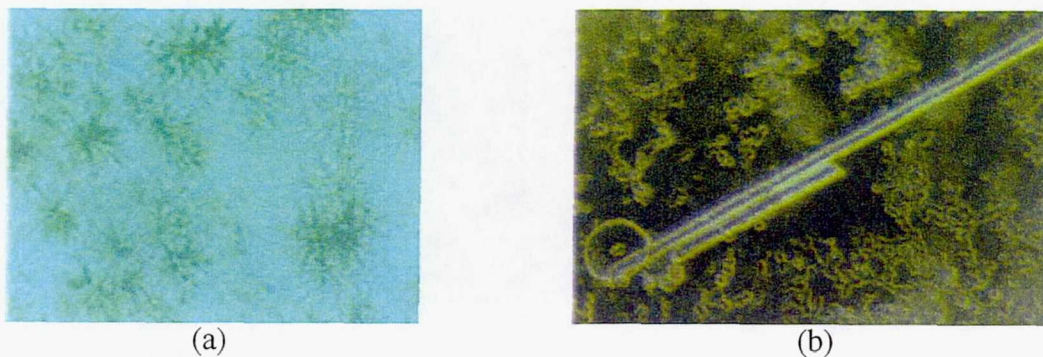


Figure 5. Raf Kinase crystals of (a) ground-based and (b) USML-2 flight at approximately the same magnification. Pictures provided courtesy of Dr. Jean-Pierre Wery and Eli Lilly and Company.

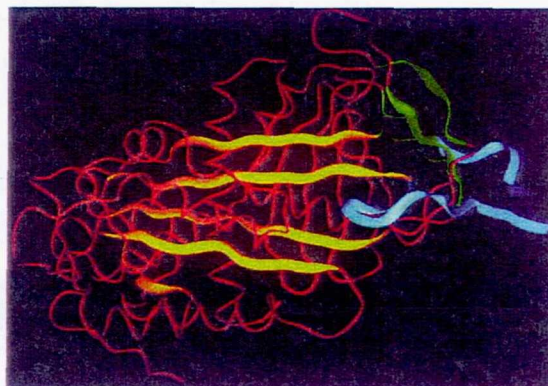


Figure 6. Structure of human antithrombin III. The reactive loop, shown in blue, was never completely visible using data from ground-based crystals. The model was first completed based on samples from STS-67, and the structure is now refined to 2.6 angstroms using crystals grown in microgravity.^{12 13}



Figure 7. Crystals of Gro EL Protein/Bacteriophage HK97 Capsid Protein Complex grown in PCAM during USML-2 (STS-73).

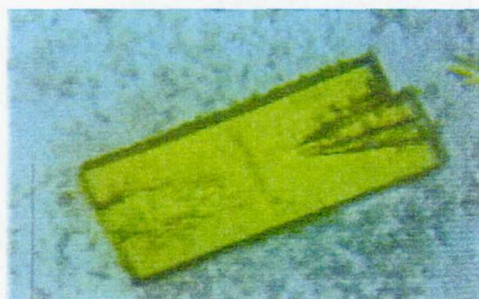


(a)

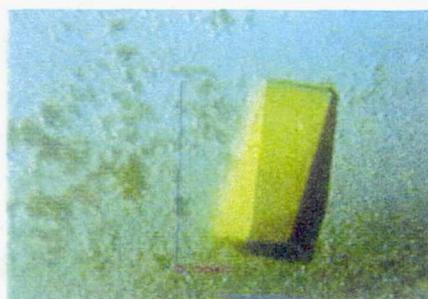


(b)

Figure 8. Ground-based (a) and flight crystals (b) of neurophysin/vasopressin complex grown in PCAM during USML-2 (STS-73).



(a)



(b)

Figure 9. Ground-based (a) and flight crystals (b) of augmentin of liver regeneration protein grown in PCAM on STS-73.

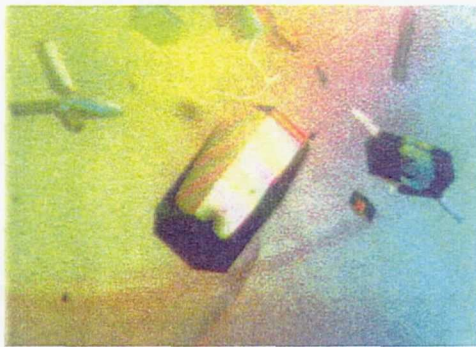


(a)

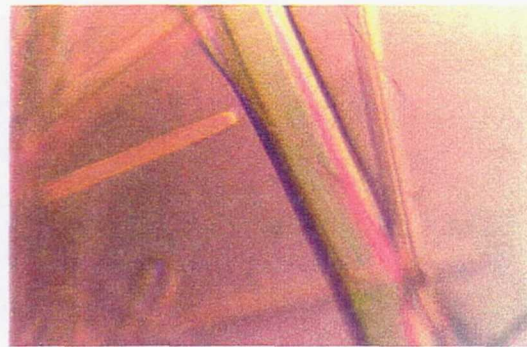


(b)

Figure 10. Ground-based (a) and flight crystals (b) of L-alanine dehydrogenase protein grown in PCAM on STS-73.



(a)



(b)

Figure 11. Crystal of nucleosome core protein grown in DCAM aboard USML-2 (a). Crystal grown during long duration *Mir* flight (b). Diffraction limit improved from 3.0 angstroms from Earth-grown crystals to 2.5 angstroms in microgravity. Crystals of the nucleosome core particle grown on *Mir* were reported to be the largest ever grown by any method (maximum dimension 3 mm).

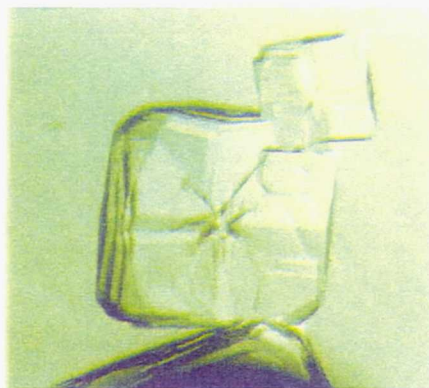


Figure 12. Two crystals of hen egg white lysozyme grown in DCAM via bulk crystallization aboard USML-2 (STS-73). Crystal dimensions: 4 mm (center) and 5 mm (bottom).

Page intentionally left blank

EXPERIMENT XII.

**COMMERCIAL PROTEIN CRYSTAL GROWTH GLOVEBOX
AND MIDDECK EXPERIMENTS**

Page intentionally left blank

EXPERIMENT XII. COMMERCIAL PROTEIN CRYSTAL GROWTH GLOVEBOX AND MIDDECK EXPERIMENTS

Lawrence J. DeLucas

Center for Macromolecular Crystallography

University of Alabama at Birmingham

Birmingham, AL 35294

Phone: 205-934-5329

Fax: 205-934-0480

E-mail: delucas@orion.cmc.uab.edu

Note: A list of co-investigators is located at the end of this report.

ABSTRACT

The commercial protein crystal growth (CPCG) experiments onboard USML-2 involved 11 proteins in three different types of experiments and hardware configurations. Ten proteins were involved in vapor diffusion experiments in the vapor diffusion apparatus (VDA) and in the protein crystal growth glovebox hardware (PCGG). Three proteins were distributed among 60 vapor diffusion experiments conducted in the VDA at 4 °C. These experiments were stored in a commercial refrigerator/incubator module (CRIM). Six proteins were involved in the glovebox experiments. The protein crystallization facility (PCF) contained one protein in a temperature-induced crystallization experiment. Diffraction-sized crystals were obtained for 4 of the 11 proteins flown. The results of x-ray diffraction studies on these crystals are presented.

1. INTRODUCTION

The general purpose of protein crystal growth experiments sponsored by the Center for Macromolecular Crystallography was to produce large, well-ordered crystals for x-ray diffraction studies. The CPCG experiments consisted of three separate experiments: (1) experiments conducted in the PCF, (2) experiments conducted in the VDA, and (3) experiments conducted in the PCGG.

The specific goal of the PCF experiments was to grow crystals of a new form of recombinant human insulin in microgravity and to use the space-grown crystals for x-ray crystallographic structure determination. This project was flown in collaboration with the Hauptman-Woodward Medical Research Institute and Eli Lilly. Four different crystal growth conditions were used to produce insulin crystals. Crystallization was induced by decreasing the temperature of the insulin solutions slowly over 3 days to decrease the insulin solubility.

Crystallization experiments were conducted on three proteins in the VDA at 4 °C. The proteins involved in these experiments were calcineurin complex, epidermal growth factor receptor, and trichomonas vaginalis ferredoxin. The long duration of USML-2 provided optimal growth time for low-temperature crystallization experiments.

In the glovebox, the vapor diffusion method was used to grow crystals of seven proteins in individual crystallization chambers. These compounds included microsomal triglyceride transfer protein, IMP dehydrogenase, feline calicivirus, lysozyme, collagen binding domain, staphylokinase, and duck delta II crystallin. Initial screening experiments were set up with each protein in the glovebox and then stored at 22 °C in a CRIM in a middeck locker. Based on the results of the screening experiments, the crystallization conditions were optimized, and additional experiments were set up. This iterative process was continued until flight day 7, and then the crystals were allowed to grow until the experiments were deactivated on flight day 13.

2. EXPERIMENTAL DESIGN

The PCF flown on USML-2 was an assembly consisting of four polysulfone bottles, four aluminum containment tubes, and two support endplates, as shown in figure 1.

Each polysulfone bottle had a capacity of 50 ml. The experimental insulin solutions were prepared and loaded into the PCF at 40 °C. The PCF assembly was stored in a CRIM and installed in a Shuttle middeck locker. The temperature was maintained at 40 °C, until the experiment was activated after orbit was attained. Crystallization was initiated by decreasing the temperature to 22 °C over 72 hours, and maintaining the temperature at 22 °C for the remainder of the flight.

The VDA hardware was comprised of three vapor diffusion apparatus trays. Each tray contained 20 individual vapor diffusion chambers. Prior to launch, each experiment was prepared by loading the protein and precipitant solutions into separate barrels of a double-barreled syringe. The syringe was then installed in the experiment chamber, and a concentrated precipitant solution injected into the polymer wicking material lining the experiment chamber. The entire loading process took place in a coldroom at 4 °C. The loaded trays were stored in a CRIM at 4 °C and the CRIM was installed in a Shuttle middeck locker. The system was maintained at that temperature for the duration of the experiments.

The PCGG was designed and built based on experience gained with glovebox crystal growth experiments performed by Dr. Larry DeLucas on USML-1. The hardware complement consisted of individual experiment chambers which were stored in containment tubes (fig. 2).

A total of 150 experiment chambers were stored in 30 containment tubes. The protein, precipitant, reservoir, and wash solutions were stored in glass vials and placed, along with the containment tubes, in a CRIM in a middeck locker at 22 °C (fig. 3).

During the flight, crew members Dr. Cady Coleman and Dr. Al Sacco set up over 80 individual crystallization experiments. The experiments were observed and video of ongoing experiments was downlinked to the UAB/CMC remote Payload Operations Control Center (POCC).

3. RESULTS

3.1 PCF Experiments

The PCF experiments yielded a large numbers of crystals of a new variant of recombinant human insulin. This project was flown in collaboration with Eli Lilly and Dr. G. David Smith at the Hauptman-Woodward Medical Research Institute. Four different crystal growing conditions were tested, and each produced crystals. Although the crystals were abundant, both the space and Earth-grown crystals were small and adhered to the walls of the PCF containers. Free-floating crystals were not observed. Previous large-scale, temperature-induction microgravity experiments with recombinant insulin had produced large free-floating crystals in addition to the crystals which adhered to the container walls. The insulin crystals which grew adhered to the PCF container walls on USML-2 were comparable in size to their Earth-grown counterparts. This result is consistent with previous results and supports our hypothesis that space-grown crystals must be free floating in a protein-rich solution in order to reach optimum size and quality. Unfortunately, the crystals produced on this flight were not large enough for x-ray data collection.

The lack of free-floating insulin crystals from STS-73 may be due to a number of factors. Previous microgravity experiments produced large, well-ordered crystals of recombinant human insulin which yielded x-ray diffraction data that gave the most detailed structure of the protein to date. Therefore, it is likely that changes in the molecular structure of this new form of recombinant human insulin resulted in the crystal growth pattern observed in the USML-2 experiments. This new variant of insulin apparently nucleated more readily on the walls of the PCF container than its parent form of insulin. Also, the temperature gradient used on STS-73 was 3 days, which may have been too long. Future microgravity experiments with this form of insulin will investigate a large number of crystallization conditions with the goal of isolating the conditions that produce the large, well-formed free-floating insulin crystals.

3.2 VDA Experiments

The VDA experiments, conducted at 4 °C, included three proteins: calcineurin complex, epidermal growth factor receptor, and trichomonas vaginalis ferredoxin. The calcineurin complex, flown in collaboration with Dr. John Thomson at Vertex Pharmaceuticals, is a protein complex whose formation leads to clinical suppression of the immune system. Understanding the structure of this large, complex, medically relevant protein through x-ray crystallography will contribute to the design of new immunosuppressant drugs. The USML-2 experiments with the calcineurin complex produced many small, well-formed cubic crystals. Unfortunately, these crystals were less than 0.1 mm on each side and were too small for x-ray diffraction data collection.

The epidermal growth factor receptor is a prototype of a family of enzyme receptors common to many human cancers. The solution of the three-dimensional structure of EGF receptor will aid in the development of new drugs for the treatment of cancerous tumors. This project was flown in collaboration with Drs. Wolfgang Weber and Christian Betzel. Microgravity crystals of EFG receptor have previously yielded the best x-ray diffraction data ever collected from crystals of this protein. However, the experiments performed on USML-2 did not produce crystals large enough for diffraction studies.

Trichomonas vaginalis ferredoxin is proposed to be the enzyme target of the antibiotic metronidazole, which is used to treat the sexually-transmitted disease trichomonis. Microgravity experiments with this protein produced thin, rod-shaped crystals, up to 1 mm in length. The crystals were larger than the typical laboratory-grown crystals but similar in shape. Unfortunately, the crystals degraded during transport to the co-investigator's laboratory, and no x-ray diffraction data was collected. However, based on the size and optical clarity of the crystals produced, co-investigator Dr. Kurt Krause is anxious to continue microgravity experiments with this protein.

In general, few diffraction-sized crystals were obtained in the 4 °C VDA experiments. The disappointing results of these experiments were thought to be related to two factors: the numerous and significant launch delays, and the unstable CRIM temperature during the mission. The multiple launch delays required that the loaded CRIM be installed in and removed from the orbiter several times, and some of the experiments were stored in the flight hardware more than 3 weeks. During ascent, the CRIM temperature rose from the nominal temperature of 4 °C to 8.9 °C. The temperature then stabilized in the 4–6 °C range, but spiked to 8.3 °C after landing. These temperature excursions were the results of fluctuations in the middeck temperature. The CRIM performed nominally but could not maintain the 4° C set point when the middeck temperature rose above 25 °C. Since the molecular stability of proteins decreases rapidly as a function of both time and temperature change, it is difficult to differentiate between the effects of the launch delays and the temperature fluctuations on the 4 °C VDA experiments. However, both factors clearly had a negative impact on the success of these experiments.

3.3 Glovebox Experiments

The PCGG included seven proteins: microsomal triglyceride transfer protein, IMP dehydrogenase, feline calicivirus, lysozyme, collagen binding domain, staphylokinase, and duck delta II crystallin.

Microsomal triglyceride transfer protein (MTPP), flown in collaboration with Dr. Howard Einspahr at Bristol-Myers Squibb, Inc., is involved in the transport of triglycerides between biological membranes. It is a novel therapeutic target to develop drugs to lower lipid and cholesterol levels in the blood. The glovebox experiments with MTPP produced several well-formed cubic crystals. However, these crystals were too small for x-ray diffraction data collection.

IMP dehydrogenase is the molecular target for the immunosuppressant drug, mycophenolic acid, and its three-dimensional structure is important in the development of better immunosuppressant drugs. IMP dehydrogenase was flown on USML-2 in collaboration with Dr. John Thomson at Vertex Pharmaceutical, Inc. The glovebox experiments produced long, thin rod-shaped crystals that were not adequate for x-ray diffraction studies.

Many perfect rectangular and square pyramidal crystals of feline calicivirus were produced in the glovebox hardware (fig. 4). This virus is a member of a family of pathogens that causes gastroenteritis in humans. The microgravity crystals were larger and appeared to be more regularly shaped than typical ground-grown crystals. The crystals were stored while the principle investigator, Dr. Ming Luo, awaited time at a synchrotron facility to collect x-ray data. Unfortunately, the long delay resulted in degradation of the crystals, and no usable x-ray diffraction data was obtained from them.

Lysozyme is a small protein that has been extensively studied in both laboratory and microgravity experiments. Therefore, lysozyme provides an excellent system for evaluating the effects of microgravity on the kinetics and thermodynamics of crystallization. Dr. Shigeo Aibara conducted experiments on USML-2 that were designed to elucidate the effect of microgravity on the crystal packing and mosaicity of lysozyme crystals. Space-grown tetragonal lysozyme crystals grown in the glovebox hardware diffracted to 1.7 Å while the ground-grown control crystals diffracted to 1.8 Å. The intensity of the diffraction data from the space crystals was greater than that from the Earth-grown crystals throughout the entire resolution range.

Staphylokinase is a potential thrombolytic agent for the treatment of heart attacks. The protein, flown in collaboration with Dr. Debasish Chattopadhyay, did not produce crystals in the glovebox hardware.

Collagen binding domain, provided by Dr. Narayana Sthanam, is a bacterial surface protein that helps bacteria enter and colonize in human joints. The three-dimensional structure of this protein will lead to a better understanding and treatment of degenerative joint disease. Microgravity experiments with collagen binding domain produced clusters of long, needle-shaped crystals that were too thin to yield usable x-ray diffraction data.

Duck delta II crystallin is a protein that is very similar to the key enzyme that causes the disease argininosuccinic aciduria. The three-dimensional structure of this protein will lead to a better understanding of the metabolic processes involved in this disease. The protein produced square pyramidal crystals up to 0.4 mm long (fig. 5).

X-ray diffraction data was collected on the microgravity crystals, and it was observed that the crystals diffracted poorly, if at all. Ground-control crystals grown from the same batch of protein diffracted to 2.8 Å. Co-investigator Dr. P. Lynne Howell observed that the microgravity experiments produced an unusual number of the square pyramidal crystals, rather than the flat plates generally grown in the laboratory. Also, the microgravity crystals, though well-formed, appeared striated. It is believed that the protein was damaged by the launch delays. Because of the volume of protein needed for these experiments, it was not possible to replace it for each launch attempt. Therefore, each time the hardware was returned to the CPCG team, the protein was stored at 4 °C to extend its lifetime. While this protocol is generally applied to proteins, the sample of duck delta II crystallin clearly suffered from the repeated temperature changes and extended time at 22 °C before the experiments were activated.

4. CONCLUSIONS

While the yield of diffraction-quality protein crystals from the CPCG experiments aboard USML-2 was disappointing, invaluable information and experience was gained from this mission. The opportunity for on-orbit optimization of crystal growth conditions provided insight into the microgravity crystallization process that will lead to improvements in crystal growth flight hardware. The video downlink and electronic still-camera image transfer provided invaluable interaction between the Shuttle crew and the science team and allowed the real-time assessment of crystal quality. KCA file transfer provided the opportunity to transmit ground-based calculations to the crew and to obtain the crew's observations of crystal growth experiments without using video or voice transmission. The establishment of a remote POCC at the University of Alabama at Birmingham (UAB) allowed the UAB science and engineering team to provide

improved mission support to the Shuttle crew and the mission management team at reduced cost. In general, the knowledge and experience gained from the CPCG experiments aboard USML-2 are vital to the future of microgravity protein crystal growth experiments.

5. CO-INVESTIGATORS

Marianna Long

Center for Macromolecular Crystallography
University of Alabama at Birmingham
Birmingham, AL 35294
Phone: 205-934-8991
Fax: 205-934-0480
E-mail: long@orion.cmc.uab.edu

Karen Moore

Center for Macromolecular Crystallography
University of Alabama at Birmingham
Birmingham, AL 35294
Phone: 205-934-0117
Fax: 205-934-0480
E-mail: moore@orion.cmc.uab.edu

Shigeo Aibara

Research Institute for Food Science
Kyoto University
4F, Room F-411
Gokasho Uji, Kyoto 611 Japan
Phone: 011-81-774-33-6907
Fax: 011-81-774-33-3004
E-mail: aibara@food.food.kyoto-u.ac.jp

Christian Betzel

DESY
Geb.22a, Notkestraße 85
22603 Hamburg, Germany
Phone: 011-49-40-8998-4744
Fax: 011-49-40-8998-4747
E-mail: betzel@embl-hamburg.de

Debasish Chattopadhyay

Center for Macromolecular Crystallography
University of Alabama at Birmingham
Birmingham, AL 35294
Phone: 205-934-0124
Fax: 205-934-0480
E-mail: debasish@orion.cmc.uab.edu

Howard Einspahr

Bristol-Myers Squibb
Route 206 & Provinceline Road
Princeton, NJ 08543-4000
Phone: 609-252-5267
Fax: 609-252-6030
E-mail: einspahr@bms.com

P. Lynne Howell

Hospital for Sick Children
Biochemistry Research
555 University Avenue
Toronto, Ontario, Canada M5G 1X8
Phone: 416-813-5378
Fax: 416-813-5022
E-mail: Howell@aragorn.psf.sickkids.on.ca

Kurt Krause

Department of Biochemical and Biophysical Sciences
University of Houston
Houston, TX 77004
Phone: 713-743-8370
Fax: 713-743-8373

Ming Luo

Center for Macromolecular Crystallography
University of Alabama at Birmingham
Birmingham, AL 35294
Phone: 205-934-4259
Fax: 205-934-0480
E-mail: ming@orion.cmc.uab.edu

G. David Smith

Hauptman-Woodward Medical Research Institute, Inc.
73 High Street
Buffalo, NY 14203-1193
Phone: 716-856-9600
Fax: 716-852-6086

Narayana Sthanam

Center for Macromolecular Crystallography
University of Alabama at Birmingham
Birmingham, AL 35294
Phone: 205-934-0119
Fax: 205-034-0480
E-mail: Narayana@orion.cmc.uab.edu

John Thomson

Vertex Pharmaceuticals, Inc.

40 Alston Street

Cambridge, MA 02139

Phone: 617-576-3111

Fax: 617-576-2109

Wolfgang Weber

Institute for Physiologische Chemi

University of Hamburg

Martinstraße 52

20246 Hamburg, Germany

Phone: 011-49-40-4717-4459

Fax: 011-49-40-4717-6818

E-mail: weber@uke.uni-hamburg.de

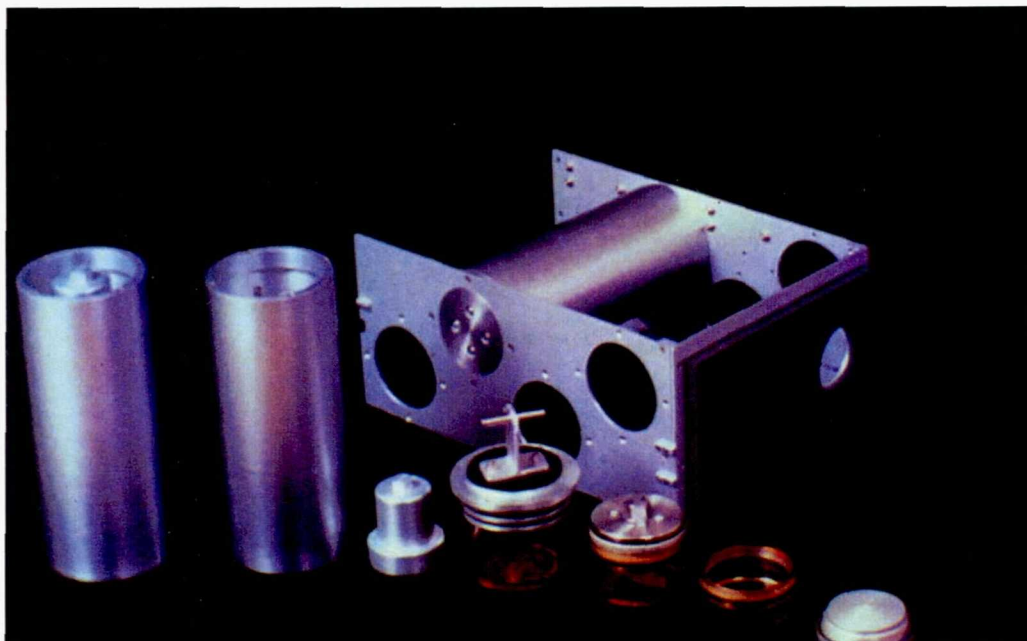


Figure 1. Protein crystallization facility hardware consisting of four polysulfone bottles, aluminum caps, aluminum containment cylinders, and the side and endplates that attach the assembly to the CRIM.



Figure 2. Protein crystal growth glovebox hardware experiment chamber and containment tube. The experiment chamber, molded from polysulfone, contained a growth chamber for a protein droplet up to 50 μl , surrounded by an annulus which held up to 0.5 ml of reservoir solution.



Figure 3. CRIM storage drawer containing crystal growth experiment chambers in containment tubes and solutions for crystallization experiments.

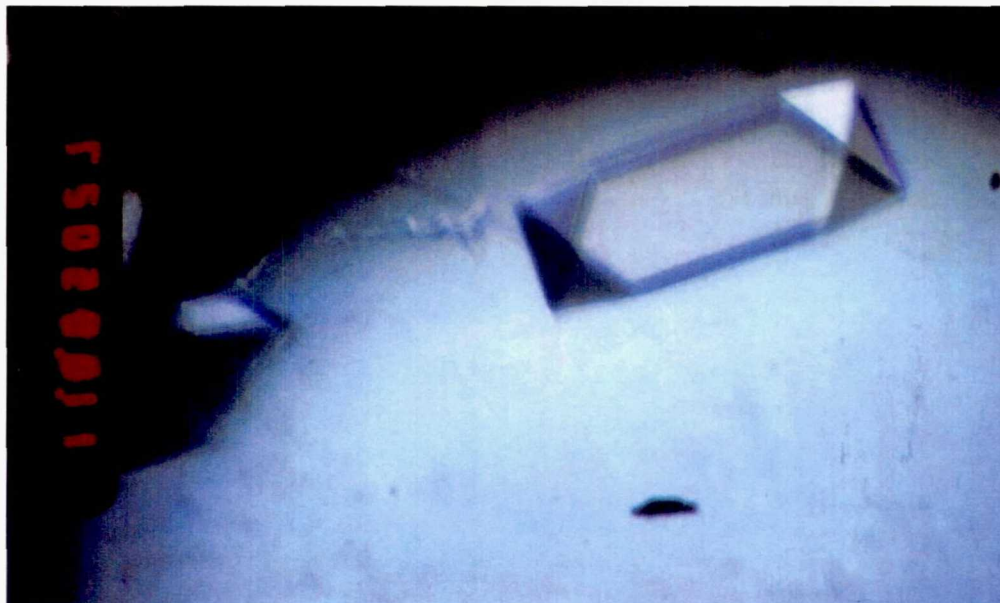


Figure 4. Crystal of feline calicivirus grown in the PCGG hardware.

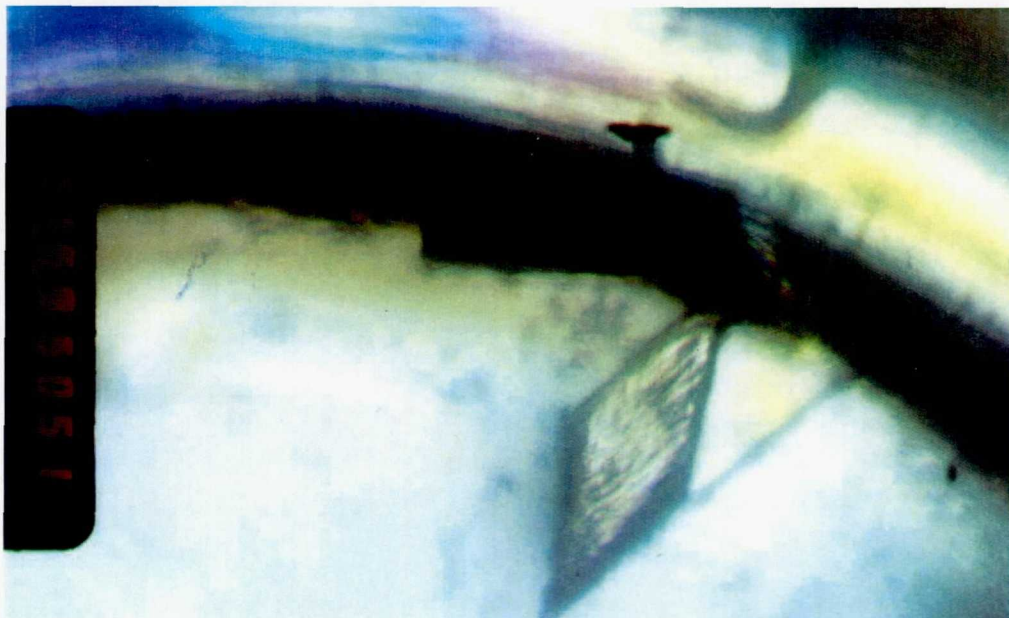


Figure 5. Square pyramidal crystals, up to 0.4 mm long, produced by Duck Delta II crystalin.

Page intentionally left blank

EXPERIMENT XIII.

THE STUDY OF DOPANT SEGREGATION BEHAVIOR DURING THE GROWTH OF GaAs IN MICROGRAVITY ON USML-2

ACKNOWLEDGMENTS

The authors would like to thank the National Aeronautics and Space Administration for their cooperation and enthusiastic support during all stages of these experiments. The following individuals are especially noted for their unwavering efforts in achieving the success of these experiments: David Schaefer, project manager; Dr. Frank Szofran and Dr. Martin Volz, project scientists from the Marshall Space Flight Center; and Dr. Michael Wargo, program manager from the Microgravity Science and Applications Division of NASA Headquarters. This work was sponsored under NASA-MSFC contract NAS8-39722.

EXPERIMENT XIII. THE STUDY OF DOPANT SEGREGATION BEHAVIOR DURING THE GROWTH OF GaAs IN MICROGRAVITY ON USML-2

D.H. Matthiesen, M.L. Kaforey, and J.M. Bly

PI: Dr. David H. Matthiesen

Case Western Reserve University
10900 Euclid Ave. White 420
Cleveland, OH 44106
Phone: 216-368-1336
Fax: 216-368-3209
E-mail: dhm5@po.cwru.edu

Co-I: James Kafalas

Viable Systems, Inc.
Medfield, MA 02254
Phone: 508-358-7140

Co-I: Dr. Monica L. Kaforey

Case Western Reserve University
10900 Euclid Ave. White 330
Cleveland, OH 44106
Phone: 216-368-4219
Fax: 216-368-3209
E-mail: mlk14@po.cwru.edu

Co-I: Dr. Douglas Carlson

M/A Com Associates
Lowell, MA 01851
Phone: 508-656-2932

Co-I: Dr. Arnon Chait

NASA Lewis Research Center
21000 Brookpark Rd.
Cleveland, OH 44135
Phone: 216-433-3558
Fax: 216-433-5033
E-mail: arnon.chait@lerc.nasa.gov

ABSTRACT

An investigation into the segregation behavior of selenium doped gallium arsenide (Se/GaAs) during directional solidification in the microgravity environment was conducted using the Crystal Growth Furnace (CGF) aboard the second United States Microgravity Laboratory (USML-2). Two crystals were successfully processed on USML-2, which lasted from October 20 to November 7, 1995. The first sample was processed for 67 hours, 45 minutes (MET 5/04:53:45—8/00:23:50) and included 19 hours of growth at 0.5 μ /sec which yielded 3.42 cm of sample length, and 5 hours of growth at 1.5 μ /sec which yielded 2.7 cm of sample. During the second experiment, the furnace temperature was adjusted to move the melt-solid

interface position towards the hot end of the furnace. The second sample was processed for 50 hours, 10 minutes (MET 8/18:48:49—10/21:58:54) and included 11 hours of growth at 0.5 μ /sec which yielded 1.98 cm of sample, and 1 hour, 25 minutes of growth at 5.0 μ /sec which yielded 2.6 cm of sample. This sample provides an order of magnitude change in growth rate and reproduces one of the growth rates used during USML-1. In contrast to the results from USML-1, no voids were present in either crystal grown on USML-2. The absence of voids in either sample indicates that growth rate changes alone were not responsible for the formation of voids found in the crystals grown on USML-1.

Sections of the ground-based and flight crystals grown on USML-2 were cut and polished. All of the interface demarcation lines expected from the current pulse interface demarcation (CPID) system have been identified. These measurements have been analyzed for interface positions, interface shapes, and growth rates.

Using a newly developed technique, based on experimental and numerical results, the seeding interface reproducibility from run to run was ≤ 2.5 mm. The seeding interface position could be controllably moved, with respect to the furnace zones, by adjusting the control set points of the heating zones. The interface shapes flattened slightly as the interface position moved closer to the hot zone but was always an unfavorable concave into the solid shape. The growth rate was found to equal the furnace translation rate, after a 2-hour transient, for growth rates ≤ 1.0 μ /sec.

Segregation measurements for the ground-based crystals are indicative of complete mixing behavior, as expected. Segregation measurements of the flight crystals are still in progress.

1. INTRODUCTION

1.1 Axial Segregation Theory

When an alloy of composition C_o is solidified, segregation of the solute occurs and is described by the alloy's equilibrium phase diagram.¹ The equilibrium segregation coefficient k_o , is defined as the ratio of the solute concentration at the interface in the solid to that in the liquid, thus:

$$k_o = \frac{C_s^{eq}}{C_l^{eq}} \quad (1)$$

If $k_o < 1$ for an alloy, then solidification causes rejection of solute into the liquid at the solid-liquid interface. There are two limiting theoretical cases, 1) complete convective mixing of the solute in the liquid, and 2) diffusive mixing of the solute in the liquid in the absence of convection.

The solute distribution for the first limiting case of complete mixing in the melt has been derived by many investigators, most notably by Scheil² and Pfann.³ In their one-dimensional analysis they assume that, 1) there is no diffusion of solute in the solid, 2) the segregation coefficient k_o , is constant, and 3) there is complete mixing in the liquid. By considering a mass balance of the solute, the composition of the solid as a function of the fraction solidified was derived to be:

$$C_s = k_o C_o (1 - f_s)^{(k_o - 1)} \quad (2)$$

where:

C_s = concentration of the solute in the solid

k_o = equilibrium segregation coefficient

C_o = initial concentration in the melt

f_s = fraction solidified

Figure 1 shows the resultant solute distribution in the solid when complete mixing due to convection was present during solidification.

The solute distribution for the second limiting case of diffusion controlled growth was originally treated by Tiller, Jackson, Rutter and Chalmers.⁴ They derived an approximate, time-independent expression to describe the solute concentration in the solid for steady-state growth as a function of the distance grown, growth rate, and diffusion coefficient of the solute in the liquid:

$$C_s = C_o \left\{ 1 - (1 - k_o) \exp \left(- \frac{k_o R x}{D_l} \right) \right\} \quad (3)$$

where:

R = microscopic growth rate

x = distance grown

D_l = diffusion coefficient in the melt

This expression assumes that a) there is a planar interface, (b) there is no diffusion in the solid, c) k_o is a constant, d) there is no convection in the melt, and (e) that solute is conserved. Also, it is assumed that the rate at which C_s approaches C_o is a function of growth distance and is proportional to $(C_s - C_o)$.

As figure 1 illustrates, growth under these conditions results in a uniform composition profile, except for initial and final transients. The characteristic length for the initial transient D_l/Rk_o , represents the build up of the solute boundary layer. The characteristic length for the final transient D_l/R , represents the impingement of the solute boundary layer on the end of the crystal.

As can be seen in figure 1, a major portion of the crystal grown in a diffusion controlled growth regime would have the desired composition of C_o . This compares to the complete mixing case, seen in figure 1, in which only a small portion of the crystal has the desired composition. Thus, a higher yield of commercially useful crystal would be achieved if diffusion controlled growth could be realized.

1.2 Diffusion Controlled Growth

Having established that diffusion controlled growth is desirable from a materials engineering point of view, how can this be achieved? In other words, how can convection in the melt be suppressed or eliminated? A review of this subject is given by Carruthers⁵ in which he discusses the factors that influence the stability and types of thermal convective flow patterns and presents the methods employed to control convection. Carruthers examines in detail the importance of thermal boundary conditions and the degree of confinement in determining the nature of thermal convective instabilities. In all types of crystal growth, the factors that influence the type and amount of thermal convection can be characterized by the dimensionless Rayleigh number, N_{Ra} :

$$N_{Ra} = N_{Gr} \times N_{Pr} = \left(\frac{\beta \vec{g} \Delta T L^3}{\alpha \nu} \right) \quad (4)$$

where:

N_{Ra} = Rayleigh number

N_{Gr} = Grashoff number

N_{Pr} = Prandtl number

β = thermal expansion coefficient

\vec{g} = effective gravitational constant (\vec{g}/g_0)

ΔT = change in temperature across L

L = characteristic distance

α = thermal diffusivity

ν = kinematic viscosity

The Rayleigh number is the ratio of buoyancy forces, which lead to the development of convective flow, to the viscous forces, which oppose flow. For small values of the Rayleigh number, where the viscous forces opposing convection are large, the fluid is stable and thermal convection is absent. At some critical value of the Rayleigh number, the onset of laminar flow occurs and, for increasingly larger Rayleigh numbers, this flow becomes oscillatory and then turbulent in nature. Engineering control of the nature and velocity of these convective flows is achieved by manipulating and controlling the variables described in the Rayleigh number, namely, the characteristic distance, the temperature gradient, and gravity.

The characteristic distance, with a third power dependence, is an obvious starting point as a variable to manipulate in order to eliminate convection in the melt. Kim et al. manipulated the melt-to-diameter aspect ratio to control the type and intensity of convection in Te-InSb⁶ and Ga-Ge⁷ in a top seeded Bridgman system using a gradient freeze growth technique. Holmes and Gatos⁸ were able to achieve diffusion controlled growth in small diameter, capillary-sized crystals of Ga-Ge in a bottom seeded Bridgman system using a gradient freeze growth technique. As they increased the diameter to larger than 1 mm, the segregation behavior quickly approached the complete mixing regime. Reduction of the characteristic distance, then, does not allow for achieving diffusion controlled growth in bulk crystals.

Another variable to manipulate would be the temperature difference across the characteristic distance. In order to solidify single crystals from their melts, it is necessary to remove the heat of solidification from the melt-solid interface during growth. Thus, temperature gradients are required during crystal growth, and the limited manipulation of these temperature differences are typically ineffective in reducing or eliminating convection in the melt. However, there have been several one-dimensional models developed to predict the axial temperature gradients,⁹ and several two-dimensional models to predict the axial and radial temperature gradients present in the growth system.¹⁰ Although manipulation of temperature gradients has limited effectiveness in eliminating convection in the melt, it is an important variable in the generation and multiplication of dislocations and other defects.¹¹

The final variable in equation (4) which can be manipulated to eliminate convective flows in the melt and thus achieve diffusion controlled growth is the effective gravity term. Experimentation in this area began during the translunar portions of the Apollo 14, 16 and 17 flights.¹² These efforts were continued during the Skylab program with several crystal growth experiments.¹³

During the Apollo-Soyuz Test Project (ASTP), Professors Witt and Gatos directed efforts to grow bottom seeded gallium doped germanium using a gradient freeze technique.¹⁴ During growth, current pulses were used to demarcate the melt-solid interface at known time intervals (Peltier Pulsing). These pulses allowed for determination of the interface shape and the growth rate. Single point spreading resistance measurements were used to determine the dopant distribution.

Since there were three growth chambers, none of them were in the thermal center of the furnace, and thus, the melt-solid interface shapes of the crystals were not symmetric. In addition, it was determined that the interface shapes changed throughout growth due to changing thermal loads in the system. Also, it was determined that the growth rate slowly increased during growth and never achieved a steady-state value.

The measured dopant distribution quickly increased in value over the first centimeter of growth and then slowly increased throughout the rest of growth. By averaging the measured left periphery, right periphery, and center values, an overall axial distribution was determined. By using the best available material property values from the literature, combined with the measured growth rate data, Witt and Gatos showed that diffusion controlled growth was achieved in the axial direction. In contrast, the ground-based experiments showed that the segregation behavior approached that of complete mixing.

The radial dopant distribution data for the crystals grown in space varied by a factor of 3 greater than the radial dopant distribution data for the crystals grown on Earth. This increased radial segregation in the presence of diffusion controlled axial segregation behavior was an unexpected result.

Another possibility which exists for lowering the Rayleigh number is to lower the kinematic viscosity of the materials by the application of a magnetic field. This is not, of course, an actual change in the material property of the liquid. A coupling occurs between the magnetic field and the electrical conductivity which can produce a damping of the fluid flow, sometimes referred to as the magnetic viscosity.⁵ In melts which have a high electrical conductivity, like germanium, large magnetic fields have been used to achieve diffusion controlled growth behavior in 1-cm diameter crystals.¹⁵

1.3 Radial Segregation Theory

The unexpected radial segregation behavior measured in Professors Witt and Gatos's experiment has lead to several analytical and numerical investigations into radial segregation behavior. Coriell and Sekerka¹⁶ assumed an interface shape with a radius of curvature expressed as:

$$R = \frac{1}{2} \left(\frac{L^2}{4\Delta d} + \Delta d \right) \quad (5)$$

where:

R = radius of curvature

L = diameter of the crystal

Δd = the interface deflection

With this assumed interface shape, they were able to solve analytically for the radial segregation due to a slightly curved interface, a small Peclet number ($N_{Pe} = LV/D$ where V is velocity) and a flat interface shape at the ampoule wall. When data from the Witt and Gatos experiment were used, their solution predicted approximately 10 percent radial segregation, which is in qualitative agreement with the measured 300 percent radial segregation data.

Coriell, Sekerka and coworkers¹⁷ followed this paper with one in which they combined analytical and numerical results to predict the radial segregation behavior due to large interface deflections, a large Peclet number and a flat interface shape at the ampoule wall.

As part of the USML-1 program, Korpela, Chait and Matthiesen¹⁸ developed an analytic expression for the radial segregation due to small interface deflections, large Peclet numbers and an arbitrary interface shape at the ampoule wall.

1.4 Computer Modeling

Numerical investigations were then initiated to provide further insight into the radial segregation behavior. The numerical simulations of Kim, Adornato and Brown¹⁹ have recently shed some insight into the problem of axial and radial segregation behavior with respect to the convection present in the melt. They predict that initially, in a bottom seeded Bridgman-Stockbarger growth system, a two cell torroidal flow pattern will exist, with an intense flow cell near the melt-solid interface. As the flow velocities are decreased, either by microgravity or applied magnetic fields, or both, the two flow cells gradually merge into one large cell. As the flow velocities are further decreased, this one flow cell eventually disappears and diffusion controlled growth is achieved.

An important conclusion of their analysis is that when the two cell patterns become one cell, the axial dopant distribution approaches that of diffusion controlled growth, but the radial segregation increases. It is only after the flow velocities are further reduced that the radial segregation finally decreases, as shown in figure 2. When the convective flows are finally suppressed, the radial segregation is controlled by the interface shape, as predicted by Coriell and Sekerka.

The work of Brown and coworkers has implicitly assumed that the gravitational vector is aligned perfectly with the temperature gradient. This will always result in a prediction of axi-symmetric flow. The work of Arnold et al. has shown that when the gravitational vector is slightly misaligned relative to the axis of the crystal, a significant change in the flow pattern can occur.²⁰

Motakef has used results from numerical modeling in combination with scaling arguments to predict the necessary reduction in the effective gravitational field to achieve diffusion controlled growth in a variety of materials for a variety of charge diameters.²¹ He predicts that for GaAs at 0.75-cm diameter, the expected microgravity environment should produce diffusion controlled behavior. In another paper, Motakef²² uses the same methodology to predict the required magnetic field strength to achieve diffusion controlled growth, again in a variety of materials and for a variety of charge diameters. He predicts that for GaAs at 0.75-cm diameter, the required magnetic field needed to produce diffusion controlled behavior is larger than any system in existence.

2. MOTIVATION AND GOALS

Although the work of Professor Brown and his coworkers has provided useful insight to the segregation behavior during the growth of electronic materials, there has been little experimental verification. In fact, the Witt and Gatos experiment is the only experiment which has had all the appropriate data necessary for comparison to these numerical simulations.

The question then arises, can these simulations be used to predict the growth of other materials in microgravity? In 1978 the Committee on Scientific and Technological Aspects of Materials Processing in Space (STAMPS) of the National Research Council²³ issued a report which reviewed the materials processing in space programs done to that date. Among their many conclusions was that, although the growth of germanium on ASTP provided a firm foundation for the growth of electronic materials in space, it was not possible *a priori* to extrapolate these results to the more technologically interesting III-V and II-IV materials. In addition, the necessary material property values needed to perform applicable numerical simulations that would predict the outcome of processing these materials in space have not been precisely determined, and in some cases, not determined at all.

3. SCIENTIFIC OBJECTIVES

The scientific objectives of these experiments were to do the following under microgravity conditions:

- To investigate techniques for uniformly distributing Se axially during GaAs growth.
- To investigate techniques for uniformly distributing Se radially during GaAs growth.
- To investigate the effect of the thermal profile on the melt/solid interface shape and the corresponding effect on radial and axial dopant distribution.

A secondary objective that was incorporated in these experiments was to test new theories for the cause of the voids found in GaAs crystals grown on USML-1.

4. EXPERIMENTAL PROCEDURE

4.1 Crystal Growth of Sample Charges

The Liquid Encapsulated Czochralski (LEC) grown crystals were oriented $\langle 111 \rangle$ and doped to achieve an average dopant concentration in the grown crystal of $\sim 10^{17}/\text{cm}^3$. These charges were prepared from the *in situ* synthesis and growth of $\sim 1,000$ g charges of selenium-doped gallium arsenide. A layer of boric oxide was used as an encapsulant and a pyrolytic boron nitride (PBN) crucible was used for the growth. An argon overpressure was maintained in the Malvern MSR-R6 high pressure crystal growth system. Typically the seed rotation rate was 7 rpm and the crucible was in counter rotation at approximately 5 rpm. The pulling rates were typically $3.5 \mu\text{m}/\text{sec}$.

The crystals were machined to approximately the right size using electric discharge machining (EDM).²⁴ This included machining a square nubbin on one end of the crystal and a round nubbin on the other end. A chemical etch was used to reduce the crystals to the final diameter to fit the PBN sleeve. Each of the crystals used on USML-2 was a single piece charge. In some of the ground-based experiments, two or three piece charges were used. On the ground, this was expected to have no effect on the resulting crystal since any bubbles generated would rise out of the PBN sleeve.

4.2 Ampoule Design and Fabrication

As shown in figure 3, each crystal was contained within a pyrolytic boron nitride crucible (sleeve). This sleeve had a 0.035-inch wall. At the cold end of the crystal was a graphite pedestal for positioning the seed crystal. At the hot end of the crystal was a graphite spring chamber, which in turn contained a graphite plunger and a PBN leaf spring assembly. This spring allowed the plunger to advance and retreat as the crystal contracted upon melting and expanded upon freezing. The spring chamber was round on the outside to match the PBN sleeve and square on the inside to allow for smooth operation of the spring. One end of the crystal was machined square to fit the spring chamber. The crystal, graphite and PBN were hermetically sealed into a fused quartz ampoule, which minimized the arsenic losses from the GaAs crystal. The ampoule was heated to 250°C under 10-millitorr vacuum before it was finally sealed. At both ends of the ampoule were molybdenum feedthroughs. These feedthroughs allowed current to pass through the ampoule to enable demarcation of the melt-solid interface by current pulsing. The CGF was modified to add a current pulse interface demarcation (CPID) system prior to USML-2. Figure 3 also shows the design for the USML-1 ampoules for comparison. Changes were made to enable interface demarcation and to improve the spring design, but no changes were made that would be expected to influence the crystal growth process.

The ampoule was then positioned into a cartridge (sample ampoule cartridge assembly, SACA). This cartridge was made of tungsten and niobium and had a molybdenum disilicide coating on the outside to inhibit thermal oxidation. As shown in figure 4, the ampoule was positioned to the correct seeding position inside the cartridge using zirconia insulation pedestals. There were six open bead, type-S thermocouples located between the ampoule and the cartridge. These thermocouples were known as the PI thermocouples. Platinum leads were used to provide current to the ampoule for current pulsing.

GaAs was determined to form 2.2 atm of arsenic pressure at 1260 °C.²⁰ To balance this internal pressure, the cartridge was evacuated and filled with 12.87-psia argon gas at room temperature and hermetically sealed. Thus, even though the fused quartz of the ampoule was in viscous flow at the processing temperature, no deformation of the ampoule was expected since the pressure forces on the ampoule balanced one another.

Before delivery each SACA was x-rayed to determine the exact location of the thermocouples relative to the seed end of the crystal.

4.3 Experimental Timelines—Ground-Based Experiments

GaAs crystals were grown successfully in four science tests and two mission simulation experiments prior to the mission. Different timelines and different furnace temperature set points were used in these experiments in an attempt to find the optimal growth conditions for achieving a flat interface.

In order to insure directional melting of the crystal, the furnace was heated prior to inserting the SACA into the hot zone of the furnace. Figure 5b shows the location of the cartridge relative to the furnace zones during heat-up. After the furnace has reached the desired temperature set points, the cartridge is inserted to the position shown in figure 5c. Translation started in this position. Figure 5a shows the location of the USML-1 cartridge relative to the furnace zones. This was the position of the cartridge during heat-up as well as at the start of translation during USML-1. Figure 6 shows a schematic graph of the various furnace set points that were used in ground-based experiments. The lengths of the zones are shown in figure 5.

4.4 Comparison of Ground-Based Results to Computational Model Results

The location of the melt-solid interface relative to the furnace zones was measured for each of the ground-based experiments. These measurements are given in table 1 as the seeding interface position relative to the cold zone/gradient zone boundary with positive numbers being in the gradient zone. As seen in these results, it was possible to adjust the furnace set points to position the melt-solid interface at the center of the gradient zone.

A model of the CGF developed by CAPE, Inc. was used to predict the furnace bore profile for given furnace temperature set points. This bore profile was used as input for a detailed model of the SACA that was developed by the Computational Modeling Laboratory at NASA Lewis Research Center. This model was used to predict the thermal profile inside the SACA. This model predicts the location of the 1511 K isotherm across the radius of the SACA. Thus, the location of the 1511 K isotherm at the center of the crystal and at the radial location of the thermocouples may be predicted. A sample output is shown in figure 7. The model predictions for the location of the 1511 K isotherm at the PI thermocouple location and at the center of the crystal were plotted on the graph shown in figure 8 for a variety of conditions. The crosses are the model predictions and the circles are the experimental results from the ground-based experiments. This plot could then be used to predict the location of the melt-solid interface in the crystal for a given location of the 1511 K isotherm at the location of the PI thermocouples.

4.5 Experimental Timelines—Flight and Ground Truth Experiments

The experimental timeline for the first flight experiment (flight No. 1) is shown in figure 9. The first ground truth experiment (GT No. 1) used the same nominal timeline. A thermal gradient was established across the 2-cm gradient zone of the CGF. The thermal gradient was approximately $10^{\circ}\text{C}/\text{cm}$ at the steepest point, as measured by the PI thermocouples. The seeding location of the crystal in relation to the furnace zones was the same as for the ground-based experiments, shown in figure 5c.

The furnace set point temperatures were adjusted in real time via uplinked commands in an attempt to position the melt-solid interface at the center of the gradient zone. The decision to modify the temperature set points from the nominal values was based on the temperature profile of the furnace produced by the PI thermocouples upon partial insertion into the fully heated furnace. Figure 10 contains a graph of the PI thermocouple values during insertion of flight No. 1. This data was compared to results from ground-based testing, specifically the GCEL mission simulation, and changes to the set points were made. The final set points are listed in table 2.

Growth included 19 hours at $0.03\text{ mm}/\text{min}$ ($0.50\text{ }\mu\text{sec}$) to grow 3.42 cm of sample. Then the rate was changed to $0.09\text{ mm}/\text{min}$ ($1.50\text{ }\mu\text{sec}$) for 4 hours (2.16 cm), halted for 5 hours 15 minutes, then resumed at $0.09\text{ mm}/\text{min}$ for 1 hour. Translation ended and a gradient freeze was used to solidify the remaining melt, principally the square nubbin located in the spring chamber. The cooling rate during the gradient freeze was designed to be no more than $14^{\circ}\text{C}/\text{hr}$ to result in a solidification rate no greater than $0.5\text{ }\mu\text{sec}$. A controlled cool down was used to cool the furnace to 800°C , followed by a power-off free-fall cool down.

The translation arrest was included in the timeline to provide an equilibrium interface position and shape in the cartridge in a position other than fully inserted in the furnace to use for comparison with the model. The duration of the translation arrest was changed from 5 hours to 5 hours 15 minutes in real time during the experiment to avoid resuming translation during a loss of signal (LOS) period when downlink data and commanding capability would be lost. The nominal LOS periods are shown in figure 9.

Current pulses were planned in periodic patterns throughout growth as described in figure 9. The maximum pulse current used was 30 A which gave a current density at the interface of $17\text{ A}/\text{cm}^2$.

The experimental timeline for the second flight experiment (flight No. 2) is shown in figure 11. In this experiment the furnace temperature set points were adjusted in an attempt to locate the melt-solid interface at the hot end of the gradient zone. A combination of the graphs shown in figures 8 and 10 were used to determine the desired thermal profile in the furnace. The nominal temperature set points are shown in figure 11 and the final temperature set points are given in table 2. Positioning the melt-solid interface in the region of the hot booster zone was expected to produce a seed approximately 1.3 cm longer than in the first flight experiment, or 4.8 cm long.

As in the first experiment, growth consisted of translation at two rates with a translation arrest near the end of the second rate period. Growth included 11 hours of growth at $0.03\text{ mm}/\text{min}$ ($0.50\text{ }\mu\text{sec}$) and 1 hour 10 minutes at $0.30\text{ mm}/\text{min}$ ($5\text{ }\mu\text{sec}$). Following a 4-hour translation arrest, 15 additional minutes of growth at $0.30\text{ mm}/\text{min}$ was included. As in the first experiment, a gradient freeze designed to be no faster than $14^{\circ}\text{C}/\text{hr}$ was used to solidify the remaining melt.

The majority of the current pulses were at 30 A as in the first flight experiment. However, the current was increased to 35 A for the first three pulses when translation resumed after the translation arrest. This was done to increase the likelihood of seeing the pulses in the concentration transient.

4.6 Sample Analysis Preparation

After flight each SACA was x-rayed and the ampoule was removed from the cartridge and inspected. The ampoules were then opened and the GaAs crystals removed. After inspection, a 0.070-inch-thick (1.778 mm) axial slice was cut from the crystal and polished on both sides to yield a 0.050-inch (1.27-mm) sample. The smaller of the two half cylinders or D-sections was cut perpendicular to the axial direction. This yielded approximately 50 to 75 0.050-inch (1.27-mm) thick D-shaped samples, which are being used for characterization analyses.

5. RESULTS AND DISCUSSION

The following sections include a discussion of the results to date for the flight and ground truth samples from the USML-2 GaAs project. The ground-based experimentation which was done will also be summarized.

The sections to be discussed include a macroscopic description of the crystals after they were removed from the ampoule and after they were sectioned; seeding interface shape measurements and analysis; growth rate determination; axial and radial segregation analyses and predictions; comparison of the predictions from the computational model to the experimental results; and a brief review of acceleration data.

5.1 Flight Data

During flight, real-time downlinked data is available to monitor the PI thermocouple temperatures, the CPID circuit resistance, and many furnace parameters such as temperatures and power values. All of the equipment ran successfully throughout both flight experiments. The CPID resistance data showed the expected trend. The CPID data is shown in figures 12 and 13 for the flight experiments.

5.2 X-Rays of the SACA's

After processing, a series of x-ray films are produced for each SACA. The x-ray films for the flight SACA's indicated that there were no voids present in either crystal; the springs had operated properly, and there had been no leakage of gallium arsenide out of the crystal chamber. These results were all confirmed after opening the ampoule and cutting the crystal.

5.3 Visual Observations

The first flight sample had a very distinct pattern of lines on the surface indicating that the PBN sleeve had probably been honed. The second flight sample had the expected dull, matte finish indicative of contact with a smooth PBN sleeve. The diameter of the remelt region was constant and the spring appeared to have worked properly. Thus, it is concluded that no free surfaces were formed on the surface of the GaAs melt during processing.

Figure 14 shows a photograph of the first flight sample boule. The meltback interface was located 32.5 mm from the seeding shoulder in the first flight sample. This compares favorably with a predicted interface location of 31 mm from the numerical model.

Polycrystalline breakdown occurs in the first flight sample from the meltback interface and can be observed in figure 15 which shows a photograph of a polished D-slice. This leaves only a very small amount of sample from the center of the crystal for use in any characterization techniques that require single crystalline samples, such as Hall effect measurements.

Figure 16 shows the GaAs boule from the second flight experiment. The meltback interface was located 50 mm from the seeding shoulder in the second flight sample. The predicted interface location for this sample was 41 mm from the numerical model.

The second flight sample remains a single crystal for approximately 5 mm before polycrystalline breakdown occurs. Figure 17 shows the polished D-slice from the second flight sample and the onset of polycrystalline growth.

The first ground truth sample boule is shown in figure 18. The position of the meltback interface was located 34 mm from the crystal shoulder. Figure 19 shows a D-slice from the same sample and the start of polycrystalline growth 3 to 5 mm from the meltback interface.

The second ground truth boule is illustrated in figure 20 with a meltback interface at 50 mm from the crystal shoulder. One D-slice from this sample, shown in figure 21, indicates the onset of polycrystalline growth at approximately 5 mm from the meltback interface.

The meltback interfaces were positioned within 1.5 mm of each other for the first flight and ground truth experiments and within 2.5 mm for the second flight and ground truth experiments.

5.4 Absence of Voids

Voids were present in both GaAs crystals grown on USML-1. Three theories were proposed to explain the formation of the voids seen in the USML-1 crystals: 1) Evolution of dissolved argon from the Liquid Encapsulated Czochralski (LEC) grown crystal could have resulted in the formation of voids during solidification; 2) Vaporization of excess arsenic at the melt/solid interface due to superheating during rapid solidification could have generated bubbles that were trapped as voids during solidification; 3) A three-piece charge geometry with nondirectional melting could have generated bubbles which were trapped in the crystal as voids during directional solidification. The USML-2 experiments were designed such that these theories could be tested. The USML-2 experiments used one-piece charges which were grown using the same LEC procedure and apparatus as the USML-1 charges, but machined with a new technique capable of producing single piece charges. The USML-2 charges were directionally melted and directionally solidified. One of the USML-2 experiments duplicated the fastest growth rate that was used on USML-1. No voids were found in either of the crystals grown on USML-2 as seen in figures 14 and 16. From these results, it is reasonable to reject the theories concerning dissolved Ar and excess As vaporization. It can be concluded that the voids found in the USML-1 crystals resulted from the combination of the three piece charge geometry and nondirectional melting prior to directional solidification.²¹

5.5 Seeding Interface Shape Measurements

Using an infrared transmission microscope, the deflection of the seeding interface (and any subsequent interface) is measured and then mapped. A fourth order curve fit is applied to the parabolic shape and then fitted to the actual data.

5.6 Interface Shapes

Figures 22–24 show the seeding interface deflections for the GCEL mission simulation, the first ground truth and space flight samples, and the second ground truth sample, respectively. All seeding interfaces are concave into the solid during crystal growth and approximately symmetric about the growth axis. The initial location of the seeding interface in the furnace was also determined.

The nominal furnace zone set point temperatures, summarized in tables 1 and 2, were the same for the GCEL and the first ground truth and flight experiments and then for the second ground truth and space flight samples (figs. 5 and 6). The location of each seeding interface within the furnace was 9.3 mm, 10.5 mm, and 12 mm with respect to the cold zone/gradient zone junction for the GCEL, the first space flight, and the first ground truth, respectively. The resulting maximum deflections of the seeding interfaces for the three samples are 1.46 mm, 1.38 mm, and 1.27 mm for the GCEL sample, the first space flight sample, and the first ground truth sample, respectively. Each interface was located near the center of the gradient zone and the slight variations in position were reflected in the slight variations of the maximum interface deflection.

The furnace zone temperatures were lowered for the second ground truth and flight experiments (fig. 8) in order to relocate the interface location high in the gradient zone near the hot main. This, in fact, was achieved as the seeding interfaces for the second ground truth and flight sample were located at 28.5 mm and 26 mm, respectively, from the junction of the gradient zone and cold zone. The maximum deflection of the seeding interface for the ground truth sample was 1.04 mm as shown in figure 21. It is expected that the deflection of the space flight sample is similar based upon their initial location in the furnace.

5.7 Demarcation Interface Shapes

Figures 26 and 27 show the shape, position, and maximum deflection of some demarcated interfaces, relative to the seeding interface, in the first space flight and ground truth crystals, respectively. The measurements and curve fits of the interfaces in each crystal during the first translation period show the deflection increasing as compared to the seeding interface. Within the first translation period, the deflection decreases slightly as the position of the interface, and therefore the growth rate, stabilizes. After the translation rate change to 1.5 m/sec, the interface shape steepens considerably in both samples. A translation arrest, followed by a thermal soak period after the rate change, allowed the interface to stabilize. This is reflected in the smaller deflection, again for both samples, compared to earlier interfaces. The deflection of the translation arrest interface is slightly larger than that of the seeding interface, most likely due to closer proximity to the end of the crystal.

5.8 Growth Rate Versus Furnace Translation Rate

The ground-based USML-2 experiments revealed that the growth rate equaled the translation rate for rates below 1 m/sec, but did not for rates higher than 1 m/sec.²⁵ The flight and ground truth experiments show similar results. Figures 28-30 illustrate the growth rate versus the time of growth for the first space flight, the first ground truth, and the second ground truth sample, respectively.

When the crystal's growth rate does not equal the furnace translation rate, the melt-solid interface position will move with respect to the furnace. This will have the undesirable effect of changing the melt-solid interface shape. It is hypothesized that the inability of the crystal's growth rate to keep up with the furnace translation rate was due to the inability to remove heat from the crystal in a low thermal gradient environment.

5.9 Dopant Distribution Measurements

Dopant distribution has been measured using the van der Pauw Hall effect technique²⁶ in each ground-based sample grown in the USML-2 program.

5.9.1 Axial Segregation Analysis

The selenium distribution for the GCEL sample is illustrated in figure 31. The results shown in this plot are representative of the results obtained from the other ground-based samples. The Se distribution is fully described by the complete mixing axial segregation profile. The k_{eff} and C_o values were obtained by fitting the distribution data to equation (2). The Se distributions in the original LEC crystals, which were used to make the GCEL mission simulation GaAs charge, were also measured. It was found that the C_o value determined and shown in the profile in figure 31 was within the range calculated from the measured Se concentration values in the LEC crystals. This validates the Hall measurements in the GCEL sample.

Dopant distribution and segregation analyses will also be carried out for each space flight and ground truth crystal.

5.9.2 Radial Segregation Analysis

Predictions of radial segregation have been made using Coriell and Sekerka's first paper¹⁵ and the Korpela, et al. paper.¹⁷ Using a k value of 0.3, a diffusion coefficient of 1×10^{-5} cm²/sec, and an experimentally measured value for a typical growth rate and interface deflection for the first space flight and ground truth sample, Coriell and Sekerka's theory predicts segregation of 57 percent and 61 percent respectively. The predictions from "the Korpela, et al. theory" are 22 percent and 40 percent, respectively, for the first space flight and ground truth samples.

A dopant distribution analysis for Se concentration will be done radially across the sample to confirm these predictions.

5.10 Comparison to Computational Model

The computational model of the USML-2 GaAs SACA was used to predict temperature isotherms, corresponding to the melt/solid interfaces, at specific positions in the crystal. A numerical model of the CGF²⁹ with a generic cartridge was used to predict a temperature profile for input to the SACA model, which contained a detailed description of the experimental SACA. A typical result from the numerical model is shown in figure 30. This illustrates the model of the ampoule at a position corresponding to the fully inserted seeding position of the crystal growth run. The deflection of the predicted interface shape is 1.53 mm and the measured seeding interface deflection was 1.52 mm. At a later position, the predicted interface deflection was 1.22 mm and the experimental deflection of the demarcation line corresponding to the interface position was 1.98 mm. The computational model assumed steady-state growth conditions and therefore only predicts the interface shape and location for steady-state processing. The experiment is actually a transient process. Thus, the model is better able to predict the melt-solid interface location and shape than the demarcated interfaces during translation.

5.11 Analysis of Acceleration Data

The Orbital Acceleration Research Experiment (OARE) and Space Acceleration Measurement System (SAMS) acceleration measurement systems were flown on the USML-2 mission. The Principal Investigator Microgravity Services (PIMS) group at NASA Lewis Research Center is helping with the analysis of the acceleration data for the time period when the GaAs was molten. Preliminary results indicate that the microgravity environment on USML-2 was similar to that found on USML-1. Moskowitz et al.^{27 28} have shown that the microgravity environment on USML-1 was of sufficient quality to produce no more than a 2 percent radial dopant segregation in the crystals 90 percent of the time. The 10 percent of the time which violated this criteria were not concentrated in a single time span. Therefore, the physical impact of this portion of time was reduced. It was concluded that the microgravity environment was sufficiently good to not cause degradation of the quality of the crystals. It is expected that this will also be true for USML-2.

6.0 CONCLUSIONS AND FUTURE WORK

The results from the USML-1 program raised questions which have been answered by the results of the USML-2 program in the following way:

Q: What was the genesis of the voids that were present in the USML-1 crystals?

A: The genesis of the voids in the USML-1 crystals was determined to be from the use of multi-piece charges that were not directionally melted. The USML-2 crystals contained no voids even when the translation rate was increased from 0.5 to 5 μ /sec.

Q: Could the interface shape during translation be determined?

A: Yes. The CPID system was used successfully to demarcate the melt-solid interface at known times throughout growth in the USML-2 samples.

Q: Is the seeding interface shape the same as the growth interface shape?

A: No. The interface shapes were concave into the solid but the interface shape was found to steepen slightly during translation as compared to the seeding interface shape.

Q: Is the furnace translation rate equal to the growth rate?

A: Sometimes. The growth rate was found to equal the translation rate, after an initial transient, when the translation rate was $\leq 1 \mu/\text{sec}$. At faster translation rates, the growth rate remained smaller than the translation rate.

Q: Can the interface position be controllably located within the gradient zone?

A: Yes. A technique was developed using a combination of experimental results and numerical modeling results to predict the interface location relative to the furnace such that the interface position could be controllably located at a desired position relative to the furnace within 2.5 mm.

Q: Can the interface shape be modified?

A: Yes, slightly. The interface shape was found to flatten slightly as the interface position was moved closer to the hot zone. However, the interface shape remained concave into the solid at all interface positions.

Q: What caused the segregation behavior seen in the USML-1 crystals?

A: The segregation behavior in one crystal grown on USML-1 initially appeared to follow diffusion controlled behavior but, after approximately 5 mm of growth switched to complete mixing behavior. In the other crystal, the segregation behavior appeared to follow a complete mixing curve.

Q: Was it caused by an acceleration event?

A: No. Analysis of acceleration data indicates that the segregation behavior seen in the USML-1 crystals was not caused by an acceleration event. Similarly, the acceleration environment on USML-2 is not expected to have caused degradation of the quality of the crystals.

Q: Was it caused by the presence of bubbles in the melt that are seen as voids in the crystals?

A: It is currently hypothesized that the presence of bubbles in the melt during processing of the USML-1 crystals may have caused mixing in the melt which could result in the segregation behavior that was observed. This remains to be investigated more fully in the future. Based on this hypothesis, it is expected that the USML-2 flight samples will exhibit diffusion controlled axial segregation. In addition, it is expected that these samples will exhibit significant radial segregation based on the measured interface curvature.

The future work to be conducted includes interface shape measurements and growth rate calculations for the second space flight sample; the measurement of dopant distributions and, correspondingly, the determination axial and radial segregation for the two space flight and two ground truth samples; and verification of dopant distribution results.

REFERENCES

1. Flemings, M.C.: *Solidification Processing*, McGraw-Hill, Inc., 1974.
2. Schiel, E.: *Z. Metallk.*, 34, 70, 1942.
3. Pfann, W.G.: *J. Metals*, 4, 763, 1952.
4. Tiller, W.A.; Jackson, K.A.; Rutter, J.W.; and Chalmers, B.: *Acta. Met.*, 1, 428, 1953.
5. Carruthers, J.R.: *Preparation and Properties of Solid State Materials*, Vol. 3, 1, 1973.
6. Kim, K.M.; Witt, A.F.; and Gatos, H.C.: *J. Electrochem. Soc.*, 119, 1218, 1972.
7. Kim, K.M.; Witt, A.F.; Lichtensteiger, M.; and Gatos, H.C.: *J. Electrochem. Soc.*, 125, 475, 1978.
8. Holmes, D.E.; and Gatos, H.C.: *J. Electrochem. Soc.*, 128, 429, 1981.
9. See for instance—
 - Chang, C.E.; and Wilcox, W.R.: *J. Crystal Growth*, 21, 135, 1974.
 - Naumann, R.J.: *J. Crystal Growth*, 58, 554, 1982.
 - Jasinski, T.; Rosenow, W.M.; and Witt, A.F.: *J. Crystal Growth*, 61, 710, 1983.
10. See for instance
 - Fu, T.F.; and Wilcox, W.R.: *J. Crystal Growth*, 48, 416, 1980.
 - Naumann, R.J.: *J. Crystal Growth*, 58, 569, 1982.
 - Jasinski, T.; Rosenow, W.M.; and Witt, A.F.: *J. Crystal Growth*, 67, 173, 1984.
 - Jasinski, T.; Rosenow, W.M.; and Witt, A.F.: *J. Crystal Growth*, 71, 295, 1985.
11. See for instance
 - Motakef, S.: *J. Crystal Growth*, 98, 711, 1989.
 - Jordan, A.S.: *J. Crystal Growth*, 49, 631, 1980.
12. Naumann, R.J.; and Herring, H.W.: *Materials Processing in Space: Early Experiments*, NASA SP-443, Washington, DC, 1980.
13. Proceedings of the Third Space Processing Symposium, *Skylab Results: Volume 1*, NASA-Marshall Space Flight Center, M-74-5, June 1974.
14. Kim, K.M.; Witt, A.F.; Lichtensteiger, M.; and Gatos, H.C.: *J. Electrochem. Soc.*, 125, 475, 1978.
15. Matthiesen, D.H.; Wargo, M.J.; Motakef, S.; Carlson, D.J.; Nakos, J.S.; and Witt, A.F.: *J. Crystal Growth*, 85, 557, 1987.

16. Coriell, S.R.; and Sekerka, R.F.: *J. Crystal Growth*, 46, 479, 1979.
17. Coriell, S.R.; Boisvert, R.F.; Rehm, R.G.; and Sekerka, R.F.: *J. Crystal Growth*, 54, 167, 1981.
18. Korpela, S.A.; Chait, A.; and Matthiesen, D.H.: *J. Crystal Growth*, in press, 1993.
19. Kim, D.H.; Adornato, P.M.; and Brown, R.A.: *J. Crystal Growth*, 89, 339, 1988.
20. Arnold, W.A.; Jacqmin, D.A.; Gaug, R.L.; and Chait, A.: "Convection Phenomena in Low-Gravity Processing: The GTE GaAs Space Experiment," 28th AIAA Aerospace Sciences Meeting, 1990.
21. Motakef, S.: *AIAA 90-0407*, 28th AIAA Aerospace Sciences Meeting, 1990.
22. Motakef, S.: *J. Crys. Growth*, 104, 833, 1990.
23. Committee on Scientific and Technological Aspects of Materials Processing in Space, *Materials Processing In Space*, National Academy of Sciences, Washington, DC, 1978.
24. Arnold, W.A.; Matthiesen, D.H.; Bennett, R.; and Jayne, D.: "An Innovative Method for Preparing Semiconductor Charges Used in Crystal Growth and Shear Cell Diffusion Experiments," *J. Crystal Growth*, in press, 1997.
25. Bly, J.M.; Kaforey, M.L.; and Matthiesen, D.H.: "Interface Shape and Growth Rate Analysis Of Se/GaAs Bulk Crystals Grown in the NASA Crystal Growth Furnace (CGF)," *J. Crystal Growth*, in press, 1997.
26. van der Pauw, L.J.: "A Method of Measuring Specific Resistivity and Hall Effect of Discs of Arbitrary Shape," *Philips Res. Reports.*, 13, 1-9, 1958.
27. Moskowitz, M.E.; Bly, J.M.; and Matthiesen, D.H.: "Comparison of OARE Accelerometer Data With Dopant Distribution in Se-Doped GaAs Crystals Grown During USML-1," *J. Crystal Growth*, in press, 1997.
28. Moskowitz, M.E.: "A Comparative Study of SAMS and OARE Acceleration Measurements During the Growth of Se-Doped GaAs Crystals Grown Aboard USML-1," M.S. Thesis, Dept. Mat. Sci. and Eng., Case Western Reserve University, 1997.
29. Furnace model developed by CAPE Simulations, Inc. Wellesley, Massachusetts.

Table 1. Results summary for USML-2 GaAs ground-based samples.

		Science Sample #1	Science Sample #2	Science Sample #3		GCEL Mission Simulation		Flight Unit Mission Simulation #2		Science Sample #4	
Furnace setpoints (°C)	CG	1220	1220	1200		1200		1208		1208	
	CM	1220	1220	1200		1200		1210		1210	
	HB	1260	1250	1242		1242		1252		1252	
	HM	1260	1250	1250		1250		1257		1257	
	HG	1260	1260	1255		1255		1262		1262	
Growth time	hours	all	all	15	10	15	10	22	5	22	5
Furnace translation rate	μ/s	0.5	0.5	0.5	1	0.5	1	0.55	1.65	0.55	1.65
Averaged crystal growth rate	μ/s±	**	0.533±	0.542±	0.947±	0.491±	0.965±	0.531±	1.590±	0.540±	**
	μ/s		0.012	0.015	0.017	0.012	0.010	0.010	0.060	0.020	
Furnace translation rate constant	sec	**	6620	4050	4080	2715	2860	3410	3720	2970	**
Seeding interface position*	mm	-13.50	-13.50	9.50		9.30		2.00		-3.10	
Maximum deflection of seeding interface	mm	1.96	1.52	1.23		1.41		1.40		1.48	

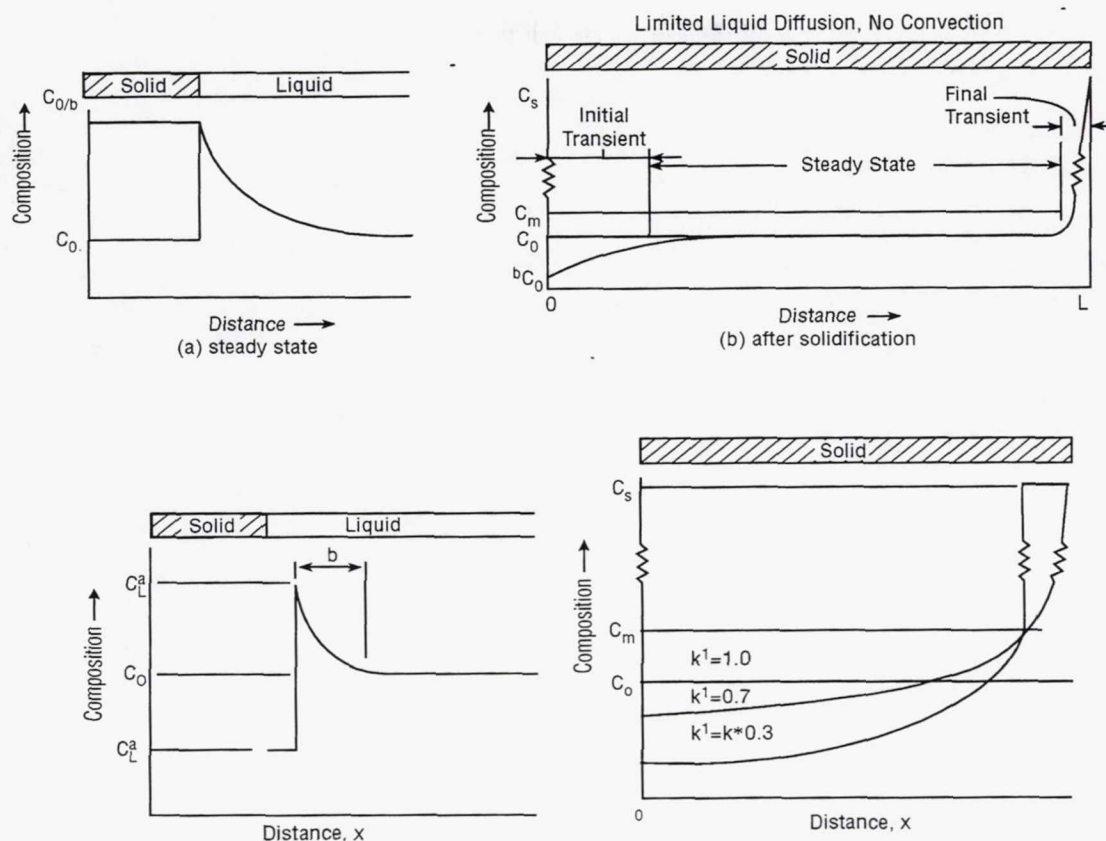
* Negative refers to distance into the cold zone; positive refers to distance into the 2.0 cm gradient zone.

** Not enough information for calculation.

Table 2. Results summary for USML-2 GaAs flight and ground truth samples.

		Flight #1				Ground #1				Flight #2				Ground #2			
Nominal thermocouple setpoints (°C)	CG	1200				1200				1193				1193			
	CM	1200				1200				1193				1193			
	HB	1242				1242				1237				1237			
	HM	1250				1250				1245				1245			
	HG	1255				1255				1248				1248			
Actual thermocouple setpoints (°C)	CG	1200				1200				1193				1190			
	CM	1200				1200				1193				1191			
	HB	1244				1242				1233				1234			
	HM	1252				1250				1242				1242			
	HG	1255				1255				1245				1245			
Total run time	hours	67 hours 30 minutes				67 hours 30 minutes				50 hours 10 minutes				50 hours 10 minutes			
Growth time	hours	19	4	5	1	19	4	5	1	11	1.17	4	0.25	11	1.17	4	0.25
Translation rate	m/s	0.5	1.5	0	0.5	0.5	1.5	0	0.5	0.5	5	0	5	0.5	5	0	5
	mm/min	0.03	0.09	0	0.03	0.03	0.09	0	0.03	0.03	0.3	0	0.3	0.03	0.3	0	0.3
	min/hr	1.8	5.4	0	1.8	1.8	5.4	0	1.8	1.8	18	0	18	1.8	18	0	18
Actual growth rate	m/s	0.52	growth rate never			0.52	growth rate never			0.51	growth rate never			To be determined (TBD)			
	mm/min	0.031	rate never			0.031	rate never			0.03	rate never						
	mm/hr	1.86±0.02	stabilized			1.86±0.05	stabilized			1.81±0.96	stabilized						
Seeding interface centerline position*	mm	10.5				12.0				26.0				28.5			
Seeding interface distance from crystal shoulder	mm	32.5				34				50				47.5			
Max. insertion point	mm	539				539				539				539			
Max. deflection of meltback interface	mm	1.38				1.27				1.04				TBD			
Max. deflection of translation arrest interface	mm	1.49				1.49				1.12				TBD			

* Relative to the cold/gradient zone junction



$$C_s = C_o \left[1 - (1 - k) e^{-(kR/D_1)x} \right]$$

$$C_s(x) = \frac{C_o}{2} \left\{ 1 + \operatorname{erf} \left(\frac{\sqrt{(R/D_1)x}}{2} \right) + (2k - 1) \exp^{-k(1-k)(R/D_1)x} \operatorname{erfc} \left[\frac{(2k - 1)}{2} \sqrt{(R/D_1)x} \right] \right\}$$

$$C_s = k_{eff} C_o (1 - f_s)^{(k_{eff} - 1)}$$

Figure 1. Solute redistribution during solidification with limited liquid diffusion and no convection. Composition profile during steady-state solidification and composition profile after solidification, top. Solute redistribution during solidification with limited liquid diffusion and convection in the melt. Composition profile during steady-state solidification showing d , the mass boundary layer and composition profile after solidification, bottom (after Flemings¹).

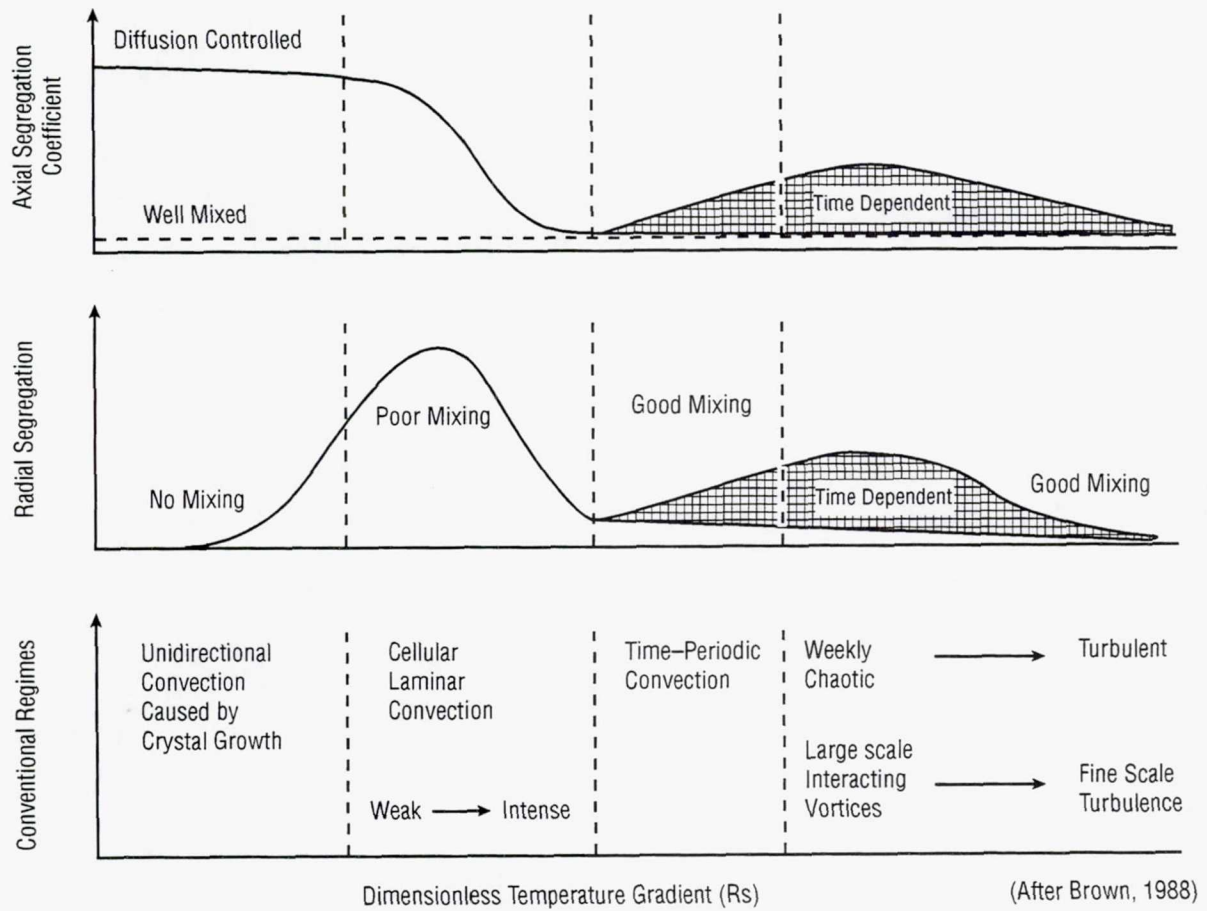


Figure 2. The effect of convection on the axial and radial segregation in a dilute binary system (after Brown¹⁷).

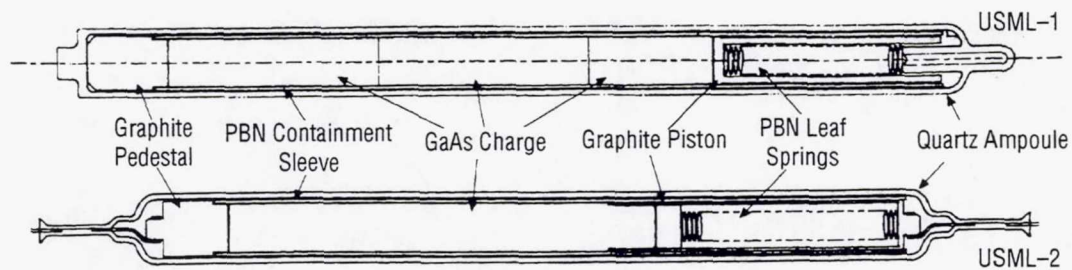


Figure 3. Schematics of ampoule designs for USML-1 and USML-2 experiments.

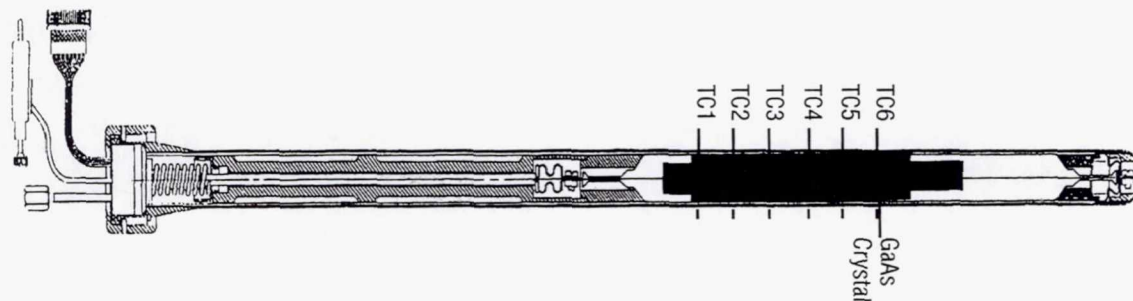


Figure 4. Schematic of cartridge design for the USML-2 experiment.

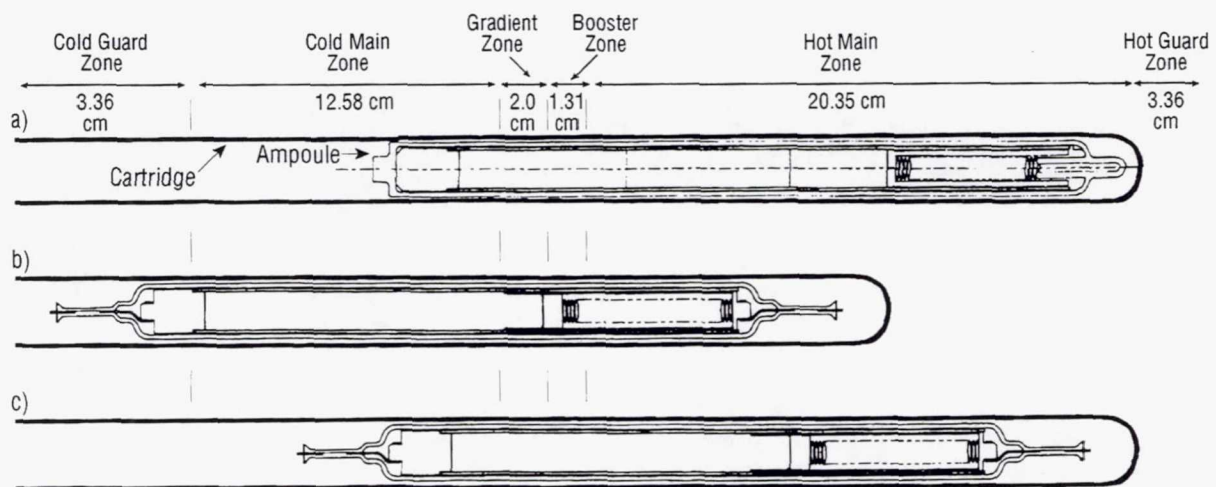


Figure 5. Schematics of sample/ampoule/cartridge assembly (SACA) relative to the six furnace zones (a) USML-1 fully inserted location during heat up and the start of translation; (b) USML-2 location during heat-up; and (c) USML-2 fully inserted location at the start of translation.

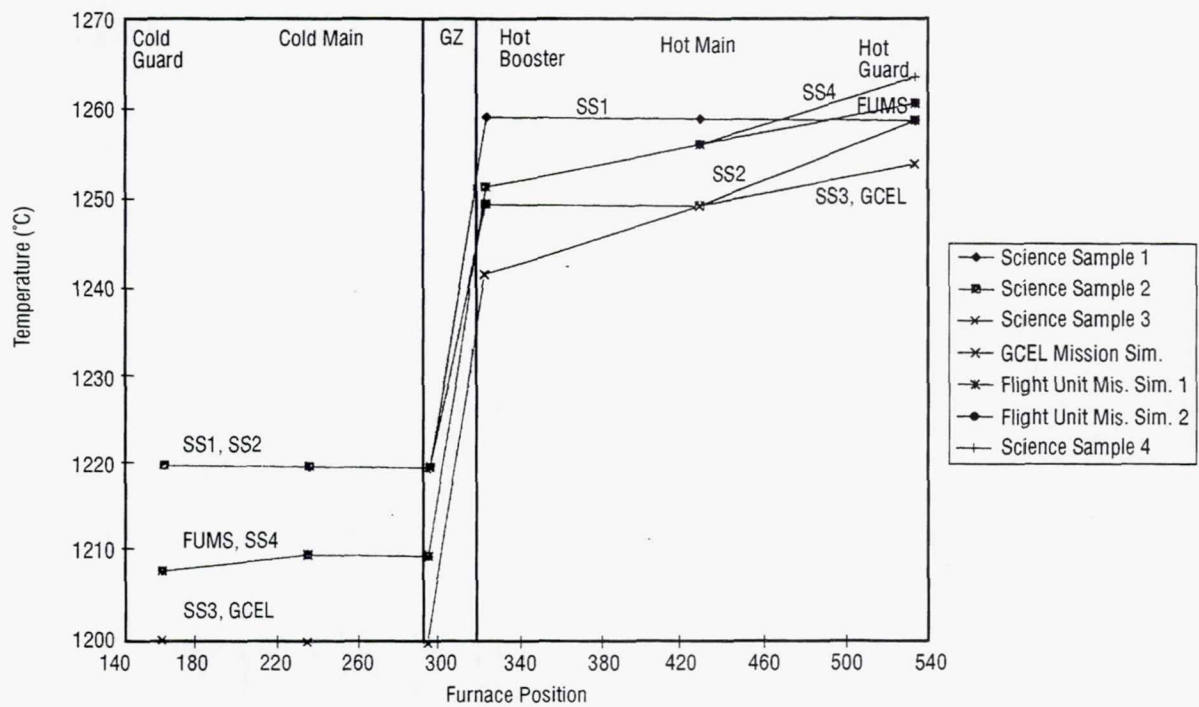


Figure 6. Schematic graph of furnace temperature setpoints versus furnace zone for USML-2 ground-based experiments.

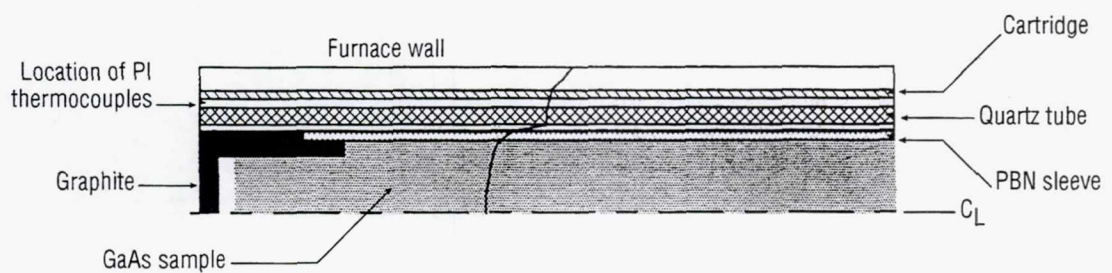


Figure 7. Sample output of computational model showing the location of the 1511 K isotherm across the layers of the SACA.

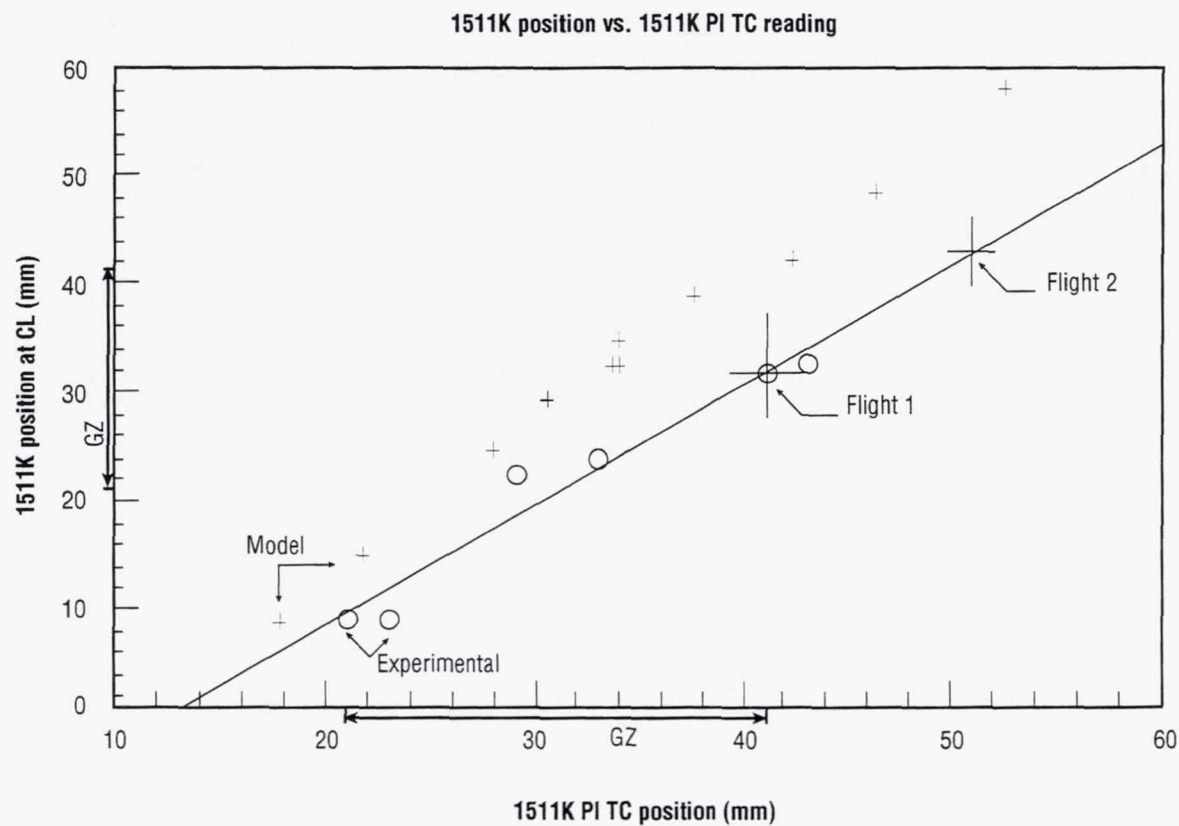
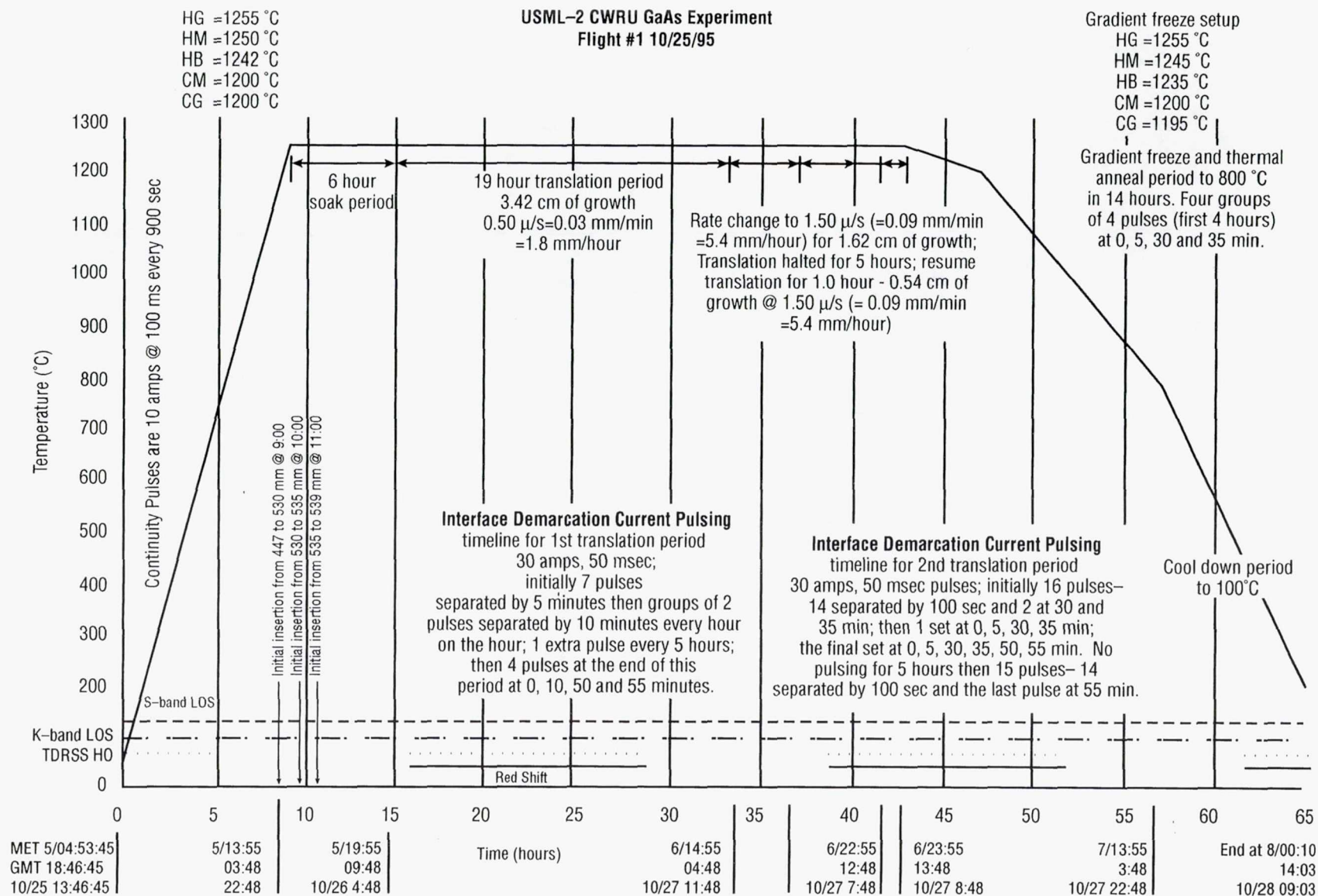


Figure 8. Graph showing the 1511 K isotherm location relative to the furnace at the centerline of the crystal and at the radial location of the PI thermocouples. The axes are numbered in the coordinate system of the computational model. The location of the gradient zone is marked on the graph for ease of use.

Figure 9. USML-2 first flight experiment (flight No. 1) timeline.



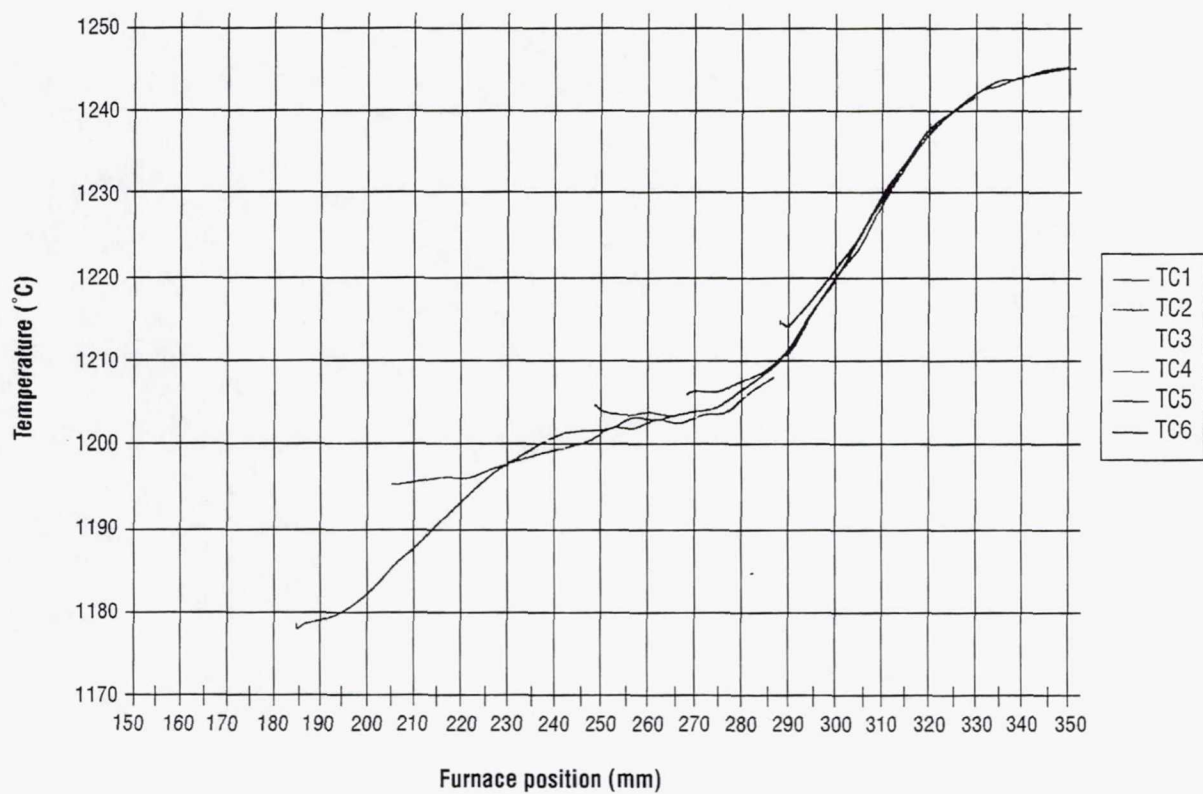
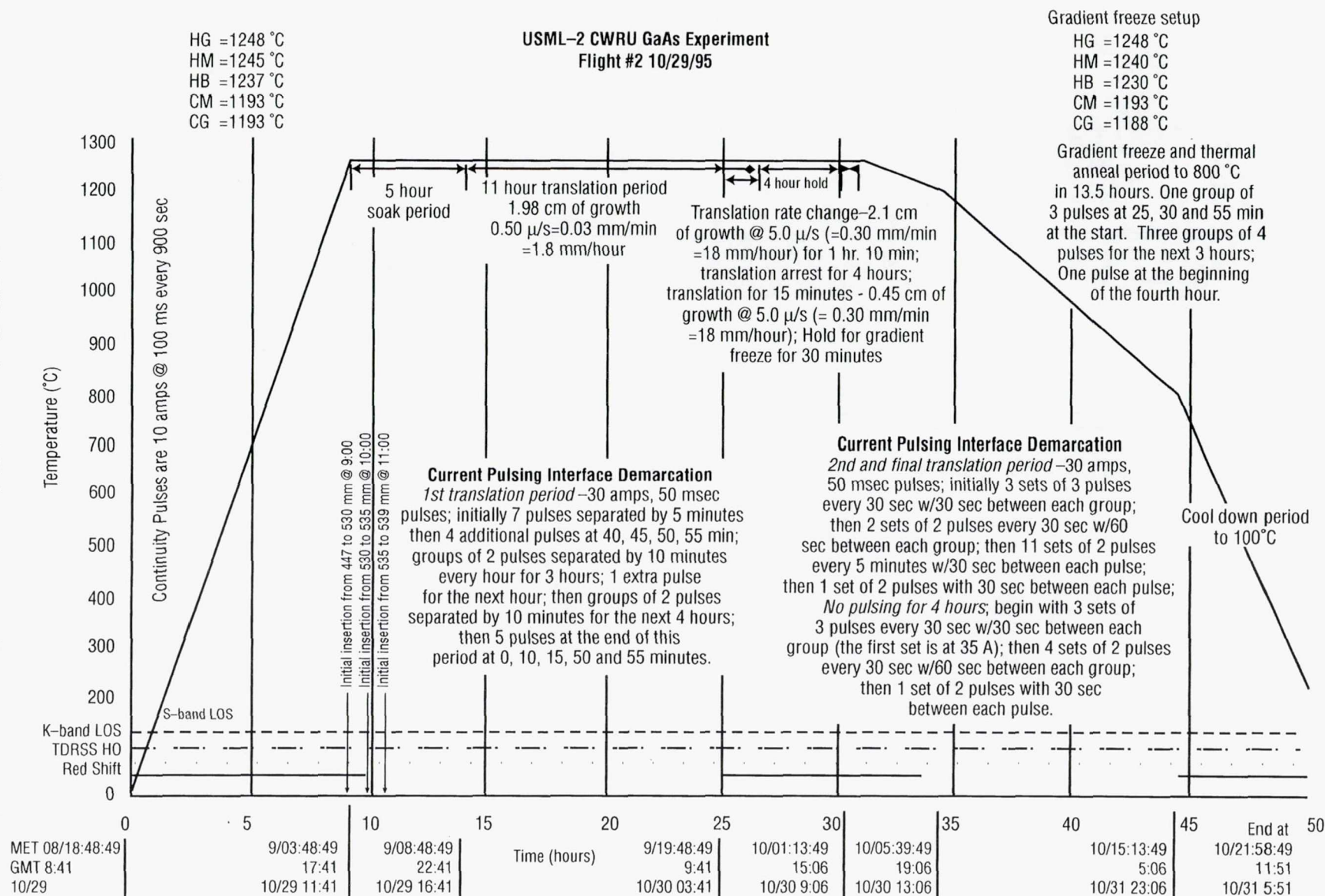


Figure 10. PI thermocouples versus furnace position during insertion of flight No. 1. The gradient zone extends from 295 to 315 mm in this plot.

Figure 11. USML-2 second flight experiment (flight No. 2) timeline.



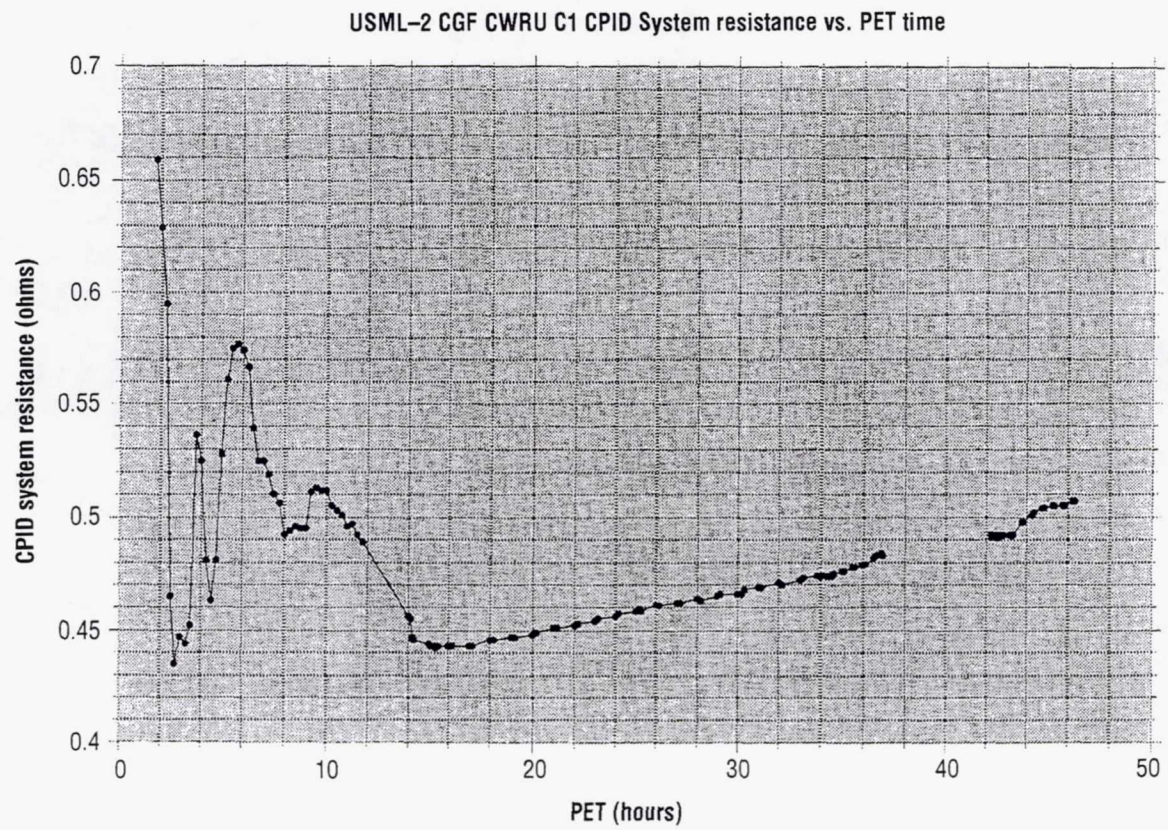


Figure 12. CPID resistance data for flight No. 1.

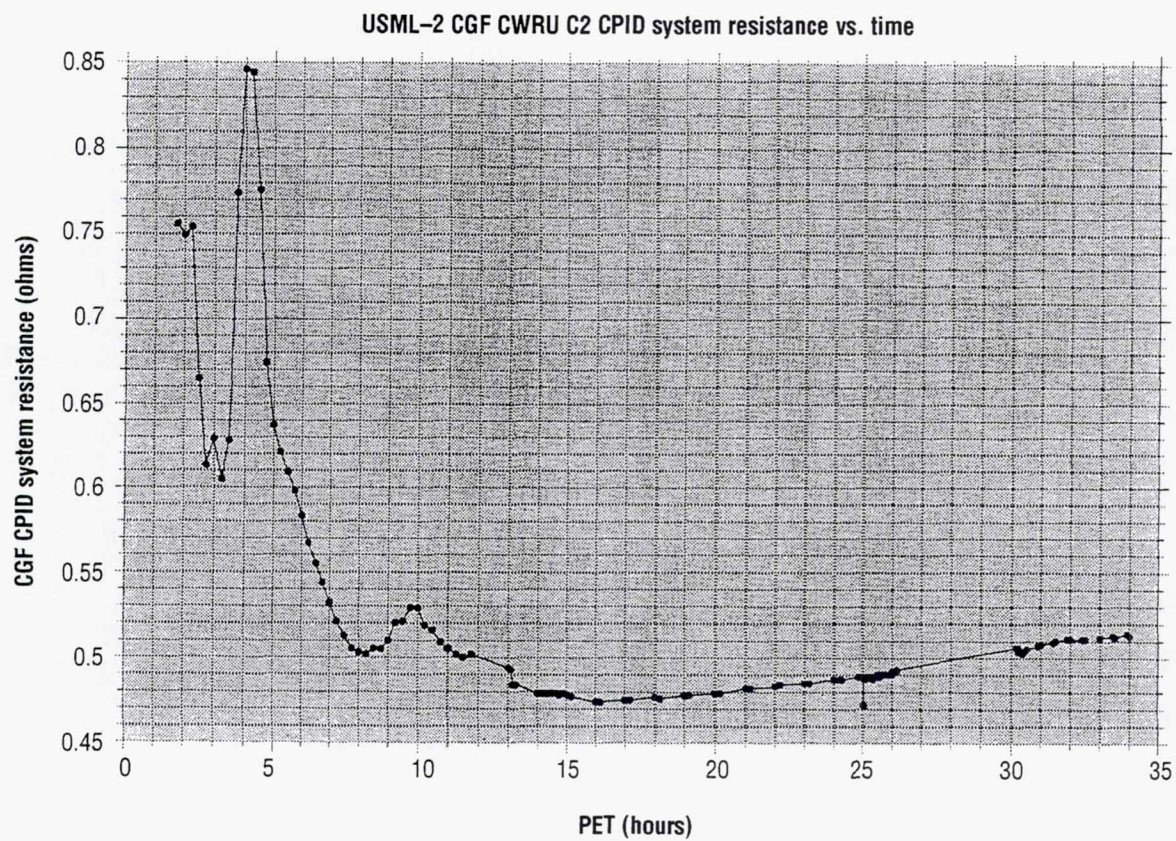


Figure 13. CPID resistance data for flight No. 2.

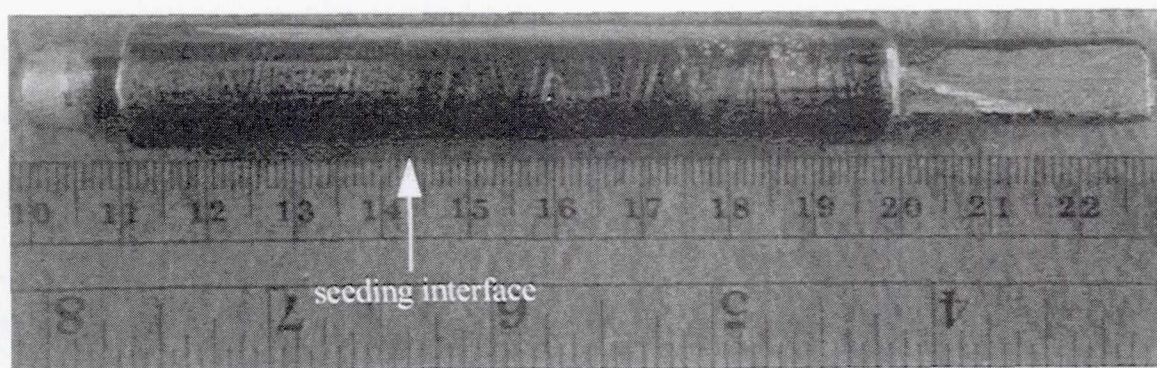


Figure 14. Photomicrograph of the first flight boule.

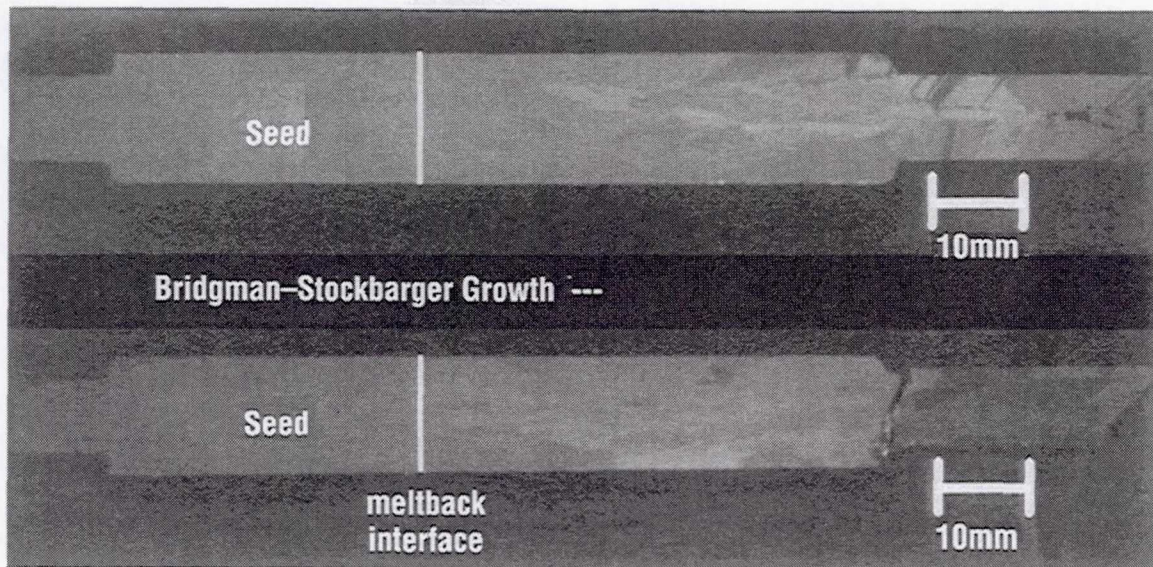


Figure 15. Macrostructure observed on the D-slice from the first flight sample.

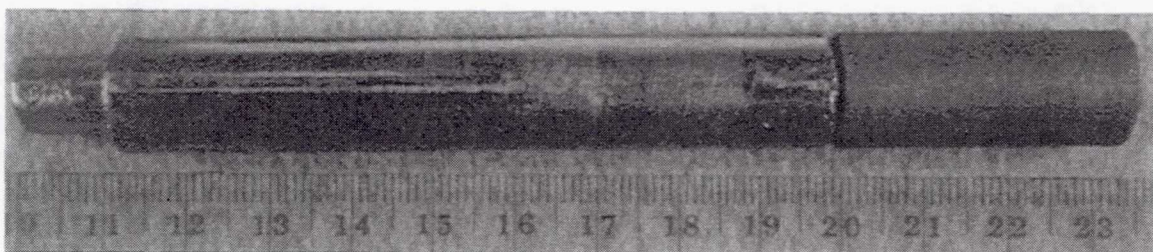


Figure 16. Photomacrograph of the second flight boule.

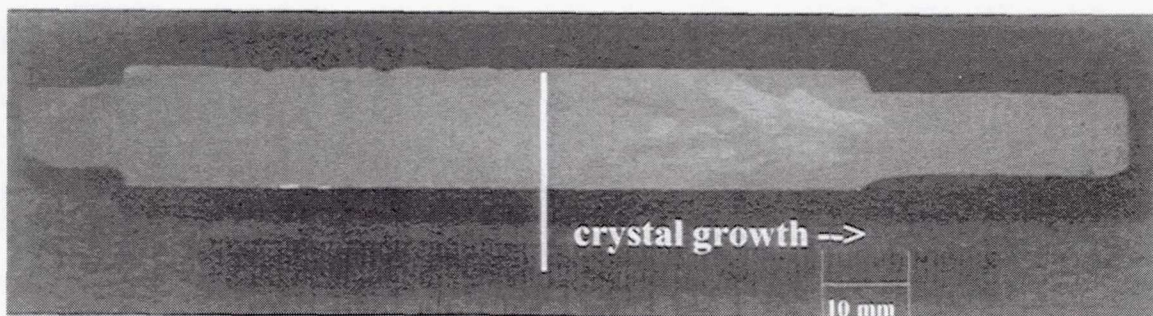


Figure 17. Macrostructure observed on the D-slice from the second flight sample.

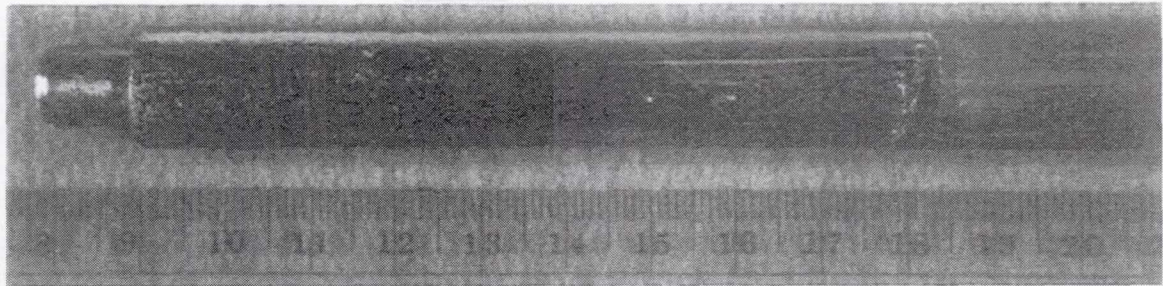


Figure 18. Photomacrograph of the first ground truth boule.

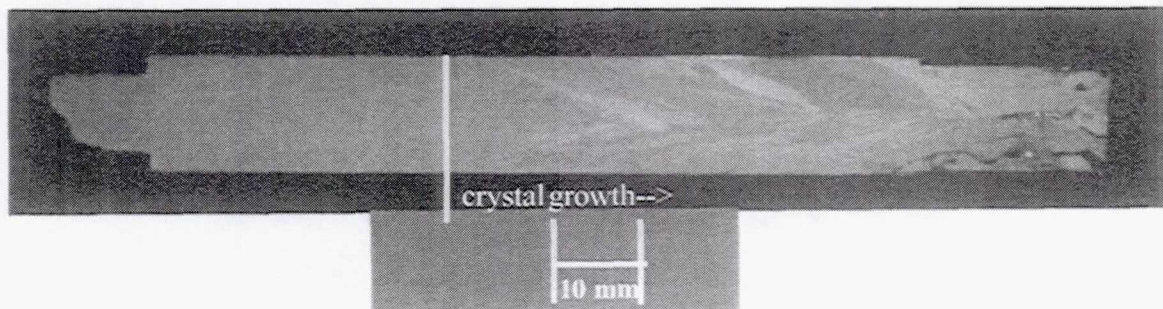


Figure 19. Macrostructure observed on the D-slice from the first ground truth sample.

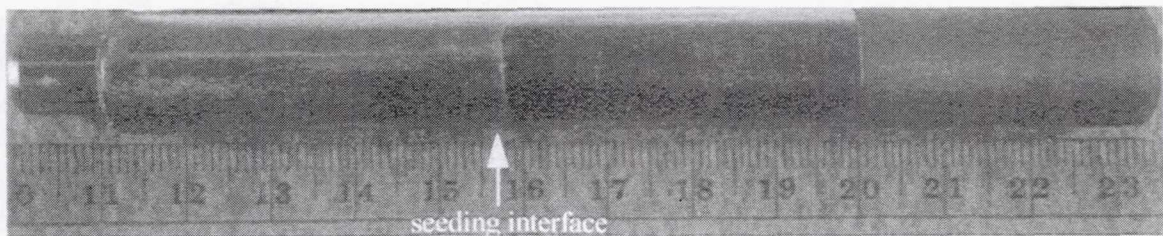


Figure 20. Photomacrograph of the second ground truth boule.

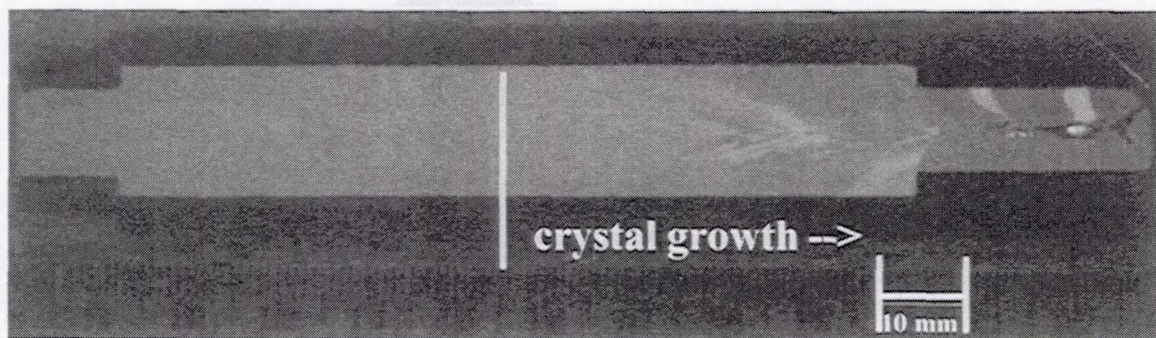


Figure 21. Macrostructure observed on the D-slice from the second ground truth sample.

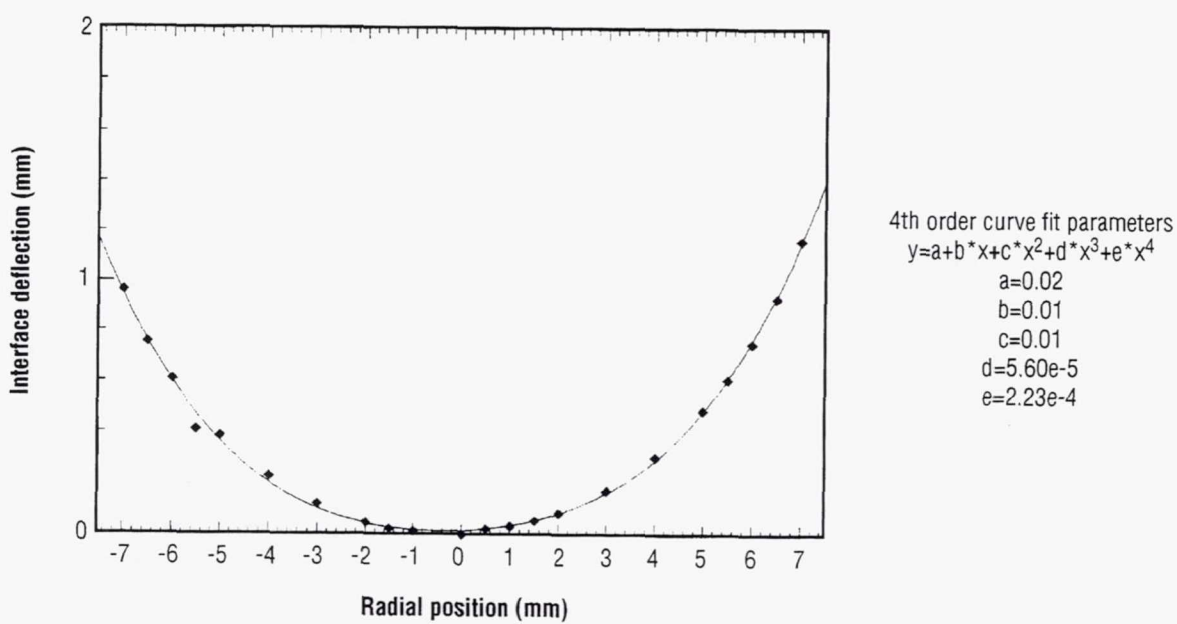


Figure 22. GCEL mission simulation interface shape and deflection.

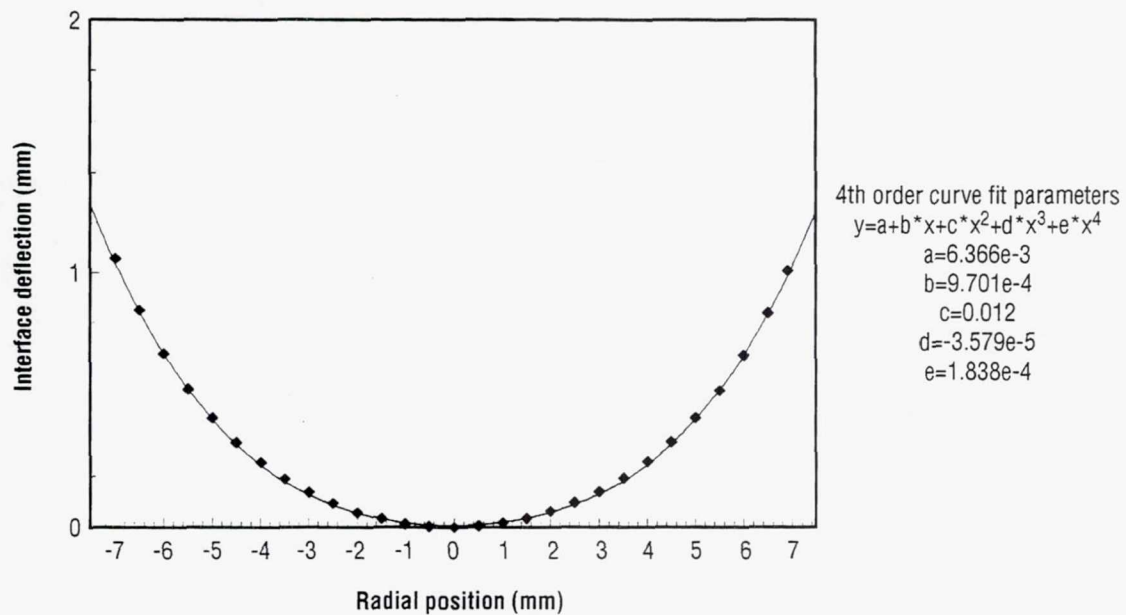


Figure 23. Space flight experiment No. 1 interface shape and deflection.

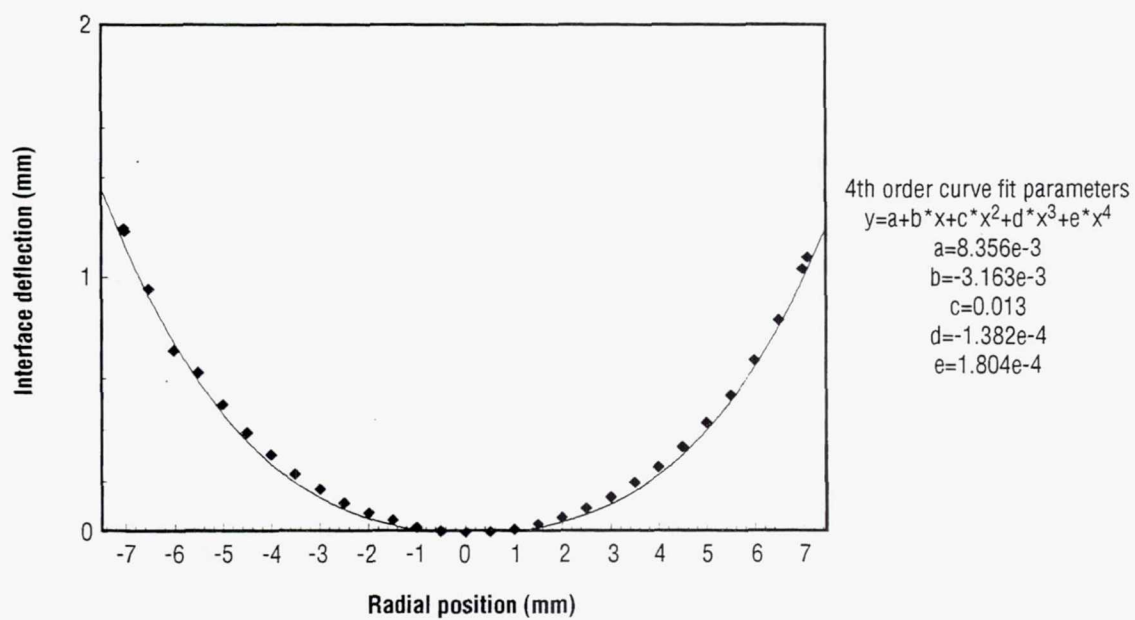


Figure 24. Ground truth experiment No. 1 interface shape and deflection.

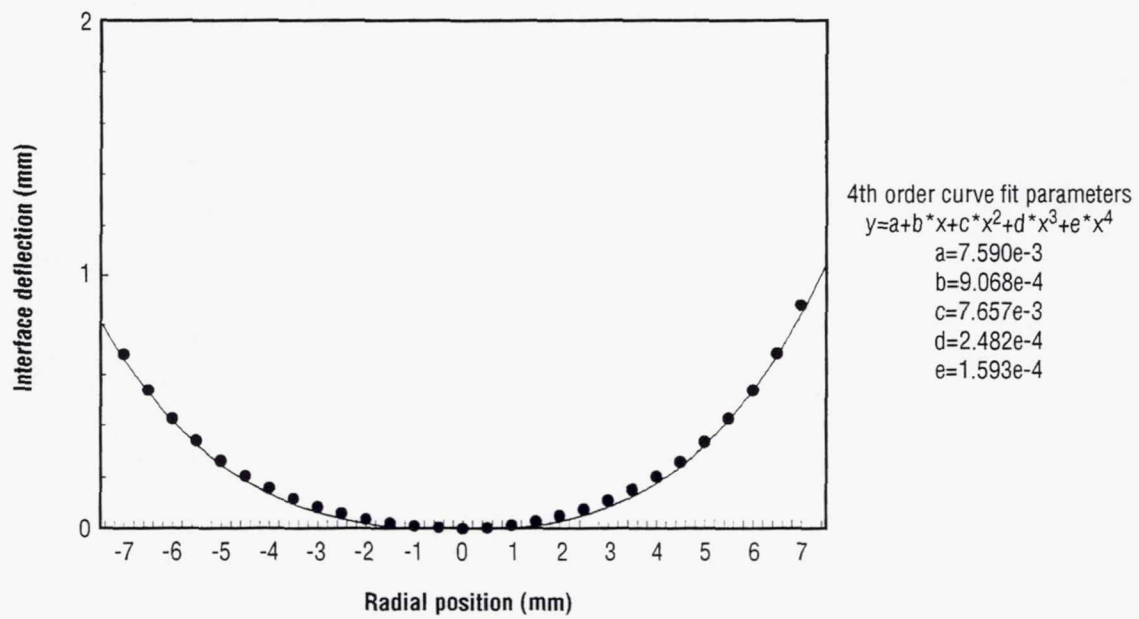


Figure 25. Ground truth experiment No. 2 interface shape and deflection.

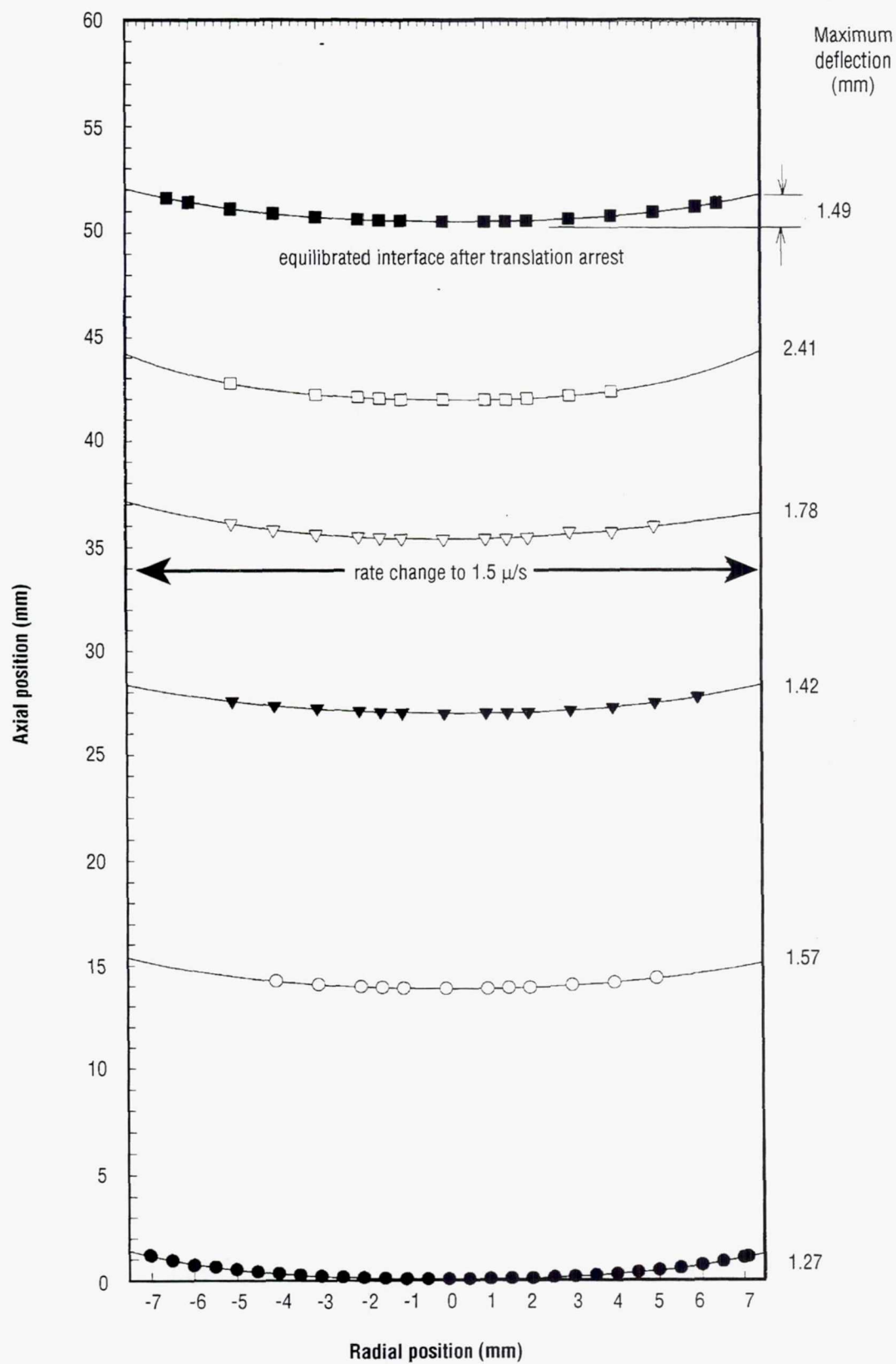


Figure 26. Space flight experiment No. 1 demarcation interface shape, position, and maximum deflection.

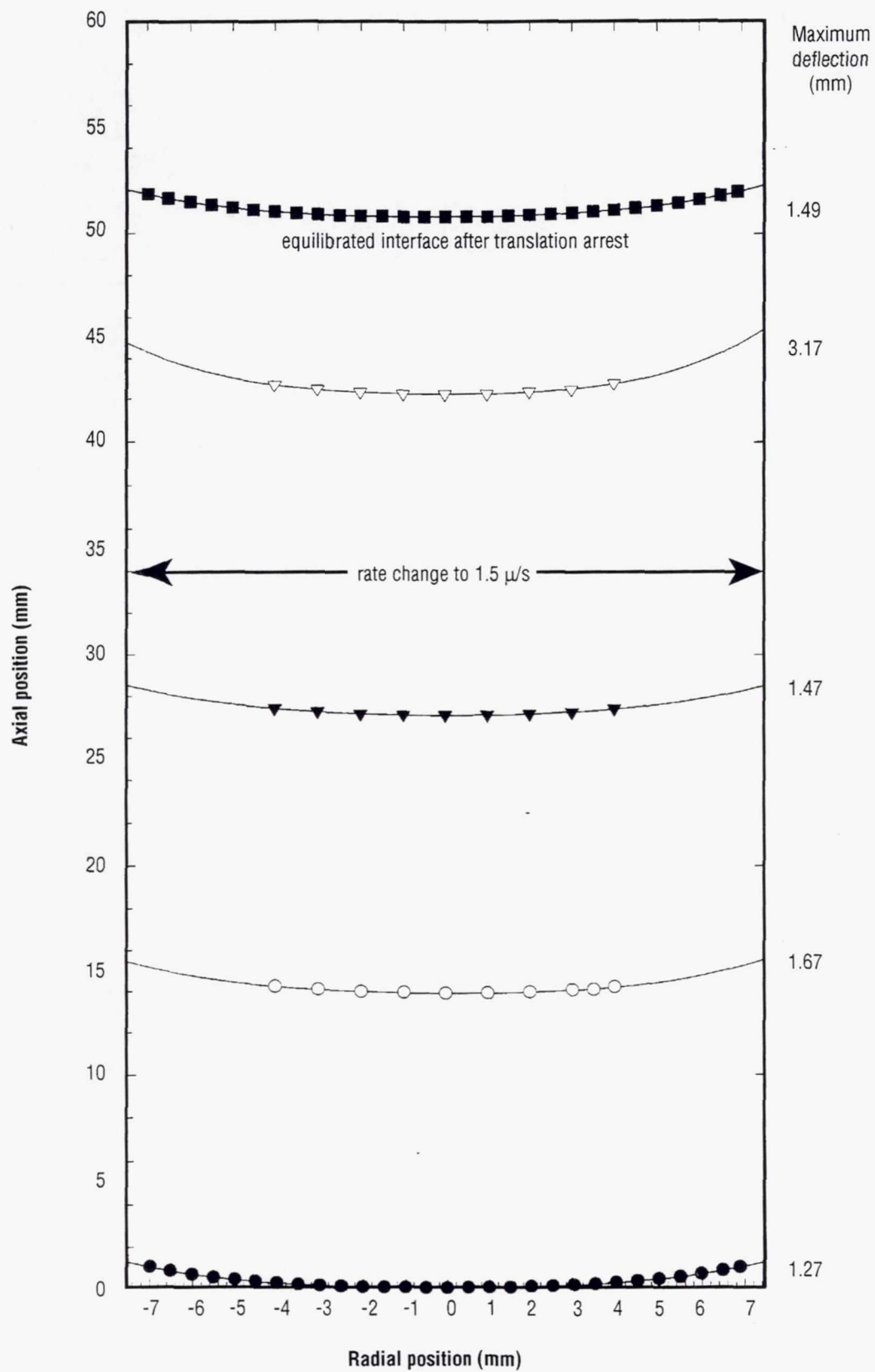


Figure 27. Ground truth experiment No. 1 demarcation interface shape, position, and maximum deflection.

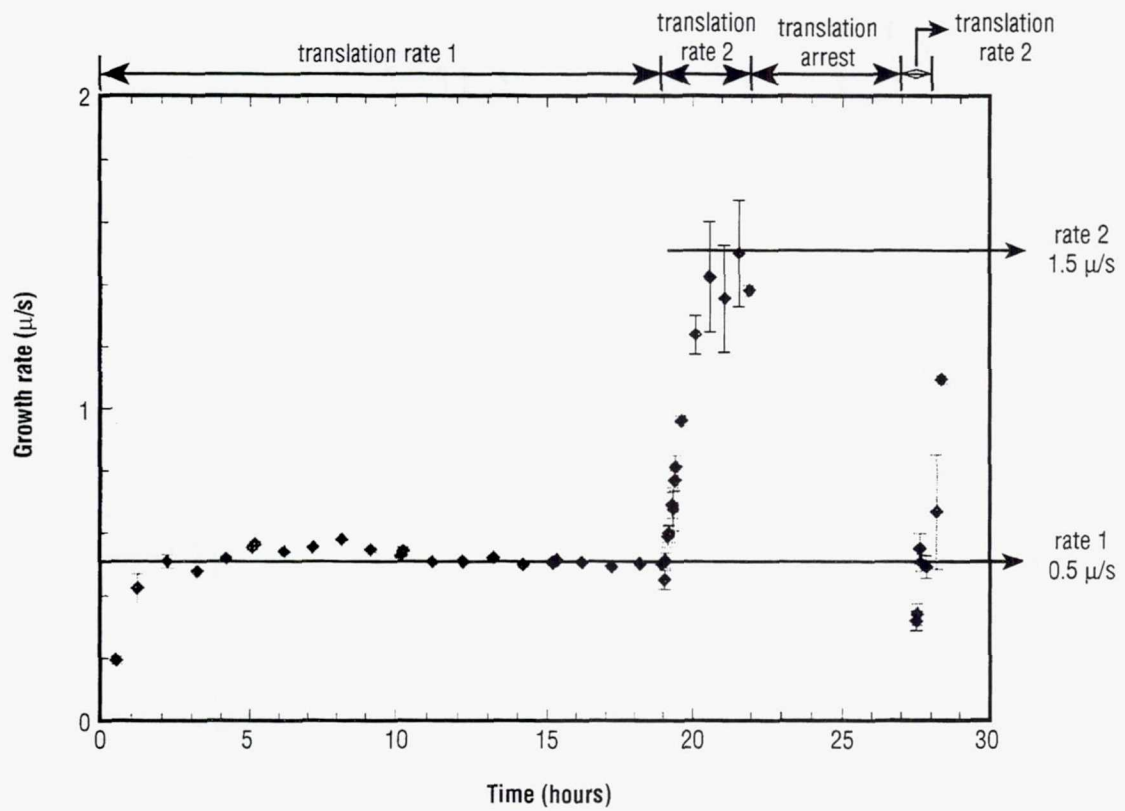


Figure 28. Space flight experiment No. 1 growth rate.

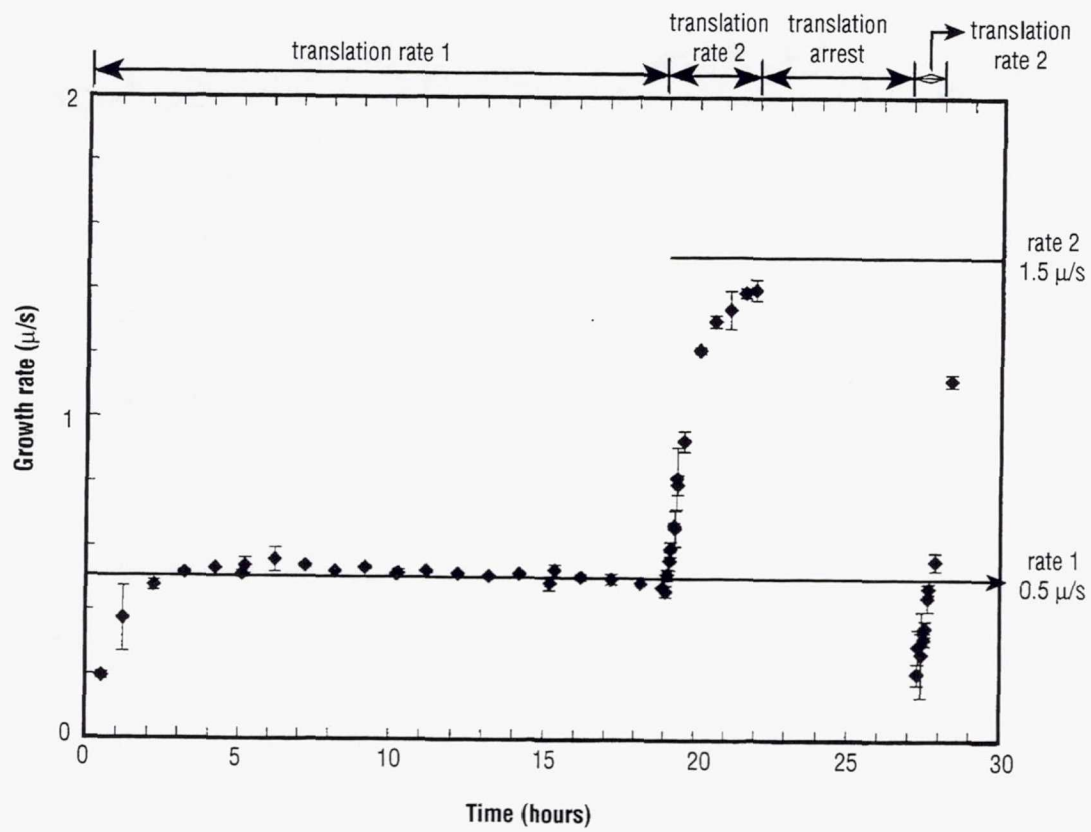


Figure 29. Ground truth experiment No. 1 growth rate.

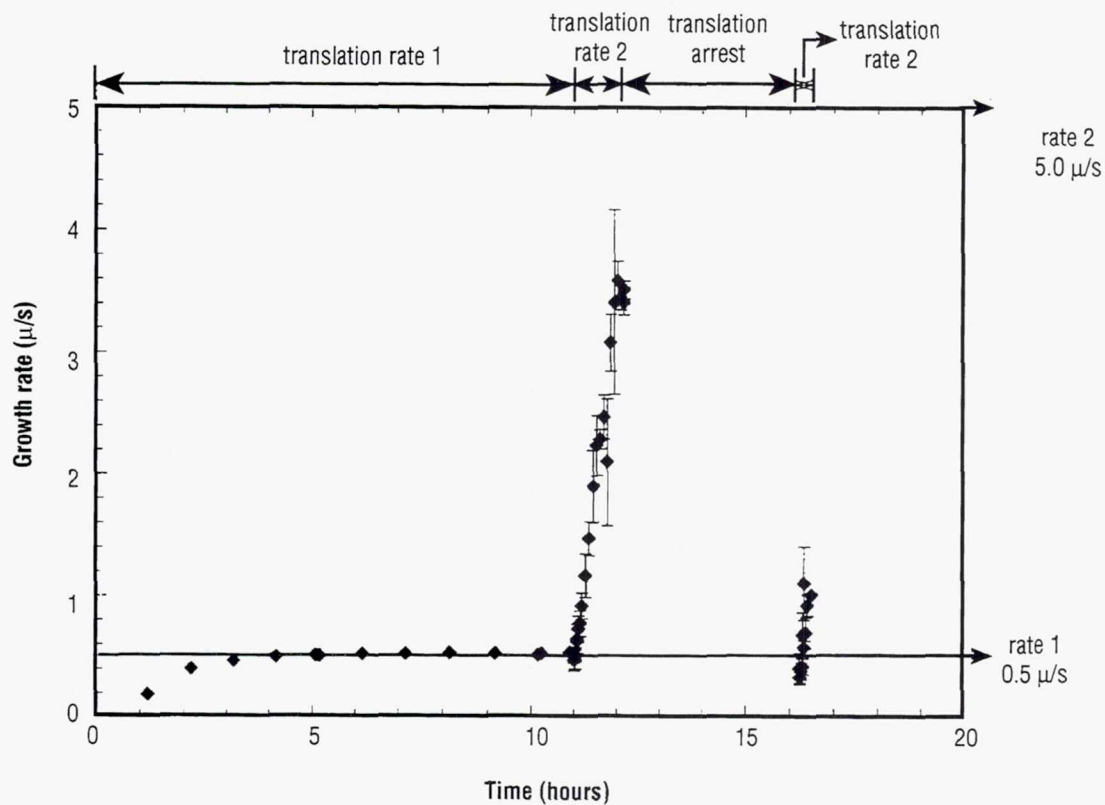


Figure 30. Ground truth experiment No. 2 growth rate.

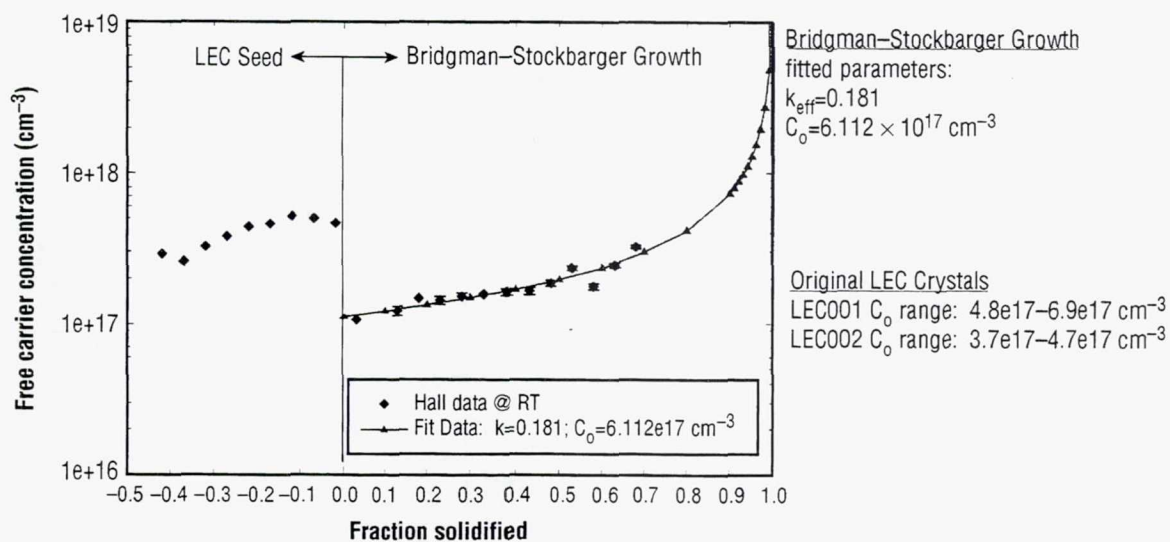


Figure 31. Dopant distribution and segregation analysis for the GCEL mission simulation ground-based sample.

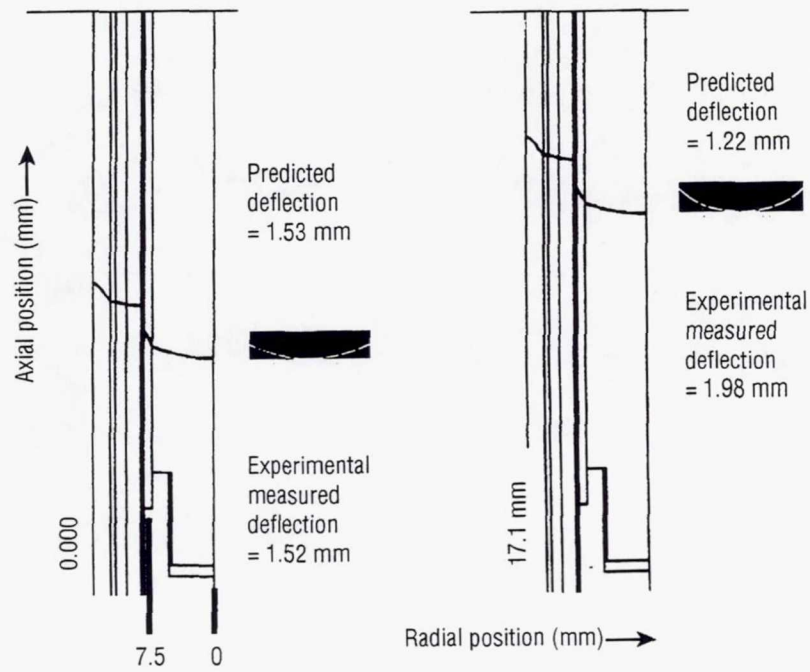


Figure 32. Predictions from numerical model compared to experimental measurements.

Page intentionally left blank

EXPERIMENT XIV.

**DIRECTIONAL SOLIDIFICATION OF GALLIUM-DOPED GERMANIUM
IN CRYSTAL GROWTH FURNACE (CGF) ON USML-2**

ACKNOWLEDGMENTS

The dedicated efforts of Richard Lamb, Fabrication Division, MSFC, who always kept a step ahead of the program requirements, are acknowledged. Special recognition is due Gene Nelson, University of Alabama in Huntsville, glassblower *extraordinaire*, for his skillful work. Thanks are due to David Schaefer, program manager CGF, MSFC, and Srinu Srinivas, Teledyne Brown Engineering, for removing many obstacles to keep the tightly scheduled program on time. Dr. Frank Szofran, Space Sciences Laboratory, MSFC, and Dr. Michael J. Wargo, MSAD, NASA Headquarters, were helpful in many discussions, as were the seminal inputs of Prof. August F. Witt, Massachusetts Institute of Technology. Lastly, the use of MRSEC Shared Facilities supported by the National Science Foundation under Award Number DMR-9400334 is acknowledged.

EXPERIMENT XIV. DIRECTIONAL SOLIDIFICATION OF GALLIUM-DOPED GERMANIUM IN CRYSTAL GROWTH FURNACE (CGF) ON USML-2

Manfred Lichtensteiger

USRA/NASA/ES75

George C. Marshall Space Flight Center

Marshall Space Flight Center, AL 35812

Phone: 205-544-7798

FAX: 205-544-1600

E-mail: manfred@mgrav1.msfc.nasa.gov

ABSTRACT

The interface demarcation flight test (IDFT) was designed to test the interface demarcation capability of the CGF system under actual growth conditions in a low-Earth orbit. The current pulse interface demarcation (CPID) subsystem passes programmable electrical pulses with a current density of up to 20 A/cm² across the solid-melt interface of the solidifying crystal which induces localized changes in the dopant segregation behavior at the interface. These current pulse introduced interface demarcation lines permit the solid-liquid interface shape of the advancing growth front to be observed. The location and shape of the interface as well as the instantaneous microscopic growth rate can therefore be determined. The interface morphology data were complemented by high spatial resolution spreading resistance profiling (SRP) measurements to determine the segregation behavior during growth. Gallium-doped single-crystalline germanium was chosen as a model substance since its thermophysical properties are well understood.

The primary purpose of this investigation was to quantitatively study the effect of a change from the CGF attitude with a minimized residual g-vector in the growth axis to a modified gravity gradient (GG) attitude during Mission STS-73 in a steady-state growth system using these analytical techniques. No significant changes in growth rate, interface morphology, and segregation behavior were identifiable during this maneuver which extended over a period of just over 8 minutes.

An additional crystal was grown with an extended translation-arrest during the solidification process to study the dynamics of the growth system. During growth, a predominantly +z-body solar inertial (+ZSI) attitude interrupted by repeated thruster firings was available.

1. INTRODUCTION

The first near zero-g crystal growth experiment employing a gallium-doped germanium matrix was flown as experiment MA060 during the Apollo-Soyuz test project (ASTP).^{1,2} Fixed cartridge assemblies were used in a three-bore gradient freeze furnace. Interface demarcation capability was requested and implemented with analog circuitry without the ability for a time-coded pulse sequence. Due to the severely asymmetrical thermal environment which led to excessive growth interface curvature and accompanying anomalous segregation behavior, this experiment posed more questions than answers.³

The present investigation had as its goal the quantitative study of the effects of a change from the CGF attitude—with a minimized residual g-vector in the growth direction, most favorable for crystal growth—to a modified GG attitude (figs. 3-5) during mission STS-73 in a steady-state growth system using two analytical techniques:

1. Interface demarcation as part of the test of the added interface demarcation capability of the CGF system under actual growth conditions in a low-Earth orbit. It passes programmable electrical pulses with a current density of up to 20 A/cm² across the solid-melt interface which induces localized changes in the dopant segregation behavior at the interface. These current pulse-introduced interface demarcation lines permit the solid-liquid interface shape of the advancing growth front to be observed. The location and shape of the interface, as well as the instantaneous microscopic growth rate, can be determined this way.
2. The interface morphology data were complemented by high spatial resolution spreading resistance profiling measurements to determine the segregation behavior during growth (appendix C). Mission timeline adjustments permitted the growth of an additional crystal with an extended translation-arrest during the solidification process to study the dynamics of the growth system. During growth a predominantly +z-body solar inertial attitude, interrupted by repeated thruster firings, was available.

Gallium-doped single-crystalline germanium was chosen as a model substance since its thermophysical properties are well understood (appendix D). The details of ampoule fabrication and sample preparation for analysis are covered in appendices A and B, respectively. The growth timelines adopted are shown in figures 1 and 2. Heat-up to growth conditions was programmed at 50 °C/min, the maximum rate for CGF, to the selected setpoints of 975 °C hot-zone and 877 °C cold-zone temperatures, followed by a nominal 4-hour thermal and compositional equilibration period. Temperatures were monitored by six type S thermocouples touching the outside ampoule wall throughout the growth experiment (a typical gradient plot is given in fig. 6). For interface demarcation purposes the basic "clock pulse" repetition rate was set to 20 sec with a positive pulse width of 75 msec at a nominal amplitude of 40 A (+ve). A double pulse of the same characteristics was inserted every 60 sec with a separation of 1 sec, and every 3,600 sec a single negative pulse of 100-msec duration at a nominal 40 A (-ve) amplitude was programmed. The translation rate established for growth was 4 µm/sec in both experiments. The late stages of growth included a gradient freeze portion by reducing the hot-zone setpoint from 975 °C to 877 °C at the rate of 1 °C/min. The

microscopic growth rate and resulting lag behind the constant furnace translation rate is illustrated in figures 7 and 8. From growth rate measurements taken at 60-sec intervals, it can be seen that the rate increased exponentially to the steady-state value of 4 $\mu\text{m}/\text{sec}$ over a period of roughly 60 minutes, while ≈ 1 cm of material had solidified. The lag approached 0.45 cm at steady-state growth rate with the established melt isotherm well within the gradient zone of the furnace (fig. 6). The original melt-back interface positions in both IDFT experiments were within 0.035 cm of each other and identical in a furnace-based coordinate system. This convincingly demonstrates the excellent thermal stability and performance of the CGF system developed jointly by Marshall Space Flight Center (MSFC) and Teledyne Brown Engineering (TBE).

2. RESULTS AND DISCUSSION

2.1 IDFT-1: Attitude Change

Figure 9 shows the overall segregation behavior derived from an axial scan of the crystal. The section between 2- to 3-cm growth was set aside for synchrotron x-ray topography to investigate its defect structure. These results are not yet available. The smaller breaks in the macrosegregation curve are due to sectioning kerf-loss and polishing edge roll-off. Note the discontinuity in segregation behavior around 9-cm growth: it is associated with the solidification front advancing into the surrounding graphite electrode where the thermal environment changes abruptly. Diffusion-controlled growth appears to have been attained over the major length of the crystal (≈ 7 cm) as can be seen by comparison with well known theoretical results by Tiller et al.⁴ for a purely diffusive growth regime plotted in figure 10 (the generally accepted value for equilibrium segregation $k_0 = 0.087$ and an effective diffusion coefficient $D_{\text{eff}} = 3.2 \times 10^{-4} \text{ cm}^2/\text{sec}$ were applied). Corrections for instantaneous growth rate values were made to the original formulation. From the data presented in figures 11, 12, and notably 13, it is evident that their boundary conditions are well met. Figure 11 shows the initial transient region with well-resolved rotational striations in the Czochralski-grown material, the meltback interface, and the beginning of regrowth. A photomicrograph of the same region (fig. 12) demonstrates the resolving power of the spreading resistance measurement technique with the interface demarcation pulses clearly visible. Finally, in figure 13 the shape of the original meltback interface is plotted radially from the axial center of the crystal; it can be seen that the slight curvature reaches a value of approximately 400 μm at the periphery. For comparison, the axial segregation profile for growth with complete mixing is given in figure 14. The measured radial segregation behavior as dependent on interface morphology and treated analytically by Coriell et al.⁵ agrees with their findings but is not presented in detail.

As mentioned in the introduction, the main thrust of this investigation was the quantitative study of the effects of a Shuttle attitude change from CGF to gravity gradient (GG) on the growth characteristics of the germanium matrix. The maneuver occurred 4:42 hours into growth at 4 $\mu\text{m}/\text{sec}$ translation rate (figs. 3-5) during which approximately 6.25 cm of material had solidified under steady-state growth conditions. No growth rate changes associated with this maneuver, which took approximately 8 minutes to complete, could be discerned. Figure 15 shows the composite free carrier concentration values of this segment derived from spreading resistance measurements with peripheral scans as well as an axial scan plotted. Note the different concentration levels of either of these traces which are otherwise undisturbed. During growth, the original meltback interface shape (fig. 13), with a slight curvature of approximately 400 μm extending symmetrically into the melt at the periphery of the 16-mm-diameter crystal, has changed to $\approx 800 \mu\text{m}$ and

has become measurably asymmetrical (fig. 16) thereby changing the established radial segregation profile. The overall appearance of the interfaces before and after the attitude change remains very similar with only minor variations in shape which are not considered indicative of residual g-vector changes. Obviously, no comparison with a ground-based experiment is possible, though an attempt was made to simulate an attitude change by slowly tilting the furnace 10° off-vertical and back during growth. No discernible effects were evidenced then either, but a larger tilt angle which would have led to measurable changes was considered unsafe based on a structural analysis by TBE.

It is therefore concluded that this gentle attitude change had no perceptible effect on the microscopic segregation behavior using these extremely sensitive analytical techniques. However, possible variations in peripheral faceting associated with growth in the $\langle 111 \rangle$ direction need to be investigated, and a three-dimensional analysis of changes in interface morphology and free carrier concentration, eight segments which include this region are available, must be attempted before this conclusion becomes unequivocal.

2.2 IDFT-2: Translation Arrest

The overall segregation behavior exhibited for this experiment is radically different from the one observed for IDFT-1 and is shown in figure 17. It only loosely follows a diffusion-controlled growth curve. The pronounced positive and negative deviations occurring around 3.5-cm and 4.8-cm regrowth are tentatively associated with orbital maneuvers involving thruster firings. As growth took place mainly in a high-g environment, correlation with acceleration data is being worked on. In the meantime, the figure caption "Tumbling through Space" seems adequate.

Referring to figure 2, we see that the translation arrest took place 3:35 hours into actual growth with a duration of 90 minutes. The composite segregation and growth rate curves for the area of immediate interest are given in figure 18 and are accompanied by the corresponding microphotograph (fig. 19) at the same magnification. The slight kink in the growth rate decay curve at approximately $-500 \mu\text{m}$ is so far unexplained but corresponds to a minute increase in free carrier concentration and also a slope change visible in the microphotograph (Nomarski differential interference contrast is sensitive to slope changes and not, as generally assumed, height differences). Residual rates fluctuate around $0.2 \mu\text{m}/\text{sec}$ and eventually become unmeasurable. The band of approximately $100 \mu\text{m}$ width prior to resumption of translation at $4 \mu\text{m}/\text{sec}$ is attributed to the minute temperature fluctuations ($\pm 0.05^\circ\text{C}$) recorded during this period and accords with the established temperature gradient of $\approx 15^\circ\text{C}/\text{cm}$ in the melt (fig. 6). Given the finite spatial resolution of the spreading resistance probe and the differentiation obtainable by etching, the resulting microscopic melt-remelt structure cannot be resolved. It is worth noting that during this time period the interface flattened from around $800 \mu\text{m}$, measured at the periphery, back to its original value of $400 \mu\text{m}$ deviation from planarity. The corresponding section, showing segregation behavior and growth rate information for the ground-based experiment, is shown in figure 20 for comparison. The general appearance is virtually identical to the results obtained in a near zero-g environment. These findings, however, are in stark contrast with results reported by Wang et al.⁶ who reported essentially opposite segregation behavior in a similar one-g experiment.

3. CONCLUSIONS AND RECOMMENDATIONS

The CPID subsystem of CGF has performed flawlessly in a low-Earth orbit environment. Its time-coded pulse capabilities have been successfully demonstrated. It would be desirable to extend these capabilities to permit bi-polar operation rather than relying on relay-switched polarity changes. Then the optical Nomarski differential interference contrast could be greatly enhanced by a pulse sequence featuring a segment passing through zero (e.g., ++++ -- ++++). Additionally, any second-order effects on segregation (except Joule heating) by the applied electric field would be cancelled. The furnace exhibited exceptional stability and control of the thermal field. The possibility of using sample thermocouples for active control over the location of the initial melt isotherm before switching to the main furnace controls by a suitable algorithm would also be desirable. Therefore, to paraphrase Roman statesman Cato the Elder: *Et ceterum censeo Fornacem Crystallis Augendis CGF iterum in caelum iactandam esse...* (CGF must fly again...).

The scheduled maneuver from CGF to GG attitude has not revealed any discernible effects on the micro-segregation behavior in the Ge-Ga system. The results obtained thus far warrant a continuing comprehensive analysis of the experiment including numerical modeling.

Initial results were reported for the second experiment which included a translation arrest. This, too, calls for a major effort to conclude this analysis successfully.

APPENDIX A: AMPOULE FABRICATION

The starting material consisted of <111> oriented 60-mm-diameter ingots of gallium-doped germanium grown by Eagle-Picher Industries, Inc. using standard Czochralski techniques with a doping level specified at $2 \times 10^{19} \pm 0.15 \times 10^{19}$ Ga-atoms/cm³ over the 152-mm length of the ingot. Individual crystals were core-drilled from the boule and then centerless ground to 16-mm diameter. Disks of 1-mm thickness were cut from both ends of the crystals for resistivity and free carrier concentration measurements. The end sections of the crystals were then reduced to 14-mm diameter over a distance of 18 mm including a 45° chamfer for attachment to cup-shaped electrodes fabricated from Unocal POCO DFP-2 graphite. Platinum wire (1 mm diameter) loops were embedded in the electrodes for fused contact with platinum-molybdenum foil-platinum feedthroughs capable of carrying a 60 A current. Prior to assembly, the crystals were etched in a mixture of equal parts of 50 percent volume hydrofluoric acid (HF), 30 percent volume hydrogen peroxide (H₂O₂), and glacial acetic acid (HAc). This ensured removal of machining damage and a tight fit to the graphite electrodes.

Individually selected pieces of GE type 214 fused quartz tubing of 20 mm OD with a wall thickness of 2 mm were used to fabricate the envelopes which were briefly etched in HF to remove possible metallic residue introduced by the gauging process. They contained an inside annulus of 10-mm length on which the cold-end electrode was positioned. The hot-end electrode was allowed a limited amount of displacement (≈ 1 mm) along the longitudinal axis to allow for thermal expansion upon heating. Figure 21 should help in visualizing the fabrication process. This exploded view of the assembly shows the vacuum current feedthroughs, graphite electrode cups, the shaped single crystal germanium ingot as well as a finished ampoule.

Both inside positioning tolerances and outside dimensions were held to ± 0.25 mm during assembly. The finished ampoules were evacuated through a seal-off tube to a system base pressure of 2×10^{-6} Torr before sealing. After forming the outside attachment loops to the cartridge assembly, inside contacts between the graphite electrodes and germanium crystal were "electroformed" by a brief 60 A current discharge, bringing the total ampoule resistance down to 0.20–0.25 ohm.

APPENDIX B: SAMPLE PREPARATION

The (211) plane crystallographic orientation was determined by Laue back-reflection taken on the seed end in all ground-based test and flight-grown crystals. They were mounted vertically with Valtron ingot mounting adhesive and sliced lengthwise into 2 mm thick slices in a Meyer+Burger 10" ID annular saw exposing the (211) plane surface. The slices were then diced into segments ranging from 10 mm to 22 mm in length with a kerf loss not exceeding 0.375 mm. After cleaning, the samples were soldered with a 99.7 percent indium–0.3 percent gallium alloy onto goldplated brass disks for polishing and subsequent etching prior to analysis.

Samples were polished to a surface finish better than $\lambda/8$ in batches of six (including a calibration sample, see appendix C) on Rodel type 204 polishing pads with a dripping slurry consisting of 600 ml DI water, 60 ml regular CLOROX bleach containing 5.25 percent sodium hypochlorite (NaOCl), and 400 ml NALCO 2360 colloidal silica. Final polishing was accomplished with the same slurry (60-6-40) but at a reduced pad pressure of 65 g/cm².

After polishing, the samples were cleaned by wiping in a detergent solution, rinsed with DI water, gently blown dry in a stream of nitrogen, inspected for surface finish and absence of haze, and then either etched immediately or scheduled for repolishing.

The samples were individually etched for 5 seconds by immersion in a mixture of equal parts of 50 vol percent hydrofluoric acid (HF), 30 vol percent hydrogen peroxide (H_2O_2), and glacial acetic acid (HAc), followed without delay by neutralization in a dilute sodium bicarbonate (NaHCO_3) solution.

The cleaning procedure described above was then repeated.

APPENDIX C: MEASUREMENT TECHNIQUES

Spreading resistance profiling (SRP) generates a resistivity and, when calibrated against known standards, a dopant profile by stepping two carefully aligned probes along the semiconductor surface and measuring the resistance between the probes at each location. To understand spreading resistance, consider a probe contacting a semiconductor surface: current I flows from the probe with diameter $2r$ into a semiconductor of resistivity ρ ; it is concentrated at the probe tip and spreads out radially from the tip, hence the name spreading resistance. Most of the voltage drop or most of the resistance is near the probe and decreases rapidly away from the probe into the semiconductor. For a nonindenting, cylindrical contact with a planar, circular interface and a highly conductive probe with negligible resistance, the spreading resistance for a semi-infinite sample is $R_{sp} = \rho/4r$. For a hemispherical, indenting probe tip of radius r , the spreading resistance is $R_{sp} = \rho/2\pi r$.

The measured spreading resistance then consists of the contact resistance, the spreading resistance under each contact, and the semiconductor resistance as given by $R_{total} = V/I = 2R_c + 2R_{sp} + R_s$ where R_c is the contact resistance at each metal probe/semiconductor contact (which depends itself on the semiconductor doping concentration), R_{sp} is the spreading resistance under each probe, and R_s is the semiconductor resistance. The spreading resistance measurement method is characterized by the following constraints:

- Specially prepared tungsten-osmium alloy probes are required with an apparatus to reproducibly lower, raise, and step the probes.
- Voltages during the measurement must be kept below kT/q . Typically 5×10^{-3} V are applied since these metal-semiconductor contacts have nonlinear I-V characteristics for applied potentials larger than kT/q .
- Sample preparation is not trivial, and the measurement is destructive.
- Since it is a comparative technique, the probe setup and the measured spreading resistances must be meticulously calibrated against known standards.
- Surface preparation must be absolutely identical and reproducible to generate calibration curves yielding accurate results for a particular set of samples.
- In single probe profiling, the second probe is replaced by a large area base contact. As it permits higher spatial resolution, it is used in scientific investigations; the additional difficulty of obtaining a reproducible base contact for measurements restricts its use to well-behaved systems.

In this investigation, all measurements were performed in single probe configuration, except for base contact evaluation where two probes were used. The instrument used was a SSM 150 Spreading Resistance Probe manufactured and modified for this analysis by Solid State Measurements, Inc.

The probe calibration procedure adopted relies on the fact that the free carrier concentration in the seed material is accurately known, and that the generally accepted value of the equilibrium distribution coefficient $k_0 = 0.087$ for the Ge-Ga system must be applicable in these seeded regrowth experiments in a near zero-g environment. Consequently, a calibration sample containing a seed portion and initial regrowth region yields a calibration algorithm for free carrier concentration applicable to the narrow range encountered in this investigation by a linear fit in $\log N \propto f(\log 1/R_{sp})$ space (fig. 11).

Optical measurements were done with a Union SG-V fab-line micromasurement microscope equipped with a 25 mm \times 25 mm x-y translation stage with a read-out accuracy of 1 μ m for linear coordinate measurements. A built-in circular stage, rotatable through 360° with 0.1° reading accuracy, was employed for precise sample orientation. The instrument was fitted with a reflected light Nomarski differential interference contrast system for observation of the interface demarcation lines made visible by the sample preparation procedure described in appendix B. Although the measurements are nontrivial since the heights of the interface demarcation lines to be observed are in the nanometer range, this optical technique can readily resolve these features.

APPENDIX D: SELECTED PHYSICAL PROPERTIES OF GERMANIUM

Atomic weight		72.59 g/mole
Atoms/cm ³		4.42×10 ²²
Lattice constant (diamond cubic)		5.646 Å
Melting point	T_{mp}	937.4 °C
Vapor pressure (T_{mp})	p_{mp}	9.0×10 ⁻⁷ Torr
Density		
solid	ρ_s	5.327 g/cm ³
liquid	ρ_l	5.48 g/cm ³
Volume thermal expansion coefficient		
solid	β_s	5.9×10 ⁻⁶ /K
liquid	β_l	5.0×10 ⁻⁴ /K
Heat of fusion	ΔH_f	33.39 KJ/mole
Specific heat		
solid	$C_{p(sol)}$	27.58 Ws/mole*K
liquid	$C_{p(liq)}$	25.41 Ws/mole*K
Thermal conductivity		
solid (600 °C)	k_s	0.18 W/cm*K
liquid (1000 °C)	k_l	0.39 W/cm*K
Kinematic viscosity (T_{mp})	ν	1.1×10 ⁻³ St
Emissivity (T_{mp})	ϵ	0.65
Equilibrium distribution coefficient (Ga)	k_0	0.087
Diffusion coefficient of Ga in Ge _{liq}	D_l	2.1×10 ⁻⁴ cm ² /s
Liquidus gradient for Ge-Ga system	m_l	3.4 K/at%
Solubility maximum of Ga in Ge (670 °C)	C_{max}	4.9×10 ²⁰ cm ⁻³

REFERENCES

1. Gatos, H.C.; Lichtensteiger, M.; Herman, C.J.; and Witt, A.F.: *Proceedings*, ESA Conference, 114, 181, 1976.
2. Gatos, H.C.; Lichtensteiger, M.; Herman, C.J.; and Witt, A.F.: NASA SP-412, 429, 1977.
3. Witt, A.F.; Gatos, H.C.; Lichtensteiger, M.; and Herman, C J.: *J. Electrochem. Soc.*, 125, 1832, 1978.
4. Tiller, W.A.; Jackson, K.A.; Rutter, J.W.; and Chalmers, B.: *Acta Met.*, 1, 428, 1953.
5. Coriell, S.R.; and Sekerka, R.F.: *J. Crystal Growth*, 46, 479, 1979.
6. Wang, C.A.; Carruthers, J.R.; and Witt, A.F.: *J. Crystal Growth*, 60, 144, 1982.

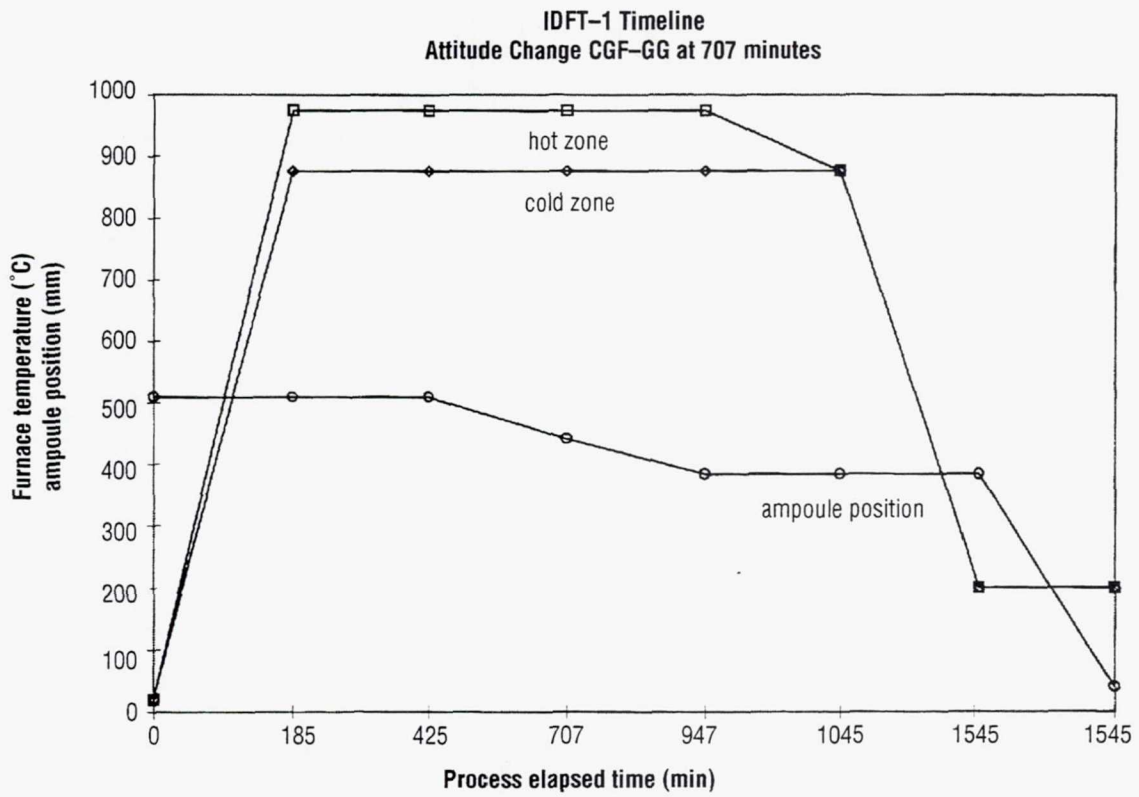


Figure 1. IDFT-1 timeline.

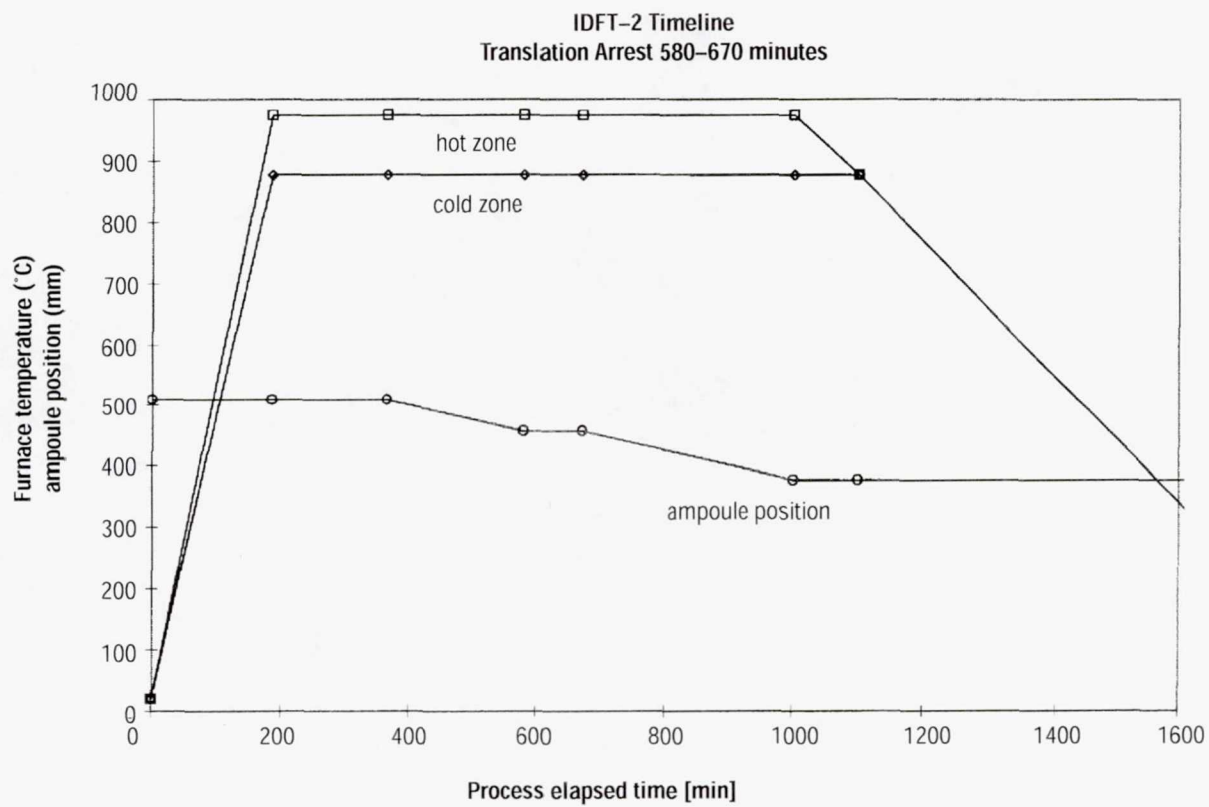


Figure 2. IDFT-2 timeline.

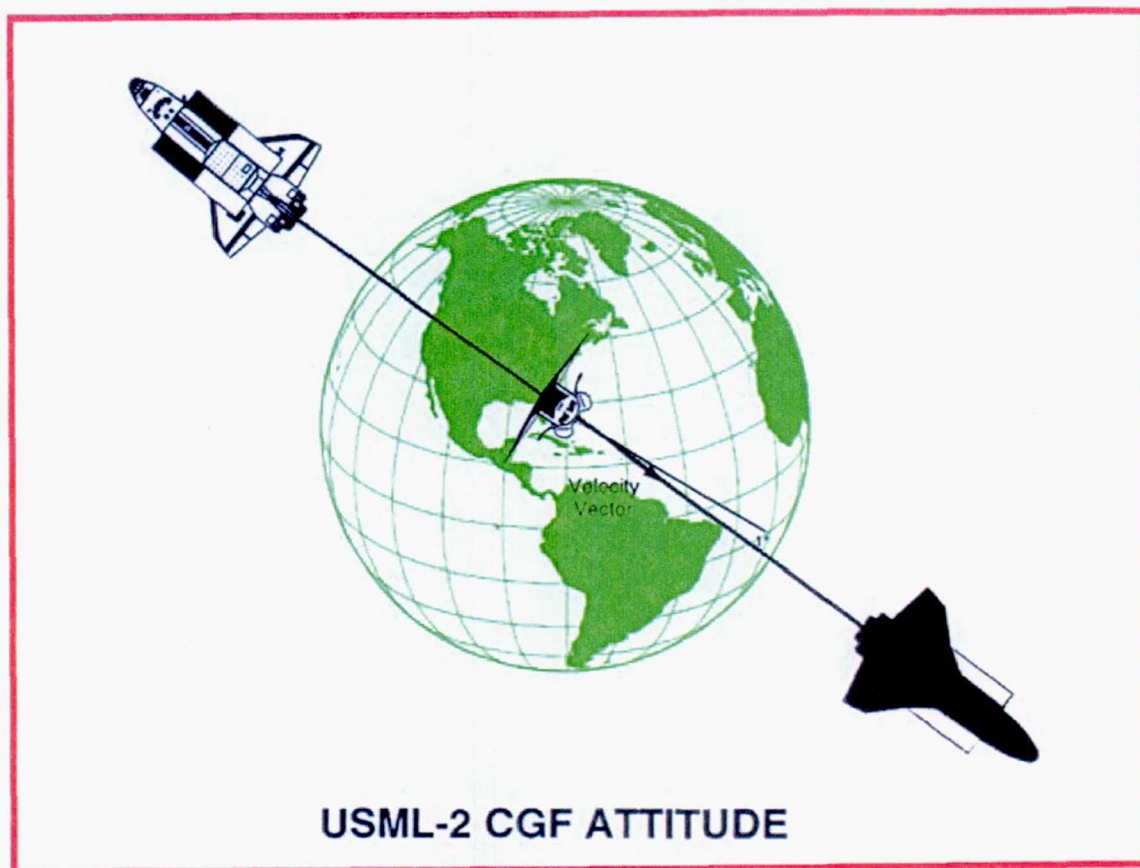


Figure 3. USML-2 CGF attitude.

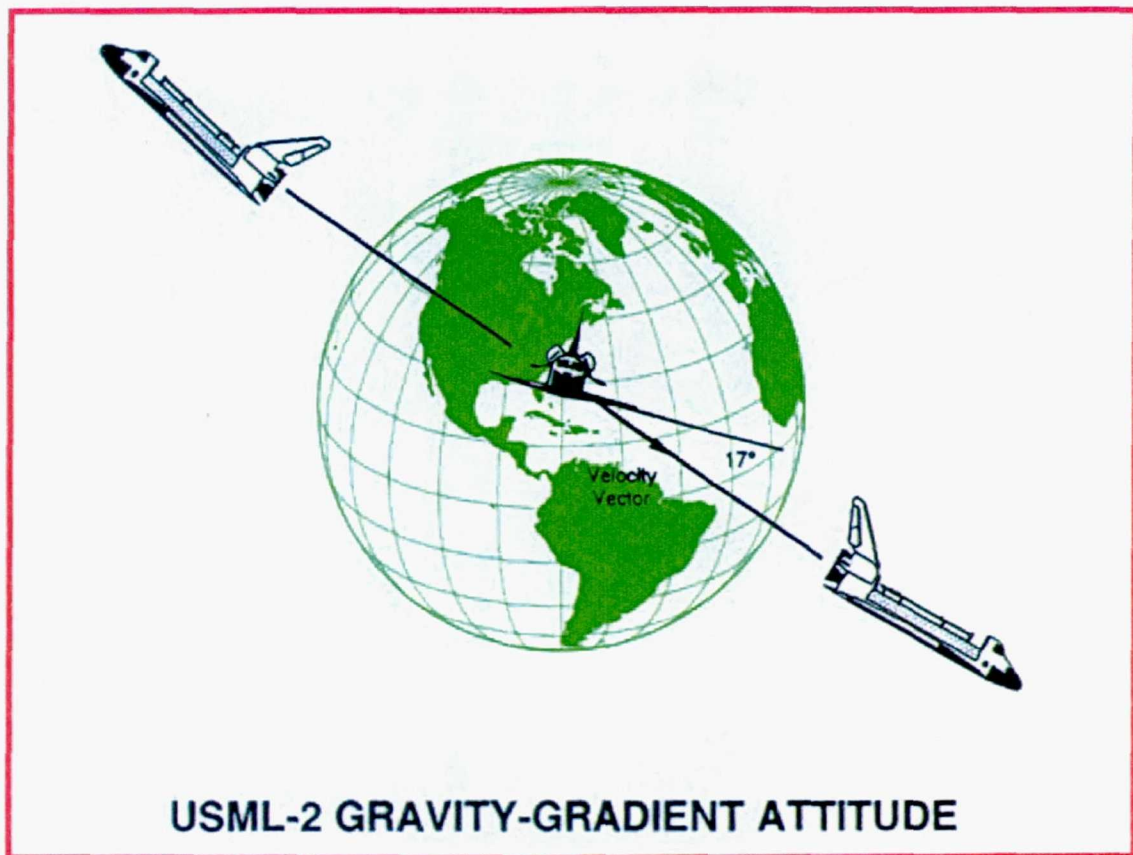


Figure 4. USML-2 gravity-gradient attitude.

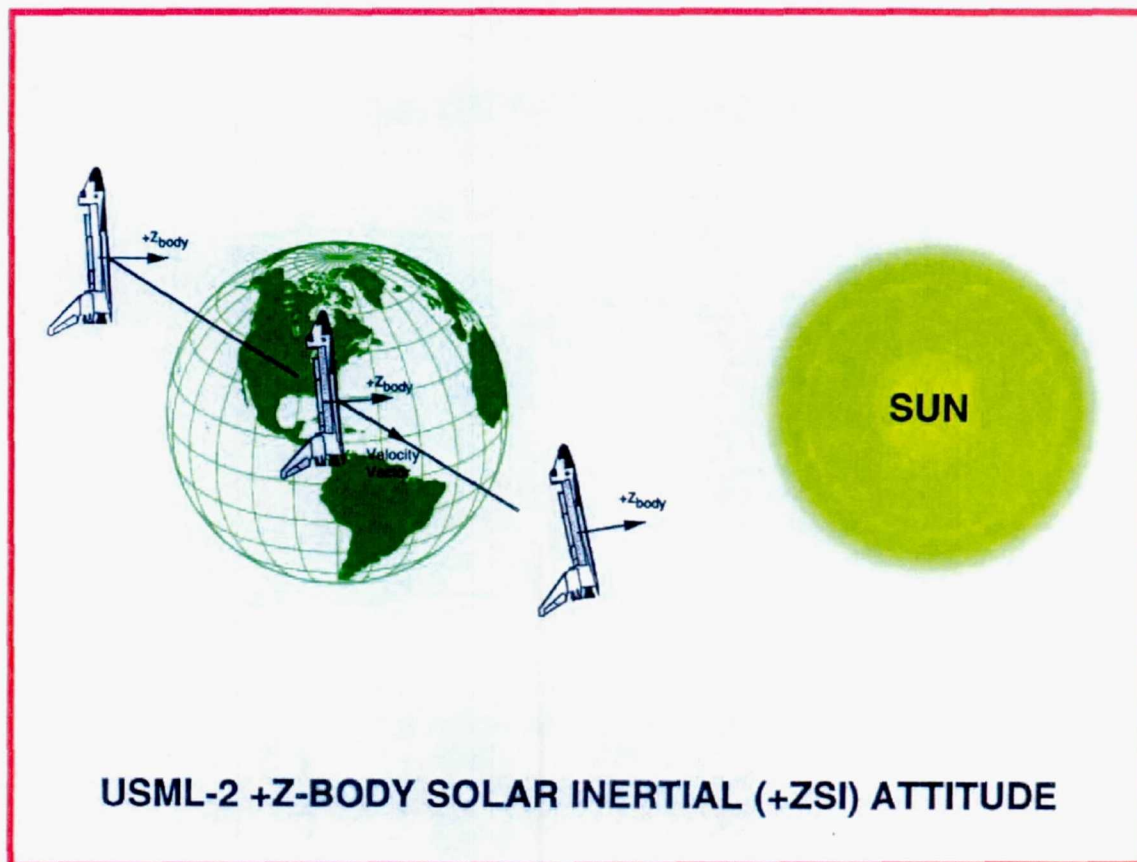


Figure 5. USML-2 +Z-body solar inertial (+ZSI) attitude.

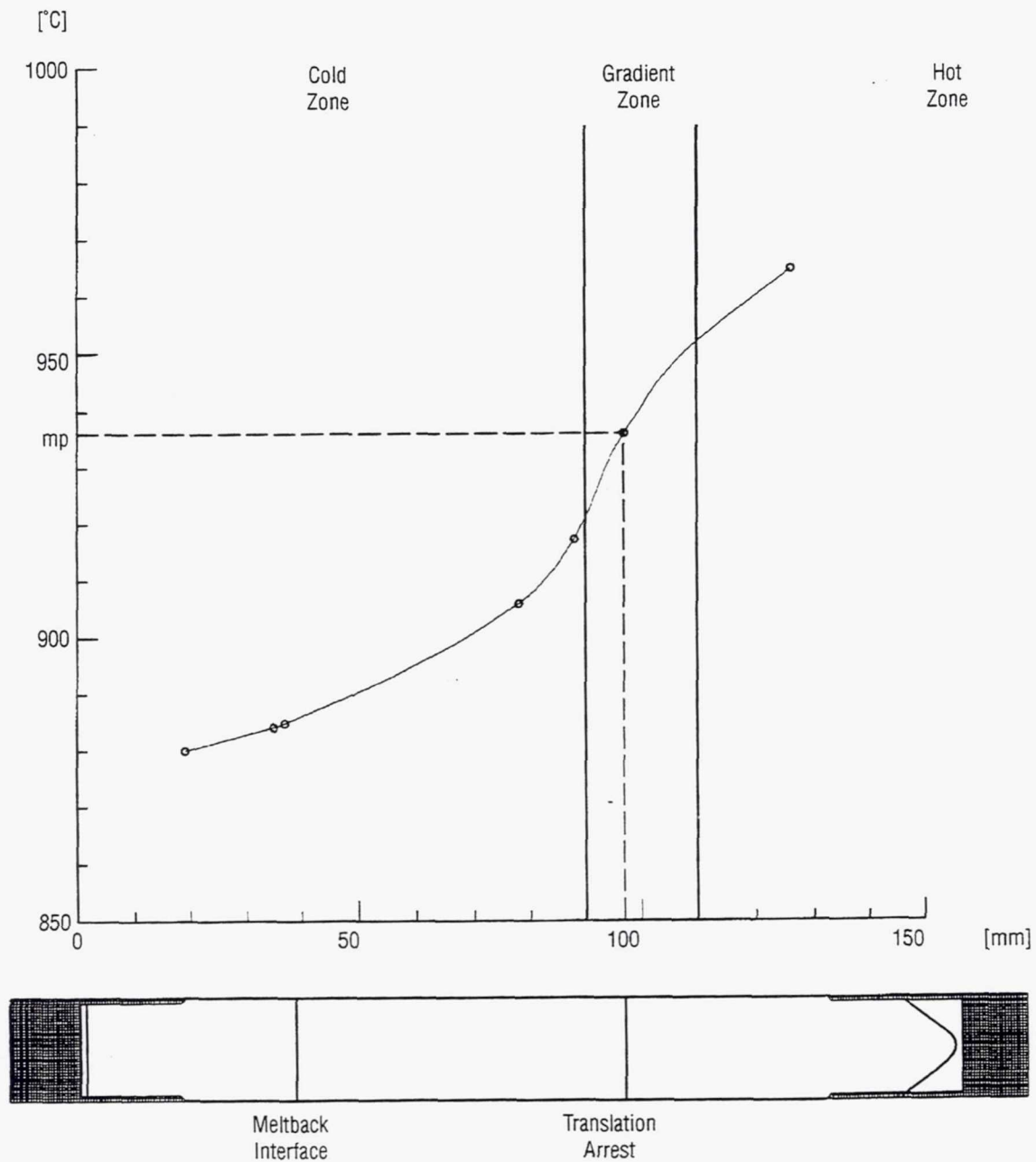


Figure 6. Temperature gradient across solid-melt interface during translation arrest (the open circles represent the location of the six thermocouples).

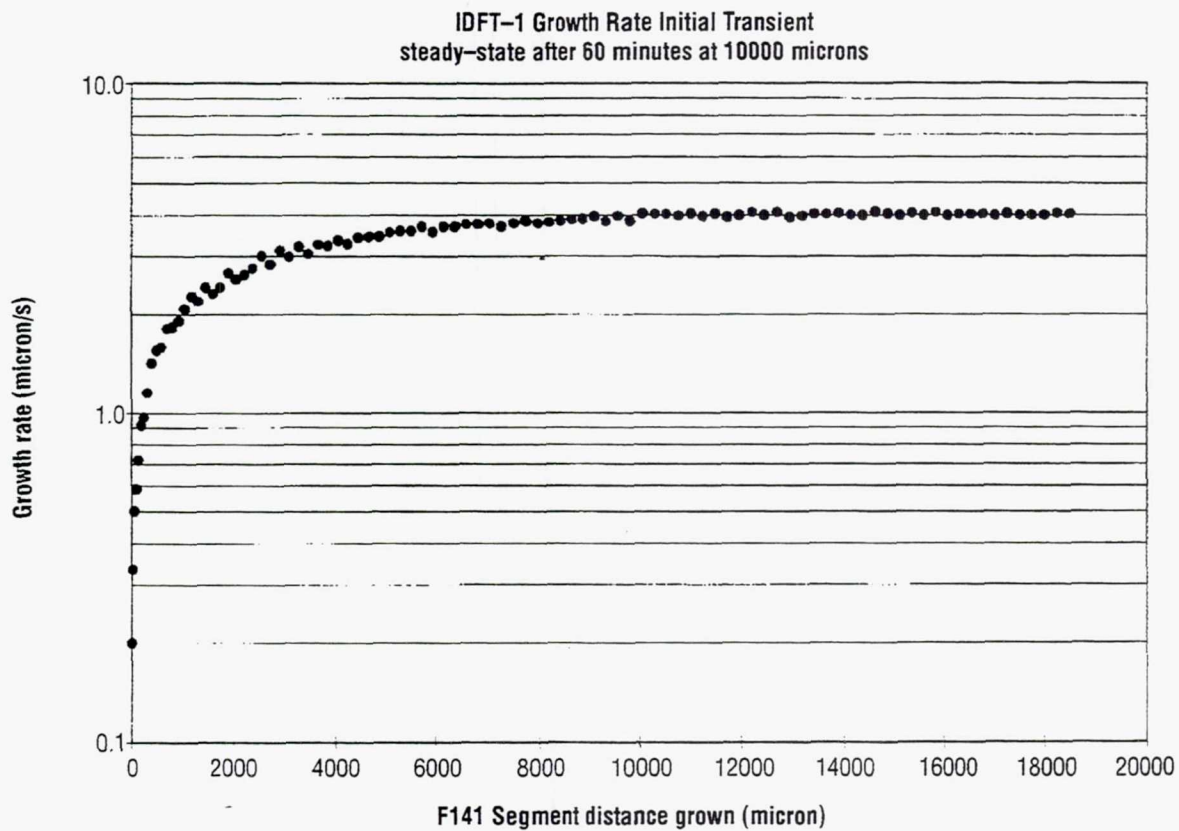


Figure 7. Initial transient growth rate.

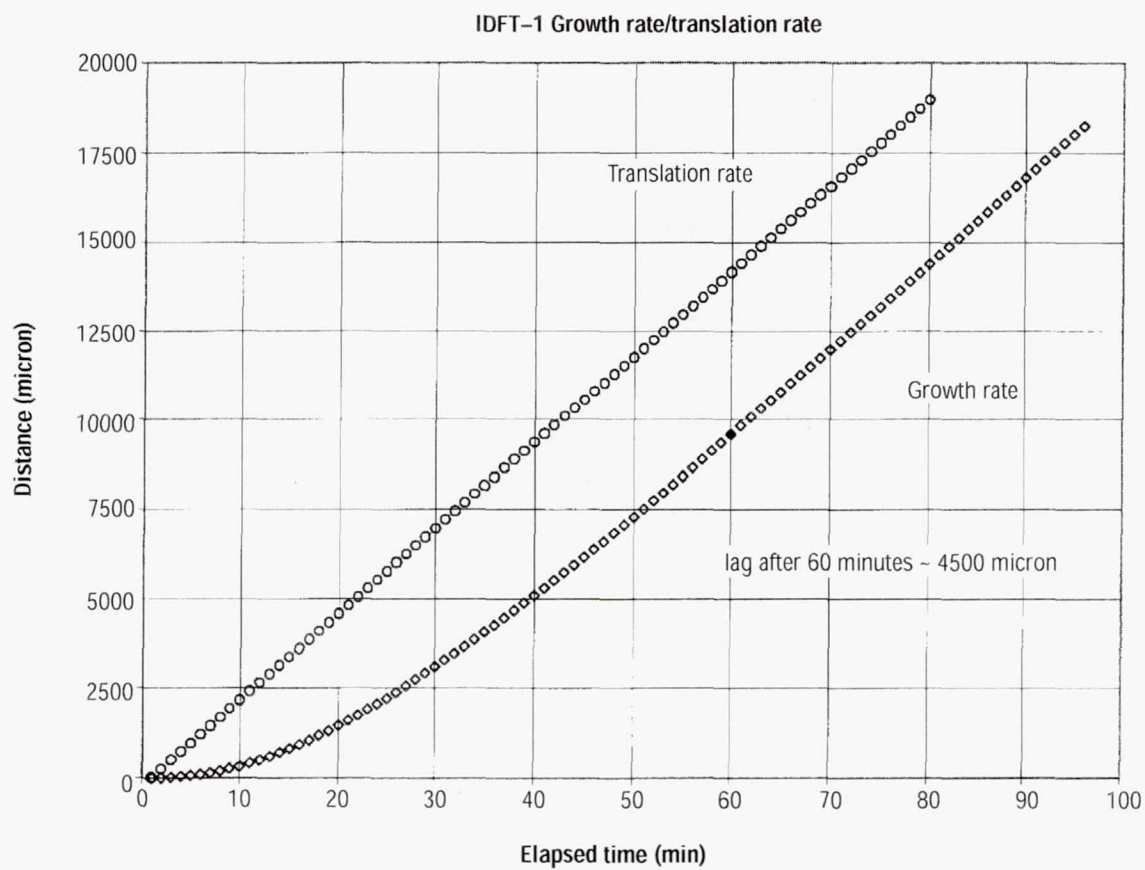


Figure 8. Growth rate lag behind translation rate.

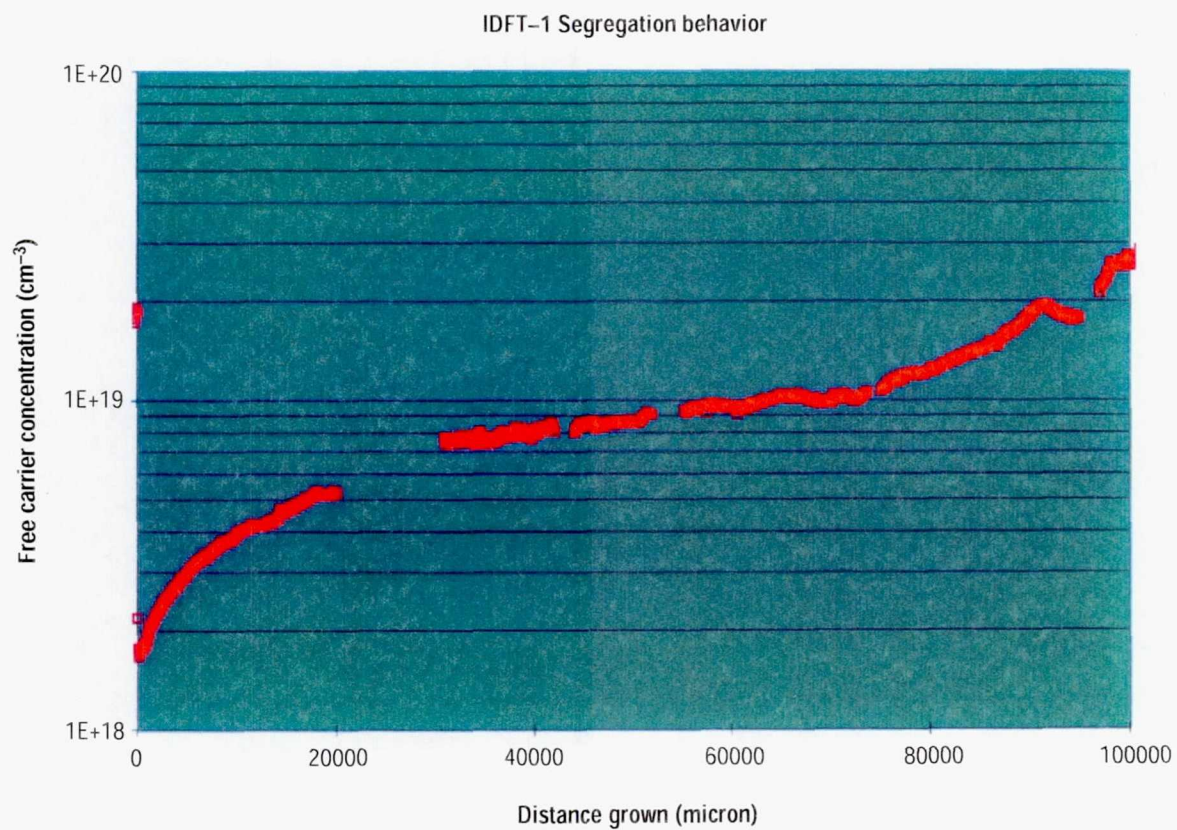


Figure 9. IDFT-1 segregation behavior.

Diffusion Limited Solute Redistribution (Tiller, et al.)
 $k(0)=0.087 \text{ g(t) corrected } D(\text{eff})=3.2 \times 10^{-4} \text{ cm}^2/\text{s}$

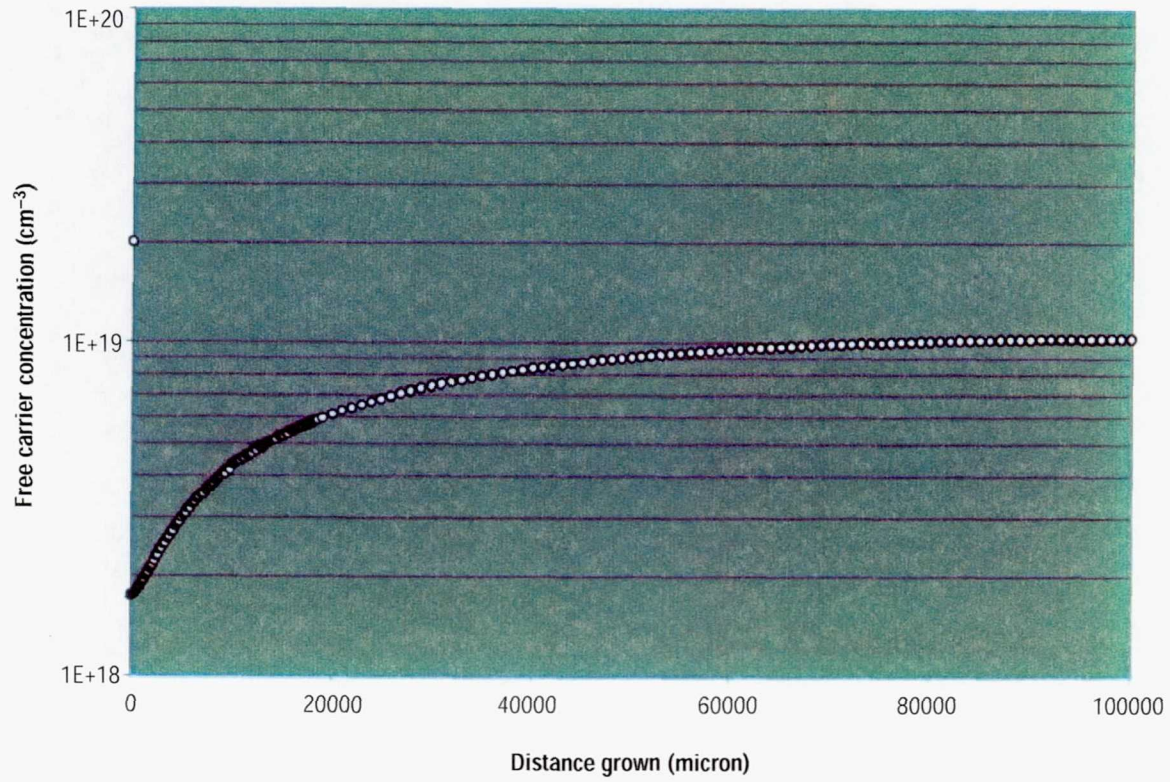


Figure 10. Diffusion limited solute redistribution.

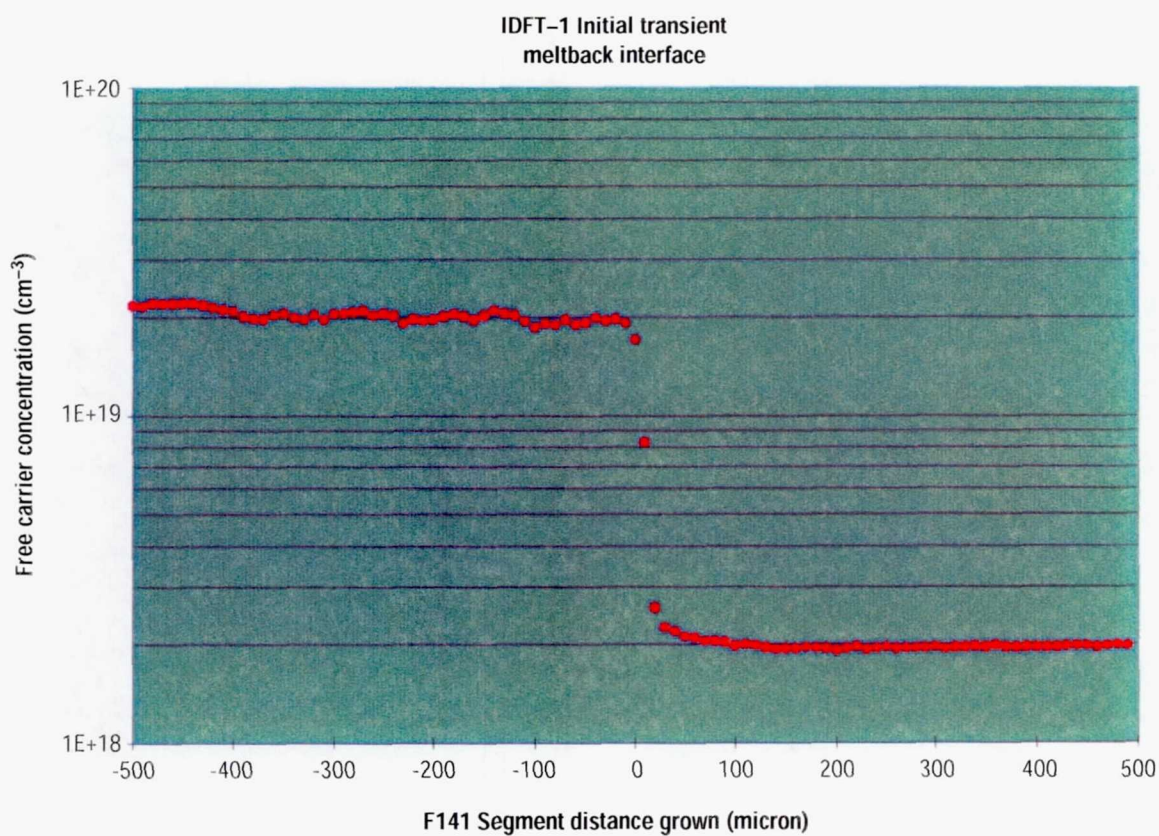


Figure 11. IDFT-1 initial transient microsegregation behavior.

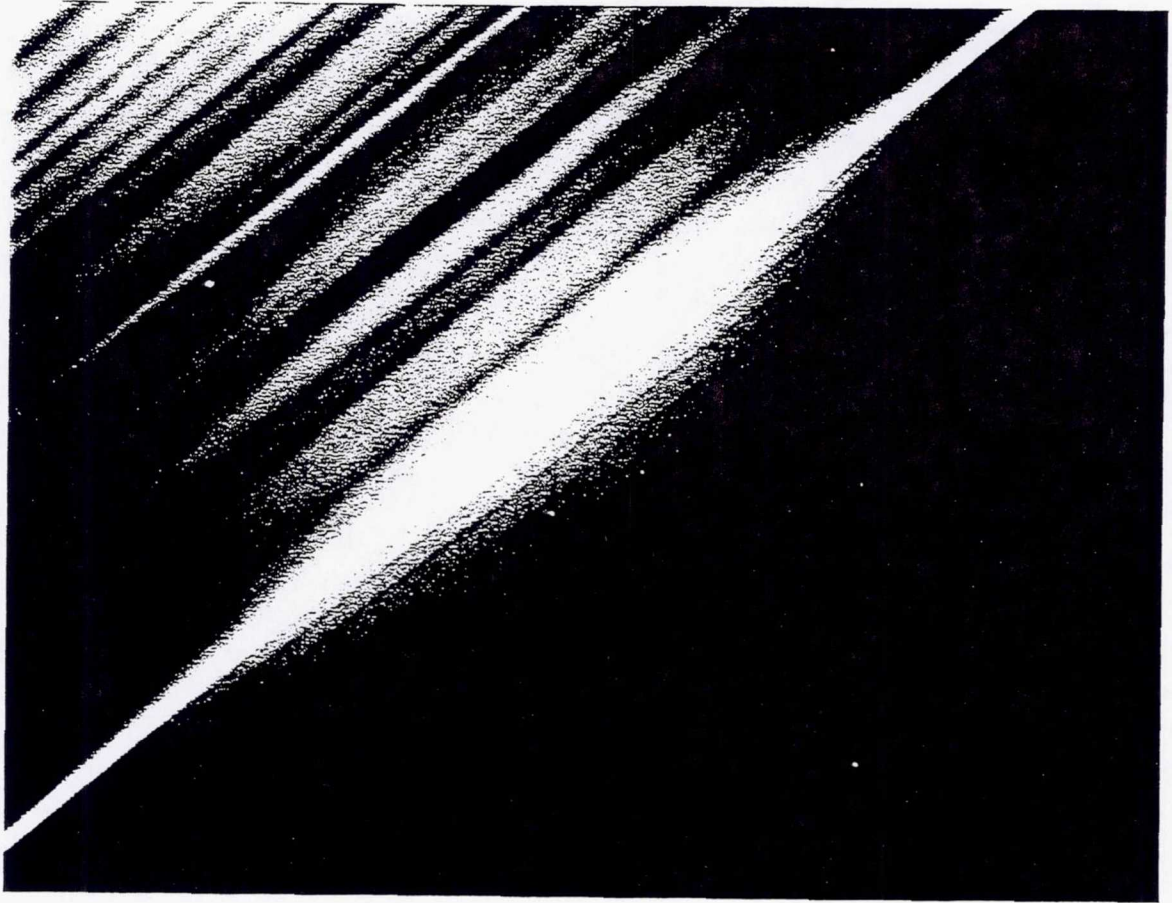


Figure 12. Microphotograph of initial transient (see text for details).

IDFT-1 Interface shape at start of growth

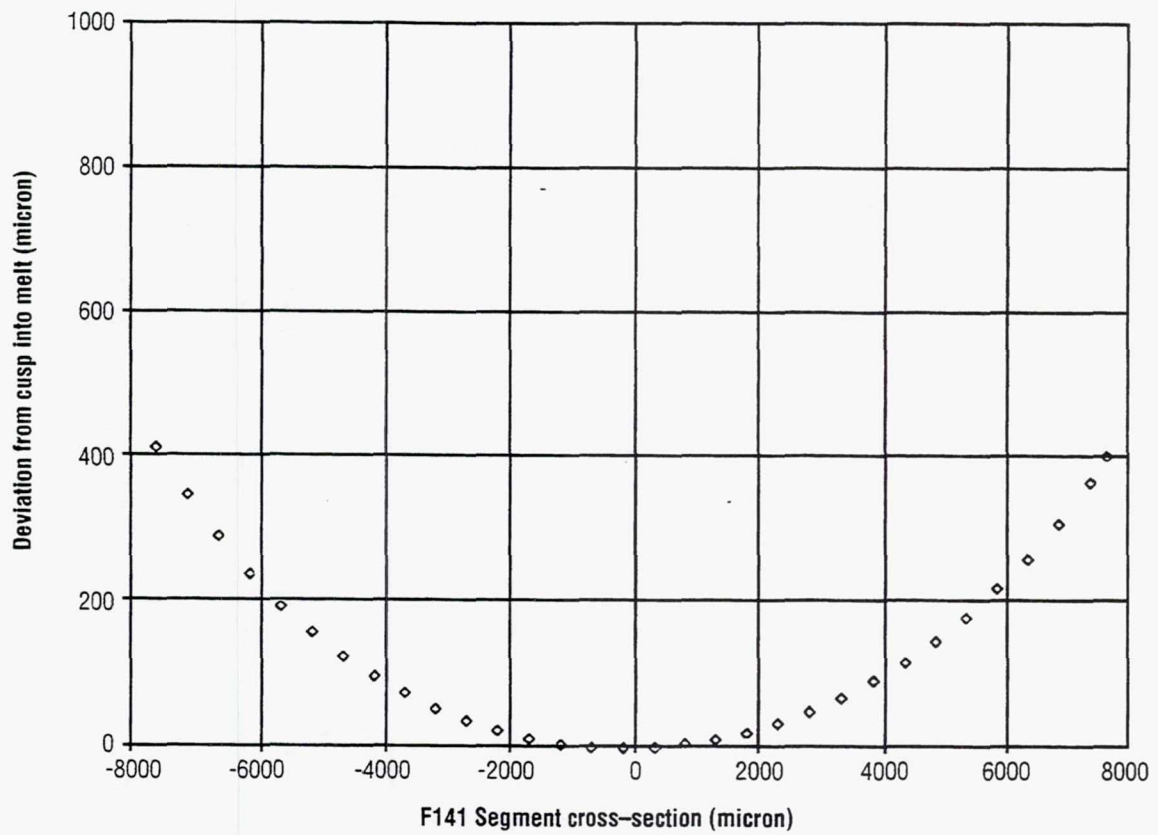


Figure 13. IDFT-1 interface shape at start of growth.

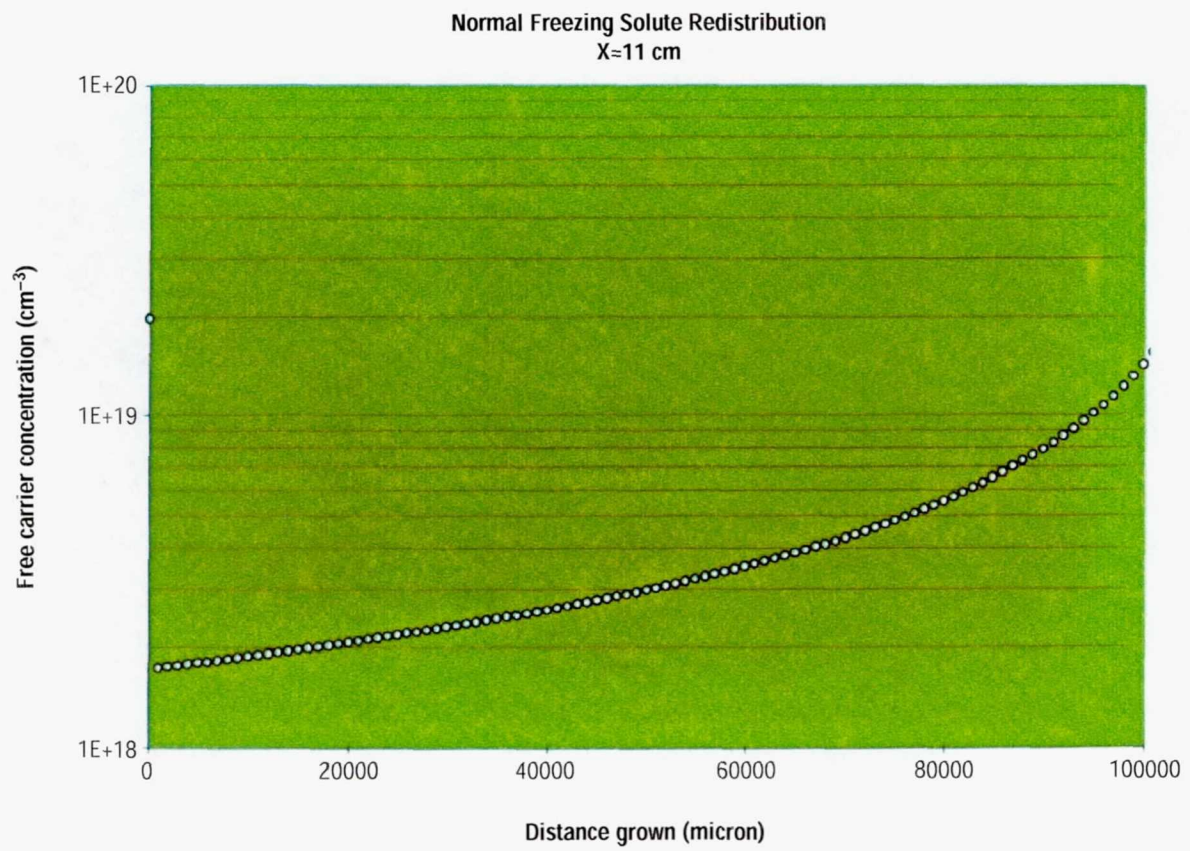


Figure 14. Convective transport solute redistribution.

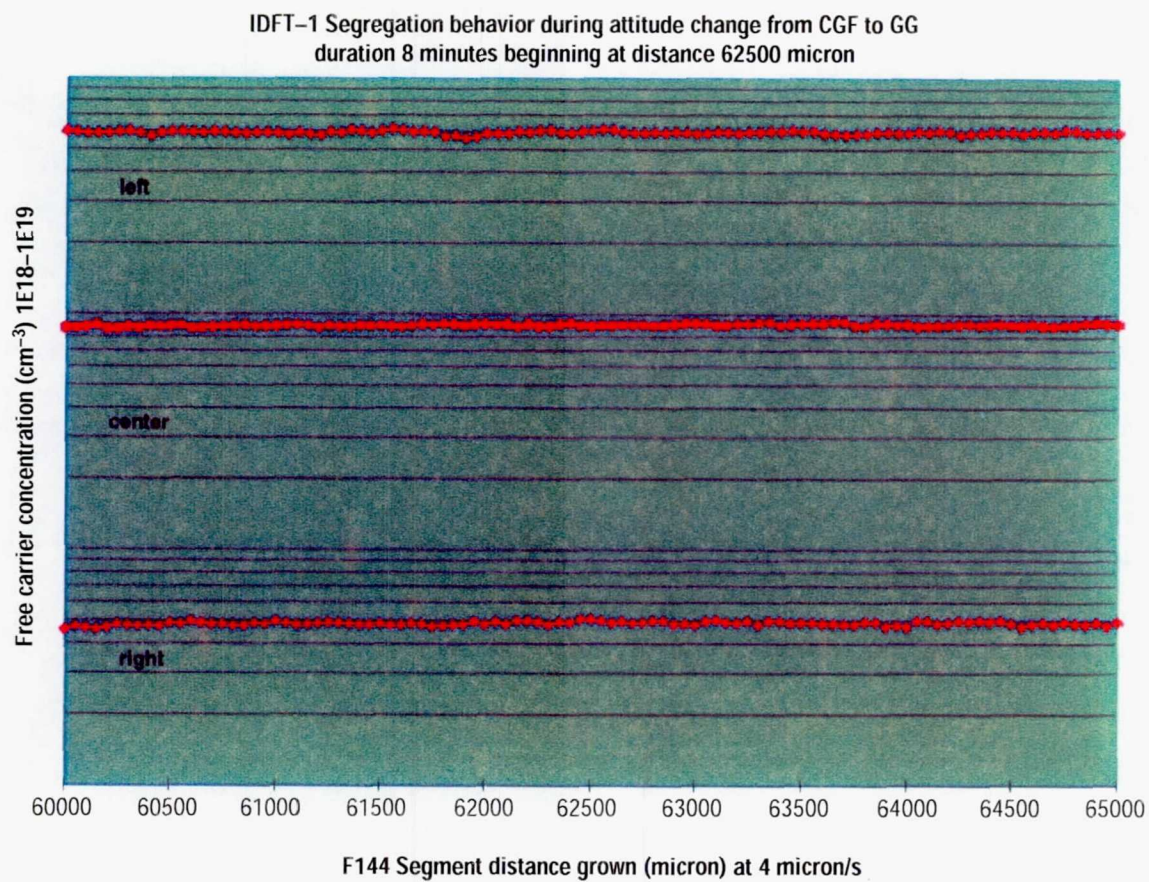


Figure 15. Microsegregation behavior during CGF to GG transition.

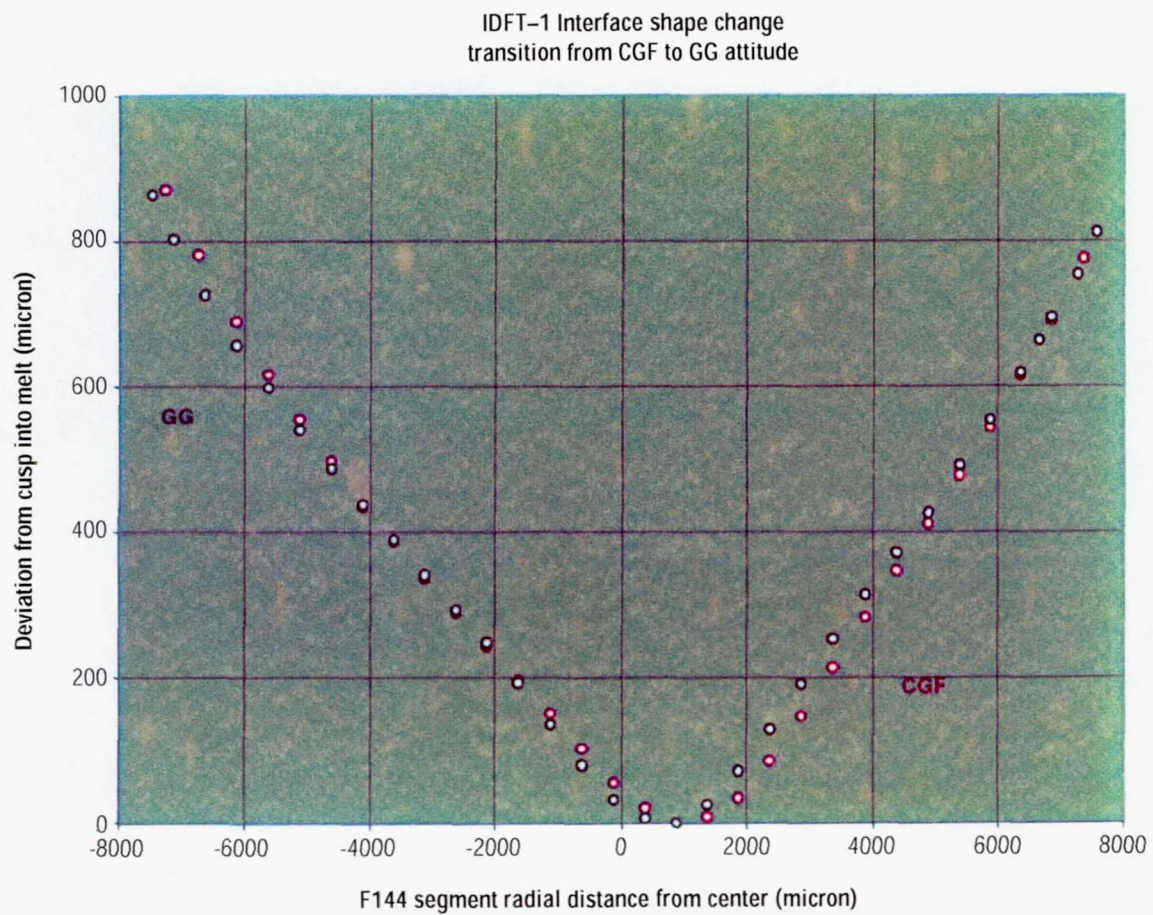


Figure 16. Interface shapes before and after CGF to GG transition.

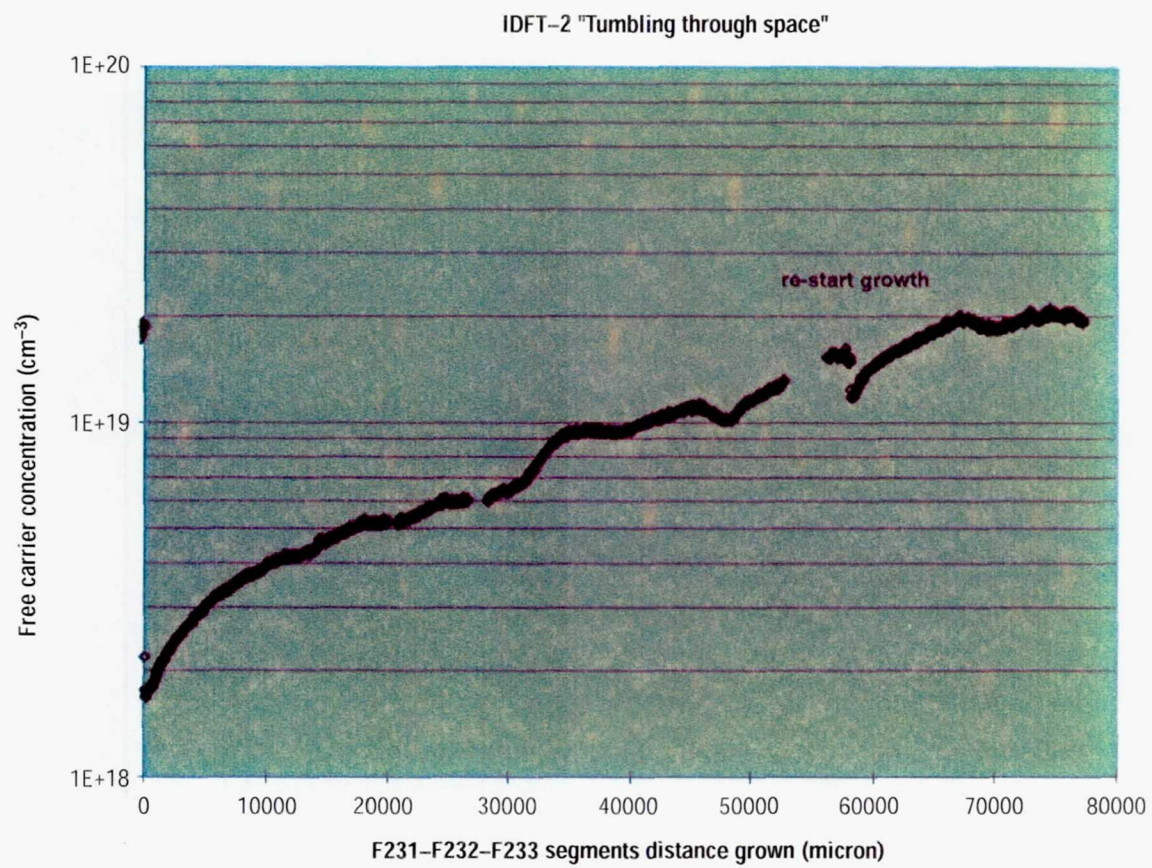


Figure 17. IDFT-2 segregation behavior.

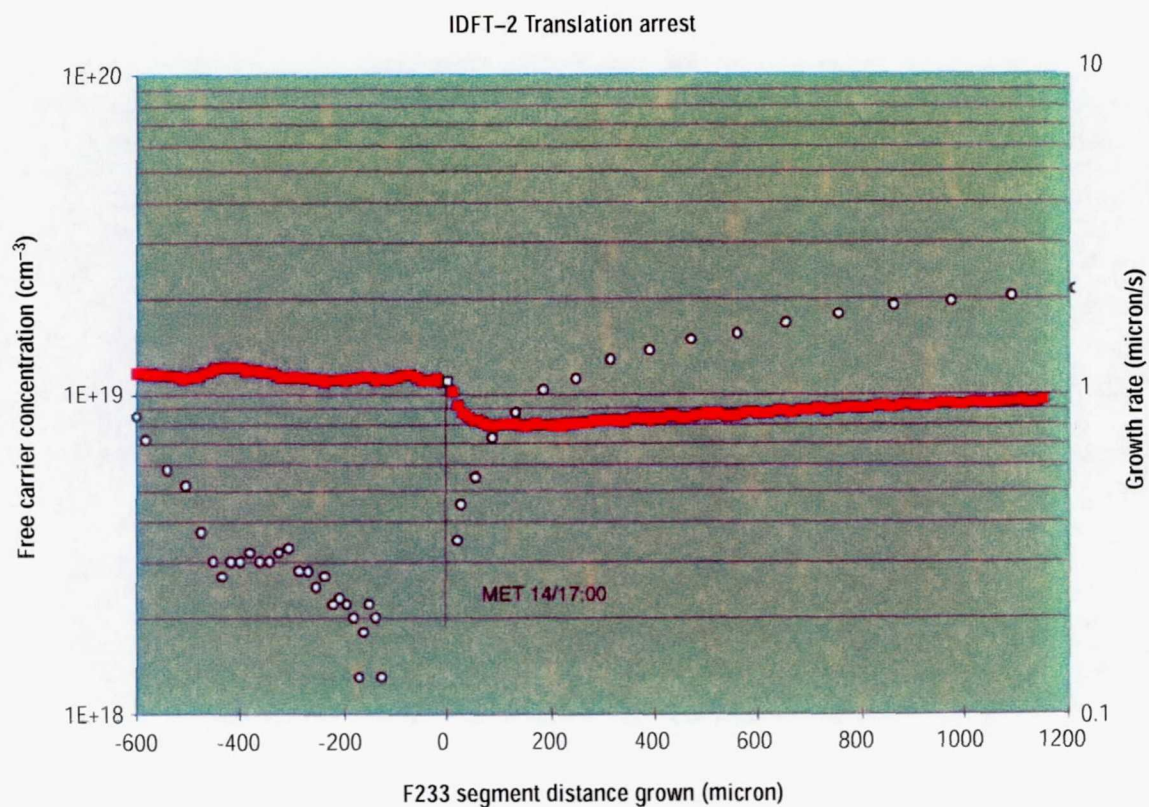


Figure 18. IDFT-2 microsegregation behavior during translation arrest (the open circles represent growth rate data)

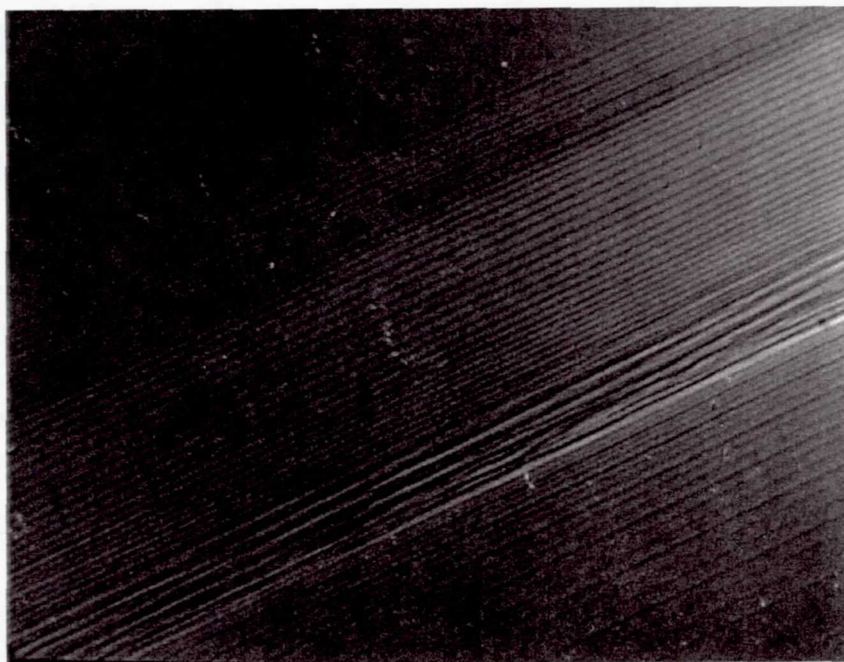


Figure 19. Microphotograph of translation arrest region (see text for details).

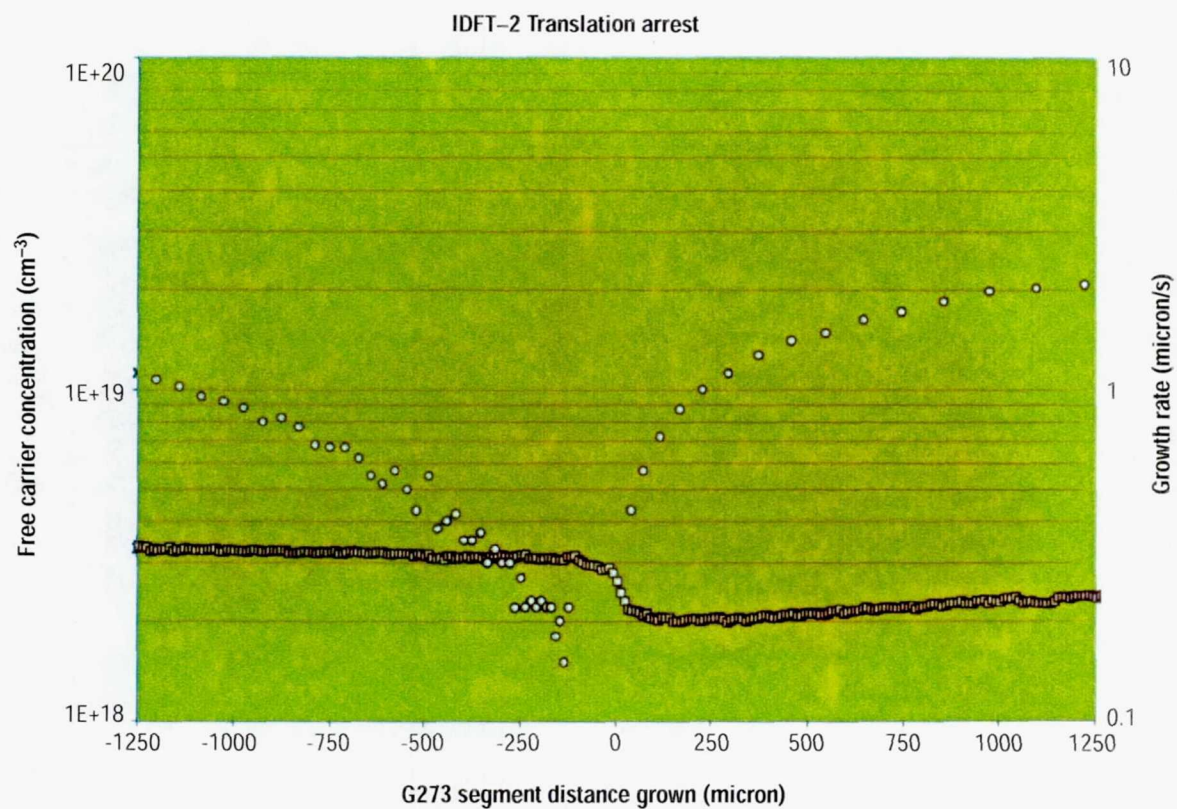


Figure 20. IDFT-2 microsegregation behavior in 1 g environment (the open circles represent growth rate data).



Figure 21. Ampoule assembly, exploded view.

REPORT DOCUMENTATION PAGE

Form Approved
OMB No. 0704-0188

Public reporting burden for this collection of information is estimated to average 1 hour per response, including the time for reviewing instructions, searching existing data sources, gathering and maintaining the data needed, and completing and reviewing the collection of information. Send comments regarding this burden estimate or any other aspect of this collection of information, including suggestions for reducing this burden, to Washington Headquarters Services, Directorate for Information Operation and Reports, 1215 Jefferson Davis Highway, Suite 1204, Arlington, VA 22202-4302, and to the Office of Management and Budget, Paperwork Reduction Project (0704-0188), Washington, DC 20503

1. AGENCY USE ONLY (Leave Blank)		2. REPORT DATE August 1998	3. REPORT TYPE AND DATES COVERED Technical Memorandum	
4. TITLE AND SUBTITLE Second United States Microgravity Laboratory: One Year Report, Volume 1			5. FUNDING NUMBERS	
6. AUTHORS M. Vlasse, D. McCauley,* and C. Walker**				
7. PERFORMING ORGANIZATION NAMES(S) AND ADDRESS(ES) George C. Marshall Space Flight Center Marshall Space Flight Center, Alabama 35812			8. PERFORMING ORGANIZATION REPORT NUMBER M-892	
9. SPONSORING/MONITORING AGENCY NAME(S) AND ADDRESS(ES) National Aeronautics and Space Administration Washington, DC 20546-0001			10. SPONSORING/MONITORING AGENCY REPORT NUMBER NASA/TM-1998-208697	
11. SUPPLEMENTARY NOTES The science reports are the culmination of research performed by the investigators in the period following the return of the 15-day USML-2 Space Shuttle mission. Prepared for Space Sciences Laboratory, Science and Engineering Directorate. * UAH ** USRA				
12a. DISTRIBUTION/AVAILABILITY STATEMENT Unclassified-Unlimited Subject Category 88 Standard Distribution			12b. DISTRIBUTION CODE	
13. ABSTRACT (Maximum 200 words) This document reports the one year science results for the important and highly successful Second United States Microgravity Laboratory (USML-2). The USML-2 mission consisted of a pressurized Spacelab module where the crew performed experiments. The mission also included a Glovebox where the crew performed additional experiments for the investigators. Together, about 36 major scientific experiments were performed, advancing the state of knowledge in fields such as fluid physics, solidification of metals, alloys, and semiconductors, combustion, and the growth of protein crystals. The results demonstrate the range of quality science that can be conducted utilizing orbital laboratories in microgravity and provide a look forward to a highly productive Space Station era.				
14. SUBJECT TERMS USML-2, Spacelab, microgravity research, materials science, protein crystal growth, fluid dynamics, drop dynamics, biotechnology, combustion			15. NUMBER OF PAGES 416	
			16. PRICE CODE A18	
17. SECURITY CLASSIFICATION OF REPORT Unclassified	18. SECURITY CLASSIFICATION OF THIS PAGE Unclassified	19. SECURITY CLASSIFICATION OF ABSTRACT Unclassified	20. LIMITATION OF ABSTRACT Unlimited	